Research Topics

Technological innovations in cardiovascular medicine: imaging, nanotechnology, tissue regeneration, genetic engineering, deep learning and beyond

Edited by
Yun Fang, Eun Ji Chung, James Dahlman, Princess Imoukhuede,
Kuei-Chun Wang and David Wu

Published in
Frontiers in Cardiovascular Medicine

ISSN 1664-8714
ISBN 978-2-83250-906-7
DOI 10.3389/978-2-83250-906-7

About Frontiers

Frontiers is more than just an open access publisher of scholarly articles: it is a pioneering approach to the world of academia, radically improving the way scholarly research is managed. The grand vision of Frontiers is a world where all people have an equal opportunity to seek, share and generate knowledge. Frontiers provides immediate and permanent online open access to all its publications, but this alone is not enough to realize our grand goals.

Frontiers journal series

The Frontiers journal series is a multi-tier and interdisciplinary set of open-access, online journals, promising a paradigm shift from the current review, selection and dissemination processes in academic publishing. All Frontiers journals are driven by researchers for researchers; therefore, they constitute a service to the scholarly community. At the same time, the *Frontiers journal series* operates on a revolutionary invention, the tiered publishing system, initially addressing specific communities of scholars, and gradually climbing up to broader public understanding, thus serving the interests of the lay society, too.

Dedication to quality

Each Frontiers article is a landmark of the highest quality, thanks to genuinely collaborative interactions between authors and review editors, who include some of the world's best academicians. Research must be certified by peers before entering a stream of knowledge that may eventually reach the public - and shape society; therefore, Frontiers only applies the most rigorous and unbiased reviews. Frontiers revolutionizes research publishing by freely delivering the most outstanding research, evaluated with no bias from both the academic and social point of view. By applying the most advanced information technologies, Frontiers is catapulting scholarly publishing into a new generation.

What are Frontiers Research Topics?

Frontiers Research Topics are very popular trademarks of the *Frontiers journals series*: they are collections of at least ten articles, all centered on a particular subject. With their unique mix of varied contributions from Original Research to Review Articles, Frontiers Research Topics unify the most influential researchers, the latest key findings and historical advances in a hot research area.

Find out more on how to host your own Frontiers Research Topic or contribute to one as an author by contacting the Frontiers editorial office: frontiersin.org/about/contact

Technological innovations in cardiovascular medicine: imaging, nanotechnology, tissue regeneration, genetic engineering, deep learning and beyond

Topic editors
Yun Fang — The University of Chicago, United States
Eun Ji Chung — University of Southern California, United States
James Dahlman — Georgia Institute of Technology, United States
Princess Imoukhuede — Washington University in St. Louis, United States
Kuei-Chun Wang — Arizona State University, United States
David Wu — The University of Chicago, United States

Citation
Fang, Y., Chung, E. J., Dahlman, J., Imoukhuede, P., Wang, K.-C., Wu, D., eds. (2022). *Technological innovations in cardiovascular medicine: imaging, nanotechnology, tissue regeneration, genetic engineering, deep learning and beyond*. Lausanne: Frontiers Media SA. doi: 10.3389/978-2-83250-906-7

Table of contents

frontiers
in Cardiovascular Medicine

ORIGINAL RESEARCH
published: 23 October 2020
doi: 10.3389/fcvm.2020.586871

Predicting Diagnostic Gene Biomarkers Associated With Immune Infiltration in Patients With Acute Myocardial Infarction

*Enfa Zhao†, Hang Xie† and Yushun Zhang**

Department of Structural Heart Disease, The First Affiliated Hospital of Xi'an Jiaotong University, Xi'an, China

Objective: The present study was designed to identify potential diagnostic markers for acute myocardial infarction (AMI) and determine the significance of immune cell infiltration in this pathology.

Methods: Two publicly available gene expression profiles (GSE66360 and GSE48060 datasets) from human AMI and control samples were downloaded from the GEO database. Differentially expressed genes (DEGs) were screened between 80 AMI and 71 control samples. The LASSO regression model and support vector machine recursive feature elimination (SVM-RFE) analysis were performed to identify candidate biomarkers. The area under the receiver operating characteristic curve (AUC) value was obtained and used to evaluate discriminatory ability. The expression level and diagnostic value of the biomarkers in AMI were further validated in the GSE60993 dataset (17 AMI patients and 7 controls). The compositional patterns of the 22 types of immune cell fraction in AMI were estimated based on the merged cohorts using CIBERSORT.

Results: A total of 27 genes were identified. The identified DEGs were mainly involved in carbohydrate binding, Kawasaki disease, atherosclerosis, and arteriosclerotic cardiovascular disease. Gene sets related to atherosclerosis signaling, primary immunodeficiency, IL-17, and TNF signaling pathways were differentially activated in AMI compared with the control. IL1R2, IRAK3, and THBD were identified as diagnostic markers of AMI ($AUC = 0.877$) and validated in the GSE60993 dataset ($AUC = 0.941$). Immune cell infiltration analysis revealed that IL1R2, IRAK3, and THBD were correlated with M2 macrophages, neutrophils, monocytes, $CD4^+$ resting memory T cells, activated natural killer (NK) cells, and gamma delta T cells.

Conclusion: IL1R2, IRAK3, and THBD can be used as diagnostic markers of AMI, and can provide new insights for future studies on the occurrence and the molecular mechanisms of AMI.

Keywords: acute myocardial infarction, immune infiltration, diagnostic, biomarker, CIBERSORT

OPEN ACCESS

Edited by:
Yun Fang,
University of Chicago, United States

Reviewed by:
Marcin Wysoczynski,
University of Louisville, United States
Salvatore De Rosa,
University of Catanzaro, Italy

****Correspondence:***
Yushun Zhang
zys2889@sina.com

†These authors have contributed equally to this work and share first authorship

Specialty section:
This article was submitted to Atherosclerosis and Vascular Medicine, a section of the journal Frontiers in Cardiovascular Medicine

Received: *24 July 2020*
Accepted: *16 September 2020*
Published: *23 October 2020*

Citation:
Zhao E, Xie H and Zhang Y (2020) Predicting Diagnostic Gene Biomarkers Associated With Immune Infiltration in Patients With Acute Myocardial Infarction. Front. Cardiovasc. Med. 7:586871. doi: 10.3389/fcvm.2020.586871

INTRODUCTION

Acute myocardial infarction (AMI) is a common event in coronary heart disease that results from interrupted blood flow to a certain area of the heart. It is considered one of the primary causes of disability and death from cardiovascular disease worldwide, and is a leading health threat in humans (1). AMI remains the primary cause of morbidity and mortality worldwide, with ∼7 million patients diagnosed with AMI each year (2, 3). AMI continues to be the primary cause of death in 2020. Approximately half of patients who suffer from cardiovascular diseases die from AMI (4). The rapid and accurate diagnosis of AMI is the first step to improve the clinical management and survival rate of AMI patients. A spectrum of biochemical markers have been related to the incidence of AMI and are widely used for the clinical diagnosis of AMI including the MB isoenzyme of creatine kinase (CK-MB), lactate dehydrogenase (LDH), cardiac myoglobin, and cardiac troponin I (cTnI) and T (cTnT) (5, 6). However, they are insufficient for the early detection of AMI because of limitations in sensitivity and specificity (7). Furthermore, the well-known risk factors for AMI, such as a history of smoking, obesity, high serum cholesterol, bad eating habits, diabetes, and hypertension, can only predict AMI prevention and outcomes and fall to adequately provide an acute diagnosis (8). These results demonstrate that genetic factors also play a vital role in the pathogenesis of AMI. In fact, AMI is a complex and multifactorial disease that occurs as a result of the interaction between genetic and environmental factors (9).

In recent years, microarray technology, together with integrated bioinformatics analysis, has been performed to identify novel genes related to various diseases that might act as diagnostic and prognostic biological markers (10–14). For example, the expression of FFAR2, also known as GPR43, in AMI patients has been found to be notably lower than in the controls, and low levels of FFAR2 expression in peripheral blood was confirmed as an independent risk predictor for AMI, with an odds ratio of 6.308 (15). The upregulation of the suppressor of cytokine signaling 3 (SOCS3) gene increases the risk of AMI by potentiating inflammatory responses (16). Moreover, research has shown that immune cell infiltration plays an increasingly significant role in the occurrence and development of various diseases (11, 17–19). With regards to AMI, mast cells, M2 macrophages, and eosinophils have been demonstrated to affect cardiac function after AMI, providing novel insights into the significance of immune modulation in the infarcted heart (20). However, to date, few studies have applied CIBERSORT to explore immune cell infiltration in AMI and investigate candidate diagnostic markers for AMI.

In this study, we downloaded two microarray datasets of AMI from the GEO database. The two datasets were merged into a meta-data cohort. Differentially expressed gene (DEG) analysis was performed between the AMI and controls. Machine-learning algorithms were used to filter and identify diagnostic biomarkers of AMI. Candidate genes strongly related to immune infiltration were identified and validated in another validation cohort and were used to construct the diagnostic prediction model using a logistic regression method. In this study, CIBERSORT was used for the first time to quantify the proportions of immune cells in samples of AMI and normal tissues based on their gene expression profiling. Furthermore, we explored the relationship between the identified biomarkers and infiltrating immune cells to provide a basis for further research.

MATERIALS AND METHODS

Microarray Data

The series of matrix files of the GSE48060 and GSE66360 datasets were obtained from http://www.ncbi.nlm.nih.gov/geo/, which were both based on the GPL570 platform of Affymetrix Human Genome U133 Plus 2.0 Array. The GSE48060 dataset included 49 AMI and 50 controls collected from circulating endothelial cells, whereas the GSE66360 dataset included 31 AMI and 21 controls collected from the peripheral blood. The probes in each dataset were changed into gene symbols based on their probe annotation files. For more than one probe corresponding to the same gene symbol, the probe average was calculated as the final expression value of the gene. These two datasets were merged into a metadata cohort for further integration analysis because they have the same platform and are significant for combining data from different datasets. Furthermore, the combat function of the "SVA" package of R software was applied to remove the batch effect (21). In addition, the GSE60993 dataset, collected from peripheral blood and containing 17 AMI and 7 control samples, was used as the validation cohort using the Illumina HumanWG-6 v3.0 expression beadchip.

Data Processing and DEG Screening

The two datasets were merged into a metadata cohort and the combat function of the SVA package was used to preprocess and remove batch effects. The limma package of R (http://www.bioconductor.org/) was used for background correction, normalization between arrays, and differential expression analysis between 80 AMI and 71 control samples. Samples with an adjusted false discovery rate $P < 0.05$ and $|\log$ fold change $(FC)| > 1.2$ were considered as the threshold points for DEGs.

Functional Enrichment Analysis

Disease ontology (DO) enrichment analyses were performed on DEGs using the "clusterProfiler" and DOSE packages in R (22, 23). Gene set enrichment analysis (GSEA) was used to identify the most significant functional terms between the AMI and control groups. The "c2.cp.kegg.v7.0.symbols.gmt" from the Molecular Signatures Database (MSigDB) was used as the reference gene set. A gene set was regarded as significantly enriched if a $P < 0.05$ and false discovery rate <0.025.

Candidate Diagnostic Biomarker Screening

To identify significant prognostic variables, two machine-learning algorithms were used to predict disease status. The least absolute shrinkage and selection operator (LASSO) is a regression analysis algorithm that uses regularization to improve the prediction accuracy. The LASSO regression algorithm was carried out using the "glmnet" package in R to identify the genes significantly associated with the discrimination of AMI and normal samples. Support vector machine (SVM) is a supervised machine-learning technique widely utilized for both classification and regression. To avoid overfitting, an RFE algorithm was employed to select the optimal genes from the meta-data cohort (24). Therefore, to identify the set of genes with the highest discriminative power, support vector machine recursive feature elimination (SVM-RFE) was applied to select the appropriate features. The overlapping genes between the two algorithms were included and the expression levels of candidate genes were further validated in the GSE60993 dataset.

Diagnostic Value of Feature Biomarkers in AMI

To test the predictive value of the identified biomarkers, we generated an ROC curve using the mRNA expression data from 80 AMI and 71 control samples. The area under the ROC curve (AUC) value was utilized to determine the diagnostic effectiveness in discriminating AMI from control samples and further validated in the GSE60993 dataset.

Discovery of Immune Cell Subtypes

To quantify the relative proportions of infiltrating immune cells from the gene expression profiles in AMI, a bioinformatics algorithm called CIBERSORT (https://cibersortx.stanford.edu/) was used to calculate immune cell infiltrations. The putative abundance of immune cells was estimated using a reference set with 22 types of immune cell subtypes (LM22) with 1,000 permutations (25). Correlation analysis and visualization of 22 types of infiltrating immune cells were performed using the R package "corrplot." Violin plots were drawn using the "vioplot" package in R to visualize the differences in immune cell infiltration between the AMI and control samples.

Correlation Analysis Between Identified Genes and Infiltrating Immune Cells

The association of the identified gene biomarkers with the levels of infiltrating immune cells was explored using Spearman's rank correlation analysis in R software. The resulting associations were visualized using the chart technique with "ggplot2" package.

Statistical Analysis

All statistical analyses were conducted using R (version 3.6.3). Group comparisons were undertaken for continuous variables using Student's *t*-test for normally distributed variables or the Mann–Whitney *U*-test for variables with an abnormal distribution. LASSO regression analysis was carried out using the "glmnet" package, and the SVM algorithm was performed using the e1071 package in R. ROC curve analysis was used to determine the diagnostic efficacy of the diagnostic biomarkers included. The relationship between the expression of gene biomarkers and infiltrating immune cells was analyzed using Spearman's correlation. All statistical analyses were two-sided with $P < 0.05$ were regarded statistically significant.

RESULTS

Identification of DEGs in AMI

Data from a total of 80 AMI and 71 control samples from two GEO datasets (GSE66360 and GSE48060) were retrospectively analyzed in this study. The DEGs of the metadata were analyzed using the limma package after removing the batch effects. A total of 27 DEGs were obtained: 25 genes were significantly upregulated and 2 genes were significantly downregulated (**Figure 1**).

Functional Correlation Analysis

DO pathway enrichment analyses were conducted to investigate the function of DEGs. The results indicated that diseases enriched by DEGs were mainly associated with arteriosclerotic cardiovascular disease, atherosclerosis, lymphadenitis, and Kawasaki disease (**Figure 2A**). The GSEA results demonstrated that the enriched pathways mainly involved cytokine–cytokine receptor interaction, atherosclerosis, IL-17 signaling pathway, primary immunodeficiency, and TNF signaling pathways (**Figure 2B**). These findings strongly suggest that the immune response plays an essential role in AMI.

Identification and Validation of Diagnostic Feature Biomarkers

Two different algorithms were used to screen potential biomarkers. The DEGs were narrowed down using the LASSO regression algorithm, resulting in the identification of 17 variables as diagnostic biomarkers for AMI (**Figure 3A**). A subset of five features among the DEGs was determined using the SVM-RFE algorithm (**Figure 3B**). The four overlapping features (IL1R2, IRAK3, NR4A2, and THBD) between these two algorithms were ultimately selected (**Figure 3C**). Furthermore, to generate more accurate and reliable results, the GSE60993 dataset was used to verify the expression levels of the four features. The expression levels of IL1R2, IRAK3, and THBD in AMI tissue were notably higher than those in the control group (**Figures 4A–C**; all $P < 0.05$). However, there was no significant difference between the two groups in terms of THBD expression (**Figure 4D**). Therefore, the three identified genes were used to establish the diagnostic model using a logistic regression algorithm in the metadata cohort.

Diagnostic Effectiveness of Feature Biomarkers in AMI

As shown in **Figure 5A**, the diagnostic ability of the three biomarkers in discriminating AMI from the control samples demonstrated a favorable diagnostic value, with an AUC of 0.849 (95% CI 0.781–0.902) in IL1R2, AUC of 0.845 (95% CI 0.778–0.899) in IRAK3, and AUC of 0.843 (95% CI 0.775–0.897) in THBD. When the three genes were combined into one variable, the diagnostic ability in terms of AUC was 0.871 (95% CI 0.807–0.920) in the meta-data cohort. Moreover, a powerful discrimination ability was confirmed in the GSE60993 dataset with an AUC of 0.782 (95% CI 0.567–0.922) in IL1R2, AUC of 0.916 (95% CI 0.729–0.990) in IRAK3, and AUC of 0.765 (95% CI 0.549–0.912) in THBD. Importantly, the diagnostic ability of

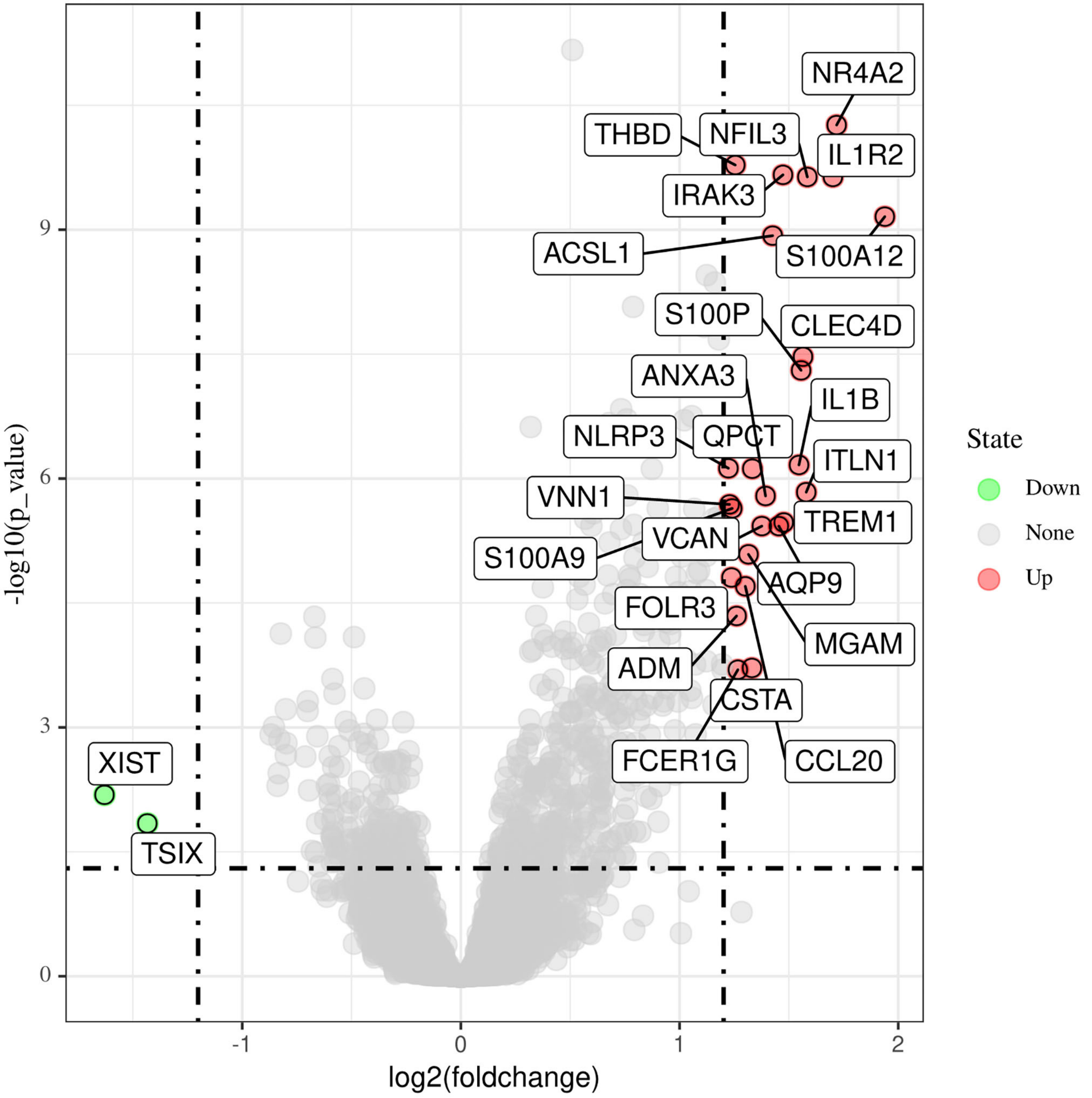

FIGURE 1 | Differentially expressed genes between acute myocardial infarction tissue and control samples.

the three biomarkers combined yielded an AUC of 0.941 (95% CI 0.764–0.996; **Figure 5B**), indicating that the feature biomarkers had a high diagnostic ability.

Immune Cell Infiltration

First, we explored the composition of immune cells in AMI tissues vs. normal control tissues. The proportions of CD4$^+$ resting memory T cells ($P < 0.001$), gamma delta T cells ($P < 0.001$), M1 macrophages ($P = 0.007$), and resting mast cells ($P < 0.001$) in AMI tissues were significantly lower than in normal tissues. However, the proportion of monocytes ($P < 0.001$), activated mast cells ($P < 0.001$), neutrophils ($P < 0.001$), and follicular helper T cells ($P = 0.012$) in AMI tissues was significantly higher than that in normal tissues (**Figure 6A**).

The correlation of 22 types of immune cells was calculated (**Figure 6B**). CD4 memory resting T cells were significantly positively correlated with memory B cells ($r = 0.23$, $P = 0.042$), but significantly negatively correlated with monocytes ($r =$

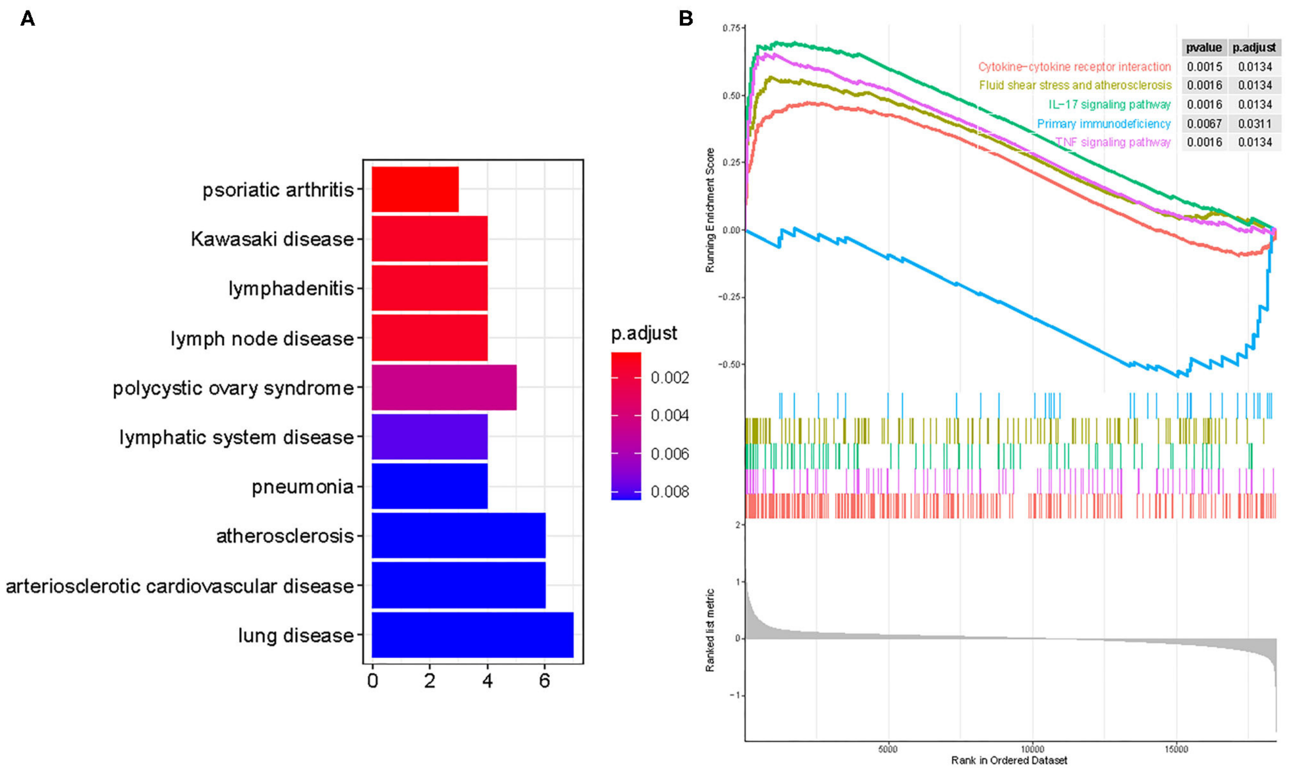

FIGURE 2 | Functional enrichment analyses to identify potential biological processes via disease ontology and gene set enrichment analysis. **(A)** Disease ontology enrichment analysis of differentially expressed genes between AMI and control samples. **(B)** Enrichment analyses via gene set enrichment analysis.

-0.42, $P = 0.023$), activated mast cells ($r = -0.43$, $P = 0.014$), and neutrophils ($r = -0.55$, $P < 0.001$). Follicular helper T cells were significantly positively correlated with plasma cells ($r = 0.42$, $P = 0.00011$) and regulatory T cells ($r = 0.42$, $P = 0.0247$), but significantly negatively correlated with CD8 T cells ($r = -0.31$, $P = 0.0051$). Gamma delta T cells were significantly positively correlated with CD8 T cells ($r = 0.22$, $P = 0.046$), but significantly negatively correlated with monocytes ($r = -0.44$, $P = 0.0092$), activated mast cells ($r = -0.44$, $P = 0.011$), and neutrophils ($r = -0.55$, $P < 0.001$). Monocytes were significantly positively correlated with follicular helper T cells ($r = 0.29$, $P = 0.0084$) and mast cell activated ($r = 0.43$, $P = 0.016$), but significantly negatively correlated with CD8 T cells ($r = -0.29$, $P = 0.0083$), CD4 memory resting T cells ($r = -0.42$, $P = 0.0001$), and gamma delta T cells ($r = -0.44$, $P < 0.0001$). M1 macrophages were significantly positively correlated with gamma delta T cells ($r = 0.25$, $P = 0.027$) and resting dendritic cells ($r = 0.49$, $P = 0.0008$). Resting mast cells were significantly positively correlated with M0 macrophages ($r = 0.26$, $P = 0.018$). Activated mast cells were significantly positively correlated with follicular helper T cells ($r = 0.31$, $P = 0.0042$), activated NK cells ($r = 0.43$, $P < 0.0001$), monocytes ($r = 0.42$, $P < 0.0001$), and M2 macrophages ($r = 0.34$, $P = 0.0017$), but significantly negatively correlated with CD8 T cells ($r = -0.23$, $P = 0.037$), CD4 memory resting T cells ($r = -0.43$, $P < 0.0001$), gamma delta T cells ($r = -0.43$, $P < 0.0001$), and M0 macrophages ($r = -0.22$, $P = 0.043$). Neutrophils were significantly positively correlated with activated NK cells ($r = 0.22$, $P = 0.045$), monocytes ($r = 0.34$, $P = 0.0017$), M2 macrophages ($r = 0.26$, $P = 0.0181$), and activated mast cells ($r = 0.51$, $P < 0.0001$), but significantly negatively correlated with CD8 T cells ($r = -0.28$, $P = 0.011$), CD4 memory resting T cells ($r = -0.55$, $P < 0.0001$), and T cells gamma delta ($r = -0.54$, $P < 0.0001$).

Correlation Analysis Between the Three Biomarkers and Infiltrating Immune Cells

As shown in **Figure 7A**, IL1R2 was positively correlated with neutrophils ($r = 0.66$, $P < 0.0001$), activated mast cells ($r = 0.55$, $P < 0.0001$), activated NK cells ($r = 0.42$, $P = 0.00011$), monocytes ($r = 0.28$, $P = 0.01$), M2 macrophages ($r = 0.25$, $P = 0.027$), and resting NK cells ($r = 0.23$, $P = 0.038$) and negatively correlated with CD4 memory resting T cells ($r = -0.48$, $P < 0.0001$), and gamma delta T cells ($r = -0.39$, $P = 0.00029$). IRAK3 was positively correlated with activated mast cells ($r = 0.65$, $P < 0.0001$), neutrophils ($r = 0.62$, $P < 0.0001$), monocytes ($r = 0.55$, $P < 0.0001$), activated NK cells ($r = 0.46$, $P < 0.0001$), resting NK cells ($r = 0.36$, $P = 0.001$), and M2 macrophages ($r = 0.29$, $P = 0.0089$) and negatively correlated with CD4 memory resting T cells ($r = -0.58$, $P < 0.0001$), gamma delta T cells ($r = -0.48$, $P < 0.0001$), CD4 naïve T cells ($r = -0.24$, $P = 0.027$), and memory B cells ($r = -0.23$, $P = 0.038$; **Figure 7B**). THBD

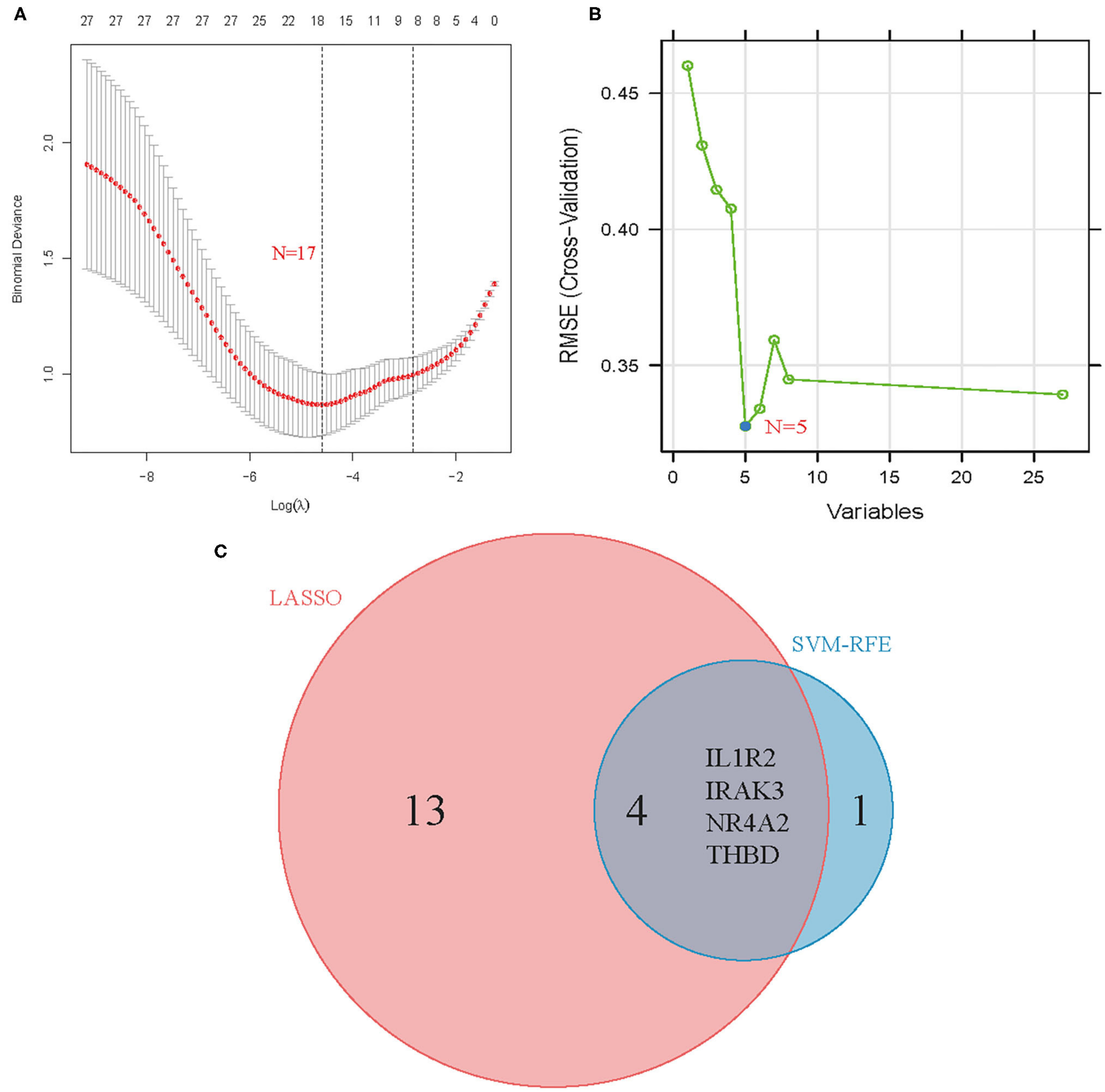

FIGURE 3 | Screening process of diagnostic biomarker candidates for acute myocardial infarction diagnosis. **(A)** Tuning feature selection in the least absolute shrinkage and selection operator model. **(B)** A plot of biomarkers selection via support vector machine-recursive feature elimination (SVM-RFE) algorithm. **(C)** Venn diagram demonstrating four diagnostic markers shared by the least absolute shrinkage and selection operator and SVM-RFE algorithms.

was positively correlated with monocytes ($r = 0.54$, $P < 0.0001$), activated mast cells ($r = 0.45$, $P < 0.0001$), activated NK cells ($r = 0.42$, $P < 0.0001$), neutrophils ($r = 0.41$, $P = 0.00012$), resting dendritic cells ($r = 0.26$, $P = 0.018$), and M2 macrophages ($r = 0.23$, $P = 0.0418$) and negatively correlated with CD4 memory resting T cells ($r = -0.36$, $P = 0.0008$), gamma delta T cells ($r = -0.32$, $P = 0.0029$), and CD8 T cells ($r = -0.26$, $P = 0.0178$; **Figure 7C**).

DISCUSSION

AMI remains a leading cause of mortality and disability despite great improvements in early diagnosis and treatment over the past decade (26). As a result, the clinical prognosis of patients with AMI is poor. Because of the lack of an effective early diagnosis, patients with AMI often lose the chance to benefit from treatment, resulting in poor outcomes. Recently,

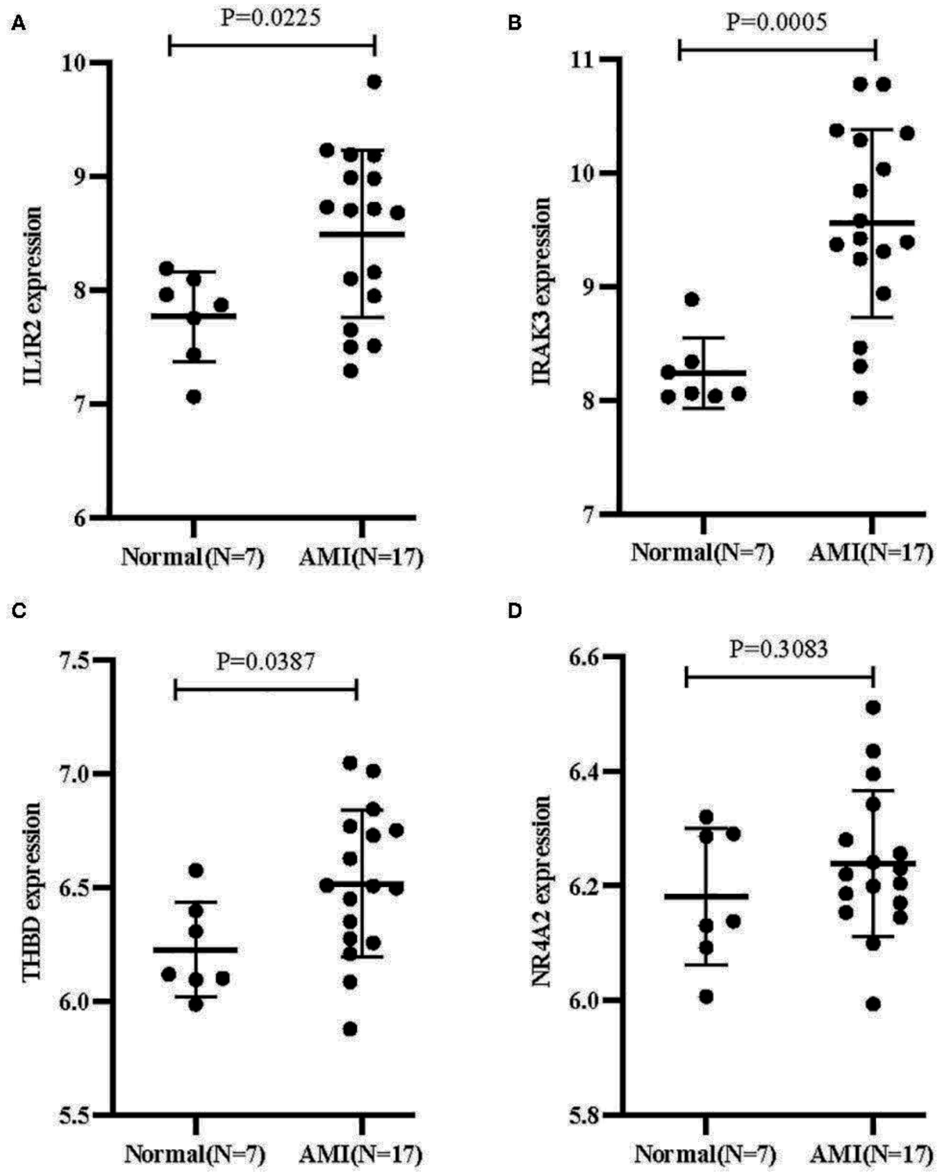

FIGURE 4 | Validation of the expression of diagnostic biomarkers in the GSE60993 dataset. **(A)** IL1R2; **(B)** IRAK3; **(C)** THBD; **(D)** NR4A2.

immune cell infiltration has been confirmed to play a vital role in the occurrence and development of AMI (20, 27, 28). Therefore, researchers are increasingly searching for novel diagnostic biomarkers and exploring the compositions of AMI immune cell infiltration, which could have a highly beneficial impact on the clinical outcomes of AMI patients. Recently, mRNAs and microRNAs have emerged as promising biomarkers in cardiovascular disease in general and in AMI in particular. For example, SOCS3 could serve as a biomarker to predict the risk of AMI, where the elevated expression of the SOCS3 gene is an independent risk factor for AMI (16). In particular, miR-34, which is known to modulate immunity, was found to be significantly modulated in post-MI heart failure, providing important information on its role in heart failure (29, 30). However, very few studies have focused on the aberrantly expressed gene biomarkers associated with immune infiltration between AMI and normal tissues. Therefore, we aimed to identify candidate diagnostic biomarkers for AMI and investigate the role of immune cell infiltration in AMI.

To the best of our knowledge, this is the first retrospective study to identify diagnostic biomarkers associated with immune cell infiltration in patients with AMI by mining multiple GEO datasets. We collected two cohorts from the GEO datasets and conducted an integrated analysis of the data. A total of 27 DEGs were identified, including 25 upregulated genes and 2 downregulated genes. The results of enrichment analyses indicated that diseases enriched by DEGs were mainly associated with atherosclerosis and arteriosclerotic cardiovascular disease.

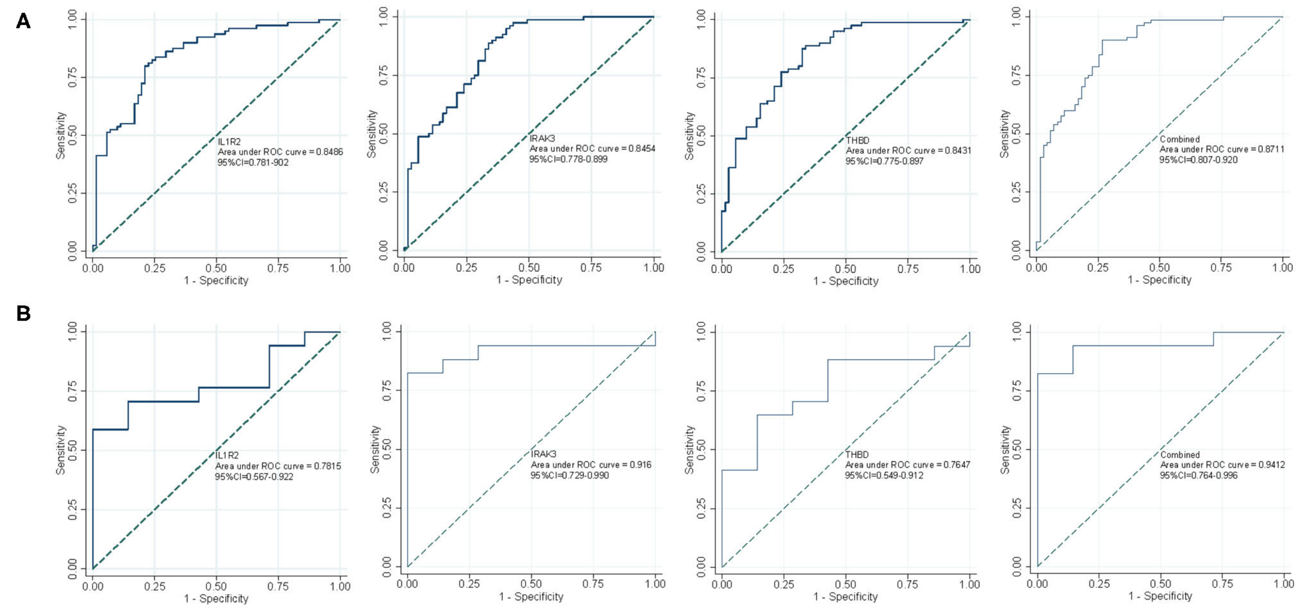

FIGURE 5 | The receiver operating characteristic (ROC) curve of the diagnostic effectiveness of the three diagnostic markers. **(A)** ROC curve of IL1R2, IRAK3, and THBD after fitting to one variable in the metadata cohort; **(B)** ROC curve of IL1R2, IRAK3, and THBD after fitting to one variable in the GSE60993 dataset.

The GSEA results demonstrated that the enriched pathways generally involved inflammation and immune response pathways, such as cytokine–cytokine receptor interaction, atherosclerosis, and TNF signaling. These findings are in general agreement with the previous finding that an inflammatory response involving leukocytes participates in the pathogenesis of AMI (31). In fact, AMI is mainly caused by atherosclerosis and is regarded as a chronic inflammatory disorder (32). A substantial amount of inflammatory responses were induced during the acute phase of cardiac injury, caused by an abrupt cessation of blood flow, resulting in MI. The tumor necrosis factor (TNF) signaling pathway participates in inflammatory cell accumulation, platelet aggregation, vulnerable plaque formation, cardiomyocyte apoptosis, and poor remodeling after AMI (33). Cytokines, such as TNF and interleukin-8, have been confirmed to be involved in cell differentiation and inflammatory response via binding to specific receptors on the cell surface during the development of AMI (34). This evidence is consistent with our results, confirming that the findings in the present study are accurate, as well as demonstrating that the immune response plays a vital role in AMI. The significance of the immune system for cardiac repair after AMI is undeniable. Perhaps the most diverse and complex reaction after AMI is the immune response, which has been confirmed to influence various repair processes. Thus, a precise control over various types of immune cells is needed to achieve a safe and effective treatment (35). Therefore, the identification of novel biomarkers of AMI correlated with the magnitude of immune cell infiltration by bioinformatics analysis will contribute to its treatment.

Based on two machine-learning algorithms, three diagnostic markers were identified. Interleukin-1 (IL-1) is a major pro-inflammatory cytokine produced by smooth muscle cells, endothelial cells, and macrophages, which can stimulate the expression of genes related to inflammation and immunity. Interleukin-1 receptor type 2 (IL1R2), a cytokine receptor that belongs to the IL-1 receptor family, has been reported to serve as a critical mediator involved in many cytokines induced by immune and inflammatory responses (36). IL1R2 gene can control cell metabolism, as well as immune response induced by many cytokines (37). IL-1-mediated inflammation contributes to the pathology of many diseases including systolic heart failure, and IL-1R2 has been implicated in atherosclerosis (38). The aforementioned evidence suggests that IL1R2 plays a key role in AMI. Interleukin 1 receptor associated kinase 3 (IRAK3), which encodes a member of the IL-1 receptor-associated kinase protein family, functions as a negative regulator of Toll-like receptor signaling and participates in innate host defense and in the control of adaptive immune responses (39). Evidence in a mouse model of AMI demonstrated that IRAK3 gene silencing could minimize AMI damage, indicated by a reduced infarct area and collagen content (40). A mutation in the thrombomodulin (THBD) gene is the main cause of thromboembolic disease. AMI is typically precipitated by thrombosis superimposed on a ruptured coronary plaque. Therefore, we believe that THBD may play a vital role in the development of AMI.

The types of immune cell infiltration in AMI and normal samples were assessed using CIBERSOTR. As a result, a variety of immune cell subtypes were found to be closely involved in important biological processes of AMI. An increased infiltration of monocytes, activated mast cells, neutrophils, and T follicular helper cells, and a decreased infiltration of $CD4^+$ resting memory T cells, gamma delta T cells, M1 macrophages, and resting mast

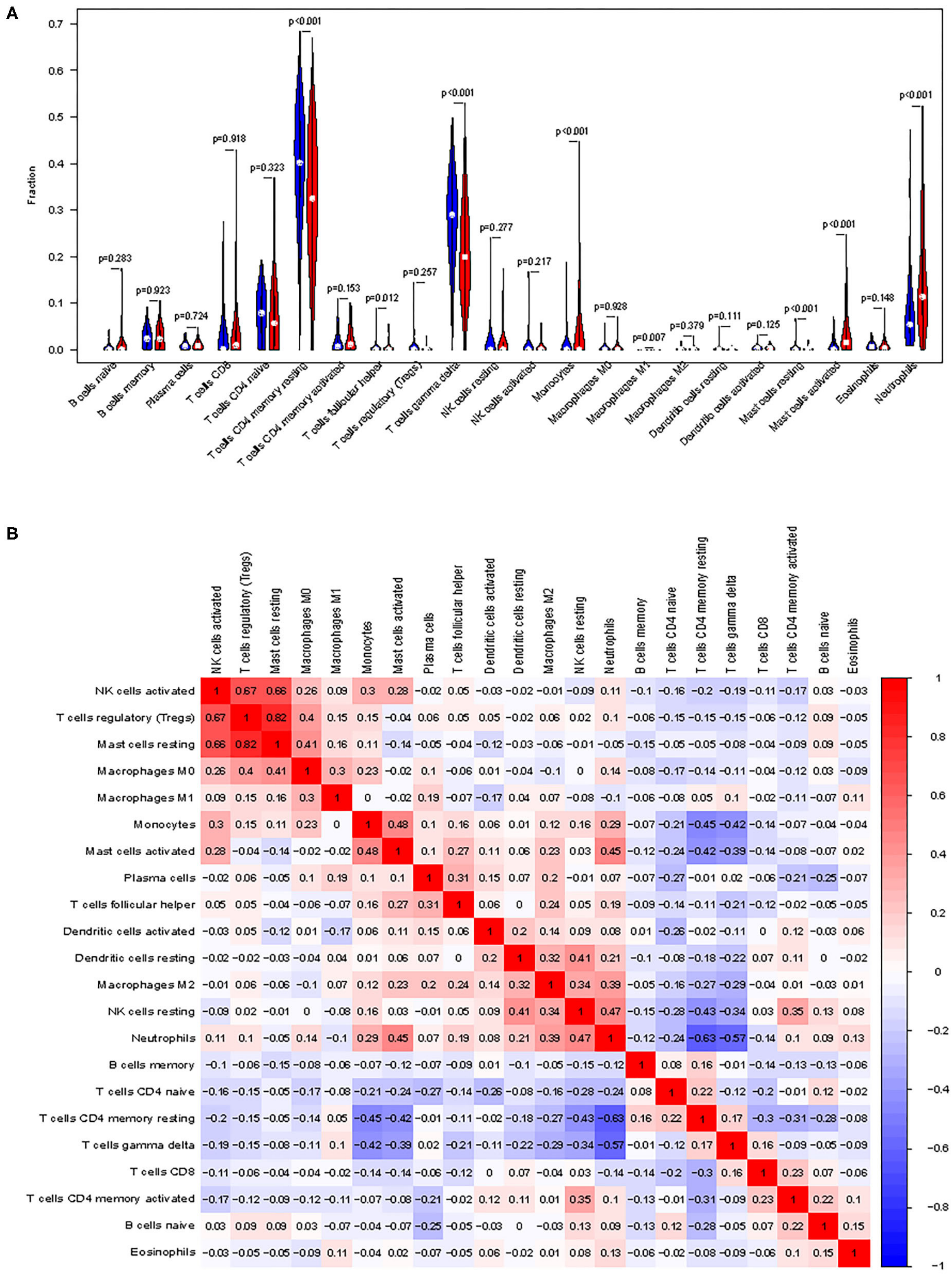

	NK cells activated	T cells regulatory (Tregs)	Mast cells resting	Macrophages M0	Macrophages M1	Monocytes	Mast cells activated	Plasma cells	T cells follicular helper	Dendritic cells activated	Dendritic cells resting	Macrophages M2	NK cells resting	Neutrophils	B cells memory	T cells CD4 naive	T cells CD4 memory resting	T cells gamma delta	T cells CD8	T cells CD4 memory activated	B cells naive	Eosinophils
NK cells activated	1	0.67	0.66	0.26	0.09	0.3	0.28	-0.02	0.05	-0.03	-0.02	-0.01	-0.09	0.11	-0.1	-0.16	-0.2	-0.19	-0.11	-0.17	0.03	-0.03
T cells regulatory (Tregs)	0.67	1	0.82	0.4	0.15	0.15	-0.04	0.06	0.05	0.05	-0.02	0.06	0.02	0.1	-0.06	-0.15	-0.15	-0.15	-0.06	-0.12	0.09	-0.05
Mast cells resting	0.66	0.82	1	0.41	0.16	0.11	-0.14	-0.05	-0.04	-0.12	-0.03	-0.06	-0.01	-0.05	-0.15	-0.05	-0.05	-0.08	-0.04	-0.09	0.09	-0.05
Macrophages M0	0.26	0.4	0.41	1	0.3	0.23	-0.02	0.1	-0.06	0.01	-0.04	-0.1	0	0.14	-0.08	-0.17	-0.14	-0.11	-0.04	-0.12	0.03	-0.09
Macrophages M1	0.09	0.15	0.16	0.3	1	0	-0.02	0.19	-0.07	-0.17	0.04	0.07	-0.08	-0.1	-0.06	-0.08	0.05	0.1	-0.02	-0.11	-0.07	0.11
Monocytes	0.3	0.15	0.11	0.23	0	1	0.48	0.1	0.16	0.06	0.01	0.12	0.16	0.29	-0.07	-0.21	-0.45	-0.42	-0.14	-0.07	-0.04	-0.04
Mast cells activated	0.28	-0.04	-0.14	-0.02	-0.02	0.48	1	0.1	0.27	0.11	0.06	0.23	0.03	0.45	-0.12	-0.24	-0.42	-0.39	-0.14	-0.08	-0.07	0.02
Plasma cells	-0.02	0.06	-0.05	0.1	0.19	0.1	0.1	1	0.31	0.15	0.07	0.2	-0.01	0.07	-0.07	-0.27	-0.01	0.02	-0.06	-0.21	-0.25	-0.07
T cells follicular helper	0.05	0.05	-0.04	-0.06	-0.07	0.16	0.27	0.31	1	0.06	0	0.24	0.05	0.19	-0.09	-0.14	-0.11	-0.21	-0.12	-0.02	-0.05	-0.05
Dendritic cells activated	-0.03	0.05	-0.12	0.01	-0.17	0.06	0.11	0.15	0.06	1	0.2	0.14	0.09	0.08	0.01	-0.26	-0.02	-0.11	0	0.12	-0.03	0.06
Dendritic cells resting	-0.02	-0.02	-0.03	-0.04	0.04	0.01	0.06	0.07	0	0.2	1	0.32	0.41	0.21	-0.1	-0.08	-0.18	-0.22	0.07	0.11	0	-0.02
Macrophages M2	-0.01	0.06	-0.06	-0.1	0.07	0.12	0.23	0.2	0.24	0.14	0.32	1	0.34	0.39	-0.05	-0.16	-0.27	-0.29	-0.04	0.01	-0.03	0.01
NK cells resting	-0.09	0.02	-0.01	0	-0.08	0.16	0.03	-0.01	0.05	0.09	0.41	0.34	1	0.47	-0.15	-0.28	-0.43	-0.34	0.03	0.35	0.13	0.08
Neutrophils	0.11	0.1	-0.05	0.14	-0.1	0.29	0.45	0.07	0.19	0.08	0.21	0.39	0.47	1	-0.12	-0.24	-0.63	-0.57	-0.14	0.1	0.09	0.13
B cells memory	-0.1	-0.06	-0.15	-0.08	-0.06	-0.07	-0.12	-0.07	-0.09	0.01	-0.1	-0.05	-0.15	-0.12	1	0.08	0.16	-0.01	-0.14	-0.13	-0.13	-0.06
T cells CD4 naive	-0.16	-0.15	-0.05	-0.17	-0.08	-0.21	-0.24	-0.27	-0.14	-0.26	-0.08	-0.16	-0.28	-0.24	0.08	1	0.22	-0.12	-0.2	-0.01	0.12	-0.02
T cells CD4 memory resting	-0.2	-0.15	-0.05	-0.14	0.05	-0.45	-0.42	-0.01	-0.11	-0.02	-0.18	-0.27	-0.43	-0.63	0.16	0.22	1	0.17	-0.3	-0.31	-0.28	-0.08
T cells gamma delta	-0.19	-0.15	-0.08	-0.11	0.1	-0.42	-0.39	0.02	-0.21	-0.11	-0.22	-0.29	-0.34	-0.57	-0.01	-0.12	0.17	1	0.16	-0.09	-0.05	-0.09
T cells CD8	-0.11	-0.06	-0.04	-0.04	-0.02	-0.14	-0.14	-0.06	-0.12	0	0.07	-0.04	0.03	-0.14	-0.14	-0.2	-0.3	0.16	1	0.23	0.07	-0.06
T cells CD4 memory activated	-0.17	-0.12	-0.09	-0.12	-0.11	-0.07	-0.08	-0.21	-0.02	0.12	0.11	0.01	0.35	0.1	-0.13	-0.01	-0.31	-0.09	0.23	1	0.22	0.1
B cells naive	0.03	0.09	0.09	0.03	-0.07	-0.04	-0.07	-0.25	-0.05	-0.03	0	-0.03	0.13	0.09	-0.13	0.12	-0.28	-0.05	0.07	0.22	1	0.15
Eosinophils	-0.03	-0.05	-0.05	-0.09	0.11	-0.04	0.02	-0.07	-0.05	0.06	-0.02	0.01	0.08	0.13	-0.06	-0.02	-0.08	-0.09	-0.06	0.1	0.15	1

FIGURE 6 | Distribution and visualization of immune cell infiltration. **(A)** Comparison of 22 immune cell subtypes between acute myocardial infarction tissues and normal tissues. Blue and red colors represent normal and acute myocardial infarction samples, respectively. **(B)** Correlation matrix of all 22 immune cell subtype compositions. Both horizontal and vertical axes demonstrate immune cell subtypes. Immune cell subtype compositions (higher, lower, and same correlation levels are displayed in red, blue, and white, respectively).

cells were found to be potentially related to the occurrence and development of AMI. Furthermore, by performing correlation analysis between IL1R2, IRAK3, THBD, and immune cells, IL1R2, IRAK3, and THBD were all found to be correlated with neutrophils, monocytes, M2 macrophages, CD4$^+$ resting memory T cells, gamma delta T cells, and activated NK cells. In fact, inflammatory and immune circulatory cells, such as neutrophils, lymphocytes, and platelets, have previously been shown to play an important role in the progression of heart disease (41, 42). The innate immune system begins immediately on the onset of necrotic cell death accompanied by intense sterile inflammation and the MI of a number of immune cell subtypes including monocytes and neutrophils during the first few days after AMI (28). Neutrophils can infiltrate the infarcted area, subsequently mediating the injury of infarcted tissues by releasing reactive oxygen species and matrix-degrading enzymes (43). CD4$^+$ and CD8$^+$ T cells, regulatory T cells, and NK T cells can infiltrate the infarcted myocardium during the proliferative phase of repair and facilitate the transition toward maturation. They may be motivated by cardiac autoantigens and limit adverse ventricular remodeling by enhancing wound healing, inflammation resolution, and scar development via collagen matrix formation (43). Furthermore, the therapeutic activation of regulatory T cells may well be an encouraging therapy for AMI to promote cardiac repair and limit adverse ventricular remodeling (44). The substantial evidence mentioned earlier together with our present findings have demonstrated that several types of infiltrating immune cells play vital roles in AMI and should be the focus of future investigations.

The limitations of this study should be acknowledged. First, the study was retrospective; thus, important clinical information was not available. Second, the number of cases in the GSE60993 validation cohort was low, which should be acknowledged as a limitation. In addition, the biomarker profiles in the blood and the immune cell profile were obtained from the two datasets, and their reproducibility should be further validated. Last, the functions of three biomarkers and immune cell infiltration in AMI were inferred by bioinformatics analysis, and prospective studies with larger sample sizes should be conducted to validate our conclusions.

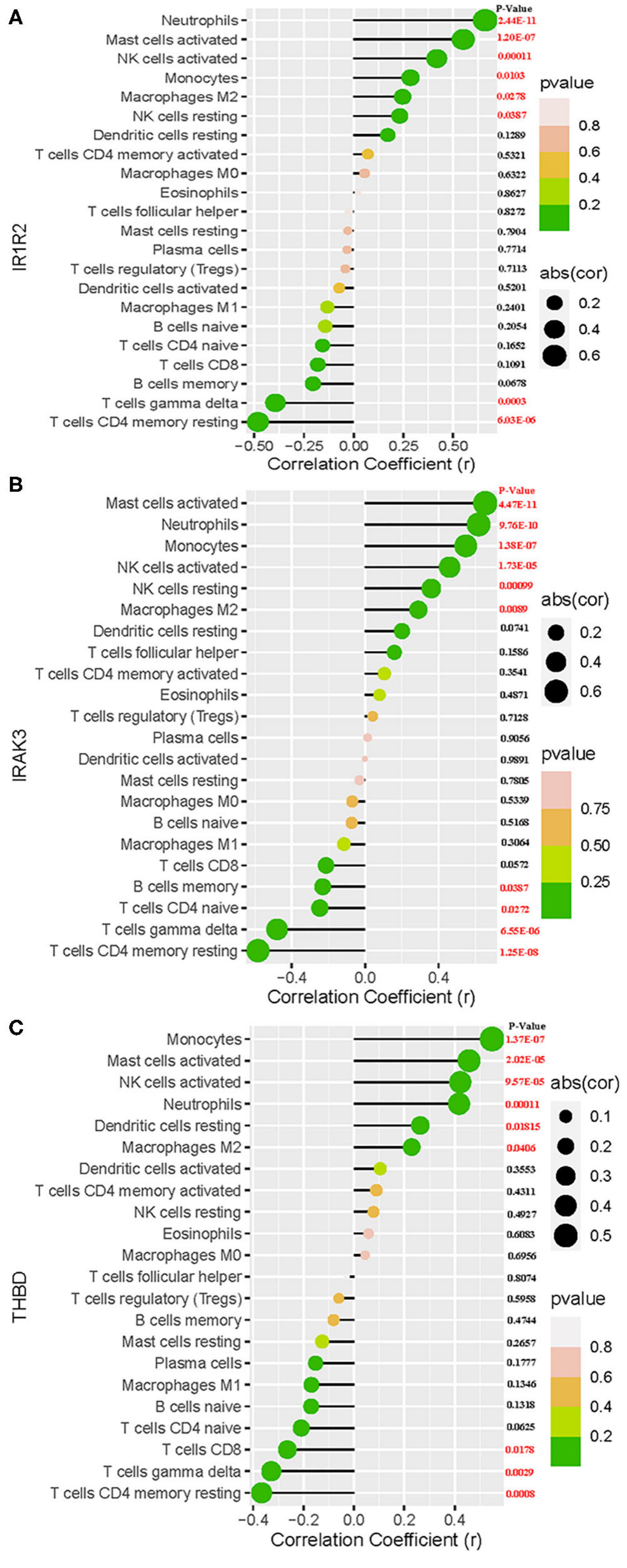

FIGURE 7 | Correlation between IL1R2 **(A)**, IRAK3 **(B)**, THBD **(C)**, and infiltrating immune cells in acute myocardial infarction.

CONCLUSION

In summary, IL1R2, IRAK3, and THBD were identified as diagnostic biomarkers of AMI. Neutrophils, monocytes, M2 macrophages, CD4$^+$ resting memory T cells, gamma delta T cells, and activated NK cells may be involved in the development of AMI. These immune cells have the potential to be developed as targets of immunotherapy in patients with AMI.

DATA AVAILABILITY STATEMENT

Publicly available datasets were analyzed in this study. This data can be found here: All the raw data used in this study are derived from the public GEO data portal (https://www.ncbi.nlm.nih.gov/geo/; Accession numbers: GSE66360, GSE48060, and GSE60993).

AUTHOR CONTRIBUTIONS

EZ and HX is the principal investigator and conducted statistical analysis and drafted the article. EZ performed data management and bioinformatics analysis. EZ, HX, and YZ edited and revised the article. All authors read and approved the final article.

ACKNOWLEDGMENTS

The authors acknowledge the Gene Expression Omnibus (GEO) database for providing data of AMI available.

REFERENCES

1. Guo J, Liu HB, Sun C, Yan XQ, Hu J, Yu J, et al. MicroRNA-155 promotes myocardial infarction-induced apoptosis by targeting RNA-binding protein QKI. *Oxid Med Cell Longev*. (2019) 2019:4579806. doi: 10.1155/2019/4579806
2. White HD, Chew DP. Acute myocardial infarction. *Lancet*. (2008) 372:570–84. doi: 10.1016/S0140-6736(08)61237-4
3. Gruzdeva O, Uchasova E, Dyleva Y, Belik E, Karetnikova V, Shilov A, et al. Multivessel coronary artery disease, free fatty acids, oxidized LDL and its antibody in myocardial infarction. *Lipids Health Dis*. (2014) 13:111. doi: 10.1186/1476-511X-13-111
4. Gehani AA, Al-Hinai AT, Zubaid M, Almahmeed W, Hasani MR, Yusufali AH, et al. Association of risk factors with acute myocardial infarction in Middle Eastern countries: the INTERHEART Middle East study. *Eur J Prev Cardiol*. (2014) 21:400–10. doi: 10.1177/2047487312465525
5. de Winter RJ, Koster RW, Sturk A, Sanders GT. Value of myoglobin, troponin T, and CK-MBmass in ruling out an acute myocardial infarction in the emergency room. *Circulation*. (1995) 92:3401–7. doi: 10.1161/01.CIR.92.12.3401
6. de Lemos JA, Drazner MH, Omland T, Ayers CR, Khera A, Rohatgi A, et al. Association of troponin T detected with a highly sensitive assay and cardiac structure and mortality risk in the general population. *JAMA*. (2010) 304:2503–12. doi: 10.1001/jama.2010.1768
7. Braunwald E. Unstable angina and non-ST elevation myocardial infarction. *Am J Respir Crit Care Med*. (2012) 185:924–32. doi: 10.1164/rccm.201109-1745CI
8. Law MR, Watt HC, Wald NJ. The underlying risk of death after myocardial infarction in the absence of treatment. *Arch Intern Med*. (2002) 162:2405–10. doi: 10.1001/archinte.162.21.2405
9. Nichols M, Townsend N, Scarborough P, Rayner M. Cardiovascular disease in Europe 2014: epidemiological update. *Eur Heart J*. (2014) 35:2950–9. doi: 10.1093/eurheartj/ehu299
10. Zhao E, Zhou C, Chen SA. Signature of 14 immune-related gene pairs predicts overall survival in gastric cancer. *Clin Transl Oncol*. (2020). doi: 10.1007/s12094-020-02414-7. [Epub ahead of print].
11. Cao Y, Tang W, Tang W. Immune cell infiltration characteristics and related core genes in lupus nephritis: results from bioinformatic analysis. *BMC Immunol*. (2019) 20:37. doi: 10.1186/s12865-019-0316-x
12. Qiu L, Liu X. Identification of key genes involved in myocardial infarction. *Eur J Med Res*. (2019) 24:22. doi: 10.1186/s40001-019-0381-x
13. Zhao E, Bai X. Nomogram based on microRNA signature contributes to improve survival prediction of clear cell renal cell carcinoma. *Biomed Res Int*. (2020) 2020:7434737. doi: 10.1155/2020/7434737
14. Zhao E, Zhou C, Chen S. Flap endonuclease 1 (FEN1) as a novel diagnostic and prognostic biomarker for gastric cancer. *Clin Res Hepatol Gastroenterol*. (2020). doi: 10.1016/j.clinre.2020.04.019. [Epub ahead of print].
15. Ruan J, Meng H, Wang X, Chen W, Tian X, Meng F. Low expression of FFAR2 in peripheral white blood cells may be a genetic marker for early diagnosis of acute myocardial infarction. *Cardiol Res Pract*. (2020) 2020:3108124. doi: 10.1155/2020/3108124
16. Meng H, Wang X, Ruan J, Chen W, Meng F, Yang P. High expression levels of the SOCS3 gene are associated with acute myocardial infarction. *Genet Test Mol Biomarkers*. (2020) 24:443–50. doi: 10.1089/gtmb.2020.0040
17. Nahrendorf M, Swirski FK. Innate immune cells in ischaemic heart disease: does myocardial infarction beget myocardial infarction? *Eur Heart J*. (2016) 37:868–72. doi: 10.1093/eurheartj/ehv453
18. Yang S, Liu T, Cheng Y, Bai Y, Liang G. Immune cell infiltration as a biomarker for the diagnosis and prognosis of digestive system cancer. *Cancer Sci*. (2019) 110:3639–49. doi: 10.1111/cas.14216
19. Deng Y-J, Ren E-H, Yuan W-H, Zhang G-Z, Wu Z-L, Xie Q-Q. GRB10 and E2F3 as Diagnostic markers of osteoarthritis and their correlation with immune infiltration. *Diagnostics*. (2020) 10:171. doi: 10.3390/diagnostics10030171
20. Xu JY, Xiong YY, Lu XT, Yang YJ. Regulation of type 2 immunity in myocardial infarction. *Front Immunol*. (2019) 10:62. doi: 10.3389/fimmu.2019.00062
21. Leek JT, Johnson WE, Parker HS, Jaffe AE, Storey JD. The sva package for removing batch effects and other unwanted variation in high-throughput experiments. *Bioinformatics*. (2012) 28:882–3. doi: 10.1093/bioinformatics/bts034
22. Yu G, Wang LG, Han Y, He QY. clusterProfiler: an R package for comparing biological themes among gene clusters. *OMICS*. (2012) 16:284–7. doi: 10.1089/omi.2011.0118
23. Yu G, Wang LG, Yan GR, He QY. DOSE: an R/Bioconductor package for disease ontology semantic and enrichment analysis. *Bioinformatics*. (2015) 31:608–9. doi: 10.1093/bioinformatics/btu684
24. Guyon I, Weston J, Barnhill S, Vapnik V. Gene selection for cancer classification using support vector machines. *Machine Learn*. (2002) 46:389–422. doi: 10.1023/A:1012487302797
25. Newman AM, Liu CL, Green MR, Gentles AJ, Feng W, Xu Y, et al. Robust enumeration of cell subsets from tissue expression profiles. *Nat Methods*. (2015) 12:453–7. doi: 10.1038/nmeth.3337
26. Boersma E, Mercado N, Poldermans D, Gardien M, Vos J, Simoons ML. Acute myocardial infarction. *Lancet*. (2003) 361:847–58. doi: 10.1016/S0140-6736(03)12712-2
27. Swirski FK, Nahrendorf M. Leukocyte behavior in atherosclerosis, myocardial infarction, and heart failure. *Science*. (2013) 339:161–6. doi: 10.1126/science.1230719
28. Weil BR, Neelamegham S. Selectins and immune cells in acute myocardial infarction and post-infarction ventricular remodeling: pathophysiology and novel treatments. *Front Immunol*. (2019) 10:300. doi: 10.3389/fimmu.2019.00300
29. Xiong XP, Kurthkoti K, Chang KY, Li JL, Ren X, Ni JQ, et al. miR-34 modulates innate immunity and ecdysone signaling in Drosophila. *PLoS Pathog*. (2016) 12:e1006034. doi: 10.1371/journal.ppat.1006034
30. de Rosa S, Eposito F, Carella C, Strangio A, Ammirati G, Sabatino J, et al. Transcoronary concentration gradients of circulating microRNAs in heart failure. *Eur J Heart Fail*. (2018) 20:1000–10. doi: 10.1002/ejhf.1119
31. Suresh R, Li X, Chiriac A, Goel K, Terzic A, Perez-Terzic C, et al. Transcriptome from circulating cells suggests dysregulated pathways associated with long-term recurrent events following first-time myocardial infarction. *J Mol Cell Cardiol*. (2014) 74:13–21. doi: 10.1016/j.yjmcc.2014.04.017
32. Sun J, Hartvigsen K, Chou MY, Zhang Y, Sukhova GK, Zhang J, et al. Deficiency of antigen-presenting cell invariant chain reduces atherosclerosis in mice. *Circulation*. (2010) 122:808–20. doi: 10.1161/CIRCULATIONAHA.109.891887
33. Xiao J, Moon M, Yan L, Nian M, Zhang Y, Liu C, et al. Cellular FLICE-inhibitory protein protects against cardiac remodelling after myocardial infarction. *Basic Res Cardiol*. (2012) 107:239. doi: 10.1007/s00395-011-0239-z
34. Bernard GR, Artigas A, Brigham KL, Carlet J, Falke K, Hudson L, et al. Report of the American-European consensus conference on acute respiratory distress syndrome: definitions, mechanisms, relevant outcomes, and clinical

trial coordination. *Consensus Committee J Crit Care.* (1994) 9:72–81. doi: 10.1016/0883-9441(94)90033-7

35. Tobin SW, Alibhai FJ, Weisel RD, Li RK. Considering cause and effect of immune cell aging on cardiac repair after myocardial infarction. *Cells*. (2020) 9:1984. doi: 10.3390/cells9081894
36. Smith AJ, Keen LJ, Billingham MJ, Perry MJ, Elson CJ, Kirwan JR, et al. Extended haplotypes and linkage disequilibrium in the IL1R1-IL1A-IL1B-IL1RN gene cluster: association with knee osteoarthritis. *Genes Immun.* (2004) 5:451–60. doi: 10.1038/sj.gene.6364107
37. Dinarello CA. The interleukin-1 family: 10 years of discovery. *FASEB J.* (1994) 8:1314–25. doi: 10.1096/fasebj.8.15.8001745
38. Peters VA, Joesting JJ, Freund GG. IL-1 receptor 2 (IL-1R2) and its role in immune regulation. *Brain Behav Immun.* (2013) 32:1–8. doi: 10.1016/j.bbi.2012.11.006
39. Pino-Yanes M, Sánchez-Machín I, Cumplido J, Figueroa J, Torres-Galván MJ, González R, et al. IL-1 receptor-associated kinase 3 gene (IRAK3) variants associate with asthma in a replication study in the Spanish population. *J Allergy Clin Immunol.* (2012) 129:573–5, 575.e571–10. doi: 10.1016/j.jaci.2011.10.001
40. Ge ZW, Wang BC, Hu JL, Sun JJ, Wang S, Chen XJ, et al. IRAK3 gene silencing prevents cardiac rupture and ventricular remodeling through negative regulation of the NF-κB signaling pathway in a mouse model of acute myocardial infarction. *J Cell Physiol.* (2019) 234:11722–33. doi: 10.1002/jcp.27827
41. Falk E. Pathogenesis of atherosclerosis. *J Am Coll Cardiol.* (2006) 47:C7–12. doi: 10.1016/j.jacc.2005.09.068
42. Davì G, Patrono C. Platelet activation and atherothrombosis. *N Engl J Med.* (2007) 357:2482–94. doi: 10.1056/NEJMra071014
43. Carbone F, Nencioni A, Mach F, Vuilleumier N, Montecucco F. Pathophysiological role of neutrophils in acute myocardial infarction. *Thromb Haemost.* (2013) 110:501–14. doi: 10.1160/TH13-03-0211
44. Nahrendorf M, Swirski FK. Regulating repair: regulatory T cells in myocardial infarction. *Circ Res.* (2014) 115:7–9. doi: 10.1161/CIRCRESAHA.114.304295

Conflict of Interest: The authors declare that the research was conducted in the absence of any commercial or financial relationships that could be construed as a potential conflict of interest.

frontiers
in Cardiovascular Medicine

ORIGINAL RESEARCH
published: 19 November 2020
doi: 10.3389/fcvm.2020.598890

Fabrication of New Hybrid Scaffolds for *in vivo* Perivascular Application to Treat Limb Ischemia

Michele Carrabba[1]*, Eva Jover[1], Marco Fagnano[1], Anita C. Thomas[1], Elisa Avolio[1], Thomas Richardson[2], Ben Carter[2], Giovanni Vozzi[3,4], Adam W. Perriman[2] and Paolo Madeddu[1]*

[1] Bristol Medical School, Translational Health Sciences, University of Bristol, Bristol, United Kingdom, [2] School of Cellular and Molecular Medicine, University of Bristol, Bristol, United Kingdom, [3] Research Centre 'E. Piaggio', University of Pisa, Pisa, Italy, [4] Dipartimento di Ingegneria dell'informazione, University of Pisa, Pisa, Italy

Cell therapies are emerging as a new therapeutic frontier for the treatment of ischemic disease. However, femoral occlusions can be challenging environments for effective therapeutic cell delivery. In this study, cell-engineered hybrid scaffolds are implanted around the occluded femoral artery and the therapeutic benefit through the formation of new collateral arteries is investigated. First, it is reported the fabrication of different hybrid "hard-soft" 3D channel-shaped scaffolds comprising either poly(ε-caprolactone) (PCL) or polylactic-co-glycolic acid (PLGA) and electro-spun of gelatin (GL) nanofibers. Both PCL-GL and PLGA-GL scaffolds show anisotropic characteristics in mechanical tests and PLGA displays a greater rigidity and faster degradability in wet conditions. The resulting constructs are engineered using human adventitial pericytes (APCs) and both exhibit excellent biocompatibility. The 3D environment also induces expressional changes in APCs, conferring a more pronounced proangiogenic secretory profile. Bioprinting of alginate-pluronic gel (AG/PL), containing APCs and endothelial cells, completes the hybrid scaffold providing accurate spatial organization of the delivered cells. The scaffolds implantation around the mice occluded femoral artery shows that bioengineered PLGA hybrid scaffold outperforms the PCL counterpart accelerating limb blood flow recovery through the formation arterioles with diameters $>50\,\mu m$, demonstrating the therapeutic potential in stimulating reparative angiogenesis.

Keywords: tissue engineering, angiogenesis, adventitial pericytes, hybrid scaffold, biomaterials, bioprinting, electrospinning

Edited by:
David Wu,
University of Chicago, United States

Reviewed by:
Saskia C. A. De Jager,
Utrecht University, Netherlands
Reto Asmis,
Wake Forest School of Medicine,
United States

***Correspondence:**
Michele Carrabba
mc14021@bristol.ac.uk
Paolo Madeddu
mdprm@bristol.ac.uk

Specialty section:
This article was submitted to Atherosclerosis and Vascular Medicine,
a section of the journal
Frontiers in Cardiovascular Medicine

Received: *25 August 2020*
Accepted: *21 October 2020*
Published: *19 November 2020*

Citation:
Carrabba M, Jover E, Fagnano M, Thomas AC, Avolio E, Richardson T, Carter B, Vozzi G, Perriman AW and Madeddu P (2020) Fabrication of New Hybrid Scaffolds for in vivo Perivascular Application to Treat Limb Ischemia.
Front. Cardiovasc. Med. 7:598890.
doi: 10.3389/fcvm.2020.598890

INTRODUCTION

Acute limb ischemia is the sudden loss of limb perfusion and is typically caused by an occluding embolus, *in situ* formation of a thrombus, trauma, or dissection of a peripheral artery. Chronic total occlusions of the femoral artery and implanted bypass grafts are common in patients with symptomatic peripheral artery disease (PAD). It is estimated more than 200 million people worldwide are affected by PAD (1). Approximately 12–20% of people over the age of 60 develop PAD with many developing critical limb ischemia (CLI), which is associated with a poor quality of life and a high risk of amputation and death (2).

Artery occlusion represents a dramatic event that threatens limb viability and requires urgent evaluation and intervention (3). The early stage of the pathology is usually treated with pharmacological administration, whilst more acute forms of PAD are treated with surgical intervention, via insertion of hydrophilic wires to dissect through the intima or the media layers of the artery (4, 5). However, surgical treatments are subjected to durability issues related to the progression of the underlying pathology and the need for repetitive interventions (6, 7). In addition, in the most severe cases of CLI, patients are not suitable for surgical revascularization due to multiple occlusions and lack of autologous vessel replacement (8).

Approaches based on cell and gene therapy are in development to promote vascular repair and tissue reperfusion, stimulating reparative angiogenesis. Several studies have demonstrated that the transplanted cells performed their therapeutic action by a number of mechanisms including, direct incorporation into the host tissue, (9) activation and recruitment of resident stem cells, (10, 11) and by the release of pro-angiogenic factors, such as growth factors and micro-RNAs, able to activate the re-vascularization process (12–14). In the last few decades, cell-based therapies have led to several promising pre-clinical studies (10, 12, 15) and ultimately, clinical trials using injected bone marrow-derived and peripheral blood-derived hematopoietic cells have shown initial evidence of safety and therapeutic efficacy (7, 16). Despite the promising results, the low efficiency of cell retention in the ischemic area with a significant reduction of stem cells a short time after the injection (17, 18) and consequent reduction of therapeutic action represent the main weaknesses of this approach. Moreover, injected stem cells are prone to accumulation in tissue sinks, such as the lungs, liver and spleen (19).

Many researchers are now focusing on scaffold-based tissue engineering approaches to develop systems to achieve optimal delivery of the cell product to the arterial occlusion. Pericytes, EPCs and mesenchymal stem cells (MSCs) have shown the ability to encourage neovascularization when encapsulated in alginate or arginine-glycine-aspartic acid conjugated alginate micro-particles (13, 20–22). Positive outcomes in ischemic tissue of myocardial infarction were also shown by the use of injectable hydrogels, such as polyethylene-glycol (PEG), fibrin glue, chitosan hydrogel, and dextran-hyaluronic acid hydrogel when combined with BM-derived stem cells and MSCs (23–26). However, approaches involving a large number of synthetic microparticle-bound cells need to achieve a minimum beneficial effect that can disrupt the ischemic region, and lead to adverse clinical outcomes. Moreover, the inability to reproduce a supportive microenvironment with relevant mechanical properties limits the potential for hydrogel-based delivery systems.

Alternative methodologies use “hard” scaffolds as cell carriers, with the advantage of selecting the appropriate design of the structure according to the specific application. Indeed, the scaffold’s material should attempt to match the topographic, mechanical, and bioresorption/remodeling features of the host tissue in order to stimulate the endogenous healing response. This approach offers the potential benefits of stimulating vasculogenesis both by delivering cells and by scaffold action directly (27, 28). Several natural and synthetic polymers have been explored and among those polycaprolactone (PCL) has been widely used. PCL nanofibers conjugated with fibronectin, and PCL 3D printed structures functionalized with gelatin (GL) nanofibers have been used to deliver MSCs (29) and adventitial pericytes (30) to infarcted myocardium and ischemic limb, respectively, to stimulate revascularization. Despite the increasing number of studies focused on using engineered scaffolds to treat ischemic tissues by stimulating spontaneous angiogenesis, the dominant mechanism of action is still largely unknown.

In this study, we show hybrid hard-soft scaffolds, comprised of microfabricated polymeric scaffolds with bioprinted hydrogel seeded with vascular cells, had beneficial pro-angiogenic effects in a murine model of LI. The novel hybrid scaffold, consisting of a 3D printed synthetic polymer [PCL or polylactic-co-glycolic acid (PLGA)] covered by a layer of electrospun GL nanofibers, were fabricated to recapitulate a rudimentary morphology and mechanical environment of the extracellular matrix (ECM) surrounding the femoral artery. In addition, the topography of the scaffold, enhanced by the cell-laden bioprinted gel, provided preferential growth direction for the seeded cells. Adventitial pericytes (APCs) isolated from saphenous veins were selected to functionalize the scaffold due to their ability to promote neovascularization or cell recruitment by secretion of paracrine factors (10, 14, 31). The scaffold was further functionalized with HUVECs to increase the therapeutic effect. Significantly, the cellularized hybrid scaffolds were highly biocompatible and promoted *in vitro* pro-angiogenic responses by the cells, with increased expression of VEGF, ANGPT-1 and FGF observed. The *in vivo* efficacy of this approach was investigated using a mouse model of LI, with the fabricated hybrid scaffolds placed around the occluded femoral artery. Here, the bioengineered PLGA hybrid scaffold outperformed the PCL counterpart by accelerating limb blood flow recovery and increasing the number of functional arterioles which supported scaffold resorption rate over matched mechanical properties as the dominate indicator of scaffold performance.

MATERIALS AND METHODS

Cell Lines and Cultures

Studies using human cells were covered by Research Ethics Committee approvals (06/Q2001/197 and 11/2009) and complied with the principles stated in the 1964 Declaration of Helsinki and later amendments. All the subjects gave informed written consent for the experimental use of donated material (**Supplementary Table 1**). APCs were obtained from saphenous vein leftovers using immunomagnetic beads sorting and an expansion protocol described previously (31). The antigenic phenotype was evaluated by flow cytometry using a FACS Canto II flow cytometer and FACS Diva software (BD Biosciences). A combination of the following antibodies was employed: anti-CD44 (eBioscience), anti-CD-105 (Life Technologies) and anti-CD90 (BD biosciences). The purity of the cell preparation was confirmed, with >95% cells expressing the above markers.

All *in vitro* and *in vivo* experiments were set up with APCs at passage 6. Commercially available human umbilical vein endothelial cells (HUVECs, Lonza cat#: CC-2517, lot:460587) were cultured at 37°C, 20% O_2, 5% CO_2 in complete Endothelial growth medium-2 (EGM-2, PromoCell) and used between passages 5 and 7.

Materials and Reagents

PCL (Mn average 80,000), Pluronic® F-127 (PL), Sodium Alginate (AG) and gelatin from porcine skin (GL) were purchased from Sigma-Aldrich. 50:50 PLGA (Inherent Viscosity = 0.55–075 dL/g) was purchased from DURECT corporation (Cupertino, US). Gelatin crosslinking agent γ-glycidoxypropyltrimethoxysilane (GPTMS) from Sigma-Aldrich. Endothelial basal medium-2 (EBM-2, cat# C-22211, Promocell) was used for *in vitro* specific assays, while complete EGM-2, consisting of EBM-2 supplemented with SupplementPack (cat#: C-39211, PromoCell), was used to culture APCs and HUVECs. Fetal bovine serum (FBS) was obtained from Hyclone (UT, USA). Phosphate buffer saline (PBS), penicillin and streptomycin were purchased from Gibco BRL, Invitrogen Corp., (Carlsbad, CA, USA).

Hybrid Scaffold Preparation

Polymeric Scaffold Fabrication

The hybrid scaffold was fabricated using different techniques which followed a bottom-up approach aiming at mimicking the hierarchical organization of the natural extracellular matrix (ECM).

The fabrication of the scaffold followed the procedure reported in the previous work (30). In brief, the nanoscale structure of natural GL polymer was overlapped to a pre-existing matrix of synthetic material. In this study, PCL and PLGA were used as a synthetic backbone to generate two types of scaffolds with different physical properties. The synthetic matrices were manufactured with a customized piston-driven 3D printing system (MandleMax3, Maker's Tool Works, US) (**Figure 1A**), which allowed the extrusion of PCL and PLGA through a layer-by-layer deposition. PCL 10% (w v^{-1}), and PLGA 15% (w v^{-1}) were dissolved in chloroform, loaded in a glass syringe with a 32 gauge needle and extruded to generate a channel pattern. The channel pattern consisted of the deposition of a first layer with the shape of a grid, to avoid the collapse of the structure, followed by six layers of parallel lines, to form the walls of the channels (**Figure 1B**). A solution of Hydrolene® LTF/K (Ecopol S.p.A., Italy) [4% (w v^{-1}) in distilled water] was used as support material during the extrusion of the polymeric solutions. The composite scaffolds were completed by the electrospinning of GL nanofibers on top of the synthetic structures to improve the biomimetic and adhesive features of the scaffold (**Figure 1C**). After dissolving porcine GL in acetic acid-water solution (ratio of 60:40) at the concentration of 15% (w v^{-1}), the crosslinking agent GPTMS was added at the concentration of 3% (v v^{-1}) and stirred for 1 h before the use of the solution. The GL solution was then electrospun using an Electrospinning Station (Nadetech®, Navarra Spain), setting parameters to the following values: 25 kV (Voltage), 20 cm (distance from the collector) and 0.2 ml h^{-1} (flow rate).

Mechanical Property of the Scaffold

Mechanical characterization of the scaffold was performed using Instron 3343 (©Illinois Tool Works Inc., US). PCL- and PLGA-based scaffolds, fabricated with the dimension of 12 × 12 mm wide specifically for this test, were clamped with pneumatic grips with an initial displacement of 5 mm. The uniaxial test machine was set with a steady deformation speed of [(0.006* l_0) min^{-1}]. Polymeric structures were tested in both axial (x) and longitudinal direction (y). In addition, mechanical properties were further evaluated in relation to the degradation rate. PCL- and PLGA-based scaffolds were conditioned with EBM-2 and incubated at 37°C, mimicking the cell culture environment, and uniaxial tests were performed at specific time-points [0, 2, 4, 7, 10 days ($n = 3$ each time-point)].

Scaffold Cellularization

APC Seeding on Scaffold

PCL- and PLGA-based scaffolds of the dimension of 6 × 6 mm wide was prepared following an established sterilization protocol. Scaffolds underwent sequential washes with 70% ethanol and PBS and then exposed to UV light for 15 min. The polymeric structures were then washed with PBS and conditioned with EGM-2 culture medium for 1 h. APCs, at passage 6, were then seeded at a density of 6,000 cell cm^{-2} onto scaffolds and cultured for 5 days, with medium changed on day 3.

Functional Assays

The cell behavior after seeding and culturing on different polymeric materials was assessed by evaluating density, viability, and proliferation. APCs were labeled with the fluorescent marker 1,1′-dioctadecyl-3,3,3′,3′-tetramethylindocarbocyanine perchlorate (Dil) (Cell-TrackerTM CM-DiI, Molecular Probes, Leiden, Netherlands) and seeded onto the scaffold as described above. After 5 days of incubation, cellularized scaffolds were washed with PBS, fixed with PFA 4%, then counterstained with DAPI, mounted with antifade mounting medium.

The viability of the APCs seeded onto PCL- and PLGA-based scaffold was assessed using the viability/cytotoxicity assay kit (Biotium Inc, US). Five days after seeding, the culture medium was removed, the scaffold washed with PBS and incubated for 30 min with a solution of Calcein [1:2000], EthD-III [1:500] and Hoechst [1:100] in serum-free medium at 37°C, 5% CO^2. Viable cells were identified using fluorescence microscopy. The ability of cells to proliferate once seeded onto scaffolds was evaluated by Click-iT® EdU Assay (Life Technologies, UK). Fluorescent images of the scaffolds were obtained using a Zeiss Fluorescent Microscope (Zeiss Axio observer Z1, Zeiss) and number of cells quantified using Image-Pro Plus software. All the functional assays in this study were performed on three cell lines, in technical triplicates.

Reverse Transcriptase-Polymerase Chain Reaction (RT-PCR)

Total RNA was isolated from APC-bioengineered PCL and PLGA scaffolds by a standardized phenol-chloroform protocol combining QIAzol lysis and miRNeasy mini kit (QIAGEN, Germany), following manufacturer's instructions.

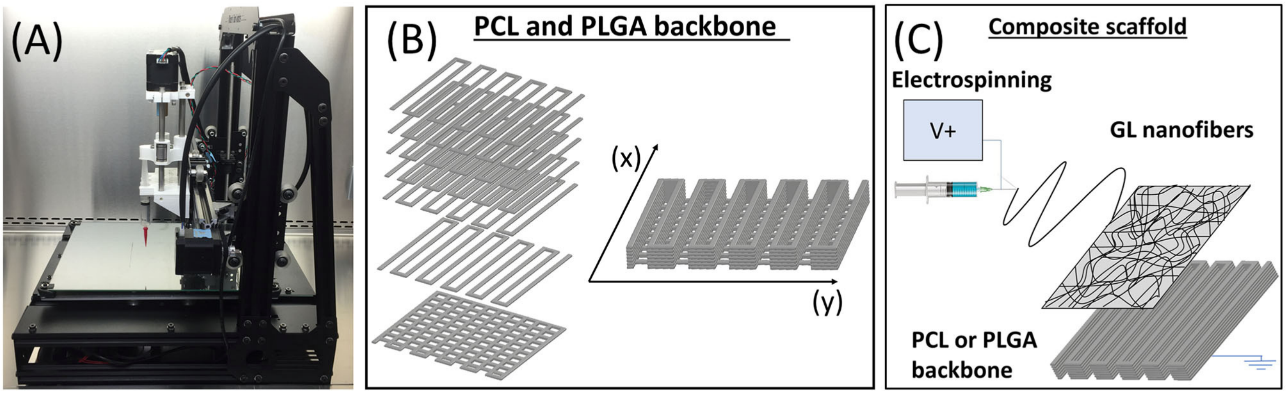

FIGURE 1 | Schematic description of scaffold fabrication process. **(A)** Image of the customized piston-driven 3D printing system (MandleMax3, Maker's Tool Works, US); **(B)** 3D render of the designed pattern for channels structures of poly(ε-caprolactone) (PCL) and polylactic-co-glycolic acid (PLGA), highlighting the piling of various layers and the directions (x) and (y); **(C)** Schematic 3D representation showing the electrospinning of the gelatin (GL) nanofibers on the upper surface of the synthetic backbone of the composite scaffold (PCL or PLGA).

Briefly, PCL- and PLGA-based scaffolds seeded with APCs for 5 days were washed once in PBS to remove non-adhered cells. Scaffolds were then collected from the culture plate, lysed in tubes with 1 ml QIAzol l, and stored on ice. The tubes were centrifuged to separate debris of polymeric structures and the supernatant was transferred to clean tubes. Cell monolayers seeded in culture petri dishes, used as control [hereafter referred to as bi-dimensional (2D) counterparts], were washed with PBS, and incubated with QIAzol; then, cell lysates were collected in tubes. Scaffold derived debris were removed by centrifuging at 10,000 g, 3 min, 4°C before chloroform separation of organic and inorganic phases. Chloroform was added to both cell lysates from scaffolds (3D) and 2D counterparts, followed by centrifugation at 12,000 × g for 15 min at 4°C.

Resulting total RNA was reverse-transcribed into single-stranded cDNA using a High Capacity RNA-to-cDNA Kit (Life Technologies, UK) (100 ng RNA), or using specific Taqman microRNA assay primers with a TaqMan® MicroRNA Reverse Transcription Kit (10 ng) for the assessment of microRNA expression (both from Life Technologies). Quantitative real-time PCR (qPCR) of first-strand cDNA was performed using TaqMan Fast Universal PCR Master Mix or SYBR Green PCR (both from Life Technologies, UK) as appropriate into a QuantStudio 6 Flex (Thermo Fisher Scientific). Targeted genes include markers for apoptosis, angiogenesis, pericyte profile and myofibroblast transformation: *BAX* (Hs00180269_m1), *BCL2* (Hs04986394_s1), *PDGFRB* (Hs01019589_m1), *ANG-1* (Hs00375822_m1), *VEGFA* (hs00900055_m1), *BACH1* (Hs00230917_m1), *FGF* (Hs01092738_m1) (all of them TaqMan® probes, Applied Biosystems); *ACTA2/SMA* (QT00088102, Hs_ACTA2_1_SG), *TGLN/SM22A* (QT00072247, Hs_TAGLN_1_SG), *COL1A1* (QT00037793, Hs_COL1A1_1_SG), *MYOC* (QT00068327, Hs_MYOC_1_SG), and *MYH11* (QT00069391, Hs_MYH11_1_SG) (all of them. QuantiTect Primer Assay-QIAGEN for SYBR Green applications).

MicroRNA profile preservation was additionally assessed with specific miRNA assay probes has-miR-132-3p (assay no. 000457), hsa-miR-532-5p (assay no. 001518), and hsa-miR-210-3p (assay no. 000512). miRNA expression was normalized to U6 snRNA (assay no.001973) (all of them TaqMan® probes, Applied Biosystems).

Relative mRNA expression was calculated using the $2^{-\Delta\Delta ct}$ method (Livack method) and expressed as fold-change compared to 2D control counterparts. All experiments were performed on three biological replicates and assessed in technical triplicates.

Enzyme-Linked Immunosorbent Assays (ELISA)

Cell conditioned media (CCM) from APC-bioengineered scaffolds (3D) or 2D control counterparts was collected and assayed for angiopoietin-1 (ANG-1) and vascular endothelial growth factor-A (VEGFA) using specific sandwich ELISA (DuoSet ELISA, R&D Systems). In brief, after 3 days in culture, EGM-2 growing media was replaced with all control and experimental conditions with fresh growth factor-depleted EBM-2. Cells were kept for 48 h more at 37°C, 5% CO_2, 21% O_2 and CCM were collected and centrifuged at 10,000 g, 3 min, 4°C to remove cell debris. CCMs were kept at −80°C until batch analysis. Data are shown as fold change by comparing to 2D control counterparts to assess for biological significance of our findings and avoid the effect of donor heterogeneity.

Final Hybrid Scaffold Preparation

Hydrogel Preparation: Sodium Alginate/Pluronic Based Gel

AG and PL solutions were produced following the protocol described by Armstrong et al. (32). Briefly, the final hydrogel working solution was produced by combining solutions of PL and AG to achieve a final gel of 13% (w v^{-1}) PL and 6% (w v^{-1}) AG in serum-free DMEM (Gibco Life Technologies™). The gel was then crosslinked with $CaCl_2$ to achieve higher water resistance.

Hydrogel Printing Characterization

Hydrogel printability and biocompatibility were further assessed before the final assembly. The extrusion of the cell-laden hydrogel was also performed with the piston-driven 3D printing system. A pattern of 12 × 12 mm grid was chosen to evaluate the gel printability. Solutions of EBM-2 with $CaCl_2$ at different concentrations were used to assess the shape maintenance of the structures after printing, followed by the analysis of cytotoxicity effect of the crosslinking agent. Both APCs and HUVECs were tested. The cell-laden gel solution of AG/PL gel, [13% (w v^{-1}) PL and 6% (w v^{-1})] with cells were loaded into a 1 ml sterile and disposable syringe, fixed to the bioprinter holder, with subsequent hydrogel printing onto a sterile coverslip. For these tests, cell concentration was fixed at 1 million·ml^{-1}; while, for the final scaffold, concentration was increased up to 4 million·ml^{-1}. The extruded structures were incubated with $CaCl_2$-EBM-2 solutions (5, 10, 20, 30, 50, and 100 mM) for 10 min at 37°C and 5% CO_2 for the first crosslinking phase. The gels were washed with PBS and incubated a second time with 5 mM $CaCl_2$ solution at 37°C and 5% CO_2. After additional 24 h, the $CaCal_2$-medium was changed with complete EGM-2 and incubated for 24 h. At the end of this period, fluorescent images acquired with Zeiss Fluorescent Microscope were used to evaluate the shape of the extruded pattern and viability of cells was assessed using a dedicated kit (Biotium Inc, US). Percentages of viable cells were quantified with Image-Pro Plus.

Cell-Laden Gel Patterning

PCL-based and PLGA-based scaffolds coated with GL nanofibers crosslinked with GPTMS were cellularized with APCs, as described above. After a culture period of 5 days, scaffolds were used as a substrate to extrude a patterned layer of the cell-laden gel. Co-culture of APCs and HUVECs [1:4] was loaded in AG/PL gel [13% (w v^{-1}) PL and 6% (w v^{-1})] with a total cell concentration of 4 million ml^{-1}, gently mixed to homogenize the solution and then transferred into a 5 ml syringe with a 27 gauge needle for the bioprinting process. The cellularized scaffold was quickly placed on the heated plate of the Bioprinter and the extrusion was activated. The cell-laden gel was deposited on the scaffold with the pattern of lines parallel to the (x) direction of the scaffolds. At the end of the extrusion, the scaffold was incubated with 100 mM $CaCl_2$-EBM-2 solution for 10 min. Then, the solution was removed and 5 mM solution of $CaCl_2$-EGM2 (supplemented with 1% penicillin/streptomycin) was added. This established protocol was used to prepare hybrid scaffold (PCL-GL + AG/PL) and PLGA-GL+AG/PL) for *in vivo* implantation.

In vivo Angiogenesis

Animal Model

Experiments involving live animals were performed in accordance with the *Guide for the Care and Use of Laboratory Animals* (The Institute of Laboratory Animal Resources, 1996) under British Home Office PPL 30/3373, after Ethical approval from the University of Bristol. Data were reported according to the ARRIVE guidelines. Male C57Bl/6J mice (8 weeks old; Charles River, UK) underwent unilateral femoral artery ligation under isoflurane anesthesia. The proximal and the distal end of the femoral artery were occluded using 6-0 silk, and the portion of the artery between the ligations was electro-coagulated. Group size was calculated to detect a 20% difference in the primary endpoint between groups with $a = 0.05$ and a power of 80%. Mice were randomly assigned to five experimental groups ($n = 10$ per group) described as follows: group I was given no treatment (vehicle); group II was implanted with PCLGL + AG/PL without cells; group III with PLGA-GL + AG/PL without cells; group IV with PCL-GL + AG/PL with cell; and group V with PLGA-GL + AG/PL with cells. Scaffolds were properly dimensioned in 3 × 3 mm squares for the *in vivo* application. During the implantation procedure, the scaffolds were positioned between the ligations and wrapped around the occluded femoral artery, with the PCL or PLGA in contact with the artery and the gel with or without cells exposed to the perivascular tissues. After being given Vetergesic analgesia, the animals were allowed to recover. The mice were given standard chow and water *ad libitum* and inspected regularly for any change in clinical signs.

The primary endpoints were blood flow recovery and vascular density. The ischemic foot was sequentially monitored by color laser Doppler at 0, 3, 7, 14, and 21 days after induction of ischemia (33). The recovery was assessed by comparing the ratio of flow in the ischemic and contralateral legs. Mice were killed under terminal anesthesia on day 21. The adductor muscles and the perivascular area (including the femoral artery and scaffold) were excised intact, fixed with PFA (4% w v^{-1} in PBS) overnight, and then embedded in optimal cutting temperature (OCT) medium. Samples were sectioned at a thickness of 5–7 μm using a Cryotome (LEICA RM2235, Germany).

Immunohistochemistry Staining

For analysis of vascularization, sections of adductor muscle and the perivascular area were incubated overnight at 4°C with primary α-SMA-Cy3 (c6198, Sigma, UK), to identify VSMCs, and Alexa 488-conjugated isolectin B4 (Life Technologies, UK) to identify ECs. Streptavidin-Alexa 488 secondary antibody. Sections were counterstained with DAPI (30 nM), to identify nuclei, and coverslips mounted using antifade mounting medium.

Statistical Analysis

Continuous variables distribution was assessed by Kolmogorov–Smirnov Z normality test and Shapiro Wilk test and are shown as mean ± standard error of the mean (SEM) or standard deviation (SD) or as median (IQR), depending on the sample distribution. Continuous variables normally distributed were compared using the Student's t-test (two-group comparison) or one-way analysis of variance followed by Tukey PostHoc analysis (ANOVA; for multiple group comparisons), as appropriate. Two-way ANOVA analysis was used to compare the mean differences between groups in the animal model (two categorical and one continuous variable) followed by pair-wise comparison using the Holm-Sidak method. Non-parametric tests, including the Mann–Whitney U test or the Kruskal-Wallis test, were used for

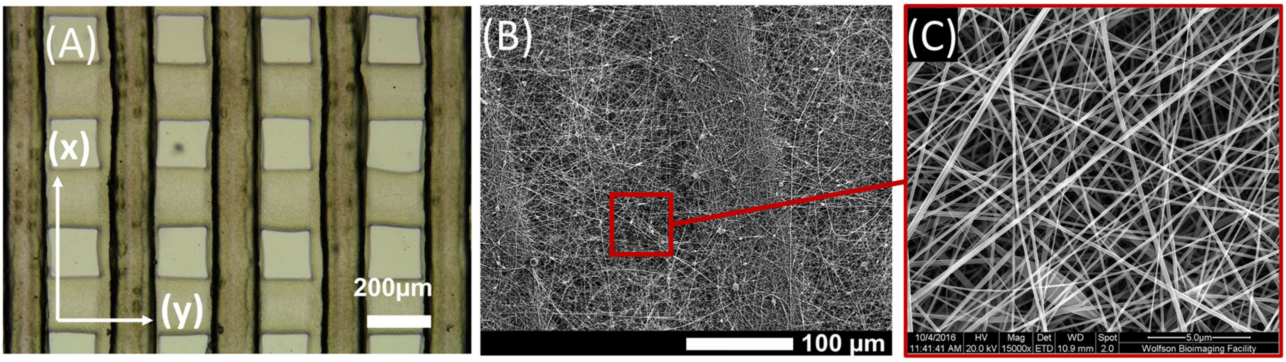

FIGURE 2 | Fabricated multi-material scaffold. **(A)** Representative image of channel structure; **(B)** Representative SEM picture of the composite scaffold formed by gelatin (GL) nanofibers covering polylactic-co-glycolic acid (PLGA) cannels structure; **(C)** Representative SEM picture of the GL nanofibers.

data not normally distributed. A *P*-value < 0.05 was considered statistically significant. Analyses were performed using GraphPad Prism 8.0 statistical software.

RESULTS

Feasibility of Composite Polymeric Scaffold Production

In order to elucidate the *in vitro* and *in vivo* responses to scaffold biomaterials, which differ systematically in mechanical properties and resorption rate, we compared two synthetic polymers, PCL and PLGA. The hybrid hard-soft scaffolds were fabricated using an adaption of a bottom-up approach with the aim being to mimic the hierarchical organization of natural ECM (30). In brief, the nanoscale structure of natural GL polymer was overlapped on a pre-existing matrix of synthetic material. In this study, PCL and PLGA were used as the synthetic backbone to generate two types of scaffolds with different physical properties. The synthetic matrices were manufactured using a customized piston-driven 3D printing system (MandleMax3, Maker's Tool Works, US), which allowed the extrusion of PCL or PLGA via a layer-by-layer deposition.

The customized piston-driven printing system (**Figure 1A**) allowed the extrusion of PCL (10% w v^{-1}) or PLGA (15% w v^{-1}) polymer solutions, following with high resolution the designed pattern of the channel (**Figure 1B**). Assessment by optical microscopy showed the full thickness of the scaffolds was 70 ± 10 μm and line width was 121 ± 15 μm for PCL and 127 ± 23 μm for PLGA, respectively **(Figure 1C)**.

The synthetic backbone of PCL or PLGA was then covered by electrospinning GL nanofibers directly onto the surface (**Figure 2A**). GL nanofibers were then crosslinked with GPTMS 3% (v v^{-1}) to improve durability in wet conditions. The successful assembling of the PCL-GL or PLGA-GL multi-material scaffolds was assessed by SEM (**Figure 2B**). The mat of GL nanofibers was uniformly distributed and adherent to the upper surface of the synthetic materials. Additionally, the GL nanofibers were randomly oriented and had an average diameter of 90 ± 18 nm and a pore size 290 ± 18 nm (**Figure 2C**).

Material Composition Confers Different Mechanical Properties to the Scaffolds

Mechanical tests were performed to evaluate the properties of the different biomaterials, the effect of the geometry and the response to incubation in wet conditions over time. The data from mechanical testing are reported in **Figure 3A** and **Table 1**. Scaffolds made of PCL had different values in the axial direction (*x*) compared with the longitudinal direction (*y*), namely higher values of Young's modulus [(*x*): 5.37 ± 0.37 vs. (*y*): 0.91 ± 0.51 MPa, $P < 0.001$] and maximum stress [(*x*): 0.43 ± 0.12 vs. (*y*): 0.09 ± 0.019 MPa, $P < 0.01$]. PLGA scaffolds followed similar patterns for both Young's modulus [(*x*): 32.86 ± 8.9 vs. (*y*): 7.44 ± 1.14 MPa, $P < 0.01$] and maximum stress [(*x*): 0.77 ± 0.16 vs. (*y*): 0.23 ± 0.07 MPa, $P < 0.01$]. These results indicate the two constructs have anisotropic mechanical characteristics.

Comparing the PLGA and PCL structures, the former had significantly higher values of Young's modulus [(*x*): $P < 0.01$ and (*y*): $P < 0.001$] and maximum stress ($P < 0.05$). Conversely, PCL showed higher values of strain at maximum stress [(*x*): $P < 0.05$ and (*x*): $P < 0.001$] and strain at rupture ($P < 0.01$). This data confirms the higher rigidity of the PLGA structure, as illustrated by the stress-strain curves in **Figure 3B**.

We next assessed the changes in mechanical features during incubation of the structure in EBM-2 for up to 10 days (**Figure 3C**). PCL showed resistance to degradation, its properties remaining steady until the end of the observational period. In contrast, the PLGA structure showed fast degradation, resulting in a drastic decrease of Young's modulus, maximum stress and strain at rupture from day 4 of incubation.

Scaffold Cellularization With APCs and Biocompatibility Assessment

Having achieved a robust production protocol for the PCL-GL and PLGA-GL composite scaffolds, we next performed

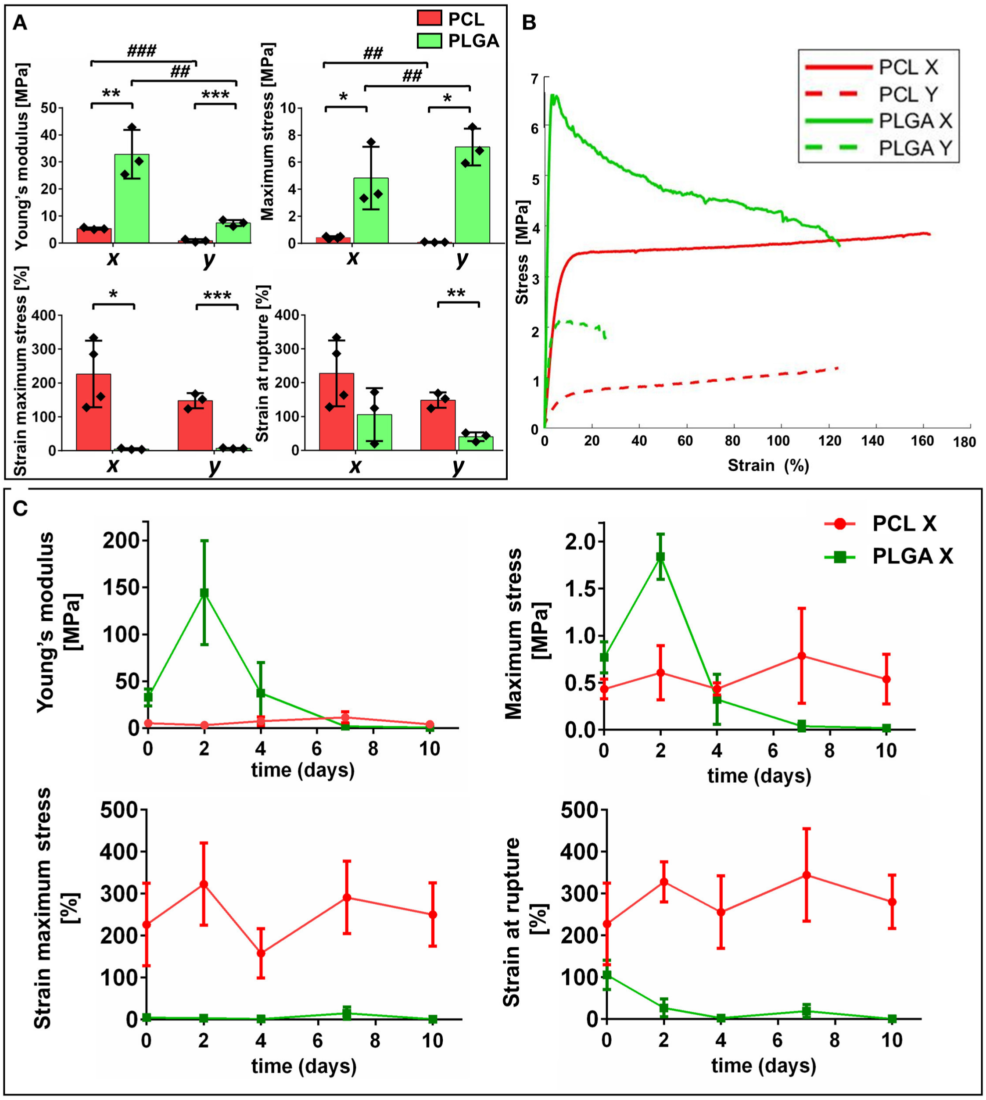

FIGURE 3 | Mechanical characterization of the scaffolds. **(A)** Bar graphs summarize results of mechanical tests on poly(ε-caprolactone) (PCL) and polylactic-co-glycolic acid (PLGA) structures namely: Young's modulus, maximum stress, strain at maximum stress and strain at rupture. Values are means ± SD, $N =$ 3 biological replicates, each one with 3 technical replicates. $^*P < 0.05$, $^{**}P < 0.01$, $^{***}P < 0.001$, vs. PCL-scaffold within same direction of testing [(x) or (y)]; $^{\#\#}P <$ 0.01, $^{\#\#\#}P < 0.001$ vs. the (x) direction of the corresponding group (PCL or PLGA). **(B)** Stress–strain curves of synthetic structures (PCL and PLGA) in both directions (x and y). **(C)** Graphs showing mechanical features of PCL and PLGA scaffolds at different timepoints.

cellularization through two stages. The first stage consisted of APC seeding by pipette deposition onto the scaffold surface, and the evaluation of the *in vitro* interaction of the cells with the different biomaterials (**Figures 4A,B**). Cell monolayers seeded in culture petri dishes were used as control [hereafter referred to as bi-dimensional (2D) counterparts].

Five days after the seeding, cell density, viability and proliferation were evaluated. Overall, the results of the assays indicated good biocompatibility for both the PCL-GL and PLGA-GL scaffolds. Fluorescent microscopy confirmed the homogeneous growth of APCs on the scaffold surfaces, with PCL scaffolds having more adherent cells ($P < 0.05$) (**Figure 4C**) than PLGA scaffolds.

APC viability was high with both materials (90 ± 3% for PLGA and 92 ± 2% for PCL scaffold) (**Figure 4D**). These data were further validated at the molecular level by measuring the mRNA expression of pro-apoptotic *BAX* and pro-survival *BCL2* genes. The APC-bioengineered scaffolds showed a *BAX/BCL2* ratio superior to 2D control counterparts, but the difference did not reach statistical significance (PCL: 2.48 ± 0.58-fold change vs. 2D; PLGA: 1.47 ± 0.19-fold change vs. 2D). Cell proliferation was observed on both PCL and PLGA-based scaffolds, with 61 ± 4% and 56 ± 17% of cells showing Edu-positive nuclei, respectively (**Figure 4E**). Despite a certain degree of directionality given by the macro-domain of the polymeric scaffolds, APCs tended to rearrange in random directions.

TABLE 1 | Mechanical properties of PCL and PLGA scaffold analyzed in both (x) and (y) direction.

	Young's modulus (MPa)	Maximum stress (MPa)	Strain at maximum stress (%)	Strain at failure (%)
PCL Ch-X	5.37 ± 0.40	0.43 ± 0.10	226.5 ± 98.5	230.7 ± 99
PCL Ch-Y	$0.91 \pm 0.51^{\#\#\#}$	$0.09 \pm 0.019^{\#\#}$	147.9 ± 22.3	148 ± 23.6
PLGA Ch-X	$32.86 \pm 8.9^{**}$	$0.77 \pm 0.16^{*}$	$4.82 \pm 2.3^{*}$	105.7 ± 70
PLGA Ch-Y	$7.44 \pm 1.14^{***,\#\#}$	$0.23 \pm 0.07^{*,\#\#}$	$7.13 \pm 1.35^{***}$	$40.4 \pm 13^{**}$

Values are means ± SD, $N = 3$ biological replicates, each one with 3 technical replicates. $^{*}P < 0.05$, $^{**}P < 0.01$, $^{***}P < 0.001$, vs. PCL-scaffold within same direction of testing (Ch-X or Ch-Y); $^{\#\#}P < 0.01$, $^{\#\#\#}P < 0.001$ vs. the Ch-X direction of the corresponding group (PCL or PLGA).

Culture in Scaffolds Modifies the Expressional Profile of APCs

In a parallel experiment, we investigated if PCL-GL or PLGA-GL scaffolds impair the characteristic antigenic and proangiogenic profile of APC. After 5 days of culture on the scaffolds, immunocytochemistry (ICC) was used to show APC protein expression of PDGFR-β, NG2 and vimentin markers (**Figure 5A**). Additionally, RNA was extracted and used to analyze the transcriptional signature of APCs by qPCR, using 2D control counterparts to calculate the relative mRNA expression. *PDGFRB*, a marker shared by pericytes and VSMC, was reduced in 3D conditions (PCL: 0.40 ± 0.16-fold change vs. 2D, $P < 0.05$; PLGA: 0.39 ± 0.15-fold change vs. 2D, $P < 0.05$). The mRNA levels of *ACTA2/SMA* (VSMC and myofibroblast marker), *TGLN/SM22A* (an early marker of smooth muscle differentiation), *COL1A1* (mainly expressed by myofibroblasts and active VSMC) and *MYH11* (a major VSMC contractile protein) were significantly down-regulated, thus suggesting the 3D environment affected the expression of genes that characterize the functional transition of pericytes toward myo-fibroblastic cells (**Figures 5B,C**). No differences were seen with respect to the mRNA expression of transcription factors *GATA4, SOX2,* and *NANOG*, which we have previously shown to be associated with the progenitor-like profile of human APCs (data not shown) (31).

Furthermore, previous studies have shown that APCs express several angiogenesis-related microRNAs (miRs) and transcription factors (34–36). The expression of miR132-3p and miR210-3p was similar in APCs embedded in PCL or PLGA compared to 2D control counterparts. However, miR532-5p was found to be down-regulated in APCs under 3D conditions, showing a significant difference vs. 2D for PLGA-embedded cells ($P < 0.05$) (**Figure 5D**). Expression of *BACH1*, a transcription factor which is a negative regulator of *ANGPT1* and heme-oxygenase-1, was downregulated in APC seeded on both polymers (PCL: 0.39 ± 0.03-fold change vs. 2D, $P < 0.05$; PLGA: 0.52 ± 0.13-fold change vs. 2D, $P < 0.05$) (**Figure 5E**). Interestingly, the three-dimensionality of the scaffold was associated with an increased expression of the arteriogenic factor *FGF* by APCs (PCL $P < 0.001$ vs. 2D and PLGA $P < 0.01$ vs. 2D). Moreover, APCs showed an upregulation of *VEGFA* mRNA in both PCL (3.92 ± 1.16-fold change, $P < 0.05$ vs. 2D) and PLGA scaffolds (3.85 ± 0.57-fold change, $P < 0.01$ vs. 2D). However, *ANGPT1* expression was significantly downregulated in cells seeded on the 3D structures (PCL: 0.44 ± 0.04-fold change vs. 2D, $P < 0.01$; PLGA: 0.45 ± 0.1-fold change vs. 2D, $P < 0.01$).

The expression of VEGFA and ANGPT1 were further verified by assaying the APC-derived secretome (**Figure 5F**). VEGFA was found to be up-regulated in both PCL (4.11 ± 0.53-fold change vs. 2D, $P < 0.01$; or 6.54 ± 1.06-fold change vs. 2D) and PLGA (5.07 ± 0.99-fold change vs. 2D, $P < 0.01$; or 7.33 ± 0.21-fold change vs. 2D). As per the qPCR results, ANGPT1 levels were reduced in PCL (0.36 ± 0.02-fold change vs. 2D, $P < 0.01$) but not in PLGA ($P = 0.441$). Altogether, the data suggest that 3D culture at this timepoint confers APCs with a pro-angiogenic growth profile, where induction cues (FGF/VEGFA) prevail over factors involved in stabilization (ANGPT1).

Characterization of Structure Fidelity of Sodium Alginate-Pluronic Gel and Evaluation of Cell Viability

Having evaluated the behavior of the APCs on the PCL-GL and PLGA-GL scaffolds, the final assembly of the hybrid scaffold consisted of the deposition of lines of gel, as described in **Figures 6A,B**. In fact, data shown above and results from a previous study (30), the polymeric scaffold itself did not ensure an ordered alignment of the cells. The spatial organization of the scaffolds was here enhanced by the deposition of gel with a specific pattern. The pattern of the scaffold improved the directionality of the cellularized structure **(Figures 6C,D)** aiming at promoting cells encapsulation and growth in specific lines.

The hydrogel was formed by a solution of AG due to its high biocompatibility and PL for its increased printability properties. Moreover, PL has the function of sacrificial material, when it is washed out it will generate bigger pores that improve cell interaction properties. AG and PL solutions were produced following the protocol described by Armstrong et al. (32). The final assembly of the hybrid scaffolds consisted of bioprinting the cell-laden gel to a specific pattern on the surface of the APC bioengineered PCL- and PLGA-based structures. The AG/PL gel was produced with a final concentration of 13% (w v^{-1}) PL and 6% (w v^{-1}) AG in serum-free DMEM.

Before incorporation into the final scaffold, the hydrogel underwent further fine-tuning of its properties. First, to improve the durability in wet conditions, the hydrogel was crosslinked with $CaCl_2$ at different concentrations (5, 10, 20, 30, 50, 100 mM) (**Figures 6E–G**). Gel grids (12 × 12 mm) were bioprinted and, after 5 days of incubation in a culture medium, the morphology of the hydrogel structure was evaluated. Immunofluorescence images showed that grids incubated with a concentration of $CaCl_2$ above 20 mM had better structure fidelity and maintained the bioprinted grid shape after 5 days of incubation (**Figures 6H,I**).

Next, we evaluated the possible cytotoxic effect of the crosslinking agent on cells loaded into the AG/PL gel. The analysis of cell viability showed that both APCs and HUVECs maintained viability (around 70%) through increasing

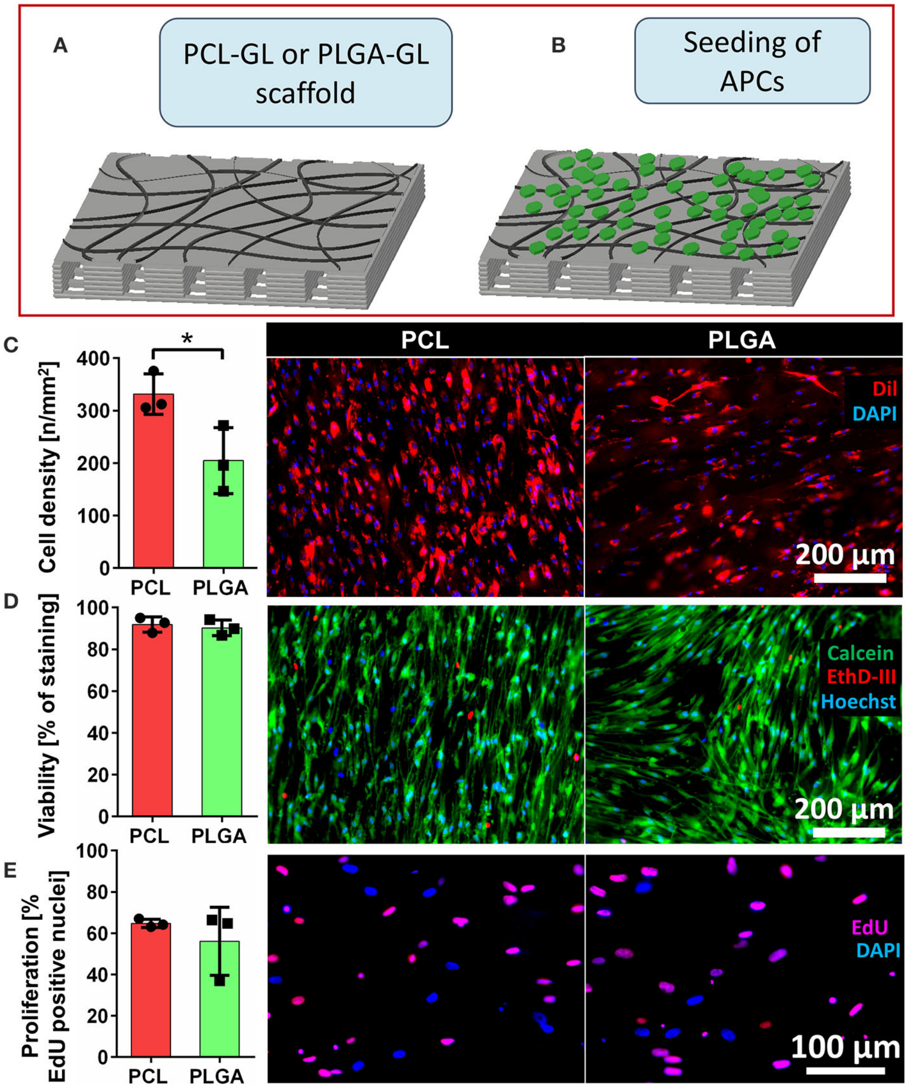

FIGURE 4 | *In vitro* cellularization of scaffolds and functional assessment. **(A,B)** Schematic representation of the Hybrid scaffold preparation following the specific steps: **(A)** step a: fabrication of the composite scaffold formed by poly(ε-caprolactone (PCL) or polylactic-co-glycolic acid (PLGA) and gelatin (GL) nanofibers, named, respectively, PCL-GL and PLGA-GL; **(B)** step b: seeding with adventitial pericytes (APCs) and culturing for 5 days; **(C)** Bar graph of cell density and representative fluorescent microscopy images of PCL and PLGA scaffolds seeded with APCs. Nuclei are stained with DAPI (blue) and cell bodies are labeled with Dil (red). **(D)** Bar graph of cell viability and representative images of APCs: viable cells stained with calcein (green), dead cells with EthD-III (red) and all the nuclei with Hoechst (blue) for assessment of cell viability. **(E)** Bar graph of cell proliferation and representative images of APCs on scaffolds [proliferating cells stained by EdU (pink) and not proliferating ones with DAPI (blue)]. Values are means ± SD, $N = 3$ biological replicates, each one with 3 technical replicates. $^*P < 0.05$, vs. PLGA-scaffold.

concentrations of $CaCl_2$ (**Figure 6J**). We selected 100 mM $CaCl_2$ to use in subsequent studies, as this combined maintenance of scaffold shape with low cytotoxicity.

Final Scaffold Cellularization: *In vitro* Evaluation of the Final Gel-Patterned Hybrid Scaffold Containing APCs and HUVECs Co-culture

The final assembly of the scaffold was performed using an AG/PL bioprinting pattern of a set of parallel lines along the (x) direction of the scaffolds to confer preferential direction of cell growth. The co-culture of APCs-HUVECs was used in the final hybrid scaffold to improve APCs action in promoting angiogenesis once implanted *in vivo*. The AG/PL gel was bioprinted with co-culture of APCs and HUVECs [at 1:4 ratio], with a total concentration of 4 million ml^{-1} cells. The shape gel lines were maintained for 5 days incubation (**Figure 6K**). From the observation of SEM images, the average line width of the extruded gel was 510 ± 33 µm and the adhesion of the AG/PL gel was confirmed (**Figure 6L**). **Figures 6M,N** illustrate higher magnification images of the complete hybrid scaffolds (PCL-GL + AG/PL and PLGA-GL + AG/PL), confirming the high preservation of the bioprinted

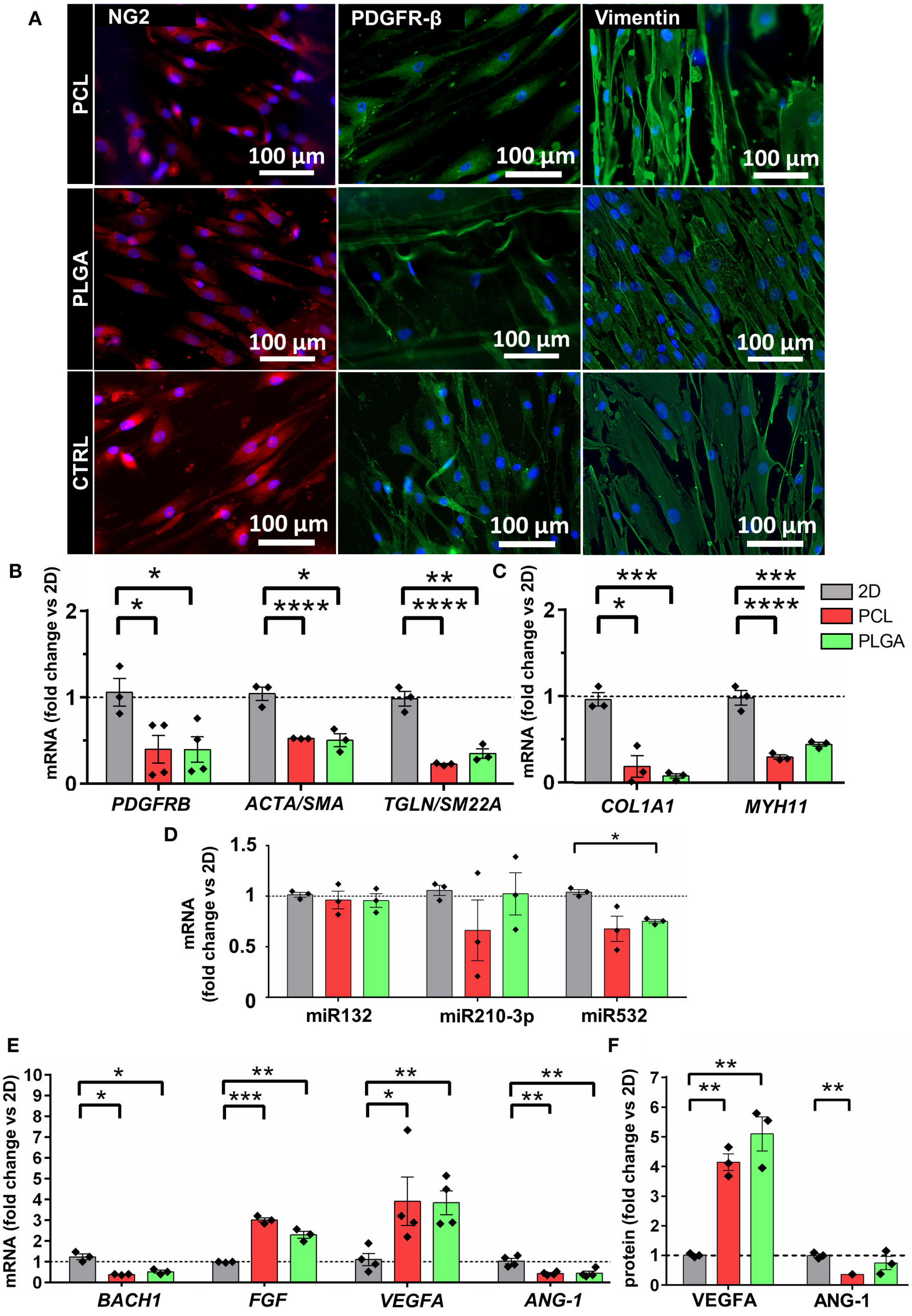

FIGURE 5 | Effect of 3D culture on poly(ε-caprolactone) with gelatin nanofibers (PCL-GL) and polylactic-co-glycolic acid with gelatin nanofibers (PLGA-GL) on APCs. Bar graphs show the average of 3 biological replicates comparing the 3D conditions to the 2D monolayer culture on petri dish. **(A)** Representative fluorescence images of specific phenotype markers (NG2, PDGFR-β and Vimentin) in APCs seeded, respectively, on PCL- and PLGA-based scaffolds; images showed that all the cells were positive for the indicated markers. **(B,C)** Expression of differentiation (PDGFRB, ACTA2/SMA, TGLN/SM22A, COL1A1, and MYH11) molecules. **(D)** Expression of angiogenic miRs: miR132, miR210-3p, and miR532. **(E)** BACH1, FGF, VEGFA, and ANG-1 molecules. **(F)** Bar graph shows the secreted of VEGFA and ANG-1. $^{*}p < 0.05$, $^{**}p < 0.01$, and $^{***}p < 0.001$ vs. 2D. Values are means ± SE, $N = 3$ biological replicates, each one with 3 technical replicates. $^{****}p < 0.0001$.

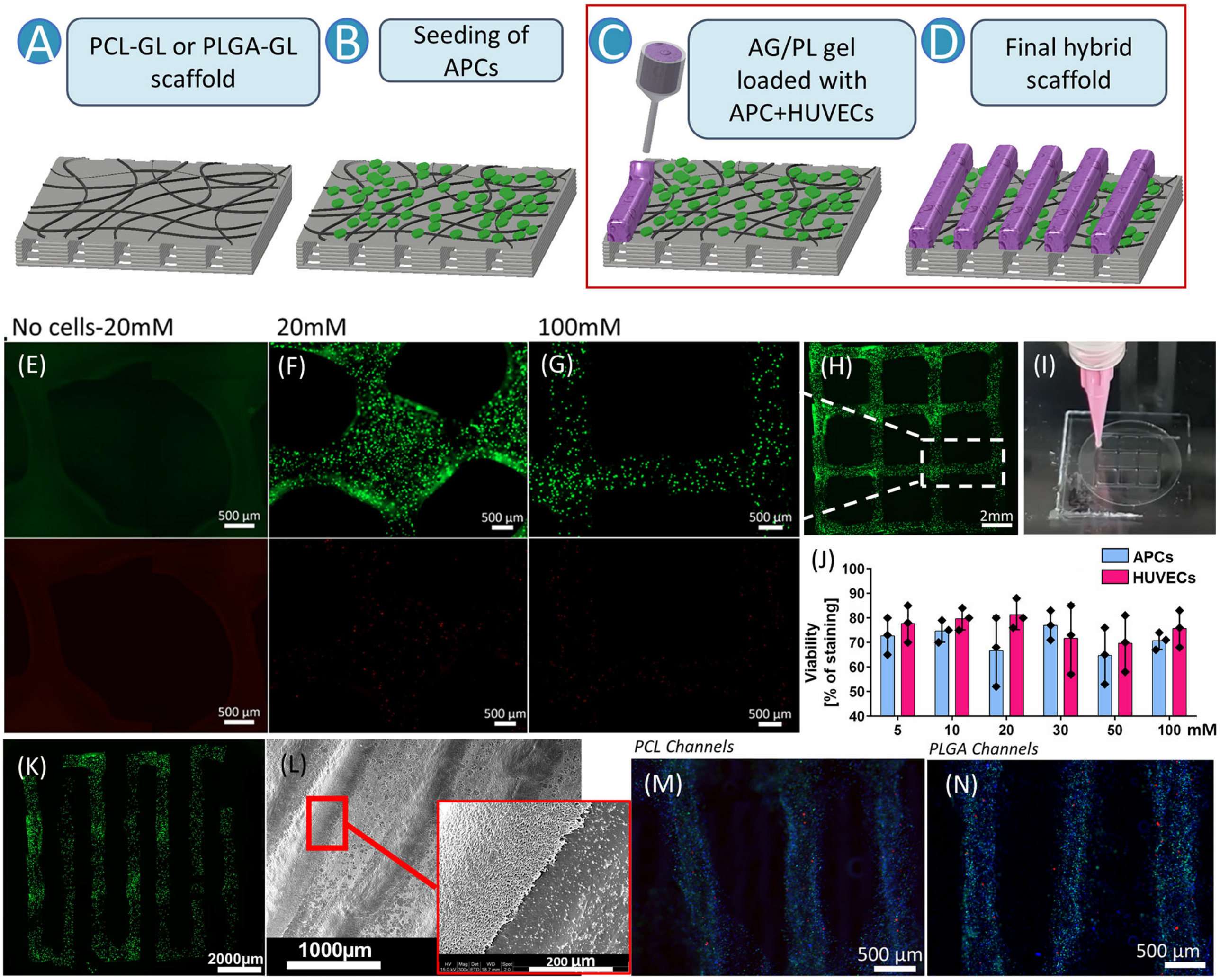

FIGURE 6 | Effect of cross-linking on structure fidelity and cell viability. **(A–D)** Schematic representation of the final hybrid scaffold preparation following the specific steps (**A,B** were already described in **Figure 3**); **(C)** incorporation of APCs-HUVECs coculture in sodium alginate/Pluronic F127 gel (AG/PL); **(D)** hydrogel patterning on the seeded scaffold for the final assembling of the Hybrid scaffold. **(E,G)** show highly magnified fields of control (no cells) **(E)** 20 mM **(F)** and 100 mM **(G)** crosslinked gel; **(E)** shows the absence of unspecific stain in the gel without cells; **(F,G)** show the living cells stained with calcein (Green) while dead cells are stained with EthD-III (red); **(H)** Fluorescent microscopy image of the structure of the bioprinted structure in the shape of a 10 × 10 mm grid; Dotted square shows the magnified filed for **(G)**; **(I)** Picture of the 10 × 10 mm bioprinted grid; **(J)** Bar graph of cell viability of APCs and HUVECs loaded into the AG/PL gel and assessed after the exposure to different concentration of $CaCl_2$. **(K)** Fluorescence image of the bioprinted structure of the final pattern for the hybrid Scaffold composition; **(L)** SEM picture of AG/PL gel printed onto the scaffold; **(M,N)** Representative images of the maintained pattern of the co-culture in the AG/PL gel extruded onto scaffold, after 5 days of incubation. APCs stained with Dil (red), HUVECs with DiO (green) and nuclei of both cell type with DAPI (blue). **(M)** poly(ε-caprolactone) with gelatin nanofibers coated with bioprinted sodium alginate/Pluronic F127 gel (PCL-GL + AG/PL) loaded with HUVECs + APCs; **(N)** polylactic-co-glycolic acid with gelatin nanofibers coated with bioprinted sodium alginate/Pluronic F127 gel (PLGA-GL + AG/PL) loaded with HUVECs + APCs.

morphology. This patterned scaffold prototype was then used in studies evaluating the potential of vascular engineering in a limb ischemia model.

Perivascular Implantation of Cellularized Scaffolds Improves Collateralization and Accelerates Blood Flow Recovery

The revascularization capacity of the hybrid scaffolds was tested in a murine model of LI. **Figures 7A,B** shows the schematic approach of implantation and the anatomical site of LI induction. Five groups were studied: the control group did not receive any treatment, while the experimental groups were implanted with PLGA-GL + AG/PL or PCL-GL + AG/PL, with or without APCs/HUVECs. Analysis of blood flow recovery in the ischemic leg (normalized to contralateral side) showed that all groups reached a similar plateau (**Figure 7C**). However, calculation of the time necessary to reach the maximum recovery showed that the group implanted with cellularized PLGA-AG/PL recovered faster as compared with vehicle (11 vs. 18 days, respectively, *P*

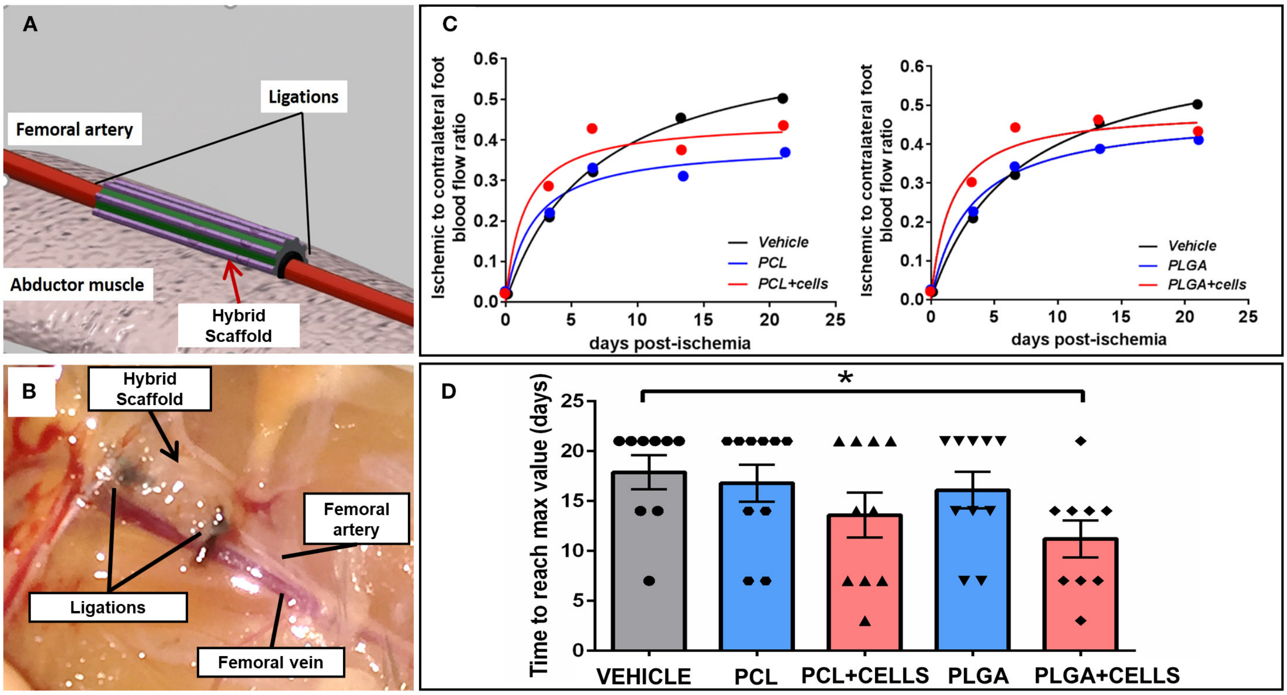

FIGURE 7 | Outcomes of the *in vivo* implantation study. **(A,B)** Schematic representation **(A)** and photograph captured with optical microscopy of hybrid scaffold implantation **(B)**; **(C)** Time course of blood flow recovery expressed as the ratio of ischemic and contralateral limb; ($N = 9$–10 per group); **(D)** Bar graph showing the velocity of blood flow recovery; data expressed as mean ± SE; $N = 9$–10 per group. Groups: (1) Vehicle: induction of unilateral limb ischemia (LI) without treatment; (2) PCL: induction of LI and implantation of PCL-GL + AG/PL without cells; (3) PCL + CELLS: induction of LI and implantation of PLC-GL + AG/PL with cells; (4) PLGA: induction of LI and implantation of PLGA-GL + AG/PL without cells; (5) PLGA + CELLS: induction of LI and implantation of PLGA-GL + AG/PL with cells. $^*p < 0.05$ vs. vehicle.

TABLE 2 | Blood flow recovery.

Group	*n*	Mean	95% CI
Vehicle	9	17.889	13.980–21.789
PCL	10	16.800	12.577–21.023
PCL + cells	10	13.600	8.472–18.728
PLGA	10	16.100	11.977–20.223
PLGA + cells	9	11.222	6.946–15.498

Table showing the time for the groups to reach maximum blood flow recovery. Values are n of replicates per group, mean and the min and max values measured.

= 0.01). Likewise, the comparison between cellularized PLGA-GL + AG/PL and acellular PLGA-GL + AG/PL was also close to statistical significance (11 vs. 16 days, $P = 0.07$) (**Figure 7D** and **Table 2**). The comparison between cellularized PCL-GL + AG/PL and vehicle showed no significant difference in time to recovery (14 vs. 18 days, $P = 0.015$).

Histological analysis of limb muscles revealed there was no difference in capillary density between groups (**Figures 8A,B**). Although the total number of arterioles was not different between groups (**Figure 8C**), narrowing the analysis to the arterioles with a diameter above 50 µm, animals given cellularized PLGA-GL + AG/PL scaffold showed a significant increase in this parameter compared with the vehicle group ($P < 0.05$) or those given cellularized PCL-GL + AG/PL scaffolds ($P < 0.01$) (**Figure 8D**). The increased collateralization induced in the mice with PLGA-GL + AG/PL scaffold may account for the accelerated perfusion recovery observed in the same group (**Figures 8E–I**).

DISCUSSION

A variety of techniques for by-passing total femoral artery occlusions and re-entering the true lumen in the distal artery are available, but few have been tested in randomized trials. The potentiation of collateralization represents a promising approach to provide relief to the ischemic tissue. In the present study, we attempted to achieve this goal through a tissue engineering approach, encompassing several innovative processes. First, we have set up a robust manufacture protocol for the hierarchical production of a hybrid scaffold made of bioprinted PCL and PLGA and electro-spun GL. Second, we verified the optimal combination of synthetic materials and natural products (GL) within the hybrid scaffold. Third, we gathered novel information regarding the ability of the scaffold to direct seeded APCs toward an angiogenic phenotype. Fourth, we succeeded in strengthening the directionality of the bioengineered scaffold by covering the initial layer of APCs with an additional patterned layer of AG/PL gel encapsulating a co-culture of APCs and HUVECs. Fifth,

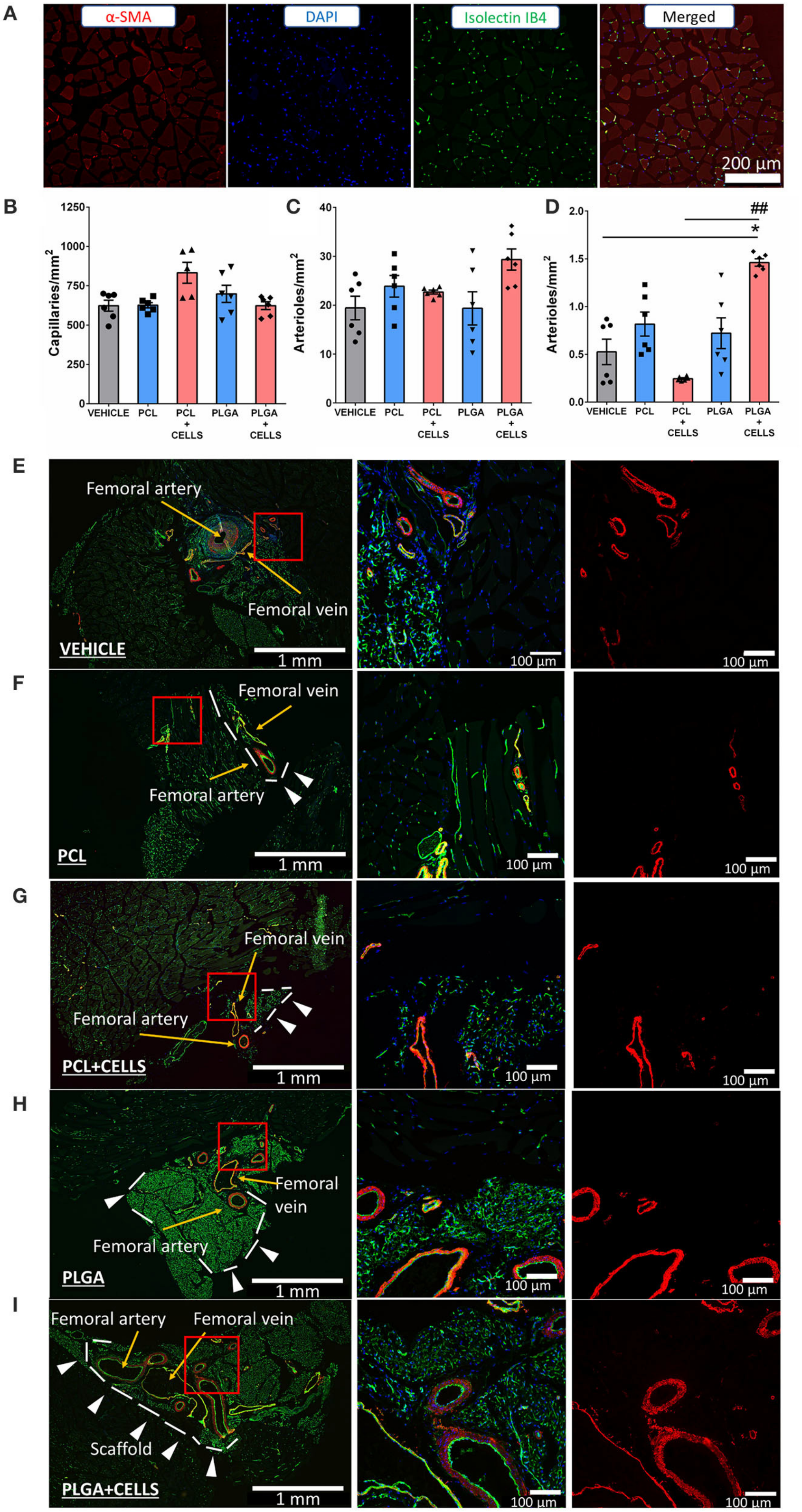

FIGURE 8 | Angiogenesis assessment. **(A)** Representative fluorescent microscopy image of staining used to detect capillaries in the ischemic leg. **(B)** Bar graph showing capillary density; **(C,D)** Bar graphs of arterioles counting in the perivascular area: **(C)** cumulative calculation of arterioles density; **(D)** calculation of arterioles

(Continued)

FIGURE 8 | with diameter >50 µm; **(E–I)** Representative images of perivascular area of the various groups: Vehicle group **(E)**, PCL **(F)**, PCL + CELLS **(G)**, PLGA **(H)** and finally PLGA + CELLS group **(I)**. White arrows indicate the scaffold. Yellow arrows indicate arterioles. $^*P < 0.05$ vs. vehicle. $^{\#\#}P < 0.01$ vs. PCL-AG/PL without cells; data expressed in mean ± SE; N = 6 per group. Groups: (1) Vehicle: induction of unilateral limb ischemia (LI) without treatment; (2) PCL: induction of LI and implantation of PCL-GL + AG/PL without cells; (3) PCL + CELLS: induction of LI and implantation of PLC-GL + AG/PL with cells; (4) PLGA: induction of LI and implantation of PLGA-GL + AG/PL without cells; (5) PLGA + CELLS: induction of LI and implantation of PLGA-GL+AG/PL with cells.

comparing two material formulations, with or without cells, in a murine model of femoral artery occlusion, we documented the superiority of cellularized PLGA-GL + AG/PL scaffolds in stimulating large arterioles formation around the blocked artery and encouraging faster blood flow recovery.

In a previous study, we set up an integrated manufacture protocol using a computer-assisted writing system to generate 3D scaffolds with woodpile or channel patterns and electrospinning to deposit GL nanofibers onto the synthetic backbone. The structure was then engineered with human APCs to confer characteristics of a living material capable of supporting revascularization after perivascular implantation (30). Here, the successful approach was refined and extended, employing two synthetic materials, PCL and PLGA, as a backbone substrate. To achieve this goal, a piston-driven bioprinting system was employed; with results demonstrating versatility of the technique in achieving high-resolution and consistent geometry features (line width and thickness) for both PCL and PLGA synthetic matrices. We focused on a channel design because this patterning is the most appropriate to encourage alignment of new arterioles in limb muscles (30) and myocardial tissues (37–39).

Owing to differences in physical properties and biocompatibility, the choice of synthetic material is crucial for the success of medical scaffolds (40). Mechanical tests confirmed the anisotropy of the channel structures made of PCL and PLGA, confirming the more rigid behavior of the latter in line with previous literature (41, 42). Moreover, PCL maintained its stability over time, confirming the typical slow degradation rate in wet conditions; while PLGA revealed a more rapid decrease in both Young's Modulus and strain at rupture, which denotes greater fragility of the material.

Like ECM, scaffold micro- and nano-scale morphology (43) and biochemical cues can impact cell behavior (44, 45). Previous studies have explored the fabrication of composite scaffolds combining different manufacturing systems with promising results. This included rapid prototyping microfabrication techniques, like 3D printing, fusion deposition modeling and solid free form deposition, in combination with electrospinning to generate composite scaffolds (46, 47). In another study, electrohydrodynamic direct-jet was used to deposit microfibrous bundles of collagen-I in order to improve cell adhesion (48). The message from these studies was that composite scaffolds are better than scaffolds made of a single material in supporting cell viability. For this reason, and following on from our previous study (30), we improved our scaffolds by applying a layer of GL nanofibers using the electrospinning technique, so as to enhance the adhesion features of the synthetic backbone.

APCs are considered progenitors of different mesenchymal cell lines. Antigenic and expressional characterization of APCs demonstrated that these cells maintained their pericyte-like phenotype when seeded on 3D structures, as demonstrated by the expression of several transcription factors associated with stemness. This, together with the observed downregulation of fibroblastic markers, suggests that the 3D environment does not promote APC differentiation. Functional assays demonstrated an overall excellent biocompatibility of the studied materials. PCL- and PLGA-based scaffolds showed a similar capacity to support the viability of seeded APCs. Nonetheless, a molecular readout of apoptosis, the BAX/BLC2 ratio, was almost 2-fold higher in APCs seeded on PCL compared with APCs on PLGA, suggesting that the latter has superior biocompatibility. On the other hand, the PCL-based scaffolds improved cell adherence, which is compatible with PCL having mechanical properties closer to natural soft tissues (40). Previous studies showed that cell proliferation is greater on PCL than PLGA, due to the difference in stiffness of the two materials (40, 49, 50). We could not detect any difference in APC proliferation, possibly because of the presence of nanofibrous GL, which acts like a biomimetic substrate for growing cells.

Our previous transplantation study showed the complexity of molecular pathways implicated in APC-induced activation of neovascularization in a model of femoral artery occlusion (51). Here, we show that the APC proangiogenic profile is remarkably modified by the culture in a 3D environment, resulting in the induction of angiogenic (VEGFA) and arteriogenic (FGF) signaling. This expressional change could be advantageous in conditions requiring the formation of collateral vessels. It should be noted that *VEGFA* mRNA levels and VEGFA secretion in conditioned media showed similar increases in both cellularized 3D PLGA and PCL scaffolds compared with 2D control counterparts (from 4 to 6-fold, respectively). Meanwhile, ANGPT1 expression in conditioned media was downregulated in the 3D transition of PCL but not of PLGA. ANGPT1 is an oligomeric secreted glycoprotein that plays a key role in the organization and maturation of newly formed vessels, promoting the quiescence and structural integrity of adult vasculature (52).

A key advancement of this study is the use of a piston-driven bioprinting system to extrude a cell-laden gel containing a mixture of APCs and ECs onto the scaffold. Bioprinted AG/PL gel had less line width resolution when compared with the bioprinted synthetic polymer (PCL and PLGA). Nevertheless, the method was highly reproducible in depositing a series of parallel lines. The AG/PL gel lines would ideally synergize with the geometry of the PCL- and PLGA-GL channels in directing arterial collaterals in a parallel direction to the occluded femoral artery.

In the present study, we used two vascular cell populations to encourage collateralization, incorporating APCs in the initial layers and APCs and ECs into the patterned AG/PL gel. The advantage of combinatory administration is highlighted by previous successful studies using human MSCs and cardiac tissue-derived stem cells (CSCs) in a pig model of MI; with the combination showing superior results compared with a single cell population (53). Similarly, we have previously demonstrated that *in vivo* co-delivery of human CSCs and APCs reduced the infarct size and promoted vascular proliferation in a murine myocardial infarction model (10). One limitation of this study is the use of HUVECs instead of arterial ECs. However, this was proof of principle study, and specific EC populations could be used according to the implantation site.

After arterial occlusion, tissue recovery occurs through the opening of pre-existing collaterals and formation of new perivascular arterioles. Moreover, hypoxia induces the formation of new muscular capillaries. Results of hemodynamic and histologic analyses indicate the superiority of PLGA scaffolds in accelerating reperfusion and promoting the perivascular formation of arterioles with a diameter above 50 µm. Characteristics of the bio-engineered material and host response to the implant were identified as major players in regenerative processes activated by hybrid scaffolds.

The balance between mechanical stability and biodegradability play key roles in the design of successful therapies. Despite the PCL scaffolds having a better match of mechanical properties with the target tissue, the rate of degradation of the scaffold should be comparable to the growth of natural tissue (54). Here PLGA was demonstrated to have a much faster degradability, with a decay rate within our window of observation of 21 days. PLGA, also reportedly causes inflammation and robust angiogenesis (27), in contrast to the absence of inflammation and poor vascularization observed after the implantation of polyurethane and collagen-chitosan-hydroxyapatite (55). In addition, both PCL- and PLGA-based scaffold showed upregulation of pro-angiogenic factors, but the secretion of ANGPT1 was downregulated only in PCL scaffolds, possibly reflecting the lack of functional collateralization.

CONCLUSION

Results of the present study represent an important step toward the clinical use of perivascular biomaterials for the revascularization around occluded limb arteries. Patients with diabetic vascular disease extending to regions below the knee could take advantage of this technique. We used xenogeneic human cells in immunocompetent mice to confirm the therapeutic efficacy of APCs in the absence of immunosuppression. This provides a scope for the use of allogeneic APCs in clinical trials. Furthermore, we have already upgraded the APC production using clinical-grade reagents, an important step forward clinical translation. However, additional improvements are necessary for scaling-up cell production and for integrating scaffold manufacture and bioengineering into a single process.

DATA AVAILABILITY STATEMENT

The raw data supporting the conclusions of this article will be made available by the authors, without undue reservation.

ETHICS STATEMENT

The animal study was reviewed and approved by Guide for 307 the Care and Use of Laboratory Animals (The Institute of Laboratory Animal Resources, 1996) 308 under British Home Office PPL 30/3373.

AUTHOR CONTRIBUTIONS

PM and MC contributed to the development of the intellectual design of the project. MC designed and performed the main stages of the *in vitro* work. EJ, MF, TR, and BC contributed to the *in vitro* development of the research with different proportions. AT and MC designed the *in vivo* study and AT performed the animal work. AP and GV provided technical and intellectual support to the project. All authors contributed to manuscript revisions and read and approved the submitted version.

FUNDING

This work was funded by BHF Ph.D. studentship (FS/15/7/31307) and BHF project grant (PG/18/38/33707). In addition, the research was also supported by a grant from the NIHR Biomedical Research Centre at University Hospitals Bristol NHS Foundation Trust and the University of Bristol. Collection of patient samples was supported by research nurses and administrators from the NIHR Biomedical Research Centre at University Hospitals Bristol NHS Foundation Trust and the University of Bristol.

SUPPLEMENTARY MATERIAL

The Supplementary Material for this article can be found online at: https://www.frontiersin.org/articles/10.3389/fcvm.2020.598890/full#supplementary-material

REFERENCES

1. Marrett E, DiBonaventura MD, Zhang Q. Burden of peripheral arterial disease in Europe and the United States: a patient survey. *Health Qual Life Outcomes.* (2013) 11:1–8. doi: 10.1186/1477-7525-11-175
2. Townsend N, Bhatnagar P, Wilkins E, Wickramasinghe K, Rayner M. *Cardiovascular Disease Statistics 2015.* London: British Heart Foundation (2015).
3. Kinlay S. Management of critical limb ischemia. *Circ Cardiovasc Interv.* (2016) 9:1–10. doi: 10.1161/CIRCINTERVENTIONS.115.001946
4. Thukkani AK, Kinlay S. Endovascular intervention for peripheral artery disease. *Circ Res.* (2015) 116:1599–613. doi: 10.1161/CIRCRESAHA.116.303503
5. Ambler GK, Radwan R, Hayes PD, Twine CP. Atherectomy for peripheral arterial disease. *Cochrane Libr.* (2014) 1–35. doi: 10.1002/14651858.CD006680.pub2

6. Oresanya L, Makam AN, Belkin M, Moneta GL, Conte MS. Factors associated with primary vein graft occlusion in a multicenter trial with mandated ultrasound surveillance. *J Vasc Surg.* (2014) 59:996–1002. doi: 10.1016/j.jvs.2013.10.096
7. Swaminathan A, Vemulapalli S, Patel MR, Jones WS. Lower extremity amputation in peripheral artery disease: improving patient outcomes. *Vasc Health Risk Manag.* (2014) 10:417–24. doi: 10.2147/VHRM.S50588
8. Norgren L, Hiatt WR, Dormandy JA, Nehler MR, Harris KA, Fowkes FGR. Inter-society consensus for the management of peripheral arterial disease (TASC II). *J Vasc Surg.* (2007) 45:S5–67. doi: 10.1016/j.jvs.2006.12.037
9. Pittenger MF, Martin BJ. Mesenchymal stem cells and their potential as cardiac therapeutics. *Circ Res.* (2004) 95:9–20. doi: 10.1161/01.RES.0000135902.99383.6f
10. Avolio E, Meloni M, Spencer HL, Riu F, Katare R, Mangialardi G. Combined intramyocardial delivery of human pericytes and cardiac stem cells additively improves the healing of mouse infarcted hearts through stimulation of vascular and muscular repair. *Circ Res.* (2015) 116:e81–94. doi: 10.1161/CIRCRESAHA.115.306146
11. Slater SC, Carrabba M, Madeddu P. Vascular stem cells—potential for clinical application. *Br Med Bull.* (2016) 118:127–37. doi: 10.1093/bmb/ldw017
12. Gnecchi M, He H, Liang OD, Melo LG, Morello F, Mu H. Paracrine action accounts for marked protection of ischemic heart by Akt-modified mesenchymal stem cells. *Nat Med.* (2005) 11:367. doi: 10.1038/nm0405-367
13. Katare R, Riu F, Rowlinson J, Lewis A, Holden R, Meloni M. Perivascular delivery of encapsulated mesenchymal stem cells improves postischemic angiogenesis via paracrine activation of VEGF-A. *Arterioscler Thromb Vasc Biol.* (2013) 33:1872–80. doi: 10.1161/ATVBAHA.113.301217
14. Katare R, Riu F, Mitchell K, Gubernator M, Campagnolo P. Transplantation of human pericyte progenitor cells improves the repair of infarcted heart through activation of an angiogenic program involving micro-RNA-132. *Circ Res.* (2011) 109:894–906. doi: 10.1161/CIRCRESAHA.111.251546
15. Tao B, Cui M, Wang C, Ma S, Wu F, Yi F. Percutaneous intramyocardial delivery of mesenchymal stem cells induces superior improvement in regional left ventricular function compared with bone marrow mononuclear cells in porcine myocardial infarcted heart. *Theranostics.* (2015) 5:196–205. doi: 10.7150/thno.7976
16. Qadura M, Terenzi DC, Verma S, Al-Omran M, Hess DA. Concise review: cell therapy for critical limb ischemia: an integrated review of preclinical and clinical studies. *Stem Cells.* (2018) 36:161–71. doi: 10.1002/stem.2751
17. Li S-H, Lai TYY, Sun Z, Han M, Moriyama E, Wilson B. Tracking cardiac engraftment and distribution of implanted bone marrow cells: comparing intra-aortic, intravenous, and intramyocardial delivery. *J Thorac Cardiovasc Surg.* (2009) 137:1225–33.e1. doi: 10.1016/j.jtcvs.2008.11.001
18. Sheikh YA, Huber CB, Narsinh HK, Spin MJ, Van der Bogt K, de Almeida EP. *In vivo* functional and transcriptional profiling of bone marrow stem cells after transplantation into ischemic myocardium. *Arterioscler Thromb Vasc Biol.* (2012) 32:92–102. doi: 10.1161/ATVBAHA.111.238618
19. Yan J, Tie G, Xu TY, Cecchini K, Messina LM. Mesenchymal stem cells as a treatment for peripheral arterial disease: current status and potential impact of type II diabetes on their therapeutic efficacy. *Stem Cell Rev Rep.* (2013) 9:360–72. doi: 10.1007/s12015-013-9433-8
20. Andrejecsk JW, Cui J, Chang WG, Devalliere J, Pober JS, Saltzman WM. Paracrine exchanges of molecular signals between alginate-encapsulated pericytes and freely suspended endothelial cells within a 3D protein gel. *Biomaterials.* (2013) 34:8899–908. doi: 10.1016/j.biomaterials.2013.08.008
21. Kim P-H, Yim H-G, Choi Y-J, Kang B-J, Kim J, Kwon S-M. Injectable multifunctional microgel encapsulating outgrowth endothelial cells and growth factors for enhanced neovascularization. *J Control Release.* (2014) 187:1–13. doi: 10.1016/j.jconrel.2014.05.010
22. Houtgraaf HJ, de Jong R, Kazemi K, de Groot D, van der Spoel TIG, Arslan F. Intracoronary infusion of allogeneic mesenchymal precursor cells directly after experimental acute myocardial infarction reduces infarct size, abrogates adverse remodeling, and improves cardiac function. *Circ Res.* (2013) 113:153–66. doi: 10.1161/CIRCRESAHA.112.300730
23. Wang T, Jiang X-J, Tang Q-Z, Li X-Y, Lin T, Wu D-Q. Bone marrow stem cells implantation with α-cyclodextrin/MPEG–PCL–MPEG hydrogel improves cardiac function after myocardial infarction. *Acta Biomater.* (2009) 5:2939–44. doi: 10.1016/j.actbio.2009.04.040
24. Nakamuta JS, Danoviz ME, Marques FLN, dos Santos L, Becker C, Gonçalves GA. Cell therapy attenuates cardiac dysfunction post myocardial infarction: effect of timing, routes of injection and a fibrin scaffold. *PLoS ONE.* (2009) 4:e6005. doi: 10.1371/journal.pone.0006005
25. Lu W-N, Lü S-H, Wang H-B, Li D-X, Duan C-M, Liu Z-Q. Functional improvement of infarcted heart by co-injection of embryonic stem cells with temperature-responsive chitosan hydrogel. *Tissue Eng Part A.* (2008) 15:1437–47. doi: 10.1089/ten.tea.2008.0143
26. Portalska KJ, Teixeira LM, Leijten JCH, Jin R, van Blitterswijk C, de Boer J. Boosting angiogenesis and functional vascularization in injectable dextran–hyaluronic acid hydrogels by endothelial-like mesenchymal stromal cells. *Tissue Eng Part A.* (2013) 20:819–29. doi: 10.1089/ten.tea.2013.0280
27. Rücker M, Laschke MW, Junker D, Carvalho C, Schramm A, Mülhaupt R. Angiogenic and inflammatory response to biodegradable scaffolds in dorsal skinfold chambers of mice. *Biomaterials.* (2006) 27:5027–38. doi: 10.1016/j.biomaterials.2006.05.033
28. Hendow EK, Moazen M, Iacoviello F, Bozec L, Pellet-Many C, Day RM. Microporous biodegradable films promote therapeutic angiogenesis. *Adv Healthc Mater.* (2020) 9:2000806. doi: 10.1002/adhm.202000806
29. Kang B-J, Kim H, Lee SK, Kim J, Shen Y, Jung S. Umbilical-cord-blood-derived mesenchymal stem cells seeded onto fibronectin-immobilized polycaprolactone nanofiber improve cardiac function. *Acta Biomater.* (2014) 10:3007–17. doi: 10.1016/j.actbio.2014.03.013
30. Carrabba M, De Maria C, Oikawa A, Reni C, Rodriguez-Arabaolaza I, Spencer H. Design, fabrication and perivascular implantation of bioactive scaffolds engineered with human adventitial progenitor cells for stimulation of arteriogenesis in peripheral ischemia. *Biofabrication.* (2016) 8:15020. doi: 10.1088/1758-5090/8/1/015020
31. Campagnolo P, Cesselli D, Al Haj Zen A, Beltrami AP, Kränkel N, Katare R. Human adult vena saphena contains perivascular progenitor cells endowed with clonogenic and proangiogenic potential. *Circulation.* (2010) 121:1735–45. doi: 10.1161/CIRCULATIONAHA.109.899252
32. Armstrong JPK, Burke M, Carter BM, Davis SA, Perriman AW. 3D bioprinting using a templated porous bioink. *Adv Healthc Mater.* (2016) 5:1724–30. doi: 10.1002/adhm.201600022
33. Spencer HL, Jover E, Cathery W, Avolio E, Rodriguez-Arabaolaza I, Thomas AC. Role of TPBG (trophoblast glycoprotein) antigen in human pericyte migratory and angiogenic activity. *Arterioscler Thromb Vasc Biol.* (2019) 39:1113–24. doi: 10.1161/ATVBAHA.119.312665
34. Katare RG, Madeddu P. Pericytes from human veins for treatment of myocardial ischemia. *Trends Cardiovasc Med.* (2013) 23:66–70. doi: 10.1016/j.tcm.2012.09.002
35. Cathery W, Faulkner A, Maselli D, Madeddu P. Concise review: the regenerative journey of pericytes toward clinical translation. *Stem Cells.* (2018) 36:1295–310. doi: 10.1002/stem.2846
36. Slater SC, Jover E, Martello A, Mitić T, Rodriguez-Arabaolaza I, Vono R. MicroRNA-532-5p regulates pericyte function by targeting the transcription regulator BACH1 and angiopoietin-1. *Mol Ther.* (2018) 26:1–15. doi: 10.1016/j.ymthe.2018.08.020
37. Zimmermann W, Melnychenko I, Wasmeier G, Didie M, Nixdorff U, Hess A. Engineered heart tissue grafts improve systolic and diastolic function in infarcted rat hearts. *Nat Med.* (2006) 12:452–8. doi: 10.1038/nm1394
38. Engelmayr GC, Papworth GD, Watkins SC, Mayer JE, Sacks MS. Guidance of engineered tissue collagen orientation by large-scale scaffold microstructures. *J Biomech.* (2006) 39:1819–31. doi: 10.1016/j.jbiomech.2005.05.020
39. Freed LE, Engelmayr GC, Borenstein JT, Moutos FT, Guilak F. Advanced material strategies for tissue engineering scaffolds. *Adv Mater.* (2009) 21:3410–8. doi: 10.1002/adma.200900303
40. Rohman G, Pettit JJ, Cameron NR, Southgate J. Influence of the physical properties of two-dimensional polyester substrates on the growth of normal human urothelial and urinary smooth muscle cells *in vitro*. *Biomaterials.* (2007) 28:2264–74. doi: 10.1016/j.biomaterials.2007.01.032
41. Middleton JC, Tipton AJ. Synthetic biodegradable polymers as orthopedic devices. *Biomaterials.* (2000) 21:2335–46. doi: 10.1016/S0142-9612(00)00101-0

42. Sung HJ, Meredith C, Johnson C, Galis ZS. The effect of scaffold degradation rate on three-dimensional cell growth and angiogenesis. *Biomaterials.* (2004) 25:5735–42. doi: 10.1016/j.biomaterials.2004.01.066
43. Jeon HJ, Simon CG, Kim GH. A mini-review: cell response to microscale, nanoscale, and hierarchical patterning of surface structure. *J Biomed Mater Res Part B Appl Biomater.* (2014) 102:1580–94. doi: 10.1002/jbm.b.33158
44. Battista S, Guarnieri D, Borselli C, Zeppetelli S, Borzacchiello A, Mayol L. The effect of matrix composition of 3D constructs on embryonic stem cell differentiation. *Biomaterials.* (2005) 26:6194–207. doi: 10.1016/j.biomaterials.2005.04.003
45. Owen SC, Shoichet MS. Design of three-dimensional biomimetic scaffolds. *J Biomed Mater Res A.* (2010) 94:1321–31. doi: 10.1002/jbm.a.32834
46. Kim GH, Son JG, Park S, Kim WD. Hybrid process for fabricating 3D hierarchical scaffolds combining rapid prototyping and electrospinning. *Macromol Rapid Commun.* (2008) 29:1577–81. doi: 10.1002/marc.200800277
47. Yoon H, Ahn SH, Kim GH. Three-dimensional polycaprolactone hierarchical scaffolds supplemented with natural biomaterials to enhance mesenchymal stem cell proliferation. *Macromol Rapid Commun.* (2009) 30:1632–7. doi: 10.1002/marc.200900264
48. Yang GH, Kim M, Kim GT. A hybrid PCL/collagen scaffold consisting of solid freeform-fabricated struts and EHD-direct-jet-processed fibrous threads for tissue regeneration. *J Colloid Interface Sci.* (2015) 450:159–67. doi: 10.1016/j.jcis.2015.02.070
49. Baker SC, Rohman G, Southgate J, Cameron NR. The relationship between the mechanical properties and cell behaviour on PLGA and PCL scaffolds for bladder tissue engineering. *Biomaterials.* (2009) 30:1321–8. doi: 10.1016/j.biomaterials.2008.11.033
50. Tan PS, Teoh SH. Effect of stiffness of polycaprolactone (PCL) membrane on cell proliferation. *Mater Sci Eng C.* (2007) 27:304–8. doi: 10.1016/j.msec.2006.03.010
51. Gubernator M, Slater SC, Spencer HL, Spiteri I, Sottoriva A, Riu F. Epigenetic profile of human adventitial progenitor cells correlates with therapeutic outcomes in a mouse model of limb ischemia. *Arterioscler Thromb Vasc Biol.* (2015) 35:675–88. doi: 10.1161/ATVBAHA.114.304989
52. Brindle NPJ, Saharinen P, Alitalo K. Signaling and functions of angiopoietin-1 in vascular protection. *Circ Res.* (2006) 98:1014–23. doi: 10.1161/01.RES.0000218275.54089.12
53. Williams A, Hatzistergos K, Addicott B, McCall F, Carvalho D. Enhanced effect of combining human cardiac stem cells and bone marrow mesenchymal stem cells to reduce infarct size and to restore cardiac function after myocardial infarction. *Circulation.* (2013) 127:213–23. doi: 10.1161/CIRCULATIONAHA.112.131110
54. Stowell CET, Wang Y. Quickening: translational design of resorbable synthetic vascular grafts. *Biomaterials.* (2018) 173:71–86. doi: 10.1016/j.biomaterials.2018.05.006
55. Laschke MW, Strohe A, Menger MD, Alini M, Eglin D. *In vitro* and *in vivo* evaluation of a novel nanosize hydroxyapatite particles/poly(ester-urethane) composite scaffold for bone tissue engineering. *Acta Biomater.* (2010) 6:2020–7. doi: 10.1016/j.actbio.2009.12.004

Conflict of Interest: The authors declare that the research was conducted in the absence of any commercial or financial relationships that could be construed as a potential conflict of interest.

frontiers
in Cardiovascular Medicine

ORIGINAL RESEARCH
published: 27 November 2020
doi: 10.3389/fcvm.2020.603621

Estimation of Major Adverse Cardiovascular Events in Patients With Myocardial Infarction Undergoing Primary Percutaneous Coronary Intervention: A Risk Prediction Score Model From a Derivation and Validation Study

Xiaoxiao Zhao[1], *Chen Liu*[1], *Peng Zhou*[1], *Zhaoxue Sheng*[1], *Jiannan Li*[1], *Jinying Zhou*[1], *Runzhen Chen*[1], *Ying Wang*[1], *Yi Chen*[1], *Li Song*[1], *Hanjun Zhao*[1] and *Hongbing Yan*[1,2]*

[1] Fuwai Hospital, Chinese Academy of Medical Sciences and Peking Union Medical College, Beijing, China, [2] Fuwai Hospital, Chinese Academy of Medical Sciences, Shenzhen, China

Edited by:
David Wu,
University of Chicago, United States

Reviewed by:
Gerald Chi,
Beth Israel Deaconess Medical Center and Harvard Medical School, United States
Daniel Duerschmied,
University of Freiburg, Germany

****Correspondence:***
Hongbing Yan
hbyanfuwai@aliyun.com

Specialty section:
This article was submitted to Atherosclerosis and Vascular Medicine, a section of the journal Frontiers in Cardiovascular Medicine

Received: *07 September 2020*
Accepted: *26 October 2020*
Published: *27 November 2020*

Citation:
Zhao X, Liu C, Zhou P, Sheng Z, Li J, Zhou J, Chen R, Wang Y, Chen Y, Song L, Zhao H and Yan H (2020) Estimation of Major Adverse Cardiovascular Events in Patients With Myocardial Infarction Undergoing Primary Percutaneous Coronary Intervention: A Risk Prediction Score Model From a Derivation and Validation Study. Front. Cardiovasc. Med. 7:603621. doi: 10.3389/fcvm.2020.603621

Background: The population with myocardial infarction (MI) undergoing primary percutaneous coronary intervention (PPCI) is growing, but validated models to guide their clinical management are lacking. This study aimed to develop and validate prognostic models to predict major adverse cardiovascular events (MACEs) in patients with MI undergoing PPCI.

Methods and Results: Models were developed in 4,151 patients with MI who underwent PPCI in Fuwai Hospital between January 2010 and June 2017, with a median follow-up of 698 days during which 544 MACEs occurred. The predictors included in the models were age, a history of diabetes mellitus, atrial fibrillation, chronic kidney disease, coronary artery bypass grafting, the Killip classification, ejection fraction at admission, the high-sensitivity C-reactive protein (hs-CRP) level, the estimated glomerular filtration rate, the d-dimer level, multivessel lesions, and the culprit vessel. The models had good calibration and discrimination in the derivation and internal validation with C-indexes of 0.74 and 0.60, respectively, for predicting MACEs. The new prediction model and Thrombolysis in Myocardial Infarction (TIMI) risk score model were compared using the receiver operating characteristic curve. The areas under the curve of the new prediction model and TIMI risk score model were 0.806 and 0.782, respectively (difference between areas $= 0.024 < 0.05$; z statistic, 1.718).

Conclusion: The new prediction model could be used in clinical practice to support risk stratification as recommended in clinical guidelines.

Keywords: myocardial infarction, primary percutaneous coronary intervention, MACE, derivation, validation

WHAT IS ALREADY KNOWN ABOUT THIS TOPIC?

Improving the quality and management of acute coronary syndrome contributed substantially to patients with cardiovascular disease. Although many clinical guidelines have been established, only a few tools are available to assess the incidence of major adverse cardiovascular events (MACEs) among patients with myocardial infarction (MI) undergoing primary percutaneous coronary intervention (PPCI) and to guide patients' clinician communication and long-term risk management.

WHAT DOES THIS ARTICLE ADD?

1. Calculated risk scores were used to develop a model that can further evaluate 1-, 2-, 3-, and 5-years risks of MACEs among patients with MI who underwent PPCI.
2. This risk score incorporates routine clinical data, biochemical tests, and coronary angiography findings, which are routinely evaluated in the clinical assessment of patients with MI who underwent PPCI. The risk score model can help doctors identify patients most at risk of MACEs.

INTRODUCTION

Cardiovascular disease (CVD) has become the leading cause of mortality worldwide (1) and a major global economic burden (2). Early primary percutaneous coronary intervention (PPCI) has increased the survival rate and decreased the mortality rate, all-cause death rate, and incidence of recurrent myocardial infarction (MI) in patients with acute coronary syndrome (ACS) (3). Thus, the identification of pretreatment risk factors is beneficial to reduce the incidence of CVD in high-risk patients using multivariable prediction equations rather than single risk factors (4, 5). Clinical guidelines have provided direction for disease management; however, only a few tools can be used to assess the incidence of major adverse cardiovascular events (MACEs) among patients with MI undergoing PPCI and to guide patients' clinician communication and long-term risk management (6).

To achieve precision medicine, healthcare decisions, practices, and interventions should be individualized on the basis of each patient's predicted risk of disease. In this study, we sought to develop a risk score model to evaluate 1 -, 2 -, 3-, and 5-years risk for patients with MI who underwent PPCI. This article was prepared in accordance with the TRIPOD reporting checklist (**Appendix File**)[1].

MATERIALS AND METHODS

Study Design and Participants

A total of 4,151 consecutive patients with MI who underwent PPCI at Fuwai Hospital in Beijing, China, between January 2010 and June 2017 were enrolled. All patients were diagnosed with MI according to established guidelines (7, 8). The derivation cohort for this study comprised patients who had experienced MI at some time.

The enrolled patients provided informed consent, and the study was approved by the Ethics Committee of Fuwai Hospital. The study flowchart is shown in **Appendix Figure 1**.

Definitions

Thrombolysis in Myocardial Infarction (TIMI) flow grade three levels less after PPCI was defined as a no-reflow phenomenon. For adverse events that occurred at follow-up, the following events were evaluated: all-cause mortality, cardiac mortality, MI recurrence, and stroke (ischemic stroke). The objective end-point index was evaluated using a single-blind method.

Follow-Up Process

The patients were followed up at least 1 year after discharge. The health status of the enrolled patients was confirmed through telephone calls and review of health records, and this method was approved by the Review Board of Fuwai Hospital. The physicians in charge of the follow-up identified and extracted primary endpoints from hospital records, laboratory reports, and clinical notes in the event of death.

Statistical Analyses

The normal distribution of the outcome variables was confirmed by the Kolmogorov–Smirnov test. For the randomization procedure, all enrolled patients were numbered 1 to 4,103. Then, cells were filled in with "=RAND ()" to create a list of randomized numbers and then sorted. The first 3,078 patients were derived queues, and the second 1,025 patients were validated queues. Baseline parameters during follow-up are presented as median [standard error (SE)] for continuous variables and as frequency and percentage for categorical variables in the table presenting the characteristics of the derivation cohort and validation cohort (**Table 1**). The variables included in the new prediction models were all pre-specified. Univariable Cox regression analysis (**Appendix Table 2**) was used to initially screen candidate factors with $P < 0.2$ for predicting MACE. The following variables were included to calculate major adverse CVD risk: sex, age, a history of hypertension, atrial fibrillation, a history of coronary artery bypass grafting (CABG), a history of PCI, diabetes status, blood pressure, the creatinine (Cr) level, the estimated glomerular filtration rate (eGFR), high-density lipoprotein cholesterol (HDL-C), low-density lipoprotein cholesterol (LDL-C), triglyceride (TG), lipase activator (LPA), and coronary angiography findings.

The least absolute shrinkage and selection operator (LASSO) method was used to screen the independent variables to realize the reduction and simplification of the model and to prevent overfitting. Multivariable Cox regression was used to develop a novel prediction risk score for MACEs using all pre-specified variables (**Appendix Table 1**). In this study, time covered the period from the index assessment to the occurrence of the following events: death from other causes, CVD, MI recurrence, cerebrovascular disease, or end of follow-up. Missing data were handled by single imputation.

---

[1] The authors have completed the TRIPOD reporting checklist.

TABLE 1 | The characteristics of derivation cohort and validation cohort.

Variables	**Derivation cohort**	**Validation cohort**	***P* value**
	***N* = 3,078**	***N* = 1,025**	
Age (years)	59.42 ± 0.217	58.82 ± 0.359	0.161
Male [% (*n*)]	78.91% (2,429)	77.37% (793)	0.158
Height (cm)	161.30 ± 0.04	161.7 ± 0.08	0.613
Weight (kg)	71.22 ± 0.29	70.86 ± 0.54	0.681
BMI (kg/m²)	25.91 ± 0.069	25.91 ± 0.116	0.997
Heart rate (beats per minute)	77 ± 0.28	78 ± 1.05	0.338
SBP (mm Hg)	124.45 ± 0.336	123.69 ± 0.581	0.254
DBP(mm Hg)	71.22 ± 0.291	70.86 ± 0.538	0.548
Hypertension [% (*n*)]	62% (1,903)	59% (604)	0.054
Diabetes [% (*n*)]	33% (1,012)	33% (335)	0.470
Hyperlipidemia [% (*n*)]	92% (2,831)	93% (957)	0.082
Smoking [% (*n*)]	59% (1,818)	59% (609)	0.307
Previous PCI [% (*n*)]	14% (419)	14% (146)	0.323
Previous CABG [% (*n*)]	1.2% (38)	1.0% (10)	0.316
Atrial fibrillation [% (*n*)]	6.2% (192)	6.0% (61)	0.403
CKD [% (*n*)]	7.8% (240)	8.6% (88)	0.229
Laboratory examinations			
HDL cholesterol at admission (mmol/L)	1.70 ± 0.02	1.97 ± 0.06	0.797
LDL cholesterol at admission (mmol/L)	2.75 ± 0.017	2.71 ± 0.028	0.307
Triglycerides at admission (mmol/L)	1.05 ± 0.005	1.05 ± 0.009	0.533
LPA at admission (mg/L)	263.87 ± 4.40	275.57 ± 8.00	0.200
hs-CRP at admission (mg/L)	7.59 ± 0.09	7.50 ± 0.16	0.622
d-Dimer at admission (μg/mL)	0.64 ± 0.03	0.68 ± 0.06	0.528
Peak level of d-dimer (μg/mL)	0.80 ± 0.04	0.80 ± 0.07	0.988
TnI at admission (ng/L)	3.58 ± 0.31	3.94 ± 0.63	0.573
Peak level of TnI (ng/L)	3.89 ± 0.25	3.98 ± 0.44	0.856
Crea at admission (μmol/L)	81.92 ± 0.45	82.73 ± 0.80	0.379
eGFR at admission (mL/min)	89.48 ± 1.49	89.96 ± 2.49	0.872
Discharge medication regimen			
Statin [% (*n*)]	91% (2,790)	91% (932)	0.287
Aspirin [% (*n*)]	96% (2,956)	96% (980)	0.412
Ticagrelor [% (*n*)]	74% (2,291)	74% (761)	0.508
ACEI/ARB [% (*n*)]	68% (2,094)	69% (709)	0.214
β-Blockers [% (*n*)]	85% (2,601)	85% (868)	0.379
Diuretic [% (*n*)]	28% (867)	28% (283)	0.401
Spironolactone [% (*n*)]	21% (649)	21% (216)	0.502
P2Y12 inhibitors	96% (2,958)	96% (986)	0.154
Endpoint events			
MACEs [% (*n*)]	11% (330)	12% (125)	0.107
Death [% (*n*)]	6.5% (200)	6.6% (68)	0.464
Recurrent MI [% (*n*)]	2.9% (90)	4.1% (42)	0.043
Stroke [% (*n*)]	1.7% (51)	2.0% (20)	0.307

Continuous data are presented as mean ± SE (standard error); categorical variables are presented as % (n). BMI, body mass index; SBP, systolic blood pressure; DBP, diastolic blood pressure; PCI, percutaneous coronary intervention; CABG, coronary artery bypass grafting; CKD, chronic kidney disease; HDL-C, high-density lipoprotein cholesterol; LDL-C, low-density lipoprotein cholesterol; TnI, troponin I; TG, triglyceride; LPA, lipse activator; hs-CRP, high sensitive C-reactive protein; eGFR, estimated glomerular filtration rate; ACEI, angiotensin-converting enzyme inhibitor; ARB, angiotensin receptor blocker; MACE, major adverse cardiovascular events.

LASSO Regression

At the beginning of the model establishment, all identified independent variables were selected to minimize model deviation caused by non-inclusion of important independent variables. Furthermore, the established model needs to find the set of independent variables with the strongest explanatory power for the dependent variables to improve the prediction accuracy. As a result, we included the LPA, HDL-C, and TG, which failed to have statistical significance by Cox regression in the LASSO regression. Therefore, index selection is significant in the modeling process. The 1996 LASSO algorithm is a compressed estimate method that simplifies the index set. A more refined model is obtained by constructing a function that compresses some coefficients and sets some coefficients to 0, 0.5, or minimization. LASSO regression is a biased estimation of data with complex collinearity and retains the advantage of contraction. LASSO programming is provided by the Lars algorithm software package of R language. Therefore, dimensionality reduction and variable selection can be achieved accurately by LASSO regression.

Nomogram Prediction Model

The corresponding nomogram prediction model was drawn according to the regression coefficient of the selected independent variables. For the variables selected in the nomogram prediction model, values of the variables can correspond to the scores on the integral line at the top of the nomogram (the score ranged from 0 to 550 points) through the projection of the vertical line, and the total score can be obtained by adding the scores corresponding to the values of each variable. The cumulative occurrence probability of MACEs at 1, 2, 3, and 5 years can be obtained from the total score on the prediction line at the bottom of the nomogram. To reduce overfitting, the self-sampling method was used to verify the nomogram prediction model. Model discrimination was quantified using Harrell's c-statistic and calibration chart. Hypertension, hyperlipidemia, a history of PCI, smoking status, sex, blood pressure, body mass index, LDL-C, HDL-C, TG, left main (LM) artery lesion, and no-flow phenomenon were controlled to draw the receiver operating characteristic (ROC) curve. The LASSO method adopts the glmnet package of R language for variable selection and the RMS package of the R language for drawing and internal verification of the nomogram (c-index and calibration chart). Cox regression analysis was performed using the survival package. Stdca.r was used to draw the clinical decision curve. The main statistical analysis software used in this study was the R language version I 386 3.6.2. Other analyses were performed using SPSS Statistics version 20.0 (SPSS, Inc., Chicago, IL). All *P*-values were two-tailed, and statistical significance was determined at $P < 0.05$.

Performance and Internal Validation of the New Risk Prediction Models

The 1-, 2-, 3-, and 5-years baseline survival probabilities of each model were obtained using R language version I 386 3.6.2 commands that were utilized to fit the models. Calibration performance was assessed graphically at 1-, 2-, 3-, and 5-years MACE risks by plotting the predicted 1-, 2-, 3-, and 5-years risks against the observed 1-, 2-, 3-, and 5-years risks. The flawlessly calibrated curve was represented by a diagonal line with a slope of 1. The observed 1-, 2-, 3-, and 5-years risks were obtained using the Kaplan–Meier method, and the slopes of regression lines comparing the predicted with the observed 1-, 2,- 3-, and 5-years risks were calculated. Standard statistical metrics of model and discrimination performance (R^2, Harrell's c-statistic) were calculated. The calibration and discrimination performance of the equations developed in the derivation subcohort were assessed in the validation subcohort and compared with the performance of models developed in the entire cohort; baseline survival functions and hazard ratios (HRs) were also compared.

Indicators of internal verification included the c-index and calibration degree, which, respectively, represent the prediction accuracy and prediction consistency of the nomogram prediction model. The degree of calibration was represented by a calibration graph. ROC plotting was used for the survival ROC package. Owing to time constraints, experimental data from other research centers were not collected. Therefore, external validation was not performed, and this point is explained in the limitation section. The model was validated in a separate MI population, which was enrolled from July 2017 to December 2018. A total of 939 consecutive patients with MI who underwent PPCI at Fuwai Hospital in Beijing, China, were enrolled. However, the separate validation cohort underwent 1–2 years of follow-up; hence, the 1- and 2-years prediction models were validated. The performance and discrimination of a separate validation cohort were quantified using a calibration chart. The calibration graph indicated that the prediction model had good calibration and was shown in the **Supplement**.

Comparison With Other Models

The accuracy of the new model and TIMI risk score model predicting MACEs among patients with MI who underwent PPCI was compared according to the area under the ROC (AUC) curve using a non-parametric test developed by DeLong et al. MedCalc for Windows version 18.2.1 (MedCalc Software, Mariakerke, Belgium) was used for comparison.

RESULTS

Demographics of the Derivation Cohort and Validation Cohort

The study population included 4,151 men and women aged 24–97 years during risk assessment from January 1, 2010, to June 30, 2017 (**Appendix Figure 1**). Forty-eight people without follow-up data were excluded. Following randomized allocation, 3,078 people constituted the derivation cohort, and 1,025 (77% men) patients comprised the validation cohort. The median duration of follow-up was 698 days in the two cohorts. In the derivation cohort, the cumulative rate of the primary composite endpoint (MI, stroke, or all-cause death) was 11 during the follow-up period. Of these patients, 2.9% experienced recurrent MI, 1.7% experienced a stroke, and 6.5% died of any causes as their first event. In the validation cohort, there were 125 MACEs, of which 68 were all-cause deaths, 42 were MI recurrence, and 20 were cerebrovascular events. Participant characteristics are outlined in **Table 1**. Outcome events were obtained exclusively from follow-up databases between August 3, 2010, and March 11, 2019. The average age of the derivation cohort was 59.42 ± 0.217 years (mean ± SE), whereas the average age of the validation cohort was 58.82 ± 0.359 years (mean ± SE). No statistical differences were found between the two groups in terms of sex, heart rate, body mass index, blood pressure, disease history, laboratory examination, and discharge medication regimen. Therefore, they can be considered as two undifferentiated populations and can be used for model establishment and validation.

Primary Screening by Univariate Cox Regression Analysis

The following variables are shown in **Appendix Table 2**: age ($P = 0.053$), hypertension ($P = 0.013$), diabetes mellitus ($P < 0.0001$), a history of atrial fibrillation ($P < 0.0001$), chronic kidney disease (CKD, $P < 0.0001$), a history of CABG ($P < 0.0001$), the Killip classification ($P < 0.0001$), ejection fraction (EF) grade ($P < 0.0001$), high-sensitivity C-reactive protein (hs-CRP) ($P < 0.0001$), eGFR ($P < 0.0001$), the D-dimer level ($P < 0.0001$), the Cr level ($P < 0.0001$), the use of intra-aortic balloon pump ($P < 0.0001$), a LM coronary artery lesion ($P < 0.0001$), the no-reflow phenomenon ($P = 0.006$), complete revascularization during hospitalization ($P < 0.0001$), triple-vessel lesions ($P < 0.0001$), culprit lesions including those in the left circumflex artery (LCX, $P < 0.0001$) and LM artery ($P < 0.0001$), the elevated LPA level ($P = 0.343$), the HDL-C level ($P = 0.50$), the TG level ($P = 0.173$), etc.

Screening of the Independent Variables by the LASSO Method

Twenty-eight variables were filtered by the LASSO regression method, as shown in **Appendix Figure 2**. Thus, it is necessary to classify the variables by factorization and then use the as.matrix() function to convert the data from a non-matrix format to a matrix format before the R language "glmet" package can call the data. The filtering and cross-validation processes of the independent variables are shown in **Appendix Figures 2A,B**, respectively. Lambda.1se is the lambda value of the simplest model in the SE range, which identifies the model with excellent performance and the least number of independent variables. At this time, a total of 12 independent variables (age, a history of diabetes, a history of atrial fibrillation, a history of CABG, a history of CKD, the Killip classification, EF grade, an increase in hs-CRP level, a decrease in eGFR, an increase in D-dimer level, the culprit lesion, and mutivessel lesions) were included in the model.

Establishment of a Multivariate Cox Regression Model and Risk Score Model

The multivariable Cox regression model established by the variables screened by LASSO method is shown in **Appendix Table 1**. Patients were categorized into four age groups: age $\leq$ 40 years, 40 < age $\leq$ 50 years, 50 < age $\leq$ 60 years, and age > 60 years. The group of patients aged 40–50 years [HR, 1.539; 95% confidence interval (CI), 0.626–3.783] was associated with a higher HR than other age groups for the incidence of MACE. In the multivariate Cox regression analysis, a history of diabetes mellitus (HR, 1.347; 95% CI, 1.054–1.723; $P = 0.0175$), atrial fibrillation (HR, 1.511; 95% CI, 1.040–2.195; $P = 0.0305$), CABG (HR, 1.937; 95% CI, 1.363–2.752; $P = 0.0002$), EF grade at admission $\leq$45 (HR, 1.530; 95% CI, 1.089, 2.150; $P = 0.0143$), and multivessel lesions (HR, 1.713; 95% CI, 1.214, 2.419; $P = 0.0022$) were relevant factors for MACEs during follow-up. The forest plot is shown in **Figure 1**.

Nomogram Depiction and Evaluation of the Risk Prediction Model

The model and discrimination metrics indicated that the risk equations performed better in predicting MACE. Additional variables available in the prediction model, when added to the LASSO regression models, are shown in **Appendix Table 1.** Age, diabetes mellitus, a family history of CKD, atrial fibrillation, CABG, the Killip score, EF grade at admission, hs-CRP, eGFR, D-dimer, the number of culprit lesions, and multivessel lesions were all statistically significant predictors of MACE risk (**Appendix Table 1**).

Interpretation of the Newly Established Risk Score

Scoring was performed during hospitalization to predict long-term events by physicians. For the variables selected in the nomogram prediction model, the values of variables can correspond to the scores on the integral line at the top of the nomogram (the score ranged from 0 to 550 points) through the projection of the vertical line, and the total score can be obtained by adding the scores corresponding to the values of each variable. The cumulative occurrence probability of MACEs at 1, 2, 3, and 5 years can be obtained from the total score on the prediction line at the bottom of the nomogram. The scores, ranging from 0 to 550 points, were assigned as follows: age < 40 years, 28.01; age 40–50 years, 18.68; age 50–60 years, 9.34; age $\geq$60 years, 0; diabetes mellitus, 30.1; without diabetes mellitus, 0; atrial fibrillation, 43.5; without atrial fibrillation, 0; history of CABG, 88.9; without history of CABG, 0; history of CKD, 59.7; without history of CKD, 0; Killip I, 0; Killip II, 33.3; Killip III, 66.7; Killip IV, 100; EF at admission $\leq$45%, 31.1; EF at admission between 45% and 55%, 15.6; EF at admission >55%, 0; hs-CRP concentration that varies from 3.5 to 10 mg/L and over 10 mg/L, 16.1 and 32.3, respectively; hs-CRP concentration $\leq$3.5 mg/L, 0; eGFR of 60–90 mL/min and <60 mL/min, 23.3 and 46.5, respectively; eGFR >90 mL/min, 0; D-dimer concentration $\geq$ 0.5 μg/mL, 26.2; D-dimer concentration <0.5 μg/mL, 0; mutivessel lesions, 53.9; without multivessel lesions, 0; vein graft culprit lesion, 18.7; LM culprit lesion, 14.02; LAD culprit lesion, 9.35; right coronary artery culprit lesion, 4.67; and LCX culprit lesion, 0. The distribution of the risk score is shown in **Figure 2**. With the increase in the total score of the nomogram prediction model, the corresponding 1-, 2-, 3-, and 5-years risk of MACEs increased (**Figure 2**). Despite the evaluation of the reliability and validity of the C-index, it provides a reliable tool for evaluating the model. The C-index was 0.74 in the derivation cohort and 0.60 in the validation cohort. **Appendix Figure 3** shows the ROC curves for the discriminatory value of the 3- and 5-years evaluation performance of the risk prediction model. **Appendix Figure 3** shows the survival ROC curves for evaluating the performance of the new risk prediction model at 1 year (A, AUC = 0.715,

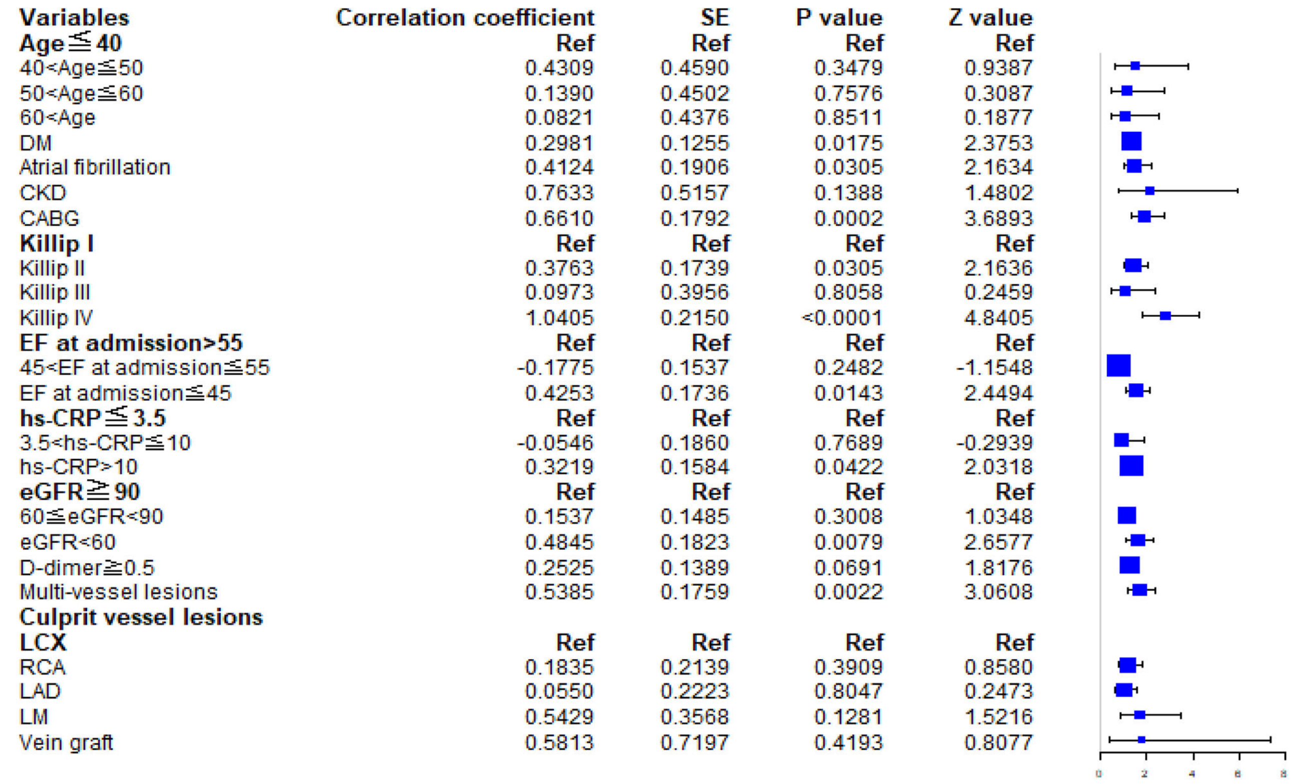

Variables	Correlation coefficient	SE	P value	Z value
Age≦40	Ref	Ref	Ref	Ref
40<Age≦50	0.4309	0.4590	0.3479	0.9387
50<Age≦60	0.1390	0.4502	0.7576	0.3087
60<Age	0.0821	0.4376	0.8511	0.1877
DM	0.2981	0.1255	0.0175	2.3753
Atrial fibrillation	0.4124	0.1906	0.0305	2.1634
CKD	0.7633	0.5157	0.1388	1.4802
CABG	0.6610	0.1792	0.0002	3.6893
Killip I	Ref	Ref	Ref	Ref
Killip II	0.3763	0.1739	0.0305	2.1636
Killip III	0.0973	0.3956	0.8058	0.2459
Killip IV	1.0405	0.2150	<0.0001	4.8405
EF at admission>55	Ref	Ref	Ref	Ref
45<EF at admission≦55	-0.1775	0.1537	0.2482	-1.1548
EF at admission≦45	0.4253	0.1736	0.0143	2.4494
hs-CRP≦3.5	Ref	Ref	Ref	Ref
3.5<hs-CRP≦10	-0.0546	0.1860	0.7689	-0.2939
hs-CRP>10	0.3219	0.1584	0.0422	2.0318
eGFR≧90	Ref	Ref	Ref	Ref
60≦eGFR<90	0.1537	0.1485	0.3008	1.0348
eGFR<60	0.4845	0.1823	0.0079	2.6577
D-dimer≧0.5	0.2525	0.1389	0.0691	1.8176
Multi-vessel lesions	0.5385	0.1759	0.0022	3.0608
Culprit vessel lesions				
LCX	Ref	Ref	Ref	Ref
RCA	0.1835	0.2139	0.3909	0.8580
LAD	0.0550	0.2223	0.8047	0.2473
LM	0.5429	0.3568	0.1281	1.5216
Vein graft	0.5813	0.7197	0.4193	0.8077

FIGURE 1 | Forest plot. The HRs and 95% CIs for predictors in the multivariable Cox model for major adverse cardiovascular events. DM, diabetes mellitus; CKD, chronic kidney disease; CABG, coronary artery bypass grafting; EF, ejection fraction; hs-CRP, high-sensitivity C-reactive protein; eGFR, estimated glomerular filtration rate.

cutoff point = 15.29396), 2 years (B, AUC = 0.692, cutoff point = 15.08561), 3 years (C, AUC = 0.674, cutoff point = 15.04044), and 5 years (D, AUC = 0.638, cutoff point = 14.87151) in the derivation cohort.

Model discrimination was quantified using Harrell's c-statistic and calibration chart. The predicted vs. observed 1-, 2-, 3-, and 5-years risk plots for MACEs using the risk prediction model showed excellent calibration performance (**Figures 3A–H**). **Figure 3** shows the MACE risk scores at 1, 2, 3, and 5 years in the derivation cohort (**Figures 3A–D**) and validation cohort (**Figures 3E–H**). Calibration is indicated by the estimated risk against survival from the Kaplan–Meier analysis. The gray line indicates perfect calibration. **Figures 4A–H** show the decision curve analysis of 1, 2, 3, and 5 years in the derivation and validation cohorts. Assuming that we choose to predict the 12% risk of MACEs and treatment, modeling queue Decision Curve Analysis (DCA) curves showed that if the new prediction model is used in every 10,000 people at the first year of follow-up, 50 people can benefit from this model without influencing any other person's interests, with 100 in 10,000 people at the second year, 200 in 10,000 people at the third year, and 500 in every 10,000 people at the fifth year. The internal validation queue DCA curves show that if the new prediction model is used in 10,000 people during the first year of follow-up, 100 people can benefit from the model without influencing any other person's interests, with 180 in 10,000 people at the second year, 250 in 10,000 people at the third year, and 500 from every 10,000 at the fifth year. **Figure 5** compares the predictive efficiency between the new prediction model and the TIMI risk score model. The AUC of the new prediction model was 0.806, and the AUC of the TIMI risk score model was 0.782 (difference between areas = 0.024; *z* statistic, 1.718). **Appendix Figure 4** shows the calibration graph of the cohorts and the excellent calibration performance.

DISCUSSION

Patient management and assessment should be individualized and precise to ensure the sustainable development of the contemporary healthcare system. For patients with ACS, care should be appropriate for the disease type and stage; however, only a few tools can be used to assist medium- to long-term management of patients with MI undergoing PPCI (9). Patients with MI do not have the same risk of recurrence, and the risk level is still relevant even after the 6-months period as predicted by the most accurate score (10, 11).

We have developed a risk score model to evaluate the 3- and 5-years risk probability for patients with MI who underwent PPCI, and this model can be used by specialists and primary healthcare professionals to enhance risk management and assessment. This risk score model incorporates routine clinical data on serum inflammatory factors and coronary angiography findings by integrating time since event, and it allows re-evaluation of

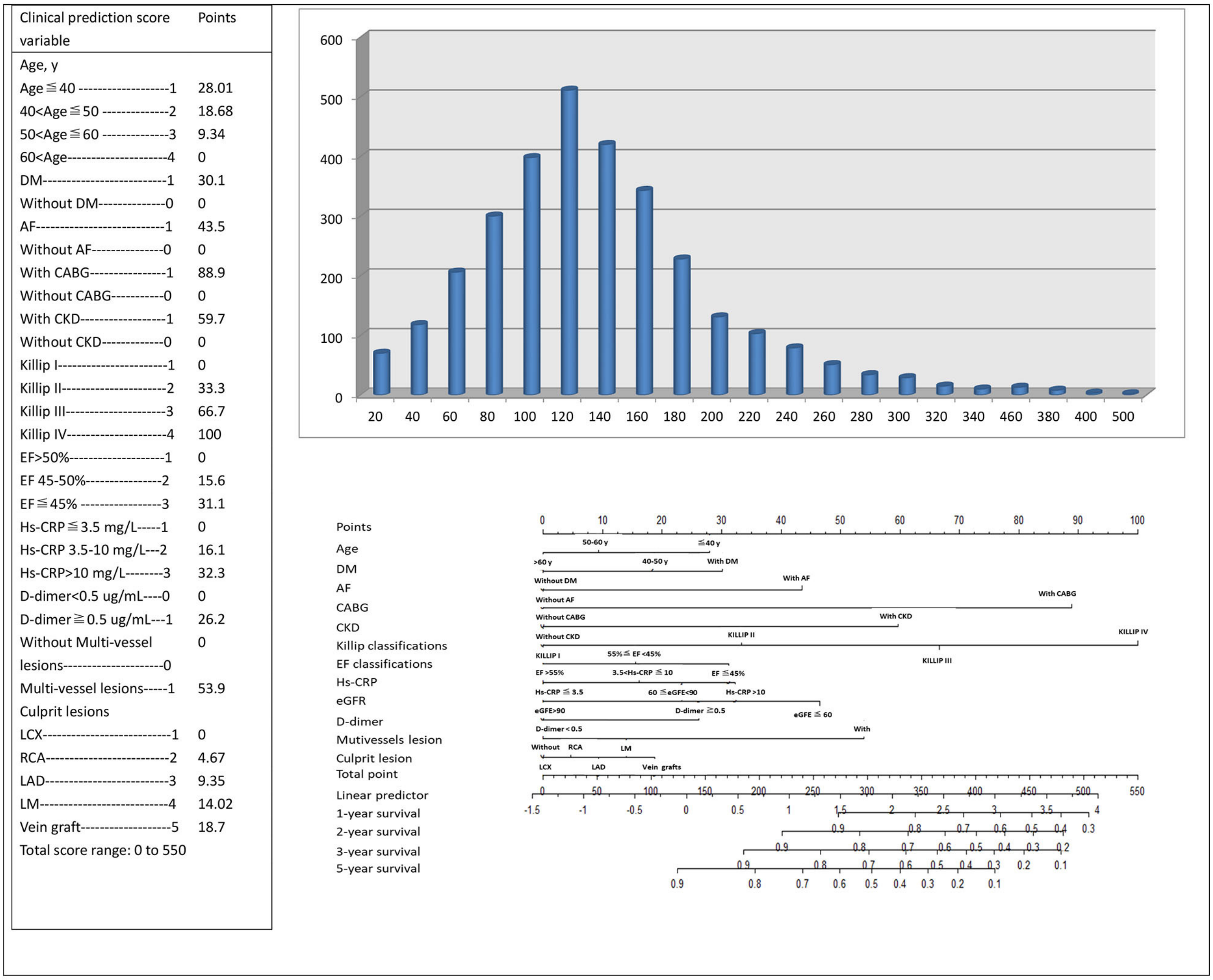

Clinical prediction score variable	Points
Age, y	
Age≦40 -------------------1	28.01
40<Age≦50 --------------2	18.68
50<Age≦60 --------------3	9.34
60<Age---------------------4	0
DM--------------------------1	30.1
Without DM--------------0	0
AF----------------------------1	43.5
Without AF---------------0	0
With CABG----------------1	88.9
Without CABG-----------0	0
With CKD------------------1	59.7
Without CKD-------------0	0
Killip I------------------------1	0
Killip II-----------------------2	33.3
Killip III----------------------3	66.7
Killip IV----------------------4	100
EF>50%--------------------1	0
EF 45-50%----------------2	15.6
EF≦45% -----------------3	31.1
Hs-CRP≦3.5 mg/L-----1	0
Hs-CRP 3.5-10 mg/L---2	16.1
Hs-CRP>10 mg/L--------3	32.3
D-dimer<0.5 ug/mL----0	0
D-dimer≧0.5 ug/mL---1	26.2
Without Multi-vessel lesions---------------------0	0
Multi-vessel lesions-----1	53.9
Culprit lesions	
LCX---------------------------1	0
RCA--------------------------2	4.67
LAD--------------------------3	9.35
LM---------------------------4	14.02
Vein graft------------------5	18.7
Total score range: 0 to 550	

FIGURE 2 | The risk score nomogram for bedside application. Histogram refers to the score distribution in the derivation cohort. For the variables selected in the nomogram model, the values of different variables can correspond to different scores on the integral line at the top of the nomogram (the score range is 0–550 points) through the projection of the vertical line, and the total score can be obtained by adding up the scores corresponding to the values of each variable. The cumulative occurrence probability of MACEs in 3 and 5 years can be obtained from the total score on the prediction line at the bottom of the nomogram.

the risk of MACEs 3 years or more following PPCI. The established risk score may be used to inform decisions about novel therapies and be tested in the context of changes in quantifiable risk.

The enrolled patients with acute MI who underwent PPCI are the most appropriate population to develop or validate a risk prediction model for MACE. However, similar cohorts are rare. While there was a statistically significant difference between the derivation and validation cohorts in terms of recurrent MI ($P = 0.043$), the model was established by derivation only, and the models had good calibration and discrimination in derivation and internal validation by the C-index and calibration graph for predicting MACE. Therefore, the proposed model does not increase the risk of recurrent MI.

How This Risk Scoring System Can and Should Influence Patient Treatment

Clinical risk factors and biochemical measurements of serum and coronary angiography findings, which are easily obtained and routinely collected at admission, are incorporated into our nomogram prediction model, which takes advantage of a novel screening method and presents as a robust predictive model of MACE. The nomogram incorporating coronary angiography results can be used to inform patients about their future risk up to 3 and 5 years and be a useful tool for clinical practice. Furthermore, the results may be used as reference for preventive therapy, such as improving renal function, enhancing heart function, and lowering inflammation in patients with a high risk of MACE.

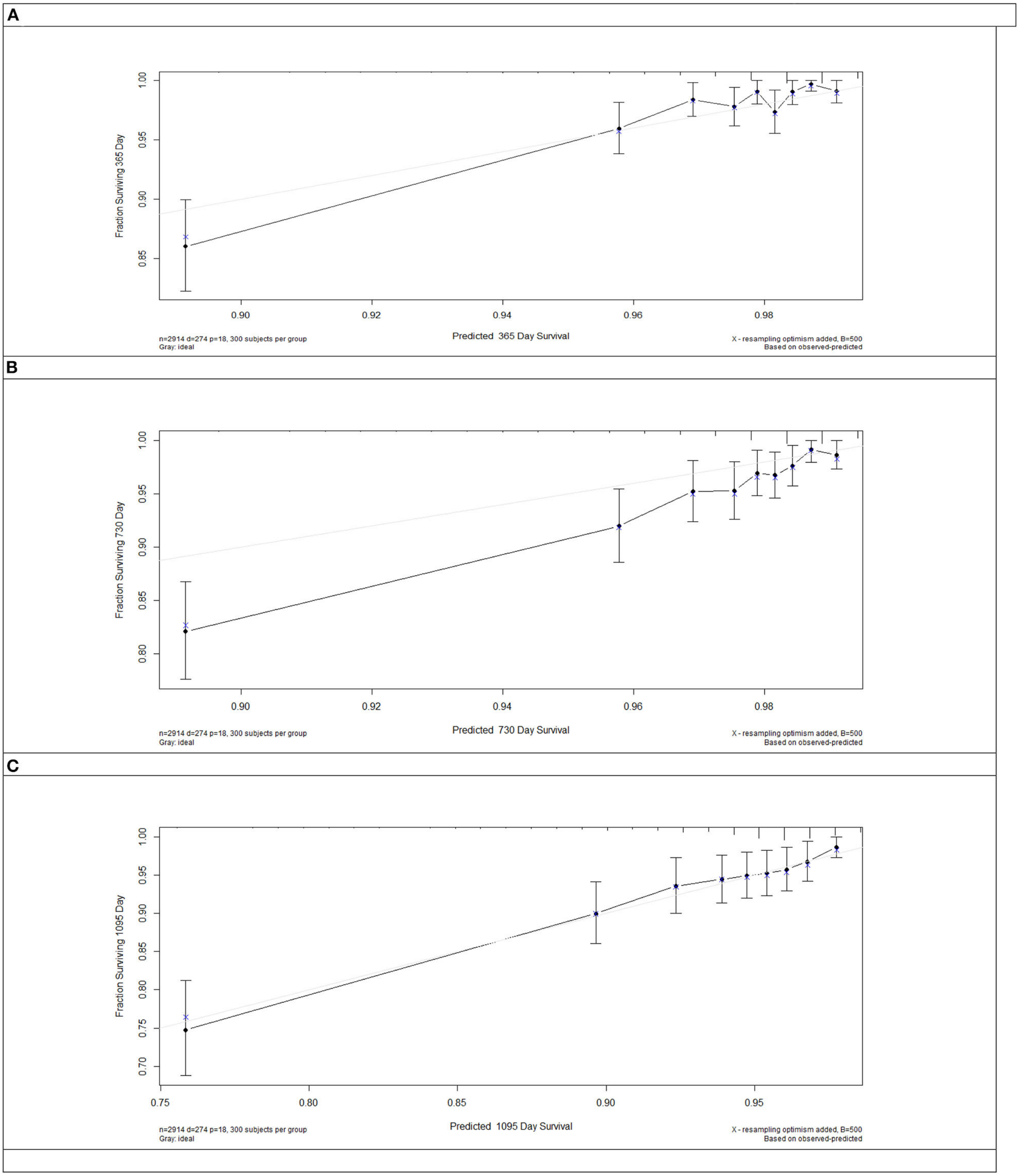

FIGURE 3 | Continued

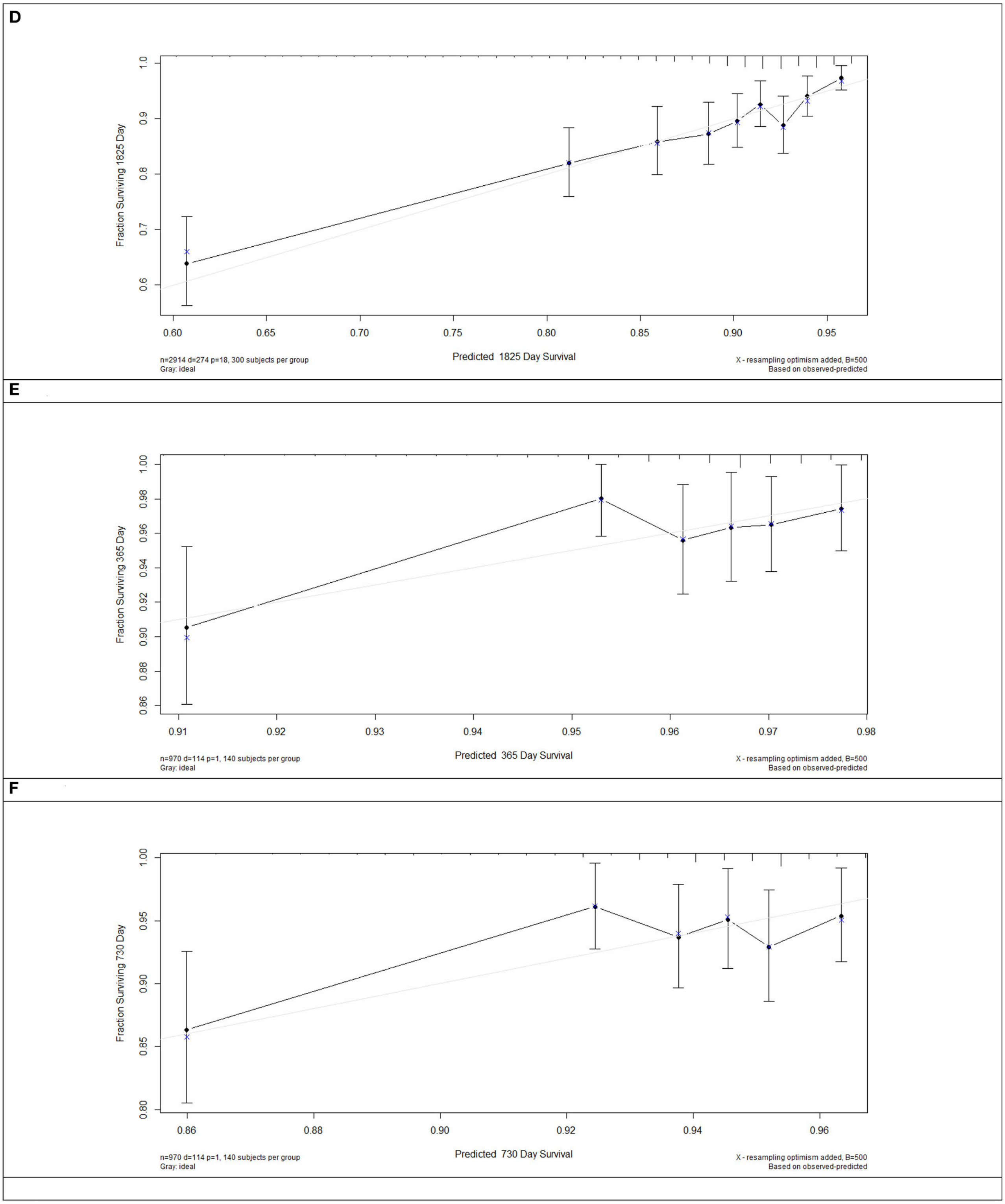

FIGURE 3 | Continued

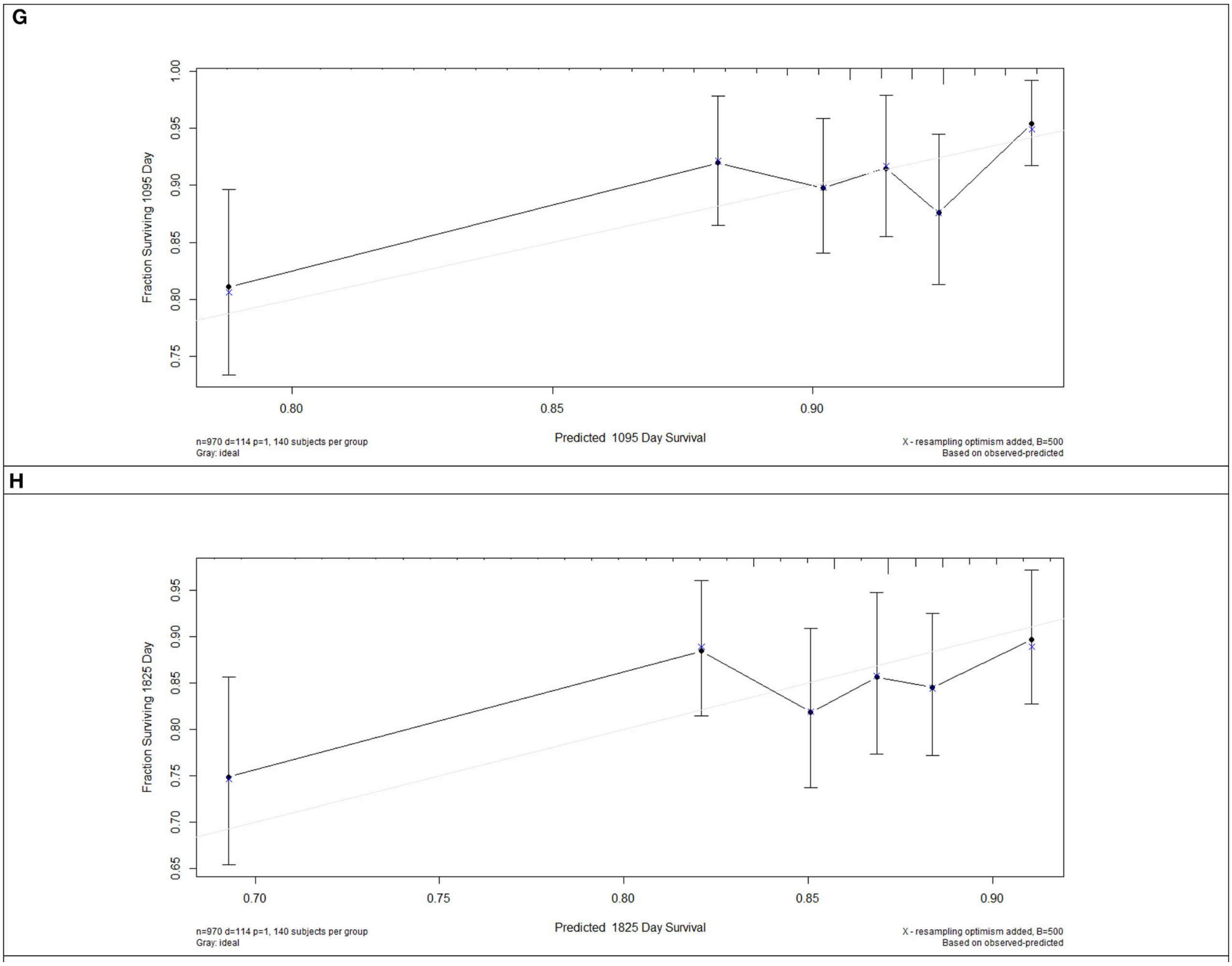

FIGURE 3 | Risk score calibration in the derivation cohort and internal validation cohort. The major adverse cardiovascular events risk score of 1 **(A)**, 2 **(B)**, 3 **(C)**, and 5 years **(D)** in the derivation cohort and 1 **(E)**, 2 **(F)**, 3 **(G)**, and 5 years **(H)** in the validation cohort. Calibration is shown as the estimated risk against survival from Kaplan–Meier analysis. Gray line = perfect calibration.

We performed a comparative study between the new prediction model and TIMI risk score model to evaluate the effect of preventive therapeutic strategies. The results show that the new prediction model has better effects and is more suited for patients with MI undergoing PPCI. MACEs could be considered an appropriate endpoint free from misclassification bias. Furthermore, we identified age, especially age <40 years, as a risk factor for MACEs following PPCI. In this study, patients were categorized into four age groups (age ≤ 40 years, $40 <$ age ≤ 50 years, $50 <$ age ≤ 60 years, age >60 years), which were assigned 28.01, 18.68, 9.34, and 0 points in the nomogram. These results were consistent with those of Dawson et al. (12); that is, the incidence rate ratio of patients aged 35–39 years (i.e., 28.1) was higher than those aged >85 years (i.e., 0.65).

Contribution of the Prediction Model

Robust evidence highlights the tremendous contribution of inflammation to the development of plaque, vulnerability, and progression of ACS. Higher plasma concentrations of inflammatory mediators such as CRP and D-dimer were significantly correlated with a greater risk for MACE. The early inflammatory response is generated by proinflammatory cytokines, with important biological functions in the cascading inflammatory reaction and critical role in the occurrence and development of acute ischemic injury. T lymphocytes, mast cells, and macrophages play critical roles in the pathogenesis of MI treated with PPCI. Furthermore, serum biomarkers reflecting systemic inflammatory levels may help establish proper clinical management and therapeutic schedules. In this study, the serum concentration of hs-CRP that varied from 3.5 to 10, and >10 was assigned 15.9 and 31.7 points, respectively. The scores of the high D-dimer concentration (≥ 0.5) and triple-vessel lesions were 27.2 and 34.2, respectively. Inflammation markers including hs-CRP and D-dimer contributed substantially to the prediction score model after screening by LASSO regression. Moreover, the role of inflammation level has been proved in plaque ruptures. Therefore, anti-inflammatory approaches could benefit patients by significantly reducing levels of serum inflammation biomarkers. Acute MI can be viewed on a life-course continuum, progressing from the presence of risk factors to occurrence of subclinical atherosclerosis and MI induced by plaque rupture. Numerous risk scores contribute to the management and primary prevention of MI (13–15). However, few equivalent scores are available for use in patients with acute MI undergoing PPCI. For these patients, cardiac imaging, coronary angiography, and advanced biomarkers are routinely available at the time of admission, so it is convenient to include them in a scoring system for this setting for long-term management.

Benefits of the Prediction Scoring Model

In the past few decades, the incidence of CVD worldwide has decreased significantly as a consequence of preventive treatments (16, 17). Most published equations and models of CVD, including the American Heart Association PCEs/2013 American College of Cardiology, are likely out of date (18). The predictive performance of the new model to identify 3- and 5-years MACE risk was calibrated. We found that adding routinely available measures of coronary angiography, renal function indices, and other easily measured predictors identified groups of patients whose risk would otherwise be appreciably underestimated or overestimated. We developed equations predicting 5-years risk rather than the more common 10-years risk because most trials of CVD risk reduction have ∼5 years of follow-up. Potential predictors and MACE definitions were prespecified to reduce overfitting. To assess the degree of overoptimism of re-substitution validation, sensitivity analyses were performed by dividing the cohort into derivation and validation subcohorts. We replicated the equation development and model performance procedures (**Appendix**) in the validation subcohorts to evaluate the performance. Equation coefficients, baseline survival functions, and performance metrics were similar irrespective of whether the whole cohort or derivation cohort was used to develop the risk score model.

Both the time of risk assessment post-event and CVD type are main factors used to evaluate the performance of the risk score for secondary prevention. The CALIBER group (19) enrolled 102,023 stable coronary artery disease patients with a mean follow-up of 4.4 years and developed a risk score for this population. They used the new model to identify high-risk patients (defined by guidelines as 3% annual mortality) and support management decisions. A recent study randomized patients post-ACS to receive clopidogrel (control) or ticagrelor on the basis of their ischemic and bleeding risks predicted by the GRACE and CRUSADE scores, suggesting that the use of an appropriate risk scoring system to guide antiplatelet therapy after ACS is safe and can improve clinical outcomes (20). Many standard clinical recommendations have been applied to all patients post-ACS by evaluating the risk factor modification and medications. Such programs have been successfully established in the context of the primary prevention and understanding of the life course of CVD. In a recent systematic review (21), 10,363 models were identified, and most CVD risk prediction models were developed in Europe and North America. The study recommended the use of uniform definitions, preferably *International Classification of Diseases*–coded events and outcome definitions. While the variables measured by coronary angiography are independently associated with MACE, most published equations include only a limited number of predictors (typically age, sex, smoking, diabetes, blood pressure, and blood lipids). One of the most comprehensive equations was from the UK QRISK3 (13), which included 22 variables, but it was difficult to assess and use outside the United Kingdom. Separate equations have been developed in the United States for black and white people, but Asians are not represented (15).

Subsequent management and risk prediction titrated against risk are all required to improve clinical outcomes for patients with MI undergoing PCI. The risk scores presented herein can be implemented alongside further medical investigations to support therapeutic decision-making and guide clinicians and patients toward individualized healthcare. A lower risk score in the post-PPCI setting would not be the reason to withdraw medications. Rather, it is a tool to enhance clinician–patient interactions to reinforce risk factor modification. The advantages of the risk tools are likely dependent on the local healthcare environment and healthcare settings. Thus, it is a logical evolution to use this experience in patients with MI undergoing PPCI.

Post-procedural Inflammation Level and Renal Function Are Associated With Increased Risk of MACE

Incorporating acute phase inflammation factors into the prediction model of long-term events based on previous literature is reasonable. Robust evidence (22–24) has shown that levels of inflammation markers, including hs-CRP and D-dimer, are constantly associated with worse mortality among patients with ACS who underwent PCI. Our previous study (25) revealed that during a median follow-up of 727 days, both low and high post-procedural hs-CRP levels were associated with a higher risk of death in patients with ACS who underwent PCI. Hs-CRP is the key marker of the interleukin (IL)-1β/IL-6/CRP pathway to synthesize and recruit leukocyte after myocardial damage (26). Hs-CRP and D-dimer could indirectly regulate the infiltration of neutrophils and macrophages into the infarcted myocardium and could lead to the delayed cleaning of apoptotic or necrotic cardiomyocytes, increasing myocardial fibrosis, and reducing EF, resulting in worse clinical outcomes during long-term follow-up. In this study, high levels of inflammation markers (D-dimer >0.5 mg/L and hs-CRP >10 mg/L) were risk factors of MACEs during a median follow-up of 698 days, which is consistent with previous studies.

CKD is correlated with a high risk of mortality from CVD (27), and patients with CVD-induced CKD are more likely to have a worse outcome during follow-up (28). Patients with severe CKD are at a high risk of diffuse obstructive coronary

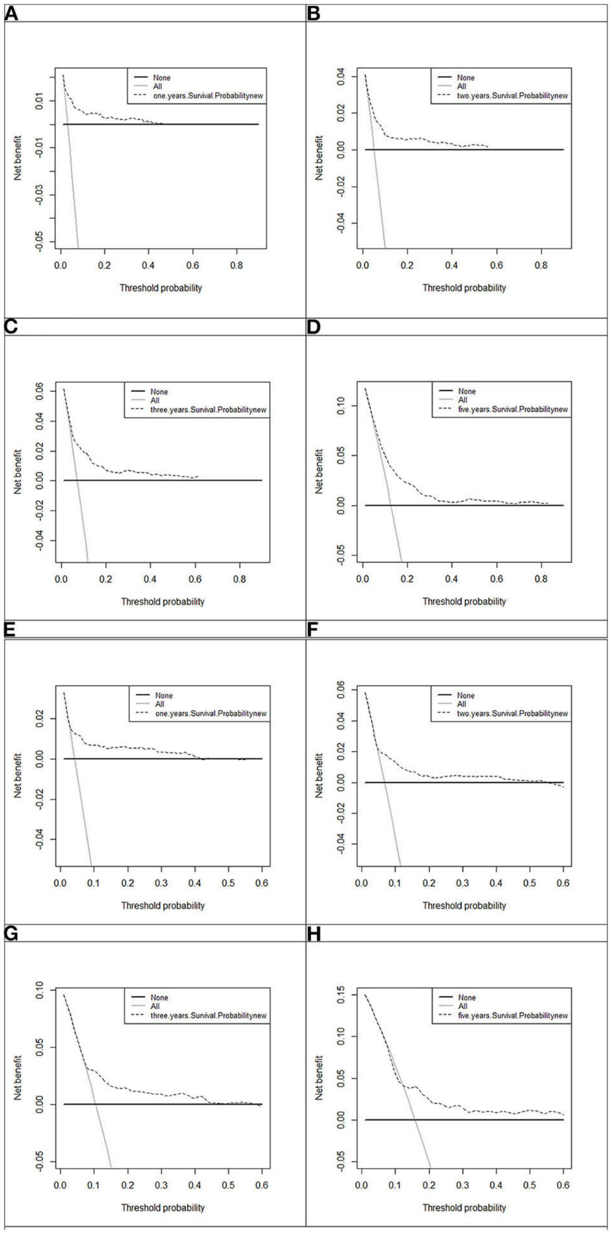

FIGURE 4 | Decision curve analysis of 1, 2, 3, and 5 years in the derivation and 1, 2, 3, and 5 years in the validation cohort. The black line, assume no patients without disease (represented by None, i.e., the horizontal line). Gray line, all the MACE patients (represented by All, i.e., the oblique line). Dotted line represents the new established model. **(A)** One-year decision curve analysis in the derivation cohort; **(B)** 2-years decision curve analysis in the derivation cohort; **(C)** 3-years decision curve analysis in the derivation cohort; **(D)** 5-years decision curve analysis in the derivation cohort; **(E)** 1-year decision curve analysis in the validation cohort; **(F)** 2-years decision curve analysis in the validation cohort; **(G)** 3-years decision curve analysis in the validation cohort; **(H)** 5-years decision curve analysis in the validation cohort.

atherosclerosis (29). The absence of reliable risk estimates in patients with CKD limits the ability of clinicians to make evidence-based decisions. A previous study (30) reported that eGFR levels in the range of 45 to 60 mL/min/1.73 m^2 and <45 mL/min/1.73 m^2 predicted MACEs (adjusted HRs, 1.25 and 2.26, respectively). In the present study, we included CKD history and eGFR levels on admission into the prediction model. eGFR tested post-PPCI reflects the renal function at that time and is non-repeatable, given the variations in CKD history.

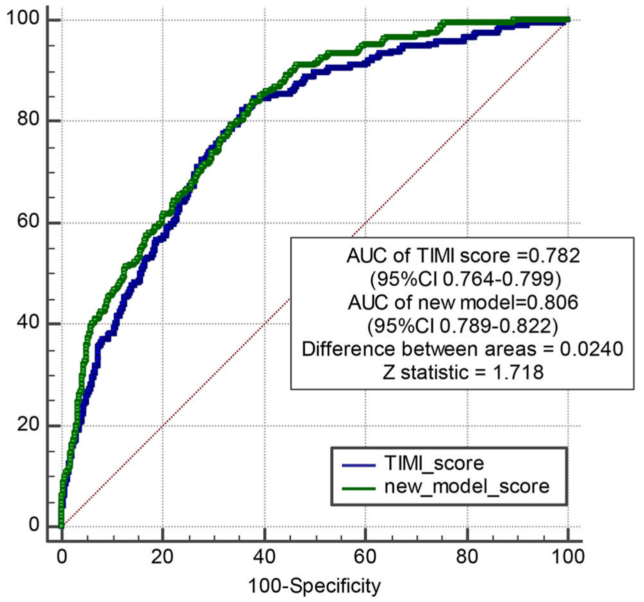

FIGURE 5 | Pairwise comparison of ROC curves between new model and TIMI risk score model. The AUC of new model is 0.806, and the AUC of TIMI score is 0.782. Difference between areas = 0.0240 $<$ 0.05; *z* statistic, 1.718.

No-Flow Phenomenon Is Associated With Increased Risk of MACE

A substantial proportion of patients still had myocardial tissue hypoperfusion after PPCI, which is termed as no-reflow phenomenon caused by microvascular obstruction (31–33). Previous studies have reported an association between the no-flow phenomenon and adverse clinical outcomes after ST-elevation MI (34–38). A metaregression study (39) reported that the no-flow phenomenon was independently correlated with increased 1-year all-cause mortality and 1-year heart failure hospitalization in the fully adjusted model. Although no-reflow phenomenon occurs in the acute phase of ACS, it is relatively significant in predicting events after more than 1 year of follow-up.

STRENGTHS AND LIMITATIONS

This study developed a risk score model to evaluate 3- and 5-years risks of patients with MI who underwent PPCI. The researchers followed strict inclusion and exclusion criteria, which enabled a reasonably streamlined and comparable hospital flow for all patients. The model incorporated variables including routine clinical data, serum inflammatory factors, coronary angiography findings, and other relevant clinical parameters that are commonly included in clinical assessment. These variables are routinely documented in electronic health records; therefore, their collection is not linked with extra costs.

Nevertheless, this study has several potential limitations. First, it is a single-center study of an ethnic population that is not diverse. Second, the large size of the dataset used to develop the models reduces the likelihood of overfitting. Third, D-dimer, hs-CRP, and EF are not routinely obtained as the standard of care for MI patients. Inclusion of these variables may increase the chance of having missing information and inability to calculate the risk score. Finally, patients have been enrolled over a long time period, which could have confounding effects due to improvements in interventional techniques and progress in medication.

CONCLUSION

In summary, we present risk prediction models for estimating the risk for MACEs on the basis of clinical parameters that are commonly available in all patients with MI undergoing PPCI. These models can be implemented alongside further medical investigations to support therapeutic decision-making. However, as with any new risk prediction model, further independent evaluation is required in different settings, including different geographic locations and healthcare organizations, to guide application in clinical management and practice.

DATA AVAILABILITY STATEMENT

The data analyzed in this study is subject to the following licenses/restrictions: The datasets used and/or analyzed during this study are available from the corresponding author on reasonable request. Requests to access these datasets should be directed to hbyanfuwai2018@163.com.

AUTHOR CONTRIBUTIONS

XZ and HY: conception and design. HY: administrative support. HY, CL, and PZ: provision of study materials or patients. XZ, CL, PZ, ZS, JL, JZ, RC, and YW: collection and assembly of data and data analysis and interpretation. All authors: manuscript writing and final approval of manuscript.

FUNDING

This study was supported by the Chinese Academy of Medical Sciences Innovation Fund for Medical Sciences (2016-I2M-1-009) and National Natural Science Funds (number: 81970308).

SUPPLEMENTARY MATERIAL

The Supplementary Material for this article can be found online at: https://www.frontiersin.org/articles/10.3389/fcvm.2020.603621/full#supplementary-material

REFERENCES

1. Lozano R, Naghavi M, Foreman K, Lim S, Shibuya K, Aboyans V, et al. Global and regional mortality from 235 causes of death for 20 age groups in 1990 and 2010: a systematic analysis for the global burden of disease study 2010. *Lancet.* (2012) 380:2095–128. doi: 10.1016/S0140-6736(12)61728-0
2. Bloom DE, Cafiero ET, Jané-Llopis E, Abrahams-Gessel S, Bloom LR, Fathima S, et al. *The Global Economic Burden of Noncommunicable Diseases*. Geneva: World Economic Forum. (2011).
3. Ibanez B, James S, Agewall S, Antunes MJ, Bucciarelli-Ducci C, Bueno H, et al. 2017 ESC Guidelines for the management of acute myocardial infarction in patients presenting with ST-segment elevation: the task force for the management of acute myocardial infarction in patients presenting with ST-segment elevation of the European Society of Cardiology (ESC). *Eur Heart J.* (2018) 39:119–77. doi: 10.1093/eurheartj/ehx393
4. Mihaylova B, Emberson J, Blackwell L, Keech A, Simes J, Barnes EH, et al. The effects of lowering LDL cholesterol with statin therapy in people at low risk of vascular disease: meta-analysis of individual data from 27 randomised trials. *Lancet.* (2012) 380:581–90. doi: 10.1016/S0140-6736(12)60367-5
5. Sundström J, Arima H, Woodward M, Jackson R, Karmali K, Lloyd-Jones D, et al. Blood pressure-lowering treatment based on cardiovascular risk: a meta-analysis of individual patient data. *Lancet.* (2014) 384:591–98. doi: 10.1016/S0140-6736(14)61212-5
6. Lear SA, Hu W, Rangarajan S, Gasevic D, Leong D, Iqbal R, et al. The effect of physical activity on mortality and cardiovascular disease in 130,000 people from 17 high-income, middle-income, and low-income countries: the PURE study. *Lancet.* (2017) 390:2643–54. doi: 10.1016/S0140-6736(17)31634-3
7. Steg PG, James SK, Atar D, Badano LP, Blömstrom-Lundqvist C, Borger MA, et al. ESC guidelines for the management of acute myocardial infarction in patients presenting with ST-segment elevation. *Eur Heart J.* (2012) 33:2569–619. doi: 10.1093/eurheartj/ehs215
8. O'Gara PT, Kushner FG, Ascheim DD, Casey DE Jr, Chung MK, de Lemos JA, et al. 2013 ACCF/AHA guideline for the management of ST-elevation myocardial infarction: executive summary: a report of the American college of cardiology foundation/American heart association task force on practice guidelines. *J Am Coll Cardiol.* (2013) 61:485–510. doi: 10.1016/j.jacc.2012.11.018
9. Banerjee A. Predicting the future of cardiovascular risk prediction. *Heart.* (2017) 103:891.2–2. doi: 10.1136/heartjnl-2016-311141
10. Kaasenbrood L, Boekholdt SM, van der Graaf Y, Ray KK, Peters RJ, Kastelein JJ, et al. Distribution of estimated 10- year risk of recurrent vascular events and residual risk in a secondary prevention population. *Circulation.* (2016) 134:1419–29. doi: 10.1161/CIRCULATIONAHA.116.021314
11. Thiele H, Akin I, Sandri M, Fuernau G, de Waha S, Meyer-Saraei R, et al. PCI strategies in patients with acute myocardial infarction and cardiogenic shock. *N Engl J Med.* (2017) 377:2419–32. doi: 10.1056/NEJMoa1710261
12. Dawson LP, Cole JA, Lancefield TF, Ajani AE, Andrianopoulos N, Thrift AG, et al. Lancefield incidence and risk factors for stroke following percutaneous coronary intervention. *Int J Stroke.* (2020) 15:909–22. doi: 10.1177/1747493020912607
13. Hippisley-Cox J, Coupland C, Brindle P. Development and validation of QrisK3 risk prediction algorithms to estimate future risk of cardiovascular disease: prospective cohort study. *BMJ.* (2017) 357:j2099. doi: 10.1136/bmj.j2099
14. Conroy RM, Pyörälä K, Fitzgerald AP, Sans S, Menotti A, De Backer G, et al. Estimation of ten- year risk of fatal cardiovascular disease in Europe: the score project. *Eur Heart J.* (2003) 24:987–1003. doi: 10.1016/S0195-668X(03)00114-3
15. Goff DC Jr, Lloyd-Jones DM, Bennett G, Coady S, D'Agostino RB, Gibbons R, et al. 2013 ACC/AHA guideline on the assessment of cardiovascular risk: a report of the American college of cardiology/ American heart association Task force on practice guidelines. *Circulation.* (2014) 129:s49–73. doi: 10.1161/01.cir.0000437741.48606.98

16. Liew SM, Doust J, Glasziou P. Cardiovascular risk scores do not account for the effect of treatment: a review. *Heart.* (2011) 97:689–97. doi: 10.1136/hrt.2010.220442
17. Grey C, Jackson R, Schmidt M, Ezzati M, Asaria P, Exeter DJ, et al. One in four major ischemic heart disease events are fatal and 60% are pre-hospital deaths: a national data-linkage study. *Eur Heart J.* (2017) 38:172–80. doi: 10.1093/eurheartj/ehv524
18. Damen JA, Hooft L, Schuit E, Debray TP, Collins GS, Tzoulaki I, et al. Prediction models for cardiovascular disease risk in the general population: systematic review. *BMJ.* (2016) 353:i2416. doi: 10.1136/bmj.i2416
19. Rapsomaniki E, Shah A, Perel P, Denaxas S, George J, Nicholas O, et al. Prognostic models for stable coronary artery disease based on electronic health record cohort of 102,023 patients. *Eur Heart J.* (2014) 35:844–52. doi: 10.1093/eurheartj/eht533
20. Antoniou S, Colicchia M, Guttmann OP, Rathod KS, Wright P, Fhadil S, et al. Risk scoring to guide antiplatelet therapy post- percutaneous coronary intervention for acute coronary syndrome results in improved clinical outcomes. *Eur Heart J Qual Care Clin Outcomes.* (2018) 4:283–9. doi: 10.1093/ehjqcco/qcx041
21. Hodgson LE, Sarnowski A, Roderick PJ, Dimitrov BD, Venn RM, Forni LG. Systematic review of prognostic prediction models for acute kidney injury (AKI) in general hospital populations. *BMJ Open.* (2017) 7:e016591. doi: 10.1136/bmjopen-2017-016591
22. Ortolani P, Marzocchi A, Marrozzini C, Palmerini T, Saia F, Taglieri N, et al. Predictive value of high sensitivity C-reactive protein in patients with ST-elevation myocardial infarction treated with percutaneous coronary intervention. *Eur Heart J.* (2008) 29:1241–9. doi: 10.1093/eurheartj/ehm338
23. Oemrawsingh RM, Cheng JM, Akkerhuis KM, Kardys I, Degertekin M, van Geuns RJ, et al. High-sensitivity C-reactive protein predicts 10-year cardiovascular outcome after percutaneous coronary intervention. *EuroIntervention.* (2016) 12:345–51. doi: 10.4244/EIJY15M07_04
24. Carrero JJ, Andersson Franko M, Obergfell A, Gabrielsen A, Jernberg T. hsCRP level and the risk of death or recurrent cardiovascular events in patients with myocardial infarction: a healthcare-based study. *J Am Heart Assoc.* (2019) 8:e012638. doi: 10.1161/JAHA.119.012638
25. Chen R, Liu C, Zhou P, Tan Y, Sheng Z, Li J, et al. Both low and high postprocedural hscrp associate with increased risk of death in acute coronary syndrome patients treated by percutaneous coronary intervention. *Mediators Inflamm.* (2020) 2020:9343475. doi: 10.1155/2020/9343475
26. Ridker PM. From C-reactive protein to interleukin-6 to interleukin-1: moving upstream to identify novel targets for atheroprotection. *Circ Res.* (2016) 118:145–56. doi: 10.1161/CIRCRESAHA.115.306656
27. Go AS, Chertow GM, Fan D, McCulloch CE, Hsu CY. Chronic kidney disease and the risks of death, cardiovascular events, and hospitalization. *N Engl J Med.* (2004) 351:1296–305. doi: 10.1056/NEJMoa041031
28. Chertow GM, Normand SL, McNeil BJ. “Renalism”: inappropriately low rates of coronary angiography in elderly individuals with renal insufficiency. *J Am Soc Nephrol.* (2004) 15:2462–68. doi: 10.1097/01.ASN.0000135969.33773.0B
29. Farkouh ME, Sidhu MS, Brooks MM, Vlachos H, Boden WE, Frye RL, et al. Impact of chronic kidney disease on outcomes of myocardial revascularization in patients with diabetes. *J Am Coll Cardiol.* (2019) 73:400–11. doi: 10.1016/j.jacc.2018.11.044
30. Stengel B, Metzger M, Froissart M, Rainfray M, Berr C, Tzourio C, et al. Epidemiology and prognostic significance of chronic kidney disease in the elderly–the Three-City prospective cohort study. *Nephrol Dial Transplant.* (2011) 26:3286–95. doi: 10.1093/ndt/gfr323
31. Wu KC, Zerhouni EA, Judd RM, Lugo-Olivieri CH, Barouch LA, Schulman SP, et al. Prognostic significance of microvascular obstruction by magnetic resonance imaging in patients with acute myocardial infarction. *Circulation.* (1998) 97:765–72. doi: 10.1161/01.CIR.97.8.765
32. Hombach V, Grebe O, Merkle N, Waldenmaier S, Höher M, Kochs M, et al. Sequelae of acute myocardial infarction regarding cardiac structure and function and their prognostic significance as assessed by magnetic resonance imaging. *Eur Heart J.* (2005) 26:549–57. doi: 10.1093/eurheartj/ehi147
33. de Waha S, Desch S, Eitel I, Fuernau G, Zachrau J, Leuschner A, et al. Impact of early versus late microvascular obstruction assessed by magnetic resonance imaging on long-term outcome after ST-elevation myocardial infarction—a comparison to traditional prognostic markers. *Eur Heart J.* (2010) 31:2660–68. doi: 10.1093/eurheartj/ehq247
34. van Kranenburg M, Magro M, Thiele H, de Waha S, Eitel I, Cochet A, et al. Prognostic value of microvascular obstruction and infarct size, as measured by CMR in STEMI patients. *JACC Cardiovasc Imaging.* (2014) 7:930–9. doi: 10.1016/j.jcmg.2014.05.010
35. Bonanad C, Monmeneu JV, Lopez-Lereu MP, Hervas A, de Dios E, Gavara J, et al. Prediction of long-term major events soon after a first ST-segment elevation myocardial infarction by cardiovascular magnetic resonance. *Eur J Radiol.* (2016) 85:585–92. doi: 10.1016/j.ejrad.2015.12.012
36. Regenfus M, Schlundt C, Krähner R, Schönegger C, Adler W, Ludwig J, et al. Six-year prognostic value of microvascular obstruction after reperfused ST-elevation myocardial infarction as assessed by contrast-enhanced cardiovascular magnetic resonance. *Am J Cardiol.* (2015) 116:1022–7. doi: 10.1016/j.amjcard.2015.06.034
37. Klug G, Mayr A, Schenk S, Esterhammer R, Schocke M, Nocker M, et al. Prognostic value at 5 years of microvascular obstruction after acute myocardial infarction assessed by cardiovascular magnetic resonance. *J Cardiovasc Magn Reson.* (2012) 14:46. doi: 10.1186/1532-429X-14-46
38. de Waha S, Desch S, Eitel I, Fuernau G, Lurz P, Leuschner A, et al. Relationship and prognostic value of microvascular obstruction and infarct size in ST-elevation myocardial infarction as visualized by magnetic resonance imaging. *Clin Res Cardiol.* (2012) 101:487–95. doi: 10.1007/s00392-012-0419-3
39. de Waha S, Patel MR, Granger CB, Ohman EM, Maehara A, Eitel I, et al. Relationship between microvascular obstruction and adverse events following primary primary percutaneous coronary intervention for ST-segment elevation myocardial infarction: an individual patient data pooled analysis from seven randomized trials. *Eur Heart J.* (2017) 38:3502–10. doi: 10.1093/eurheartj/ehx414

Conflict of Interest: The authors declare that the research was conducted in the absence of any commercial or financial relationships that could be construed as a potential conflict of interest.

frontiers
in Cardiovascular Medicine

ORIGINAL RESEARCH
published: 02 February 2021
doi: 10.3389/fcvm.2021.614204

Development and Validation of a Predictive Model for Coronary Artery Disease Using Machine Learning

Chen Wang[1], Yue Zhao[1], Bingyu Jin[1], Xuedong Gan[2], Bin Liang[1], Yang Xiang[1], Xiaokang Zhang[1], Zhibing Lu[2] and Fang Zheng[1]*

[1] *Department of Laboratory Medicine, Center for Gene Diagnosis, Zhongnan Hospital of Wuhan University, Wuhan, China,*
[2] *Department of Cardiology, Zhongnan Hospital of Wuhan University, Wuhan, China*

Early identification of coronary artery disease (CAD) can prevent the progress of CAD and effectually lower the mortality rate, so we intended to construct and validate a machine learning model to predict the risk of CAD based on conventional risk factors and lab test data. There were 3,112 CAD patients and 3,182 controls enrolled from three centers in China. We compared the baseline and clinical characteristics between two groups. Then, Random Forest algorithm was used to construct a model to predict CAD and the model was assessed by receiver operating characteristic (ROC) curve. In the development cohort, the Random Forest model showed a good AUC 0.948 (95%CI: 0.941–0.954) to identify CAD patients from controls, with a sensitivity of 90%, a specificity of 85.4%, a positive predictive value of 0.863 and a negative predictive value of 0.894. Validation of the model also yielded a favorable discriminatory ability with the AUC, sensitivity, specificity, positive predictive value, and negative predictive value of 0.944 (95%CI: 0.934–0.955), 89.5%, 85.8%, 0.868, and 0.886 in the validation cohort 1, respectively, and 0.940 (95%CI: 0.922–0.960), 79.5%, 94.3%, 0.932, and 0.823 in the validation cohort 2, respectively. An easy-to-use tool that combined 15 indexes to assess the CAD risk was constructed and validated using Random Forest algorithm, which showed favorable predictive capability (http://45.32.120.149:3000/randomforest). Our model is extremely valuable for clinical practice, which will be helpful for the management and primary prevention of CAD patients.

Keywords: coronary artery disease, prediction model, machine learning, random forest, primary prevention

Edited by:
Yun Fang,
University of Chicago, United States

Reviewed by:
Joan T. Matamalas,
Brigham and Women's Hospital and Harvard Medical School,
United States
Massimo Mancone,
Sapienza University of Rome, Italy

***Correspondence:**
Fang Zheng
zhengfang@whu.edu.cn

Specialty section:
This article was submitted to Atherosclerosis and Vascular Medicine,
a section of the journal
Frontiers in Cardiovascular Medicine

***Received:** 05 October 2020*
***Accepted:** 15 January 2021*
***Published:** 02 February 2021*

Citation:
Wang C, Zhao Y, Jin B, Gan X, Liang B, Xiang Y, Zhang X, Lu Z and Zheng F (2021) Development and Validation of a Predictive Model for Coronary Artery Disease Using Machine Learning.
Front. Cardiovasc. Med. 8:614204.
doi: 10.3389/fcvm.2021.614204

INTRODUCTION

Currently, coronary artery disease (CAD) continues to be the principal cause of worldwide incidence and mortality (1, 2). The main pathogenic mechanism of CAD is atherosclerosis, a complicated and constantly progressing process of chronic inflammation characterized by dysfunction of endothelial cells, cumulative deposition of lipoprotein particles, migration of monocyte and macrophage, proliferation of vascular smooth muscle cells (VSMCs), and ultimately contributes to a narrowing of the vessel that impedes blood supply to the heart (3, 4). The reference standard of CAD diagnosis is invasive coronary angiography, which allows for real-time evaluation of the location and the degree of coronary stenosis, and to decide the most suitable therapy (5). However, its use for population screening has been limited by the demand for specialized catheterization laboratory and the possible radiation exposure (6, 7). Consequently, sensitive, specific, and non-invasive indicators for CAD risk assessment are urgently desirable.

Development and progression of coronary atherosclerosis is modulated by multiple interplays between genetic and environmental factors (8). Consistent and convincing evidence has authenticated a casual correlation between lipoprotein-related lipid contents and cardiovascular disease prevalence (9–11). High level of circulating low-density lipoprotein cholesterol (LDL-C) and triglyceride (TG)-rich lipoproteins were related with high risk of CAD, whereas high level of high-density lipoprotein cholesterol (HDL-C) was correlated with low CAD risk. Furthermore, pedigree studies have demonstrated that triglyceride, LDL-C, and HDL-C concentrations are strongly determined by the individual genetic architecture. For instance, rare variants in the apolipoprotein B (*APOB*) and LDL receptor (*LDLR*) genes and common variants in the apolipoprotein E (*APOE*) gene could increase LDL-C contents and were also correlated with increased susceptibility to CAD (12). In addition to cholesterol, the epidemiological studies have also substantiated other canonical risk factors, such as age, male gender, smoking, alcohol drinking, hypertension, diabetes, and obesity. To devise and improve preventive tactics for CAD, it is indispensable to comprehend and properly calculate the etiological contribution of these risk factors. In this study, we sought to evaluate the predictive value of these traditional risk factors in CAD by machine learning algorithms.

MATERIALS AND METHODS

Study Design and Data Collection

This three-stage case-control study, involving 3,112 CAD patients and 3,182 controls, was retrospectively collected from three clinical centers: the development cohort with 2014 CAD cases and 2018 controls from Wuhan Asia Heart Hospital between March 2014 and October 2016, the validation cohort 1 with 837 CAD cases and 876 controls from Zhongnan Hospital of Wuhan University between January 2016 and December 2017 and the validation cohort 2 with 261 CAD cases and 258 controls from Shandong Provincial Hospital between January 2017 and February 2018. The diagnosis of CAD was determined by coronary angiography that stenosis $\geq$50% in at least one main coronary artery or their major branches. Patients with other cardiac diseases, autoimmune diseases, systemic diseases, and cancers were excluded. The control groups were non-CAD individuals based on physical examination and medical history evaluations. Traditional CAD risk factors such as age, gender, alcohol drinking, cigarette smoking and histories of hyperlipidemia, hypertension, and type 2 diabetes mellitus (T2DM) and clinical information, including blood pressure, body mass index (BMI), fasting plasma glucose (FPG), total cholesterol (TC), total triglyceride (TG), LDL-C, and HDL-C were retrospectively collected from the database of electronic medical records and laboratory test reports. The study was approved by the Ethics Committees of Wuhan Asia Heart Hospital, Zhongnan Hospital of Wuhan University, and Shandong Provincial Hospital and adhered to the tenets of the Declaration of Helsinki. Informed consent was obtained from all participants.

Machine Learning Algorithms

Logistic regression is a kind of probabilistic statistical classification model, which can be applied to predict the classification of nominal variable based on certain features. The classification is completed by utilizing the logit function to evaluate the outcome probability. As a supervised machine learning algorithm, support vector machines (SVM) can be fitted for both classification and regression. It first maps the data into a multidimensional feature space constructed by the kernel function, and then determines the optimal hyperplane that partitions the training set by the maximum boundary. Decision trees, one of the easiest kinds of decision model, use a tree structure built by recursive partitioning to simulate the correlations between the features and the potential outcomes. Once the model is created, the resulting structure is shown in a human-readable format. Random forests (RF) are modified bagged trees that randomly select the predictor features to split at each node and incorporate the voting results of many decision trees for classification. It retains the many strengths of the decision tree and exhibits high accurateness in disease diagnosis and risk prediction.

Statistical Analysis

Qualitative variables were expressed as frequencies with proportions, and the differences between cases and controls were examined by Chi-square test. Quantitative variables were shown as mean with standard deviation (SD) and were assessed for normality distribution by the Kolmogorov-Smirnov test. Independent t-test and Mann-Whitney U-test were performed to compare two groups of continuous variables with or without normal distribution, respectively. A two-sided $P < 0.05$ was considered to be statistically significant.

Least absolute shrinkage and selection operator (LASSO) regression analysis was applied to identify relatively important features. The logistic regression can be fitted to the data using the glm function with the family argument set to binomial and the summary function was used to check the coefficients and their p-values. We use the e1071 package to build linear SVM model since it contains the tune.svm function which can optimize the tuning parameters and kernel functions through cross-validation. To build the classification tree model, we use rpart function from party package and inspect the error per split in order to determine the optimal number of splits in the tree, then prune function was used to prune the tree. Randomforest function from randomForest package was used to build random forest model. The specific and optimal tree was determined by the minimum mean of squared residuals and the number of trees constructed in this model was 178, and three variables were randomly selected to split at each node. The prediction model was established by the four aforementioned machine learning algorithms and the predictive capability was evaluated by the area under the receiver operating characteristic curve (ROC) and the precision-recall curve, using precrec package. For final model, ROCR package was conducted to assess the classification accuracy in the development and validation cohorts. The methods and the interpretation of the results are guaranteed by a machine learning algorithm expert. All data analysis was performed in R software (version 3.6.0).

RESULTS

Baseline and Clinical Characteristics of Study Population

In the development cohort, CAD patients had significantly higher age, higher body mass index (BMI), higher proportions of smoking, alcohol drinking, histories of hyperlipidemia, hypertension, and T2DM, higher concentrations of TC, TG, LDL-C, and FPG, and lower level of HDL-C, systolic blood pressure (SBP), and diastolic blood pressure (DBP) comparing with controls (**Table 1**). In two validation cohorts, the baseline and clinical characteristics of study population were basically similar to that of the development cohort (**Table 1**).

Machine Learning Model Evaluation

By LASSO regression filtration, all these variables remain significant (**Figure 1**). Therefore, we utilized four machine learning algorithms (logistic regression, RF, decision tree classification, and SVM) to construct the full model with all these variables, and the ROC curve (**Figure 2**) and the precision-recall curve (**Figure 3**) were implemented to assess their performance. Ultimately, random forests model was chosen for further analysis owing to its highest predictive accuracy.

Model Construction and Validation

We constructed a risk prediction model with all these variables by the random forests. The out-of-bag (OOB) estimate of error rate was 12.26%, indicating that the generalization error of this model is relatively small. The degree of Gini coefficient average decrease implied that HDL-C, followed by LDL-C, TG, BMI, and TC are important features for the risk evaluation of CAD (**Figure 4**). In the development cohort, this model yielded a high AUC 0.948 (95%CI: 0.941–0.954) to identify CAD patients from controls, with a sensitivity of 90%, a specificity of 85.4%, a positive predictive value of 0.863 and a negative predictive value of 0.894 (**Figure 5A**). In consistent with the development cohort, favorable discriminatory ability was also demonstrated by two validation cohorts, with an AUC, sensitivity, specificity, positive predictive value, and negative predictive value of 0.944 (95%CI: 0.934–0.955), 89.5%, 85.8%, 0.868, and 0.886 in the validation cohort 1 (**Figure 5B**), respectively, and 0.940 (95%CI: 0.922–0.960), 79.5%, 94.3%, 0.932, and 0.823 in the validation cohort 2 (**Figure 5C**), respectively. The model is further shown as a web calculator to facilitate its application (http://45.32.120.149:3000/randomforest).

DISCUSSION

In the current study, we elucidated the significant contributions of age, gender, alcohol drinking, cigarette smoking, hyperlipidemia, hypertension and T2DM, TC, TG, HDL-C, LDL-C, SBP, DBP, and FBG to the risk of CAD. Subsequently, we constructed and validated a Random Forest model integrated these indexes with a favorable discriminability that can be helpful for the non-invasive identification of CAD patients.

The most important features identified by Random Forest was HDL-C. HDL-C has been regarded as "good cholesterol" largely owing to an inverse association between high HDL-C levels and low CAD risk (13, 14). The main functions of HDL are to facilitate reverse cholesterol transport and regulate inflammation (15). The potential atheroprotective effects of HDL from healthy individuals were remarkably impaired in CAD patients (16, 17). The Framingham study suggested that about 44% CAD clinical

TABLE 1 | Baseline and clinical characteristics of the study cohort.

Variables	**Development cohort**			**Validation cohort1**			**Validation cohort2**		
	Control (*N* = 2,048)	**CAD (*N* = 2,014)**	***P***	**Control (*N* = 876)**	**CAD (*N* = 837)**	***P***	**Control (*N* = 258)**	**CAD (*N* = 261)**	***P***
Age, year	60.22 ± 9.81	62.56 ± 9.77	<0.001	59.23 ± 11.62	61.97 ± 9.33	<0.001	57.26 ± 9.81	60.68 ± 9.87	<0.001
Male, *n* (%)	1,268 (61.91)	1,230 (61.07)	0.582	536 (61.19)	498 (59.5)	0.475	163 (63.18)	200 (76.63)	0.001
BMI, kg/m^2	23.8 ± 2.45	25.11 ± 3.71	<0.001	23.69 ± 2.4	25.04 ± 3.68	<0.001	24.11 ± 2.15	25.61 ± 4.37	0.001
Smoking, *n* (%)	573 (27.98)	843 (41.86)	<0.001	240 (27.4)	322 (38.47)	<0.001	58 (22.48)	137 (52.49)	<0.001
Alcohol drinking, *n* (%)	511 (24.95)	555 (27.56)	<0.001	215 (24.54)	231 (27.6)	0.023	56 (21.71)	123 (47.13)	<0.001
Hypertension, *n* (%)	786 (38.38)	1,230 (61.07)	<0.001	365 (41.67)	484 (57.83)	<0.001	86 (33.33)	161 (61.69)	<0.001
T2DM, *n* (%)	521 (25.44)	636 (31.58)	<0.001	220 (25.11)	262 (31.3)	0.004	78 (30.23)	102 (39.08)	0.034
Hyperlipidemia, *n* (%)	477 (23.39)	585 (29.05)	<0.001	199 (22.72)	248 (29.63)	0.001	56 (21.71)	84 (32.18)	0.007
TC, mmol/L	4.59 ± 0.82	4.61 ± 1.09	0.009	4.59 ± 0.85	4.63 ± 1.14	0.016	4.81 ± 0.85	4.47 ± 1.4	<0.001
TG, mmol/L	1.24 ± 0.61	1.7 ± 1.07	<0.001	1.26 ± 0.63	1.74 ± 1.07	<0.001	1.14 ± 0.48	1.96 ± 1.29	<0.001
HDL-C, mmol/L	1.3 ± 0.25	1 ± 0.19	<0.001	1.3 ± 0.25	1.02 ± 0.19	<0.001	1.33 ± 0.28	1 ± 0.19	<0.001
LDL-C, mmol/L	2.69 ± 0.61	2.75 ± 0.87	<0.001	2.7 ± 0.65	2.74 ± 0.86	0.003	2.89 ± 0.74	2.86 ± 1	0.143
SBP, mmHg	139.78 ± 25	132.56 ± 19.68	<0.001	139.65 ± 25.18	131.74 ± 19.09	<0.001	128.76 ± 16.67	132.22 ± 17.25	0.02
DBP, mmHg	85.05 ± 16.94	81.02 ± 11.8	<0.001	85.5 ± 17.83	81.47 ± 11.57	0.005	80.97 ± 11.83	79.62 ± 11.48	0.348
FBG, mmol/L	5.37 ± 1.47	5.85 ± 2.02	<0.001	5.36 ± 1.52	5.86 ± 2.26	<0.001	5.41 ± 0.64	6.48 ± 1.95	<0.001

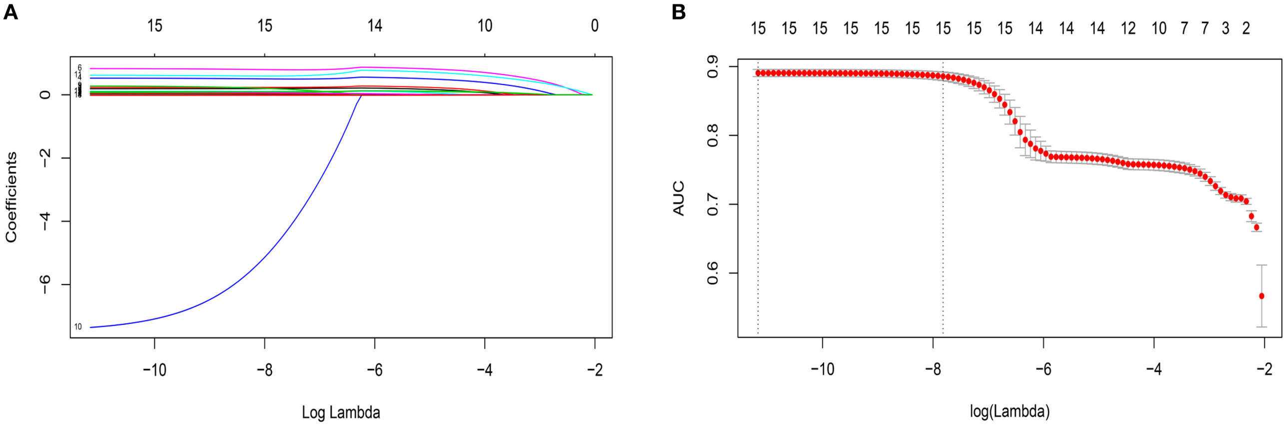

FIGURE 1 | Features selection by least absolute shrinkage and selection operator (LASSO). **(A)** LASSO coefficients profiles (*y*-axis) of the 15 features. The upper *x*-axis is the average numbers of predictors and the lower x-axis is the log(λ). **(B)** Five-fold cross-validation for tuning parameter selection in the LASSO model. The area under the receiver operating characteristic (AUC) with error bar is plotted against log(λ), where λ is the tuning parameter. The dotted vertical lines are drawn at the optimal values by minimum criteria and the one standard error of the minimum criteria (1se criteria). The upper *x*-axis is the average numbers of predictors and the lower *x*-axis is the log(λ). To avoid overfitting, 1se criteria (λ = 0.000402) was selected.

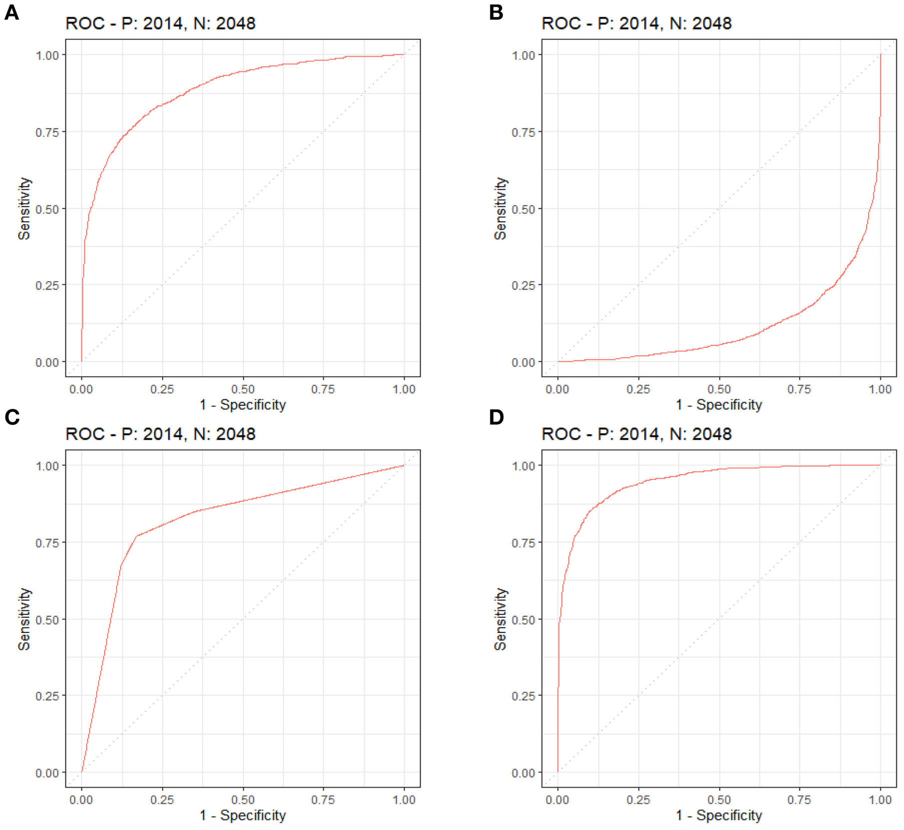

FIGURE 2 | Each machine learning model was assessed by the ROC curve, which plots a curve according to its true positive rate (*y*-axis) against its false positive rate (*x*-axis). The larger area under the curve, the better the prediction accuracy of the model. **(A)** Logistic regression. **(B)** Support vector machine (SVM). **(C)** Decision tree classification. **(D)** Random forest (RF).

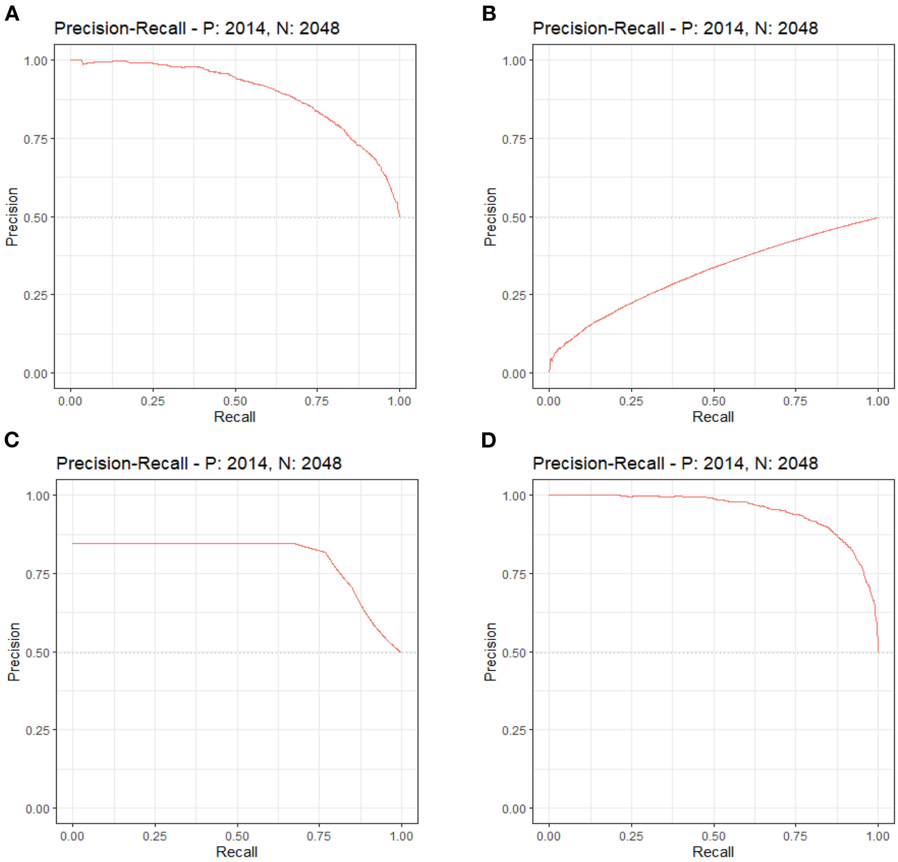

FIGURE 3 | Each machine learning model was evaluated by the precision-recall curve, which displays the trade-off between recall (*x*-axis) and precision (*y*-axis). The bigger area under the curve, the greater predictive capability of the model. **(A)** Logistic regression. **(B)** Support vector machine (SVM). **(C)** Decision tree classification. **(D)** Random forest (RF).

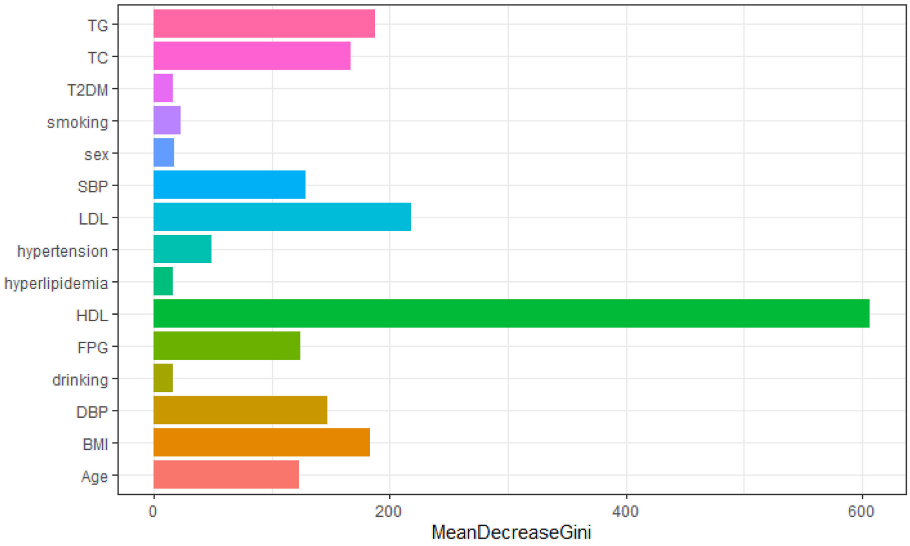

FIGURE 4 | Variable importance plot for the Random Forest model. The *x*-axis is the average decrease in the Gini coefficient, the *y*-axis is 15 risk factors of CAD. The more the average decrease of the Gini coefficient, the more important of the variable.

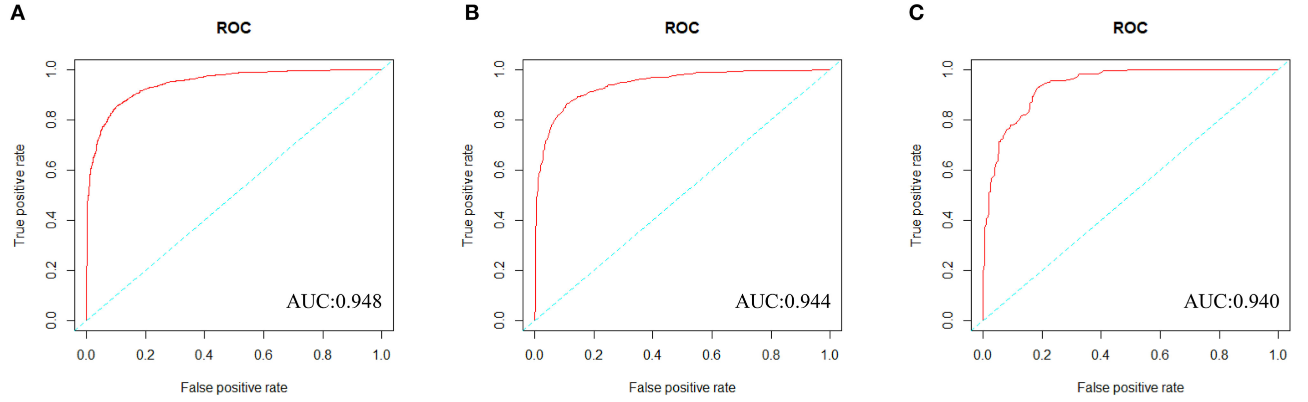

FIGURE 5 | The ROC curves of the Random Forest model in three cohorts. **(A)** To evaluate discrimination performance in the development cohort, area under the curve (AUC) of ROC curve was 0.948. **(B)** To assess the discrimination capability in the validation cohort 1, AUC was 0.944. **(C)** To assess the predictive capability in the validation cohort 2, AUC was 0.940.

events in men with HDL-C >40 mg/dL and near 43% in women with HDL-C >50 mg/dL. In addition, Mendelian randomization genetic studies have suggested that genetically raised HDL-C levels were not correlated with a decreased risk of myocardial infarction comparing with genetic variants associated with lowering LDL-C levels (18). Furthermore, recent large-scale clinical studies had also failed to validate the preventive effect of HDL-C raising treatments on coronary disease (19, 20). These results highlighted that HDL-C levels were not necessarily causally associated with coronary disease and normal serum HDL-C levels did not guarantee free of CAD events (15). Nevertheless, our model illustrated that HDL-C levels made a greatest contribution in CAD risk prediction.

A high serum LDL-C level is a well-established risk factor for cardiovascular disease, especially CAD. Genetic studies have revealed that variants in PSCK9 (proprotein convertase subtilisin/kexin type 9), HMGCR (HMG-coenzyme A reductase), and NPC1L1 (Niemann-Pick C1-like intracellular cholesterol transporter 1) are correlated with decreasing LDL-C levels and low CAD risk (21–23). Moreover, large-scale clinical studies have suggested that decreasing LDL-C by targeting these proteins has been proven to be a safe and effectual approach to reduce risk of coronary disease. Additionally, lowering serum LDL-C levels can reduce mortality and morbidity of cardiovascular diseases in both primary and secondary prevention (24, 25). Consistent with this result, our model also showed that LDL-C levels were the important feature in CAD risk assessment.

Large triglyceride-rich lipoprotein particles including chylomicrons (CM) and very low-density lipoprotein (VLDL) particles pass through the arterial wall via transcytosis in specialized vesicles instead of direct penetration. These particles can be swallowed by arterial macrophages, with enormous cholesterol depositing and foam cell formation in coronary arteries (26). Therefore, elevated blood triglyceride levels were associated with the development of CAD by directly participating in atherosclerotic plaque formation and progression (27). However, the relationship between increased plasma triglyceride levels and cardiovascular disease were controversial in epidemiological studies. A large meta-analysis comprising 10,158 CAD patients from 262,525 individuals in 29 prospective studies suggested a modestly significant correlation between triglyceride levels and CAD risk (28). In contrast, other studies didn't find significance after multivariable adjustments for smoking, hypertension, diabetes, BMI, and glucose levels. Meanwhile, some of these studies also implied that even a little elevated triglyceride levels were correlated with high risk of recurrent CVD events in patients receiving stain treatment and should be regarded as a useful risk indicator (29). Moreover, genetic studies have demonstrated that increased blood triglyceride levels were causally associated with high CAD risk (30). In addition, a Mendelian randomization study revealed that genetically decreased non-fasting plasma triglyceride concentrations could reduce all-cause mortality (31). In accord with these reports, our model hinted that blood triglyceride levels were helpful for CAD risk prediction.

Aside from HDL-C, LDL-C, and triglyceride levels, other variables such as BMI, TC, DBP, SBP, FBG, age, hypertension, smoking, sex, T2DM, hyperlipidemia, and drinking are of relative importance in stratifying a patient's risk. Age is the most important factor associated with the progression of CAD, as well as death when coronary atherosclerosis occurs (32). Previous studies have demonstrated that there is a conspicuous sex difference in CAD incidence and mortality (33, 34). In general, men develop CAD earlier than women (35). Dietary cholesterol could raise the concentration of serum total cholesterol, which was associated with a high risk of cardiovascular disease (36). Obesity has been shown to be an usual cause of cardiovascular mortality in the developed countries (37). Abdominal visceral with an excess fat overload can result in atherosclerotic disease (37). Dysregulation of endocrine factors originating from adipocyte in overnutrition has been presumed to be implicated in the progression of atherosclerosis (38). Hypertension was pathologically related with CAD and arterial hypertension could aggravate CAD (39). Furthermore, hypertension was also often correlated with other risk factors of CAD, such as dyslipidemia and insulin resistance (40). Diabetes was reported to frequently correlated with high levels of triglyceride and low levels of HDL-C (41). Smoking could induce endothelial exposure and platelet adhering to subintimal layer, thus increasing lipoprotein particle penetration and proliferation of smooth muscle cells (SMCs) (42). Meanwhile, the cardiovascular system is sensitive to the toxic effects of alcohol. High-dose alcohol drinking could induce extensive coronary arterial damage and increase the risk of developing CAD (43).

The Framingham risk score is a well-known prediction algorithm that has been widely applied to evaluate CAD risk in different populations including Chinese (44, 45). However, since the risk equation was developed in 1976 and more than 99% participants are of European descent, it is necessary to reconfirm the predictive values of traditional risk factors for Chinese due to the intrinsic discrepancy of diet and life style, social environment and genetic predisposition. Furthermore, rapidly increasing per-capita income, westernization of lifestyle, an aging population and longer life spans contributed to conspicuous changes in the CVD epidemics and risk factors pattern in China during the past decade (46). Therefore, an evolutionary CAD risk appraisal tool developed from recent information of Chinese population would be better generalized. Some recent studies utilized nomogram to assess CAD risks based on the results of multivariate logistic regression or Cox proportional hazard regression (47–50). Albeit these studies provided powerful clinical benefits, these models had the inherent drawback that the algorithm is sensitive to multicollinearity and missing values. Random forest is an ensemble classifier which applies lots of decision trees to the dataset and integrates results from all the trees by taking a majority vote. It can ameliorate prediction accuracy without considerably increasing the calculation amount. Our study established and validated a Random Forest model, which shows favorable predictive capability and clinical application value.

Some possible limitations in our study should be emphasized. First, this is a retrospective study, some potential inherent biases cannot be ignored and causal inference is limited. Second, we only took 15 CAD traditional risk factors into account, future studies with more variables including individual genetic information are necessitated to further confirm our results. Finally, this was a three-center study of only Chinese population from two provinces, which may restrict its generalizability. Therefore, future prospective multicenter studies from other areas of China are required to validate the findings of our study.

Collectively, an easy-to-use tool that combined 15 indexes to assess the CAD risk was constructed and validated using Random Forest algorithm, which showed favorable predictive capability (http://45.32.120.149:3000/randomforest). Our model is extremely valuable for clinical practice, which will be helpful for the primary prevention and management of CAD patients.

DATA AVAILABILITY STATEMENT

The raw data supporting the conclusions of this article will be made available by the authors, without undue reservation.

ETHICS STATEMENT

The studies involving human participants were reviewed and approved by the Ethics Committees of Wuhan Asia Heart Hospital, Zhongnan Hospital of Wuhan University, and Shandong Provincial Hospital. The patients/participants provided their written informed consent to participate in this study.

AUTHOR CONTRIBUTIONS

XG, BL, YX, XZ, and ZL collected clinical information and laboratory data. CW and BJ analyzed the data. CW and YZ generated the figures and wrote the manuscript. FZ designed and supervised this study and revised the manuscript. All authors read and approved the final manuscript.

FUNDING

This work was supported by the National Natural Science Foundation of China (81871722 and 82072373).

ACKNOWLEDGMENTS

We thank Mr. Xinping Huang for his kind help in web calculator production.

REFERENCES

1. Zhu KF, Wang YM, Zhu JZ, Zhou QY, Wang NF. National prevalence of coronary heart disease and its relationship with human development index: a systematic review. *Eur J Prev Cardiol.* (2016) 23:530–43. doi: 10.1177/2047487315587402
2. Roth GA, Abate D, Abate KH, Abay SM, Abbafati C, Abbasi N, et al. Global, regional, and national age-sex-specific mortality for 282 causes of death in 195 countries and territories, 1980-2017: a systematic analysis for the Global Burden of Disease Study 2017. *Lancet.* (2018) 392:1736–88. doi: 10.1016/s0140-6736(18)32203-7
3. Hansson GK. Inflammation, atherosclerosis, and coronary artery disease. *N Engl J Med.* (2005) 352:1685–95. doi: 10.1056/NEJMra043430
4. Willer CJ, Sanna S, Jackson AU, Scuteri A, Bonnycastle LL, Clarke R, et al. Newly identified loci that influence lipid concentrations and risk of coronary artery disease. *Nat Genet.* (2008) 40:161–9. doi: 10.1038/ng.76
5. Levine GN, Bates ER, Blankenship JC, Bailey SR, Bittl JA, Cercek B, et al. 2015 ACC/AHA/SCAI focused update on primary percutaneous coronary intervention for patients with ST-elevation myocardial infarction: an update of the 2011 ACCF/AHA/SCAI guideline for percutaneous coronary intervention and the 2013 ACCF/AHA guideline for the management of ST-elevation myocardial infarction: a report of the American College of Cardiology/American Heart Association Task Force on Clinical Practice Guidelines and the Society for Cardiovascular Angiography and Interventions. *Circulation.* (2016) 133:1135–47. doi: 10.1161/cir.0000000000000336

6. de Gonzalo-Calvo D, Vilades D, Martínez-Camblor P, Vea À, Nasarre L, Sanchez Vega J, et al. Circulating microRNAs in suspected stable coronary artery disease: a coronary computed tomography angiography study. *J Intern Med.* (2019) 286:341–55. doi: 10.1111/joim.12921
7. Messerli M, Panadero AL, Giannopoulos AA, Schwyzer M, Benz DC, Gräni C, et al. Enhanced radiation exposure associated with anterior-posterior x-ray tube position in young women undergoing cardiac computed tomography. *Am Heart J.* (2019) 215:91–4. doi: 10.1016/j.ahj.2019.05.006
8. Khera AV, Emdin CA, Drake I, Natarajan P, Bick AG, Cook NR, et al. Genetic risk, adherence to a healthy lifestyle, and coronary disease. *N Engl J Med.* (2016) 375:2349–58. doi: 10.1056/NEJMoa1605086
9. Kuulasmaa K, Tunstall-Pedoe H, Dobson A, Fortmann S, Sans S, Tolonen H, et al. Estimation of contribution of changes in classic risk factors to trends in coronary-event rates across the WHO MONICA Project populations. *Lancet.* (2000) 355:675–87. doi: 10.1016/s0140-6736(99)11180-2
10. Law MR, Wald NJ, Rudnicka AR. Quantifying effect of statins on low density lipoprotein cholesterol, ischaemic heart disease, and stroke: systematic review and meta-analysis. *BMJ.* (2003) 326:1423. doi: 10.1136/bmj.326.7404.1423
11. Clarke R, Emberson JR, Parish S, Palmer A, Shipley M, Linksted P, et al. Cholesterol fractions and apolipoproteins as risk factors for heart disease mortality in older men. *Arch Intern Med.* (2007) 167:1373–8. doi: 10.1001/archinte.167.13.1373
12. Breslow JL. Genetics of lipoprotein abnormalities associated with coronary artery disease susceptibility. *Annu Rev Genet.* (2000) 34:233–54. doi: 10.1146/annurev.genet.34.1.233
13. Castelli WP. Cholesterol and lipids in the risk of coronary artery disease–the Framingham Heart Study. *Can J Cardiol.* (1988) 4(Suppl A):5–10a
14. Di Angelantonio E, Sarwar N, Perry P, Kaptoge S, Ray KK, Thompson A, et al. Major lipids, apolipoproteins, and risk of vascular disease. *JAMA.* (2009) 302:1993–2000. doi: 10.1001/jama.2009.1619
15. Navab M, Reddy ST, Van Lenten BJ, Fogelman AM. HDL and cardiovascular disease: atherogenic and atheroprotective mechanisms. *Nat Rev Cardiol.* (2011) 8:222–32. doi: 10.1038/nrcardio.2010.222
16. Besler C, Heinrich K, Rohrer L, Doerries C, Riwanto M, Shih DM, et al. Mechanisms underlying adverse effects of HDL on eNOS-activating pathways in patients with coronary artery disease. *J Clin Invest.* (2011) 121:2693–708. doi: 10.1172/jci42946
17. Huang Y, Wu Z, Riwanto M, Gao S, Levison BS, Gu X, et al. Myeloperoxidase, paraoxonase-1, and HDL form a functional ternary complex. *J Clin Invest.* (2013) 123:3815–28. doi: 10.1172/jci67478
18. Voight BF, Peloso GM, Orho-Melander M, Frikke-Schmidt R, Barbalic M, Jensen MK, et al. Plasma HDL cholesterol and risk of myocardial infarction: a mendelian randomisation study. *Lancet.* (2012) 380:572–80. doi: 10.1016/s0140-6736(12)60312-2
19. Schwartz GG, Olsson AG, Abt M, Ballantyne CM, Barter PJ, Brumm J, et al. Effects of dalcetrapib in patients with a recent acute coronary syndrome. *N Engl J Med.* (2012) 367:2089–99. doi: 10.1056/NEJMoa1206797
20. Landray MJ, Haynes R, Hopewell JC, Parish S, Aung T, Tomson J, et al. Effects of extended-release niacin with laropiprant in high-risk patients. *N Engl J Med.* (2014) 371:203–12. doi: 10.1056/NEJMoa1300955
21. Cannon CP, Blazing MA, Giugliano RP, McCagg A, White JA, Theroux P, et al. Ezetimibe added to statin therapy after acute coronary syndromes. *N Engl J Med.* (2015) 372:2387–97. doi: 10.1056/NEJMoa1410489
22. Collins R, Reith C, Emberson J, Armitage J, Baigent C, Blackwell L, et al. Interpretation of the evidence for the efficacy and safety of statin therapy. *Lancet.* (2016) 388:2532–61. doi: 10.1016/s0140-6736(16)31357-5
23. Sabatine MS, Giugliano RP, Keech AC, Honarpour N, Wiviott SD, Murphy SA, et al. Evolocumab and clinical outcomes in patients with cardiovascular disease. *N Engl J Med.* (2017) 376:1713–22. doi: 10.1056/NEJMoa1615664
24. Graham I, Cooney MT, Bradley D, Dudina A, Reiner Z. Dyslipidemias in the prevention of cardiovascular disease: risks and causality. *Curr Cardiol Rep.* (2012) 14:709–20. doi: 10.1007/s11886-012-0313-7
25. Reiner Ž. Statins in the primary prevention of cardiovascular disease. *Nat Rev Cardiol.* (2013) 10:453–64. doi: 10.1038/nrcardio.2013.80
26. Goldstein JL, Ho YK, Brown MS, Innerarity TL, Mahley RW. Cholesteryl ester accumulation in macrophages resulting from receptor-mediated uptake and degradation of hypercholesterolemic canine beta-very low density lipoproteins. *J Biol Chem.* (1980) 255:1839–48.
27. Alaupovic P, Mack WJ, Knight-Gibson C, Hodis HN. The role of triglyceride-rich lipoprotein families in the progression of atherosclerotic lesions as determined by sequential coronary angiography from a controlled clinical trial. *Arterioscler Thromb Vasc Biol.* (1997) 17:715–22. doi: 10.1161/01.atv.17.4.715
28. Sarwar N, Danesh J, Eiriksdottir G, Sigurdsson G, Wareham N, Bingham S, et al. Triglycerides and the risk of coronary heart disease: 10,158 incident cases among 262,525 participants in 29 Western prospective studies. *Circulation.* (2007) 115:450–8. doi: 10.1161/circulationaha.106.637793
29. Faergeman O, Holme I, Fayyad R, Bhatia S, Grundy SM, Kastelein JJ, et al. Plasma triglycerides and cardiovascular events in the Treating to New Targets and Incremental Decrease in End-Points through Aggressive Lipid Lowering trials of statins in patients with coronary artery disease. *Am J Cardiol.* (2009) 104:459–63. doi: 10.1016/j.amjcard.2009.04.008
30. Do R, Willer CJ, Schmidt EM, Sengupta S, Gao C, Peloso GM, et al. Common variants associated with plasma triglycerides and risk for coronary artery disease. *Nat Genet.* (2013) 45:1345–52. doi: 10.1038/ng.2795
31. Thomsen M, Varbo A, Tybjærg-Hansen A, Nordestgaard BG. Low nonfasting triglycerides and reduced all-cause mortality: a mendelian randomization study. *Clin Chem.* (2014) 60:737–46. doi: 10.1373/clinchem.2013.219881
32. Goff DC Jr, Lloyd-Jones DM, Bennett G, Coady S, D'Agostino RB, Gibbons R, et al. 2013 ACC/AHA guideline on the assessment of cardiovascular risk: a report of the American College of Cardiology/American Heart Association Task Force on Practice Guidelines. *Circulation.* (2014). 129(25 Suppl. 2), S49–73. doi: 10.1161/01.cir.0000437741.48606.98
33. Jousilahti P, Vartiainen E, Tuomilehto J, Puska P. Sex, age, cardiovascular risk factors, and coronary heart disease: a prospective follow-up study of 14 786 middle-aged men and women in Finland. *Circulation.* (1999) 99:1165–72. doi: 10.1161/01.cir.99.9.1165
34. Rosamond W, Flegal K, Friday G, Furie K, Go A, Greenlund K, et al. Heart disease and stroke statistics—2007 update: a report from the American Heart Association Statistics Committee and Stroke Statistics Subcommittee. *Circulation.* (2007) 115:e69–171. doi: 10.1161/circulationaha.106.179918
35. Anand SS, Islam S, Rosengren A, Franzosi MG, Steyn K, Yusufali AH, et al. Risk factors for myocardial infarction in women and men: insights from the INTERHEART study. *Eur Heart J.* (2008) 29:932–40. doi: 10.1093/eurheartj/ehn018
36. Berger S, Raman G, Vishwanathan R, Jacques PF, Johnson EJ. Dietary cholesterol and cardiovascular disease: a systematic review and meta-analysis. *Am J Clin Nutr.* (2015) 102:276–94. doi: 10.3945/ajcn.114.100305
37. Matsuzawa Y, Nakamura T, Shimomura I, Kotani K. Visceral fat accumulation and cardiovascular disease. *Obes Res*. (1995) 3(Suppl. 5):645–7s. doi: 10.1002/j.1550-8528.1995.tb00481.x
38. Kumada M, Kihara S, Sumitsuji S, Kawamoto T, Matsumoto S, Ouchi N, et al. Association of hypoadiponectinemia with coronary artery disease in men. *Arterioscler Thromb Vasc Biol.* (2003) 23:85–9. doi: 10.1161/01.atv.0000048856.22331.50
39. Chobanian AV, Alexander RW. Exacerbation of atherosclerosis by hypertension. Potential mechanisms and clinical implications. *Arch Intern Med.* (1996) 156:1952–1956.
40. DeFronzo RA, Ferrannini E. Insulin resistance. A multifaceted syndrome responsible for NIDDM, obesity, hypertension, dyslipidemia, and atherosclerotic cardiovascular disease. *Diabetes Care.* (1991) 14:173–94. doi: 10.2337/diacare.14.3.173
41. Haffner SM. Diabetes, hyperlipidemia, and coronary artery disease. *Am J Cardiol.* (1999) 83:17–21f. doi: 10.1016/s0002-9149(99)00213-1
42. Malakar AK, Choudhury D, Halder B, Paul P, Uddin A, Chakraborty S. A review on coronary artery disease, its risk factors, and therapeutics. *J Cell Physiol.* (2019) 234:16812–23. doi: 10.1002/jcp.28350
43. Kim MK, Shin J, Kweon SS, Shin DH, Lee YH, Chun BY, et al. Harmful and beneficial relationships between alcohol consumption and subclinical atherosclerosis. *Nutr Metab Cardiovasc Dis.* (2014) 24:767–76. doi: 10.1016/j.numecd.2014.02.004
44. Wilson PW, D'Agostino RB, Levy D, Belanger AM, Silbershatz H, Kannel WB. Prediction of coronary heart disease using risk factor categories. *Circulation.* (1998) 97:1837–47. doi: 10.1161/01.cir.97.18.1837
45. Chen G, Levy D. Contributions of the framingham heart study to the epidemiology of coronary heart disease.

JAMA Cardiol. (2016) 1:825–30. doi: 10.1001/jamacardio.2016.2050

46. Cheng J, Zhao D, Zeng Z, Critchley JA, Liu J, Wang W, et al. The impact of demographic and risk factor changes on coronary heart disease deaths in Beijing, 1999-2010. *BMC Public Health.* (2009) 9:30. doi: 10.1186/1471-2458-9-30
47. Naoum C, Berman DS, Ahmadi A, Blanke P, Gransar H, Narula J, et al. Predictive value of age- and sex-specific nomograms of global plaque burden on coronary computed tomography angiography for major cardiac events. *Circ Cardiovasc Imaging.* (2017) 10:e004896. doi: 10.1161/circimaging.116.004896
48. Hartaigh BÓ, Gransar H, Callister T, Shaw LJ, Schulman-Marcus J, Stuijfzand WJ, et al. Development and validation of a simple-to-use nomogram for predicting 5-, 10-, and 15-year survival in asymptomatic adults undergoing coronary artery calcium scoring. *JACC Cardiovasc Imaging.* (2018) 11:450–8. doi: 10.1016/j.jcmg.2017.03.018
49. Wu N, Chen X, Li M, Qu X, Li Y, Xie W, et al. Predicting obstructive coronary artery disease using carotid ultrasound parameters: a nomogram from a large real-world clinical data. *Eur J Clin Invest.* (2018) 48:e12956. doi: 10.1111/eci.12956
50. Huang S, Xie X, Sun Y, Zhang T, Cai Y, Xu X, et al. Development of a nomogram that predicts the risk for coronary atherosclerotic heart disease. *Aging.* (2020) 12:9427–39. doi: 10.18632/aging.103216

Conflict of Interest: The authors declare that the research was conducted in the absence of any commercial or financial relationships that could be construed as a potential conflict of interest.

frontiers in Cardiovascular Medicine

ORIGINAL RESEARCH
published: 23 April 2021
doi: 10.3389/fcvm.2021.654392

Agreement of Angiography-Derived and Wire-Based Fractional Flow Reserves in Percutaneous Coronary Intervention

Hu Ai[1†], Naixin Zheng[1†], Le Li[1†], Guojian Yang[1], Hui Li[1], Guodong Tang[1], Qi Zhou[2], Huiping Zhang[1], Xue Yu[1], Feng Xu[1], Ying Zhao[1*] and Fucheng Sun[1*]

[1] *Department of Cardiology, National Center of Gerontology, Institute of Geriatric Medicine, Beijing Hospital, Chinese Academy of Medical Sciences, Beijing, China,* [2] *The MOH Key Laboratory of Geriatrics, National Center of Gerontology, Beijing Hospital, Beijing, China*

Background: Coronary angiography-derived fractional flow reserve (caFFR) measurements have shown good correlations and agreement with invasive wire-based fractional flow reserve (FFR) measurements. However, few studies have examined the diagnostic performance of caFFR measurements before and after percutaneous coronary intervention (PCI). This study sought to compare the diagnostic performance of caFFR measurements against wire-based FFR measurements in patients before and after PCI.

Methods: Patients who underwent FFR-guided PCI were eligible for the acquisition of caFFR measurements. Offline caFFR measurements were performed by blinded hospital operators in a core laboratory. The primary endpoint was the vessel-oriented composite endpoint (VOCE), defined as a composite of vessel-related cardiovascular death, vessel-related myocardial infarction, and target vessel revascularization.

Results: A total of 105 pre-PCI caFFR measurements and 65 post-PCI caFFR measurements were compared against available wire-based FFR measurements. A strong linear correlation was found between wire-based FFR and caFFR measurements ($r = 0.77$; $p < 0.001$) before PCI, and caFFR measurements also showed a high correlation ($r = 0.82$; $p < 0.001$) with wire-based FFR measurements after PCI. A total of 6 VOCEs were observed in 61 patients during follow-up. Post-PCI FFR values ($\leq$0.82) in the target vessel was the strongest predictor of VOCE [hazard ratio (HR): 5.59; 95% confidence interval (CI): 1.12–27.96; $p = 0.036$). Similarly, patients with low post-PCI caFFR values ($\leq$0.83) showed an 8-fold higher risk of VOCE than those with high post-PCI caFFR values (>0.83; HR: 8.83; 95% CI: 1.46–53.44; $p = 0.017$).

Conclusion: The study showed that the caFFR measurements were well-correlated and in agreement with invasive wire-based FFR measurements before and after PCI. Similar to wire-based FFR measurements, post-PCI caFFR measurements can be used to identify patients with a higher risk for adverse events associated with PCI.

Keywords: fractional flow reserve, stable ischemic heart disease, percutaneous coronary intervention, vessel-oriented composite endpoint, coronary angiography-derived fractional flow reserve

Edited by:
Kuei-Chun Wang,
Arizona State University, United States

Reviewed by:
Masashi Fukunaga,
Morinomiya Hospital, Japan
Paolo Severino,
Sapienza University of Rome, Italy

Correspondence:
Ying Zhao
zybjhmoh@163.com
Fucheng Sun
sunfc2016@yahoo.com

[†] *These authors have contributed equally to this work*

Specialty section:
This article was submitted to Atherosclerosis and Vascular Medicine, a section of the journal Frontiers in Cardiovascular Medicine

Received: *16 January 2021*
Accepted: *30 March 2021*
Published: *23 April 2021*

Citation:
Ai H, Zheng N, Li L, Yang G, Li H, Tang G, Zhou Q, Zhang H, Yu X, Xu F, Zhao Y and Sun F (2021) Agreement of Angiography-Derived and Wire-Based Fractional Flow Reserves in Percutaneous Coronary Intervention. Front. Cardiovasc. Med. 8:654392. doi: 10.3389/fcvm.2021.654392

INTRODUCTION

Angiography-derived fractional flow reserve (FFR) measurements represent a novel technique for evaluating physiological function in cardiovascular disease (1, 2). Over the past few years, four angiography-derived FFR measurement methods have shown good correlation and agreement with the conventional invasive wire-based FFR method in the FAVOR II China study (3), FAST-FFR study (4), FLASH FFR study (5), and FAST study (6). Among patients who are suspected of coronary heart disease, these clinical trials have shown that angiography-derived FFR measurement techniques have good diagnostic performance for guiding revascularization in percutaneous coronary intervention (PCI). However, few studies have examined the diagnostic performance of coronary angiography-derived FFR (caFFR) before and after PCI. The value of initial wire-derived FFR is typically below 0.8 among patients who have previously undergone PCI, which might challenge the diagnostic abilities of caFFR. Furthermore, whether computational fluid dynamics have diagnostic value in coronary arteries implanted with exogenous metal stents remains unknown.

The objective of the current retrospective study was to compare the diagnostic performance of caFFR measurement against wire-based FFR measurement among patients before and after PCI. The FlashAngio caFFR system includes the Flash pressure transducer, console, and software (Rainmed Ltd., Suzhou, China). In this study, pre-PCI and post-PCI caFFR measurements were compared with corresponding wire-based FFR measurements. We also investigated the post-PCI FFR and caFFR cutoff values for the prediction of long-term adverse cardiac outcomes.

METHODS

Study Population

Patients (≥18 years of age) with stable ischemic heart disease (SIHD) who underwent elective invasive FFR-guided PCI for a *de novo* lesion from June 2012 to May 2020 at Beijing Hospital were included in this study. The angiographic inclusion criterion was at least one lesion with diameter stenosis of 50–90% by visual assessment. The angiographic exclusion criteria (5), as required by the FlashAngio caFFR system, included: (1) poor angiographic image quality, precluding contour detection; (2) severe vascular overlap or distortion of the interrogated vessel; (3) stenoses caused by myocardial bridge; and (4) ostial lesions. The clinical data were obtained from electronic medical records and analyzed retrospectively. The study was approved by the Institutional Ethics Committee (2020BJYYEC-038-01) at Beijing Hospital. All patients signed informed consent to undergo invasive FFR-guided PCI and agreed to the use of their data for research purposes.

Determination of Wire-Based FFR

Intracoronary nitroglycerine (200 mg) was routinely injected before FFR measurement. The coronary pressure wire-based FFR was measured using a commercially available pressure

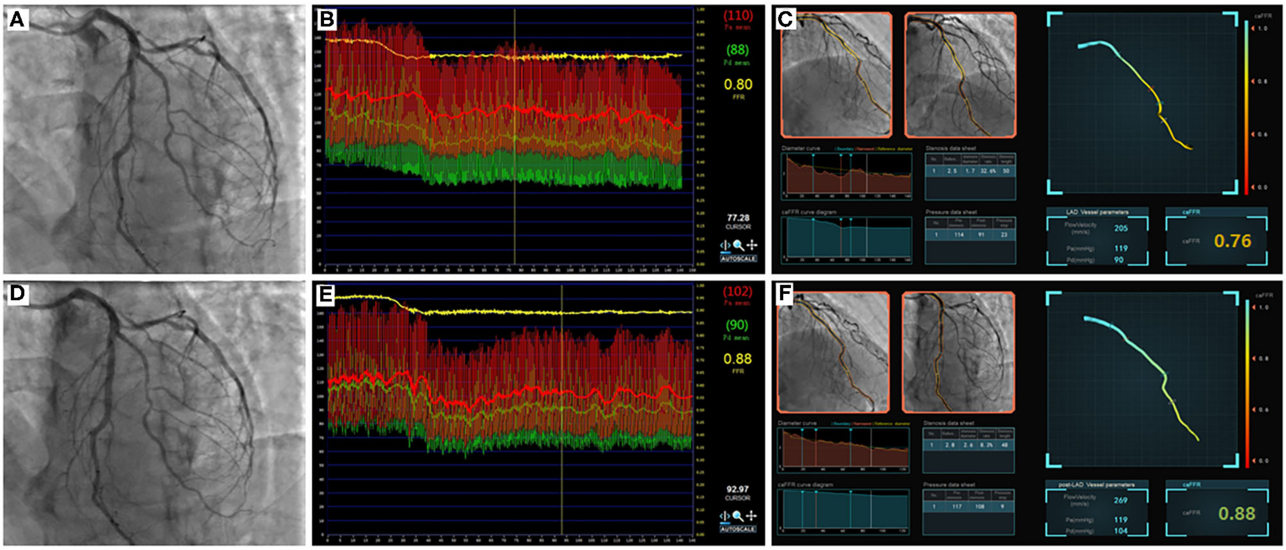

FIGURE 1 | Example of comparisons between pre- and post-PCI FFR and caFFR values. Images were obtained from a 61-year-old patient in the study. **(A)** Coronary angiography shows moderate stenosis lesion located in the middle of the LAD. **(B)** The value of pre-PCI FFR, measured by invasive pressure wire, was 0.80. **(C)** The pre-PCI caFFR value was 0.76. **(D)** Post-PCI coronary angiography after 2.5 × 24 mm and 2.75 × 24 mm stent implantation. **(E)** The invasive post-PCI wire-based FFR value was 0.88. **(F)** The post-PCI caFFR value was 0.88. LAD, left descending artery; FFR, fractional flow reserve; PCI, percutaneous coronary intervention; caFFR, coronary angiography-derived FFR.

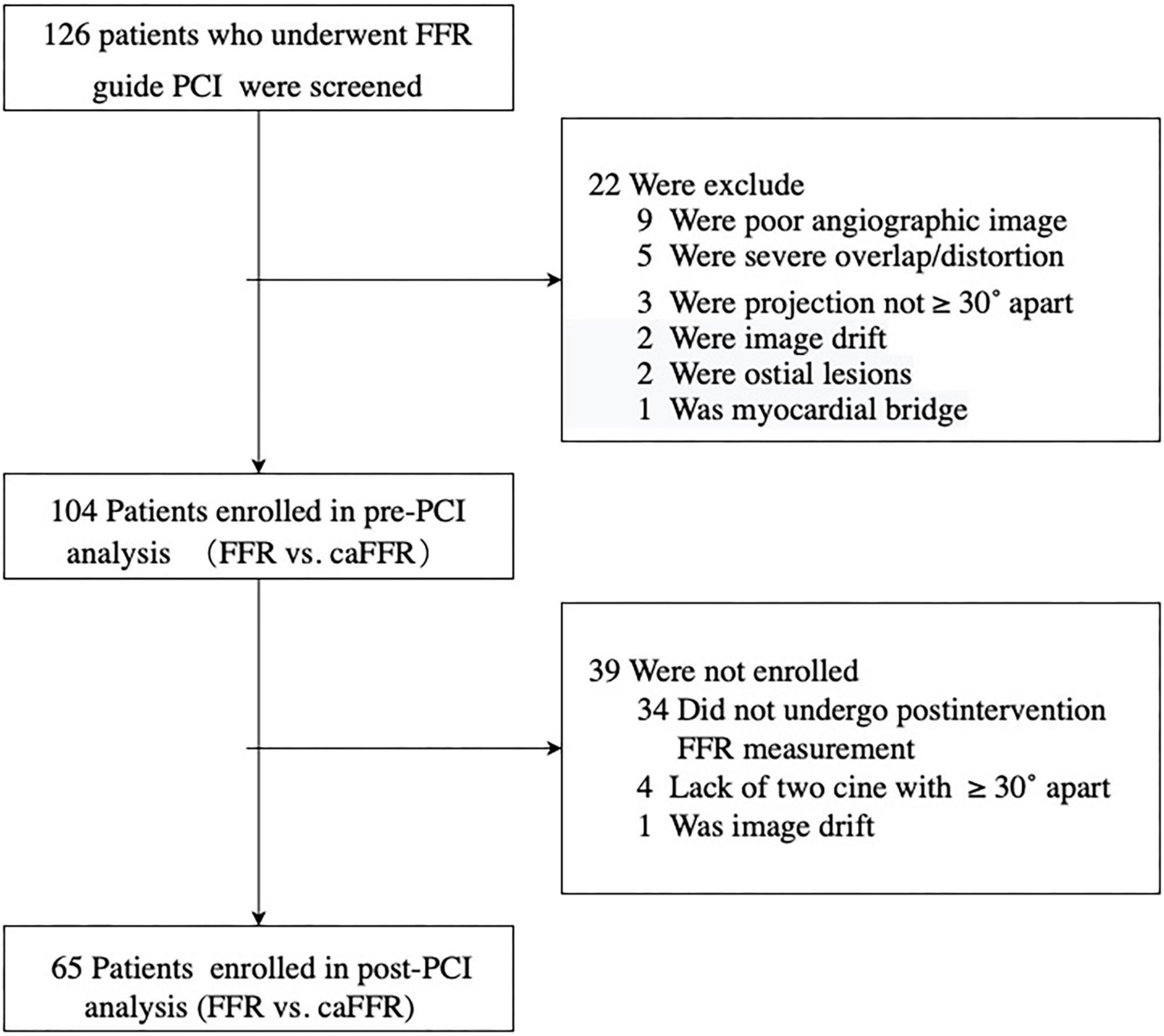

FIGURE 2 | Study flow diagram. SIHD, stable ischemic heart disease; LAD, left descending artery; FFR, fractional flow reserve; PCI, percutaneous coronary intervention; caFFR, coronary angiography-derived FFR.

wire system (Certus, Abbott Vascular, Santa Clara, CA). The pressure wire was inserted such that the pressure transducer was ≥2 cm downstream from the most distal stenosis. The position of the pressure wire was captured on cine angiography for offline comparisons. Hyperemic blood flow was induced by the intravenous administration of adenosine-5'-triphosphate (ATP) at ≥140 µg/kg/min and recorded after at least 60 s in the presence of stable aortic pressure decrease relative to baseline pressure that was sustained for at least 10 beats. FFR pullback was performed at the operator's judgment. Pressure drift was measured after the withdrawal of the pressure wire to the guiding catheter tip and was defined as a resting distal-to-aortic coronary pressure ratio (Pd/Pa) from 0.97 to 1.03.

Coronary Revascularization and Image Transfer

Coronary angiography was performed based on 9 conventional projection views (7), which were recorded at 15 frames/s. A mechanical pump was used to inject the contrast agent at a rate of 3.5 mL/s. The PCI procedures were determined by an interventional cardiologist following the best local practices. At the end of the procedure, at least two angiographic projection views for the targeted vessel were recorded. During the operation, the aortic pressure value was routinely recorded in the Catheter Laboratory Database.

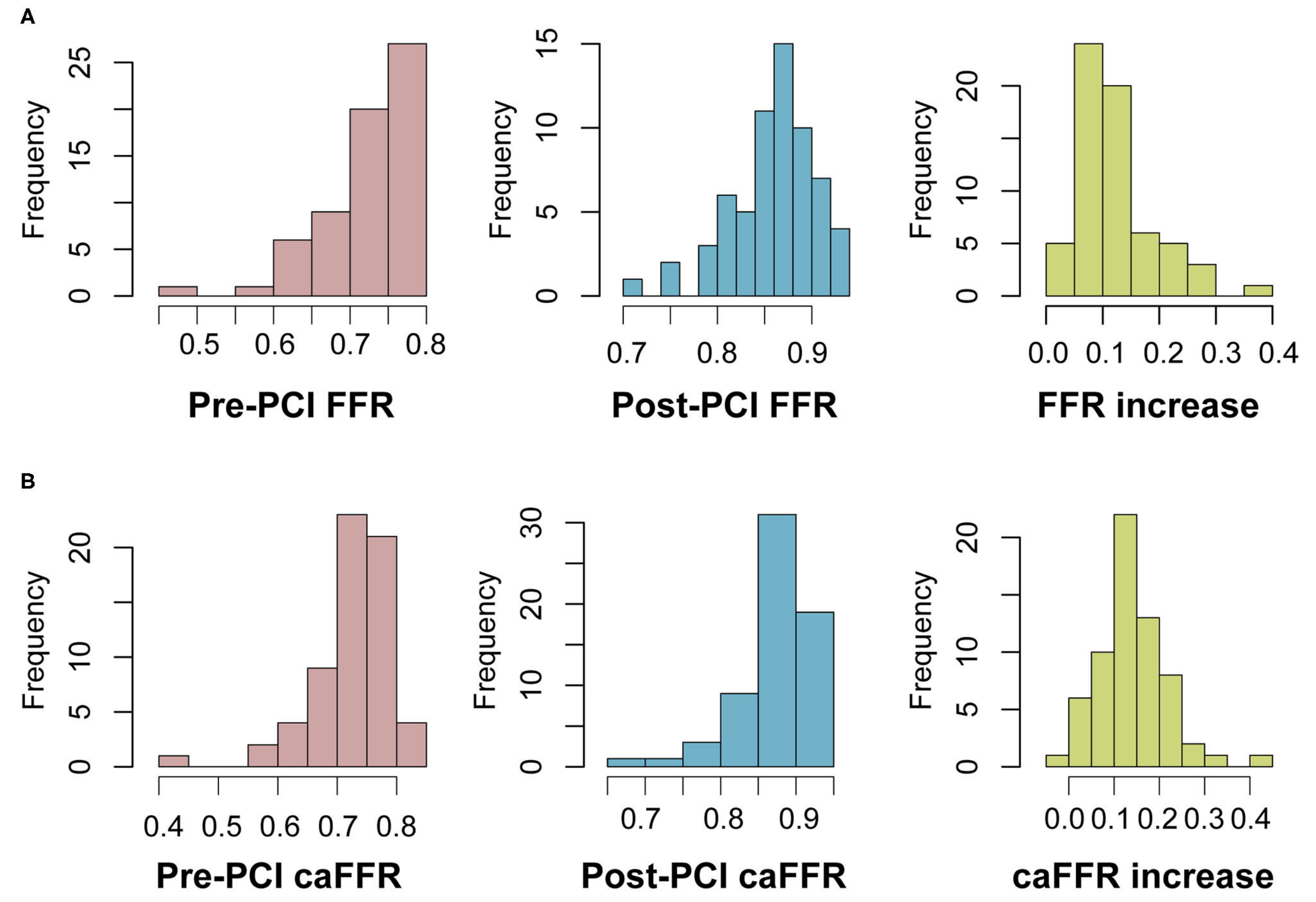

FIGURE 3 | Frequency distribution of FFR and caFFR values and increased values. **(A)** Frequency distribution and increased values of FFR. **(B)** Frequency distribution and increased values of caFFR. LAD, left descending artery; FFR, fractional flow reserve; PCI, percutaneous coronary intervention; caFFR, coronary angiography-derived FFR.

Offline caFFR Measurement

At least two angiographic projections, avoiding vessel overlap and separated by ≥30°, without table movement, were required to generate caFFR. Digital Imaging and Communications in Medicine (DICOM) images of coronary angiography and mean aortic pressure (MAP) were exported to the FlashAngio console. A simulated three-dimensional (3D) mesh reconstruction of the coronary artery was generated along the artery path from the inlet to the most distal location. The caFFR computation was performed by blinded hospital operators using the method described previously (5). The values of pre-PCI and post-PCI caFFR were reported separately, as shown in **Figure 1**.

Follow-Up and End Points

Clinical follow-up data were recorded in a dedicated database, including admission records and outpatient notes, maintained at Beijing Hospital. All patients were followed individually by direct telephone contact or outpatient visits to confirm clinical data every 6 months. The primary endpoint was the vessel-oriented composite endpoint (VOCE), defined as the composite of vessel-related cardiovascular death, vessel-related myocardial infarction (MI), and target vessel revascularization (TVR) (8). Secondary endpoints were the individual components of the VOCE. Death of unknown etiology was considered cardiovascular death. MI was defined as new Q waves or one plasma level of creatine kinase-myocardial band (CK-MB) $\geq 5 \times$ upper limit of normal (ULN; or troponin $\geq 35 \times$ ULN if CK-MB was not available) in the context of acute coronary syndrome (ACS) (9). TVR was defined as the repeat revascularization or bypass grafting of the target vessel.

Statistical Analysis

Continuous variables are expressed as the mean and standard deviation. Categorical data are summarized as the number and percentage. The Student's *t*-test and the Chi-square test were used to compare group differences. The correlation between wire-based FFR and caFFR measurements was assessed by Spearman's correlation coefficient (r) with a 95% confidence interval (CI). Bland–Altman analysis was used to estimate the agreement between the two indices. Patients were separated into two groups (high-risk and low-risk groups) according to the post-PCI wire-based FFR and caFFR values. The cumulative survival probability of VOCE was estimated by Kaplan–Meier curves; the difference between high-risk and low-risk groups was compared by a log-rank test and plotted using the "survival" package of R language (Version 3.6.1). In parallel, Cox regression was fitted to estimate the risks of VOCE (hazard ratio [HR], 95% CI) for the two groups. The cutoff post-PCI FFR value for the prediction of long-term adverse cardiac outcomes varied from 0.81 to 0.95 (10). We tested the threshold starting at 0.81 to determine the optimal cutoff value for post-PCI FFR measurements to predict VOCE to determine whether caFFR measurements have similar prognostic power as traditional wire-based FFR measurements for VOCE prediction. All statistical analyses were performed with SPSS software (Version 24.0, IBM Corp., Armonk, NY) and R language. The significance level was set at $p < 0.05$, and all probability values were two-sided.

TABLE 1 | Clinical and angiographic characteristics of patients.

Patients ($n = 104$)	
Sex, male (%)	78 (75.0)
Age (years)	61.6 ± 9.6
BMI (kg/m^2)	25.9 ± 3.5
Smoking (%)	43 (41.3)
Hypertension (%)	67 (64.4)
Diabetes (%)	42 (40.4)
Dyslipidemia (%)	69 (66.3)
Hemoglobin (g/L)	135.0 ±14.8
FBG (mmol/L)	6.4 ± 2.0
Creatinine (μmol/L)	71.6 ± 17.2
LDL-C (mmol/L)	2.1 ± 0.8
LVEF (%)	64.2 ± 5.4
Multivessel disease, *n* (%)	55 (52.9)
Target vessel ($n = 105$)	
Location of lesion	
LAD, *n* (%)	96 (91.4)
LCX, *n* (%)	5 (4.8)
RCA, *n* (%)	4 (3.8)
ACC/AHA lesion type	
A (%)	17 (16.2)
B_1 (%)	29 (27.6)
B_2 (%)	25 (23.8)
C (%)	34 (32.4)
Quantitative coronary angiography	
Pre-PCI Minimal lumen diameter, mm	1.6 ± 0.4
Reference vessel diameter, mm	3.0 ± 0.6
% Diameter stenosis	48.5 ± 9.3
Lesion length, mm	19.3 ± 10.0
Post-PCI	
Minimal lumen diameter, mm	2.4 ± 0.5
Reference vessel diameter, mm	2.8 ± 0.5
% Diameter stenosis	14.3 ± 7.1
Lesion length, mm	14.7 ± 8.5
Interventional characteristics	
DES implantation	80 (76.19)
DCB dilation	25 (23.81)

FFR, fractional flow reserve; caFFR, coronary angiography-derived FFR; BMI, body mass index; FBG, fasting blood glucose; LDL-C, low-density lipoprotein cholesterol; LVEF, Left ventricular ejection fraction; LAD, left anterior descending artery; RCA, right coronary artery; LCX, left circumflex artery; ACC, American College of Cardiology; AHA, American Heart Association; PCI, percutaneous coronary intervention; DES, drug-eluting stent; DCB, drug-coated balloon.

RESULTS

Feasibility and Characteristics of Patients

From 2012 to 2020, 126 patients with SIHD who underwent FFR-guided PCI were enrolled in this study, and caFFR was analyzed in 104 patients (105 vessels). Post-PCI FFR measurement was performed in 70 patients (67.3%, 71 vessels), and post-PCI caFFR measurements could be performed in 65 patients (65 vessels). The primary causes of caFFR computation failure were poor image quality ($n = 9$ of 126, 7.14%), severe overlap or distortion ($n = 5$ of 126, 3.97%), and the lack of 2 cines with projection angles $\geq 30^\circ$ ($n = 3$ of 126, 2.38%), as shown in **Figure 2**. **Figure 3** shows the frequency distribution of FFR measurements, caFFR measurements, and increased relative values to baseline. Clinical and interventional characteristics are reported in **Table 1**.

Agreement Between FFR and caFFR

Pre-PCI caFFR values were well-correlated with wire-based FFR values (caFFR = 0.76 × FFR + 0.18, $R = 0.77$, **Figure 4A**). The Bland–Altman analysis of pre-PCI caFFR and wire-based FFR values showed no systematic differences, with a bias of -0.0003 ± 0.0420 (95% limit of agreement: -0.0826 to 0.0820, **Figure 4B**). The post-PCI caFFR values were also correlated with wire-based FFR values (caFFR = 0.93 × FFR + 0.88, $R = 0.817$, **Figure 5A**). Bland–Altman analysis of post-PCI caFFR and wire-based FFR values showed no systematic differences, with a bias of -0.0123 ± 0.0299 (95% limit of agreement: -0.0709 to 0.0463, **Figure 5B**). **Figure 6** shows the increase in the wire-based FFR values after PCI, similar to those observed by caFFR measurement (0.13 ± 0.07 vs. 0.14 ± 0.08; $p = 0.25$).

Prognostic Implications of Post-PCI caFFR

In 65 patients with post-PCI wire-based FFR and caFFR measurements, 61 (93.9%) patients had clinical follow-up data. During a follow-up period of 6–105 months (86.9% >12-month follow-up; 50.9% >36-month follow-up), 6 (9.8%) VOCEs were repo rted: 1 cardiovascular death (1.6%), 1 MI (1.6%), and 4 TVRs (6.6%). The post-PCI caFFR values showed consistent power with post-PCI wire-based FFR values for the prediction of VOCEs, although different cutoff values were identified for the two measurement methods (**Supplementary Figure 1**). Patients with low post-PCI wire-based FFR values (≤ 0.82) had a higher risk of VOCE than those with high post-PCI wire-based FFR values (> 0.82; HR: 5.59; 95% CI: 1.12–27.96; $p = 0.036$). Similarly, patients with low post-PCI caFFR values (≤ 0.83) showed an 8-fold higher risk of VOCE than those with high post-PCI caFFR values (> 0.83; HR: 8.83; 95% CI: 1.46–53.44; $p = 0.017$; **Figure 7**).

When the patients were grouped according to their post-PCI wire-based FFR values (>0.82 vs. ≤ 0.82; **Table 2**), a significant difference was found in the numbers and total lengths of the stents used (1.50 ± 0.55 vs. 1.0 and 30.96 ± 10.45 vs. 19.75 ± 3.73, respectively; $p < 0.01$). Similarly, both the numbers and total lengths of stents in the high caFFR value group (>0.83 vs. ≤ 0.83) were significantly higher than those in the low caFFR value

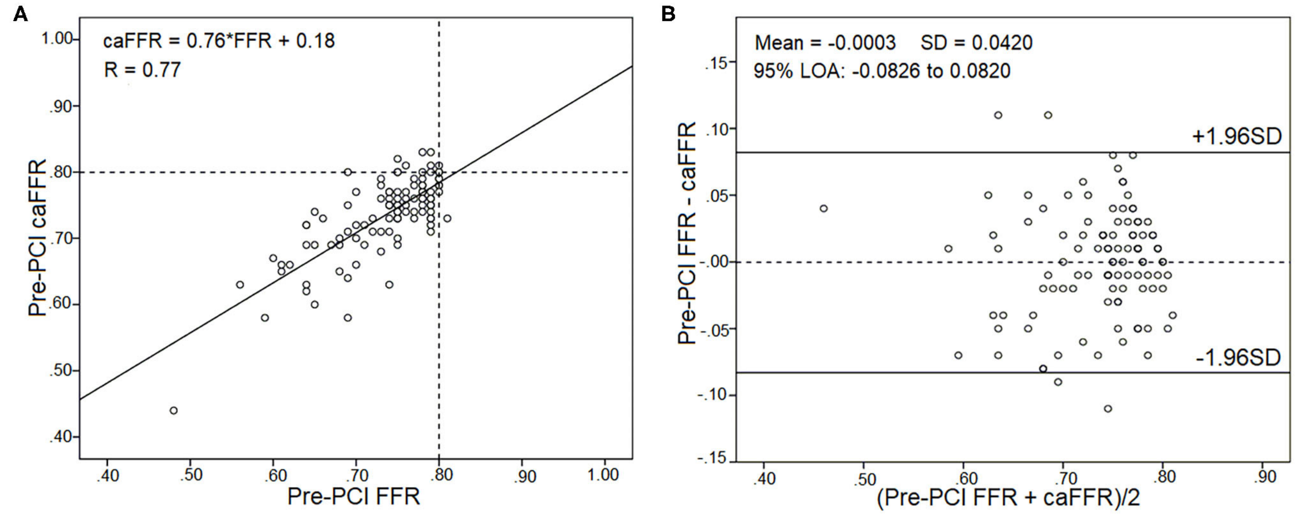

FIGURE 4 | Correlation and agreement between pre-PCI wire-based FFR and caFFR values (*n* = 105). **(A)** Strong correlation between pre-PCI wire-based FFR and caFFR values (caFFR = 0.76 × FFR + 0.18, *R* = 0.77, 95% CI: 0.53–0.78). **(B)** Good agreement between pre-PCI wire-based FFR and caFFR values by the Bland–Altman analysis (bias: −0.0003 ± 0.0420; 95% LOA −0.0826 to 0.0820). CI, confidence interval; LOA, limits of agreement; LAD, left descending artery; FFR, fractional flow reserve; PCI, percutaneous coronary intervention; caFFR, coronary angiography-derived FFR.

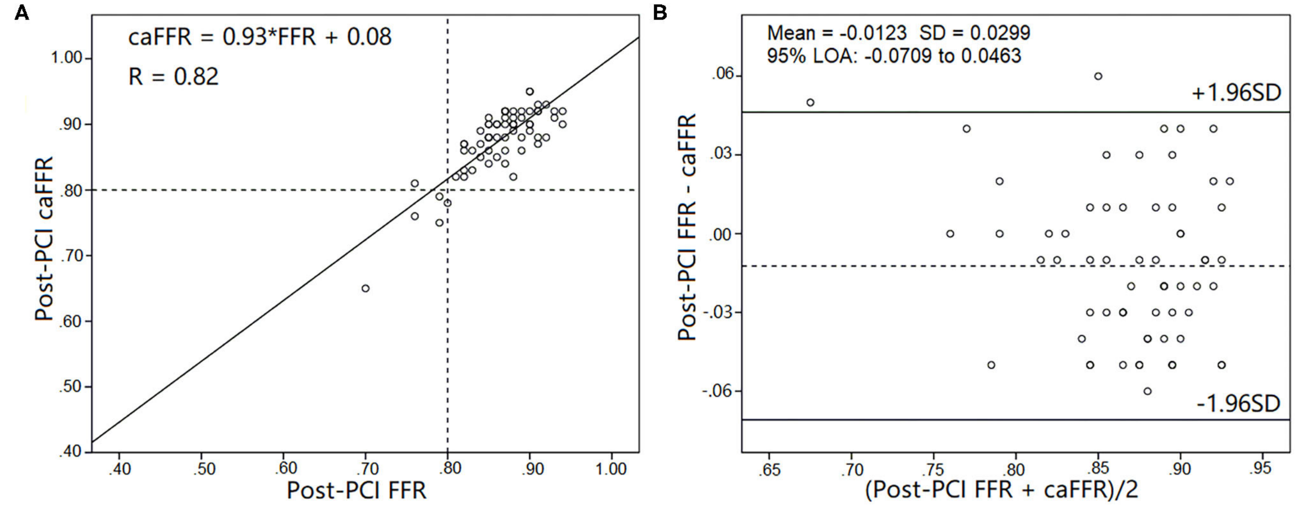

FIGURE 5 | Correlation and agreement between post-PCI wire-based FFR and caFFR values (*n* = 65). **(A)** Strong correlation between post-PCI wire-based FFR and caFFR values (caFFR = 0.93 × FFR + 0.08, *R* = 0.82, 95% CI: 0.762–1.092). **(B)** Good agreement between post-PCI wire-based FFR and caFFR values by the Bland–Altman analysis (bias: −0.0123 ± 0.0299; 95% LOA −0.0709 to 0.0463). CI, confidence interval; LOA, limits of agreement; LAD, left descending artery; FFR, fractional flow reserve; PCI, percutaneous coronary intervention; caFFR, coronary angiography-derived FFR.

group (1.48 ± 0.55 vs. 1.0; 30.52 ± 10.51 vs. 19.50 ± 2.66; $p < 0.01$; **Table 2**).

DISCUSSION

The present study validated caFFR measurement against those obtained using conventional wire-based FFR measurements before and after PCI. The major findings were as follows: (1) caFFR analysis could be applied to most conventional coronary angiography images; (2) caFFR and wire-based FFR measurements had good correlation and agreement both before and after PCI; and (3) post-PCI wire-based FFR and caFFR measurements had similar prognostic values.

FFR measurement has been used in the cardiac catheter laboratory to identify functionally significant coronary stenoses (11, 12). Random trials have demonstrated that

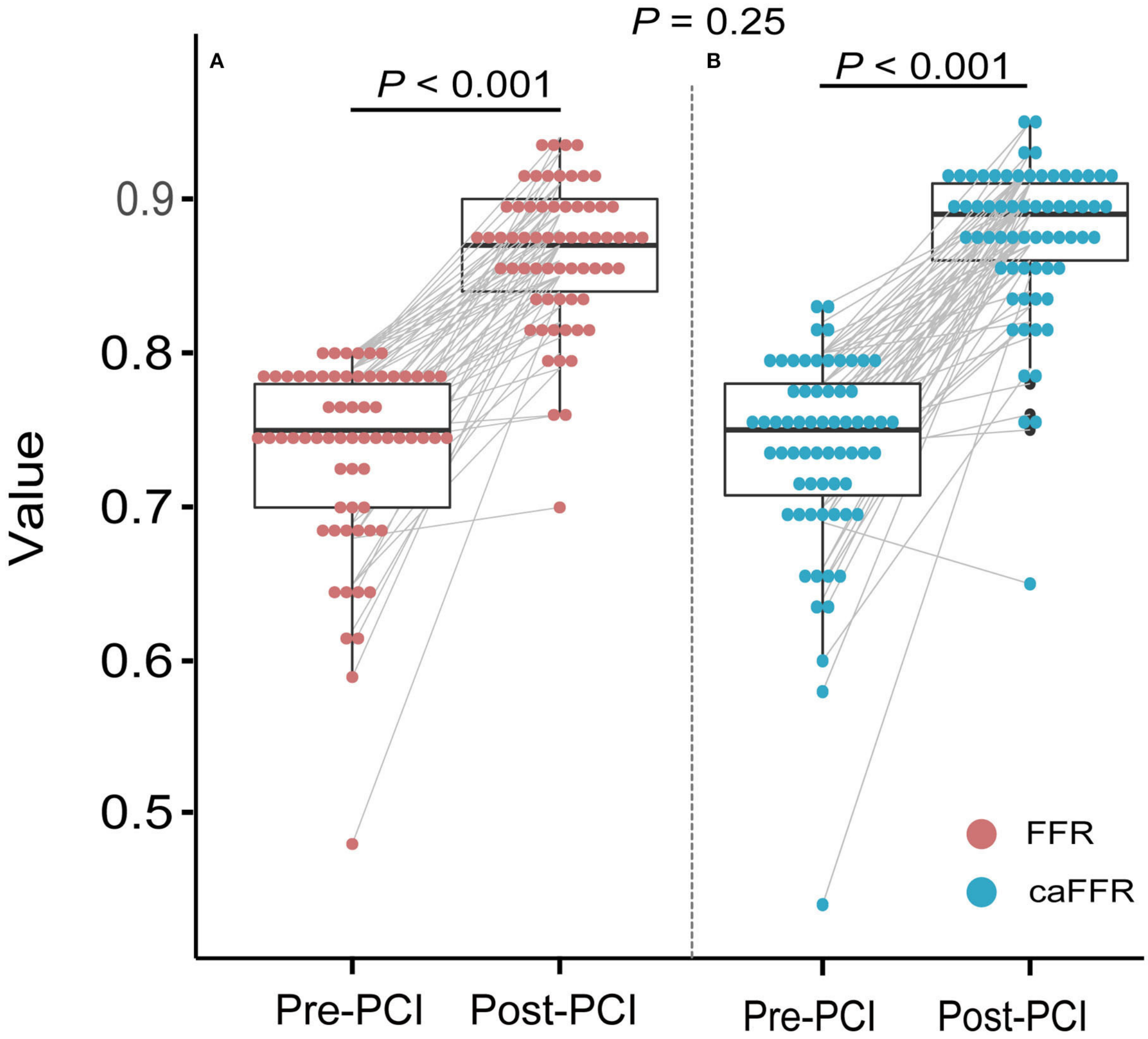

FIGURE 6 | Improvements in wire-based FFR and caFFR values after PCI ($n = 65$). **(A)** The wire-based FFR values increased significantly after PCI (0.74 ± 0.07 vs. 0.86 ± 0.05, $p < 0.001$). **(B)** The caFFR values increased significantly after PCI (0.74 ± 0.07 vs. 0.88 ± 0.05, $p < 0.001$). The increase in wire-based FFR values after PCI were similar to that of caFFR values (0.13 ± 0.07 vs. 0.14 ± 0.08; $p = 0.25$). LAD, left descending artery; FFR, fractional flow reserve; PCI, percutaneous coronary intervention; caFFR, coronary angiography-derived FFR.

FFR-guided PCI improves clinical outcomes and reduces the need for stenting, in addition to reducing costs (13–15). FFR measurement is recommended as a standard protocol in the revascularization guidelines for stable coronary heart disease (16, 17). Angiography-derived FFR and wire-based FFR measurements showed similar diagnostic accuracy. Using wire-based FFR as the reference standard, the area under the curve (AUC) for caFFR (5) was 0.979, and similar results were demonstrated in studies of the quantitative flow ratio (QFR) (3), FFRangio (4), and Vessel FFR (vFFR) (6) measurement methods, which reported AUC values of 0.96, 0.94, and 0.93, respectively. In this study, pre-PCI caFFR values showed good diagnostic accuracy in patients who underwent elective PCI for a *de novo* lesion compared with the diagnostic accuracy of wire-based FFR values.

FFR measurement after PCI can be used to discriminate suboptimal PCI procedures and predict clinical outcomes. Pijls et al. (18) investigated 750 patients following successful bare-metal stent implantation and found that lower post-PCI FFR values were associated with an increased major adverse cardiovascular event (MACE) rate (for groups based on FFR values > 0.95, 0.8–0.9, and < 0.80, MACE rates were 4.9% 20.3% and 29.5%, respectively; $p < 0.05$) at the 6-month follow-up time point. The DK CRUSH VII Registry Study (19) revealed that a post-PCI FFR value < 0.88 was the predominant predictor of target vessel failure (12.3 vs. 6.1%; $p < 0.01$) 3 years after drug-eluting stent implantation. An increase in the FFR value after PCI was directly associated with MI recovery (20), whereas a small increase in the FFR value (<15%) was a prognostic indicator of poor clinical outcomes, similar to low

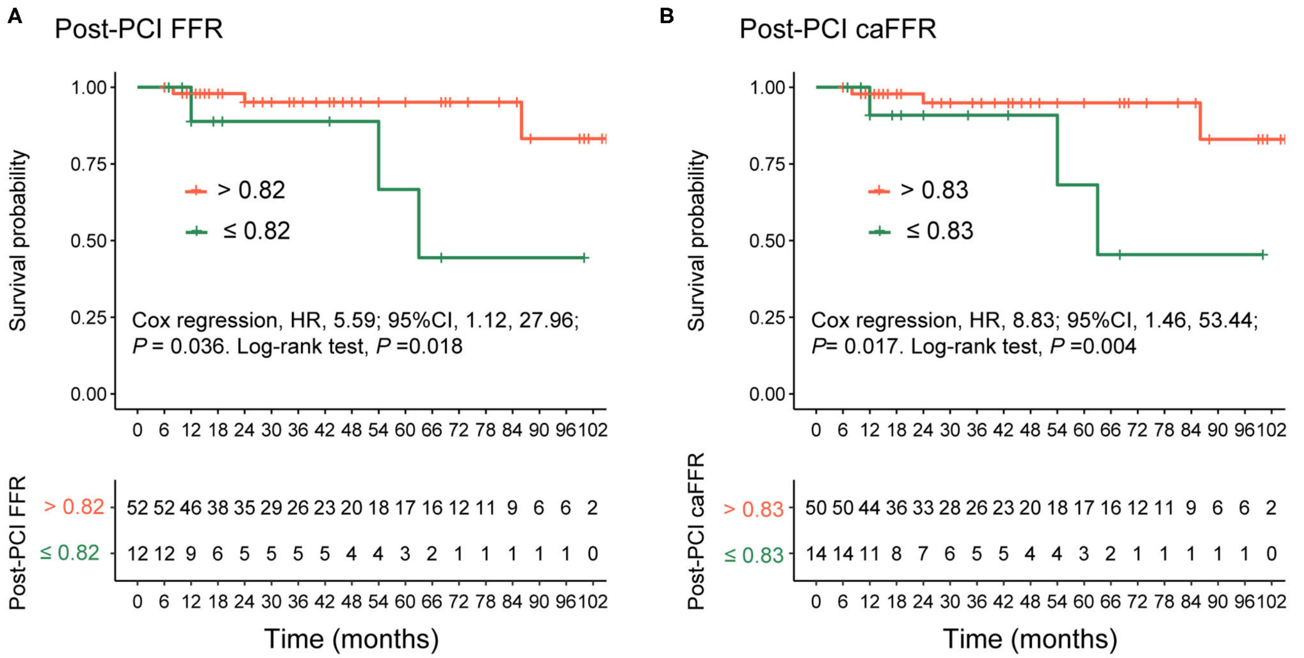

FIGURE 7 | Comparison of VOCEs according to post-PCI FFR or caFFR values. Kaplan–Meier curves showing that **(A)** patients with post-PCI wire-based FFR values > 0.82 had a higher survival free of VOCE compared with patients with post-PCI wire-based FFR values ≤ 0.82. **(B)** Patients with post-PCI caFFR values > 0.83 had a higher survival free of VOCE compared with patients with post-PCI caFFR values ≤ 0.83 group. VOCE, vessel-oriented composite endpoint; LAD, left descending artery; FFR, fractional flow reserve; PCI, percutaneous coronary intervention; caFFR, coronary angiography-derived FFR.

absolute post-PCI FFR values (<0.84) (21). The FFR-search study unexpectedly showed that post-PCI FFR values did not correlate with clinical events at the 30-day follow-up time point (22), which was thought to be due to the follow-up period being too short. The reasons for ineffective FFR changes after PCI include incomplete stent expansion, stent malapposition, geographical plaque miss, plaque protrusion, edge dissection, and plaque shift at the stent edge (23). To achieve functional optimization, unsatisfactory changes in FFR can safely and effectively be corrected by further interventions (post-dilation or additional stenting) (24).

Despite a Class 1a recommendation for use in the guidance of coronary revascularization in patients with stable angina, only 18.5%–21% of patients undergo FFR measurement (25, 26). Moreover, post-PCI FFR measurement was only performed in 69.2 and 64.2% of patients in the FAME 1 and FAME 2 studies (27). caFFR measurement represents a new technique that can be performed without the use of a pressure wire and hyperemic stimulus. The FLASH FFR study demonstrated that caFFR measurement has a good correlation with wire-based FFR measurement, and caFFR measurement requires a shorter operation time (< 5 min) than wire-based FFR measurement (5). The present study demonstrated that caFFR measurement had a good correlation with wire-based FFR measurement both before and after PCI. Similarly, post-PCI QFR and vFFR measurements correlated reasonably well-with post-PCI wire-based FFR measurements (28, 29). However, in a retrospective study of data collected by more than 50 centers, a weak correlation was reported between vFFR measurement and wire-based FFR measurement because of poor image quality and the difficulty tracking aortic pressure (30). The prognostic value of QFR measurements has been confirmed under various conditions (8, 9, 31), although the optimal cutoff values for post-PCI QFR measurements have been reported as 0.89, 0.91, and 0.80 in different studies. In the current single-center, retrospective study, patients with low post-PCI wire-based FFR (≤0.82) or caFFR (≤0.83) values were associated with a significantly higher risk of VOCE than those with high post-PCI FFR (>0.82) or caFFR (>0.83) values. The numbers and lengths of stents implanted in the high post-PCI FFR and caFFR value groups were significantly higher than those in the low post-PCI FFR and caFFR value groups. Insufficient stent implantation has been shown to result in incomplete coronary lesion coverage, which may explain the suboptimal FFR and caFFR values measured after the intervention in some patients. Currently, no consensus exists regarding the optimal post-PCI FFR value, although a higher FFR value is generally believed to be preferable. This study showed that a higher post-PCI caFFR value could predict a better clinical outcome.

LIMITATIONS

The present study has several limitations. First, this study was performed as a retrospective study in a single center

TABLE 2 | Comparison of general and procedural characteristics according to post-PCI wire-based FFR and caFFR values.

	Post-PCI wire-based FFR value			Post-PCI caFFR value		
	High FFR ($>$0.82, $n = 53$)	**Low FFR ($\leq$0.82, $n = 12$)**	***P*-Value**	**High caFFR ($>$0.83, $n = 54$)**	**Low caFFR ($\leq$0.83, $n = 11$)**	***P*-Value**
Sex, male (%)	41 (77.36)	10 (83.33)	0.948	43 (79.63)	8 (72.73)	0.916
Age (years)	61.21 ± 9.97	59.75 ± 9.98	0.649	60.89 ± 9.73	61.18 ± 11.25	0.93
BMI (kg/m^2)	26.02 ± 3.37	27.74 ± 6.26	0.351	25.84 ± 3.23	28.22 ± 6.57	0.07
Smoking (%)	22 (41.51)	8 (66.67)	0.208	25 (46.30)	5 (45.45)	1.0
Hypertension (%)	33 (63.26)	7 (58.33)	0.801	33 (61.11)	7 (63.64)	0.875
Diabetes (%)	19 (35.85)	4 (33.33)	0.869	19 (35.19)	4 (36.36)	0.941
Dyslipidemia (%)	34 (64.15)	10 (83.33)	0.347	36 (66.67)	8 (72.73)	0.970
Target lesion location						
LAD, *n* (%)	50 (94.34)	11 (91.67)	0.567	51 (94.44)	10 (90.91)	0.533
LCX, *n* (%)	1 (1.89)	1 (8.33)		2 (3.70)	0	
RCA, *n* (%)	2 (3.77)	0		1 (1.85)	1 (9.09)	
ACC/AHA lesion type						
A (%)	8 (0.15)	1 (8.33)	0.889	8 (14.81)	1 (9.09)	0.296
B_1 (%)	13 (24.53)	3 (25.00)		13 (24.07)	3 (27.27)	
B_2 (%)	12 (22.64)	4 (33.33)		11 (20.37)	5 (45.45)	
C (%)	20 (37.74)	4 (33.33)		22 (40.74)	2 (18.18)	
Quantitative coronary angiography						
Pre-PCI reference vessel diameter, mm	3.05 ± 0.62	2.96 ± 0.49	0.699	3.05 ± 0.63	2.98 ± 0.39	0.676
Pre-PCI diameter stenosis, %	49.24 ± 8.95	44.68 ± 5.32	0.028	49.38 ± 8.89	43.57 ± 4.36	0.039
Pre-PCI lesion length, mm	19.96 ± 10.29	17.18 ± 8.47	0.389	20.22 ± 10.33	15.61 ± 7.28	0.093
Post-PCI diameter stenosis, %	12.71 ± 6.31	13.54 ± 3.41	0.662	12.90 ± 6.08	12.70 ± 4.95	0.917
Procedural characteristics						
DES/DCB	46/7	8/4	0.21	48/6	6/5	0.020
Number of DES	1.50 ± 0.55	1.00	0.000	1.48 ± 0.55	1.00	0.000
Diameter of DES, mm	3.08 ± 0.46	2.75 ± 0.34	0.08	3.08 ± 0.46	2.70 ± 0.25	0.06
Total length of DES, mm	30.96 ± 10.45	19.75 ± 3.73	< 0.001	30.52 ± 10.51	19.50 ± 2.66	< 0.001
Number of DCB	1.14 ± 0.38	1.50 ± 0.58	0.241	1.17 ± 0.41	1.40 ± 0.51	0.438
Diameter of DCB, mm	3.14 ± 0.28	3.00 ± 0.35	0.479	3.17 ± 0.30	3.00 ± 0.31	0.389
Total length of DCB, mm	20.71 ± 6.73	28.75 ± 9.46	0.132	20.83 ± 7.35	27.00 ± 9.08	0.244

FFR, fractional flow reserve; caFFR, coronary angiography-derived FFR; BMI, body mass index; FBG, fasting blood glucose; LDL-C, low-density lipoprotein cholesterol; LVEF, Left ventricular ejection fraction; LAD, left anterior descending artery; RCA, right coronary artery; LCX, left circumflex artery; ACC, American College of Cardiology; AHA, American Heart Association; PCI, percutaneous coronary intervention; DES, drug-eluting stent; DCB, drug-coated balloon.

with a relatively small study population. Second, only patients with stable coronary heart disease were enrolled in this study. High-risk patients, such as those with ACS, ostial lesions, or left main lesions, were excluded, which restrains the generalizability of the results. Third, aortic root pressure was obtained from an interventional database maintained by the cardiac catheterization laboratory rather than measuring real-time invasive pressure. The retrospective methodology of obtaining aortic root pressure might affect the results slightly. Fourth, the retrospective study lacked a sufficient sample size and preconditions. We cannot recommend a powerful post-PCI FFR or caFFR cutoff value for the prediction of long-term adverse cardiac outcomes, and we did not obtain sufficient adverse event data to analyze any other VOCE predictors. Finally, macrovascular and microvascular diseases can affect coronary physiology after PCI. Evidence suggests that microvascular dysfunctions may falsify the results of FFR and be associated with adverse events after PCI (32–34). We will perform experimental and computational analyses of post-PCI microvascular dysfunction in future studies to quantify this effect.

CONCLUSIONS

This study showed that caFFR measurements are feasible, reproducible, and well-correlated with invasive wire-based FFR measurements both before and after PCI. Similar to wire-based FFR measurements, post-PCI caFFR measurements might be a useful tool for performing coronary physiological functional assessments and identifying patients with a higher risk for adverse events related to PCI.

DATA AVAILABILITY STATEMENT

The original contributions presented in the study are included in the article/**Supplementary Material**, further inquiries can be directed to the corresponding authors.

ETHICS STATEMENT

The studies involving human participants were reviewed and approved by The institutional Ethics Committee approved the study at Beijing Hospital (decision no. 2020BJYYEC-038-01). The patients/participants provided their written informed consent to participate in this study. Written informed consent was obtained from the individual(s) for the publication of any potentially identifiable images or data included in this article.

AUTHOR CONTRIBUTIONS

HA, NZ, and LL: study conception and design. NZ, LL, GY, HL, GT, HZ, XY, and FX: acquisition of data. HA and QZ: analysis and interpretation of data. HA: writing, review, and/or revision of the manuscript. YZ and FS: study supervision. All authors contributed to the article and approved the submitted version.

FUNDING

This project was supported by the Beijing Hospital Clinical Research 121 Project (BJ-2019-193).

ACKNOWLEDGMENTS

Thanks to Suzhou Rainmed, LTD, for providing the FlashAngio FFR System free of charge for research purposes. We also thank all participants in the study.

SUPPLEMENTARY MATERIAL

The Supplementary Material for this article can be found online at: https://www.frontiersin.org/articles/10.3389/fcvm.2021.654392/full#supplementary-material

Supplementary Figure 1 | Subjects whose post-PCI wire-based FFR or caFFR values were lower than the cutoff values were categorized as the high-risk groups. LAD, left descending artery; FFR, fractional flow reserve; PCI, percutaneous coronary intervention; caFFR, coronary angiography-derived FFR.

REFERENCES

1. Randles A, Frakes DH, Leopold JA. Computational fluid dynamics and additive manufacturing to diagnose and treat cardiovascular disease. *Trends Bio.* (2017) 35:1049–61. doi: 10.1016/j.tibtech.2017.08.008
2. Morris PD, Narracott A, von Tengg-Kobligk H, Silva Soto DA, Hsiao S, Lungu A, et al. Computational fluid dynamics modelling in cardiovascular medicine. *Heart.* (2016) 102:18–28. doi: 10.1136/heartjnl-2015-308044
3. Xu B, Tu S, Qiao S, Qu X, Chen Y, Yang J, et al. Diagnostic accuracy of angiography-based quantitative flow ratio measurements for online assessment of coronary stenosis. *J Am Coll Cardiol.* (2017) 70:3077–87. doi: 10.1016/j.jacc.2017.10.035
4. Fearon WF, Achenbach S, Engstrom T, Assali A, Shlofmitz R, Jeremias A, et al. Accuracy of fractional flow reserve derived from coronary angiography. *Circulation.* (2019) 139:477–84. doi: 10.1161/CIRCULATIONAHA.118.037350
5. Li J, Gong Y, Wang W, Yang Q, Liu B, Lu Y, et al. Accuracy of computational pressure-fluid dynamics applied to coronary angiography to derive fractional flow reserve: FLASH FFR. *Cardiovasc Res.* (2020) 116:1349–56. doi: 10.1093/cvr/cvz289
6. Masdjedi K, van Zandvoort LJC, Balbi MM, Gijsen FJH, Ligthart JMR, Rutten MCM, et al. Validation of a three-dimensional quantitative coronary angiography-based software to calculate fractional flow reserve: the FAST study. *EuroIntervention.* (2020) 16:591–9. doi: 10.4244/EIJ-D-19-00466
7. Popma JJ. Coronary Angiography and Intravascular Ultrasound Imaging. In: Zipes DP, Libby P, Bonow RO, Braunwald E, editors. *Braunwald's Heart Disease: A Textbook of Cardiovascular Medicine*. 7th ed. St. Singapore: Elsevier Pre Ltd. (2006). p. 423–56.
8. Biscaglia S, Tebaldi M, Brugaletta S, Cerrato E, Erriquez A, Passarini G, et al. Prognostic value of QFR measured immediately after successful stent implantation: the international multicenter prospective HAWKEYE study. *JACC Cardiovasc Interv.* (2019) 12:2079–88. doi: 10.1016/j.jcin.2019.06.003
9. Kogame N, Takahashi K, Tomaniak M, Chichareon P, Modolo R, Chang CC, et al. Clinical implication of quantitative flow ratio after percutaneous coronary intervention for 3-vessel disease. *JACC Cardiovasc Interv.* (2019) 12:2064–75. doi: 10.1016/j.jcin.2019.08.009
10. Hakeem A, Uretsky BF. Role of postintervention fractional flow reserve to improve procedural and clinical outcomes. *Circulation.* (2019) 139:694–706. doi: 10.1161/CIRCULATIONAHA.118.035837
11. Pijls NH, De Bruyne B, Peels K, Van Der Voort PH, Bonnier HJ, Bartunek J Koolen JJ, et al. Measurement of fractional flow reserve to assess the functional severity of coronary-artery stenoses. *N Engl J Med.* (1996) 334:1703–8. doi: 10.1056/NEJM199606273342604
12. Ragosta M, Bishop AH, Lipson LC, Watson DD, Gimple LW, Sarembock IJ, et al. Comparison between angiography and fractional flow reserve versus single-photon emission computed tomographic myocardial perfusion imaging for determining lesion significance in patients with multivessel coronary disease. *Am J Cardiol.* (2007) 99:896–902. doi: 10.1016/j.amjcard.2006.11.035
13. Pijls NH, van Schaardenburgh P, Manoharan G, Boersma E, Bech JW, van't Veer M, et al. Percutaneous coronary intervention of functionally nonsignificant stenosis: 5-year follow-up of the DEFER study. *J Am Coll Cardiol.* (2007) 49:2105–11. doi: 10.1016/j.jacc.2007.01.087
14. Pijls NH, Fearon WF, Tonino PA, Siebert U, Ikeno F, Bornschein B, et al. Fractional flow reserve versus angiography for guiding percutaneous coronary intervention in patients with multivessel coronary artery disease: 2-year follow-up of the FAME (fractional flow reserve versus angiography for multivessel evaluation) study. *J Am Coll Cardiol.* (2010) 56:177–84. doi: 10.1016/j.jacc.2010.04.012
15. De Bruyne B, Pijls NH, Kalesan B, Barbato E, Tonino PA, Piroth Z, et al. Fractional flow reserve-guided PCI versus medical therapy in stable coronary disease. *N Engl J Med.* (2012) 367:991–1001. doi: 10.1056/NEJMoa1205361
16. Patel MR, Calhoon JH, Dehmer GJ, Grantham JA, Maddox TM, Maron DJ, et al. ACC/AATS/AHA/ASE/ASNC/SCAI/SCCT/STS 2017 appropriate use criteria for coronary revascularization in patients with stable ischemic heart disease: a report of the American college of cardiology appropriate use criteria task force, American association for thoracic surgery, American heart association, American society of echocardiography, American society of nuclear cardiology, society for cardiovascular angiography and interventions, society of cardiovascular computed tomography, and society of thoracic surgeons. *J Am Coll Cardiol.* (2017) 69:2212–41. doi: 10.1016/j.jacc.2017.02.001

17. Neumann FJ, Sousa-Uva M, Ahlsson A, Alfonso F, Banning AP, Benedetto U, et al. 2018 ESC/EACTS guidelines on myocardial revascularization. *Eur Heart J*. (2019) 40:87–165. doi: 10.1093/eurheartj/ehy394
18. Pijls NH, Klauss V, Siebert U, Powers E, Takazawa K, Fearon WF, et al. Coronary pressure measurement after stenting predicts adverse events at follow-up: a multicenter registry. *Circulation*. (2002) 105:2950–4. doi: 10.1161/01.CIR.0000020547.92091.76
19. Li SJ, Ge Z, Kan J, Zhang JJ, Ye F, Kwan TW, et al. Cutoff value and long-term prediction of clinical events by FFR measured immediately after implantation of a drug-eluting stent in patients with coronary artery disease: 1- to 3-year results from the DKCRUSH VII registry study. *JACC Cardiovasc Interv*. (2017) 10:986–95. doi: 10.1016/j.jcin.2017.02.012
20. Driessen RS, Danad I, Stuijfzand WJ, Schumacher SP, Knuuti J, Mäki M, et al. Impact of revascularization on absolute myocardial blood flow as assessed by serial $[^{15}O]H_2O$ positron emission tomography imaging: a comparison with fractional flow reserve. *Circ Cardiovasc Imaging*. (2018) 11:e007417. doi: 10.1161/CIRCIMAGING.117.007417
21. Lee JM, Hwang D, Choi KH, Rhee TM, Park J, Kim HY, et al. Prognostic implications of relative increase and final fractional flow reserve in patients with stent implantation. *JACC Cardiovasc Interv*. (2018) 11:2099–109. doi: 10.1016/j.jcin.2018.07.031
22. van Bommel RJ, Masdjedi K, Diletti R, Lemmert ME, van Zandvoort L, Wilschut J, et al. Routine fractional flow reserve measurement after percutaneous coronary intervention. *Circ Cardiovasc Interv*. (2019) 12:e007428. doi: 10.1161/CIRCINTERVENTIONS.118.007428
23. Wolfrum M, Fahrni G, de Maria GL, Knapp G, Curzen N, Kharbanda RK, et al. Impact of impaired fractional flow reserve after coronary interventions on outcomes: a systematic review and meta-analysis. *BMC Cardiovasc Disord*. (2016) 16:177. doi: 10.1186/s12872-016-0355-7
24. Agarwal SK, Kasula S, Hacioglu Y, Ahmed Z, Uretsky BF, Hakeem A. Utilizing post-intervention fractional flow reserve to optimize acute results and the relationship to long-term outcomes. *JACC Cardiovasc Interv*. (2016) 9:1022–31. doi: 10.1016/j.jcin.2016.01.046
25. Parikh RV, Liu G, Plomondon ME, Sehested TSG, Hlatky MA, Waldo SW, et al. Utilization and outcomes of measuring fractional flow reserve in patients with stable ischemic heart disease. *J Am Coll Cardiol*. (2020) 75:409–19. doi: 10.1016/j.jacc.2019.10.060
26. Toth GG, Toth B, Johnson NP, De Vroey F, Di Serafino L, Pyxaras S, et al. Revascularization decisions in patients with stable angina and intermediate lesions: results of the international survey on interventional strategy. *Circ Cardiovasc Interv*. (2014) 7:751–9. doi: 10.1161/CIRCINTERVENTIONS.114.001608
27. Piroth Z, Toth GG, Tonino PAL, Barbato E, Aghlmandi S, Curzen N, et al. Prognostic value of fractional flow reserve measured immediately after drug-eluting stent implantation. *Circ Cardiovasc Interv*. (2017) 10:e005233. doi: 10.1161/CIRCINTERVENTIONS.116.005233
28. Rubimbura V, Guillon B, Fournier S, Amabile N, Chi Pan C, Combaret N, et al. Quantitative flow ratio virtual stenting and post stenting correlations to post stenting fractional flow reserve measurements from the DOCTORS (Does optical coherence tomography optimize results of stenting) study population. *Catheter Cardiovasc Interv*. (2020) 96:1145–53. doi: 10.1002/ccd.28615
29. Masdjedi K, van Zandvoort LJ, Balbi MM, Nuis RJ, Wilschut J, Diletti R, et al. Validation of novel 3-dimensional quantitative coronary angiography based software to calculate fractional flow reserve post stenting [published online ahead of print, 2020 Oct 6]. *Catheter Cardiovasc Interv*. (2020) 10. doi: 10.1002/ccd.29311
30. Ely Pizzato P, Samdani AJ, Vergara-Martel A, Palma Dallan LA, Tensol Rodrigues Pereira G, Zago E, et al. Feasibility of coronary angiogram-derived vessel fractional flow reserve in the setting of standard of care percutaneous coronary intervention and its correlation with invasive FFR. *Int J Cardiol*. (2020) 301:45–9. doi: 10.1016/j.ijcard.2019.10.054
31. Buono A, Mühlenhaus A, Schäfer T, Trieb AK, Schmeißer J, Koppe F, et al. QFR predicts the incidence of long-term adverse events in patients with suspected CAD: feasibility and reproducibility of the method. *J Clin Med*. (2020) 9:220. doi: 10.3390/jcm9010220
32. Severino P, D'Amato A, Pucci M, Infusino F, Adamo F, Birtolo LI, et al. Ischemic heart disease pathophysiology paradigms overview: from plaque activation to microvascular dysfunction. *Int J Mol Sci*. (2020) 21:8118. doi: 10.3390/ijms21218118
33. Xu H, Liu J, Zhou D, Jin Y. Influence of microcirculation load on FFR in coronary artery stenosis model. *BMC Cardiovasc Disord*. (2020) 20:144. doi: 10.1186/s12872-020-01437-w
34. Severino P, D'Amato A, Netti L, Pucci M, Mariani MV, Cimino S, et al. Susceptibility to ischaemic heart disease: focusing on genetic variants for ATP-sensitive potassium channel beyond traditional risk factors [published online ahead of print, 2020 Jun 2]. *Eur J Prev Cardiol*. (2020). doi: 10.1177/2047487320926780

Conflict of Interest: The authors declare that the research was conducted in the absence of any commercial or financial relationships that could be construed as a potential conflict of interest.

frontiers
in Cardiovascular Medicine

ORIGINAL RESEARCH
published: 09 June 2021
doi: 10.3389/fcvm.2021.675291

Automatic Segmentation and Cardiac Mechanics Analysis of Evolving Zebrafish Using Deep Learning

Bohan Zhang[1,2], Kristofor E. Pas[1], Toluwani Ijaseun[1], Hung Cao[3], Peng Fei[2] and Juhyun Lee[1,4*]

[1] Joint Department of Bioengineering, University of Texas (UT) Arlington/(UT) Southwestern, Arlington, TX, United States, [2] School of Optical and Electronic Information-Wuhan National Laboratory for Optoelectronics, Huazhong University of Science and Technology, Wuhan, China, [3] Department of Electrical Engineering and Computer Science, University of California, Irvine, Irvine, CA, United States, [4] Department of Medical Education, Texas Christian University (TCU) and University of North Texas Health Science Center (UNTHSC) School of Medicine, Fort Worth, TX, United States

Background: In the study of early cardiac development, it is essential to acquire accurate volume changes of the heart chambers. Although advanced imaging techniques, such as light-sheet fluorescent microscopy (LSFM), provide an accurate procedure for analyzing the heart structure, rapid, and robust segmentation is required to reduce laborious time and accurately quantify developmental cardiac mechanics.

Methods: The traditional biomedical analysis involving segmentation of the intracardiac volume occurs manually, presenting bottlenecks due to enormous data volume at high axial resolution. Our advanced deep-learning techniques provide a robust method to segment the volume within a few minutes. Our U-net-based segmentation adopted manually segmented intracardiac volume changes as training data and automatically produced the other LSFM zebrafish cardiac motion images.

Results: Three cardiac cycles from 2 to 5 days postfertilization (dpf) were successfully segmented by our U-net-based network providing volume changes over time. In addition to understanding each of the two chambers' cardiac function, the ventricle and atrium were separated by 3D erode morphology methods. Therefore, cardiac mechanical properties were measured rapidly and demonstrated incremental volume changes of both chambers separately. Interestingly, stroke volume (SV) remains similar in the atrium while that of the ventricle increases SV gradually.

Conclusion: Our U-net-based segmentation provides a delicate method to segment the intricate inner volume of the zebrafish heart during development, thus providing an accurate, robust, and efficient algorithm to accelerate cardiac research by bypassing the labor-intensive task as well as improving the consistency in the results.

Keywords: U-net, LSFM, segmentation, zebrafish, cardiac mechanics

Edited by:
Yun Fang,
University of Chicago, United States

Reviewed by:
Tzung Hsiai,
University of California, Los Angeles, United States
Paolo Severino,
Sapienza University of Rome, Italy

****Correspondence:***
Juhyun Lee
juhyun.lee@uta.edu

Specialty section:
This article was submitted to Atherosclerosis and Vascular Medicine, a section of the journal Frontiers in Cardiovascular Medicine

Received: *02 March 2021*
Accepted: *20 April 2021*
Published: *09 June 2021*

Citation:
Zhang B, Pas KE, Ijaseun T, Cao H, Fei P and Lee J (2021) Automatic Segmentation and Cardiac Mechanics Analysis of Evolving Zebrafish Using Deep Learning. Front. Cardiovasc. Med. 8:675291. doi: 10.3389/fcvm.2021.675291

INTRODUCTION

Biomechanical analysis is vital during cardiac development, as assessment of biomechanics is closely associated with regulation of valve formation, ventricular septum, and trabecular morphology related to cardiogenic transcriptional and growth/differentiation factors (1, 2). Lack of intracardiac biomechanical force could induce genetic programming's malfunction resulting in congenital heart defects in humans and mice (3). For example, understanding potential malfunctions within the heart's subcellular structure could point toward indications of different maladies such as ischemic heart disease (IHD). Severino et al. (4) reported that IHD is associated with coronary microvascular dysfunction, which is affected by the role of ATP-sensitive potassium channel, and this ATP-sensitive potassium channel modulates the degree of contractile tone in vascular muscle (5). Thus, investigating biomechanics to link disease models including contractility is an important assessment in cardiac research field.

Volume change-based cardiac mechanics measurements (e.g., ejection fraction) from the complex trabeculated and beating heart are most commonly used and play an essential role in evaluating the cardiac health condition. Such measurement relies on the accurate reconstruction of the heart's volume, which depends on the accurate segmentation of the biomedical images. Although the segmentation of biomedical images for volume reconstruction has been extensively studied in radiation imaging techniques such as MRI or CT (6–8), these imaging methods are challenging to be adopted for optical fluorescent images. Although various optical microscopes have been extensively used to study in biomedical research due to inexpensive approach, high resolution, and amenable fluorescent tagging (9–11), it suffers from light scattering and different intensity of the fluorescent signal. In addition, imaging dynamic samples is another challenge for microscopes. Unlike conventional microscopes, however, light-sheet fluorescent microscopy (LSFM) circumvents these challenges to capture *in vivo* dynamic samples, such as zebrafish heart, with a high axial resolution, deep axial scanning, fast image acquisition, and low photobleaching (12, 13).

Despite having a two-chambered heart and a lack of a pulmonary system, the zebrafish represents an emerging vertebrate model for studying developmental biology (14, 15). Its transparency and short organ developmental timeline enable rapid and high throughput analysis of developmental stages with optical fluorescent technology (16). Such advantages of zebrafish and LSFM systems make a powerful tool for studying *in vivo* cardiac development.

To understand the cardiac function and mechanics and further analysis, intracardiac segmentation is a necessary step (2, 17). Previously, segmentation of the LSFM images for measuring cardiac mechanics was accomplished manually by recognizing different intensities from large amounts of samples or tissue scatterings engenders many variables (18). The time-consuming task of manually segmenting the LSFM images is infeasible when processing high axial resolution data, as the number of images required is enormous (19, 20). On the other hand, lower axial resolution degrades the volume measurement's accuracy, while inconsistent manual segmentation poses a threat to the cardiac mechanic analysis' overall quality. Recently, Akerberg et al. (21) nicely demonstrated SegNet-based deep-learning segmentation of zebrafish hearts at the early ventricular developmental stage before trabeculation. However, accurate segmentation of complex ventricular morphology after initiating trabeculation is critical to cardiac mechanics analysis. Therefore, we utilize the advancements in a specific convolution neural network (CNN) architecture, namely, U-net (22), which performs binary classification of the LSFM images' pixels. Unlike natural images, in which rich color and texture information are provided, LSFM images offer limited information. To reliably segment an LSFM image, the pixel location has to be considered. Our proposed U-net utilizes such information via a multiscale processing pipeline, which uses downsampling to extract the features while using upsampling to convert features to specific pixel positions. The main contribution of this paper is to propose and demonstrate a practical and robust U-net architecture for optical imaging, which is tailored to segment LSFM images of the developing zebrafish heart. The synchronization of the LSFM image sequence is applied before segmentation as a preprocessing step.

For our application, the U-net was trained to utilize LSFM images of a zebrafish during ventricular development from 2 to 5 days postfertilization (dpf). In this paper, we explore the potential use of the U-Net architecture to expedite the segmentation of the intracardiac zebrafish heart, including the atrium and ventricle and further biomechanical analysis of the extracted results from the network.

METHODS

Zebrafish Preparation for Imaging

The zebrafish used for this study was raised and maintained in our zebrafish core facility under the required UT Arlington Institutional Animal Care and Use Committee (IACUC) protocol. Transgenic *tg*(*cmlc2:gfp*) zebrafish lines were used in this study to observe myocardium and chamber development. To ensure a clear image, a medium composed of 0.0025% phenylthiourea (PTU) was used to suppress pigmentation at 20 h postfertilization (hpf) (23). Before imaging, zebrafish embryos were anesthetized in 0.05% Tricaine and immersed in a solution of 0.5% low-melt-agarose at 37°C. The embryos were then transferred to a fluorinated ethylene propylene (FEP) tube (refractive index, 1.33) to minimize refraction along the path of light before image acquisition. This FEP tube was then immersed in water (refractive index, 1.33) and connected to an in-house LSFM to scan 500 images per slice from the anterior to posterior of zebrafish heart with 2 μm thickness (24).

4D Reconstruction of Beating Zebrafish Heart

4D reconstruction of *in vivo* beating zebrafish heart was performed using previously described methods (18, 25). Performed 4D reconstruction procedure is based on assumption that zebrafish heartbeat is regular throughout the image acquisition. However, experiments demonstrate that this assumption is not reliable. To minimize the natural irregularity of zebrafish heartbeat, we added an extra parameter (δ) to detect phase lock at period determination to observe irregularity during the experiments (18, 25). This latent variable window, δ, can be set roughly −0.3 to +0.3 ms after finding the estimated cardiac period manually (26).

Segmentation of Intracardiac Domain

Well-reconstructed 4D images were selected for manual segmentation of the intracardiac domain. 3D images of each time point from the beating heart were loaded into the Amira software (Thermofisher Scientific, Waltham, MA) or 3DSlicer. First, the inner cavity of each 2D slice was carefully selected manually and reconstruct 3D volume segmentation for each time point of the beating heart. We repeated this process at all developmental points to make segmentation masks. Manual segmentation masks were used for training our U-net architecture.

Application of U-Net Architecture

The U-net architecture revolves around two distinct paths: the contracting path and the expansive path (22). The network takes the input of size: A × A × n {A = 2k|k∈N} array, where "n" is the color channel or the depth of image. Since our LSFM provides a grayscale image of singular depth, "n" was 1. The input is pushed initially through the contracting path, which processes the input through a series of 3 × 3 convolutions, the application of a rectified linear unit (ReLU) following each convolution, then a 2 × 2 max-pooling operation. This yields an output of A/2 × A/2 × 2n, expanding the feature channel by double. This process is repeated four times before the final output is started to processed by the expansive path, which undergoes a similar process, with the exception of using a 2 × 2 convolution operation instead of max pooling (**Figure 1**). The loss function used for this particular project was a binary cross-entropy loss function, and the Adam optimizer was used. The computer used was an Intel Xeon E5 (CPU) and NVIDIA Quadro P5000 (GPU). Most of the calculations were done by GPU; it consumes 3.39 GB of memory, and performance scales with more memory allotted. With the current setup, it costs around 180 ms to train each slice; the minimal request for training dataset (400 slices) and epoch number (50 epochs) would be 48 minutes. It takes about 60 ms to predict one slice. In a few minutes, the network can process the whole 4D data.

Network Training With Manually Segmented Images

Training data for CNN learning is divided into two separate bins: training volumes and labels. Four individual heart samples models were used to study the developmental stages from 2 to 5 dpf. The raw data came from 4D images of the beating heart. From these 4D images, each 3D images were isolated from every 20 equally spaced sample of each heart. For these, we selected the entire slices of the 20 samples of 3D volume of the heart from 4D dataset, representing three cardiac cycles, with each volume containing m numbers of 2D sliced images (m∈N), which was dependent on the slice selected. This particular parameter was related to the spatial depth of the volume being observed. Following data acquisition, hand segmentation was performed using 3DSlicer GUI application on the 2D axial plane spanning the entirety of the zebrafish heart captured. Both of these training bins were converted into 8-bit format and imported into U-NET as a 512 × 512 × 1 8-bit array, with bijective correspondence between volumes and labels. The U-NET program featured trained blind to the spatial depth of the volume itself, only having access to segmentation of the 2D axial slice input. From here, the training data took up approximately 80% of the data used for experimentation, while 20% was used for future validation.

Dice Similarity Coefficient Correlation

The primary method to which our automatic segmentation was assessed was using the Dice similarity coefficient correlation, which compares the amount of space of which the volumes of the automatic and hand segmentation overlap in comparison with the summation of the total number of pixels. The calculation of this is as follows for area A, representing autosegmentation, and area B, representing our manually labeled segmentation:

$$\text{Similarity} = \frac{2 \times |(A \cap B)|}{|A| + |B|} \tag{1}$$

The outcome yields some value x for $x \in [0, 1]$, with the value 1 (approximating a near-perfect segmentation match with respect to the initial hand segmentation used) and 0 (showing essentially no correlation between the two).

Cardiac Mechanics Analysis

After segmented volume, we multiplied voxel resolution to obtain the actual volume of zebrafish heart. We capture the size of most dilated points and most contracted points as end-diastolic volume (EDV) and end-systolic volume (ESV), respectively. Stroke volume (SV) was calculated by subtracting ESV from EDV. Ejection fraction (EF) is the ratio of blood ejection, which can be simply calculated from EF = (SV/EDV) × 100.

RESULTS

Manual Segmentation From LSFM for U-Net Training

Manual segmentation was performed along the 2D axial plane of the zebrafish heart for each studied sample. The methodology for manual segmentation, which served as our ground truth and labels, was performed using a contour-based segmentation method provided by 3DSlicer and was done in conjunction with *ad hoc* edits done on the resulting figures. Manually segmented images were used as training datasets for U-net (**Figure 1**). The concept of U-net architecture was to supplement a usual contracting network by successive layers, where pooling operators were replaced by upsampling operators (22). Here, original 512 × 512 pixels LSFM images were deconstructed to detect features of intracardiac boundaries. Then, upsampling of each layer increased the resolution of the output. For localization, higher resolution features from the downsampling path were combined with the upsampled output. As the manual

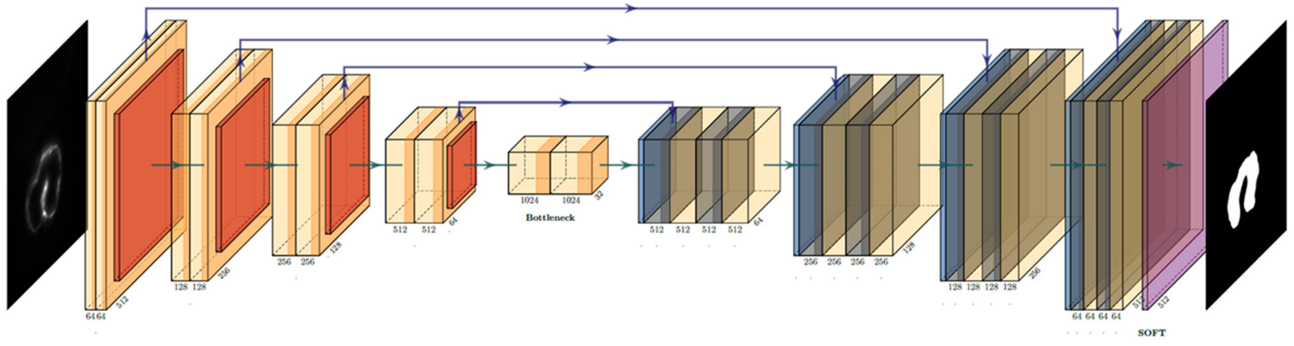

FIGURE 1 | U-net convolution neural network (CNN) architecture utilized to generate the binary mask of the intracardiac domain of zebrafish. Each box represents a multichannel feature map that allows for efficient and accurate extraction of anatomical features. In our specific application, the input was a 512 × 512 pixel map.

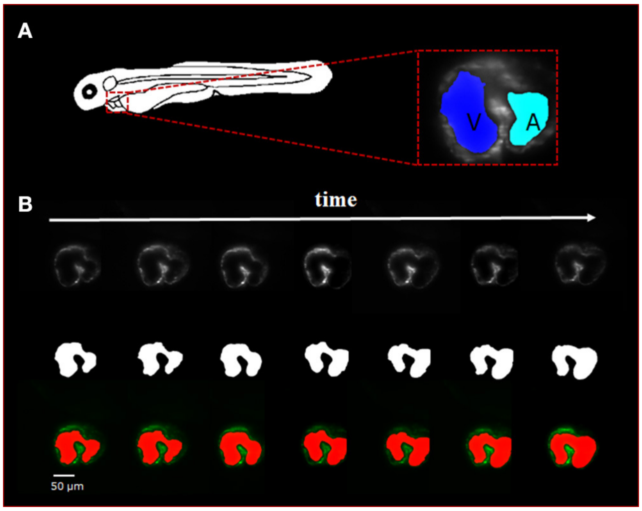

FIGURE 2 | Sequence of selected light-sheet fluorescent microscopy (LSFM) images with the manual hand segmentation mask from 4 dpf zebrafish heart. **(A)** Diagram showing the anatomical feature of the zebrafish heart as well as a single axial slice with corresponding binary mask generated by the U-net. It is observed that there is a clear distinction between the atria and ventricle of the specimen. **(B)** A sequence of selected axial slices with corresponding binary masks generated by our U-net program; the reference scale bar is 50 μm.

segmentation images were input for training, a successive convolution layer learned to assemble a more precise output based on this information. In addition, a Gaussian 2D filter of kernel size of 2.0 μm was applied to smooth manual segmentation. Contour interpolation was further applied to the 3D structure output to minimize the step size of later 3D reconstruction. The fidelity of the manual segmentation was done observationally through inspecting the spatial comparison between the label generated and the intracardiac area of the 2D slice (**Figure 2**).

Validation of U-Net Based Autosegmented Image

We visualize the segmentation ability of our networks by reconstructing the diastolic and systolic stages of zebrafish (**Figures 3A,B**; **Supplementary Videos 1, 2**). Although there is a small segmentation discrepancy between ground truth and autosegmentation around fluorescent boundaries (**Figures 3C,D**), U-net-based segmentation accuracy for each frame has a mean Dice coefficient score of 0.95 with a standard deviation of 0.02 (**Figure 3E**). Due to trabeculation in the ventricle at 4 dpf, manual segmentation was more sophisticatedly segmented in rough fluorescent boundaries. Although our autosegmentation was performed to detect rough boundaries in the trabeculated area, the roughness was relatively smooth. However, the atrium's smooth surface and innermost area of the ventricle were captured closer to the fluorescent signal. This discrepancy could be from the dataset that we used to train the network, the result of inconsistences from manual segmentation judged by the user. These statistics demonstrate our U-net-based segmentation's remarkable ability to segment intracardiac chamber with a high dice coefficient score and reduces inherent manual segmentation.

Automatic Morphology to Separate Inner Chamber Space

To validate the U-net-based autosegmentation and allow for further application, it was deemed necessary to derive some function for separating the inner-chamber structure to allow for independent analysis of the two-volume components and their disjoint biomechanical characteristics. This was done using an in-house Matlab code utilizing an iterative process of applying an erosion operator relying on a 3D structuring element until fracturing the single master volume. Following this, a dilation operator was applied to the individual subvolumes to recover lost space, and the resulting dilated volumes were intersected in 3D space with the initial master volume. The output of this program was the resulting intersected space.

This program's use proved to be critical in studying the resulting biomechanical elements of the atria and ventricle, as it allowed for consistency in determining the chambers (**Figure 4A**; **Supplementary Videos 3, 4**). The methodology was used successfully to distinguish the atrium and ventricle within the program on a three-dimensional level (**Figure 4B**). The resulting axial scans of the separated atria and ventricle show

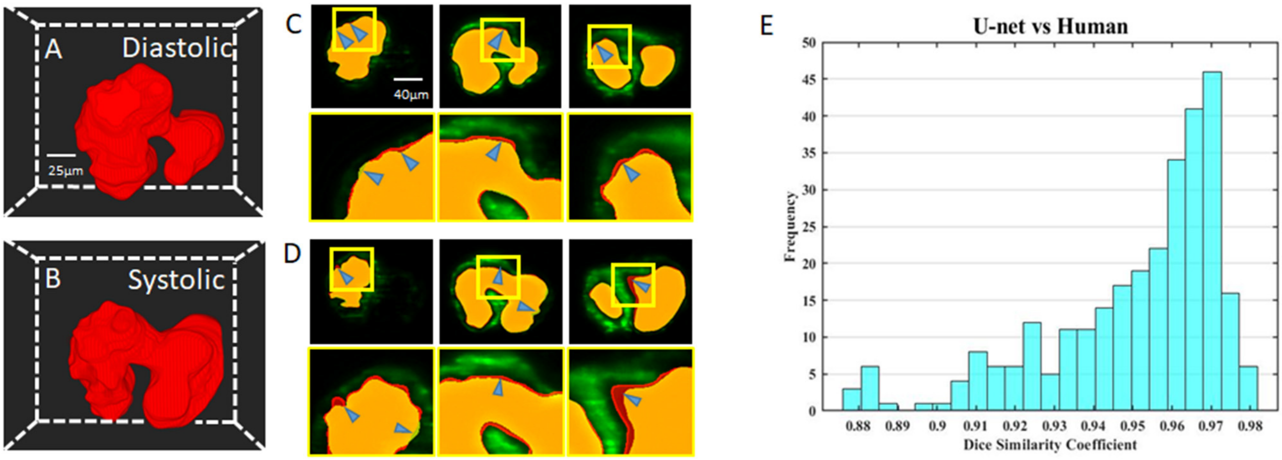

FIGURE 3 | Comparison of U-net based autosegmentation to manual hand segmentation. **(A,B)** Geometric representation of both the diastolic and systolic stages of the heart cycle. **(C,D)** Comparison in the 2D axial plane between autosegmentation of the U-net and ground truth in both the diastolic and systolic stages, respectively. The blue arrows indicate areas of disjoint space within the segmentations, shown in red (manual segmentation), green (autosegmentation), and yellow (intersection). **(E)** Corresponding Dice similarity coefficient comparing the results between our ground truth and automatic segmentation demonstrated the ability of autosegmentation.

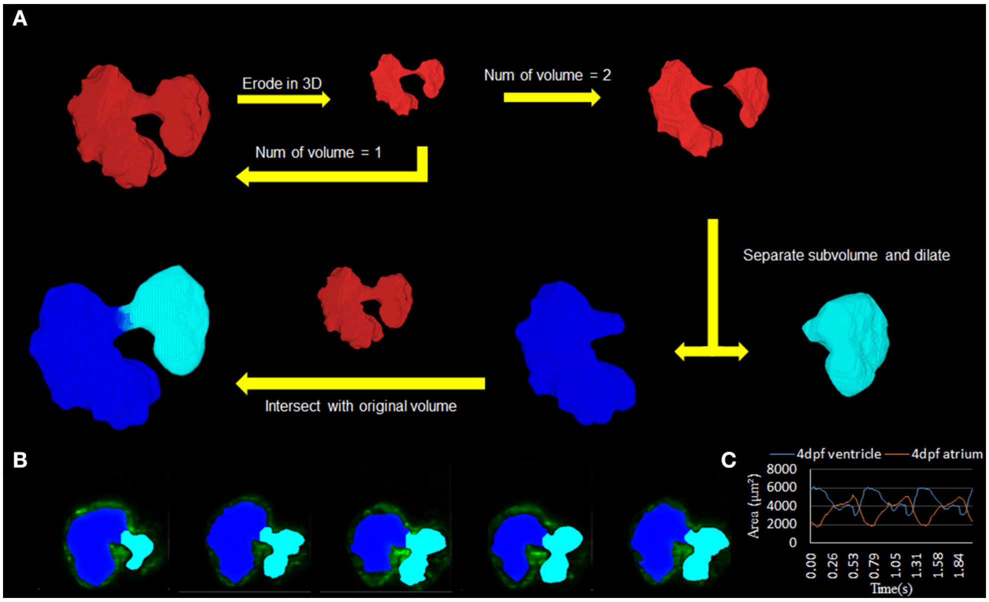

FIGURE 4 | Subdivision of atrium and ventricle. **(A)** Methodology of using the automatic segmentation to define the morphology of inner volume of the zebrafish heart. This method relies on an iterative process that uses an erosion operator on the 3D structure of the inner volume until division occurs. Following the division of the volume into two separate components, extraction of each individual piece follows with a dilation operation and intersection with the original volume. **(B)** 2D axial slices showing the differentiation of the atrium (teal) and ventricle (blue) of various slices. **(C)** Area change over time from 2D slice **(B)** was successfully demonstrated.

a clear distinction between the two different chamber areas per slice at 4 dpf (**Figure 4C**).

Volumetric Analysis

We have applied 4D synchronization methods to reconstruct volume change over time (2, 18). Analysis of the volume change along three cardiac cycles was provided to study the biomechanical changes over time (**Figure 5A**). The volume of the atria and ventricle and the total intracardiac volume of both chambers were plotted independently (**Figure 5B**). Although the total cardiac volume of 4 dpf is oscillating during pumping, the mean value is roughly 9.5 × 105 μm^3. At 4 dpf, trabeculae developed in the ventricle; thus, 4D reconstruction showed the motion of the corrugated surface of the ventricle. Due to the lack of trabeculae (27), the atrium has a relatively tranquil curvature motion during atrial contraction and relaxation. Our results reveal the potential power of complex morphology and functional analysis.

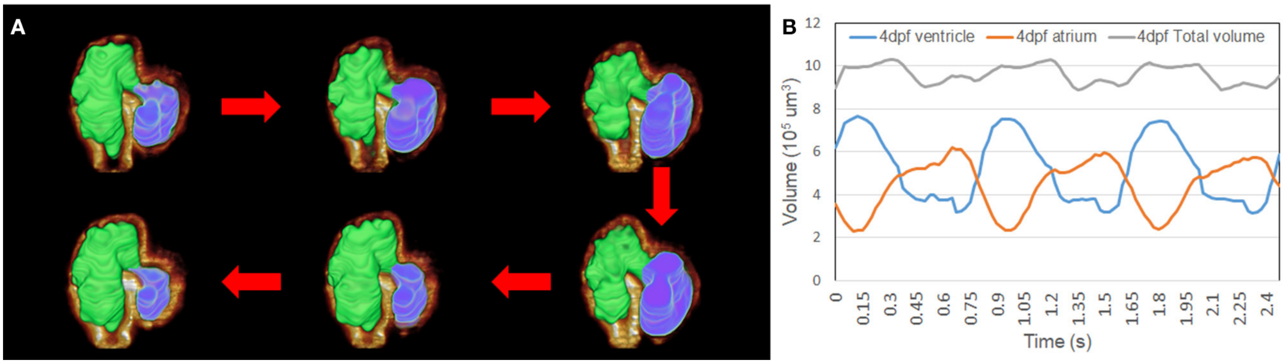

FIGURE 5 | Representation of the contraction to dilation of zebrafish heart volume change over time. **(A)** Autosegmented successfully reconstructed 4D image captured the rough inner surface of zebrafish due to trabeculation after merging with fluorescent-labeled *tg*(*cmlc2:gfp*) zebrafish from light-sheet fluorescent microscopy (LSFM) images. **(B)** Volume change in the ventricle and atrium was measured from autosegmentation. Total volume of atrium and ventricle represented around 9.5 × 10^5 μm^3 when zebrafish was at 4 dpf.

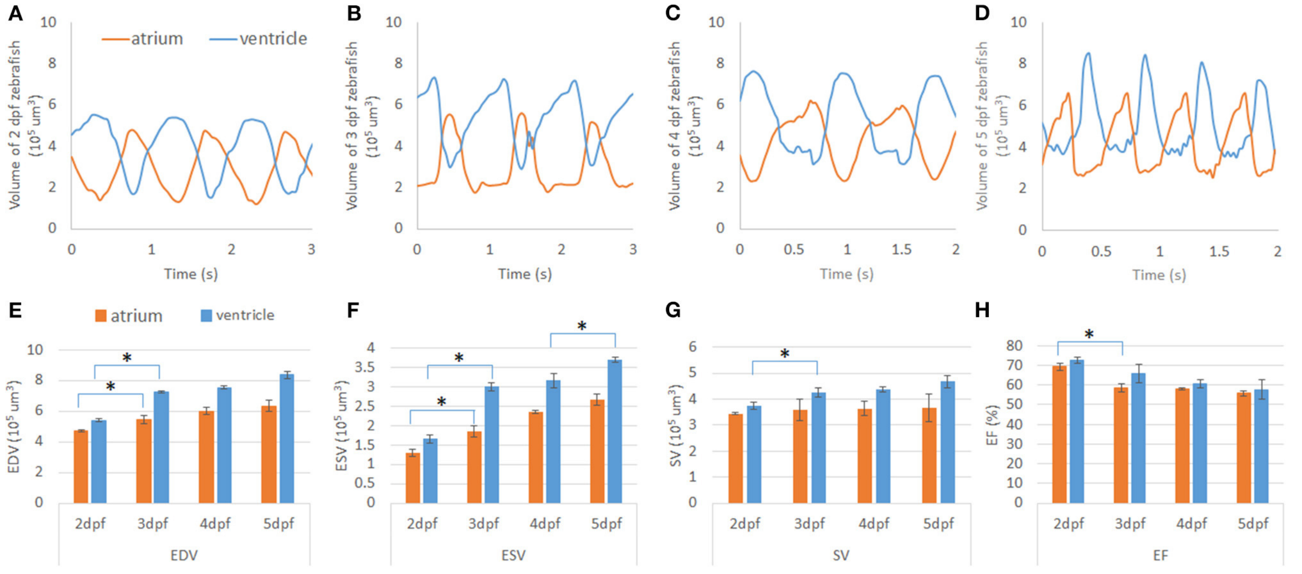

FIGURE 6 | Cardiac mechanics analysis of developing zebrafish heart. **(A–D)** Volume change of developing zebrafish heart was measured by U-net-based autosegmentation, showing consistent increase in volume in both the atrium and ventricle. **(E,F)** After notable morphology change after cardiac looping, end-diastolic volume (EDV) and end-systolic volume (ESV) were increased significantly in both the atrium and ventricle. At 5 dpf, ESV was also significantly increased compared to 4 dpf. **(G)** While SV of the ventricle showed an increasing trend, that if the atrium remained at a similar level from 2 to 5 dpf. **(H)** Ejection fraction (EF) analysis demonstrated a decreasing trend from high EF at 2 dpf. *$p \leq 0.05$.

Assessment of Cardiac Mechanics of Developing Zebrafish Heart

In studying the volumetric change of the zebrafish heart during early-stage development between 2 and 5 dpf, observations allowed for the analysis of the atria and ventricle volumetric loads. Interestingly, we recognize that the ventricular contraction pattern shifts left from 2 to 3 dpf and shifts right from 4 to 5 dpf. Similarly, a pattern was observed within the atrium's volumetric change, albeit in an inverse manner (**Figures 6A–D**). Furthermore, based on volume change data, we have performed cardiac mechanics analysis during development. We first analyze the end-diastolic volume (EDV) and end-systolic volume (ESV) of the atrium and ventricle. Although the EDV and ESV trend of both the atrium and ventricle consistently increased, there was a significant increase between 2 and 3 dpf where morphology changed by cardiac looping (28) (**Figures 6E,F**). The active trabeculation process (18, 27), which increases the ventricle's contractility, affects the ESV of the ventricle at 5 from 4 dpf. Interestingly, the ventricle's stroke volume (SV) consistently increased, while the SV of the atrium remains consistent around 3.6 × 105 μm^3 during early cardiogenesis (**Figure 6G**). We have further analyzed ejection fraction (EF) from EDV and ESV of the atrium and ventricle to understand how much blood each chamber pumps out with each contraction. Although, at 2 dpf, EF was high in both the atrium and ventricle, it continuously decreased throughout development (**Figure 6H**).

DISCUSSION

Our U-net-based segmentation methods successfully provided intracardiac 3D volume structure for studying the biomechanics of zebrafish hearts trained with manually segmented LSFM images. The previously created manual segmented volume was a tedious and taxing process for the researcher, leading to a possible room for error as time requirements increase. Furthermore, inconsistency would be induced between individuals, yielding different results of the same volume for two people. Although Akerberg et al. (21) used a SegNet-based autosegmentation nicely segmented zebrafish intracardiac volume and analyzed the cardiac function, their application was visualized in an early stage of zebrafish heart before trabeculation. We have adopted U-net for the segmentation to apply complex geometry of inner ventricular surface until 5 dpf zebrafish heart. This study relies on a fully convolutional neural network, which allows for quick segmentations with as little as five datasets. Within this experiment, our application revolved around pairing U-net with LSFM. This particular study's novelty was the new relation between the LSFM and U-net structure, which allows for high-level sectioning capabilities of the LSFM to generate the 3D structure of the complex zebrafish heart with ease, followed by automatic morphological analyses.

There are currently a few limitations to our approach from this paper, which we feel necessary to touch upon. A limitation to the algorithm is that it relies on manual segmentation as its ground truth. Furthermore, the quality of the manual segmentation also depends on the image quality of each raw LSFM image slice. If the raw images are perhaps not precise enough for various reasons, the algorithm may not be able to generate the most precise results it is capable of. As for manual segmentation, there is a high possibility of human error. There are many variables that change in the manual segmentation depending on the user. One aspect of this is smoothing of the 2D slices in the manual segmentation. The smoothing is done based on each user's discerning eye, which can lead to minor discrepancies in the manual segmentation. In addition, the data for the algorithm are trained separately by day instead of a single dataset, which limits efficiency due to the complex nature of the morphology and different developmental environment. As a consequence of the change in morphological structure observed over the time period of which this project was performed, it was not feasible to create some singular model that could automatically segment any 2D axial input for any developmental stage. As a consequence, we found it necessary to create four different models, one for each corresponding developmental stage for independent processing. This limitation required extra work in terms of computational requirements; however, we see it as necessary for the moment. Despite these limitations, the current algorithm designed has been able to create highly accurate autosegmentation from the use of manual segmentation of four different developmental datasets.

This study's primary objective was to determine if the conjunctional use of this modality-program pair provided feasible results. This objective was satisfied with a high degree of success, as seen from the Dice similarity correlation coefficient having a value perceived as exceptional, showing similarity between our perceived ground truth and the autosegmentation (**Figure 3E**). Although we have observed errors between manual and autosegmentation, we assume that the fluorescent intensity threshold point was vague when segmentation was performed manually (**Figures 3C,D**). Therefore, our autosegmentation network could help to process more detailed cardiac mechanical analysis compared to manual segmentation. Most interestingly, in our cardiac mechanics analysis, relatively rapid contraction and slower relaxation of the atrium at 2 and 3 dpf transitions to slower contraction and rapid relaxation at 4 and 5 dpf (**Figures 6A–D**). At 2 and 3 dpf, zebrafish atrium pumps blood in peristaltic motion due to lack of valves, while it relies on impedance pumping mechanism at 4 and 5 dpf (29). Therefore, we may observe that the atrial volume change curve shifts left at 2 and 3 dpf and shifts right at 4 and 5 dpf. In addition, after cardiac looping, cardiac function significantly changed as the ventricle developed faster in size. In the heart's tubular shape before cardiac looping, the atrium is bigger than the ventricle (21). At 5 dpf, when active trabeculation increases the ventricle's contractility, contraction of the ventricle increased significantly in corroboration with previous findings (**Figure 6F**) (18). Atrial SV stayed consistent during development in the interim of increasing SV of the ventricle (**Figure 6G**).

Despite rapid process and consistent results, the experiment conducted has some mild limitations when considering the overall capabilities being used. The most critical component for this study, including any deep-learning-based segmentation process, requires a high-quality input dataset, as the output test labels are only as good as those they are trained from. In our case, using the fluorescent label zebrafish, *tg*(*cmlc2:gfp*), yielded overall strong results from the ventricle but, on occasion, could have issues with the atria due to lower cardiomyocyte density and its location deeper in the chest, leading to more imaging issues. Circumventing this issue was not a trivial action, as exploring extensive preprocessing methods was required to be able to find the boundary of the inner volume of the heart (30). Other limitations that could be found in the experimentation process could be issues within the imaging process, in which user and systematic errors could hinder image fidelity.

Our methods will be compatible with other fluorescent optical imaging, such as z-scanned confocal microscopy images, providing quality 3D reconstruction. Our powerful U-net-based segmentation could be a new tool for studying a variety of future biomedical research applications. To begin, the parameters of the U-net could be tweaked to increase the accuracy and precision of the program for the zebrafish hearts; this would lead to a better quality autosegmentation, which would lead to progress in the field of mechanobiology by using computational fluid dynamics to understand the shear stress or pressure that could affect cardiac morphogenesis (2, 17).

CONCLUSION

Our U-net-based segmentation provides a delicate method to segment the intricate inner volume of zebrafish heart during development, thus providing an accurate and convenient algorithm to accelerate cardiac research by bypassing the labor-intensive task as well as improving the consistency in the results.

DATA AVAILABILITY STATEMENT

The raw data supporting the conclusions of this article will be made available by the authors, without undue reservation. Our all source codes are available in our **Supplementary Materials**.

ETHICS STATEMENT

The experiments were performed in compliance the approval from the UT Arlington Institutional Animal Care and Use Committee (IACUC) protocol (#A17.014).

AUTHOR CONTRIBUTIONS

BZ and KP: developing U-net for cardiac segmentation. KP and TI: image data acquisition and image processing for training. BZ, KP, and TI: training network and data analysis. HC, PF, and JL: conceptual design, research guide, and data interpretation. All authors edited and revised the article.

FUNDING

This study was supported by grants from AHA 18CDA34110150 (JL) and NSF 1936519 (JL).

SUPPLEMENTARY MATERIAL

The Supplementary Material for this article can be found online at: https://www.frontiersin.org/articles/10.3389/fcvm.2021.675291/full#supplementary-material

REFERENCES

1. Chen H, Shi S, Acosta L, Li W, Lu J, Bao S, et al. BMP10 is essential for maintaining cardiac growth during murine cardiogenesis. *Development.* (2004) 131:2219–31. doi: 10.1242/dev.01094
2. Lee J, Vedula V, Baek KI, Chen J, Hsu JJ, Ding Y, et al. Spatial and temporal variations in hemodynamic forces initiate cardiac trabeculation. *JCI Insight.* (2018) 3:e96672. doi: 10.1172/jci.insight.96672
3. High FA, Epstein JA. The multifaceted role of Notch in cardiac development and disease. *Nat Rev Genet.* (2008) 9:49–61. doi: 10.1038/nrg2279
4. Severino P, D'Amato A, Netti L, Pucci M, Mariani MV, Cimino S, et al. Susceptibility to ischaemic heart disease: focusing on genetic variants for ATP-sensitive potassium channel beyond traditional risk factors. *Eur J Prev Cardiol.* (2020). doi: 10.1177/2047487320926780. [Epub ahead of print].
5. Fedele F, Mancone M, Chilian WM, Severino P, Canali E, Logan S, et al. Role of genetic polymorphisms of ion channels in the pathophysiology of coronary microvascular dysfunction and ischemic heart disease. *Basic Res Cardiol.* (2013) 108:387. doi: 10.1007/s00395-013-0387-4
6. de Albuquerque VHC, de A Rodrigues D, Ivo RF, Peixoto SA, Han T, Wu W, et al. Fast fully automatic heart fat segmentation in computed tomography datasets. *Comput Med Imaging Graph.* (2020) 80:101674. doi: 10.1016/j.compmedimag.2019.101674
7. Higaki T, Nakamura Y, Zhou J, Yu Z, Nemoto T, Tatsugami F, et al. Deep learning reconstruction at CT: phantom study of the image characteristics. *Acad Radiol.* (2020) 27:82–7. doi: 10.1016/j.acra.2019.09.008
8. Dong J, Fu J, He Z. A deep learning reconstruction framework for X-ray computed tomography with incomplete data. *PLoS One.* (2019) 14:e0224426. doi: 10.1371/journal.pone.0224426
9. Arridge SR, Hebden JC. Optical imaging in medicine: II Modelling and reconstruction. *Phys Med Biol.* (1997) 42:841–53. doi: 10.1088/0031-9155/42/5/008
10. Hebden JC, Arridge SR, Delpy DT. Optical imaging in medicine: I. Experimental techniques. *Phys Med Biol.* (1997) 42:825–40. doi: 10.1088/0031-9155/42/5/007
11. Wilkinson JM, Frigault MM, Lacoste J, Swift JL, Brown CM. Live-cell microscopy-tips and tools. *J Cell Sci.* (2009) 122:753–67. doi: 10.1242/jcs.033837
12. Mickoleit M, Schmid B, Weber M, Fahrbach FO, Hombach S, Reischauer S, et al. High-resolution reconstruction of the beating zebrafish heart. *Nat Methods.* (2014) 11:919–22. doi: 10.1038/nmeth.3037
13. Huisken J, Stainier DY. Selective plane illumination microscopy techniques in developmental biology. *Development.* (2009) 136:1963–75. doi: 10.1242/dev.022426
14. Yu F, Huang J, Adlerz K, Jadvar H, Hamdan MH, Chi N, et al. Evolving cardiac conduction phenotypes in developing zebrafish larvae: implications to drug sensitivity. *Zebrafish.* (2010) 7:325–31. doi: 10.1089/zeb.2010.0658
15. Milan DJ, Jones IL, Ellinor PT, MacRae CA. *In vivo* recording of adult zebrafish electrocardiogram and assessment of drug-induced QT prolongation. *Am J Physiol Heart Circ Physiol.* (2006) 291:H269–73. doi: 10.1152/ajpheart.00960.2005
16. Bakkers J. Zebrafish as a model to study cardiac development and human cardiac disease. *Cardiovasc Res.* (2011) 91:279–88. doi: 10.1093/cvr/cvr098
17. Vedula V, Lee J, Xu H, Kuo CJ, Hsiai TK, Marsden AL. A method to quantify mechanobiologic forces during zebrafish cardiac development using 4-D light sheet imaging and computational modeling. *PLoS Comput Biol.* (2017) 13:e1005828. doi: 10.1371/journal.pcbi.1005828
18. Lee J, Fei P, Packard RR, Kang H, Xu H, Baek KI, et al. 4-Dimensional light-sheet microscopy to elucidate shear stress modulation of cardiac trabeculation. *J Clin Invest.* (2016) 126:1679–90. doi: 10.1172/JCI83496
19. Wang X, Zeng W, Yang X, Fang C, Han Y, Fei P. Bi-channel image registration and deep-learning segmentation (BIRDS) for efficient, versatile 3D mapping of mouse brain. *eLife.* (2021) 10:e63455. doi: 10.7554/eLife.63455
20. Wang Z, Zhu L, Zhang H, Li G, Yi C, Li Y, et al. Real-time volumetric reconstruction of biological dynamics with light-field microscopy and deep learning. *Nat Methods.* (2021) 18:551–6. doi: 10.1038/s41592-021-01058-x
21. Akerberg AA, Burns CE, Burns CG, Nguyen C. Deep learning enables automated volumetric assessments of cardiac function in zebrafish. *Dis Models Mech.* (2019) 12:dmm040188. doi: 10.1242/dmm.040188
22. Ronneberger O, Fischer P, Brox T. U-Net: convolutional networks for biomedical image segmentation. In: *International Conference on Medical Image Computing and Computer-Assisted Intervention.* Cham: Springer (2015). p. 234–41.
23. Lee J, Moghadam ME, Kung E, Cao H, Beebe T, Miller Y, et al. Moving domain computational fluid dynamics to interface with an embryonic model of cardiac morphogenesis. *PLoS One.* (2013) 8:e72924. doi: 10.1371/journal.pone.0072924
24. Fei P, Lee J, Packard RR, Sereti KI, Xu H, Ma J, et al. Cardiac light-sheet fluorescent microscopy for multi-scale and rapid imaging of architecture and function. *Sci Rep.* (2016) 6:22489. doi: 10.1038/srep22489
25. Messerschmidt V, Bailey Z, Baek KI, Bryant R, Li R, Hsiai TK, et al. Light-sheet fluorescence microscopy to capture 4-dimensional images of the effects of modulating shear stress on the developing zebrafish heart. *J Vis Exp.* (2018) 57763. doi: 10.3791/57763

26. Liebling M, Forouhar AS, Gharib M, Fraser SE, Dickinson ME. Four-dimensional cardiac imaging in living embryos via postacquisition synchronization of nongated slice sequences. *J Biomed Opt.* (2005) 10:054001. doi: 10.1117/1.2061567
27. Rasouli SJ, Stainier DYR. Regulation of cardiomyocyte behavior in zebrafish trabeculation by Neuregulin 2a signaling. *Nat Commun.* (2017) 8:15281. doi: 10.1038/ncomms15281
28. Lombardo VA, Heise M, Moghtadaei M, Bornhorst D, Manner J, Abdelilah-Seyfried S. Morphogenetic control of zebrafish cardiac looping by Bmp signaling. *Development.* (2019) 146:dev180091. doi: 10.1242/dev.180091
29. Hu N, Sedmera D, Yost HJ, Clark EB. Structure and function of the developing zebrafish heart. *Anat Rec.* (2000) 260:148–57. doi: 10.1002/1097-0185(20001001)260:2<148::AID-AR50>3.0.CO;2-X
30. Teranikar T, Messerschmidt V, Lim J, Bailey Z, Chiao JC, Cao H, et al. Correcting anisotropic intensity in light sheet images using dehazing and image morphology. *APL Bioeng.* (2020) 4:036103. doi: 10.1063/1.5144613

Conflict of Interest: The authors declare that the research was conducted in the absence of any commercial or financial relationships that could be construed as a potential conflict of interest.

frontiers
in Cardiovascular Medicine

REVIEW
published: 14 July 2021
doi: 10.3389/fcvm.2021.709871

Engineering the Cellular Microenvironment of Post-infarct Myocardium on a Chip

Natalie N. Khalil[1] **and Megan L. McCain**[1,2]*

[1] Laboratory for Living Systems Engineering, Department of Biomedical Engineering, USC Viterbi School of Engineering, University of Southern California, Los Angeles, CA, United States, [2] Department of Stem Cell Biology and Regenerative Medicine, Keck School of Medicine of USC, University of Southern California, Los Angeles, CA, United States

Myocardial infarctions are one of the most common forms of cardiac injury and death worldwide. Infarctions cause immediate necrosis in a localized region of the myocardium, which is followed by a repair process with inflammatory, proliferative, and maturation phases. This repair process culminates in the formation of scar tissue, which often leads to heart failure in the months or years after the initial injury. In each reparative phase, the infarct microenvironment is characterized by distinct biochemical, physical, and mechanical features, such as inflammatory cytokine production, localized hypoxia, and tissue stiffening, which likely each contribute to physiological and pathological tissue remodeling by mechanisms that are incompletely understood. Traditionally, simplified two-dimensional cell culture systems or animal models have been implemented to elucidate basic pathophysiological mechanisms or predict drug responses following myocardial infarction. However, these conventional approaches offer limited spatiotemporal control over relevant features of the post-infarct cellular microenvironment. To address these gaps, Organ on a Chip models of post-infarct myocardium have recently emerged as new paradigms for dissecting the highly complex, heterogeneous, and dynamic post-infarct microenvironment. In this review, we describe recent Organ on a Chip models of post-infarct myocardium, including their limitations and future opportunities in disease modeling and drug screening.

Keywords: tissue engineering, myocardial infarction, organ on a chip, hypoxia, stiffness, strain, cardiac myocytes, cardiac fibroblasts

OPEN ACCESS

Edited by:
David Wu,
University of Chicago, United States

Reviewed by:
Walter Emerson Cromer,
Texas A&M Health Science Center,
United States
Giuseppe Militello,
Mirimus Inc., United States

****Correspondence:***
Megan L. McCain
mlmccain@usc.edu

Specialty section:
This article was submitted to
Atherosclerosis and Vascular
Medicine,
a section of the journal
Frontiers in Cardiovascular Medicine

Received: *14 May 2021*
Accepted: *14 June 2021*
Published: *14 July 2021*

Citation:
Khalil NN and McCain ML (2021)
Engineering the Cellular
Microenvironment of Post-infarct
Myocardium on a Chip.
Front. Cardiovasc. Med. 8:709871.
doi: 10.3389/fcvm.2021.709871

INTRODUCTION

Cardiovascular disease is the leading cause of death worldwide, responsible for over 17.9 million deaths annually (1). One of the most common causes of cardiovascular disease is coronary artery disease, in which plaque buildup in the coronary arteries deprives downstream myocardium of vital, oxygenated blood. Complete occlusion of the coronary arteries can ultimately lead to myocardial infarction, commonly referred to as a heart attack. Myocardial infarction is among the top five most expensive conditions treated by US hospitals annually and is a common cause of heart failure (2–4).

When a patient presents with a myocardial infarction, percutaneous coronary intervention is often performed, which is a catheterization procedure to restore flow to the interrupted artery and minimize the initial insult (5, 6). Rapid identification of myocardial infarction is essential for timely reperfusion of the occluded coronary artery, which can, in some cases, lead to reperfusion injury that further increases the size of the initial insult (7). After revascularization procedures, treatment is predominantly focused on pharmaceutical interventions to reduce adverse cardiovascular events, including stroke, recurrent infarctions, and death (8). Common treatments include renin-angiotensin-aldosterone system (RAAS) inhibitors, such as angiotensin-converting enzyme inhibitors, which decrease the load on the heart by lowering blood pressure (9) and may also reduce fibrotic remodeling (10). Another therapeutic target is beta adrenergic receptors, which are activated by epinephrine or norepinephrine to stimulate heart rate, strength of contraction, and cardiac output. Similar to RAAS inhibitors, beta blockers, such as bisoprolol, carvedilol, and metoprolol, can reduce blood pressure following myocardial infarction (8, 10). Thus, existing pharmacological interventions are primarily focused on reducing the load on the damaged heart instead of attempting to repair the initial injury or mitigate the ensuing fibrotic remodeling process.

One challenge facing the development of new therapies for post-infarct myocardium is that conventional preclinical models are limited primarily to non-human animal models or static, uniform monolayers of cultured cells that poorly replicate the clinical setting, especially the complex, dynamic remodeling that occurs post-infarction (3). Thus, developing the next generation of treatments for myocardial infarction can be accelerated by new preclinical model systems that more closely replicate native pathophysiology across multiple spatial scales, including the post-infarct cellular microenvironment.

Organs on Chips are engineered *in vitro* systems that mimic the fundamental structural and functional units of native tissues and have been shown to mimic responses to drugs at clinical doses in various tissue models with higher fidelity than conventional *in vitro* methods (11). Organs on Chips can also provide enhanced spatiotemporal control over multiple distinct features of the cellular microenvironment, which is especially relevant to modeling post-infarct myocardium. Thus, Organ on Chip approaches have vast potential to provide new mechanistic insights into post-infarct remodeling and to inform future pharmacological interventions.

In this review, we will first describe the cellular and molecular remodeling that occurs after myocardial infarction in humans, which will provide a framework for the microenvironmental features that are important to model on a chip. Next, we will describe existing strategies for engineering aspects of the cellular microenvironment of post-infarct myocardium on a chip, which have until now focused on hypoxia, fibrosis, and strain in both 2-dimensional (2-D) and 3-dimensional (3-D) tissue constructs. Lastly, we will describe considerations for future work to promote clinical mimicry and translation of Organ on a Chip models of myocardial infarction.

VENTRICULAR REMODELING POST-MYOCARDIAL INFARCTION

The initial coronary occlusion of a myocardial infarction deprives downstream myocardium of vital oxygen and nutrients, causing cardiac myocyte necrosis within hours (10, 12, 13). Due to tissue necrosis, the infarct zone is vulnerable to deformation and thinning, which can lead to infarct expansion (14, 15). Cardiac myocytes in the surviving infarct border zone myocardium also begin to rapidly remodel. For example, the normal distribution of intercalated disc protein complexes (gap junctions, desmosomes, and adherens junctions) is lost as early as 6 h post-infarction. Because intercalated disks are necessary for the heart to function as an electromechanical syncytium, changes in their expression and localization are thought to contribute to arrhythmogenesis after infarction (16).

As a result of infarct expansion, diastolic and systolic wall stresses increase (17, 18). To normalize the increased load, the myocardium undergoes cardiac hypertrophy in the weeks and months after an infarction by increasing muscle mass and wall thickness (19). These changes are reflected in the morphology of individual cardiac myocytes, which can increase in both length and diameter. Due to the spatial arrangement of cardiac myocytes in the ventricles, increased diameter and lengthening of individual cells ultimately results in changes in chamber geometry (6, 20, 21), which contributes to ventricular enlargement. Increasing chamber volume through ventricular enlargement may be compensatory in order to maintain stroke volume after the initial loss of contractility (14, 22) but is ultimately associated with increased likelihood of mortality (14, 23).

Tissue necrosis and infarct expansion can also increase the likelihood of myocardial rupture (14, 15). Because mammalian cardiac myocytes have limited regenerative capacity, maintaining tissue integrity is dependent on the formation of a scar. Scar formation occurs through three overlapping phases: the inflammatory phase, proliferative phase, and maturation phase (**Figure 1**). The inflammatory phase occurs in the first few days following a myocardial infarction and is initiated when necrotic cardiac myocytes release their intracellular contents, which activate pro-inflammatory signaling pathways in innate immune cells (24). Next, inflammatory chemokine and cytokine gradients [comprised of tumor necrosis factor-α (TNF-α), interleukin (IL)-1β, and IL-6] promote leukocyte migration into the infarct zone to clear dead cell debris and damaged extracellular matrix. After 1 week, tissue inhibitors of metalloproteinases are upregulated to conclude this degradative phase (24). Ultimately, as neutrophils undergo apoptosis, macrophages are directed toward a resolving phenotype and begin secreting anti-inflammatory signals [such as transforming growth factor-β (TGF-β) and IL-10] that repress the inflammatory response and drive cardiac fibroblast activation in the subsequent proliferative phase (10).

The proliferative phase occurs over the next few weeks and is characterized by cardiac fibroblast proliferation, migration into the site of injury, and differentiation into an activated myofibroblast phenotype. Cardiac fibroblasts are the most abundant non-myocyte cell population in the mammalian myocardium (24) and, after expansion in the proliferative phase in combination with cardiac myocyte necrosis, they become the most abundant cell type in the infarcted region (10). Myofibroblasts play an important role in depositing collagen, fibronectin, and other matrix proteins to maintain tissue integrity and prevent myocardial rupture. They also express α-smooth muscle actin (α-SMA) and non-muscle myosin, which provide

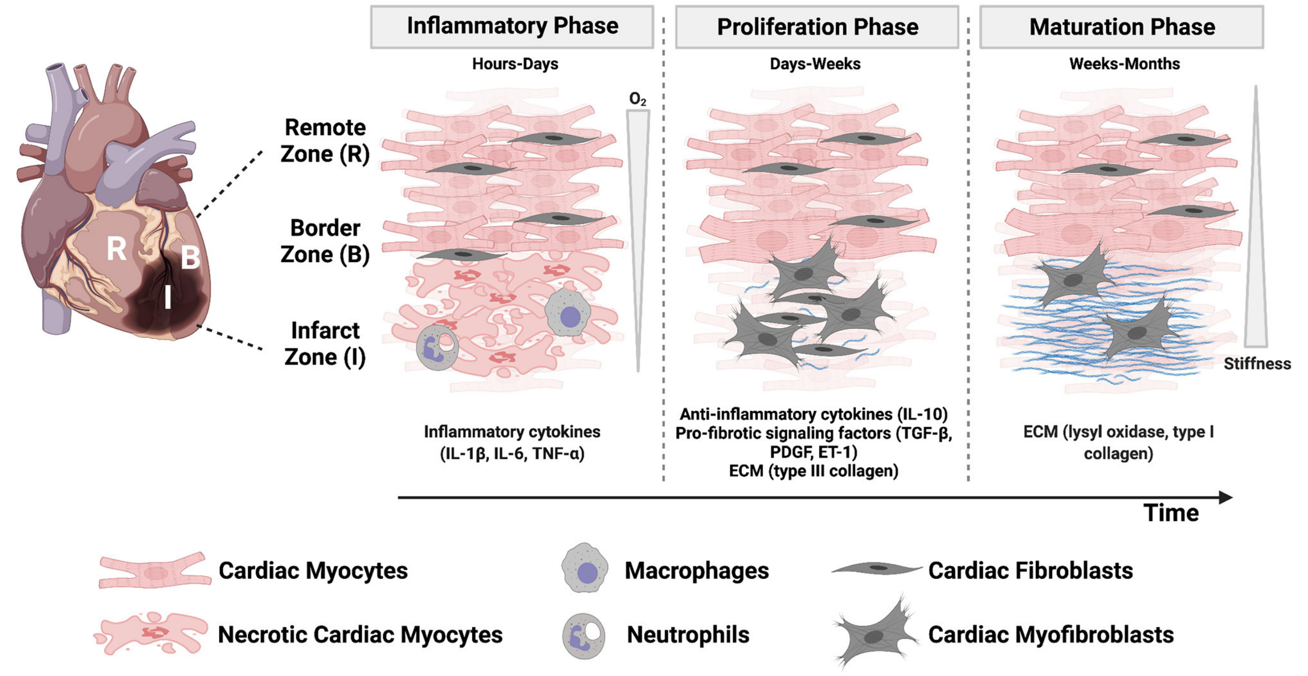

FIGURE 1 | The post-infarct microenvironment is characterized by dynamic physical, mechanical, and biochemical cues that orchestrate the three phases of healing. Regional and temporal changes of oxygen concentration, stiffness, inflammatory cytokines, cell, and matrix composition characterize the myocardium as injured tissue is replaced with a scar. Created with BioRender.com.

them with the ability to generate force to migrate and facilitate wound contracture (10).

The final phase is scar maturation, which occurs on a timescale of weeks to months. In this phase, myofibroblasts initiate collagen turnover and begin secreting type I collagen, which has the tensile strength of steel (12), in place of type III collagen. The depletion of growth factors necessary for myofibroblast survival ultimately leads to myofibroblast apoptosis (10, 25). Further enzymatic cross-linking of collagen occurs through lysyl oxidase, which progressively increases the tensile strength of the myocardium for months after myocardial infarction (10). While myofibroblasts play a vital role in maintaining structural integrity after the initial loss of tissue, they may also be driven by many cellular and molecular events toward a pathological fibrotic response. Myofibroblast persistence in the myocardium can occur for months, or even years, after injury and is a common feature of heart failure (12). Fibrotic tissue, which was historically considered an inert tissue, is now known to secrete factors (such as angiotensin II and TGF-β) that can traverse the interstitial space and promote fibrosis in non-infarcted regions (12, 26).

In summary, post-infarct myocardium is characterized by multiple biochemical and biomechanical properties changing in both space and time, which are correlated to complex remodeling of several cell types and the extracellular matrix in parallel (**Figure 1**). Some or all of these remodeling processes ultimately impact cardiac function and patient outcomes. However, the relationships between these biochemical, biomechanical, cellular, and molecular factors are incompletely understood, hindering the discovery of new therapies to mitigate the effects of the initial injury. Thus, there is a great need for controlled experimental models of post-infarct myocardium that account for remodeling of the cellular microenvironment to uncover mechanisms of pathophysiology.

IN VITRO MODELS OF MYOCARDIAL ISCHEMIA AND HYPOXIA

Due to the high metabolic activity of cardiac myocytes, the myocardium is a highly vascularized tissue, with capillaries separated by approximately 20 µm (27). This translates to about one blood vessel between every two cardiac myocytes (28). As a result, hypoxia is one of the most injurious effects of a myocardial infarction. Conventionally, hypoxia has been induced by culturing cells in environments with uniformly low oxygen. However, phosphorescent oxygen probes have demonstrated that a spatial gradient ranging from 0 to 10% oxygen bridges injured tissue with neighboring viable tissue in post-infarct myocardium (29, 30). In addition, oxygen concentrations change over time as the infarct zone is re-oxygenated during reperfusion. Thus, *in vitro* systems that can modulate oxygen concentrations in space or time have more recently been developed to mimic the hypoxic landscape of post-infarct myocardium. In this section, we will describe conventional hypoxia models that replicate uniform hypoxia as well as engineered systems that offer spatial or temporal control over oxygen tension.

Conventional Hypoxia Models

To recapitulate myocardial hypoxia *in vitro* (3), one of the most common approaches is to place cardiac cells in incubators or hypoxia chambers and replace oxygen with nitrogen. This enables the stable, long-term induction of hypoxia, with tunable control over global oxygen levels by selecting a gas composition of choice. To enable cell handling, hypoxia workstations have also been developed that contain gloveboxes to allow for the manipulation of cells in a hypoxic enclosure. However, these approaches for physical induction of hypoxia require access to specialized equipment, such as incubators with oxygen regulation, and are limited to uniform gas concentrations.

Hypoxia can also be simulated in cells cultured in ambient oxygen by adding hypoxia mimetic agents, such as cobalt chloride, to cell media. Hypoxia mimetic agents often work by stabilizing hypoxia inducible factors (HIF), a family of transcription factors that facilitates the cellular response to hypoxia by upregulating genes associated with survival in low oxygen. In normoxia, HIF is constantly degraded through hydroxylation of the HIF-α subunit by the enzyme prolyl hydroxylase, which marks it for ubiquitination by Von Hippel Lindau protein and subsequent degradation. Cobalt chloride chemically stabilizes HIF in normoxia by replacing Fe^{2+} with Co^{2+} in the prolyl hydroxylase active site, thereby inhibiting its hydroxylation of HIF-α and the ensuing degradation pathway. Other successful hypoxia mimetics include dimethyloxalylglycine and deferoxamine, which similarly work by inhibiting prolyl hydroxylase activity (31). Hypoxia mimetics enable easy access to cells during cell culture, are inexpensive, and can quickly simulate hypoxic conditions *in vitro*. However, they can have adverse effects on other signaling pathways that are not affected by low oxygen (31, 32), may be cytotoxic (33), and likely do not capture all the effects of true hypoxia.

Conventional *in vitro* models have shown that hypoxia results in structural and functional changes that may contribute to the development of arrhythmias. Specifically, the gap junction protein connexin 43 (Cx43) is known to be affected, which plays a critical role in conducting electrical impulses in the myocardium. Hypoxia has been shown to drive electrical uncoupling *in vitro*, with effects including decreased Cx43 signal at gap junctions (34, 35), increased Cx43 internalization (35) and dephosphorylation (36), and decreased conduction velocity (34). Hypoxia is also associated with inactivation of sodium potassium pumps (Na,K ATPase), which regulate cardiac action potentials (37, 38). Hypoxic cardiac myocytes also upregulate fetal, T type calcium channels, which are absent in healthy, adult myocardium, in a mechanism dependent on HIF-1*α* (39). Finally, hypoxia has also been shown to promote apoptosis in cardiac myocytes (40–43). These remodeling processes are possibly related to the increased incidence of arrhythmias observed in post-infarct myocardium.

Studies have also shown that cardiac fibroblasts and other non-myocyte cell populations are generally more resistant to hypoxia (40–42). In response to hypoxic stimuli *in vitro*, cardiac fibroblasts undergo differentiation into the activated, myofibroblast phenotype, which is signified by increased α-SMA expression (44–46), collagen type I expression (44–47), and migration capacity (46). However, there have been differing reports of cardiac fibroblast proliferation in response to hypoxia (44–46), which may result from differences in basal levels of fibroblast differentiation, or from differences in cell source, oxygen concentration, and hypoxia duration. In response to prolonged hypoxia exposure *in vitro,* cardiac fibroblasts ultimately undergo apoptosis (48–50).

Hypoxia also changes the secretion of paracrine factors that are involved in many processes of infarct healing, such as angiogenesis, fibroblast differentiation, and remodeling of the extracellular matrix. Hypoxic cardiac myocytes upregulate vascular endothelial growth factor (VEGF) (51, 52), insulin-like growth factor 2 (52), inflammatory cytokines (TNF-α, IL-1β, IL-6), and TGF-β (53). As TGF-β is known to promote fibroblast differentiation into myofibroblasts, medium conditioned by hypoxic myocytes has been reported to drive cardiac fibroblast migration (54) and facilitate faster wound closure in cultured skin fibroblasts (53). Similar to cardiac myocytes, hypoxic cardiac fibroblasts upregulate TGF-β1 and also its receptor, TGFβ-R1, which can play a role in autocrine signaling pathways to promote fibroblast differentiation (46, 48). Hypoxic fibroblasts also exhibit increased secretion of inflammatory cytokines [TNF-α (55–57) and IL-6 (57)], matrix metalloproteinases [MMP-2 and MMP-9 (56)] and VEGF (56), and conditioned medium from hypoxic fibroblasts has been shown to reduce cardiac myocyte viability (55, 58). Thus, hypoxia likely alters cellular cross-talk between distinct cardiac cell types in post-infarct myocardium.

Engineered Models With Spatial Oxygen Gradients

Although conventional hypoxia systems have revealed valuable insights into oxygen-dependent remodeling of cardiac cell types, they do not replicate the spatial or temporal changes in oxygen that are characteristic of post-infarct myocardium. To mimic spatial oxygen gradients, more complex *in vitro* systems have been engineered. In one example, a microfluidic device was fabricated with a central channel designated for cell culture embedded between two lateral media channels. By flowing media containing a chemical hypoxia mimetic through one channel and standard media through the other, a chemical hypoxia gradient was established in the central cell-containing channel. Cardiac myoblasts near the hypoxic end of the gradient exhibited altered morphology, including reduced cell area and actin disintegration, which was accompanied by mitochondrial dysfunction and decreased cell viability (59). In addition to chemical methods (60–63), microfluidic devices have also been developed to generate physical oxygen gradients by culturing cells on a gas-permeable membrane above microchannels for gas flow (64–66). However, these methods have not been extensively applied to cardiac cell types.

Ischemic gradients have also been developed by stacking thin layers of hydrogels that are mechanically supported by a paper scaffold, a technique termed "cells-in-gels-in-paper." To control oxygen and nutrient diffusion into the stack, one end of the construct was placed in a base that is impermeable to gases and liquids. Nutrients become depleted as they diffuse into the stack, which creates an ischemic environment in the lower layers. Cardiac myocytes in the ischemic, lower layers exhibited reduced viability and circular morphology when compared with upper layers. Cell-tracking demonstrated that cardiac fibroblasts embedded in upper layers migrate toward ischemic cardiac myocytes. Fibroblast migration increased when myocytes were exposed to higher levels of ischemia (generated through taller stacks) and was reduced in the absence of cardiac myocytes or with the pharmacological inhibition of TGF-β (27). Other methods have been developed that similarly modify hydrogels to generate oxygen gradients (67) by using oxygen-consuming enzymes during hydrogel cross-linking (68, 69), embedding a hydrogel between gas flow channels (70), or linearly increasing cell density and thus oxygen consumption rates (71), but these methods have not yet been implemented to model post-infarct myocardium.

Lastly, cardiac spheroids have also been implemented to mimic hypoxia gradients. Cardiac spheroids are 3-D aggregates of cardiac cells that recapitulate select aspects of native tissue structure and function (72–76). Because the diffusion limit of oxygen in tissues is around 100–200 microns (77), cardiac spheroids intrinsically generate oxygen gradients, for which oxygen tension is highest at the surface and decreases toward the necrotic core. Though this is conventionally thought of as a limitation of spheroids, recent work has harnessed this property to develop "infarct spheroids" that are exposed to ambient 10% oxygen to generate spatial hypoxia gradients (0–10% oxygen) that mimic the infarct, border, and remote zones after infarction (**Figure 2A**). These infarct spheroids contained cardiac myocytes, endothelial cells, and stromal cells and were treated with noradrenaline to mimic neurohormonal stimulation after infarction. Infarct spheroids demonstrated similar global gene-expression profiles to human ischemic cardiomyopathy and animal myocardial infarction samples. Furthermore, when compared with control spheroids in ambient oxygen, infarct spheroids exhibited a metabolic shift toward glycolysis, increased stiffness, increased expression of myofibroblast markers, decreased cardiac myocyte contraction amplitude (**Figure 2A**), and asynchronization of contractions (78).

Engineered Models of Ischemia-Reperfusion

In vitro models have also been engineered to replicate dynamic changes in oxygen characteristic of ischemia-reperfusion. Microfluidic devices are particularly suitable for this application because they contain chambers of small volumes that can be rapidly filled with hypoxic gas or cell medium. For example, a microfluidic device with integrated bioelectronics was used to measure intracellular action potential and extracellular beat rate and propagation velocity in cardiac myocytes cultured in a microchannel. The microchannel was rapidly filled with hypoxic cell medium followed by recovery medium to mimic ischemia-reperfusion. Hypoxic cardiac myocytes demonstrated substantially reduced depolarization times and beat rates, as well as irregular propagation patterns, which recovered within 30 min after reintroducing normoxic cell media (80). A similar microfluidic device was fabricated to contain small chamber volumes that can be quickly filled with hypoxic gas. Gas from the upper chamber diffused across a thin, gas-permeable membrane to reach cells cultured in lower microfluidic channels. This device demonstrated that hypoxic conditions below 5% oxygen induce changes in cardiac myocyte calcium transients, including a decrease in amplitude that could be mimicked using L-type calcium channel antagonists. After a subsequent 10 min of reperfusion with normoxic gas, cardiac myocytes recovered with normal calcium transients (81). Together, these studies suggest that hypoxia induces reversible alterations in cardiac myocyte electrophysiology.

In another model of ischemia-reperfusion, cardiac myocytes were cultured as an aligned tissue on silicone cantilever substrates with embedded strain sensors (**Figure 2B**). The cardiac myocytes were aligned using microcontact printing, which involves the preparation of silicone "stamps" that are used to transfer extracellular matrix proteins to a substrate in desired geometries. With a spatial resolution of approximately 1 μm, microcontact printing can direct tissue orientation (82–84), single-cell shape (85), and even subcellular structures (86). When the aligned cardiac tissues contracted on the cantilever substrates, the cantilevers deflected, leading to a resistance change in the embedded strain sensors proportional to the contractile stress (87, 88). This system was used to provide real-time measurements of contractile stress in a simulated ischemia-reperfusion injury by switching cells from ischemic media at 1% oxygen to standard media at ambient 21% oxygen. Integrated sensor readouts demonstrated that cardiac tissues stopped contracting during ischemia and displayed a minor recovery of twitch stress during reperfusion. In contrast, pre-treatment with endothelial cell-derived extracellular vesicles was cardioprotective and enabled cardiac tissues to continue contracting during simulated ischemia and exhibit higher recovery of twitch stress after reperfusion (**Figure 2B**) (79).

In summary, several technologies, including microfluidic devices, hydrogels, spheroids, and strain sensors, have been implemented to mimic the spatial and temporal oxygen gradients characteristic of post-infarct myocardium and subsequently quantify changes in cardiac cell phenotypes. Unlike conventional systems, these approaches can be used to explore oxygen-dependent regional and temporal changes in cellular phenotypes at high resolution and uncover cross-talk between cells in distinct oxygen environments to identify new mechanisms of infarct remodeling.

IN VITRO MODELS OF MYOCARDIAL FIBROSIS AND STIFFNESS

Healthy myocardium is a moderately stiff tissue, with an elastic modulus of around 10 kPa. After myocardial infarction, local elastic modulus in the infarcted region increases to 20–100 kPa due to scar formation and fibrosis (89–92). Rat models with coronary artery ligation demonstrate myocardial stiffening over

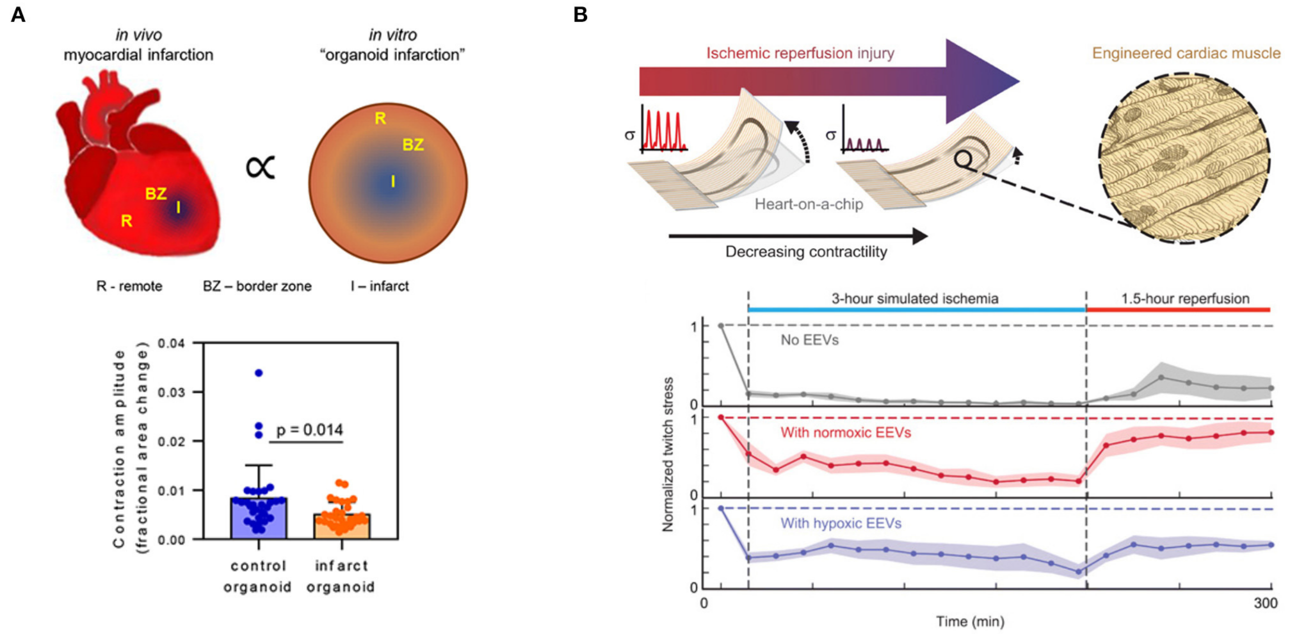

FIGURE 2 | Engineered *in vitro* hypoxia models that modulate oxygen in **(A)** space and **(B)** time. **(A)** Infarct spheroids generate intrinsic spatial oxygen gradients to model the infarct, border, and remote zones after myocardial infarction. Infarct spheroids exhibit higher levels of myofibroblast marker expression, exhibit asynchronous contraction of myocytes, and have lower contraction amplitudes than control spheroids. Reprinted by permission from Springer Nature: Nat. Biomed. Eng. (78). **(B)** Muscular thin films with integrated strain gauges can measure changes in contractility in cardiac myocytes pre-treated with endothelial extracellular vesicles in a simulated ischemia-reperfusion injury. Endothelial extracellular vesicles enhanced the contractility of engineered cardiac tissues during both ischemia and reperfusion. From Yadid et al. (79). Reprinted with permission from AAAS.

time, with elastic modulus increasing from 18 to 55 kPa (90), and increased stiffness has been observed in the infarct zone as early as 1 day post-infarction (93). In addition to temporal changes, regional stiffness varies between the infarct zone, border zone, and remote zone by 3 days post-infarction (94). Elastic modulus progressively decreases in the border zone at a rate of 8.5 kPa/mm toward remote tissue (90). Because investigating the effects of tissue stiffness with *in vivo* models is confounded by many other concurrent changes, including matrix composition (93), *in vitro* models have been implemented to elucidate the effects of stiffness and other aspects of fibrosis on cardiac cell phenotypes. In this section, we will describe 2-D and 3-D *in vitro* models of cardiac fibrosis that focus primarily on recapitulating uniform or spatiotemporal changes in stiffness.

2-D Models With Uniform Stiffness

Because standard polystyrene dishes used for cell culture are nearly five orders of magnitude more stiff than the native myocardium (95), mechanically tunable biomaterials have been developed to mimic the rigidity of healthy or fibrotic myocardium (96). For example, hydrogels are cross-linked, hydrophilic polymers with high water content that are commonly used as cell culture substrates because they can be tuned to resemble the elasticity of soft tissue and allow for efficient mass transfer. Hydrogels can incorporate natural polymer chains, such as mammalian matrix proteins, or synthetic polymer chains, such as polyacrylamide or polyethylene glycol (97, 98). Other biomaterials commonly used to recapitulate physiological or pathological stiffness *in vitro* include elastomers like polydimethylsiloxane (PDMS), which is biocompatible, mechanically tunable, and transparent (99–102).

When cultured on rigid hydrogel or elastomer substrates, cardiac myocytes exhibit disorganized sarcomeres, reduced sarcoplasmic calcium stores (103), lower amplitude calcium currents (103, 104), decreased cell shortening during contraction (103), and a progressive decrease in beat frequency over time (105) when compared to substrates that mimic the elasticity of healthy myocardium. Using traction force microscopy, in which fluorescent beads embedded in substrates are displaced during cell contraction, several studies have established non-monotonic relationships between force generation and substrate rigidity. In these studies, cardiac myocytes generally generate maximum forces on physiological stiffness, which decrease on substrates that are either more soft or stiff in both isotropic (103, 106) and aligned microtissues (107). However, some studies have reported linearly increasing force generation with increased substrate stiffness (101, 108, 109), which may be attributed to differences in experimental methods, such as cell source, biomaterial substrate, or analysis techniques. Similar results are observed in cocultures of cardiac myocytes and fibroblasts on polyacrylamide substrates, in which increased stiffness results in reduced troponin I staining, increased fibroblast density, and poor electrical excitability (106).

Micropatterning has also been used in combination with tunable hydrogel or elastomer substrates to modulate both cellular architecture and substrate stiffness because both of these features remodel concurrently in post-infarct myocardium. Substrate stiffness and cellular architecture has been shown to modulate metabolic activity (99, 100, 107) and mitochondrial structure in cardiac myocytes (102). Microcontact printed hydrogels have also been used to characterize the contractility of single (85) or coupled (110) cardiac myocytes as a function of both cellular architecture and substrate stiffness. At the single cell level, cardiac myocytes with low cell aspect ratios that mimic concentric hypertrophy do more work on stiff substrates that resemble fibrotic myocardium, demonstrating a functional advantage of cell shape remodeling in response to mechanical overload (85). In coupled myocytes, stiff substrates caused increased focal adhesion formation at the cell-cell interface, possibly contributing to cellular uncoupling in post-infarct myocardium (110).

To model both the cellular and biomechanical aspects of fibrosis, tissues have also been engineered with cardiac myocytes and fibroblasts on substrates with tunable stiffness. For example, microcontact printing has been implemented to engineer aligned microtissues on polyacrylamide hydrogels with both cardiac myocytes and fibroblasts. Microtissues generated less work on rigid substrates, irrespective of cell adhesion ligand or presence of fibroblasts, revealing the dominant role of substrate elasticity in regulating contractile output (111). To engineer an artificial infarct boundary, cardiac myocytes and fibroblasts have been cocultured on separate halves of cell culture substrates with rigidities that range from healthy, 1-week post-infarct, and 2- to 6-weeks post-infarct myocardium. The presence of cardiac fibroblasts in this coculture setting attenuated mechanical signal propagation across the infarct boundary in a stiffness-dependent manner (112).

In addition to affecting cardiac myocytes, rigid substrates that mimic fibrotic myocardium also promote fibroblast activation to myofibroblasts. On stiff substrates, cardiac fibroblasts notably activate into a myofibroblast phenotype, exhibiting increased α-SMA coverage (113–116), increased contractile force generation measured through traction force microscopy (117), and increased nuclear localization of the mechanosensitive transcription factors yes-associated protein (YAP) and transcriptional co-activator with PDZ-binding motif (TAZ) (114). Knockdown of YAP and TAZ reversed or attenuated stiffness-dependent changes in cell morphology and function, suggesting YAP and TAZ coordinate fibroblast mechanoactivation (114). In other work, limiting focal adhesion size through microcontact printing was also sufficient to interrupt the recruitment of α-SMA to stress fibers on stiff substrates, indicating that focal adhesion size may control α-SMA localization (113). Studies that establish mechanisms behind fibroblast mechanoactivation may reveal new targets for anti-fibrotic strategies to mitigate adverse remodeling following myocardial infarction.

In vitro models have also identified stiffness-dependent secretion of paracrine factors, which may regulate several processes involved in infarct remodeling. For example, cardiac myocytes on stiff substrates secrete more VEGF. Consistent with this finding, media conditioned by myocytes on stiff substrates promotes angiogenesis, including increased migration capacity and tube length of microvascular endothelial cells (118). Fibroblasts cultured on stiff hydrogels and treated with TGF-β have also been shown to upregulate several cytokines, including osteopontin, a known regulator of collagen cross-linking via lysyl oxidase, and insulin-like growth factor 1, which regulates cardiac myocyte hypertrophy. As a result, conditioned media from TGF-β-treated fibroblasts cultured on stiff hydrogels has been shown to induce cardiac myocyte hypertrophy, indicated by increased cell volume, when compared with medium from cardiac fibroblasts without TGF-β, regardless of substrate stiffness (119). This echoes previous work that demonstrates TGF-β may be a more potent regulator of the myofibroblast phenotype than substrate rigidity (116). Together, 2-D models that resemble the elasticity of fibrotic myocardium recapitulate many cellular and molecular events following myocardial infarction.

2-D Models With Spatiotemporal Control of Stiffness

2-D models with uniform stiffness do not encompass regional changes in stiffness between the infarct, border, or remote zones following myocardial infarction. Spatial stiffness gradients have been fabricated through graded material cross-linking (120), including gradient-patterned (121–124) or sliding (125, 126) photomasks, layering of hydrogels of different elasticities (127), applying a temperature gradient to PDMS during curing (128), or microfluidic-mixing of prepolymer solutions with different cross-linker concentrations (129). However, most of these have not been implemented with cardiac cell types to model post-infarct myocardium. In one example, a polyethylene glycol hydrogel was patterned with soft and stiff concentric circles using a photomask. Cardiac fibroblasts cultured on stiff regions of the substrate expressed increased α-SMA and collagen when compared with soft regions. Live imaging demonstrated a directional cellular migration toward the inner stiff region. Treatment with a ROCK inhibitor reduced the population of myofibroblasts, demonstrating that the model can be used as an antifibrotic drug screening platform (130). To investigate the effects of pathological matrix stiffening in lung fibroblasts, a stiffness gradient was made from polyacrylamide gels polymerized through gradient photomasks. Human lung fibroblasts cultured on the stiffness gradient show a progressive increase in fibroblast activation, indicated by increased proliferation and matrix synthesis, toward the stiff end of the gradient. Addition of prostaglandin E2, an inhibitor of fibrogenesis, inhibited fibroblast activation (131). Similar phenotypes may also be observed in cardiac fibroblasts over stiffness gradients, though this has not yet been tested.

Mechanical properties can also be controlled *in situ* to model changes in stiffness over time, which is characteristic of infarct scar maturation. This can be achieved with materials that polymerize in response to light exposure (132, 133) or by varying the molecular weight of the cross-linking agent in real-time (134). Engineered models to capture dynamic stiffening have been used to model development, wound healing, and disease (135), but few have been implemented in the context of myocardial infarction. In one study, hyaluronic acid hydrogels seeded with

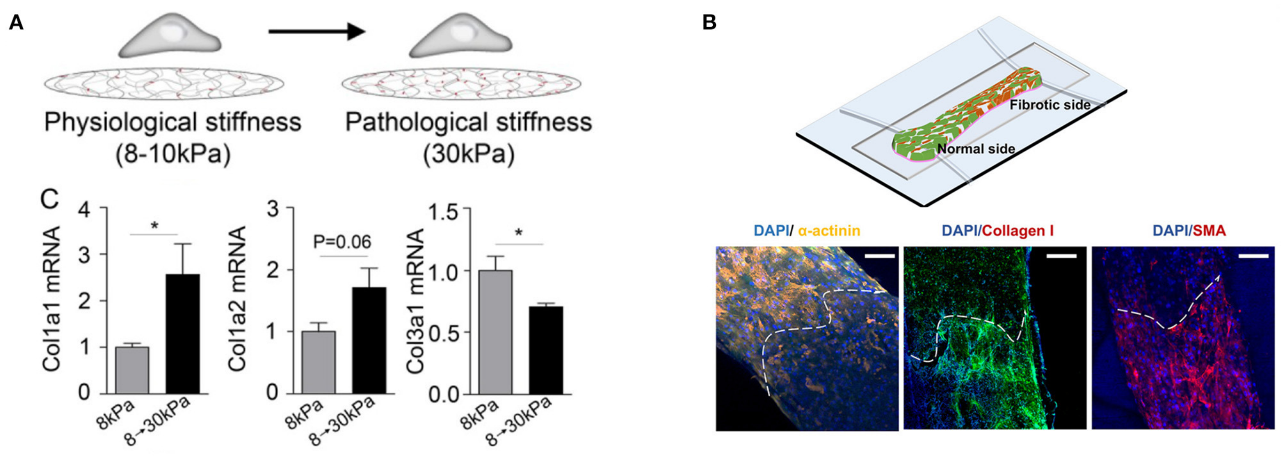

FIGURE 3 | Engineered *in vitro* fibrosis models that modulate stiffness in **(A)** time and **(B)** space. **(A)** A hyaluronic acid hydrogel is polymerized *in situ* upon exposure to UV light to mimic scar maturation after myocardial infarction. Stiffening from 8 to 30 kPa results in collagen turnover ($*p < 0.05$). Republished with permission of the American Society for Cell Biology, from Herum et al. (115); permission conveyed through Copyright Clearance Center, Inc. **(B)** A heteropolar biowire integrates normal (7.6 kPa) and fibrotic (61.1 kPa) cardiac tissue. The white dashed line indicates the interface between normal and fibrotic regions. Normal regions exhibit increased α-actinin, a component of sarcomeres in cardiac myocytes, while fibrotic regions have increased collagen and α-smooth muscle actin, indicating increased presence of myofibroblasts. Images reproduced with permission of the American Chemical Society, from https://pubs.acs.org/doi/full/10.1021/acscentsci.9b00052 (136). Further permissions related to the material excerpted should be directed to the American Chemical Society.

cardiac fibroblasts were modified to dynamically increase in stiffness in response to UV exposure. Dynamic stiffening to model scar maturation resulted in increased cell spreading, α-SMA formation, and collagen I expression (**Figure 3A**) (115). Although fibroblast activation correlates with increased stiffness in 2-D spatiotemporal models, cardiac myocyte phenotype and function has been relatively unexplored in these settings.

3-D Models With Uniform Stiffness

Modulating stiffness in 2-D only exposes one side of cells to the fibrotic microenvironments experienced *in vivo*. To more closely mimic cell-cell and cell-matrix interactions that occur in native myocardium, cardiac cells have been mixed into hydrogels to form 3-D tissues. Similar to findings in 2-D, cardiac myocytes encapsulated in rigid polyethylene glycol hydrogels demonstrate reduced cell shortening and increased relaxation time when compared with soft hydrogels, which was also accompanied by increased intracellular localization of the mechanosensitive transcription factor YAP (133). In 3-D, matrix stiffness promotes fibroblast differentiation into myofibroblasts, demonstrated by increased stellate morphology, α-SMA and collagen type III levels, and gel compaction (137), consistent with findings in 2-D. The simple aggregation of cardiac fibroblasts in 3-D using low-attachment plates has also been shown to induce gene expression changes associated with adverse cardiac remodeling and the extracellular matrix. Conditioned media from 3-D fibroblast aggregates also causes cardiac myocyte hypertrophy relative to media from fibroblasts cultured in 2-D (138), indicating that phenotypes in 2-D do not always translate to 3-D.

Using microfabricated templates, 3-D cardiac tissues have also been engineered with control over cell composition, matrix stiffness, and tissue architecture. In one model, cardiac myocytes and fibroblasts were embedded in collagen hydrogels of varying fibroblast cell densities or collagen concentrations and suspended between uniaxial PDMS microposts. Microposts serve as tissue constraints that promote alignment. Increasing fibroblast density decreased tissue contraction force and hampered beating frequency, as measured by displacement of the microposts (139). In a similar paper, the system was modified to contain biaxial PDMS microposts to generate isotropic cardiac matrices, designed to mimic "diseased" architecture. 3-D microtissues of cardiac myocytes and fibroblasts in isotropic matrices display more stellate morphology, characteristic of myofibroblasts, and more heterogeneous force distribution when compared with "healthy" aligned matrices. Furthermore, increasing the proportion of fibroblasts in the tissues reduces the overall tissue beating frequency, suggesting that both matrix organization and cellular composition regulate cardiac function (140).

Although hydrogels are mechanically tunable, they fail to recapitulate the fibrous architecture of native cardiac extracellular matrix. A 3-D fibrous network functionalized with fibronectin, which anchors cardiac cells *in vivo*, was fabricated through electrospinning. Spin speed was adjusted to tune fiber alignment while photo-initiated cross-linking was used to tune fiber stiffness to mimic physiologic (9–14 kPa) or pathophysiologic (>20 kPa) tissues. Cardiac myocytes in stiff, fibrous networks exhibit slower calcium flux, indicated by increased decay time and increased peak-to-peak irregularity (141). In another example, fibrous scaffolds with varying fiber stiffness were fabricated through two-photon polymerization and seeded with cardiac myocytes that lack expression of cardiac myosin binding protein C, which is thought to play a role in sarcomere sliding during contraction. Mutations in this protein are also associated with hypertrophic and dilated cardiomyopathy. While control cells were able to adapt to the increased load with increasing contraction force, cells with the mutation displayed impaired contraction on stiffer fibers. This work demonstrates the combined effects of mechanical stress and genetic factors on contraction deficits (142).

Interestingly, fibroblasts in 3-D fibrous matrices depart from the conventional relationships established between stiffness and fibroblast activation in 2-D cell culture or 3-D hydrogels (143). In human lung fibroblasts seeded in the same fibrous matrices, increasing fiber stiffness actually reduced proliferation and myofibroblast activation (α-SMA) when compared with cells on soft and deformable fibrous matrices. This is correlated with reduced cell spreading and focal adhesion formation that was also observed with increasing stiffness (144). Fiber density, on the other hand, has been shown to promote differentiation in lung fibroblasts, signified by increased fibronectin synthesis, nuclear localization of YAP, proliferation, and cytokine secretion (145). Similar relationships may also exist for cardiac fibroblasts but have yet to be investigated.

3-D Models With Spatiotemporal Control of Stiffness

Engineered 3-D cardiac tissues have also been fabricated with increasing spatiotemporal control over stiffness. A 3-D fibrosis model was developed using the biowire platform, in which cardiac cells are encapsulated in a fibrin-based hydrogel and suspended between a pair of polymer wires that function to promote microtissue alignment. Tissue contractile stress is measured based on the deflection of the intrinsically fluorescent polymer wires. To model healthy (7.6 kPa) or fibrotic (61.1 kPa) myocardium, cardiac myocytes were cocultured with 25 or 75% cardiac fibroblasts, respectively. Fibrotic tissues underwent more rapid compaction and had higher collagen content, disrupted myofibril structures, altered Cx43 distribution, prolonged time to peak, and lower contractile force generation when compared with healthy tissues. To next create a spatially heterogeneous stiffness model, which can mimic the interface between the infarct zone and viable tissue, fibrotic and healthy tissue were integrated at opposing sides of a single biowire platform (**Figure 3B**). The fibrotic side of the microtissue underwent more rapid compaction, contained increased collagen content and myofibroblast activation, and had slower calcium transients with a lower amplitude compared to the healthy side. In addition, propagation velocity at the healthy side was diminished when compared with uniform healthy biowire tissues. Arrhythmic waves were also observed, especially in the interface region. This platform was also used to screen antifibrotic drugs (136), demonstrating the potential impact of these approaches in drug development.

To alter substrate rigidity over time, one approach is to encapsulate cells into hydrogels that either degrade or cross-link in response to specific wavelengths of light. In one example, a 3-D photodegradable hydrogel was used to demonstrate that valvular myofibroblasts can be redirected into a quiescent phenotype by decreasing stiffness. This work demonstrates fibroblast phenotypic plasticity and the potential role of the mechanical environment in de-differentiating fibroblasts, which has therapeutic applications in resolving fibrotic disease (146). Lastly, one study demonstrated that cardiac myocytes encapsulated in photopolymerizable polyethylene glycol hydrogels do not exhibit differences in cell viability after UV exposure (133), though the impact of progressive stiffening in 3-D on cardiac cell phenotypes has not been further established.

IN VITRO MODELS OF PATHOLOGICAL STRAIN

Cardiac cells are constantly under cyclic stretch in the healthy, beating heart. Myocardial infarction results in an initial loss of contractility in the infarct zone followed by arrhythmogenesis, which alters strain rates experienced by surviving cardiac cells, as quantified through echocardiographic imaging (147). To stretch myocytes and non-myocytes *in vitro*, experimental platforms include microchips with stretchable silicone membranes, custom-built bioreactors, or commercially available cell straining units in which strain can be applied to cell culture plates with integrated loading posts.

Chronic cyclic stretch over several days to mimic the diastolic and systolic movement of cardiac muscle has been shown to promote the maturation of "engineered heart tissues," which are generally defined as cardiac myocytes embedded in hydrogels and cast around uniaxial tissue constraints or circular molds. Stretched heart tissues exhibit increased cell alignment (148–151), sarcomere organization (151, 152), Cx43 expression (150, 151), and contractile force generation (148, 150, 153). In some studies, morphological changes were also observed that indicate cardiac myocyte hypertrophy through increased cell size (148, 152) and mitochondrial density (148). In 2-D aligned cardiac tissues fabricated through microcontact printing, chronic cyclic stretch has also been shown to induce pathological changes in cell aspect ratio and sarcomere alignment, promote gene expression profiles associated with pathological remodeling, and diminish calcium transients and force generation (**Figure 4A**) (154). Thus, chronic cyclic stretch can be beneficial or detrimental to cardiac myocytes, depending on the specific parameters.

Cardiac fibroblast responses to strain have also been relatively inconsistent. In some cases, stretching activates many hallmarks of cardiac fibrosis, including increased fibroblast proliferation, hydrogel stiffening (156), increased gel compaction and strength (157, 158), extracellular matrix deposition (156–158), and enhanced secretion of TNF-α (159). However, responses are dependent on baseline levels of fibroblast activation, which is highly sensitive to culture conditions. Cardiac fibroblasts that are cultured for 1 day on rigid substrates and have lower initial levels of α-SMA respond to static tensile forces with increased α-SMA, while cells cultured for 3 days with higher basal levels of α-SMA respond to the same force with decreased α-SMA production (160). Consistent with this, fibroblasts grown on soft hydrogels with minimal basal α-SMA expression and exposed to static stretch show elevated α-SMA mRNA levels and expression of various extracellular matrix proteins, including collagen and fibronectin (115). Fibroblasts also show differing

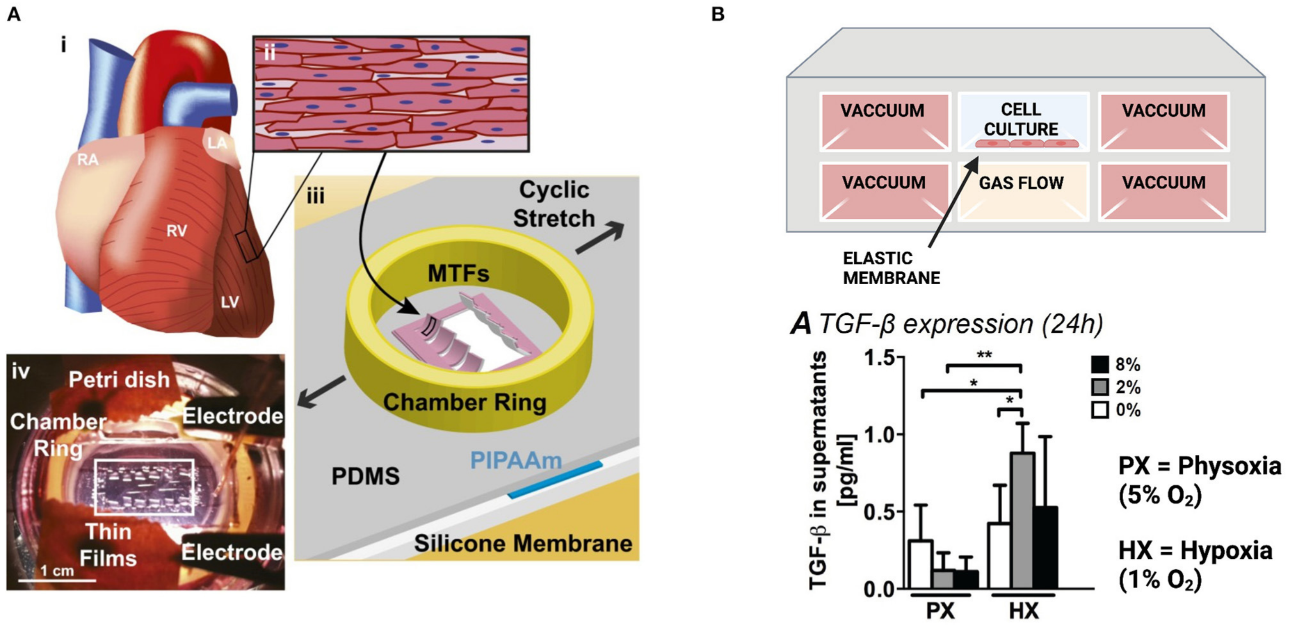

FIGURE 4 | Engineered *in vitro* models to mimic pathological strain post-infarction. **(A)** Muscular thin films on a stretchable silicone membrane provide real-time measurements of contractile stress during stretch. Images reproduced from McCain et al. (154). **(B)** A microfluidic device to evaluate the combined effects of hypoxia and strain on cardiac fibroblasts. Created with BioRender.com. Both hypoxia (1% O_2) and reduced contractility (2% strain) are required for cardiac fibroblasts to upregulate TGF-β and IL-1β ($^*p < 0.05$, $^{**}p < 0.01$). Image reproduced from Ugolini et al. (155) (https://creativecommons.org/licenses/by/4.0/).

proliferative behavior in response to mechanical strain, which may be dependent on baseline α-SMA levels, strain rate (161), ECM composition (162, 163), serum concentration (164), or substrate stiffness (115), which highlights a need for more standardized cell culture methods (165).

To assess the combined effects of strain and hypoxia, cardiac fibroblasts have been cultured in a microfluidic device containing a stretchable, gas-permeable membrane situated above a microchannel for gas flow and between lateral actuation channels (**Figure 4B**). Uniform hypoxia (1% oxygen) or reduced contractility to mimic post-infarct myocardium (2% strain) are alone sufficient to induce proliferation and collagen type 1 production, although the combined effects of hypoxia and reduced strain are required to trigger fibroblast secretion of IL-1β or TGF-β (155).

Paracrine signals secreted by stretched cardiac cells may also regulate critical aspects of infarct healing. Recent work has characterized the transcriptomic profile of stretched cardiac myocytes, which show differentially expressed genes and regulatory networks that may lead to hypertrophic growth of cardiac myocytes (166). Consistent with this, stretched cardiac myocytes upregulate miR208, a mediator of cardiac hypertrophy, hypertrophic proteins, such as β-myosin heavy chain, and secretion of TGF-β (167). Neonatal rat cardiac myocytes on stretched silicone membranes have also been reported to undergo apoptosis, accompanied by mitochondrial dysfunction (168). One study explored factors secreted by stretched cardiac myocytes by fabricating a coculture device that enables paracrine signaling between cardiac myocytes and fibroblasts while exposing cardiac myocytes to strains that mimic the border zone after infarction *in vivo*. In this device, coculture with stretched cardiac myocytes increases cardiac fibroblast proliferation. A media screen indicated the presence of cytokines such as colony stimulating factor 1 and platelet derived growth factor B, which were sufficient to increase proliferation in fibroblast monocultures (115).

OUTLOOK

As described above, post-infarct myocardium is characterized by distinct biochemical and biomechanical changes in the cellular microenvironment that vary in both space and time and are thought to contribute to excessive fibrosis, hypertrophy, and arrhythmias. Unlike conventional *in vitro* and *in vivo* models, Organs on Chips are able to dissect the impact of these complex and dynamic changes to the post-infarct microenvironment by offering a unique combination of multi-modal microenvironmental control and accessibility to physiological readouts. For example, the gradient systems described above showed that cardiac fibroblasts migrate toward both ischemic cardiac myocytes (27) and stiffer environments (130), two hallmark features of post-infarct myocardium. These studies also demonstrated that myofibroblast phenotypes can be reduced by inhibiting TGF-β (27) or ROCK (130), suggesting that these molecules or pathways could be exploited as anti-fibrotic therapies. As another example, microfluidic devices that offer precise control over oxygen concentration showed that the electrophysiology of cardiac myocytes becomes irregular in response to hypoxia but can recover after 10–30 min of reperfusion (80, 81). Another Organ on a Chip system showed that pre-treatment with endothelial cell-derived vesicles reduces ischemia-reperfusion injury in engineered cardiac tissues (79). Collectively, these and the other examples highlighted above demonstrate how Organ on a Chip models of post-infarct myocardium are powerful for determining how disease evolution is regulated by spatiotemporal heterogeneity while also serving as platforms for therapeutic development.

Despite the advantages of Organs on Chips, there are still many challenges that limit their widescale adoption for disease modeling and drug discovery. First, some findings in response to hypoxia, stiffness, or strain have produced conflicting results. For example, studies have reported increased (45, 155), decreased (46), or unchanged (44) proliferation of cardiac fibroblasts in response to hypoxia. Similarly, fibroblast proliferation has been shown to increase (155, 161) or decrease (162) in response to strain. This may be due to the inherent heterogeneity of the biological responses or may highlight a need for more standardized experimental methods. There is also a need for more characterization of injured myocardium *in vivo* and *ex vivo* through techniques such as atomic force microscopy, fluorescent oxygen probes, and high-resolution imaging to ensure that Organs on Chips are accurately modeling relevant features of post-infarct myocardium and to establish more universal design parameters.

Another limitation of existing Organ on a Chip models of post-infarct myocardium is their over-simplified architecture. As described above, current *in vitro* models have been predominantly 2-D monocultures that can be micropatterned to control tissue architecture or 3-D cocultured tissues or spheroids with relatively random tissue architecture. Thus, future work should focus on engineering cardiac tissues with distinct control over the positioning of multiple cell types and matrix components, leading to more granular models of post-infarct myocardium. Emerging methods to pattern multiple cell types in 2-D (169) and 3-D (170, 171) can improve the architectural relevance and reproducibility of engineered tissues. 3-D bioprinting has also advanced considerably in recent years to provide increasing structural complexity (172, 173), including spatial gradients in porosity (174) and material and cell composition (175), and can be implemented to make more precise tissue models. Model systems should also strive to incorporate relevant cell types beyond cardiac myocytes and fibroblasts, such as neurons (176) and immune cells (177). In addition, there are other types of spatial and temporal gradients beyond those described above, such as cytokine and chemokine gradients that orchestrate the inflammatory cascade after myocardial infarction. Recent approaches to control gradients of soluble factors using microfluidics (178, 179) or 3-D hydrogels (180) will enable more complex modeling of small molecule gradients in the context of myocardial infarction.

Another limitation of many of the studies described above is their reliance on primary cardiac cells from other species (usually neonatal rats), which have historically been the most accessible cardiac cell source. Cells from neonatal rats exhibit species-specific differences and are relatively resistant to hypoxia, a key feature of the infarct microenvironment (3). Thus, model systems will be improved as the field continues to adopt human induced pluripotent stem cell (hiPSC)-derived cardiac myocytes. In addition to providing human relevance, hiPSC-derived cardiac myocytes can also help identify genetic contributions to post-infarct remodeling (181) and contribute to patient-specific models and treatment regimens. However, a major concern is that these cells demonstrate fetal-like maturity, which is especially problematic for modeling myocardial infarctions, a condition that affects almost exclusively adults. Recent approaches to mature hiPSC-derived cardiac myocytes with electromechanical or biochemical stimuli may help mitigate this concern (182, 183), but achieving adult-like maturity in hiPSC-derived cardiac myocytes remains a major hurdle for the field.

Lastly, Organ on a Chip systems need to be more high-throughput and scalable to be integrated into the drug discovery pipeline. Thus, the field also needs more scalable fabrication methods, such as rapid, multimaterial bioprinting of cardiac biowire scaffolds into 96-well plate formats (184) or the development of substrates with integrated electrodes to streamline electrical stimulation (185). Throughput can also be improved by integrating sensors for real-time readouts of parameters such as tissue contractility (87, 88), action potentials (186), the consumption or secretion of biomolecules (187, 188), or physical aspects of the microenvironment, such as oxygen concentration and temperature (189). These types of multi-sensor systems will provide more continuous and detailed insight into cellular phenotypes in response to drug treatments while also requiring less manual handling, thereby increasing throughput and reproducibility.

In summary, engineered Organ on a Chip models of post-infarct myocardium have exciting potential to address many of the gaps presented by oversimplified 2-D cell culture models and animal models that lack human relevance. As technologies continue to develop, next-generation multi-dimensional models could provide simultaneous control over spatial and temporal changes in the physical, biochemical, and mechanical microenvironment that correspond to the phases of infarct healing. When further advanced with patient-derived cells, scalable fabrication techniques, and integrated sensors, these models have potential to emerge as new standards for disease modeling and drug screening and lead to new breakthrough therapies for mitigating post-infarction remodeling.

AUTHOR CONTRIBUTIONS

Both authors were involved in the conceptualization and writing of this manuscript.

FUNDING

This work was supported by NIH R01 HL153286 (MM), NSF CAREER 1944734 (MM), and the Provost Fellowship at the USC Viterbi School of Engineering (NK).

REFERENCES

1. Cardiovascular Diseases [Online]. World Health Organization (2020). Available online at: https://www.who.int/health-topics/cardiovascular-diseases/#tab=tab_1 (accessed May 14, 2021).
2. Torio CM, Moore BJ. *National Inpatient Hospital Costs: The Most Expensive Conditions by Payer [Online]*. Healthcare Cost and Utilization Project (HCUP): Agency for Healthcare Research and Quality (2016). Available online at: https://www.hcup-us.ahrq.gov/reports/statbriefs/sb204-Most-Expensive-Hospital-Conditions.jsp
3. Lindsey ML, Bolli R, Canty JM, Du XJ, Frangogiannis NG, Frantz S, et al. Guidelines for experimental models of myocardial ischemia and infarction. *Am J Physiol Heart Circ Physiol.* (2018) 314:H812–38. doi: 10.1152/ajpheart.00335.2017
4. Heart Disease Facts [Online]. Centers for Disease Control and Prevention (2020). Available online at: https://www.cdc.gov/heartdisease/facts.htm (accessed May 14, 2021).
5. Montalescot G, Andersen HR, Antoniucci D, Betriu A, de Boer MJ, Grip L, et al. Recommendations on percutaneous coronary intervention for the reperfusion of acute ST elevation myocardial infarction. *Heart.* (2004) 90:e37. doi: 10.1136/hrt.2003.016014
6. Bagai A, Dangas GD, Stone GW, Granger CB. Reperfusion strategies in acute coronary syndromes. *Circ Res.* (2014) 114:1918–28. doi: 10.1161/CIRCRESAHA.114.302744
7. Hausenloy DJ, Botker HE, Engstrom T, Erlinge D, Heusch G, Ibanez B, et al. Targeting reperfusion injury in patients with ST-segment elevation myocardial infarction: trials and tribulations. *Eur Heart J.* (2017) 38:935–41. doi: 10.1093/eurheartj/ehw145
8. Mercado MG, Smith DK, McConnon ML. Myocardial infarction: management of the subacute period. *Am Fam Physician.* (2013) 88:581–8.
9. Iravanian S, Dudley SC. The renin-angiotensin-aldosterone system (RAAS) and cardiac arrhythmias. *Heart Rhythm.* (2008) 5:S12–17. doi: 10.1016/j.hrthm.2008.02.025
10. Talman V, Ruskoaho H. Cardiac fibrosis in myocardial infarction-from repair and remodeling to regeneration. *Cell Tissue Res.* (2016) 365:563–81. doi: 10.1007/s00441-016-2431-9
11. Ingber DE. Is it time for reviewer 3 to request human organ chip experiments instead of animal validation studies? *Adv Sci.* (2020) 7:2002030. doi: 10.1002/advs.202002030
12. Weber KT, Sun Y, Bhattacharya SK, Ahokas RA, Gerling IC. Myofibroblast-mediated mechanisms of pathological remodelling of the heart. *Nat Rev Cardiol.* (2013) 10:15–26. doi: 10.1038/nrcardio.2012.158
13. Prabhu SD, Frangogiannis NG. The biological basis for cardiac repair after myocardial infarction: from inflammation to fibrosis. *Circ Res.* (2016) 119:91–112. doi: 10.1161/CIRCRESAHA.116.303577
14. Pfeffer MA, Braunwald E. Ventricular remodeling after myocardial infarction. Experimental observations and clinical implications. *Circulation.* (1990) 81:1161–72. doi: 10.1161/01.CIR.81.4.1161
15. Azevedo PS, Polegato BF, Minicucci MF, Paiva SA, Zornoff LA. Cardiac remodeling: concepts, clinical impact, pathophysiological mechanisms and pharmacologic treatment. *Arq Bras Cardiol.* (2016) 106:62–9. doi: 10.5935/abc.20160005
16. Matsushita T, Oyamada M, Fujimoto K, Yasuda Y, Masuda S, Wada Y, et al. Remodeling of cell-cell and cell-extracellular matrix interactions at the border zone of rat myocardial infarcts. *Circ Res.* (1999) 85:1046–55. doi: 10.1161/01.RES.85.11.1046
17. Cohn JN, Ferrari R, Sharpe N. Cardiac remodeling–concepts and clinical implications: a consensus paper from an international forum on cardiac remodeling. Behalf of an international forum on cardiac remodeling. *J Am Coll Cardiol.* (2000) 35:569–82. doi: 10.1016/S0735-1097(99)00630-0
18. Sutton MG, Sharpe N. Left ventricular remodeling after myocardial infarction: pathophysiology and therapy. *Circulation.* (2000) 101:2981–88. doi: 10.1161/01.CIR.101.25.2981
19. Lorell BH, Carabello BA. Left ventricular hypertrophy: pathogenesis, detection, and prognosis. *Circulation.* (2000) 102:470–9. doi: 10.1161/01.CIR.102.4.470
20. Konstam MA, Kramer DG, Patel AR, Maron MS, Udelson JE. Left ventricular remodeling in heart failure: current concepts in clinical significance and assessment. *JACC Cardiovasc Imaging.* (2011) 4:98–108. doi: 10.1016/j.jcmg.2010.10.008
21. Savinova OV, Gerdes AM. Myocyte changes in heart failure. *Heart Fail Clin.* (2012) 8:1–6. doi: 10.1016/j.hfc.2011.08.004
22. Korup E, Dalsgaard D, Nyvad O, Jensen TM, Toft E, Berning J. Comparison of degrees of left ventricular dilation within three hours and up to six days after onset of first acute myocardial infarction. *Am J Cardiol.* (1997) 80:449–53. doi: 10.1016/S0002-9149(97)00393-7
23. Armstrong PW. Left ventricular dysfunction: causes, natural history, and hopes for reversal. *Heart*. (2000) 84(Suppl 1):i15–7; discussion: i50. doi: 10.1136/heart.84.suppl_1.i15
24. Frangogiannis NG. The inflammatory response in myocardial injury, repair, and remodelling. *Nat Rev Cardiol.* (2014) 11:255–65. doi: 10.1038/nrcardio.2014.28
25. Shinde AV, Frangogiannis NG. Fibroblasts in myocardial infarction: a role in inflammation and repair. *J Mol Cell Cardiol.* (2014) 70:74–82. doi: 10.1016/j.yjmcc.2013.11.015
26. Rog-Zielinska EA, Norris RA, Kohl P, Markwald R. The living scar–cardiac fibroblasts and the injured heart. *Trends Mol Med.* (2016) 22:99–114. doi: 10.1016/j.molmed.2015.12.006
27. Mosadegh B, Dabiri BE, Lockett MR, Derda R, Campbell P, Parker KK, et al. Three-dimensional paper-based model for cardiac ischemia. *Adv Healthc Mater.* (2014) 3:1036–43. doi: 10.1002/adhm.2013 00575
28. Chiu LL, Radisic M, Vunjak-Novakovic G. Bioactive scaffolds for engineering vascularized cardiac tissues. *Macromol Biosci.* (2010) 10:1286–301. doi: 10.1002/mabi.201000202
29. Rumsey WL, Pawlowski M, Lejavardi N, Wilson DF. Oxygen pressure distribution in the heart *in vivo* and evaluation of the ischemic "border zone". *Am J Physiol.* (1994) 266(4 Pt 2):H1676–80. doi: 10.1152/ajpheart.1994.266.4.H1676
30. Sen CK, Khanna S, Roy S. Perceived hyperoxia: oxygen-induced remodeling of the reoxygenated heart. *Cardiovasc Res.* (2006) 71:280–8. doi: 10.1016/j.cardiores.2006.01.003
31. Muñoz-Sánchez J, Chánez-Cárdenas ME. The use of cobalt chloride as a chemical hypoxia model. *J Appl Toxicol.* (2019) 39:556–70. doi: 10.1002/jat.3749
32. Zhao RZ, Jiang S, Ru NY, Jiao B, Yu ZB. Comparison of hypoxic effects induced by chemical and physical hypoxia on cardiomyocytes. *Can J Physiol Pharmacol.* (2019) 97:980–8. doi: 10.1139/cjpp-2019-0092
33. Pavlacky J, Polak J. Technical feasibility and physiological relevance of hypoxic cell culture models. *Front Endocrinol.* (2020) 11:57. doi: 10.3389/fendo.2020.00057
34. Zeevi-Levin N, Barac YD, Reisner Y, Reiter I, Yaniv G, Meiry G, et al. Gap junctional remodeling by hypoxia in cultured neonatal rat ventricular myocytes. *Cardiovasc Res.* (2005) 66:64–73. doi: 10.1016/j.cardiores.2005.01.014
35. Danon A, Zeevi-Levin N, Pinkovich DY, Michaeli T, Berkovich A, Flugelman M, et al. Hypoxia causes connexin 43 internalization in neonatal rat ventricular myocytes. *Gen Physiol Biophys.* (2010) 29:222–33. doi: 10.4149/gpb_2010_03_222
36. Turner MS, Haywood GA, Andreka P, You L, Martin PE, Evans WH, et al. Reversible connexin 43 dephosphorylation during hypoxia and reoxygenation is linked to cellular ATP levels. *Circ Res.* (2004) 95:726–33. doi: 10.1161/01.RES.0000144805.11519.1e
37. Xu KY, Kuppusamy SP, Wang JQ, Li H, Cui H, Dawson TM, et al. Nitric oxide protects cardiac sarcolemmal membrane enzyme function and ion active transport against ischemia-induced inactivation. *J Biol Chem.* (2003) 278:41798–803. doi: 10.1074/jbc.M306865200
38. Yakushev S, Band M, Tissot van Patot MC, Gassmann M, Avivi A, Bogdanova A. Cross talk between S-nitrosylation and S-glutathionylation in control of the Na,K-ATPase regulation in hypoxic heart. *Am J Physiol Heart Circ Physiol*. (2012) 303:H1332–43. doi: 10.1152/ajpheart.001 45.2012
39. González-Rodríguez P, Falcón D, Castro MJ, Ureña J, López-Barneo J, Castellano A. Hypoxic induction of T-type Ca(2+) channels in rat cardiac myocytes: role of HIF-1α and RhoA/ROCK signalling. *J Physiol.* (2015) 593:4729–45. doi: 10.1113/JP271053

40. Tanaka M, Ito H, Adachi S, Akimoto H, Nishikawa T, Kasajima T, et al. Hypoxia induces apoptosis with enhanced expression of Fas antigen messenger RNA in cultured neonatal rat cardiomyocytes. *Circ Res.* (1994) 75:426–33. doi: 10.1161/01.RES.75.3.426
41. Long X, Boluyt MO, Hipolito ML, Lundberg MS, Zheng JS, O'Neill L, et al. p53 and the hypoxia-induced apoptosis of cultured neonatal rat cardiac myocytes. *J Clin Invest.* (1997) 99:2635–43. doi: 10.1172/JCI119452
42. Chen SJ, Bradley ME, Lee TC. Chemical hypoxia triggers apoptosis of cultured neonatal rat cardiac myocytes: modulation by calcium-regulated proteases and protein kinases. *Mol Cell Biochem.* (1998) 178:141–9. doi: 10.1023/A:1006893528428
43. Kang PM, Haunstetter A, Aoki H, Usheva A, Izumo S. Morphological and molecular characterization of adult cardiomyocyte apoptosis during hypoxia and reoxygenation. *Circ Res.* (2000) 87:118–25. doi: 10.1161/01.RES.87.2.118
44. Gao Y, Chu M, Hong J, Shang J, Xu D. Hypoxia induces cardiac fibroblast proliferation and phenotypic switch: a role for caveolae and caveolin-1/PTEN mediated pathway. *J Thorac Dis.* (2014) 6:1458–68. doi: 10.3978/j.issn.2072-1439.2014.08.31
45. Watson CJ, Collier P, Tea I, Neary R, Watson JA, Robinson C, et al. Hypoxia-induced epigenetic modifications are associated with cardiac tissue fibrosis and the development of a myofibroblast-like phenotype. *Hum Mol Genet.* (2014) 23:2176–88. doi: 10.1093/hmg/ddt614
46. Zhao X, Wang K, Liao Y, Zeng Q, Li Y, Hu F, et al. MicroRNA-101a inhibits cardiac fibrosis induced by hypoxia via targeting TGFβRI on cardiac fibroblasts. *Cell Physiol Biochem.* (2015) 35:213–26. doi: 10.1159/000369689
47. Tamamori M, Ito H, Hiroe M, Marumo F, Hata RI. Stimulation of collagen synthesis in rat cardiac fibroblasts by exposure to hypoxic culture conditions and suppression of the effect by natriuretic peptides. *Cell Biol Int.* (1997) 21:175–80. doi: 10.1006/cbir.1997.0130
48. Chu W, Li X, Li C, Wan L, Shi H, Song X, et al. TGFBR3, a potential negative regulator of TGF-β signaling, protects cardiac fibroblasts from hypoxia-induced apoptosis. *J Cell Physiol.* (2011) 226:2586–94. doi: 10.1002/jcp.22604
49. Yang B, He K, Zheng F, Wan L, Yu X, Wang X, et al. Over-expression of hypoxia-inducible factor-1 alpha *in vitro* protects the cardiac fibroblasts from hypoxia-induced apoptosis. *J Cardiovasc Med.* (2014) 15:579–86. doi: 10.2459/JCM.0b013e3283629c52
50. Zhao X, Wang K, Hu F, Qian C, Guan H, Feng K, et al. MicroRNA-101 protects cardiac fibroblasts from hypoxia-induced apoptosis via inhibition of the TGF-β signaling pathway. *Int J Biochem Cell Biol.* (2015) 65:155–64. doi: 10.1016/j.biocel.2015.06.005
51. Ladoux A, Frelin C. Hypoxia is a strong inducer of vascular endothelial growth factor mRNA expression in the heart. *Biochem Biophys Res Commun.* (1993) 195:1005–10. doi: 10.1006/bbrc.1993.2144
52. Hwang JM, Weng YJ, Lin JA, Bau DT, Ko FY, Tsai FJ, et al. Hypoxia-induced compensatory effect as related to Shh and HIF-1alpha in ischemia embryo rat heart. *Mol Cell Biochem.* (2008) 311:179–87. doi: 10.1007/s11010-008-9708-6
53. Ontoria-Oviedo I, Dorronsoro A, Sánchez R, Ciria M, Gómez-Ferrer M, Buigues M, et al. Extracellular vesicles secreted by hypoxic AC10 cardiomyocytes modulate fibroblast cell motility. *Front Cardiovasc Med.* (2018) 5:152. doi: 10.3389/fcvm.2018.00152
54. Shi H, Zhang X, He Z, Wu Z, Rao L, Li Y. Metabolites of hypoxic cardiomyocytes induce the migration of cardiac fibroblasts. *Cell Physiol Biochem.* (2017) 41:413–21. doi: 10.1159/000456531
55. Shivakumar K, Sollott SJ, Sangeetha M, Sapna S, Ziman B, Wang S, et al. Paracrine effects of hypoxic fibroblast-derived factors on the MPT-ROS threshold and viability of adult rat cardiac myocytes. *Am J Physiol Heart Circ Physiol.* (2008) 294:H2653–8. doi: 10.1152/ajpheart.91443.2007
56. Gao Q, Guo M, Zeng W, Wang Y, Yang L, Pang X, et al. Matrix metalloproteinase 9 secreted by hypoxia cardiac fibroblasts triggers cardiac stem cell migration *in vitro*. *Stem Cells Int.* (2015) 2015:836390. doi: 10.1155/2015/836390
57. Wang JH, Zhao L, Pan X, Chen NN, Chen J, Gong QL, et al. Hypoxia-stimulated cardiac fibroblast production of IL-6 promotes myocardial fibrosis via the TGF-β1 signaling pathway. *Lab Invest.* (2016) 96:1035. doi: 10.1038/labinvest.2016.84
58. Cosme J, Guo H, Hadipour-Lakmehsari S, Emili A, Gramolini AO. Hypoxia-induced changes in the fibroblast secretome, exosome, and whole-cell proteome using cultured, cardiac-derived cells isolated from neonatal mice. *J Proteome Res.* (2017) 16:2836–47. doi: 10.1021/acs.jproteome.7b00144
59. Ren L, Liu W, Wang Y, Wang JC, Tu Q, Xu J, et al. Investigation of hypoxia-induced myocardial injury dynamics in a tissue interface mimicking microfluidic device. *Anal Chem.* (2013) 85:235–44. doi: 10.1021/ac3025812
60. Wang L, Liu W, Wang Y, Wang JC, Tu Q, Liu R, et al. Construction of oxygen and chemical concentration gradients in a single microfluidic device for studying tumor cell-drug interactions in a dynamic hypoxia microenvironment. *Lab Chip.* (2013) 13:695–705. doi: 10.1039/C2LC40661F
61. Chang CW, Cheng YJ, Tu M, Chen YH, Peng CC, Liao WH, et al. A polydimethylsiloxane-polycarbonate hybrid microfluidic device capable of generating perpendicular chemical and oxygen gradients for cell culture studies. *Lab Chip.* (2014) 14:3762–72. doi: 10.1039/C4LC00732H
62. Shih HC, Lee TA, Wu HM, Ko PL, Liao WH, Tung YC. Microfluidic collective cell migration assay for study of endothelial cell proliferation and migration under combinations of oxygen gradients, tensions, and drug treatments. *Sci Rep.* (2019) 9:8234. doi: 10.1038/s41598-019-44594-5
63. Kang YBA, Eo J, Bulutoglu B, Yarmush ML, Usta OB. Progressive hypoxia-on-a-chip: an *in vitro* oxygen gradient model for capturing the effects of hypoxia on primary hepatocytes in health and disease. *Biotechnol Bioeng.* (2020) 117:763–75. doi: 10.1002/bit.27225
64. Polinkovsky M, Gutierrez E, Levchenko A, Groisman A. Fine temporal control of the medium gas content and acidity and on-chip generation of series of oxygen concentrations for cell cultures. *Lab Chip.* (2009) 9:1073–84. doi: 10.1039/b816191g
65. Lo JF, Sinkala E, Eddington DT. Oxygen gradients for open well cellular cultures via microfluidic substrates. *Lab Chip.* (2010) 10:2394–401. doi: 10.1039/c004660d
66. Rexius-Hall ML, Rehman J, Eddington DT. A microfluidic oxygen gradient demonstrates differential activation of the hypoxia-regulated transcription factors HIF-1α and HIF-2α. *Integr Biol.* (2017) 9:742–50. doi: 10.1039/C7IB00099E
67. Lavrentieva A. Advances in biochemical engineering/biotechnology. In: Lavrentieva A, Pepelanova I, Seliktar D, editors. *Tunable Hydrogels.* Cham: Springer. (2020). p. 1–25. doi: 10.1007/978-3-030-76769-3
68. Park KM, Gerecht S. Hypoxia-inducible hydrogels. *Nat Commun.* (2014) 5:4075. doi: 10.1038/ncomms5075
69. Blatchley M, Park KM, Gerecht S. Designer hydrogels for precision control of oxygen tension and mechanical properties. *J Mater Chem B.* (2015) 3:7939–49. doi: 10.1039/C5TB01038A
70. Boyce MW, Simke WC, Kenney RM, Lockett MR. Generating linear oxygen gradients across 3D cell cultures with block-layered oxygen controlled chips (BLOCCs). *Anal Methods.* (2020) 12:18–24. doi: 10.1039/C9AY01690B
71. Pedron S, Becka E, Harley BA. Spatially gradated hydrogel platform as a 3D engineered tumor microenvironment. *Adv Mater.* (2015) 27:1567–72. doi: 10.1002/adma.201404896
72. Khademhosseini A, Eng G, Yeh J, Kucharczyk PA, Langer R, Vunjak-Novakovic G, et al. Microfluidic patterning for fabrication of contractile cardiac organoids. *Biomed Microdev.* (2007) 9:149–57. doi: 10.1007/s10544-006-9013-7
73. Iyer RK, Chui J, Radisic M. Spatiotemporal tracking of cells in tissue-engineered cardiac organoids. *J Tissue Eng Regen Med.* (2009) 3:196–207. doi: 10.1002/term.153
74. Chiu LL, Iyer RK, King JP, Radisic M. Biphasic electrical field stimulation aids in tissue engineering of multicell-type cardiac organoids. *Tissue Eng A.* (2011) 17:1465–77. doi: 10.1089/ten.tea.2007.0244
75. Iyer RK, Odedra D, Chiu LL, Vunjak-Novakovic G, Radisic M. Vascular endothelial growth factor secretion by nonmyocytes modulates Connexin-43 levels in cardiac organoids. *Tissue Eng A.* (2012) 18:1771–83. doi: 10.1089/ten.tea.2011.0468
76. Mills RJ, Titmarsh DM, Koenig X, Parker BL, Ryall JG, Quaife-Ryan GA, et al. Functional screening in human cardiac organoids reveals a metabolic

mechanism for cardiomyocyte cell cycle arrest. *Proc Natl Acad Sci USA*. (2017) 114:E8372–81. doi: 10.1073/pnas.1707316114

77. Cai Y, Zhang J, Wu J, Li ZY. Oxygen transport in a three-dimensional microvascular network incorporated with early tumour growth and preexisting vessel cooption: numerical simulation study. *Biomed Res Int*. (2015) 2015:476964. doi: 10.1155/2015/476964
78. Richards DJ, Li Y, Kerr CM, Yao J, Beeson GC, Coyle RC, et al. Human cardiac organoids for the modelling of myocardial infarction and drug cardiotoxicity. *Nat Biomed Eng*. (2020) 4:446–62. doi: 10.1038/s41551-020-0539-4
79. Yadid M, Lind JU, Ardoña HAM, Sheehy SP, Dickinson LE, Eweje F, et al. Endothelial extracellular vesicles contain protective proteins and rescue ischemia-reperfusion injury in a human heart-on-chip. *Sci Transl Med*. (2020) 12:eaax8005. doi: 10.1126/scitranslmed.aax8005
80. Liu H, Bolonduro OA, Hu N, Ju J, Rao AA, Duffy BM, et al. Heart-on-a-chip model with integrated extra- and intracellular bioelectronics for monitoring cardiac electrophysiology under acute hypoxia. *Nano Lett*. (2020) 20:2585–93. doi: 10.1021/acs.nanolett.0c00076
81. Martewicz S, Michielin F, Serena E, Zambon A, Mongillo M, Elvassore N. Reversible alteration of calcium dynamics in cardiomyocytes during acute hypoxia transient in a microfluidic platform. *Integr Biol (Camb)*. (2012) 4:153–64. doi: 10.1039/C1IB00087J
82. Bursac N, Parker KK, Iravanian S, Tung L. Cardiomyocyte cultures with controlled macroscopic anisotropy: a model for functional electrophysiological studies of cardiac muscle. *Circ Res*. (2002) 91:e45–54. doi: 10.1161/01.RES.0000047530.88338.EB
83. Feinberg AW, Alford PW, Jin H, Ripplinger CM, Werdich AA, Sheehy SP, et al. Controlling the contractile strength of engineered cardiac muscle by hierarchal tissue architecture. *Biomaterials*. (2012) 33:5732–41. doi: 10.1016/j.biomaterials.2012.04.043
84. Petersen AP, Lyra-Leite DM, Ariyasinghe NR, Cho N, Goodwin CM, Kim JY, et al. Microenvironmental modulation of calcium wave propagation velocity in engineered cardiac tissues. *Cell Mol Bioeng*. (2018) 11:337–52. doi: 10.1007/s12195-018-0522-2
85. McCain ML, Yuan H, Pasqualini FS, Campbell PH, Parker KK. Matrix elasticity regulates the optimal cardiac myocyte shape for contractility. *Am J Physiol Heart Circ Physiol*. (2014) 306:H1525–39. doi: 10.1152/ajpheart.00799.2013
86. Watson JL, Aich S, Oller-Salvia B, Drabek AA, Blacklow SC, Chin J, et al. High-efficacy subcellular micropatterning of proteins using fibrinogen anchors. *J Cell Biol*. (2021) 220:e202009063. doi: 10.1083/jcb.202009063
87. Lind JU, Busbee TA, Valentine AD, Pasqualini FS, Yuan H, Yadid M, et al. Instrumented cardiac microphysiological devices via multimaterial three-dimensional printing. *Nat Mater*. (2017) 16:303–8. doi: 10.1038/nmat4782
88. Lind JU, Yadid M, Perkins I, O'Connor BB, Eweje F, Chantre CO, et al. Cardiac microphysiological devices with flexible thin-film sensors for higher-throughput drug screening. *Lab Chip*. (2017) 17:3692–703. doi: 10.1039/C7LC00740J
89. Litwin SE, Litwin CM, Raya TE, Warner AL, Goldman S. Contractility and stiffness of noninfarcted myocardium after coronary ligation in rats. Effects of chronic angiotensin converting enzyme inhibition. *Circulation*. (1991) 83:1028–37. doi: 10.1161/01.CIR.83.3.1028
90. Berry MF, Engler AJ, Woo YJ, Pirolli TJ, Bish LT, Jayasankar V, et al. Mesenchymal stem cell injection after myocardial infarction improves myocardial compliance. *Am J Physiol Heart Circ Physiol*. (2006) 290:H2196–203. doi: 10.1152/ajpheart.01017.2005
91. van Putten S, Shafieyan Y, Hinz B. Mechanical control of cardiac myofibroblasts. *J Mol Cell Cardiol*. (2016) 93:133–42. doi: 10.1016/j.yjmcc.2015.11.025
92. Herum KM, Lunde IG, McCulloch AD, Christensen G. The soft- and hard-heartedness of cardiac fibroblasts: mechanotransduction signaling pathways in fibrosis of the heart. *J Clin Med*. (2017) 6:53. doi: 10.3390/jcm6050053
93. Rusu M, Hilse K, Schuh A, Martin L, Slabu I, Stoppe C, et al. Biomechanical assessment of remote and postinfarction scar remodeling following myocardial infarction. *Sci Rep*. (2019) 9:16744. doi: 10.1038/s41598-019-53351-7
94. Torres WM, Jacobs J, Doviak H, Barlow SC, Zile MR, Shazly T, et al. Regional and temporal changes in left ventricular strain and stiffness in a porcine model of myocardial infarction. *Am J Physiol Heart Circ Physiol*. (2018) 315:H958–67. doi: 10.1152/ajpheart.00279.2018
95. Landry NM, Rattan SG, Dixon IMC. An improved method of maintaining primary murine cardiac fibroblasts in two-dimensional cell culture. *Sci Rep*. (2019) 9:12889. doi: 10.1038/s41598-019-49285-9
96. Ariyasinghe NR, Lyra-Leite DM, McCain ML. Engineering cardiac microphysiological systems to model pathological extracellular matrix remodeling. *Am J Physiol Heart Circ Physiol*. (2018) 315:H771–89. doi: 10.1152/ajpheart.00110.2018
97. Zhu J, Marchant RE. Design properties of hydrogel tissue-engineering scaffolds. *Expert Rev Med Devices*. (2011) 8:607–26. doi: 10.1586/erd.11.27
98. Hu W, Wang Z, Xiao Y, Zhang S, Wang J. Advances in crosslinking strategies of biomedical hydrogels. *Biomater Sci*. (2019) 7:843–55. doi: 10.1039/C8BM01246F
99. Lyra-Leite DM, Andres AM, Petersen AP, Ariyasinghe NR, Cho N, Lee JA, et al. Mitochondrial function in engineered cardiac tissues is regulated by extracellular matrix elasticity and tissue alignment. *Am J Physiol Heart Circ Physiol*. (2017) 313:H757–67. doi: 10.1152/ajpheart.00290.2017
100. Lyra-Leite DM, Andres AM, Cho N, Petersen AP, Ariyasinghe NR, Kim SS, et al. Matrix-guided control of mitochondrial function in cardiac myocytes. *Acta Biomater*. (2019) 97:281–95. doi: 10.1016/j.actbio.2019.08.007
101. Guo J, Simmons DW, Ramahdita G, Munsell MK, Oguntuyo K, Kandalaft B, et al. Elastomer-grafted iPSC-derived micro heart muscles to investigate effects of mechanical loading on physiology. *ACS Biomater Sci Eng*. (2020). doi: 10.1021/acsbiomaterials.0c00318
102. Lyra-Leite DM, Petersen AP, Ariyasinghe NR, Cho N, McCain ML. Mitochondrial architecture in cardiac myocytes depends on cell shape and matrix rigidity. *J Mol Cell Cardiol*. (2021) 150:32–43. doi: 10.1016/j.yjmcc.2020.10.004
103. Jacot JG, McCulloch AD, Omens JH. Substrate stiffness affects the functional maturation of neonatal rat ventricular myocytes. *Biophys J*. (2008) 95:3479–87. doi: 10.1529/biophysj.107.124545
104. Boothe SD, Myers JD, Pok S, Sun J, Xi Y, Nieto RM, et al. The effect of substrate stiffness on cardiomyocyte action potentials. *Cell Biochem Biophys*. (2016) 74:527–35. doi: 10.1007/s12013-016-0758-1
105. Engler AJ, Carag-Krieger C, Johnson CP, Raab M, Tang HY, Speicher DW, et al. Embryonic cardiomyocytes beat best on a matrix with heart-like elasticity: scar-like rigidity inhibits beating. *J Cell Sci*. (2008) 121(Pt 22):3794–802. doi: 10.1242/jcs.029678
106. Bhana B, Iyer RK, Chen WL, Zhao R, Sider KL, Likhitpanichkul M, et al. Influence of substrate stiffness on the phenotype of heart cells. *Biotechnol Bioeng*. (2010) 105:1148–60. doi: 10.1002/bit.22647
107. Pasqualini FS, Agarwal A, O'Connor BB, Liu Q, Sheehy SP, Parker KK. Traction force microscopy of engineered cardiac tissues. *PLoS ONE*. (2018) 13:e0194706. doi: 10.1371/journal.pone.0194706
108. Bajaj P, Tang X, Saif TA, Bashir R. Stiffness of the substrate influences the phenotype of embryonic chicken cardiac myocytes. *J Biomed Mater Res A*. (2010) 95:1261–9. doi: 10.1002/jbm.a.32951
109. Hersch N, Wolters B, Dreissen G, Springer R, Kirchgeßner N, Merkel R, et al. The constant beat: cardiomyocytes adapt their forces by equal contraction upon environmental stiffening. *Biol Open*. (2013) 2:351–61. doi: 10.1242/bio.20133830
110. McCain ML, Lee H, Aratyn-Schaus Y, Kléber AG, Parker KK. Cooperative coupling of cell-matrix and cell-cell adhesions in cardiac muscle. *Proc Natl Acad Sci USA*. (2012) 109:9881–6. doi: 10.1073/pnas.1203007109
111. Ariyasinghe NR, Reck CH, Viscio AA, Petersen AP, Lyra-Leite DM, Cho N, et al. Engineering micromyocardium to delineate cellular and extracellular regulation of myocardial tissue contractility. *Integr Biol*. (2017) 9:730–41. doi: 10.1039/C7IB00081B
112. Nguyen DT, Nagarajan N, Zorlutuna P. Effect of substrate stiffness on mechanical coupling and force propagation at the infarct boundary. *Biophys J*. (2018) 115:1966–80. doi: 10.1016/j.bpj.2018.08.050
113. Goffin JM, Pittet P, Csucs G, Lussi JW, Meister JJ, Hinz B. Focal adhesion size controls tension-dependent recruitment of alpha-smooth muscle actin

to stress fibers. *J Cell Biol.* (2006) 172:259–68. doi: 10.1083/jcb.200506179

114. Liu F, Lagares D, Choi KM, Stopfer L, Marinković A, Vrbanac V, et al. Mechanosignaling through YAP and TAZ drives fibroblast activation and fibrosis. *Am J Physiol Lung Cell Mol Physiol.* (2015) 308:L344–57. doi: 10.1152/ajplung.00300.2014
115. Herum KM, Choppe J, Kumar A, Engler AJ, McCulloch AD. Mechanical regulation of cardiac fibroblast profibrotic phenotypes. *Mol Biol Cell.* (2017) 28:1871–82. doi: 10.1091/mbc.e17-01-0014
116. Cho N, Razipour SE, McCain ML. Featured Article: TGF-β1 dominates extracellular matrix rigidity for inducing differentiation of human cardiac fibroblasts to myofibroblasts. *Exp Biol Med.* (2018) 243:601–12. doi: 10.1177/1535370218761628
117. Marinković A, Mih JD, Park JA, Liu F, Tschumperlin DJ. Improved throughput traction microscopy reveals pivotal role for matrix stiffness in fibroblast contractility and TGF-β responsiveness. *Am J Physiol Lung Cell Mol Physiol.* (2012) 303:L169–80. doi: 10.1152/ajplung.00108.2012
118. Shen J, Xie Y, Liu Z, Zhang S, Wang Y, Jia L, et al. Increased myocardial stiffness activates cardiac microvascular endothelial cell via VEGF paracrine signaling in cardiac hypertrophy. *J Mol Cell Cardiol.* (2018) 122:140–51. doi: 10.1016/j.yjmcc.2018.08.014
119. Ceccato TL, Starbuck RB, Hall JK, Walker CJ, Brown TE, Killgore JP, et al. Defining the cardiac fibroblast secretome in a fibrotic microenvironment. *J Am Heart Assoc.* (2020) 9:e017025. doi: 10.1161/JAHA.120.017025
120. Li C, Ouyang L, Armstrong JPK, Stevens MM. Advances in the fabrication of biomaterials for gradient tissue engineering. *Trends Biotechnol.* (2021) 39:150–64. doi: 10.1016/j.tibtech.2020.06.005
121. Marklein RA, Burdick JA. Spatially controlled hydrogel mechanics to modulate stem cell interactions. *Soft Matter.* (2010) 6:136–43. doi: 10.1039/B916933D
122. Tse JR, Engler AJ. Stiffness gradients mimicking *in vivo* tissue variation regulate mesenchymal stem cell fate. *PLoS ONE.* (2011) 6:e15978. doi: 10.1371/journal.pone.0015978
123. Major LG, Holle AW, Young JL, Hepburn MS, Jeong K, Chin IL, et al. Volume adaptation controls stem cell mechanotransduction. *ACS Appl Mater Interfaces.* (2019) 11:45520–30. doi: 10.1021/acsami.9b19770
124. Kim C, Young JL, Holle AW, Jeong K, Major LG, Jeong JH, et al. Stem cell mechanosensation on gelatin methacryloyl (GelMA) stiffness gradient hydrogels. *Ann Biomed Eng.* (2020) 48:893–902. doi: 10.1007/s10439-019-02428-5
125. Sunyer R, Jin AJ, Nossal R, Sackett DL. Fabrication of hydrogels with steep stiffness gradients for studying cell mechanical response. *PLoS ONE.* (2012) 7:e46107. doi: 10.1371/journal.pone.0046107
126. Dou J, Mao S, Li H, Lin JM. Combination stiffness gradient with chemical stimulation directs glioma cell migration on a microfluidic chip. *Anal Chem.* (2020) 92:892–8. doi: 10.1021/acs.analchem.9b03681
127. Hadden WJ, Young JL, Holle AW, McFetridge ML, Kim DY, Wijesinghe P, et al. Stem cell migration and mechanotransduction on linear stiffness gradient hydrogels. *Proc Natl Acad Sci USA.* (2017) 114:5647–52. doi: 10.1073/pnas.1618239114
128. Wang PY, Tsai WB, Voelcker NH. Screening of rat mesenchymal stem cell behaviour on polydimethylsiloxane stiffness gradients. *Acta Biomater.* (2012) 8:519–30. doi: 10.1016/j.actbio.2011.09.030
129. Lavrentieva A, Fleischhammer T, Enders A, Pirmahboub H, Bahnemann J, Pepelanova I. Fabrication of stiffness gradients of GelMA hydrogels using a 3D printed micromixer. *Macromol Biosci.* (2020) 20:e2000107. doi: 10.1002/mabi.202000107
130. Zhao H, Li X, Zhao S, Zeng Y, Zhao L, Ding H, et al. Microengineered *in vitro* model of cardiac fibrosis through modulating myofibroblast mechanotransduction. *Biofabrication.* (2014) 6:045009. doi: 10.1088/1758-5082/6/4/045009
131. Liu F, Mih JD, Shea BS, Kho AT, Sharif AS, Tager AM, et al. Feedback amplification of fibrosis through matrix stiffening and COX-2 suppression. *J Cell Biol.* (2010) 190:693–706. doi: 10.1083/jcb.201004082
132. Kloxin AM, Kasko AM, Salinas CN, Anseth KS. Photodegradable hydrogels for dynamic tuning of physical and chemical properties. *Science.* (2009) 324:59–63. doi: 10.1126/science.1169494
133. Crocini C, Walker CJ, Anseth KS, Leinwand LA. Three-dimensional encapsulation of adult mouse cardiomyocytes in hydrogels with tunable stiffness. *Prog Biophys Mol Biol.* (2020) 154:71–9. doi: 10.1016/j.pbiomolbio.2019.04.008
134. Young JL, Engler AJ. Hydrogels with time-dependent material properties enhance cardiomyocyte differentiation *in vitro*. *Biomaterials.* (2011) 32:1002–9. doi: 10.1016/j.biomaterials.2010.10.020
135. Burdick JA, Murphy WL. Moving from static to dynamic complexity in hydrogel design. *Nat Commun.* (2012) 3:1269. doi: 10.1038/ncomms2271
136. Wang EY, Rafatian N, Zhao Y, Lee A, Lai BFL, Lu RX, et al. Biowire model of interstitial and focal cardiac fibrosis. *ACS Cent Sci.* (2019) 5:1146–58. doi: 10.1021/acscentsci.9b00052
137. Galie PA, Westfall MV, Stegemann JP. Reduced serum content and increased matrix stiffness promote the cardiac myofibroblast transition in 3D collagen matrices. *Cardiovasc Pathol.* (2011) 20:325–33. doi: 10.1016/j.carpath.2010.10.001
138. Yu J, Seldin MM, Fu K, Li S, Lam L, Wang P, et al. Topological arrangement of cardiac fibroblasts regulates cellular plasticity. *Circ Res.* (2018) 123:73–85. doi: 10.1161/CIRCRESAHA.118.312589
139. van Spreeuwel ACC, Bax NAM, van Nierop BJ, Aartsma-Rus A, Goumans MTH, Bouten CVC. Mimicking cardiac fibrosis in a dish: fibroblast density rather than collagen density weakens cardiomyocyte function. *J Cardiovasc Transl Res.* (2017) 10:116–27. doi: 10.1007/s12265-017-9737-1
140. van Spreeuwel AC, Bax NA, Bastiaens AJ, Foolen J, Loerakker S, Borochin M, et al. The influence of matrix (an)isotropy on cardiomyocyte contraction in engineered cardiac microtissues. *Integr Biol.* (2014) 6:422–9. doi: 10.1039/C3IB40219C
141. DePalma SJ, Davidson CD, Stis AE, Helms AS, Baker BM. Microenvironmental determinants of organized iPSC-cardiomyocyte tissues on synthetic fibrous matrices. *Biomater Sci.* (2021) 9:93–107. doi: 10.1039/D0BM01247E
142. Ma Z, Huebsch N, Koo S, Mandegar MA, Siemons B, Boggess S, et al. Contractile deficits in engineered cardiac microtissues as a result of MYBPC3 deficiency and mechanical overload. *Nat Biomed Eng.* (2018) 2:955–67. doi: 10.1038/s41551-018-0280-4
143. Baker BM, Trappmann B, Wang WY, Sakar MS, Kim IL, Shenoy VB, et al. Cell-mediated fibre recruitment drives extracellular matrix mechanosensing in engineered fibrillar microenvironments. *Nat Mater.* (2015) 14:1262–8. doi: 10.1038/nmat4444
144. Davidson CD, Jayco DKP, Matera DL, DePalma SJ, Hiraki HL, Wang WY, et al. Myofibroblast activation in synthetic fibrous matrices composed of dextran vinyl sulfone. *Acta Biomater.* (2020) 105:78–86. doi: 10.1016/j.actbio.2020.01.009
145. Matera DL, DiLillo KM, Smith MR, Davidson CD, Parikh R, Said M, et al. Microengineered 3D pulmonary interstitial mimetics highlight a critical role for matrix degradation in myofibroblast differentiation. *Sci Adv.* (2020) 6:eabb5069. doi: 10.1126/sciadv.abb5069
146. Wang H, Haeger SM, Kloxin AM, Leinwand LA, Anseth KS. Redirecting valvular myofibroblasts into dormant fibroblasts through light-mediated reduction in substrate modulus. *PLoS ONE.* (2012) 7:e39969. doi: 10.1371/journal.pone.0039969
147. Gorcsan J, Tanaka H. Echocardiographic assessment of myocardial strain. *J Am Coll Cardiol.* (2011) 58:1401–13. doi: 10.1016/j.jacc.2011.06.038
148. Fink C, Ergün S, Kralisch D, Remmers U, Weil J, Eschenhagen T. Chronic stretch of engineered heart tissue induces hypertrophy and functional improvement. *FASEB J.* (2000) 14:669–79. doi: 10.1096/fasebj.14.5.669
149. Zimmermann WH, Schneiderbanger K, Schubert P, Didié M, Münzel F, Heubach JF, et al. Tissue engineering of a differentiated cardiac muscle construct. *Circ Res.* (2002) 90:223–30. doi: 10.1161/hh0202.103644
150. Salazar BH, Cashion AT, Dennis RG, Birla RK. Development of a cyclic strain bioreactor for mechanical enhancement and assessment of bioengineered myocardial constructs. *Cardiovasc Eng Technol.* (2015) 6:533–45. doi: 10.1007/s13239-015-0236-8
151. Massai D, Pisani G, Isu G, Rodriguez Ruiz A, Cerino G, Galluzzi R, et al. Bioreactor platform for biomimetic culture and *in situ* monitoring of the mechanical response of *in vitro* engineered models of cardiac tissue. *Front Bioeng Biotechnol.* (2020) 8:733. doi: 10.3389/fbioe.2020.00733

152. Tulloch NL, Muskheli V, Razumova MV, Korte FS, Regnier M, Hauch KD, et al. Growth of engineered human myocardium with mechanical loading and vascular coculture. *Circ Res.* (2011) 109:47–59. doi: 10.1161/CIRCRESAHA.110.237206
153. Naito H, Melnychenko I, Didié M, Schneiderbanger K, Schubert P, Rosenkranz S, et al. Optimizing engineered heart tissue for therapeutic applications as surrogate heart muscle. *Circulation*. (2006) 114:I72–8. doi: 10.1161/CIRCULATIONAHA.105.001560
154. McCain ML, Sheehy SP, Grosberg A, Goss JA, Parker KK. Recapitulating maladaptive, multiscale remodeling of failing myocardium on a chip. *Proc Natl Acad Sci USA*. (2013) 110:9770–5. doi: 10.1073/pnas.1304913110
155. Ugolini GS, Pavesi A, Rasponi M, Fiore GB, Kamm R, Soncini M. Human cardiac fibroblasts adaptive responses to controlled combined mechanical strain and oxygen changes *in vitro*. *eLife*. (2017) 6:e22847. doi: 10.7554/eLife.22847.020
156. Occhetta P, Isu G, Lemme M, Conficconi C, Oertle P, Räz C, et al. A three-dimensional *in vitro* dynamic micro-tissue model of cardiac scar formation. *Integr Biol.* (2018) 10:174–83. doi: 10.1039/C7IB00199A
157. Balestrini JL, Billiar KL. Equibiaxial cyclic stretch stimulates fibroblasts to rapidly remodel fibrin. *J Biomech.* (2006) 39:2983–90. doi: 10.1016/j.jbiomech.2005.10.025
158. Balestrini JL, Billiar KL. Magnitude and duration of stretch modulate fibroblast remodeling. *J Biomech Eng.* (2009) 131:051005. doi: 10.1115/1.3049527
159. Yokoyama T, Sekiguchi K, Tanaka T, Tomaru K, Arai M, Suzuki T, et al. Angiotensin II and mechanical stretch induce production of tumor necrosis factor in cardiac fibroblasts. *Am J Physiol.* (1999) 276:H1968–76. doi: 10.1152/ajpheart.1999.276.6.H1968
160. Wang J, Chen H, Seth A, McCulloch CA. Mechanical force regulation of myofibroblast differentiation in cardiac fibroblasts. *Am J Physiol Heart Circ Physiol.* (2003) 285:H1871–81. doi: 10.1152/ajpheart.00387.2003
161. Ugolini GS, Rasponi M, Pavesi A, Santoro R, Kamm R, Fiore GB, et al. On-chip assessment of human primary cardiac fibroblasts proliferative responses to uniaxial cyclic mechanical strain. *Biotechnol Bioeng.* (2016) 113:859–69. doi: 10.1002/bit.25847
162. Atance J, Yost MJ, Carver W. Influence of the extracellular matrix on the regulation of cardiac fibroblast behavior by mechanical stretch. *J Cell Physiol.* (2004) 200:377–86. doi: 10.1002/jcp.20034
163. Watson CJ, Phelan D, Collier P, Horgan S, Glezeva N, Cooke G, et al. Extracellular matrix sub-types and mechanical stretch impact human cardiac fibroblast responses to transforming growth factor beta. *Connect Tissue Res.* (2014) 55:248–56. doi: 10.3109/03008207.2014.904856
164. Butt RP, Bishop JE. Mechanical load enhances the stimulatory effect of serum growth factors on cardiac fibroblast procollagen synthesis. *J Mol Cell Cardiol.* (1997) 29:1141–51. doi: 10.1006/jmcc.1996.0347
165. Li X, Garcia-Elias A, Benito B, Nattel S. The effects of cardiac stretch on atrial fibroblasts: analysis of the evidence and potential role in atrial fibrillation. *Cardiovasc Res*. (2021). doi: 10.1093/cvr/cvab035. [Epub ahead of print].
166. Rysä J, Tokola H, Ruskoaho H. Mechanical stretch induced transcriptomic profiles in cardiac myocytes. *Sci Rep*. (2018) 8:4733. doi: 10.1038/s41598-018-23042-w
167. Wang BW, Wu GJ, Cheng WP, Shyu KG. Mechanical stretch via transforming growth factor-β1 activates microRNA-208a to regulate hypertrophy in cultured rat cardiac myocytes. *J Formos Med Assoc.* (2013) 112:635–43. doi: 10.1016/j.jfma.2013.01.002
168. Liao XD, Wang XH, Jin HJ, Chen LY, Chen Q. Mechanical stretch induces mitochondria-dependent apoptosis in neonatal rat cardiomyocytes and G2/M accumulation in cardiac fibroblasts. *Cell Res.* (2004) 14:16–26. doi: 10.1038/sj.cr.7290198
169. Stevens KR, Ungrin MD, Schwartz RE, Ng S, Carvalho B, Christine KS, et al. InVERT molding for scalable control of tissue microarchitecture. *Nat Commun.* (2013) 4:1847. doi: 10.1038/ncomms2853
170. Hoang P, Wang J, Conklin BR, Healy KE, Ma Z. Generation of spatial-patterned early-developing cardiac organoids using human pluripotent stem cells. *Nat Protoc.* (2018) 13:723–37. doi: 10.1038/nprot.2018.006
171. Nikolaev M, Mitrofanova O, Broguiere N, Geraldo S, Dutta D, Tabata Y, et al. Homeostatic mini-intestines through scaffold-guided organoid morphogenesis. *Nature.* (2020) 585:574–8. doi: 10.1038/s41586-020-2724-8
172. Skylar-Scott MA, Uzel SGM, Nam LL, Ahrens JH, Truby RL, Damaraju S, et al. Biomanufacturing of organ-specific tissues with high cellular density and embedded vascular channels. *Sci Adv.* (2019) 5:eaaw. doi: 10.1126/sciadv.aaw2459
173. Mirdamadi E, Tashman JW, Shiwarski DJ, Palchesko RN, Feinberg AW. FRESH 3D bioprinting a full-size model of the human heart. *ACS Biomater Sci Eng.* (2020) 6:6453–9. doi: 10.1021/acsbiomaterials.0c01133
174. Bittner SM, Smith BT, Diaz-Gomez L, Hudgins CD, Melchiorri AJ, Scott DW, et al. Fabrication and mechanical characterization of 3D printed vertical uniform and gradient scaffolds for bone and osteochondral tissue engineering. *Acta Biomater.* (2019) 90:37–48. doi: 10.1016/j.actbio.2019.03.041
175. Liu W, Zhang YS, Heinrich MA, De Ferrari F, Jang HL, Bakht SM, et al. Rapid continuous multimaterial extrusion bioprinting. *Adv Mater*. (2017) 29:1604630. doi: 10.1002/adma.201604630
176. Hausenloy DJ, Bøtker HE, Ferdinandy P, Heusch G, Ng GA, Redington A, et al. Cardiac innervation in acute myocardial ischaemia/reperfusion injury and cardioprotection. *Cardiovasc Res.* (2019) 115:1167–77. doi: 10.1093/cvr/cvz053
177. Gentek R, Hoeffel G. The innate immune response in myocardial infarction, repair, and regeneration. *Adv Exp Med Biol.* (2017) 1003:251–72. doi: 10.1007/978-3-319-57613-8_12
178. Frick C, Dettinger P, Renkawitz J, Jauch A, Berger CT, Recher M, et al. Nano-scale microfluidics to study 3D chemotaxis at the single cell level. *PLoS ONE.* (2018) 13:e0198330. doi: 10.1371/journal.pone.0198330
179. Li Y, Xuan J, Hu R, Zhang P, Lou X, Yang Y. Microfluidic triple-gradient generator for efficient screening of chemical space. *Talanta.* (2019) 204:569–75. doi: 10.1016/j.talanta.2019.06.018
180. Gandavarapu NR, Azagarsamy MA, Anseth KS. Photo-click living strategy for controlled, reversible exchange of biochemical ligands. *Adv Mater.* (2014) 26:2521–6. doi: 10.1002/adma.201304847
181. Dai X, Wiernek S, Evans JP, Runge MS. Genetics of coronary artery disease and myocardial infarction. *World J Cardiol.* (2016) 8:1–23. doi: 10.4330/wjc.v8.i1.1
182. Yang X, Pabon L, Murry CE. Engineering adolescence: maturation of human pluripotent stem cell-derived cardiomyocytes. *Circ Res.* (2014) 114:511–23. doi: 10.1161/CIRCRESAHA.114.300558
183. Ronaldson-Bouchard K, Ma SP, Yeager K, Chen T, Song L, Sirabella D, et al. Advanced maturation of human cardiac tissue grown from pluripotent stem cells. *Nature.* (2018) 556:239–43. doi: 10.1038/s41586-018-0016-3
184. Zhao Y, Wang EY, Davenport LH, Liao Y, Yeager K, Vunjak-Novakovic G, et al. A multimaterial microphysiological platform enabled by rapid casting of elastic microwires. *Adv Healthc Mater.* (2019) 8:e1801187. doi: 10.1002/adhm.201801187
185. Yip JK, Sarkar D, Petersen AP, Gipson JN, Tao J, Kale S, et al. Contact photolithography-free integration of patterned and semi-transparent indium tin oxide stimulation electrodes into polydimethylsiloxane-based heart-on-a-chip devices for streamlining physiological recordings. *Lab Chip*. (2021) 21:674–87. doi: 10.1039/D0LC00948B
186. Dipalo M, Rastogi SK, Matino L, Garg R, Bliley J, Iachetta G, et al. Intracellular action potential recordings from cardiomyocytes by ultrafast pulsed laser irradiation of fuzzy graphene microelectrodes. *Sci Adv*. (2021) 7:eabd5175. doi: 10.1126/sciadv.abd5175
187. Marasco CC, Enders JR, Seale KT, McLean JA, Wikswo JP. Real-time cellular exometabolome analysis with a microfluidic-mass spectrometry platform. *PLoS ONE.* (2015) 10:e0117685. doi: 10.1371/journal.pone.0117685
188. McKenzie JR, Cognata AC, Davis AN, Wikswo JP, Cliffel DE. Real-time monitoring of cellular bioenergetics with a multianalyte screen-printed electrode. *Anal Chem.* (2015) 87:7857–64. doi: 10.1021/acs.analchem.5b01533
189. Zhang YS, Aleman J, Shin SR, Kilic T, Kim D, Mousavi Shaegh SA, et al. Multisensor-integrated organs-on-chips platform for automated and continual *in situ* monitoring of organoid behaviors. *Proc Natl Acad Sci USA.* (2017) 114:E2293–302. doi: 10.1073/pnas.1612906114

Conflict of Interest: MM is an inventor on US patent US9857356B2 filed by Harvard University and licensed to Emulate, Inc.

The remaining author declares that the research was conducted in the absence of any commercial or financial relationships that could be construed as a potential conflict of interest.

frontiers
in Cardiovascular Medicine

MINI REVIEW
published: 14 September 2021
doi: 10.3389/fcvm.2021.708470

Wnt Signaling in Vascular Calcification

Kaylee Bundy, Jada Boone and C. LaShan Simpson*

Agricultural and Biological Engineering, Mississippi State University, Starkville, MS, United States

Cardiovascular disease is a worldwide epidemic and considered the leading cause of death globally. Due to its high mortality rates, it is imperative to study the underlying causes and mechanisms of the disease. Vascular calcification, or the buildup of hydroxyapatite within the arterial wall, is one of the greatest contributors to cardiovascular disease. Medial vascular calcification is a predictor of cardiovascular events such as, but not limited to, hypertension, stiffness, and even heart failure. Vascular smooth muscle cells (VSMCs), which line the arterial wall and function to maintain blood pressure, are hypothesized to undergo a phenotypic switch into bone-forming cells during calcification, mimicking the manner by which mesenchymal stem cells differentiate into osteoblast cells throughout osteogenesis. RunX2, a transcription factor necessary for osteoblast differentiation and a target gene of the Wnt signaling pathway, has also shown to be upregulated when calcification is present, implicating that the Wnt cascade may be a key player in the transdifferentiation of VSMCs. It is important to note that the phenotypic switch of VSMCs from a healthy, contractile state to a proliferative, synthetic state is necessary in response to the vascular injury surrounding calcification. The lingering question, however, is if VSMCs acquire this synthetic phenotype through the Wnt pathway, how and why does this signaling occur? This review seeks to highlight the potential role of the canonical Wnt signaling pathway within vascular calcification based on several studies and further discuss the Wnt ligands that specifically aid in VSMC transdifferentiation.

Keywords: vascular calcification, Wnt signaling, phenotypes, transdifferentiation, Runx2

Edited by:
David Wu,
University of Chicago, United States

Reviewed by:
Cécile Oury,
University of Liège, Belgium
Subhi Marwari,
The Scripps Research Institute,
United States

***Correspondence:**
C. LaShan Simpson
clsimpson@abe.msstate.edu

Specialty section:
This article was submitted to Atherosclerosis and Vascular Medicine,
a section of the journal
Frontiers in Cardiovascular Medicine

Received: *12 May 2021*
Accepted: *26 July 2021*
Published: *14 September 2021*

Citation:
Bundy K, Boone J and Simpson CL (2021) Wnt Signaling in Vascular Calcification.
Front. Cardiovasc. Med. 8:708470.
doi: 10.3389/fcvm.2021.708470

INTRODUCTION

Cardiovascular disease (CVD) is a worldwide epidemic. As the leading cause of death across the world, many researchers are working to better understand the causes and mechanisms resulting in the disease (1). One of the contributors and predictors of cardiovascular mortalities is vascular calcification, the buildup of hydroxyapatite deposits within the arterial wall. The mineral deposition can occur in either the intimal or medial layers of the arteries; the location depends upon the causative factors and can result in different effects within the body (2). Conditions conducive of calcification include, but are not limited to, hypercalcemia, hyperphosphatemia, and mechanical stress which induce changes to the arteries on a cellular level. Medial calcification, which occurs within the vascular smooth muscle cells (VSMCs) lining the middle layer of the arterial wall, has been linked to hypertension, stiffness, and increased risk of heart failure (3). A comprehensive understanding of the various changes within the VSMCs during calcification may help to identify a key regulator to target with a treatment. VSMCs are derived from mesenchymal stem cells and are not terminally differentiated; they are known to maintain their plasticity and can differentiate into other mesenchymal cell derivatives (4). During calcification, studies have shown VSMCs undergo a cellular mediated phenotypic switch into cells resembling bone forming osteoblasts, characterized by a loss of smooth muscle markers and an upregulation of osteogenic markers (5). Runx2, a transcription factor necessary for osteoblast differentiation, is upregulated within calcifying VSMCs and may be the cause of this transdifferentiation (6). Runx2 is a target gene of the Wnt signaling cascade, which is known to regulate bone development during embryogenesis, as well as direct bone turnover and remodeling (7). Because mineral deposition in VSMCs appears to be very similar to bone formation, many studies have begun investigating Wnt signaling as a possible mechanism and regulator of vascular calcification. This mini review seeks to culminate the observations made so far on VSMC phenotypes and the regulatory role of Wnt in VSMC plasticity to help construct a holistic but focused view of the cellular factors influencing vascular calcification.

VSMC PHENOTYPES

Before the 1960s, it was commonly thought that there were two cell types in the arterial media: smooth muscle cells and fibroblasts. The reason for this assumption was due to the presence of connective tissue within the middle layer, like that formed by fibroblasts. However, in the early 1960s, studies began providing evidence for only one cell type, smooth muscle cells, within the arterial media (8, 9). In 1967, Wissler suggested that the medial cells are a multifunctional mesenchyme cell type capable of both contracting and fabricating connective tissue. Wissler was one of the first to realize smooth muscle cell plasticity and that the once thought fibroblasts are really a dedifferentiated smooth muscle cell (10). Over the next few decades, much more was learned about the range of VSMC phenotypes. The principal function of VSMCs within the body is to maintain blood pressure. To achieve this function, the cells primarily maintain a contractile phenotype that is characterized by slow proliferation, response to neurotransmitters, and expression of cellular markers such as α-smooth muscle actin, smooth muscle myosin heavy chains 1 and 2, calponin, and smoothelin (4). When in the contractile state, the cell has a spindle shape with many focal adhesions and integrin receptors to connect the cell to the ECM and allow for contraction. The cytoplasm contains primarily myofilaments, with a low number of other organelles such as rough endoplasmic reticulum, Golgi, and free ribosomes (11). In response to a necessary change in function, such as the need for increased proliferation, VSMCs may display a dedifferentiated phenotype commonly referred to as synthetic. The synthetic state is characterized primarily by proliferation, migration, and extracellular matrix production, so the cytoplasm of the cells contains a greater amount of rough endoplasmic reticulum, Golgi, and free ribosomes and a smaller number of myofilaments (11). The distinctions between the contractile and synthetic phenotypes can be seen in **Figure 1** (12). The need for greater proliferation as seen in the synthetic state can arise in various circumstances but has been particularly characterized in response to vascular injury.

VSMC TRANSDIFFERENTIATION

Following injury and for vascular repair to occur, the VSMCs revert to the synthetic state explained above. However, as the synthetic phenotype occurs as a dedifferentiated state, the cells can then further differentiate into other cell types depending on environmental cues. VSMCs have been shown to downregulate contractile proteins and display characteristics of other mesenchymal lineage cell types, including those of osteoblasts, chondrocytes, and adipocytes (13). In pro-calcifying conditions, such as high levels of serum phosphate, VSMCs begin to express osteogenic markers including Runx2, Sp7, osteopontin, osteocalcin, alkaline phosphatase, Sox9, and collagen types II and X (4). A study done by Patel et al. sought to evaluate the similarity between bone formation and calcification by comparing mouse osteoblast with control and calcifying VSMCs (14). The quantity of calcium deposition between osteoblasts and calcifying VSMCs was similar, but osteoblasts formed many large bone nodules whereas calcifying VSMCs formed small discrete regions of calcification. Calcifying VSMCs saw a 6-fold increase in early osteoblast markers Runx2 and Sp7 compared to control VSMCs but still a 3-fold lower amount compared to the osteoblasts. The study concluded that calcifying VSMCs take on a transitional phenotype between but distinct from that of healthy VSMCs and bone-forming osteoblasts (14). Many other studies have also noted the increase and possible requirement of Runx2 expression, a transcription factor necessary for osteoblast differentiation, in calcifying VSMCs (15–18). Though it is well understood that Runx2 is at least partially responsible for the osteogenic switch, it is necessary to determine why the transcription factor is being upregulated in the cells. Gaur et al. determined the Runx2 gene is directly targeted by the canonical Wnt signaling pathway which activates the gene and regulates bone production during development and in adults (19). Because of the governing role of Runx2 in osteoblast differentiation and vascular calcification, studies are investigating Wnt signaling as a possible mechanism of calcification.

THE WNT SIGNALING CASCADE

A family of 19 secreted glycoproteins, Wnt signaling is conserved among metazoan animals to regulate many cellular functions during development including cell fate determination, migration, polarity, primary axis formation, organogenesis, and stem cell renewal (20). Wnt ligands each consist of 350-400 amino acids including 22–24 conserved cysteine residues (7). The signaling cascade is activated when one of the extracellular Wnt ligands binds to a Frizzled (Fz) receptor. Fz is a family of 10 different seven-member transmembrane proteins. A Wnt signal binds to the cysteine-rich extracellular N-terminal of a Fz receptor associated with co-receptors such as LRP5 and LRP6

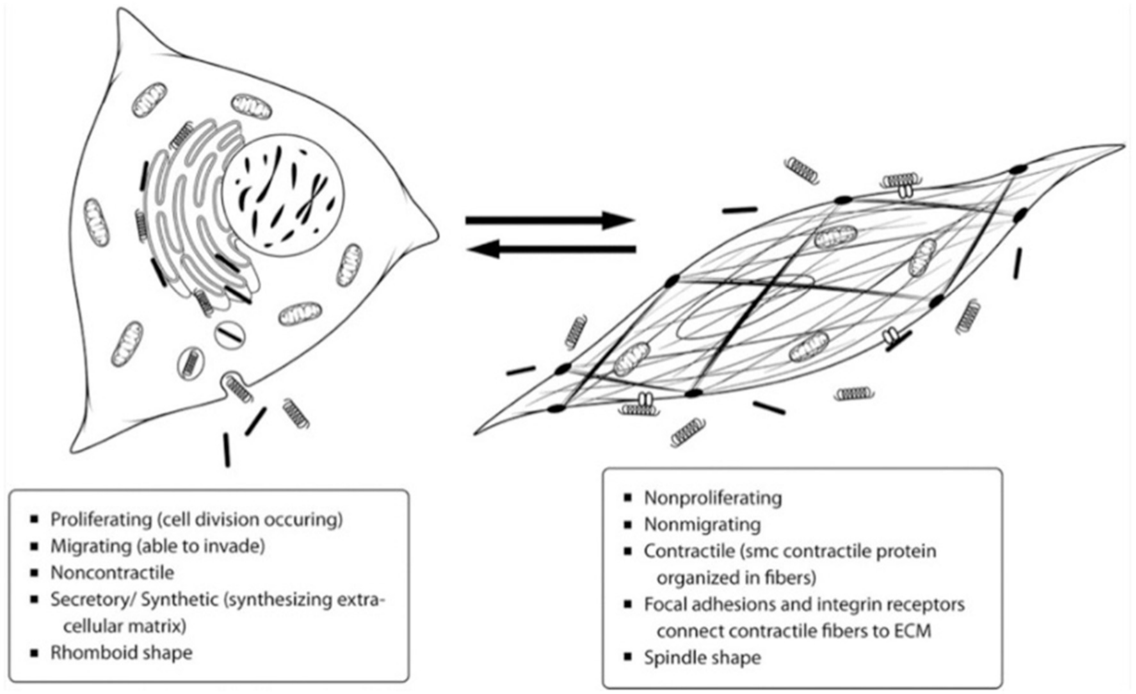

FIGURE 1 | Depiction of the differences between the contractile and synthetic VSMC phenotypes. Most VSMCs exist in the contractile state on the right to maintain blood pressure, but they can dedifferentiate into the synthetic phenotype on the left as necessary for proliferation and tissue repair (12).

of the low-density lipoprotein receptor family (20). LRP5 and LRP6 are transmembrane proteins that help Fz to induce the canonical Wnt pathway (7). After Wnt binds to Fz, the signal recruits the cytoplasmic phosphoprotein Disheveled (Dsh) to the plasma membrane. At this point, the signaling pathway diverges into three separate branches: Canonical (β-catenin dependent), Planar Cell Polarity, and Wnt/Ca^{2+} (20). The canonical branch has been most widely studied and is the segment hypothesized to play a role in vascular calcification. Dsh aids in the recruitment of an Axin and GSK3 complex (21). Under normal, non-activated Wnt conditions, Axin is the scaffolding protein of a β-catenin destruction complex. The destruction complex is made up of Axin, glycogen synthase kinase 3 (GSK-3), casein kinase 1 (CK1), adenomatous polyposis coli (APC) protein, and the E3-ubiquitin ligase β-TrCP (22). The complex typically phosphorylates and proteolytically degrades any accumulation of β-catenin in the cytoplasm. When Axin is recruited to the plasma membrane because of Wnt signaling, the destruction complex is disassembled, resulting in an upregulation of β-catenin (21). β-catenin then translocates to the nucleus and forms a transcriptional complex with LEF-1/TCF DNA-binding transcription factors. The complex associates to the promoter of Wnt target genes that results in the upregulation of those genes (20). In summary, during canonical Wnt signaling, the binding of Wnt ligands to the cell membrane inhibits the β-catenin destruction complex resulting in the translocation of β-catenin to the nucleus where the transcription of Wnt target genes is induced, as shown in **Figure 2** (20).

WNT AND RUNX2 IN OSTEOGENESIS

As stated before, studies have shown that Runx2 is a target gene of Wnt signaling, and activation of Runx2 by Wnt stimulates osteoblast differentiation and bone formation (19). In mesenchymal stem cells, Runx2 regulates the expression of other bone related proteins, such as osterix, osteocalcin, and sclerostin, directing the cell to an osteogenic phenotype (6). Expression of Runx2 begins in uncommitted stem cells, increases in osteoblast precursors, peaks in immature osteoblast, and decreases once osteoblasts mature (23). This expression of Runx2 is modulated by canonical Wnt signaling, resulting in an inhibition of chondrocyte differentiation in early mesenchymal cells and directing the progenitors to become osteoblasts (23). The process occurs during embryonic development when establishing the body axis and tissue and organ development and functions after birth in bone maintenance and repair (24).

WNT IN VASCULAR CALCIFICATION

Because Wnt is involved in bone turnover and calcifying smooth muscle cells resemble osteoblasts, Wnt may play a governing role in calcification. A recent comprehensive review by Tyson et al. highlights the role of mechanotransduction, explaining how the compressive and tensile strains experienced by VSMC under increased stress may induce bone-like Wnt mediated remodeling in the arterial wall (25). Interestingly, Wnt ligands and signals are found in noncalcifying VSMCs and may contribute to normal

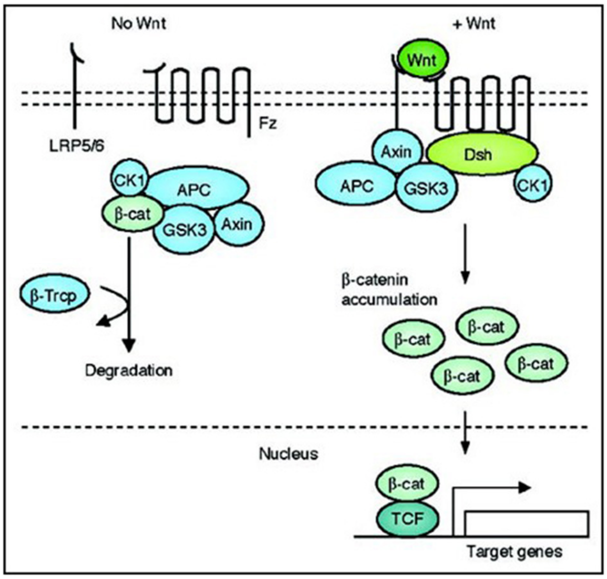

FIGURE 2 | Schematic of the canonical Wnt signaling cascade. Binding of a Wnt ligand to the cell surface causes the translocation of β-catenin to the nucleus and the upregulation of Wnt target genes (20).

regulation of the VSMC phenotype, proliferation, and survival, particularly in response to vascular injury. Studies from the early 2000s indicate the presence of Wnt proteins in VSMCs. A study done in 2004 by Wang et al. used a transfection assay to show that loss of the Wnt coreceptor LRP6 function in VSMCs inhibited cell cycle progression, demonstrating a role for LRP6 and Wnt in VSMC growth and fate (26). Another study done by Wang et al. in 2005 noted that Fz1 is highly expressed in VSMC tissues indicating active Wnt signaling, and they suggest a role in development and response to environmental stimulus (27). In agreement with these studies, in 2014 Wu et al. found that a Wnt ligand influences VSMC migration and adhesion to collagen type I (28). A transwell migration and wound healing assay showed that Wnt3a significantly increased VSMC migration, and an adhesion assay showed that Wnt3a treated VSMCs were able to adhere more to collagen type I. The study also used Western blot analysis to test for several canonical Wnt components, including β-catenin, GSK-3β, ILK, and β1-integrin. Wnt3a treatment upregulated phosphorylated β-catenin, phosphorylated GSK-3β, and ILK and activated β1-integrin in VSMCs, providing additional evidence of Wnt effecting protein expression and potential therapeutic targets (28).

Other studies have looked at the involvement of Wnt particularly in calcifying VSMCs. Mikhaylova et al. found that Wnt3a induced a 3.5-fold increase in mineralization when used with hypertrophic chondrocyte conditioned media, suggesting Wnt paired with other chondrocyte-derived factors, such as VEGF, may be a positive regulator of calcification (29). Rong et al. used phosphate and BMP-2 to induce calcification in VSMCs, and then tested the cultures for various cellular markers (5). They were able to observe a phenotypic change as SM 22α and α-SMA were downregulated and osteogenic markers including Msx2, RunX2, Pit1, and β-catenin were upregulated. When β-catenin was knocked down using a transfection assay, these results were reversed, indicating a dependent role of β-catenin and Wnt signaling in VSMC transdifferentiation (5). In 2016, Cai et al. also provided strong evidence for the involvement of Wnt signaling in VSMC transdifferentiation and mineralization (6). In a pro-calcifying high phosphate environment, RunX2 expression was induced in a time-dependent manner, observed by Western blot analysis. To determine if the increase in RunX2 expression was caused by Wnt signaling, they used Western blots to track β-catenin activity and found that both dephosphorylated and phosphorylated β-catenin was upregulated. Immunostaining showed the high phosphate treatment also promoted β-catenin translocation to the nucleus, a typical cellular response to Wnt signaling, and they were able to use luciferase reporter assays to identify two specific TCF binding elements that mediate the interaction with TCF in response to β-catenin translocation. Further evidence of Wnt included a positive result for phosphorylation of LRP6, a Wnt dependent reaction. To confirm these results, a Wnt inhibitor was used that abolished RunX2 induction during high phosphate treatment. VSMCs were then treated with Wnt3a, which successfully induced calcium deposition and osteocalcin induction. The results from Cai et al. suggest a specific pathway in which Wnt3a can activate β-catenin and induce RunX2 and osteocalcin expression and promote calcification of VSMCs (6).

WHICH WNT?

Though there is surmounting evidence of the involvement of Wnt in vascular calcification, each study identifies different inducers, inhibitors, and regulatory proteins relative to Wnt and even other signaling pathways, such as VEGF and BMPs mentioned previously. Although they must be studied independently, it is likely that each of these different processes may contribute and work together to create an environment conducive to VSMC transdifferentiation and thus calcification. As Wnt has been more heavily investigated as a possible mechanism, some studies have begun testing specific Wnt ligands to determine if one contributes most significantly toward calcification. Wnt7b has been shown to play a role in vascular development and can activate canonical Wnt signaling (27). Wnt16 is also expressed in VSMCs. In a recent study by Behrmann et al., *in vitro* and *in vivo* studies showed that Wnt16 suppressed the contractile phenotype, supported osteofibrogenic matrix metabolism, and contributed to aortic stiffening (30). However, the most studied Wnt ligand in vascular calcification is Wnt3a. Some of these studies were referenced in the previous section (6, 28, 29). These studies provide some of the most convincing support for the Wnt signaling cascade in calcification indicating that Wnt3a may be the focus of future studies working toward a treatment.

CONCLUSION

In conclusion, VSMCs display a range of phenotypes within two key states: contractile and synthetic. When VSMCs exist in the synthetic state, they exhibit a less differentiated phenotype and can be directed down different cell lineages in response to abnormal environmental cues. A high phosphate environment can induce calcification in VSMCs and direct them toward an osteogenic phenotype. This transdifferentiation is characterized by a loss of VSMC markers and an increase in osteogenic markers, most notably RunX2. Because of the upregulation of RunX2, many believe the canonical Wnt signaling pathway may be the cellular mechanism resulting in the osteogenic switch of VSMCs. RunX2 is a target gene of Wnt, which also involves many other proteins, including β-catenin, LRPs, Fzd, Dsh, and Axin. Wnt has been found to regulate normal VSMC phenotype and proliferation, and much data has been elucidated for a role in VSMC transdifferentiation during calcification. Many studies have used Western blots, PCR, and luciferase assays to identify various Wnt proteins, notably β-catenin, and track the Wnt cascade to determine its involvement in the initiation and regulation of medial vascular calcification. Future research strategies should focus these methods on regular time intervals to determine at what point during VSMC transdifferentiation Wnt is activated. Experiments should also begin investigating other Wnt proteins in addition to β-catenin to identify any other major regulatory factors. If a particular fate-determining time point and feedback loop is identified as the primary mechanism of action for VSMCS transdifferentiation, Wnt could be manipulated as a potential therapy for vascular calcification. Knocking out Wnt, or its regulators, with Wnt inhibitors, such as sclerostin, and determining the effect will help determine whether Wnt is a valuable therapeutic target. Additional studies should be done like McArthur et al. who found that sclerostin could successfully prevent Wnt proteins from attaching to their corresponding receptors and ultimately resulted in reduction of calcification (16). The study illustrates the potential of manipulating Wnt for calcification treatment, though much more extensive preclinical trails are necessary. The most common preclinical disease model for atherosclerosis, which closely mimics calcification, is Apoe$^{-/-}$ mice (31). More recently, a model utilizing calcium chloride to induce calcification has been established (32). Using these models to further test Wnt targeted calcification treatments may be a logical next step. This literature review has summarized the current understanding of the role of VSMCs in calcification and helped to identify ways in which to further study the mechanism of the disease. However, there are some limitations and current gaps in knowledge. Though Wnt must be isolated to study the pathway independently, more than likely the Wnt cascade operates dependently upon other pathways and external factors. In addition, to our knowledge there has not yet been significant investigation into the presence of Wnt ligands under normal conditions, and it is unclear whether Wnt is always present within the arterial media. Furthermore, if this is the case, studies have not explored what activates Wnt signaling leading to calcification. As the Wnt family consists of extracellular ligands, cell-to-cell signaling and mechanical stimulus could be contributors. Thought it appears targeting Wnt could be a potential treatment, it is yet unclear whether a Wnt therapy would reverse calcification or only prevent further buildup. Based on these theories, there remains a need for investigating further into the typical behavior of Wnt under healthy and disease conditions, as well as the underlying mechanism behind the activation of the Wnt cascade. As a result, additional research may lead to preclinical trials and eventually allow for a targeted treatment for vascular calcification.

AUTHOR CONTRIBUTIONS

KB conducted a comprehensive literature review and transcribed the bulk of the manuscript. JB contributed to the literature review and writing of the manuscript. CS helped to develop the concept for the work and played a supervisory and editorial role. All authors contributed to the article and approved the submitted version.

FUNDING

This work was supported by the Mississippi Agricultural and Forestry Experiment Station.

ACKNOWLEDGMENTS

The authors would like to acknowledge the Shackouls Honors College and Bagley College of Engineering of Mississippi State University.

REFERENCES

1. Okwuosa IS, Lewsey SC, Adesiyun T, Blumenthal RS, Yancy CW. Worldwide disparities in cardiovascular disease: Challenges and solutions. *Int J Cardiol.* (2016) 202:433–440. doi: 10.1016/j.ijcard.2015.08.172
2. Demer LL, Tintut Y. Vascular calcification: Pathobiology of a multifaceted disease. Circulation. (2008) 117:2938–2948. doi: 10.1161/CIRCULATIONAHA.107.743161
3. Persy V, D'Haese P. Vascular calcification and bone disease: the calcification paradox. *Trends Mol Med.* (2009) 15:405–16. doi: 10.1016/j.molmed.2009.07.001
4. Durham AL, Speer MY, Scatena M, Giachelli CM, Shanahan CM. Role of smooth muscle cells in vascular calcification: implications in atherosclerosis and arterial stiffness. *Cardiovasc Res.* (2018) 114:590–600. doi: 10.1093/cvr/cvy010
5. Rong S, Zhao X, Jin X, Zhang Z, Chen L, Zhu Y, et al. Vascular calcification in chronic kidney disease is induced by bone morphogenetic protein-2 via a mechanism involving the Wnt/β-catenin pathway. *Cell Physiol Biochem.* (2014) 34:2049–60. doi: 10.1159/000366400
6. Cai T, Sun D, Duan Y, Wen P, Dai C, Yang J, et al. WNT/β-catenin signaling promotes VSMCs to osteogenic transdifferentiation and calcification through directly modulating Runx2 gene expression. *Exp Cell Res.* (2016) 345:206–217. doi: 10.1016/j.yexcr.2016.06.007
7. Kobayashi Y, Maeda K, Takahashi N. Roles of Wnt signaling in bone formation and resorption. *Jpn Dent Sci Rev.* (2008) 44:76–82. doi: 10.1016/j.jdsr.2007.11.002

8. Buck RC. Histogenesis and morphology of arterial tissue. *Atheroscler Orig.* (1963) 1–38.
9. Pease DC, Paule W. Electron microscopy of elastic arteries; the thoracic aorta of the rat. *J Ultrastruct Res.* (1960) 3:469–483. doi: 10.1016/S0022-5320(60)90023-X
10. Wissler RW. The arterial medial cell, smooth muscle, or multifunctional mesenchyme? *Circulation.* (1967) 36:1–4. doi: 10.1161/01.CIR.36.1.1
11. Campbell G, Campbell J. Smooth muscle phenotypic changes in arterial wall homeostasis: implications for the pathogenesis of atherosclerosis. *Exp Mol Pathol.* (1985) 42:139–162. doi: 10.1016/0014-4800(85)90023-1
12. Byanova K. Effects of the Acta2 R258C mutation on vascular smooth muscle cell phenotype and properties. *UT GSBS Diss Theses* (2012).
13. Iyemere VP, Proudfoot D, Weissberg PL, Shanahan CM. Vascular smooth muscle cell phenotypic plasticity and the regulation of vascular calcification. *J Intern Med.* (2006) 260:192–210. doi: 10.1111/j.1365-2796.2006.01692.x
14. Patel JJ, Bourne LE, Davies BK, Arnett TR, MacRae VE, Wheeler-Jones CP, et al. Differing calcification processes in cultured vascular smooth muscle cells and osteoblasts. *Exp Cell Res.* (2019) 380:100–113. doi: 10.1016/j.yexcr.2019.04.020
15. Lin ME, Chen T, Leaf EM, Speer MY, Giachelli CM. Runx2 expression in smooth muscle cells is required for arterial medial calcification in mice. *Am J Pathol.* (2015) 185:1958–1969. doi: 10.1016/j.ajpath.2015.03.020
16. Mcarthur KM, Kay AM, Mosier JA, Grant JN, Stewart JA, Simpson CL. Manipulating the plasticity of smooth muscle cells to regulate vascular calcification. *AIMS Cell Tissue Eng.* (2017) 1:165–79. doi: 10.3934/celltissue.2017.3.165
17. Chen Y, Zhao X, Wu H. Transcriptional programming in arteriosclerotic disease: a multifaceted function of the Runx2. *Arterioscler Thromb Vasc Biol.* (2020) 41:20–34. doi: 10.1161/ATVBAHA.120.313791
18. Cobb AM, Yusoff S, Hayward R, Ahmad S, Sun M, Verhulst A, et al. Runx2 (Runt-Related Transcription Factor 2) Links the DNA Damage Response to Osteogenic Reprogramming and Apoptosis of Vascular Smooth Muscle Cells. *Arterioscler Thromb Vasc Biol.* (2020) 2:1339–57. doi: 10.1161/ATVBAHA.120.315206
19. Gaur T, Lengner CJ, Hovhannisyan H, Bhat RA, Bodine PVN, Komm BS, et al. Canonical WNT signaling promotes osteogenesis by directly stimulating Runx2 gene expression. *J Biol Chem.* (2005) 280:33132–40. doi: 10.1074/jbc.M500608200
20. Komiya Y, Habas R. Wnt signal transduction pathways. *Organogenesis.* (2008) 4:68–75. doi: 10.4161/org.4.2.5851
21. Song X, Wang S, Li L. New insights into the regulation of Axin function in canonical Wnt signaling pathway. *Protein Cell.* (2014) 5:186–93. doi: 10.1007/s13238-014-0019-2
22. Stamos JL, Weis WI. The β-catenin destruction complex. *Cold Spring Harb Perspect Biol.* (2013) 5:1–16. doi: 10.1101/cshperspect.a007898
23. Komori T. Regulation of proliferation, differentiation and functions of osteoblasts by runx2. *Int J Mol Sci.* (2019) 20:1694. doi: 10.3390/ijms20071694
24. Duan P, Bonewald LF. The role of the WNT/β-catenin signaling pathway in formation and maintenance of bone and teeth. *Int J Biochem Cell Biol.* (2016) 77:23–9. doi: 10.1016/j.biocel.2016.05.015
25. Tyson J, Bundy K, Roach C, Douglas H, Ventura V, Segars MF, et al. Mechanisms of the osteogenic switch of smooth muscle cells in vascular calcification: Wnt signaling, bmps, mechanotransduction, and endmt. *Bioengineering.* (2020) 7:88. doi: 10.3390/bioengineering7030088
26. Wang X, Adhikari N, Li Q, Hall JL. LDL receptor-related protein LRP6 regulates proliferation and survival through the Wnt cascade in vascular smooth muscle cells. *Am J Physiol Heart Circ Physiol.* (2004) 287:2376–83. doi: 10.1152/ajpheart.01173.2003
27. Wang Z, Shu W, Lu MM, Morrisey EE. Wnt7b activates canonical signaling in epithelial and vascular smooth muscle cells through interactions with Fzd1, Fzd10, and LRP5. *Mol Cell Biol.* (2005) 25:5022–30. doi: 10.1128/MCB.25.12.5022-5030.2005
28. Wu X, Wang J, Jiang H, Hu Q, Chen J, Zhang J, et al. Wnt3a activates β1-integrin and regulates migration and adhesion of vascular smooth muscle cells. *Mol Med Rep.* (2014) 9:1159–64. doi: 10.3892/mmr.2014.1937
29. Mikhaylova L, Malmquist J, Nurminskaya M. Regulation of in vitro vascular calcification by BMP4, VEGF and Wnt3a. *Calcif Tissue Int.* (2007) 81:372–81. doi: 10.1007/s00223-007-9073-6
30. Behrmann A, Zhong D, Sabaeifard P, Li L, Goodarzi M, Lemoff A, et al. Wnt16 regulates vascular matrix metabolism and arterial stiffness in the ldlr-/- mouse model of diet-induced metabolic syndrome. *Arterioscler Thromb Vasc Biol.* (2020) 40:A331.
31. MacAskill MG, McDougald W, Alcaide-Corral C, Newby DE, Tavares AAS, Hadoke PWF, et al. Characterisation of an atherosclerotic micro-calcification model using ApoE−/− mice and PET/CT. *IJC Hear Vasc.* (2020) 31:10–12. doi: 10.1016/j.ijcha.2020.100672
32. Abrao S, Campos C, Cavalcante R, Eggermont J, Lemos P, Lederman A, et al. Percutaneous endovascular delivery of calcium chloride to the intact porcine carotid artery: A novel animal model of arterial calcification. *Catheter Cariovascular Interv.* (2020) 96:E484–92. doi: 10.1002/ccd.29070

Conflict of Interest: The authors declare that the research was conducted in the absence of any commercial or financial relationships that could be construed as a potential conflict of interest.

frontiers in Cardiovascular Medicine

ORIGINAL RESEARCH
published: 28 September 2021
doi: 10.3389/fcvm.2021.707897

Notch Intracellular Domain Plasmid Delivery via Poly(Lactic-Co-Glycolic Acid) Nanoparticles to Upregulate Notch Pathway Molecules

Victoria L. Messerschmidt [1,2†], Uday Chintapula [1,2†], Aneetta E. Kuriakose [1,2], Samantha Laboy [1], Thuy Thi Dang Truong [1], LeNaiya A. Kydd [1], Justyn Jaworski [1], Zui Pan [3], Hesham Sadek [2], Kytai T. Nguyen [1,2] and Juhyun Lee [1,2*]*

[1] Department of Bioengineering, University of Texas at Arlington, Arlington, TX, United States, [2] Department of Internal Medicine, University of Texas Southwestern Medical Center, Dallas, TX, United States, [3] College of Nursing and Health Innovation, University of Texas at Arlington, Arlington, TX, United States

Edited by:
Yun Fang,
University of Chicago, United States

Reviewed by:
Kuei-Chun Wang,
Arizona State University, United States
Eun Ji Chung,
University of Southern California, United States

***Correspondence:**
Kytai T. Nguyen
knguyen@uta.edu
Juhyun Lee
juhyun.lee@uta.edu

† These authors have contributed equally to this work

Specialty section:
This article was submitted to Atherosclerosis and Vascular Medicine, a section of the journal Frontiers in Cardiovascular Medicine

Received: 10 May 2021
Accepted: 20 August 2021
Published: 28 September 2021

Citation:
Messerschmidt VL, Chintapula U, Kuriakose AE, Laboy S, Truong TTD, Kydd LA, Jaworski J, Pan Z, Sadek H, Nguyen KT and Lee J (2021) Notch Intracellular Domain Plasmid Delivery via Poly(Lactic-Co-Glycolic Acid) Nanoparticles to Upregulate Notch Pathway Molecules. Front. Cardiovasc. Med. 8:707897. doi: 10.3389/fcvm.2021.707897

Notch signaling is a highly conserved signaling system that is required for embryonic development and regeneration of organs. When the signal is lost, maldevelopment occurs and leads to a lethal state. Delivering exogenous genetic materials encoding Notch into cells can reestablish downstream signaling and rescue cellular functions. In this study, we utilized the negatively charged and FDA approved polymer poly(lactic-co-glycolic acid) to encapsulate Notch Intracellular Domain-containing plasmid in nanoparticles. We show that primary human umbilical vein endothelial cells (HUVECs) readily uptake the nanoparticles with and without specific antibody targets. We demonstrated that our nanoparticles are non-toxic, stable over time, and compatible with blood. We further demonstrated that HUVECs could be successfully transfected with these nanoparticles in static and dynamic environments. Lastly, we elucidated that these nanoparticles could upregulate the downstream genes of Notch signaling, indicating that the payload was viable and successfully altered the genetic downstream effects.

Keywords: Notch signaling, PLGA, nanoparticles, gene delivery, non-viral transfection

INTRODUCTION

Notch signaling is highly conserved cell signaling pathway, which is involved in diverse embryonic organs or tissue development as well as regeneration (1–10). Notch signaling regulates cell-fate determination during activation by signal sending and receiving, affected through ligand-receptor crosstalk. During the cell-fate decisions in cardiac (8, 11, 12), neuronal (13–15), immune (16, 17), and endocrine (18, 19) development, the Notch signaling pathway acts as a key regulator of cell proliferation and differentiation (2, 4, 20). Notch receptors are single-pass transmembrane proteins composed of functional Notch extracellular domain (NECD), transmembrane (TM), and Notch intracellular domains (NICD). Notch receptors are processed in the endoplasmic reticulum and Golgi apparatus within the signal-receiving cell, through cleavage and glycosylation, generating a Ca^{2+}-stabilized heterodimer composed of NECD non-covalently attached to the transmembrane NICD inserted in the membrane called S1 cleavage.

Regulation of arteriovenous specification and differentiation in both endothelial cells and vascular smooth muscle cells are also involved in Notch signaling including regulation of blood vessel sprouting, branching during normal and pathological angiogenesis, and the physiological responses of vascular smooth muscle cells (4, 6, 7, 21–23). Defects in Notch signaling also cause inherited cardiovascular diseases, such as Left Ventricular Non-compaction and Alagille syndrome (4, 7, 22). In endothelium, Delta-like ligand 4 (DLL4) is one of main ligands to send a signal to Notch in the adjacent cell (4, 6) (**Figure 1A**). This in turn signals the surrounding cells to determine the cell-fate (4). Once Notch is activated, the NICD is cleaved by γ-secretase and translocated into the nucleus (**Figures 1B,C**). Here, the NICD binds directly to the DNA, physically moving corepressors and histones, recruiting coactivators, and activating gene transcription (2, 4, 6) (**Figure 1D**).

When a disruption in this Notch pathway occurs, either by chemical or genetic means, it causes developmental malformations. For example, significant reduction of Notch signaling causing cardiac trabeculation is usually associated with deficient compaction in the ventricle (6, 24). It has been shown that lack of cardiac trabeculation results in the inability to dissipate the kinetic energy, resulting in a malformed heart due to a decrease in Notch related signaling (24, 25). Interestingly, when given NICD mRNA injection treatment, the heart function—including end diastolic function, end systolic function, stroke volume, and ejection fraction—were all partially or fully restored by rescuing downstream Notch signaling (25, 26). Regardless of whether the defect comes from the γ-secretase's inability to cleave the NICD, or if the native NICD is defective and unable to pass through the nucleus, by providing NICD mRNA to the cell it partially rescued the trabeculation. Similarly, when Notch signaling is inhibited from NICD cleavage or NICD translocation into the nucleus, Notch related downstream genes can rescue the feedback loop of Notch pathway (24). These data demonstrate the possible impact of spatiotemporal NICD treatment for therapeutic approach to rescue Notch signaling.

Traditionally, retroviruses or liposomes have been used to deliver cDNA plasmids (2, 27–29). These methods have various benefits such as DNA protection and DNA viability, but also have limitations of non-specific delivery, stability after formulation, or host immune responses (30, 31). Therefore, many groups are attempting to deliver the genetic materials such as cDNA plasmids via nanoparticles to mitigate these negative effects. Various polymers have been used for gene delivery (32–37). Cationic polymers have been used extensively to deliver genetic materials, as DNA condenses quickly on the oppositely charged positive polymer. These polymers can be synthetic or organic and usually include polyethylenimine (38, 39), polyamidoamine (40, 41), chitosan (42, 43), and cationic proteins (44), or peptides. However, the drawbacks of these highly positively charged polymers are mainly due to its toxicity (30, 31) and often require extensive surface modifications to alleviate those effects (31). Poly(lactic-co-glycolic acid) (PLGA), an FDA-approved biodegradable polymer (45), is a negatively charged polymer that has been extensively used for cancer treatment (46–49). More recently, PLGA has been used to load both hydrophilic and hydrophobic materials such as cDNA plasmids (33) and RNAs (50), proteins (51–53), dyes (54), and drugs (55).

In this study, we developed the PLGA nanoparticles encapsulating plasmids containing NICD for upregulation of Notch pathway molecules in cultured HUVECs. Using a flow chamber mimicking the *in vivo* circulation system, we evaluated the toxicity, stability, and compatibility in blood of the PLGA nanoparticles and our data suggested that we have here demonstrated NICD cDNA plasmid in the PLGA nanoparticles could upregulate Notch pathway molecules.

METHODS

Nanoparticle Synthesis and Conjugation

Poly(D, L-lactide-*co*-glycolic acid) nanoparticles (PLGA, 50:50, Akina Inc., West Lafayette, IN, USA) of two different molecular weights including 55–65 kDa [High Molecular Weight (HMW) Nanoparticles] and 5–10 kDa [Low Molecular Weight (LMW) Nanoparticles] were fabricated by a standard double emulsion method as previously described (36). In brief, PLGA was dissolved in chloroform (Sigma-Aldrich, St. Luis, MO, USA) at a 20 $\text{mg}\cdot\text{mL}^{-1}$ concentration. Following which, the water phase with 1% (w/w) rhodamine B (Rh B) was added to the oil phase dropwise under stirring and sonicated. The primary emulsion is then emulsified into 5% (w/v) Poly(vinyl) Alcohol (PVA, 13 kDa, Sigma-Aldrich) solution and then sonicated at 40 Watts for 5 min (30 s off every 1 min). Nanoparticles were then collected via centrifugation at 15,000 RPM for 15 min, then lyophilized until completely dry. Coumarin-6 loaded PLGA nanoparticles were prepared to track the nanoparticles' interaction with the cells. For this, coumarin-6 was added into the oil phase at a ratio of 1:100 with respect to the amount of PLGA used during the nanoparticle synthesis. Rh B loaded nanoparticles were exclusively used to study model drug release kinetics.

TetO-FUW-NICD was a gift from Rudolf Jaenisch (Addgene plasmid #61540) and pCAG-GFP was a gift from Connie Cepko (Addgene plasmid #11150). pCAG-GFP or TetO-FUW-NICD loaded HMW nanoparticles were also prepared based on the same standard double emulsion method with slight modifications according to past literature (56). In brief, 250 μg of plasmid was diluted in 5% glucose solution to 200 μL which was then emulsified into 0.5 mL of 5% (w/v) PLGA solution in chloroform using a probe sonicator at 40 W energy output for 15 s to form primary water/oil emulsion. The primary emulsion was then emulsified into 3 mL of 4% (w/v) PVA solution by sonication and later dropped into 7.5 mL of 0.3% (w/v) PVA solution while stirring. The final mixture was then stirred for 3 h at room temperature and particles were collected by centrifugation. Nanoparticles were then lyophilized until completely dry before use.

PLGA nanoparticles were conjugated either with anti-EGFL7 antibody (ab92939, Abcam) or anti-Tie2+Tie1 antibody (ab151704, Abcam) via EDC-NHS chemistry as described elsewhere with modification (36). In brief, nanoparticles were suspended in 0.1M MES buffer at a concentration of 2 mg/ml. Following which, 120 mg of EDC and 150 mg of NHS was added into the solution. After 2 h of incubation at room temperature, nanoparticles were collected by centrifugation and resuspended in PBS (2 mg/ml). Twenty five microliter

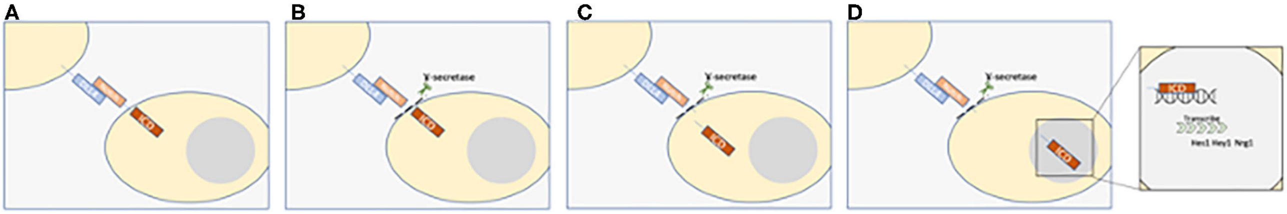

FIGURE 1 | Notch signal activation. **(A)** Notch Receptor and DLL4 ligand bind together. **(B)** γ-secretase cleaves the Intracellular domain (ICD) from the extracellular domain. **(C,D)** The ICD is released and travels into the nucleose. (**D** inset) The ICD binds onto the DNA as a transcription factor to transcribe downstream Notch genes such as Hes1, Hey1, and Nrg1.

of antibody solution was added into nanoparticles solution and incubated overnight at 4°C. The supernatant was used to determine the antibody conjugation efficiency using Bradford assay following manufacturers' instructions. Pellets were resuspended in DI water, freeze-dried, and stored for use.

Characterization and Stability of Nanoparticles

To determine the size and surface charge, nanoparticle suspension was added to a transparent cuvette and was then inserted into the ZetaPALS dynamic light scattering (DLS) detector (NanoBrook 90Plus PALS, Brookhaven Instruments, Holtsville, NY) as previously described (36). Scanning electron microscopy (SEM, Hitachi S-3000N, Hitachi, Pleasanton, CA) was used to visualize the morphology of nanoparticles. Briefly, 50 μl of the nanoparticle suspension air-dried on a coverslip was silver sputter-coated and inserted into the SEM instrument. To determine the *in vitro* stability, nanoparticles were suspended in saline (0.9% Sodium Chloride, NaCl, Crystalline, Fisher Scientific, Hampton, NH, USA) or Vasculife VEGF basal cell media with 10% Fetal Bovine Serum (LL-0003, Lifeline Cell Technologies) and incubated at 37°C for 48 h. Particle size was measured on predetermined time points using DLS as described earlier. The stability of the nanoparticles was represented as the percentage change of nanoparticle size measured at each time point with respect to initial particle size according to the following equation:

$$Size\ (\%) = \frac{Nanoparticle\ Size_{t=t_0}}{Nanoparticle\ Size_{t=0}} * 100 \tag{1}$$

Loading and Release Studies

The encapsulation efficiency of entrapped reagent including, pCAG-GFP or TetO-FUW-NICD, within PLGA nanoparticles was determined based on indirect loading analysis. Briefly, the un-loaded reagent in the supernatant (PVA solution) following the nanoparticle synthesis, was used to calculate the encapsulation efficiency (Equation 2). The amount of plasmid was determined using Picogreen DNA assay (#E2670, Promega, Madison, WI) following the manufacturers' instructions.

$$Encapsulation\ Efficiency\ (\%) = \frac{Plasmid\ initially\ added - plamid\ in\ supernatant}{Plasmid\ initially\ added} * 100 \tag{2}$$

For *in vitro* plasmid release studies, solutions of pCAG-GFP or TetO-FUW-NICD plasmid-loaded nanoparticles were prepared in 1X PBS at a concentration of 1.5 mg/mL. At predetermined time points, the samples were centrifuged at 12,000 RPM for 5 min. The supernatant was then collected and stored at −20°C for further analysis. Pellet was again resuspended in fresh 1 mL of PBS solution and incubated until next time point. Four replicates were used for analysis. For analysis, the plasmid solutions were incubated with Nb.Bsmi nicking enzyme (R0706S, New England Biolabs) for 60 min at 65°C in NEBuffer 3.1. The enzyme was then inactivated for 20 min at 80°C. The nicked plasmid supernatant was analyzed for plasmid release using the Picogreen DNA assays. The plasmid standards were made to determine the cumulative percentage of plasmid release over time.

In vitro Compatibility of Nanoparticles

HUVECs were cultured in M199 media (M4530, Sigma-Aldrich) supplemented with Vasculife VEGF LifeFactors kit (LS-1020, Lifeline Cell Technologies) up to passage 7 in a 5% CO_2 environment. To determine the compatibility of nanoparticles, HUVECs were seeded in 96 well plates at seeding density of 8,000 cells/well and cultured overnight. HMW nanoparticles and LMW nanoparticles of various concentrations (25, 50, 100, 250, 500, 1,000 $\mu g\ mL^{-1}$) were prepared in complete M199 media and added to the cells. After 24 h of incubation at 37°C, the nanoparticle containing media was removed, and cells were carefully washed with 1X PBS. The cellular viability was then determined using MTS assays per manufacturer's instructions.

In addition, HMW nanoparticles and LMW nanoparticles compatibility was evaluated using human whole blood, to determine hemolysis and whole blood clotting kinetics assay as previously mentioned. For these studies, whole blood was drawn from healthy adult volunteers into acid citrate dextrose anticoagulant tubes (ACD, Solution A; BD Franklin Lakes, NJ). Consent from the volunteers was obtained prior to the blood collection, and all the procedures strictly adhered to the IRB standards approved at the University of Texas at Arlington.

To perform whole blood clotting study, the blood was initially activated by adding 0.01 M of calcium chloride (Sigma). Following which, 50 μL of activated blood was added into 10 μL of saline diluted nanoparticle solution at concentration of 1 mg/mL and incubated for predetermined time points. At each time point, 1.5 mL of DI water was added to lyse the un-clotted blood and the absorbance of the supernatant was measured at 540 nm. Untreated blood served as a control. In the hemolysis study, nanoparticles were suspended in saline at the following concentrations (0, 10, 25, 50, 100, 250, 500, 1,000 $\mu g \cdot mL^{-1}$) and then incubated with 200 μL of saline-diluted blood for 2 h at 37°C. Following the incubation, the samples were centrifuged, and the absorbance of the supernatant was quantified at 545 nm. Untreated blood that was diluted with DI water and saline solution served as positive and negative controls, respectively. The percent hemolysis was calculated using the following equation:

$$\% = \frac{Abs_{sample} - Abs_{neg\ ctl}}{Abs_{pos\ ctl} - Abs_{neg\ ctl}} \times 100 \tag{3}$$

In vitro Cellular Uptake and Interaction of Nanoparticles

To determine the uptake of coumarin-6 loaded HMW- and LMW-PLGA nanoparticles by HUVECs, cells were seeded in 96 well-plates at a density of 8,000 cells/well. After overnight culture, nanoparticles of various concentrations 50, 100, 250, 500, 1,000 $\mu g \cdot mL^{-1}$ were added to the cells and incubated for 4 h in 37°C. Nanoparticles were then removed, cells were carefully washed with PBS solution and lysed using 1% Triton X-100. Fluorescence intensity measurement of nanoparticles in cellular lysate was quantified at a wavelength of 457 nm (excitation)/500 nm (emission) using a spectrophotometer. These measurements were analyzed against a nanoparticle standard. The measurements were further normalized with respect to the sample cellular protein amount as determined based on BCA assay (Thermofisher Scientific).

Similarly, interaction between antibody (anti-EGFL7 or anti-Tie2+Tie1) conjugated HMW nanoparticles loaded with coumarin-6 and HUVECs were also determined under static conditions. In brief, nanoparticle suspensions were treated with cells for 30 min and following which, cells were washed and lysed. Cellular lysate was used to determine the amount of nanoparticle attachment and internalization with HUVECs based on coumarin-6 fluorescence intensity. These fluorescence measurements values were then normalized with the total DNA content per sample using Picogreen DNA assays per manufacturer's instructions. In parallel, nanoparticle interaction with HUVECs were observed using a fluorescence microscope under FITC channel. The cells were counterstained using Nucblue (Invitrogen) to visualize the cell nuclei. To show the specificity of the optimal antibody to endothelial cells, HL-1 cells were cultured overnight in a 96-well plate overnight in Claycomb media supplemented with 10% FBS, 1% pen-strep, 0.1 mM Norepinephrine, and 2 mM of L-Glutamine. The following day, nanoparticles conjugated with anti-Tie2+Tie1 were added to the HL1 cells at 100, 250, 500, 1,000 $\mu g \cdot mL^{-1}$ for 4 h. After the incubation, cells were lysed, and fluorescence read under the same conditions. The fluorescence was normalized to DNA content.

In addition, the ability of a coumarin-6 loaded, antibody (anti-EGFL7 or anti-Tie2+Tie1) conjugated HMW nanoparticles to adhere and interact with HUVECs under physiological relevant flow condition was investigated. HUVEC's were seeded at 2^*10^6 cells/mL into μSlide $VI^{0.4}$ channel and cultured overnight. Following the cell attachment, nanoparticles suspended in M199 media at a concentration of 200 μg/mL were perfused through the channels of the flow slide using Ibidi pump system at a shear stress of 5 dyne/cm^2 for 30 min. Later, cells within the channels were fixed with paraformaldehyde solution and treated with Nucblue (Invitrogen) to stain cell nuclei. The cellular images were then taken using fluorescence microscope under FITC and DAPI channel to visualize the nanoparticles and nuclei, respectively. The fluorescence intensity of nanoparticles was later quantified using NIH ImageJ software and normalized by cell number.

To further prove our nanoparticle selectivity, we coated μ-Slide IV 0.4 (Ibidi, #80606) with 14.4 μg of bovine serum albumin (BSA), a 1:1 solution of Tie1 and Tie2 protein at 14.4 μg, or 1X PBS. The solutions were left at room temperature for 2 h. The remaining solution was washed off. Coumarin 6 nanoparticles were prepared as above, and conjugated with either BSA, anti-Tie2+Tie1, or were unconjugated. Nanoparticle media at a concentration of 250 μg/mL was flowed through at 5 dyne·cm^2 for 15 min. The media was removed and washed with 1x PBS to remove unbound nanoparticles. The slides were imaged at 100× to visualize the bound content. Using ImageJ, the intensity of the fluorescence was measured to quantitatively evaluate the binding.

Plasmid Transfection

HUVECs were seeded 24 h prior to the transfection study at $n = 4$. The following day, Lipofectamine 3000 or no treatment were applied to the cells for 6 h. After the treatment, the cells were washed three times with 1X PBS and incubated until the next time point. HMW PLGA nanoparticles were prepared as described above. The nanoparticles at a concentration of 250 μg/mL were then applied to HUVECs for 6 h. The cells were then gently washed with 1X PBS three times and new media given. The cells treated with Lipofectamine, nanoparticles, or no treatment were then grown for 24, 48, or 72 h post transfection. Cells transfected with pCAG-GFP plasmid-loaded nanoparticles were imaged in a fluorescent microscope on FITC channel, nuclei were stained with Nucblu. The intensity of each fluorescent channel was measured via ImageJ. The data was then normalized by cell number, via Nucblu intensity, then normalized to the untreated cell group following the Equation 4.

$$Mean\ Correlated\ Total\ Cell\ Fluorescence = (GFP\ Intensity)/(NucBlu\ Intensity) \tag{4}$$

Before loaded into nanoparticles, the quality and quantity of TetO-FUW-NICD plasmid were analyzed by digestion to ensure positive clones were used. Four biological repeats were carried out for each experiment.

RT-PCR Data

Cells were first washed with 1X PBS two to three times. Then, 0.025% trypsin was added for 5 min at 37°C to allow cell detachment. The trypsin was then neutralized by adding media twice the volume of trypsin to the wells. The cells were collected, centrifuged at 150 × g for 5 min, and the supernatant discarded. The cells were then used to isolate the total RNA using the Aurum Total RNA Mini Kit (Biorad, #7326820) following the manufacturer's instructions. RNA concentration was determined via NanoDrop, by reading each sample 3 times. The total RNA was then used to synthesize 200 ng of cDNA using the iScript Synthesis Kit (Biorad, #1708890) following the manufacturer's instructions. PCR was conducted using the iTaq Universal SYBR Green Supermix (Biorad, #1725121) following manufacturer's instructions. The primer sequences for human mRNA are as follows: *Dll4* (Frd CTGCGAGAAGAAAGTGGACAGG, Rev ACAGTCGCTGACGTGGAGTTCA), *Hes1* (Frd GGAAAT GACAGTGAAGCACCTCC, GAAGCGGGTCACCTCGTT CATG*), Hey1* (Frd ACCATCGAGGTGGAGAAGGA, Rev AAA AGCACTGGGTACCAGCC), *Notch1* Receptor (Frd GGTG AACTGCTCTGAGGAGATC, Rev GGATTGCAGTCGTCCA CGTTGA), NICD (Frd ACCAATACAACCCTCTGCGG, Rev GGCCCTGGTAGCTCATCATC), and *β-Actin* (CGACAGGAT GCAGAAGGAG, Rev ACATCTGCTGGAAGGTGGA).

Western Blot

Cells were cultured in a 6-well plate overnight. The following day, nanoparticles loaded with NICD plasmid, nanoparticles loaded with NICD plasmid and conjugated anti-Tie2+Tie1, blank nanoparticles, or cell media were added to the culture. After an additional 24 h with treatment and shear stress, the media was removed, cells washed with 1x PBS, and lysed with radio-immunoprecipitation assay buffer supplemented with protease inhibitor cocktail (Roche). Protein concentrations were determined via the Pierce BCA Assay Kit (ThermoFisher). Antibodies against Notch1 (Invitrogen, MA5-32080), Hey1 (Abnova, H00023462-M02), Hes1 (OriGene, TA400013), and GAPDH (Proteintech, HRP-60004) were probed at suggested dilutions. Secondary antibodies conjugated with horseradish peroxidase were incubated and detected by enhanced chemiluminescence reagent (BioRad). The total protein of each well was measured using ImageJ's Gel Analysis. Similarly, each individual band was measured using the same technique, then normalized to the total protein amount.

Statistical Analysis

All statistics were evaluated in the statistical program R. For the percent change in size, a one-way ANOVA was used to compare each sample to its' original size. A one-way ANOVA was also used to determine significance of nanoparticle uptake between anti-Tie2+Tie1 or anti-EGFL7 nanoparticles, antibody uptake in dynamic culture, nanoparticle dose study, and gene expression between static and dynamic culture. A two-sample *t*-test was used to compare the HMW to LMW in the cell viability and nanoparticle cellular interaction studies. Similarly, the gene expression was evaluated to compare dynamic culture at 12 dyne·cm^{-2} to static culture for each gene. All values where $p < 0.05$ were considered significant. *Post-hoc* Tukey tests were conducted if ANOVA results showed significance to determine differences between groups.

RESULTS

Optimization of Nanoparticles Based on Molecular Weight of PLGA

Before performing the cell study, nanoparticles were characterized based on their size, poly dispersity, and zeta potential (**Table 1**). The diameter of high molecular weight (HMW) PLGA nanoparticles, at 55–65 kDa, were smaller than the low molecular weight (LMW), 1–5 kDa, PLGA nanoparticles at 234 ± 90 and 246 ± 85 nm, respectively. The zeta potential, or surface charge of the nanoparticles, indicates the presence of the negatively charged carboxyl and hydroxyl groups present on the polymer. The HMW PLGA nanoparticles have a charge of −31 ± 3.4 mV, and the LMW PLGA nanoparticles have a charge of −29 ± 2.8 mV. The poly dispersity of both the HMW and LMW PLGA nanoparticles, 0.13 ± 0.05 and 0.08 ± 0.02, respectively, shows that the particles are uniformly dispersed. SEM images also indicated that both the HMW- and LMW-nanoparticles were uniformly dispersed and have spherical morphology (**Figure 2A**).

TABLE 1 | PLGA nanoparticle physical attributes.

PLGA nanoparticles	Size (nm)	Poly dispersity	Zeta potential (mV)
MW: 55–65 kDa	234 ± 90	0.13 ± 0.05	−31 ± 3.4
MW: 1–5 kDa	246 ± 85	0.08 ± 0.02	−29 ± 2.8

Following *in vitro* stability studies using HMW- and LMW-nanoparticles in both saline (0.9% NaCl) and 10% serum, the nanoparticle percent size change was determined. Accordingly, the diameter of HMW nanoparticles were constant in both formulations over 48 h of incubation, which indicates the superior stability properties of HMW nanoparticles. On other hand, the size of LMW nanoparticles steadily increased over time and showed significant aggregation following their incubation with the saline solution at 24 h. In serum, the LMW nanoparticles increased in size, but was not significantly different (**Figure 2B**). This suggests that LMW nanoparticles may exhibit aggregation behavior following their suspension and/or administration. Then, the drug release kinetics were then compared between the two molecular weights using a model hydrophilic drug Rh B. High and low molecular weight nanoparticles were incubated in 1X PBS over a period to assess Rh B release kinetics. Both molecular weights of PLGA nanoparticles showed a burst release of Rh B dye with LMW releasing all the dye within 5 days and the HMW nanoparticles with a sustained release of over 20% by day 28 (**Supplementary Figure 1**).

To assess the cytocompatibility of nanoparticles, HUVECs were subjected to varying concentrations of both HMW and LMW nanoparticles. Across all tested concentrations, the HMW nanoparticles were all above 90% viability, while the LMW had >90% viability in only 25, 50, 100, and 250 μg/mL (**Figure 2C**). At both 500 and 1,000 μg/mL, the LMW nanoparticles were significantly lower at 88 ± 10 and 76 ± 13% viability, respectively ($p < 0.05$). The uptake of the nanoparticles was evaluated using HUVECs incubated with varying amounts of nanoparticles. At each tested concentration, the HMW nanoparticles had a significantly higher uptake compared to that of the LMW. Additionally, there is a trend showing a dose-dependent relationship between the number of nanoparticles applied, and the number of nanoparticles endocytosed by the cells (**Figure 2D**).

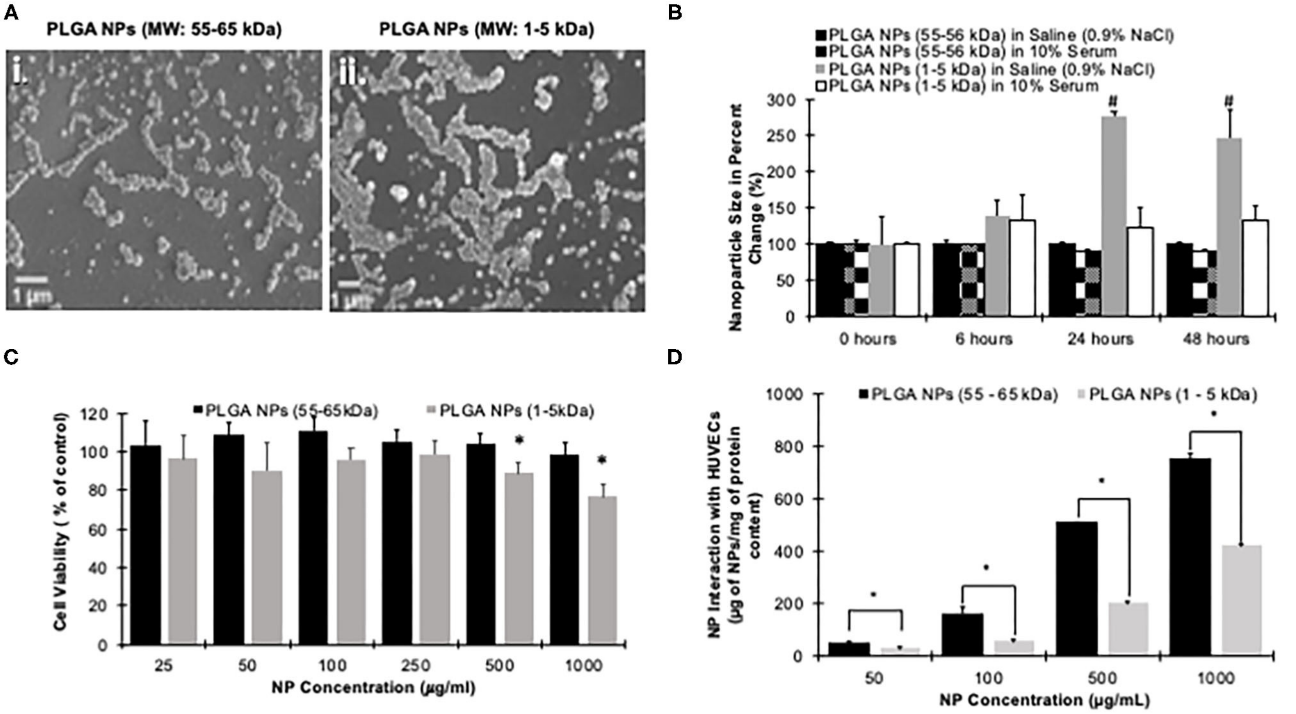

FIGURE 2 | Characterization of PLGA nanoparticles. **(A)** SEM images of (i) PLGA at 55–65 kDa and (ii) PLGA at 1– 5 kDa nanoparticles. Aggregation occurs during the air-drying process due to the shrinking water droplet on the glass slide for taking this images. Scale bar is 1 μm. **(B)** Nanoparticles stability in saline (0.9% NaCl) or 10% Serum over time shows that the HMW PLGA nanoparticles' size is steady in both solutions, while the LMW PLGA nanoparticles vary in both the Saline and 10% Serum. Error bars denote standard error. #Indicates a significant difference from the samples' time point 0 ($p < 0.05$) evaluated via one-way ANOVA. **(C)** Cytocompatibility test comparing HMW to LMW PLGA nanoparticles. This shows at all concentrations the HMW PLGA nanoparticles are insignificantly toxic to the cells. The LMW nanoparticles are tolerated up to a concentration of 250 μg/mL. *Indicates a significant difference from 100% viability evaluated via two-way ANOVA ($p < 0.05$). **(D)** HUVEC uptake of both HMW and LMW PLGA nanoparticles shows HMW had significantly higher uptake than LMW at all tested concentrations. Data shown as mean + standard error. *Indicates a significant difference between HMW and LMW Nanoparticle uptake evaluated at each time point via a *t*-test ($p < 0.05$).

Compatibility in Blood

To simulate the effect of nanoparticles on human blood, hemolysis and whole blood clotting tests were conducted. For whole blood clotting, the nanoparticles significantly affected the clotting cascade only during the first 10 min of exposure. Afterwards, the progress of blood clotting gradually reduced and there were no significant results compared to whole blood without exposing PLGA nanoparticles (**Figure 3A**). After 60 min, blood exposed to either HMW or LMW nanoparticles had great low supernatant absorbance, 0.1, similar to whole blood which indicates blood clot. Our results reflect those who have performed similar studies showing little red blood cell lysis or reduced clotting kinetics (57). Furthermore, the interaction between red blood cells and nanoparticles were evaluated by incubation with diluted blood to determine if hemolysis occurred. Compared to lysed cells as the positive control, both the HMW and LMW nanoparticles were significantly lower (<0.25%) in hemolysis (**Figure 3B**).

Selection of Optimal Endothelial Target

For this study, HMW nanoparticles were used because the HMW has greater cell uptake and cell viability properties even though LMW nanoparticles have a rapid release profile. Anti-EGFL7 and Anti-Tie2+1 were conjugated to PLGA HMW nanoparticles and characterized. The nanoparticles conjugated with anti-EGFL7 increased to 249 ± 55 nm, while the nanoparticles conjugated with anti-Tie2+Tie1 are 243 ± 41 nm. Both antibody conjugations had a low poly dispersity, indicating that most of the nanoparticles were uniform in size. The antibodies changed the surface charge of the nanoparticles from −31 ± 3.4 to −23.5 ± 1.7 mV for anti-EGFL7 nanoparticles, and −31 ± 3.4 to −27.4 ± 1.8 mV for anti-Tie2+Tie1 nanoparticles. The antibodies had a conjugation efficiency of 59.6 ± 1.5 and 47.5 ± 1.2% for anti-EGFL7 conjugated nanoparticles and anti-Tie2+Tie1 conjugated nanoparticles, respectively (**Table 2**).

Furthermore, we tested our antibody conjugated particles on their uptake abilities under static and physiological flow conditions. Under static conditions, we saw concentration-dependent uptake of nanoparticles by endothelial cells (**Figure 4A**). As the concentration of anti-Tie2+Tie1 conjugated nanoparticles increases, the rate of cellular uptake increases 3.5 and 8.4 folds from 100 to 250 and 500 μg/mL, respectively (**Figure 4A**). Similarly, anti-EGFL7 conjugated nanoparticles increase 2.4-folds and 5.1-folds from 100 to 250 and 500 μg/mL, respectively. Additionally, the unconjugated nanoparticles increase 5.2 and 7.3-fold from concentrations of 100 to 250,

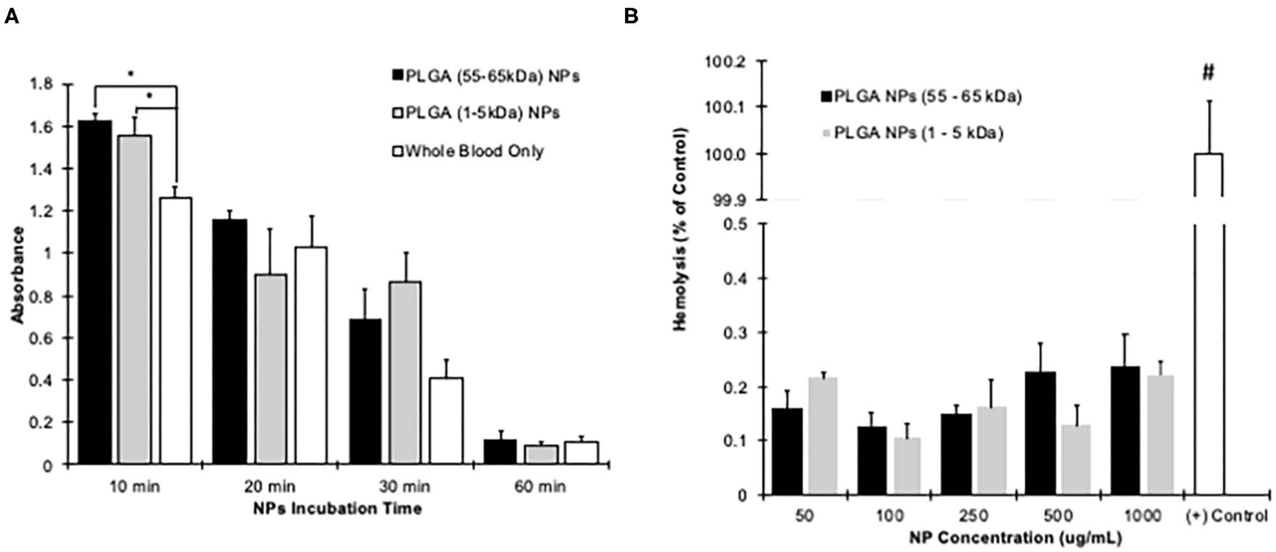

FIGURE 3 | Hemocompatibility of PLGA nanoparticles. **(A)** Nanoparticles at a concentration of 1 mg/mL were subjected to human blood for up to 1 h. The clotting was significantly affected only during the first 10 min of nanoparticle exposure ($p < 0.05$). At all other time points, the nanoparticles did not affect the clotting ability of the human blood. Blood exposed to only air was kept as a control. *Denoted a significant difference with $p < 0.05$ evaluated via one-way ANOVA at each time point. **(B)** Nanoparticles were incubated with blood for 1 h. Compared to RO water treatment (Positive control), both nanoparticle groups had significantly less hemolysis at all tested concentrations. #Indicates that the Positive control is significantly higher than all other groups with $p < 0.05$ evaluated using a two-way ANOVA. All data is shown as mean + standard error.

TABLE 2 | Endothelial cell targeted PLGA nanoparticles.

Antibody conjugated nanoparticles	Size (nm)	Poly dispersity	Zeta potential (mV)	Conjugation efficiency (%)
Anti-EGFL7 nanoparticles	249 ± 55	0.21 ± 0.01	−23.5 ± 1.7	59.6 ± 1.5
Anti-Tie2+Tie1 nanoparticles	243 ± 41	0.19 ± 0.13	−27.4 ± 1.8	47.5 ± 1.2

and 500 μg/mL, respectively. Additionally, antibody conjugated nanoparticles had a greater interaction with the cells compared to unconjugated ones. Coumarin-6 loaded HMW nanoparticles conjugated to either anti-EGFL7 or anti-Tie2+Tie1 supported the quantitative data (**Supplementary Figure 2**).

Compared to unconjugated nanoparticles, antibody conjugated nanoparticles to target endothelial cells show higher uptake efficiency although the diameter of nanoparticles were increased (**Figure 4B**). Tested with flow system, nanoparticles conjugated with anti-EGFL7 has significantly higher cellular uptake. However, nanoparticles conjugated with anti-Tie2+Tie1 were significantly higher in cellular uptake than that of anti-EGFL7 conjugated. With fluorescent imaging, we can visualize that under flow conditions at 5 dyne·cm^{-2}, the antibody conjugated nanoparticles were able to be endocytosed into cells at a higher rate compared to unconjugated nanoparticles (**Figure 4C**). To further prove the targeting ability of our anti-Tie2+Tie1 nanoparticles, we tested their binding ability to different protein coatings. In addition to anti-Tie2+Tie1 coated nanoparticles, we compared BSA conjugated and unconjugated nanoparticles on their binding ability to Tie1/Tie2-coated, BSA-coated, or uncoated slides. The Tie2+Tie1 nanoparticles bound to the Tie2+Tie1-coated slides significantly higher than both the BSA conjugated nanoparticles and the unconjugated nanoparticles (**Supplementary Figures 4A,B**). Additionally, we cultured cardiomyocytes, HL1 cells, with anti-Tie2+Tie1 nanoparticles to investigate if the NP uptake was specific to endothelial cells. There was a significant difference at all tested concentrations between HUVECs and HL1 cells (**Supplementary Figure 4C**). Due to the increase in cellular uptake of nanoparticles conjugated with anti-Tie2+Tie1 and its specificity toward Tie1/Tie2 coating and endothelial cells, this antibody was determined to be superior for endothelial targeting.

Characterization of Plasmid Loaded PLGA Nanoparticles

Both pCAG-GFP and TetO-FUW-NICD were loaded into HMW PLGA nanoparticles at 62.3 ± 2.2 μg plasmid per mg of nanoparticles and 89.1 ± 6.4 μg plasmid/mg nanoparticles, respectively. The encapsulation efficiency of 56.3 ± 4.1 and 38.9 ± 2.17% for NICD and GFP plasmids, respectfully, is similar to previous reports (58–60) (**Table 3**). Additionally, previously reported particles were larger (59) and the encapsulated plasmids were 6- to 2-times smaller in size (58–60) of our largest plasmid, at 10,671 bp, the genetic material encapsulated into the nanoparticles was released in a similar

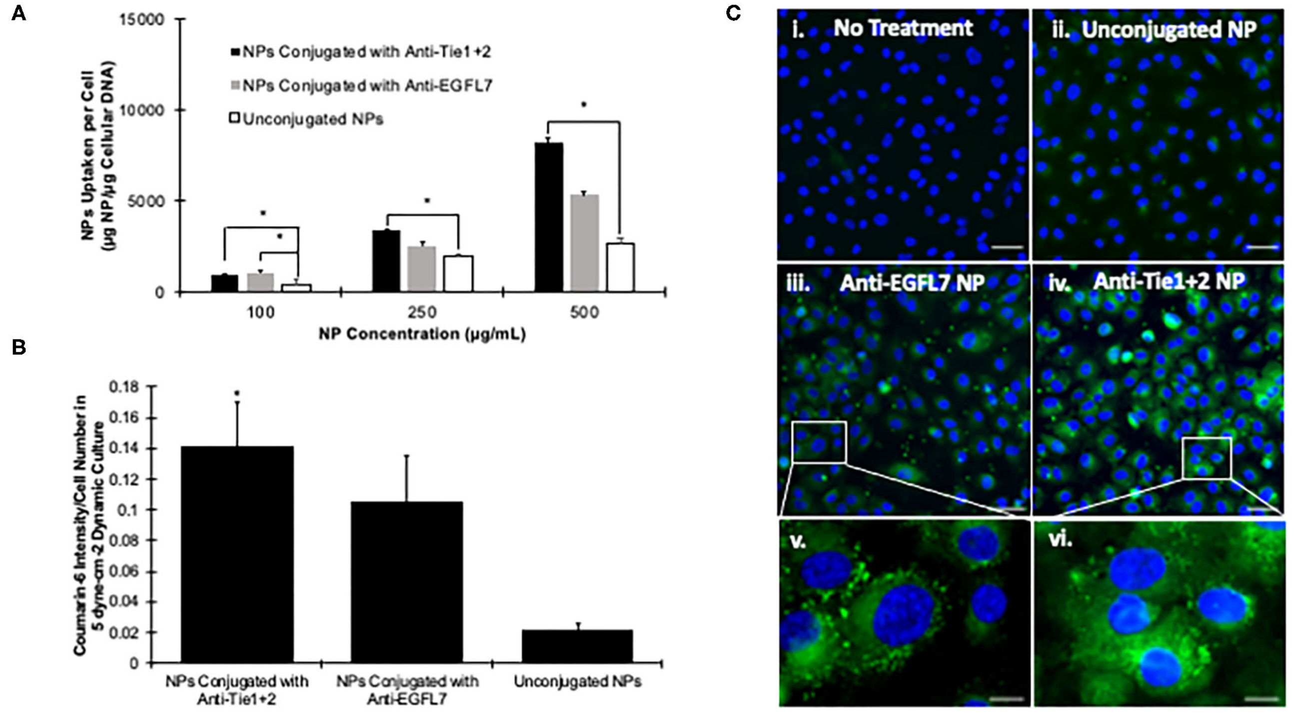

FIGURE 4 | Targeting efficiency of antibody conjugated PLGA nanoparticles. **(A)** HUVEC Cellular uptake of endothelium specific anti-EGFL7, anti-Tie2+Tie1 conjugated nanoparticles or unconjugated nanoparticles after 4 h. *Indicates a significant difference via one-way ANOVA ($p < 0.05$). Data is shown as mean + standard deviation. **(B)** HUVEC Cellular uptake under 5 dyne·cm^{-2} of endothelium specific anti-EGFL7 and anti-Tie1+2 conjugated nanoparticles, or unconjugated nanoparticles. *Denotes a significant difference between anti-Tie2+Tie1 nanoparticles and unconjugated nanoparticles via one-way ANOVA ($p < 0.05$). Data is shown as mean + standard deviation. **(C)** Fluorescent images of HUVEC's incubated in flow culture of 5 dyne·cm^{-2} with (i) No Treatment, (ii) Unconjugated Nanoparticles, (iii) Anti-EGFL7 conjugated nanoparticles, (iv) anti-Tie1+2 conjugated nanoparticles. Scale bar = 20 μm. Zoomed in portions of HUVEC's incubated in flow culture at 5 dyne·cm^{-2} with (v) Anti-EGFL7 conjugated nanoparticles, and (vi) anti-Tie2+Tie1 conjugated nanoparticles. Scale bar = 5 μm.

TABLE 3 | NICD plasmid loaded PLGA nanoparticle characteristics.

	Size (nm)	Poly dispersity	Zeta potential (mV)	Encapsulated efficiency (%)
NICD-loaded PLGA nanoparticle	272 ± 51	0.12 ± 0.05	−12.9 ± 1.90	56.3 ± 4.1%
NICD-loaded PLGA nanoparticle conjugated with anti-Tie2+Tie1	268 ± 26	0.11 ± 0.01	−17.0 ± 0.83	

form to our model hydrophilic drug, Rh B (**Figure 5A, Supplementary Figures 1, 3**). The NICD plasmid released up to 1 μg of plasmid within the first 24 h. The plasmid continued to be released over 14 days to a total of 1.2 μg (**Figure 5A**). Our GFP plasmid loaded nanoparticles similarly released 0.5 μg of plasmid over 14 days (**Supplementary Figure 3**). With the addition of the plasmids, the zeta potential and size both increased, indicating a change. However, the polydispersity value was still low illustrating their homogeneous size.

TetO-FUW-NICD loaded nanoparticles were also given to HUVECs at varying doses. Compared to the untreated group, Notch target gene, *Hey1* was upregulated in each tested concentration. Additionally, another target gene, *Hes1,* was upregulated with NICD plasmid concentrations of 100, 250, and 500 μg of nanoparticles while 1,000 μg of NICD plasmid loaded nanoparticle decrease the expression level of *Hey1* (**Figure 5B**). Based on the trend, the NICD plasmid concentration of nanoparticle, affects the gradual expression level of target gene expressions until adding 250 ug of NICD plasmid loaded NP.

GFP Expression Over Time

HUVECs were subjected to 5 μg of plasmid, either through Lipofectamine 3000, or our GFP Plasmid-loaded nanoparticles. After 6 h, the treatments were removed, and fresh media applied to the cells. At 12 h, Lipofectamine had significantly higher GFP expression than the plasmid nanoparticles (**Figure 6B**). However, after 24 h, the GFP plasmid loaded nanoparticles had a significantly higher GFP expression level per cell. Additionally, the GFP plasmid-loaded nanoparticles had an even expression of GFP across most cells. At 24 h, the lipofectamine group had few GFP positive cells compared to that of the nanoparticle treated group. At 48 h post transfection, GFP was observed in

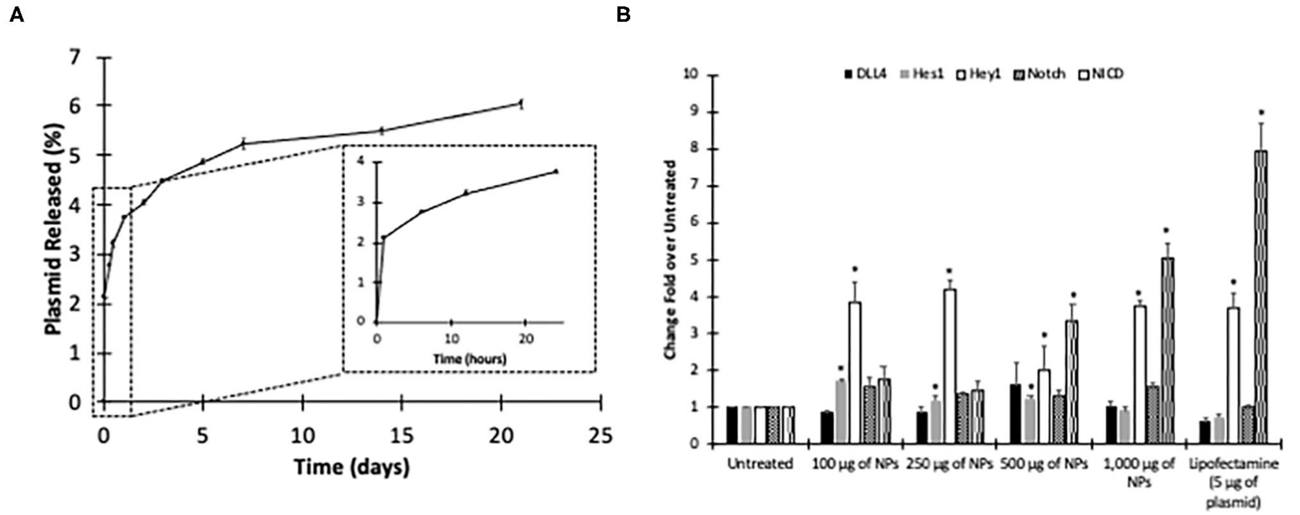

FIGURE 5 | Characterization of NICD Loaded Nanoparticles. Release curve of **(A)** NICD Plasmid-loaded nanoparticles measured via Promega dsDNA assay after 21 days. $n = 3$. Data shown as mean ± standard deviation. **(B)** Quantitative expression of NICD after TetO-FUW-NICD Nanoparticle transfection at varying dosages. *Significantly different from Untreated Group evaluated via two-way ANOVA ($p < 0.05$).

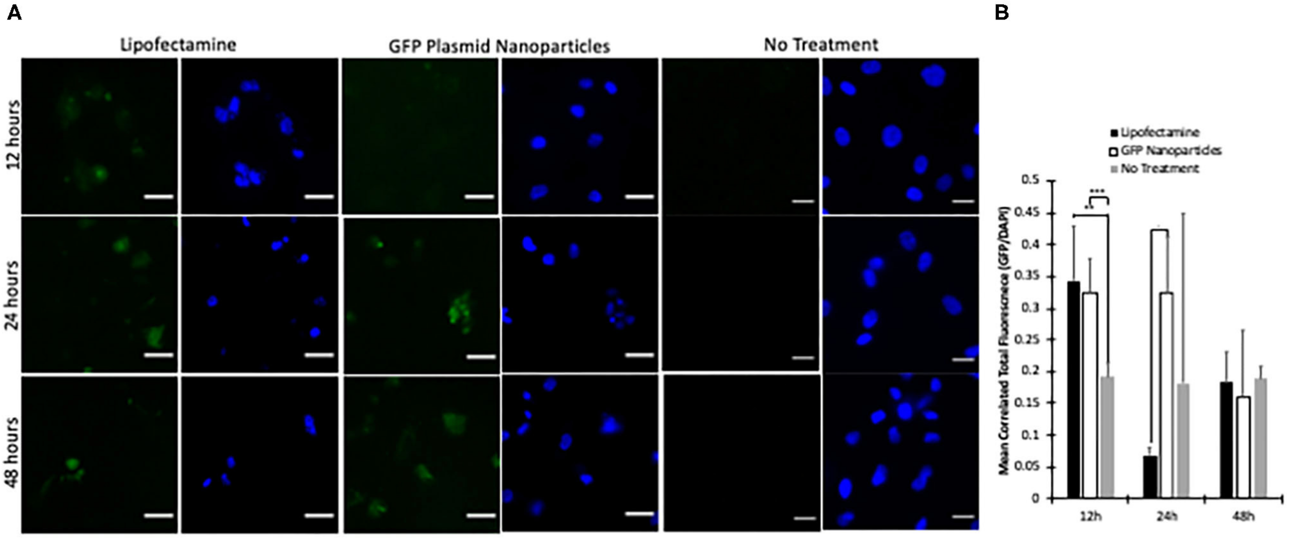

FIGURE 6 | GFP plasmid-loaded nanoparticle transfection. **(A)** After 6 h of treatment, nanoparticles or lipofectamine were washed off with 1X PBS and media replaced. At 12 h, slight GFP expression can be seen (**A**, first row). After 24 h, there is significantly more GFP expression in GFP plasmid-loaded nanoparticles than lipofectamine treated cells (**A**, second row). Additionally, after 48 h, lipofectamine transfected cells had a high GFP signal in few cells. Whereas, nanoparticle transfected cells had many cells expressing GFP, resulting in a lower over signal. **(B)** Normalized GFP intensity to nuclei intensity shows significantly higher lipofectamine at 12 h, significantly higher Nanoparticle at 24 h, and no difference at 48 h. • indicates ($p < 0.1$), **indicates ($p < 0.01$) and ***indicates significance at ($p < 0.001$) via one-way ANOVA per time point.

both lipofectamine treated and GFP plasmid-loaded nanoparticle treated groups (**Figure 6**).

Nanoparticle Mediated HUVEC Transfection Based on NICD Expression

HUVECs were subjected to 12 dyne·cm^{-2} for 24 h, then an additional 24 h of flow treatment with blank nanoparticles, TetO-FUW-NICD loaded HMW nanoparticles, TetO-FUW-NICD loaded HMW nanoparticles conjugated with anti-Tie2+Tie1, or cell media only for control. Each nanoparticle group was given at a concentration of 250 µg/mL due to highest Notch target efficiency concentration (**Figure 5B**). The plasmid-loaded nanoparticles with targeting antibody had significantly higher expression of Notch related genes, but not *Hes1* although expression level was upregulated (**Figure 7**). The expression

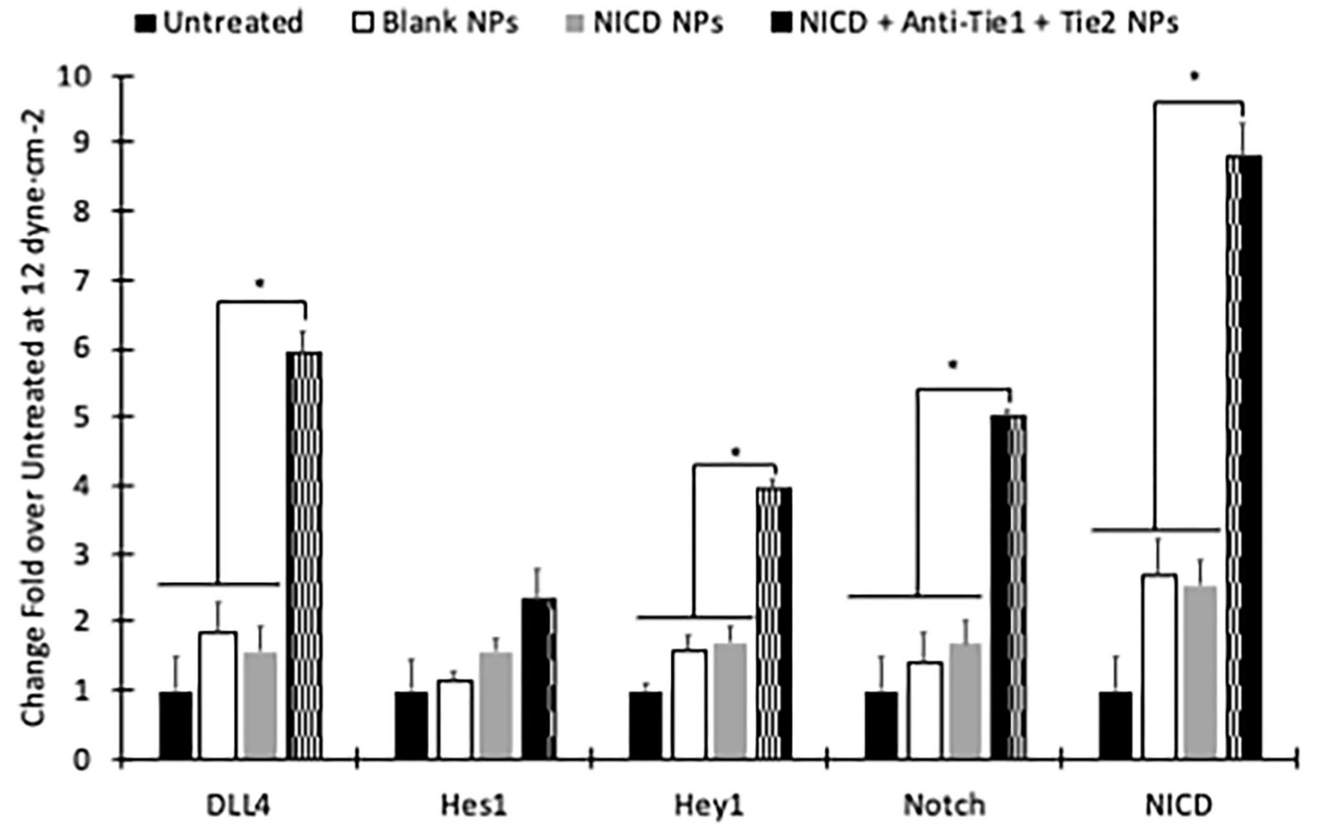

FIGURE 7 | NICD plasmid-loaded nanoparticles can enhance NICD expression in dynamic culture conditions. RT-PCR results showing that NPs conjugated to anti-Tie2+Tie1 significantly upregulate DLL4, Hey1, Notch Receptor, and NICD in 12 dyne·cm^{-2} flow conditions. *NICD+Anti-Tie1+Tie2 is significantly higher mRNA expression evaluated with one-way ANOVA per gene group ($p < 0.05$).

of Notch related genes when exposed to plasmid-loaded nanoparticles without a conjugating antibody were not significantly different from that of the blank nanoparticles. Both were upregulated most likely due to the increased viscosity of the media after adding the nanoparticles. The higher viscosity causes a higher shear stress, which upregulates shear responsive Notch signaling **Supplementary Figure 5**. We then analyzed the protein expression after application of the NICD loaded nanoparticles, NICD loaded nanoparticles conjugated with anti-Tie2+Tie1, or no treatment. After 24 h of treatment, we found that the nanoparticles containing NICD plasmid and conjugated with anti-Tie2+Tie1 had a significantly higher amount of NICD protein than both the NICD-loaded nanoparticles and the no treatment group. This indicates that the plasmid was able to be released from the nanoparticle and be translated into protein by the cell **Supplementary Figure 6**. Additionally, the NICD-loaded nanoparticles had significantly higher Hes1 and Hey1 proteins (**Supplementary Figure 6**).

DISCUSSION

In this work, we have demonstrated the successful transfection of NICD plasmid to upregulated Notch signaling via PLGA nanoparticles. PLGA is one of the most characterized biopolymers with respect to drug delivery design and performance (61), which has been widely utilized for delivering proteins (51, 62–64) and hydrophobic drugs (65–68). More recently, PLGA nanoparticle has been used as a delivery vehicles for gene delivery for vaccines (32), immunotherapy (29), or gene therapy (38, 58, 60, 69, 70). Therefore, we have used PLGA for NICD DNA plasmid delivery to overcome the limitations of traditional viral vector methods such as negative immunological effects, random gene integration, base pair size restrictions, and cytotoxicity (71).

First, we optimized the molecular weight of the PLGA. Our data shows that the higher molecular weight, 55–65 kDa, PLGA was more cytocompatible, hemocompatible, and stable in various solutions. Even though the low molecular weight, 5–10 kDa, released the plasmid quickly, the nanoparticles were unstable in saline, a common liquid vehicle used for intravenous drug delivery (68, 72–75). Similarly, it has been shown that low molecular weight PLGA nanoparticles release the payload at a higher rate (76–78). Therefore, the molecular weight can influence how long a drug of interest is released and exposed to the area of interest (77, 78). These previous studies support our data showing that the low molecular weight releases the payload after 5 days. Interestingly, molecular weight differences of 5 kDa can have significantly different release profiles (76). Additionally, lower molecular weight PLGA increases the pH of the surrounding fluid, which leads to cell death (79). This would explain why at high concentrations, our lower molecular weight PLGA nanoparticles become significantly more toxic (**Figure 2C**). Mittal et al. showed that the poly-lactic acid to poly-glycolic acid ratio (PLA: PGA) have a significant effect of drug release as well (78). Mittal et al. shows that the 50:50 composition allows for the highest release of the payload compared to 65:35 and 85:15 ratios (78). They also show that *in vivo*, the higher molecular weight polymers allow for a higher cumulative drug in the blood stream in both oral and intravenous administration (78). Additionally, others have shown that PLGA (50:50, 24–38 kDa) is non-toxic to cells with survival rates >90%, and hemolysis of <0.4% (80). Our results support that of Thasneem et al. with cell viability of >90% at all tested concentrations for high molecular weight PLGA. We expanded that other molecular weights of PLGA, that are 10× lower and 2× higher than Thasneem's, have <0.3% hemolysis at all tested concentrations. Combining our data with those mentioned, PLGA is shown to be non-toxic, hemocompatible, and stable. Specifically, we show that higher molecular weight PLGA has superior performance over that of the low molecular weight PLGA, therefore, we have chosen the high molecular weight PLGA nanoparticles for antibody optimization.

As intravenous injection is the most common method to administer therapeutics, it is critical to ensure that the nanoparticle reaches its targeted destination. Although research reported that encapsulated DNA into particles have modified their nanoparticles to be less toxic, have higher cellular uptake, or increase payload (39, 41, 81), there still is the limitation of off target delivery which causes systemic effects (82, 83). For this reason, we investigated two endothelial cell specific antibodies, anti-EGFL7 and anti-Tie2+Tie1, on their ability to enhance cellular uptake in static and dynamic environments. We show that anti-Tie2+Tie1 has superior cellular uptake in both static and dynamic cell culture environments (**Figures 4**, **6**). Additionally, we have demonstrated that compared to HL1 cells, there was significantly more cellular uptake of anti-Tie2+Tie1 conjugated nanoparticles in HUVECs, which is due to the fact that HL1 cells do not express Tie2 or Tie1 proteins (84) (**Supplementary Figure 4C**). With our binding study, the anti-Tie2+Tie1 conjugated nanoparticles were bound significantly more than BSA conjugated or unconjugated nanoparticles. Additionally, the anti-Tie2+Tie1 nanoparticles bound significantly more to the Tie1+Tie2 coated slides than BSA-coated or uncoated slides (**Supplementary Figures 4A,B**). Others have shown that even in co-cultures of MCF-10A neoT and Caco-2, targeting antibodies for ductal breast carcinoma selectively target the MCF-10A neoT cells (85). Unconjugated nanoparticles were up taken by both cell types in the co-culture (85). Other targeting nanoparticles have been able to repress expression of particular genes at a higher rate than the standard (75). Compared to unconjugated nanoparticles, our targeting nanoparticles had significantly higher cellular uptake in the dynamic culture, supporting the notion that without targeting, the therapeutic clearance may diffuse the efficacy of the therapeutic.

In addition to site specific delivery, the encapsulated DNA needs to be bioactive. Others have shown that the sonication time or power, additives, or polymer molecular weight can affect the integrity of the plasmid (60). We have shown that our synthesis method ensures plasmid delivery at several nanoparticle concentrations, and that the plasmid is bioactive. To find optimum concentration of NICD to upregulate Notch signaling related genes, the 100 and 250 μg nanoparticle of NICD encapsulating nanoparticles significantly upregulated Notch target genes, *Hes1* and *Hey1,* compared to the gold standard lipofectamine with 5 μg of NICD (**Figure 5B**). We show that GFP protein can be synthesized in HUVECs by delivering the plasmid. Additionally, Notch and its related genes were quantified showing upregulation. However, in 500 and 1,000 μg nanoparticle groups, while NICD was also significantly upregulated, expression levels of target genes were downregulated. This indicates that the 100 μg or 250 μg of NICD nanoparticle concentrations were preferred to induce a downstream genetic effect although the higher concentrations were able to increase expression of NICD. Accordance with previous report, increment of NICD does not proportionally increase target gene expression levels (26).

Although we demonstrated PLGA nanoparticles at HMW (55–65 kDa) are an appropriate material to deliver NICD plasmid to upregulate Notch signaling with *in vitro* flow experiment, we still need to evaluate our nanoparticle in an *in vivo* environment. Specifically, our *in vitro* experiment was limited in laminar flow, while *in vivo* injection of nanoparticle would be exposed to pulsatile blood flow environment. In addition, our optimal endothelial targeting antibody, anti-Tie2+Tie1, for this study may bind to only activated Tie2 and Tie1 proteins when phosphorylated during vasculogenesis and vessel maturation (86, 87). Although our antibodies target toward to Tie1 and Tie2 heterodimer after activation from shear stress application (86), application of conjugated PLGA nanoparticles was mainly for fluid shear studies to enhance the targeting ability toward endothelial cells; thus, our nanoparticles could successfully target endothelial cells in this study. In future studies, we will optimize the NICD plasmid concentration, and the anti-Tie2+Tie1 concentration for conjugation to PLGA nanoparticles for upregulated Notch signaling in an animal model. This future experiment will help to translate our technology to effective therapeutic approach for translational medicine.

In this study, we have synthesized a PLGA nanoparticle that can deliver NICD plasmids to primary endothelial cells to upregulate Notch related components. In addition to being a non-viral transfection agent, the optimized nanoparticle was compatible with human cells and blood, and effectively delivered bioactive plasmid DNA to endothelial cells. These results demonstrate that PLGA targeting nanoparticles could increase the genetic delivery in complex environments, such as *in vivo*, with minimal adverse effects.

CONCLUSION

In this work, we have shown that higher molecular weight PLGA outperforms the low molecular weight PLGA nanoparticles in cytotoxicity, cellular uptake, stability, and hemocompatibility. Additionally, the conjugation of anti-Tie2+Tie1 to the nanoparticles allows for a significant increase in endocytosis compared to those conjugated with anti-EGFL7. Lastly, our pCAG-GFP and TetO-FUW-NICD plasmids were both successfully encapsulated and transfected into HUVECs. Most importantly, the plasmid was bioactive after transfection as indicated by GFP imaging and RT-PCR analysis. In conclusion, we can show that plasmid loaded nanoparticles have a higher transfection efficiency and create a significant genetic effect when applied to hard-to-transfect cells like HUVECs.

DATA AVAILABILITY STATEMENT

The datasets presented in this study can be found in online repositories. The names of the repository/repositories and accession number(s) can be found below: https://www.addgene.org/61540/. https://www.addgene.org/11150/.

ETHICS STATEMENT

The studies involving human participants were reviewed and approved by the University of Texas at Arlington Institutional Biosafety Committee (IBC 18.001). The patients/participants provided their written informed consent to participate in this study.

AUTHOR CONTRIBUTIONS

VM and AK: nanoparticle characterization, hemocompatibility, and antibody optimization. VM and UC: plasmid loading, plasmid release analysis, and flow study RT-PCR. VM, UC, and TD: HUVEC cell culture. VM and SL: nanoparticle release study. VM, SL, and LK: bacteria culture, and plasmid isolation. JJ, ZP, HS, KN, and JL: project support, guide, and financial support. All authors contributed to the article and approved the submitted version.

FUNDING

VM and AK are supported by the National Institutes of Health (NIH) training award, T32 HL134613 (KN). JL is supported by the American Heart Association 18CDA34110150 (JL) and NSF 1936519 (JL).

ACKNOWLEDGMENTS

The authors would like to thank Dr. Hesham Sadek, MD PhD at the University of Texas Southwestern for his valuable insight and support for this manuscript.

SUPPLEMENTARY MATERIAL

The Supplementary Material for this article can be found online at: https://www.frontiersin.org/articles/10.3389/fcvm.2021.707897/full#supplementary-material

REFERENCES

1. Chadwick N, Nostro MC, Baron M, Mottram R, Brady G, Buckle AM. Notch signaling induces apoptosis in primary human CD34+ hematopoietic progenitor cells. *Stem Cells*. (2007) 25:203–10. doi: 10.1634/stemcells.2005-0303
2. Chau MD, Tuft R, Fogarty K, Bao ZZ. Notch signaling plays a key role in cardiac cell differentiation. *Mech Dev*. (2006) 123:626–40. doi: 10.1016/j.mod.2006.06.003
3. Challice CE, Viragh S. The architectural development of the early mammalian heart. *Tissue Cell*. (2005) 6:447–62. doi: 10.1016/0040-8166(74)90037-8
4. D'Amato G, Luxán G, de la Pompa JL. Notch signalling in ventricular chamber development and cardiomyopathy. *FEBS J*. (2016) 283:4223–37. doi: 10.1111/febs.13773
5. Da'as S, Coombs AJ, Balci TB, Grondin CA, Ferrando AA, Berman JN. The zebrafish reveals dependence of the mast cell lineage on notch signaling *in vivo*. *Blood*. (2019) 119:3585–94. doi: 10.1182/blood-2011-10-385989
6. de la Pompa JL, Epstein JA. Coordinating tissue interactions: notch signaling in cardiac development and disease. *Dev Cell*. (2012) 22:244–54. doi: 10.1016/j.devcel.2012.01.014
7. High FA, Epstein JA. The multifaceted role of notch in cardiac development and disease. *Nat Rev*. (2008) 9:49–61. doi: 10.1038/nrg2279
8. Raya A, Koth CM, Buscher D, Kawakami Y, Itoh T, Raya RM, et al. Activation of Notch signaling pathway precedes heart regeneration in zebrafish. *Proc Natl Acad Sci USA*. (2003) 100:11889–95. doi: 10.1073/pnas.1834204100
9. Gazave E, Lapebie P, Richards GS, Brunet F, Ereskovsky AV, Degnan BM, et al. Origin and evolution of the Notch signalling pathway: an overview from eukaryotic genomes. *BMC Evol Biol*. (2009) 9:249. doi: 10.1186/1471-2148-9-249
10. Richards GS, Degnan BM. The dawn of developmental signaling in the metazoa. *Cold Spring Harb Symp Quant Biol*. (2009) 74:81–90. doi: 10.1101/sqb.2009.74.028
11. Samsa LA, Yang B, Liu J. Embryonic cardiac chamber maturation: trabeculation, conduction and cardiomyocyte proliferation. *Am J Med Genet C Semin Med Genet*. (2013) 163:157–68. doi: 10.1002/ajmg.c.31366
12. Tu S, Chi NC. Zebrafish models in cardiac development and congenital heart birth defects. *Differentiation*. (2012) 84:4–16. doi: 10.1016/j.diff.2012.05.005
13. Engler A, Zhang R, Taylor V. *Molecular Mechanisms of Notch Signaling*. Springer: Cham (2018).
14. Kopan R, Ilagan MX. The canonical Notch signaling pathway: unfolding the activation mechanism. *Cell*. (2009) 137:216–33. doi: 10.1016/j.cell.2009.03.045
15. Wilson C, Kavaler J, Ahmad ST. Expression of a human variant of CHMP2B linked to neurodegeneration in Drosophila external sensory organs leads to cell fate transformations associated with increased Notch activity. *Dev Neurobiol*. (2020) 80:85–97. doi: 10.1002/dneu.22722
16. Garis M, Garrett-Sinha LA. Notch signaling in B cell immune responses. *Front Immunol*. (2020) 11:609324. doi: 10.3389/fimmu.2020.609324
17. Dell'Aringa M, Reinhardt RL. Notch signaling represents an important checkpoint between follicular T-helper and canonical T-helper 2 cell fate. *Mucosal Immunol*. (2018) 11:1079–91. doi: 10.1038/s41385-018-0012-9
18. Huang D, Wang R. Exploring the mechanism of pancreatic cell fate decisions via cell-cell communication. *Math Biosci Eng*. (2021) 18:2401–24. doi: 10.3934/mbe.2021122
19. Bankaitis ED, Bechard ME, Gu G, Magnuson MA, Wright CVE. ROCK-nmMyoII, Notch and Neurog3 gene-dosage link epithelial morphogenesis

with cell fate in the pancreatic endocrine-progenitor niche. *Development.* (2018) 145:dev162115. doi: 10.1242/dev.162115

20. Lu Z, Liu H, Xue L, Xu P, Gong T, Hou G. An activated Notch1 signaling pathway inhibits cell proliferation and induces apoptosis in human esophageal squamous cell carcinoma cell line EC9706. *Int J Oncol.* (2007) 32:643–51. doi: 10.3892/ijo.32.3.643
21. Diaz-Trelles R, Scimia MC, Bushway P, Tran D, Monosov A, Monosov E, et al. Notch-independent RBPJ controls angiogenesis in the adult heart. *Nat Commun.* (2016) 7:12088. doi: 10.1038/ncomms12088
22. Luxán G, Casanova JC, Martínez-Poveda B, Prados B, D'Amato G, MacGrogan D, et al. Mutations in the NOTCH pathway regulator MIB1 cause left ventricular noncompaction cardiomyopathy. *Nat Med.* (2013) 19:193–201. doi: 10.1038/nm.3046
23. Nemir M, Pedrazzini T. Functional role of Notch signaling in the developing and postnatal heart. *J Mol Cell Cardiol.* (2008) 45:495–504. doi: 10.1016/j.yjmcc.2008.02.273
24. Lee J, Fei P, Packard RRS, Kang H, Xu H, Baek KI, et al. 4-Dimensional light-sheet microscopy to elucidate shear stress modulation of cardiac trabeculation. *J Clin Invest.* (2016) 126:1679–90. doi: 10.1172/JCI83496
25. Lee J, Vedula V, Baek KI, Chen J, Hsu JJ, Ding Y, et al. Spatial and temporal variations in hemodynamic forces initiate cardiac trabeculation. *JCI Insight.* (2018) 3:e96672. doi: 10.1172/jci.insight.96672
26. Baek KI, Packard RRS, Hsu JJ, Saffari A, Ma Z, Luu AP, et al. Ultrafine particle exposure reveals the importance of FOXO1/Notch Activation Complex for vascular regeneration. *Antioxid Redox Signal.* (2018) 28:1209–23. doi: 10.1089/ars.2017.7166
27. Meade BR, Dowdy SF. Exogenous siRNA delivery using peptide transduction domains/cell penetrating peptides. *Adv Drug Deliv Rev.* (2007) 59:134–40. doi: 10.1016/j.addr.2007.03.004
28. Klibanov AL, Khaw Ba Fau N, Nossiff SM, Nossiff NF, O'Donnell L, O'Donnell SF, et al. Targeting of macromolecular carriers and liposomes by antibodies to myosin heavy chain. *Am J Physiol.* (1991) 261:60–5. doi: 10.1152/ajpheart.1991.261.4.60
29. Oberli MA, Reichmuth AM, Dorkin JR, Mitchell MJ, Fenton OS, Jaklenec A, et al. Lipid nanoparticle assisted mRNA delivery for potent cancer immunotherapy. *Nano Lett.* (2017) 17:1326–35. doi: 10.1021/acs.nanolett.6b03329
30. Lv H, Zhang S, Wang B, Cui S, Yan J. Toxicity of cationic lipids and cationic polymers in gene delivery. *J Control Release.* (2006) 114:100–9. doi: 10.1016/j.jconrel.2006.04.014
31. Zubareva A, Shagdarova B, Varlamov V, Kashirina E, Svirshchevskaya E. Penetration and toxicity of chitosan and its derivatives. *Eur Polym J.* (2017) 93:743–9. doi: 10.1016/j.eurpolymj.2017.04.021
32. Coolen AL, Lacroix C, Mercier-Gouy P, Delaune E, Monge C, Exposito JY, et al. Poly(lactic acid) nanoparticles and cell-penetrating peptide potentiate mRNA-based vaccine expression in dendritic cells triggering their activation. *Biomaterials.* (2019) 195:23–37. doi: 10.1016/j.biomaterials.2018.12.019
33. Menon JU, Ravikumar P, Pise A, Gyawali D, Hsia CC, Nguyen KT. Polymeric nanoparticles for pulmonary protein and DNA delivery. *Acta Biomater.* (2014) 10:2643–52. doi: 10.1016/j.actbio.2014.01.033
34. Yan Y, Xiong H, Zhang X, Cheng Q, Siegwart DJ. Systemic mRNA delivery to the lungs by functional polyester-based carriers. *Biomacromolecules.* (2017) 18:4307–15. doi: 10.1021/acs.biomac.7b01356
35. Guerrero-Cázares H, Tzeng SY, Young NP, Abutaleb AO, Quiñones-Hinojosa A, Green JJ. Biodegradable polymeric nanoparticles show high efficacy and specificity at DNA delivery to human glioblastoma *in vitro* and *in vivo*. *ACS Nano.* (2014) 8:5141–53. doi: 10.1021/nn501197v
36. Inyang E, Kuriakose A, Chen B, Nguyen K, Cho M. Engineering delivery of nonbiologics using Poly(lactiv-co-glycolic acid) Nanoparticles for repair of disrupted brain endothelium. *ACS Omega.* (2020) 5:14730–40. doi: 10.1021/acsomega.0c01517
37. Zangi L, Lui KO, von Gise A, Ma Q, Ebina W, Ptaszek LM, et al. Modified mRNA directs the fate of heart progenitor cells and induces vascular regeneration after myocardial infarction. *Nat Biotechnol.* (2013) 31:898–907. doi: 10.1038/nbt.2682
38. Amani A, Kabiri T, Shafiee S, Hamidi A. Preparation and characterization of PLA-PEG-PLA/PEI/DNA Nanoparticles for improvement of transfection efficiency and controlled release of DNA in gene delivery systems. *Iran J Pharm Res.* (2019) 18:125—41.
39. Ryu N, Kim M-A, Park D, Lee B, Kim Y-R, Kim K-H, et al. Effective PEI-mediated delivey of CRISPR-Cas9 complex for targeted gene therapy. *Nanomedicine.* (2018) 14:2095–102. doi: 10.1016/j.nano.2018.06.009
40. Cooper RC, Yang H. Duplex of polyamidoamine dendrimer/custom-designed nuclear-localization sequence peptide for enhanced gene delivery. *Bioelectrcity.* (2020) 2:150–7. doi: 10.1089/bioe.2020.0009
41. Srinageshwar B, Florendo M, Clark B, Johnson K, Munro N, Peruzzaro S, et al. A mixed-surface polyamidoamine dendrimer for *in vitro* and *in vivo* delivery of large plasmids. *Pharmaceutics.* (2020) 12:619. doi: 10.3390/pharmaceutics12070619
42. Huang T, Song X, Jing J, Zhao K, Shen Y, Zhang X, et al. Chitosan-DNA nanoparticles enhanced the immunogenicity of multivalent DNA vaccination on mice against Trueperella pyogenes infection. *J Nanobiotechnology.* (2018) 16:8. doi: 10.1186/s12951-018-0337-2
43. Rahmani S, Hakimi S, Esmaeily A, Samadi FY, Mortazavian E, Nazari M, et al. Novel chitosan based nanoparticles as gene delivery systems to cancerous and noncancerous cells. *Int J Pharm.* (2019) 560:306–14. doi: 10.1016/j.ijpharm.2019.02.016
44. Nematollahi MH, Torkzadeh-Mahanai M, Pardakhty A, Meimand HAE, Asadikaram G. Ternary complex of plasmid DNA with NLS-Mu-Mu protein and cationic niosome for biocompatible and efficient gene delivery: a comparative study with protamine and lipofectamine. *Artif Cells Nanomed Biotechnol.* (2017) 46:1781–91. doi: 10.1080/21691401.2017.1392316
45. Marin E, Briceño MI, Caballero-George C. Critical evaluation of biodegradable polymers used in nanodrugs. *Int J Nanomed.* (2013) 8:3071–91. doi: 10.2147/IJN.S47186
46. Patel J, Amrutiya J, Bhatt P, Javia A, Jain M, Misra A. Targeted delivery of monoclonal antibody conjugated docetaxel loaded PLGA nanoparticles into EGFR overexpressed lung tunour cells. *J Microencapsul.* (2018) 35:204–17. doi: 10.1080/02652048.2018.1453560
47. Malinovskaya Y, Melnikov P, Baklaushev V, Gabashvili A, Osipova N, Mantrov S, et al. Delivery of doxorubicin-loaded PLGA nanoparticles into U87 human glioblastoma cells. *Int J Pharm.* (2017) 524:77–90. doi: 10.1016/j.ijpharm.2017.03.049
48. Madani F, Esnaashari SS, Mujokoro B, Dorkoosh F, Khosravani M, Adabi M. Investigation of effective parameters on size of paclitaxel loaded PLGA nanoparticles. *Adv Pharm Bull.* (2018) 8:77–84. doi: 10.15171/apb.2018.010
49. Khan I, Gothwal A, Sharma AK, Kesharwani P, Gupta L, Iyer AK, et al. PLGA nanoparticles and their versatile role in anticancer drug delivery. *Crit Rev Ther Drug Carrier Syst.* (2016) 33:159–93. doi: 10.1615/CritRevTherDrugCarrierSyst.2016015273
50. Cun D, Jensen DK, Maltesen MJ, Bunker M, Whiteside P, Scurr D, et al. High loading efficiency and sustained release of siRNA encapsulated PLGA nanoparticles; Quality by design optimization and characterization. *Eur J Pharm Biopharm.* (2011) 77:26–35. doi: 10.1016/j.ejpb.2010.11.008
51. Golub JS, Kim YT, Duvall CL, Bellamkonda RV, Gupta D, Lin AS, et al. Sustained VEGF delivery via PLGA nanoparticles promotes vascular growth. *Am J Physiol Heart Circ Physiol.* (2010) 298:H1959–65. doi: 10.1152/ajpheart.00199.2009
52. Oduk Y, Kannappan R, Wuqiang Z, Zhang J. Abstract 19225: sustained release of VEGF via PLGA nanoparticles improves vascularization *in vitro* and *in vivo*. *Circulation.* (2016) 134:A19225.
53. Jeon SG, Cha M-Y, Kim J-I, Hwang TW, Kim KA, Song KC, et al. Vitamin D-binding protein-loaded PLGA nanoparticles suppress Alzheimer's disease-related pathology in 5XFAD mice. Nanomedicine: *Nanotechnol Biol Med.* (2019) 17:297–307. doi: 10.1016/j.nano.2019.02.004
54. Zhang E, Zhukova V, Semyonkin A, Osipova N, Malinovskaya Y, Maksimenko O, et al. Release kinetics of fluorescent dyes from PLGA nanoparticles in retinal blood vessels: in vivo monitoring and *ex vivo* localization. *Eur J Pharm Biopharm.* (2020) 150:131–42. doi: 10.1016/j.ejpb.2020.03.006
55. Dalpiaz A, Sacchetti F, Baldisserotto A, Pavan B, Maretti E, Iannuccelli V, et al. Application of the "in-oil nanoprecipitation" method in the encapsulation of hydrophillic drugs in PLGA nanoparticles. *J Drug Deliv Sci Technol.* (2016) 32:283–90. doi: 10.1016/j.jddst.2015.07.020

56. Liang GF, Zhu YL, Sun B, Hu FH, Tian T, Li SC, et al. PLGA-based gene delivering nanoparticle enhance suppression effect of miRNA in HePG2 cells. *Nanoscale Res Lett.* (2011) 6:447. doi: 10.1186/1556-276X-6-447
57. Menon JU, Kuriakose A, Iyer R, Hernandez E, Gandee L, Zhang S, et al. Dual-drug containing core-shell nanoparticles for lung cancer therapy. *Sci Rep.* (2017) 7:13249. doi: 10.1038/s41598-017-13320-4
58. Kalvanagh PA, Ebtekar M, Kokhaei P, Soleimanjahi H. Preparation and characterization of PLGA nanoparticles containng plasmid DNA Encoding HUman IFN-lambda-1/IL-29. *Iran J Pharm Res.* (2019) 18:156−67.
59. Dastan T, Turan K. *In vitro* characterization and delivery of chitosan-DNA microparticles into mamalian cells. *J Pharm Pharmaceut Sci.* (2004) 7:205−14.
60. Gvili K, Benny O, Danino D, Machluf M. Poly(D,L-lactide-co-glycolide acid) nanoparticles for DNA delivery: waiving preparation complexity and increasing efficiency. *Biopolymers.* (2007) 85:379–91. doi: 10.1002/bip.20697
61. Makadia HK, Siegel SJ. Poly Lactic-co-Glycolic Acid (PLGA) as biodegradable controlled drug delivery carrier. *Polymers.* (2011) 3:1377–97. doi: 10.3390/polym3031377
62. Allahyari M, Mohit E. Peptide/protein vaccine delivery system based on PLGA particles. *Hum Vaccin Immunother.* (2016) 12:806–28. doi: 10.1080/21645515.2015.1102804
63. Roces CB, Christensen D, Perrie Y. Translating the fabrication of protein-loaded poly(lactic-co-glycolic acid) nanoparticles from bench to scale-independent production using microfluidics. *Drug Deliv Transl Res.* (2020) 10:582–93. doi: 10.1007/s13346-019-00699-y
64. Mansor MH, Najberg M, Contini A, Alvarez-Lorenzo C, Garcion E, Jerome C, et al. Development of a non-toxic and non-denaturing formulation process for encapsulation of SDF-1alpha into PLGA/PEG-PLGA nanoparticles to achieve sustained release. *Eur J Pharm Biopharm.* (2018) 125:38–50. doi: 10.1016/j.ejpb.2017.12.020
65. Shi Y, Zhou M, Zhang J, Lu W. Preparation and cellular targeting study of VEGF-conjugated PLGA Nanoparticles. *J Microencapsul.* (2015) 32:699–704. doi: 10.3109/02652048.2015.1035683
66. Lu B, Lv X, Le Y. Chitosan-Modified PLGa nanoparticles for control-released drug delivery. *Polymers.* (2019) 11:304. doi: 10.3390/polym11020304
67. Wilkosz N, Lazarski G, Kovacik L, Gargas P, Nowakowska M, Jamroz D, et al. Molecular insight into drug-loading capacity of PEG-PLGA nanoparticles for itraconazole. *J Phys Chem B.* (2018) 122:7080–90. doi: 10.1021/acs.jpcb.8b03742
68. Yu X, Sun L, Tan L, Wang M, Ren X, Pi J, et al. Preparation and characterization of PLGA-PEG-PLGA nanoparticles containing salidroside and tamoxifen for breast cancer therapy. *AAPS Pharm Sci Tech.* (2020) 21:85. doi: 10.1208/s12249-019-1523-8
69. Bettinger T, Carlisle RC, Read ML, Ogris M, Seymour LW. Peptide-mediated RNA delivery: a novel approach for enhanced transfection of primary and post-mitotic cells. *Nucleic Acids Res.* (2001) 29:3882–91. doi: 10.1093/nar/29.18.3882
70. Panyam J, Labhasetwar V. Biodegradable nanoparticles for drug and gene delivery to cells and tissue. *Adv Drug Deliv Rev.* (2003) 55:329–47. doi: 10.1016/S0169-409X(02)00228-4
71. Kamimura K, Suda T, Zhang G, Liu D. Advances in gene delivery systems. *Pharm Med N Z.* (2011) 25:293–306. doi: 10.1007/BF03256872
72. Oh MH, Lee N, Kim H, Park SP, Piao Y, Lee J, et al. Large-scale synthesis of bioinert tantalum oxide nanoparticles for X-ray computed tomography imaging and bimodal image-guided sentinel lymph node mapping. *J Am Chem Soc.* (2011) 133:5508–15. doi: 10.1021/ja200120k
73. Takahama H, Minamino T, Asanuma H, Fujita M, Asai T, Wakeno M, et al. Prolonged targeting of ischemic/reperfused myocardium by liposomal adenosine augments cardioprotection in rats. *J Am Coll Cardiol.* (2009) 53:709–17. doi: 10.1016/j.jacc.2008.11.014
74. Turnbull IC, Eltoukhy AA, Fish KM, Nonnenmacher M, Ishikawa K, Chen JQ, et al. Myocardial delivery of lipidoid nanoparticle carrying modRNA induces rapid and transient expression. *Mol Ther.* (2016) 24:66–75. doi: 10.1038/mt.2015.193
75. Wu F-L, Zhang J, Li W, Bian B-X, Hong Y-D, Song Z-Y, et al. Enhanced antiproliferative activity of antibody-functionalized polymeric nanoparticles for targeted delivery of anti-miR-21 to HER2 positive gastric cancer. *Oncotarget.* (2017) 8:67189–202. doi: 10.18632/oncotarget.18066
76. Kumskova N, Ermolenko Y, Osipova N, Semyonkin A, Kildeeva N, Gorshkova M, et al. How subtle differences in polymer molecular weight affect doxorubicin-loaded PLGA nanoparticles degradation and drug release. *J Microencapsul.* (2020) 37:283–95. doi: 10.1080/02652048.2020.1729885
77. Choi Y, Yoon HY, Kim J, Yang S, Lee J, Choi JW, et al. Doxorubicin-Loaded PLGA nanoparticles for cancer therapy: molecular weight effect of PLGA in doxorubicin release for controlling immunogenic cell death. *Pharmaceutics.* (2020) 12:1165. doi: 10.3390/pharmaceutics12121165
78. Mittal G, Sahana DK, Bhardwaj V, Ravi Kumar MN. Estradiol loaded PLGA nanoparticles for oral administration: effect of polymer molecular weight and copolymer composition on release behavior *in vitro* and *in vivo*. *J Control Release.* (2007) 119:77–85. doi: 10.1016/j.jconrel.2007.01.016
79. Ozturk AA, Yenilmez E, Senel B, Kiyan HT, Guven UM. Effect of different molecular weight PLGA on flurbiprofen nanoparticles: formulation, characterization, cytotoxicity, and *in vivo* anti-inflammatory effect by using HET-CAM assay. *Drug Dev Ind Pharm.* (2020) 46:682–95. doi: 10.1080/03639045.2020.1755304
80. Thasneem YM, Sajeesh S, Sharma CP. Effect of thiol functionalization on the hemo-compatibility of PLGA nanoparticles. *J Biomed Mater Res A.* (2011) 99:607–17. doi: 10.1002/jbm.a.33220
81. Zhang J, Lei Y, Dhaliwal A, Ng QK, Du J, Yan M, et al. Protein-Polymer nanoparticles for novel gene delivery. *Biomacromolecules.* (2011) 12:1006–14. doi: 10.1021/bm101354a
82. Chen J, Wang K, Wu J, Tian H, Chen X. Polycations for gene delivery: dilemmas and solutions. *Bioconjug Chem.* (2019) 30:338–49. doi: 10.1021/acs.bioconjchem.8b00688
83. Amreddy N, Babu A, Muralidharan R, Munshi A, Ramesh R. Polymeric Nanoparticle-Mediated gene delivery for lung cancer treatment. *Top Curr Chem.* (2017) 375:35. doi: 10.1007/s41061-017-0128-5
84. Uhlén M, Fagerberg L, Hallström BM, Lindskog C, Oksvold P, Mardinoglu A, et al. Tissue-based map of the human proteome. *Science.* (2015) 347:1260419. doi: 10.1126/science.1260419
85. Kocbek P, Obermajer N, Cegnar M, Kos J, Kristl J. Targeting cancer cells using PLGA nanoparticles surface modified with monoclonal antibody. *J Control Release.* (2007) 120:18–26. doi: 10.1016/j.jconrel.2007.03.012
86. Leppanen VM, Saharinen P, Alitalo K. Structural basis of Tie2 activation and Tie2/Tie1 heterodimerization. *Proc Natl Acad Sci USA.* (2017) 114:4376–81. doi: 10.1073/pnas.1616166114
87. Lee HJ, Koh GY. Shear stress activates Tie2 receptor tyrosine kinase in human endothelial cells. *Biochem Biophys Res Commun.* (2003) 304:399–404. doi: 10.1016/S0006-291X(03)00592-8

Conflict of Interest: The authors declare that the research was conducted in the absence of any commercial or financial relationships that could be construed as a potential conflict of interest.

frontiers in Cardiovascular Medicine

CORRECTION
published: 26 October 2021
doi: 10.3389/fcvm.2021.785910

Corrigendum: Notch Intracellular Domain Plasmid Delivery via Poly(Lactic-Co-Glycolic Acid) Nanoparticles to Upregulate Notch Pathway Molecules

Victoria L. Messerschmidt [1,2†], Uday Chintapula [1,2†], Aneetta E. Kuriakose [1,2], Samantha Laboy [1], Thuy Thi Dang Truong [1], LeNaiya A. Kydd [1], Justyn Jaworski [1], Zui Pan [3], Hesham Sadek [2], Kytai T. Nguyen [1,2] and Juhyun Lee [1,2]**

[1] Department of Bioengineering, University of Texas at Arlington, Arlington, TX, United States, [2] Department of Internal Medicine, University of Texas Southwestern Medical Center, Dallas, TX, United States, [3] College of Nursing and Health Innovation, University of Texas at Arlington, Arlington, TX, United States

Approved by:
Frontiers Editorial Office,
Frontiers Media SA, Switzerland

****Correspondence:***
Kytai T. Nguyen
knguyen@uta.edu
Juhyun Lee
juhyun.lee@uta.edu

†These authors have contributed equally to this work

Specialty section:
This article was submitted to Atherosclerosis and Vascular Medicine,
a section of the journal
Frontiers in Cardiovascular Medicine

Received: *29 September 2021*
Accepted: *30 September 2021*
Published: *26 October 2021*

Citation:
Messerschmidt VL, Chintapula U, Kuriakose AE, Laboy S, Truong TTD, Kydd LA, Jaworski J, Pan Z, Sadek H, Nguyen KT and Lee J (2021) Corrigendum: Notch Intracellular Domain Plasmid Delivery via Poly(Lactic-Co-Glycolic Acid) Nanoparticles to Upregulate Notch Pathway Molecules. Front. Cardiovasc. Med. 8:785910. doi: 10.3389/fcvm.2021.785910

Keywords: Notch signaling, PLGA, nanoparticles, gene delivery, non-viral transfection

A Corrigendum on

Notch Intracellular Domain Plasmid Delivery via Poly(Lactic-Co-Glycolic Acid) Nanoparticles to Upregulate Notch Pathway Molecules
by Messerschmidt, V. L., Chintapula, U., Kuriakose, A. E., Laboy, S., Truong, T. T. D., Kydd, L. A., Jaworski, J., Pan, Z., Sadek, H., Nguyen, K. T., and Lee, J. (2021). Front. Cardiovasc. Med. 8:707897. doi: 10.3389/fcvm.2021.707897

An author name was incorrectly spelled as **Hashem Sadek**. The correct spelling is **Hesham Sadek**.

****Incorrect version****

Victoria L. Messerschmidt[1,2†], Uday Chintapula[1,2†], Aneetta E. Kuriakose[1,2], Samantha Laboy[1], Thuy Thi Dang Truong[1], LeNaiya A. Kydd[1], Justyn Jaworski[1], Zui Pan[3], Hashem Sadek[2], Kytai T. Nguyen[1,2]* and Juhyun Lee[1,2]*

[1] Department of Bioengineering, University of Texas at Arlington, Arlington, TX, United States

[2] Department of Internal Medicine, University of Texas Southwestern Medical Center, Dallas, TX, United States

[3] College of Nursing and Health Innovation, University of Texas at Arlington, Arlington, TX, United States

****CORRECT version****

Victoria L. Messerschmidt[1,2†], Uday Chintapula[1,2†], Aneetta E. Kuriakose[1,2], Samantha Laboy[1], Thuy Thi Dang Truong[1], LeNaiya A. Kydd[1], Justyn Jaworski[1], Zui Pan[3], Hesham Sadek[2], Kytai T. Nguyen[1,2]* and Juhyun Lee[1,2]*

[1] Department of Bioengineering, University of Texas at Arlington, Arlington, TX, United States

[2] Department of Internal Medicine, University of Texas Southwestern Medical Center, Dallas, TX, United States

[3] College of Nursing and Health Innovation, University of Texas at Arlington, Arlington, TX, United States

The authors apologize for this error and state that this does not change the scientific conclusions of the article in any way. The original article has been updated.

frontiers in Cardiovascular Medicine

MINI REVIEW
published: 08 November 2021
doi: 10.3389/fcvm.2021.707890

Transplantation of Human Pluripotent Stem Cell-Derived Cardiomyocytes for Cardiac Regenerative Therapy

Sophia E. Silver[1,2], *Ryan W. Barrs*[1,2] *and Ying Mei*[1,2]*

[1] Bioengineering Department, Clemson University, Clemson, SC, United States, [2] Department of Regenerative Medicine and Cell Biology, Medical University of South Carolina, Charleston, SC, United States

Cardiovascular disease is the leading cause of death worldwide and bears an immense economic burden. Late-stage heart failure often requires total heart transplantation; however, due to donor shortages and lifelong immunosuppression, alternative cardiac regenerative therapies are in high demand. Human pluripotent stem cells (hPSCs), including human embryonic and induced pluripotent stem cells, have emerged as a viable source of human cardiomyocytes for transplantation. Recent developments in several mammalian models of cardiac injury have provided strong evidence of the therapeutic potential of hPSC-derived cardiomyocytes (hPSC-CM), showing their ability to electromechanically integrate with host cardiac tissue and promote functional recovery. In this review, we will discuss recent developments in hPSC-CM differentiation and transplantation strategies for delivery to the heart. We will highlight the mechanisms through which hPSC-CMs contribute to heart repair, review major challenges in successful transplantation of hPSC-CMs, and present solutions that are being explored to address these limitations. We end with a discussion of the clinical use of hPSC-CMs, including hurdles to clinical translation, current clinical trials, and future perspectives on hPSC-CM transplantation.

Keywords: human pluripotent stem cell-derived cardiomyocytes, cardiovascular disease, cell therapy, regenerative medicine, tissue engineering

Edited by:
James Dahlman,
Georgia Institute of Technology,
United States

Reviewed by:
Minglin Ma,
Cornell University, United States
Timothy Mark O'Shea,
Boston University, United States

****Correspondence:***
Ying Mei
mei@clemson.edu

Specialty section:
This article was submitted to
Atherosclerosis and Vascular
Medicine,
a section of the journal
Frontiers in Cardiovascular Medicine

Received: *10 May 2021*
Accepted: *20 October 2021*
Published: *08 November 2021*

Citation:
Silver SE, Barrs RW and Mei Y (2021)
Transplantation of Human Pluripotent
Stem Cell-Derived Cardiomyocytes for
Cardiac Regenerative Therapy.
Front. Cardiovasc. Med. 8:707890.
doi: 10.3389/fcvm.2021.707890

INTRODUCTION

Cardiovascular disease (CVD) is the leading cause of death worldwide (1). In the United States alone, CVD is responsible for ∼655,000 deaths and contributes to $200 billion in spending each year (2). CVD can lead to myocardial infarction (MI), also known as a "heart attack," which results in restricted blood flow and extensive cell death within the infarct zone. Due to the limited regenerative capacity of the human heart, infarcted myocardium is replaced by fibrotic scar tissue with inferior contractile performance. Over time, pathological remodeling leads to ventricular wall thinning, which can progress to heart failure (3). There is currently no treatment available that can restore lost cardiomyocytes after MI, and conventional therapies typically only manage the symptoms (3, 4). Heart transplantation is the only therapy capable of replacing a failing heart, but the shortage of viable donor organs and need for lifelong immunosuppression presents its own set of challenges for heart transplantation as a therapy (5). Therefore, alternative approaches that can restore the function of the patient's heart and replace infarcted myocardium would be a transformative development in cardiovascular medicine.

Stem cell therapy for cardiac regenerative medicine has drawn major interest due to the promising capacity of stem cells to differentiate into functional tissue. Several sources have been investigated for stem cell-mediated cardiac regenerative therapy, including both human adult stem cells and human pluripotent stem cells (hPSCs) (6). Unlike adult stem cells, hPSCs have a proven capacity to derive functional cardiomyocytes, and their scalable production *in vitro* has made hPSCs a favorable cell source for cardiac regenerative medicine (7, 8).

This review will discuss the origins and characteristics of human pluripotent stem cell-derived cardiomyocytes (hPSC-CMs) and how they are implemented in transplantation techniques (**Figure 1**). Additionally, we will discuss the potential mechanisms through which these transplantation strategies improve cardiac function and what challenges limit effective hPSC-CM transplantation. Finally, we will end with a discussion of challenges facing clinical translation of these transplantation strategies (**Figure 1**), current clinical trials involving hPSC-CMs, and future considerations in the field of transplantation of hPSC-CM for cardiac regenerative therapies.

HUMAN PLURIPOTENT STEM CELL SOURCES AND DIFFERENTIATION INTO CARDIOMYOCYTES

Human embryonic stem cells (hESCs) are a form of hPSCs isolated from human blastocysts cultured for *in vitro* fertilization. hESCs are capable of unlimited self-renewal and can differentiate into derivatives of all three germ layers (9). The differentiation potential of hESCs has been harnessed to reproducibly generate cardiomyocytes (hESC-CMs) (10). As the production of hESCs involves the destruction of human embryos, there are many ethical controversies that accompany the use of hESCs (11). To overcome these ethical concerns, human induced pluripotent stem cells (hiPSCs) have been explored as a cardiomyocyte source. hiPSCs are reprogrammed somatic cells with the capacity to differentiate into cells of all three embryonic germ layers. The concept behind the development of hiPSCs was that the genes that allow a cell to maintain its pluripotency could be overexpressed in a somatic cell and reprogram it to an ESC-like state (12). Viral vectors (12, 13) as well as recombinant proteins (14) and micro RNAs (15, 16) have been used to reprogram adult human cells to a pluripotent state.

The major methods to derive CMs from hPSCs are embryoid body differentiation, monolayer differentiation, and inductive differentiation (17). Common among all of these methods is the principle of mimicking endogenous embryonic cardiovascular development, including modulation of Wnt, Activin/Nodal, TGF-β, and BMP signaling pathways (18–21). Currently, hPSC-CM purity following differentiation can reach over 90% (18, 19, 21). The phenotype of hPSC-CMs resembles that of fetal CMs. For instance, they are morphologically small, spontaneously beat, lack T-tubules, and have underdeveloped and inefficient calcium handling (22). Developments in methods for differentiation and culture are working toward the goal of producing hPSC-CMs with a more mature phenotype, as will be discussed later in this review.

TRANSPLANTATION STRATEGIES

Delivery routes for cardiac cell therapies have included intravenous injection, intramyocardial injection, intracoronary injection, intrapericardial transplantation, and epicardial patches. Each of these methods have their own strengths and weaknesses regarding cell retention and functional outcomes (23). For hPSC-CM transplantation, intramyocardial injection and epicardial patches have been the most popular delivery routes in pre-clinical studies and first-in-human clinical trials. Therefore, we will focus on these two transplantation strategies in this review.

Intramyocardial Injection

Early studies in the transplantation of hPSC-CM involved intramyocardial injection of single cell suspensions in mouse (24), rat (25), guinea pig (26), and swine models (27). Although hPSC-CMs demonstrated the ability of to partially remuscularize the animal hearts, cell retention and survival rates were low, and there was insufficient evidence of functional integration. To improve hPSC-CM survival post-transplantation, Murry et al. developed a pro-survival cocktail that led to enhanced cell survival after transplantation, robust cardiac remuscularization, and functional improvement in both small (28–32) and large (33) animal models of ischemic injury. Murry's group later showed that hPSC-CM injection in a non-human primate model of MI results in extensive remuscularization and electromechanical coupling of grafted cells to host myocardium (33, 34). They further confirmed the ability of the engrafted hPSC-CMs to restore function in the non-human primate heart by demonstrating improved left ventricular ejection fraction. However, they also observed transient graft-associated ventricular arrhythmias, which was attributed to the ectopic pacemaker activity of the engrafted hPSC-CMs (33, 34).

To aid in cell retention following engraftment of hPSC-CM, recent studies have explored injectable three-dimensional hPSC-CM microtissues to provide critical cell-cell interactions and reduce anoikis. For example, Moon et al. demonstrated reduced fibrosis, improved fractional shortening, and prolonged survival of 5–10 cell hPSC-CM aggregates injected into infarcted rat hearts (35). Larger scale hPSC-CM spheroids containing 200,000 cells each have also been implemented to promote improvement in fractional shortening and engraftment rates following infarction in a murine model (36). Spheroids consisting of hPSC-CMs have also been implanted into a porcine model of heart failure, leading to functional improvement (37). However, graft-associated arrhythmias were observed in the swine transplanted with hiPSC-CM spheroids.

Epicardial Patches

Epicardial patches refer to engineered heart tissues that are attached to the outer surface of the heart, usually adjacent to the infarct region. In addition to providing mechanical support, epicardial patches function as a scaffold to provide cell-ECM interactions that promote hPSC-CM survival and engraftment post-transplantation as well as secretion of cardioprotective paracrine factors (38, 39). For example, rodent models of chronic ischemia have been treated with epicardial patches

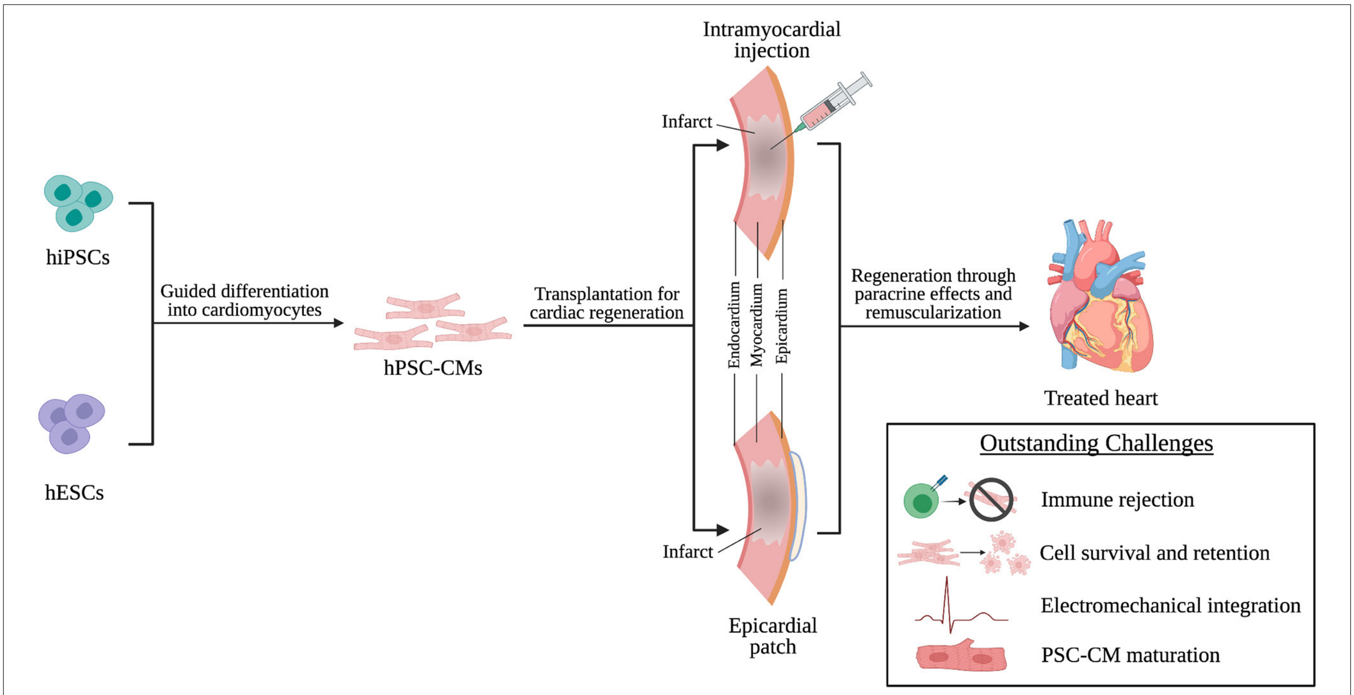

FIGURE 1 | hPSC-CMs are differentiated from hiPSCs and hESCs and transplanted into the infarcted heart through intramyocardial injection or epicardial patches as a cardiac regenerative therapy. Following transplantation, regeneration is driven by paracrine effects of and remuscularization of myocardial tissue by engrafted hPSC-CMs. However, challenges persist that limit successful transplantation of hPSC-CMs and will need to be addressed to achieve effective clinical translation.

and demonstrated long-term retention of grafts (40). Despite this progress, patches are not immediately perfused post-transplantation and can be isolated from host myocardium by a layer of fibrotic tissue, limiting nutrient diffusion to cells within the construct post-transplantation (40). To address this, porous patches seeded with hPSC-CMs have been investigated to examine whether the porous nature of the patch would allow sufficient nutrient and oxygen exchange to engrafted cardiomyocytes (41). Munarin et al. have also recently demonstrated that the incorporation of alginate microspheres containing angiogenic factors in hPSC-CM scaffolds could lead to enhanced host vasculature infiltration into the scaffolds and improved cell survival when implanted in a rodent model of acute MI (42).

To improve vascular integration with host myocardium, vascular cells (i.e., endothelial cells) have been incorporated into epicardial patches with hPSC-CMs. Biodegradable scaffolds seeded with a triculture of hPSC-CMs, human umbilical vein endothelial cells (HUVECs), and embryonic fibroblasts promoted graft vascularization and anastomosis with host coronary vasculature in rodent hearts (43). Ye et al. combined the use of biomaterials and multiple cell types to investigate a 3D fibrin patch loaded with the pro-survival factor insulin-like growth factor-1 (IGF-1)-encapsulated microspheres seeded with hPSC-CMs, endothelial cells (ECs), and smooth muscle cells (SMCs). When implanted in a porcine model of acute MI, all three cell types integrated with the host, and physiological improvements were observed in terms of improved left ventricle function, myocardial metabolism, and ventricular wall stress (44). Advances in engineered heart tissue have led to the fabrication of clinical scale human cardiac muscle patches (hCMP) consisting of 3D fibrin scaffolds seeded with hPSC-CMs, -ECs, and -SMCs (45, 46). The hCMPs exhibited 10% engraftment at 4 weeks post-implantation and promoted significant improvement in cardiac function and reduction in wall stress and infarct size (46).

Scaffold-free approaches have also been used to create epicardial patches. Cell sheet technology, developed by Okano et al., involves coating culture dishes with PNIPAAm, a thermo-responsive polymer, to release cells and produce cell sheets upon changing temperature (47). This technique was recently used to fabricate cardiac tissue sheets from hPSCs, which were then implanted into small and large animal injury models to demonstrate their therapeutic potential (48–51). In addition, Murry et al. developed pre-vascularized cell sheets with enhanced survival and anastomosis with host vasculature upon transplantation in healthy rodent hearts (52).

MECHANISMS OF IMPROVING CARDIAC FUNCTION

Remuscularization

A major goal of cardiac regenerative medicine is to remuscularize the infarcted myocardium, restoring the muscle that was lost to ischemic injury (53). Intramyocardial injection of hPSC-CMs allows the engrafted hPSC-CMs to integrate with host myocardium and directly contribute to contractile function. Functional integration has been evidenced by the formation of gap junctions between host and engrafted cardiomyocytes in various small (28, 29, 39) and large (33, 34) animal models.

Epicardial patches can improve hPSC-CM engraftment, provide partial remuscularization to infarcted myocardium, and augment left ventricular function in a dose-dependent manner (54). However, the fibrotic tissue between the patch and myocardium can reduce long-term survival of the hPSC-CMs and prohibit the formation of electromechanical junctions between the engrafted hPSC-CMs and host myocardium, leading to unsynchronized contractions (29).

Paracrine Effects

In many instances of intramyocardial hPSC-CM transplantation, functional recovery has occurred even without significant hPSC-CM engraftment, leading researchers to hypothesize that paracrine factors (e.g., cytokines, extracellular vesicles, etc.) released by the transplanted cells are partially responsible for improvements in damaged myocardium. This concept was explored through single-cell profiling of hPSC-CMs following their transplantation in a murine acute MI model. Left ventricular function was improved despite limited engraftment, and hPSC-CMs were found to release high levels of proangiogenic and anti-apoptotic factors, suggesting functional benefits came from paracrine activity (55). This is further supported by similar functional recovery obtained by injection of hPSC-cardiac cells and hPSC-cardiac cell-secreted exosomes into infarcted porcine hearts (56). Cardioprotective microRNAs have been identified in hiPSC-CM-derived extracellular vesicles, and extended delivery *via* a hydrogel patch improved cardiac recovery (57).

Due to subnormal formation of electromechanical junctions with host myocardium, epicardial patches typically repair injured hearts through mechanical support and paracrine effects. Given the fibrotic separation, vascular integration between epicardial patches and host myocardium may play a critical role in transporting patch-derived paracrine factors into myocardium (39, 41).

CHALLENGES TO IMPROVE hPSC-CM TRANSPLANTATION STRATEGIES

Although progress has been made in the field of hPSC-CM transplantation, challenges still face transplantation and clinical translation of hPSC-CM therapies. In the next two chapters, we will first discuss the challenges that face the development of successful hPSC-CM transplantation techniques and then the outstanding challenges that limit safe and effective clinical translation of these techniques.

Immune Rejection

Transplantation of allogenic cells or tissues can elicit an immune response that ultimately leads to graft rejection and can have harmful consequences for the transplant recipient. Solutions include major histocompatibility (MHC)-matching and the production of hPSC banks (58). Shiba et al. performed an MHC matching study in which they transplanted allogenic non-human primate PSC-CMs 14 days after injury in a cynomolgus monkey model of MI. They observed improved cardiac function, along with electrical coupling with the host myocardium and no evidence of immune rejection in the MHC-matched PSC-CM group, suggesting the safety of transplanting MHC-matched, donor-derived hPSC-CMs in humans (59). Eventually, autologous transplantation of hPSC-CMs would be ideal and hiPSC-CMs, in particular, offer a promising source of patient-derived cells. However, manufacturing challenges must be overcome to make autologous hPSC-CM transplantation practical for clinical use.

Cell Survival and Retention

Low cell survival and retention after transplantation is a central obstacle in the development of effective hPSC-CM-based cardiac regenerative therapy (60, 61). To improve survival of intramyocardial injected hPSC-CM single cells, a pro-survival cocktail for injection was developed to address common causes of graft death (62). A recent study found that co-transplantation of hiPSC-CMs with ready-made microvessels from adipose tissue resulted in a six-fold improvement in hiPSC-CM cell survival (63). To promote cell survival in epicardial patches, pre-vascularization strategies have been explored to promote anastomosis of the patches with host vasculature (64, 65). Going forward, novel bioengineering approaches (e.g., biomaterials and cellular engineering) could improve hPSC-CM retention (23).

Electromechanical Integration of the Graft

Due to the wound healing response following MI and intramyocardial injections, fibrosis develops around transplanted hPSC-CMs. This affects signal propagation and proper electromechanical integration of the graft, leading to arrhythmias (66). In studies of hPSC-CM transplantation, intramyocardial engraftment into non-human primates (33, 59) and porcine models (67) was associated with transient ventricular arrhythmias (68). To solve these issues, conductive scaffolds can be used to aid in signal propagation (66). Furthermore, engrafted hPSC-CMs have an immature phenotype associated with spontaneous beating, which will affect the electrical signaling in the heart (68). To decrease the presence of arrhythmias, hPSC-CM maturation and ventricular subtype-specific differentiation protocols would be useful to eliminate pacemaker-like activity from engrafted cells (22, 34). Epicardial transplantation of hPSC-CM patches has not been shown to elicit arrhythmias in guinea pig (69) and porcine (46) hearts. However, this could be due to fibrotic isolation of the graft and lack of electromechanical coupling with host myocardium (70).

hPSC-CM Maturation

As mentioned, hPSC-CM have an immature phenotype. Maturation of hPSC-CM involves physiological hypertrophy associated with organization of sarcomeric structure, along with presence of T-tubules (71). hPSC-CM maturation also involves more efficient calcium handling, improved electrophysiological properties and higher contractile force (72). Therefore, transplanted CM with properties that more closely resemble adult myocardium would reduce the risk of arrhythmias and have improved contractile properties (73). Several methods have been investigated for maturation of hPSC-CM, including long-term culture, changes in the culture substrate stiffness, electrical stimulation, and biochemical cues (73). Mechanical loading has also been used to stimulate maturation in iPSC-derived cardiac tissue (74, 75). Additionally, tissue engineering methods have been employed to promote maturation. Engineered heart tissue made from a co-culture of hESC-CM and hESC-derived epicardium promoted hESC-CM maturation in terms of enhanced contractility, myofibril structure, and calcium handling (76). Electrical training of hPSC-CMs in three-dimensional culture system has also contributed to advanced morphological maturation of hiPSCs (77). Three-dimensional culture containing multiple cell types has also been shown to promote a more mature phenotype of hiPSC-CMs (78, 79).

CLINICAL APPLICATIONS OF hPSC-CMs

Challenges in Clinical Translation of hPSC-CMs

There are several safety concerns in the clinical use of hPSC-CM treatments. In addition to potential tumorigenicity and immune rejection, a major roadblock for intramyocardial injection is hPSC-CM graft-associated arrhythmias. Recent evidence has demonstrated the feasibility of pharmacological therapy for hPSC-CM-induced arrhythmias after intramyocardial injection (80). Arrhythmia risk may increase with graft size and, therefore, thorough cell dose-response studies are needed. While studies with hPSC-CM epicardial patches have mostly indicated no arrhythmic burden, the long-term effects of their subnormal electromechanical integration are unclear (81).

Most cardiac injury models to date can be classified as acute or subacute MI, with transplantation occurring within minutes to days after infarction. In a clinical setting, hPSC-CM therapy would often be performed months to years after MI as a last resort in patients with chronic heart failure (68). While hPSC-CM transplantation at 2 weeks post-MI can improve cardiac function in rats (82), transplantation at 1 month post-MI showed no functional benefit in rats (83) or guinea pigs (84). Sawa et al. showed that hPSC-CM cell sheet transplantation 1 month post-MI can improve cardiac function in swine, but there was no evidence of graft-host electromechanical integration and very few cells survived long-term (50), which could be attributed to the established fibrotic environment in chronic MI. These discrepancies necessitate further evaluation of animal models of chronic heart failure to determine the potential of hPSC-CM transplantation in a more clinically applicable setting.

Scalable manufacturing of clinical-grade hPSC-CMs is also a serious challenge for clinical use and, therefore, several recent studies have focused on large-scale production of clinical-grade hPSC-CMs. Master iPSC cell banks have been developed for clinically compliant sourcing of PSC-derived cells under current good manufacturing practice (cGMP) (85). To increase cell production, PSC aggregate culture and differentiation systems that produce 10^9 hPSC-CMs in a 1 L flask have been developed (86). Serum-free (87) and human serum-based (54) construction

TABLE 1 | Current clinical trials involving hPSC-CM transplantation for heart repair.

Trial ID	Sponsor	Title	Condition	Intervention	Estimated enrollment	Start date	Country
NCT03763136	Help therapeutics	The study of human epicardial injection with allogenic induced pluripotent stem cell-derived cardiomyocytes in ischemic heart failure	Heart failure	Intramyocardial injection of allogenic hiPSC-CMs at time of coronary artery bypass grafting surgery	5	May 2019	China
jRCT2053190081	Osaka University Hospital	Clinical trial of human (allogeneic) iPS cell-derived cardiomyocytes sheet for ischemic cardiomyopathy	Ischemic cardiomyopathy	Human (allogeneic) iPS cell derived-cardiomyocyte sheet transplantation	10	January 2020	Japan
NCT04396899	University Medical Center Goettingen	Safety and efficacy of induced pluripotent stem cell-derived engineered human myocardium as biological ventricular assist tissue in terminal heart failure	Heart failure	Implantation of EHM on dysfunctional left or right ventricular myocardium in patients with HFrEF (EF <35%).	53	February 2020	Germany
jRCTa032200189	Heartseed Inc.	Safety study of regenerative therapy with allogeneic induced pluripotent stem cell-derived cardiac spheres for severe heart failure (Regenerative cardiac spheres)	Severe heart failure patients with NYHA class III or higher (HFrEF by Dilated Cardiomyopathy)	Intramyocardial injection of 5×10^7 iPSC-derived cardiomyocytes by open-heart surgery	3	November 2020	Japan

protocols for engineered heart tissue (EHT) patches have also been developed to adapt to cGMP for clinical applications.

Finally, there is a lack of consensus on the characterization and assessment of hPSC-CM differentiation and maturity (i.e., cell surface markers). Consistency in the assessment of hPSC-CM products is necessary to ensure their quality, reproducibility, and safety for use in humans. To this end, an unbiased integrative proteomics approach could offer comprehensive assessment of hPSC-cardiomyocyte maturation (88).

First In-human Clinical Trials With hPSC-CMs

Despite the outstanding challenges in the field, first-in-human clinical trials have recently begun involving the transplantation of hPSC-CMs (**Table 1**). The first use of hPSC-CMs in humans took place in 2019 in Nanjing, China, and involved intramyocardial injection of hiPSC-CMs in patients with chronic ischemic cardiomyopathy (89). However, cell injection occurred alongside coronary artery bypass grafting, limiting the ability to delineate the therapeutic benefits of hiPSC-CM transplantation. In Japan, a trial at Osaka University is exploring transplantation of an allogeneic hiPSC-CM cell sheet as a sole therapy for ischemic cardiomyopathy (90). Heartseed Inc., a Japan-based biotechnology company led by Prof. Keiichi Fukuda, recently gained approval for a Phase I/II clinical trial of intramyocardial injection of three-dimensional hiPSC-CM spheres to treat heart failure. The largest trial to date has been registered in Germany at University Medical Center Goettingen, investigating the remuscularization capacity of engineered heart tissue containing hiPSC-CMs and stromal cells in patients with heart failure with reduced ejection fraction (HFrEF).

CONCLUSIONS AND FUTURE CONSIDERATIONS

Transplantation of hPSC-CMs has proven to be a viable strategy for cardiac regenerative therapies. Single-cell injection and tissue-level engineered constructs have served as the basis for promoting functional improvements in injured myocardium. Future research needs to focus on addressing the limitations currently facing the field, as discussed in this review. In particular, the development of a viable strategy to prevent graft-associated arrythmia will have immediate clinical impacts for intramyocardial injection of hPSC-CMs. In addition, paracrine factors play a central role in hPSC-CM mediated functional recoveries; therefore, developing methods to enhance hPSC-CM cardioprotective secretome would have significant impacts to the field. Lastly, optimal doses of PSC-CMs for heart repair need to be determined for safe and effective application in humans.

In summary, although the clinical translation of hPSC-CM transplantation faces several significant limitations, immense progress has been made in recent years in the development of potential strategies for hPSC-CM regenerative therapies. It has been proven that engrafted hPSC-CM can make meaningful connections with host cardiomyocytes and provide paracrine factors that stimulate functional recovery of host myocardium. Furthermore, strategies for producing cells at a clinical scale have been explored, as well as methods to mitigate immune rejection, reduce incidence of cardiac arrhythmias, and mature hPSC-CMs.

AUTHOR CONTRIBUTIONS

SS was responsible for manuscript development and primary authorship under the guidance of YM. RB contributed to organization and conceptualization of the work and was lead author on section First In-Human Clinical Trials With hPSC-CMs. YM contributed to article organization and conceptualization. All authors contributed to the article and approved the submitted version.

FUNDING

This work was supported by the National Institutes of Health (1F31 HL156541, 1R01HL133308, 8P20 GM103444), and the National Science Foundation (NSF—EPS-0903795, NSF1655740).

REFERENCES

1. Nowbar AN, Gitto M, Howard JP, Francis DP, Al-Lamee R. Mortality from ischemic heart disease. *Circ Cardiovasc Qual Outcomes.* (2019) 12:e005375. doi: 10.1161/CIRCOUTCOMES.118.005375
2. Benjamin EJ, Muntner P, Alonso A, Bittencourt MS, Callaway CW, Carson AP, et al. Heart disease and stroke statistics-2019 update: a report from the American Heart Association. *Circulation.* (2019) 139:e56–e528. doi: 10.1161/CIR.0000000000000659
3. Cohn JN, Ferrari R, Sharpe N. Cardiac remodeling–concepts and clinical implications: a consensus paper from an international forum on cardiac remodeling. Behalf of an international forum on cardiac remodeling. *J Am Coll Cardiol.* (2000) 35:569–82. doi: 10.1016/S0735-1097(99)00630-0
4. Mazurek JA, Jessup M. Understanding heart failure. *Heart Fail Clin.* (2017) 13:1–19. doi: 10.1016/j.hfc.2016.07.001
5. Tonsho M, Michel S, Ahmed Z, Alessandrini A, Madsen JC. Heart transplantation: challenges facing the field. *Cold Spring Harb Perspect Med.* (2014) 4:a015636. doi: 10.1101/cshperspect.a015636
6. Nguyen PK, Rhee JW, Wu JC. Adult stem cell therapy and heart failure, 2000 to 2016: a systematic review. *JAMA Cardiol.* (2016) 1:831–41. doi: 10.1001/jamacardio.2016.2225
7. Romito A, Cobellis G. Pluripotent stem cells: current understanding and future directions. *Stem Cells Int.* (2016) 2016:9451492. doi: 10.1155/2016/9451492
8. Rikhtegar R, Pezeshkian M, Dolati S, Safaie N, Afrasiabi Rad A, Mahdipour M, et al. Stem cells as therapy for heart disease: iPSCs, ESCs, CSCs, and skeletal myoblasts. *Biomed Pharmacother.* (2019) 109:304–13. doi: 10.1016/j.biopha.2018.10.065
9. Thomson JA, Itskovitz-Eldor J, Shapiro SS, Waknitz MA, Swiergiel JJ, Marshall VS, et al. Embryonic stem cell lines derived from human blastocysts. *Science.* (1998) 282:1145–7. doi: 10.1126/science.282.5391.1145
10. Kehat I, Kenyagin-Karsenti D, Snir M, Segev H, Amit M, Gepstein A, et al. Human embryonic stem cells can differentiate into myocytes with structural and functional properties of cardiomyocytes. *J Clin Invest.* (2001) 108:407–14. doi: 10.1172/JCI200112131
11. Lo B, Parham L. Ethical issues in stem cell research. *Endocr Rev.* (2009) 30:204–13. doi: 10.1210/er.2008-0031

12. Takahashi K, Yamanaka S. Induction of pluripotent stem cells from mouse embryonic and adult fibroblast cultures by defined factors. *Cell.* (2006) 126:663–76. doi: 10.1016/j.cell.2006.07.024
13. Yu J, Vodyanik MA, Smuga-Otto K, Antosiewicz-Bourget J, Frane JL, Tian S, et al. Induced pluripotent stem cell lines derived from human somatic cells. *Science.* (2007) 318:1917–20. doi: 10.1126/science.1151526
14. Zhou H, Wu S, Joo JY, Zhu S, Han DW, Lin T, et al. Generation of induced pluripotent stem cells using recombinant proteins. *Cell Stem Cell.* (2009) 4:381–4. doi: 10.1016/j.stem.2009.04.005
15. Anokye-Danso F, Trivedi CM, Juhr D, Gupta M, Cui Z, Tian Y, et al. Highly efficient miRNA-mediated reprogramming of mouse and human somatic cells to pluripotency. *Cell Stem Cell.* (2011) 8:376–88. doi: 10.1016/j.stem.2011.03.001
16. Judson RL, Babiarz JE, Venere M, Blelloch R. Embryonic stem cell-specific microRNAs promote induced pluripotency. *Nat Biotechnol.* (2009) 27:459–61. doi: 10.1038/nbt.1535
17. Mummery CL, Zhang J, Ng ES, Elliott DA, Elefanty AG, Kamp TJ. Differentiation of human embryonic stem cells and induced pluripotent stem cells to cardiomyocytes: a methods overview. *Circ Res.* (2012) 111:344–58. doi: 10.1161/CIRCRESAHA.110.227512
18. Lian X, Hsiao C, Wilson G, Zhu K, Hazeltine LB, Azarin SM, et al. Robust cardiomyocyte differentiation from human pluripotent stem cells *via* temporal modulation of canonical wnt signaling. *Proc Natl Acad Sci USA.* (2012) 109:E1848–57. doi: 10.1073/pnas.1200250109
19. Zhang J, Klos M, Wilson GF, Herman AM, Lian X, Raval KK, et al. Extracellular matrix promotes highly efficient cardiac differentiation of human pluripotent stem cells: the matrix sandwich method. *Circ Res.* (2012) 111:1125–36. doi: 10.1161/CIRCRESAHA.112.273144
20. Kattman SJ, Witty AD, Gagliardi M, Dubois NC, Niapour M, Hotta A, et al. Stage-specific optimization of activin/nodal and BMP signaling promotes cardiac differentiation of mouse and human pluripotent stem cell lines. *Cell Stem Cell.* (2011) 8:228–40. doi: 10.1016/j.stem.2010.12.008
21. Burridge PW, Matsa E, Shukla P, Lin ZC, Churko JM, Ebert AD, et al. Chemically defined generation of human cardiomyocytes. *Nat Methods.* (2014) 11:855–60. doi: 10.1038/nmeth.2999
22. Oikonomopoulos A, Kitani T, Wu JC. Pluripotent stem cell-derived cardiomyocytes as a platform for cell therapy applications: progress and hurdles for clinical translation. *Mol Ther.* (2018) 26:1624–34. doi: 10.1016/j.ymthe.2018.02.026
23. Li J, Hu S, Zhu D, Huang K, Mei X, Lopez de Juan Abad B, et al. All roads lead to Rome (the heart): cell retention and outcomes from various delivery routes of cell therapy products to the heart. *J Am Heart Assoc.* (2021) 10:e020402. doi: 10.1161/JAHA.120.020402
24. van Laake LW, Passier R, Monshouwer-Kloots J, Verkleij AJ, Lips DJ, Freund C, et al. Human embryonic stem cell-derived cardiomyocytes survive and mature in the mouse heart and transiently improve function after myocardial infarction. *Stem Cell Res.* (2007) 1:9–24. doi: 10.1016/j.scr.2007.06.001
25. Laflamme MA, Gold J, Xu C, Hassanipour M, Rosler E, Police S, et al. Formation of human myocardium in the rat heart from human embryonic stem cells. *Am J Pathol.* (2005) 167:663–71. doi: 10.1016/S0002-9440(10)62041-X
26. Xue T, Cho HC, Akar FG, Tsang SY, Jones SP, Marban E, et al. Functional integration of electrically active cardiac derivatives from genetically engineered human embryonic stem cells with quiescent recipient ventricular cardiomyocytes: insights into the development of cell-based pacemakers. *Circulation.* (2005) 111:11–20. doi: 10.1161/01.CIR.0000151313.18547.A2
27. Kehat I, Khimovich L, Caspi O, Gepstein A, Shofti R, Arbel G, et al. Electromechanical integration of cardiomyocytes derived from human embryonic stem cells. *Nat Biotechnol.* (2004) 22:1282–9. doi: 10.1038/nbt1014
28. Shiba Y, Fernandes S, Zhu WZ, Filice D, Muskheli V, Kim J, et al. Human ES-cell-derived cardiomyocytes electrically couple and suppress arrhythmias in injured hearts. *Nature.* (2012) 489:322–5. doi: 10.1038/nature11317
29. Gerbin KA, Yang X, Murry CE, Coulombe KL. Enhanced electrical integration of engineered human myocardium *via* intramyocardial versus epicardial delivery in infarcted rat hearts. *PLoS ONE.* (2015) 10:e0131446. doi: 10.1371/journal.pone.0131446
30. Caspi O, Huber I, Kehat I, Habib M, Arbel G, Gepstein A, et al. Transplantation of human embryonic stem cell-derived cardiomyocytes improves myocardial performance in infarcted rat hearts. *J Am Coll Cardiol.* (2007) 50:1884–93. doi: 10.1016/j.jacc.2007.07.054
31. Guan X, Xu W, Zhang H, Wang Q, Yu J, Zhang R, et al. Transplantation of human induced pluripotent stem cell-derived cardiomyocytes improves myocardial function and reverses ventricular remodeling in infarcted rat hearts. *Stem Cell Res Ther.* (2020) 11:73. doi: 10.1186/s13287-020-01673-z
32. Funakoshi S, Miki K, Takaki T, Okubo C, Hatani T, Chonabayashi K, et al. Enhanced engraftment, proliferation, and therapeutic potential in heart using optimized human iPSC-derived cardiomyocytes. *Sci Rep.* (2016) 6:19111. doi: 10.1038/srep19111
33. Chong JJ, Yang X, Don CW, Minami E, Liu YW, Weyers JJ, et al. Human embryonic-stem-cell-derived cardiomyocytes regenerate non-human primate hearts. *Nature.* (2014) 510:273–7. doi: 10.1038/nature13233
34. Liu YW, Chen B, Yang X, Fugate JA, Kalucki FA, Futakuchi-Tsuchida A, et al. Human embryonic stem cell-derived cardiomyocytes restore function in infarcted hearts of non-human primates. *Nat Biotechnol.* (2018) 36:597–605. doi: 10.1038/nbt.4162
35. Moon SH, Kang SW, Park SJ, Bae D, Kim SJ, Lee HA, et al. The use of aggregates of purified cardiomyocytes derived from human ESCs for functional engraftment after myocardial infarction. *Biomaterials.* (2013) 34:4013–26. doi: 10.1016/j.biomaterials.2013.02.022
36. Mattapally S, Zhu W, Fast VG, Gao L, Worley C, Kannappan R, et al. Spheroids of cardiomyocytes derived from human-induced pluripotent stem cells improve recovery from myocardial injury in mice. *Am J Physiol Heart Circ Physiol.* (2018) 315:H327–H39. doi: 10.1152/ajpheart.00688.2017
37. Kawaguchi S, Soma Y, Nakajima K, Kanazawa H, Tohyama S, Tabei R, et al. Intamyocardial transplantation of human iPS cell-derived cardiac spheroids improves cardiac function in heart failure animals. *J Am Coll Cardiol Basic Trans Sci.* (2021) 6:239–54. doi: 10.1016/j.jacbts.2020.11.017
38. Sayed N, Liu C, Wu JC. Translation of human-induced pluripotent stem cells: from clinical trial in a dish to precision medicine. *J Am Coll Cardiol.* (2016) 67:2161–76. doi: 10.1016/j.jacc.2016.01.083
39. Weinberger F, Breckwoldt K, Pecha S, Kelly A, Geertz B, Starbatty J, et al. Cardiac repair in guinea pigs with human engineered heart tissue from induced pluripotent stem cells. *Sci Transl Med.* (2016) 8:363ra148. doi: 10.1126/scitranslmed.aaf8781
40. Riegler J, Tiburcy M, Ebert A, Tzatzalos E, Raaz U, Abilez OJ, et al. Human engineered heart muscles engraft and survive long term in a rodent myocardial infarction model. *Circ Res.* (2015) 117:720–30. doi: 10.1161/CIRCRESAHA.115.306985
41. Sugiura T, Hibino N, Breuer CK, Shinoka T. Tissue-engineered cardiac patch seeded with human induced pluripotent stem cell derived cardiomyocytes promoted the regeneration of host cardiomyocytes in a rat model. *J Cardiothorac Surg.* (2016) 11:163. doi: 10.1186/s13019-016-0559-z
42. Munarin F, Kant RJ, Rupert CE, Khoo A, Coulombe KLK. Engineered human myocardium with local release of angiogenic proteins improves vascularization and cardiac function in injured rat hearts. *Biomaterials.* (2020) 251:120033. doi: 10.1016/j.biomaterials.2020.120033
43. Lesman A, Habib M, Caspi O, Gepstein A, Arbel G, Levenberg S, et al. Transplantation of a tissue-engineered human vascularized cardiac muscle. *Tissue Eng Part A.* (2010) 16:115–25. doi: 10.1089/ten.tea.2009.0130
44. Ye L, Chang YH, Xiong Q, Zhang P, Zhang L, Somasundaram P, et al. Cardiac repair in a porcine model of acute myocardial infarction with human induced pluripotent stem cell-derived cardiovascular cells. *Cell Stem Cell.* (2014) 15:750–61. doi: 10.1016/j.stem.2014.11.009
45. Gao L, Kupfer ME, Jung JP, Yang L, Zhang P, Da Sie Y, et al. Myocardial tissue engineering with cells derived from human-induced pluripotent stem cells and a native-like, high-resolution, 3-dimensionally printed scaffold. *Circ Res.* (2017) 120:1318–25. doi: 10.1161/CIRCRESAHA.116.310277
46. Gao L, Gregorich ZR, Zhu W, Mattapally S, Oduk Y, Lou X, et al. Large cardiac muscle patches engineered from human induced-pluripotent stem cell-derived cardiac cells improve recovery from myocardial infarction in Swine. *Circulation.* (2018) 137:1712–30. doi: 10.1161/CIRCULATIONAHA.117.030785
47. Okano T, Yamada N, Sakai H, Sakurai Y. A novel recovery system for cultured cells using plasma-treated polystyrene dishes grafted with poly(N-isopropylacrylamide). *J Biomed Mater Res.* (1993) 27:1243–51. doi: 10.1002/jbm.820271005

48. Masumoto H, Ikuno T, Takeda M, Fukushima H, Marui A, Katayama S, et al. Human iPS cell-engineered cardiac tissue sheets with cardiomyocytes and vascular cells for cardiac regeneration. *Sci Rep.* (2014) 4:6716. doi: 10.1038/srep06716
49. Kawamura M, Miyagawa S, Fukushima S, Saito A, Miki K, Funakoshi S, et al. Enhanced therapeutic effects of human iPS cell derived-cardiomyocyte by combined cell-sheets with omental flap technique in porcine ischemic cardiomyopathy model. *Sci Rep.* (2017) 7:8824. doi: 10.1038/s41598-017-08869-z
50. Kawamura M, Miyagawa S, Miki K, Saito A, Fukushima S, Higuchi T, et al. Feasibility, safety, and therapeutic efficacy of human induced pluripotent stem cell-derived cardiomyocyte sheets in a porcine ischemic cardiomyopathy model. *Circulation.* (2012) 126(Suppl. 1):S29–37. doi: 10.1161/CIRCULATIONAHA.111.084343
51. Ishida M, Miyagawa S, Saito A, Fukushima S, Harada A, Ito E, et al. Transplantation of human-induced pluripotent stem cell-derived cardiomyocytes is superior to somatic stem cell therapy for restoring cardiac function and oxygen consumption in a porcine model of myocardial infarction. *Transplantation.* (2019) 103:291–8. doi: 10.1097/TP.0000000000002384
52. Stevens KR, Pabon L, Muskheli V, Murry CE. Scaffold-free human cardiac tissue patch created from embryonic stem cells. *Tissue Eng Part A.* (2009) 15:1211–22. doi: 10.1089/ten.tea.2008.0151
53. Hartman ME, Chong JJH, Laflamme MA. State of the art in cardiomyocyte transplantation. *Card Vasc Biol.* (2017) 4:177–218. doi: 10.1007/978-3-319-56106-6_9
54. Querdel E, Reinsch M, Castro L, Köse D, Bähr A, Reich S, et al. Human engineered heart tissue patches remuscularize the injured heart in a dose-dependent manner. *Circulation.* (2021) 143:1991–2006. doi: 10.1161/CIRCULATIONAHA.120.047904
55. Ong SG, Huber BC, Lee WH, Kodo K, Ebert AD, Ma Y, et al. Microfluidic single-cell analysis of transplanted human induced pluripotent stem cell-derived cardiomyocytes after acute myocardial infarction. *Circulation.* (2015) 132:762–71. doi: 10.1161/CIRCULATIONAHA.114.015231
56. Gao L, Wang L, Wei Y, Krishnamurthy P, Walcott GP, Menasche P, et al. Exosomes secreted by hiPSC-derived cardiac cells improve recovery from myocardial infarction in swine. *Sci Transl Med.* (2020) 12:e aay1318. doi: 10.1126/scitranslmed.aay1318
57. Liu B, Lee BW, Nakanishi K, Villasante A, Williamson R, Metz J, et al. Cardiac recovery *via* extended cell-free delivery of extracellular vesicles secreted by cardiomyocytes derived from induced pluripotent stem cells. *Nat Biomed Eng.* (2018) 2:293–303. doi: 10.1038/s41551-018-0229-7
58. Neofytou E, O'Brien CG, Couture LA, Wu JC. Hurdles to clinical translation of human induced pluripotent stem cells. *J Clin Invest.* (2015) 125:2551–7. doi: 10.1172/JCI80575
59. Shiba Y, Gomibuchi T, Seto T, Wada Y, Ichimura H, Tanaka Y, et al. Allogeneic transplantation of iPS cell-derived cardiomyocytes regenerates primate hearts. *Nature.* (2016) 538:388–91. doi: 10.1038/nature19815
60. Wu KH, Mo XM, Han ZC, Zhou B. Stem cell engraftment and survival in the ischemic heart. *Ann Thorac Surg.* (2011) 92:1917–25. doi: 10.1016/j.athoracsur.2011.07.012
61. Nguyen PK, Neofytou E, Rhee JW, Wu JC. Potential strategies to address the major clinical barriers facing stem cell regenerative therapy for cardiovascular disease: a review. *JAMA Cardiol.* (2016) 1:953–62. doi: 10.1001/jamacardio.2016.2750
62. Laflamme MA, Chen KY, Naumova AV, Muskheli V, Fugate JA, Dupras SK, et al. Cardiomyocytes derived from human embryonic stem cells in pro-survival factors enhance function of infarcted rat hearts. *Nat Biotechnol.* (2007) 25:1015–24. doi: 10.1038/nbt1327
63. Sun X, Wu J, Qiang B, Romagnuolo R, Gagliardi M, Keller G, et al. Transplanted microvessels improve pluripotent stem cell-derived cardiomyocyte engraftment and cardiac function after infarction in rats. *Sci Transl Med.* (2020) 12:eaax2992. doi: 10.1126/scitranslmed.aax2992
64. Dvir T, Kedem A, Ruvinov E, Levy O, Freeman I, Landa N, et al. Prevascularization of cardiac patch on the omentum improves its therapeutic outcome. *Proc Natl Acad Sci USA.* (2009) 106:14990–5. doi: 10.1073/pnas.0812242106
65. Stevens KR, Kreutziger KL, Dupras SK, Korte FS, Regnier M, Muskheli V, et al. Physiological function and transplantation of scaffold-free and vascularized human cardiac muscle tissue. *Proc Natl Acad Sci USA.* (2009) 106:16568–73. doi: 10.1073/pnas.0908381106
66. Huang NF, Serpooshan V, Morris VB, Sayed N, Pardon G, Abilez OJ, et al. Big bottlenecks in cardiovascular tissue engineering. *Commun Biol.* (2018) 1:199. doi: 10.1038/s42003-018-0202-8
67. Romagnuolo R, Masoudpour H, Porta-Sanchez A, Qiang B, Barry J, Laskary A, et al. Human embryonic stem cell-derived cardiomyocytes regenerate the infarcted pig heart but induce ventricular tachyarrhythmias. *Stem Cell Reports.* (2019) 12:967–81. doi: 10.1016/j.stemcr.2019.04.005
68. Kadota S, Shiba Y. Pluripotent stem cell-derived cardiomyocyte transplantation for heart disease treatment. *Curr Cardiol Rep.* (2019) 21:73. doi: 10.1007/s11886-019-1171-3
69. Shadrin IY, Allen BW, Qian Y, Jackman CP, Carlson AL, Juhas ME, et al. Cardiopatch platform enables maturation and scale-up of human pluripotent stem cell-derived engineered heart tissues. *Nat Commun.* (2017) 8:1825. doi: 10.1038/s41467-017-01946-x
70. Zimmermann W-H, Melnychenko I, Wasmeier G, Didié M, Naito H, Nixdorff U, et al. Engineered heart tissue grafts improve systolic and diastolic function in infarcted rat hearts. *Nat Med.* (2006) 12:452–8. doi: 10.1038/nm1394
71. Nakamura M, Sadoshima J. Mechanisms of physiological and pathological cardiac hypertrophy. *Nat Rev Cardiol.* (2018) 15:387–407. doi: 10.1038/s41569-018-0007-y
72. Sun X, Nunes SS. Bioengineering approaches to mature human pluripotent stem cell-derived cardiomyocytes. *Front Cell Dev Biol.* (2017) 5:19. doi: 10.3389/fcell.2017.00019
73. Yang X, Pabon L, Murry CE. Engineering adolescence: maturation of human pluripotent stem cell-derived cardiomyocytes. *Circ Res.* (2014) 114:511–23. doi: 10.1161/CIRCRESAHA.114.300558
74. Ruan JL, Tulloch NL, Razumova MV, Saiget M, Muskheli V, Pabon L, et al. Mechanical stress conditioning and electrical stimulation promote contractility and force maturation of induced pluripotent stem cell-derived human cardiac tissue. *Circulation.* (2016) 134:1557–67. doi: 10.1161/CIRCULATIONAHA.114.014998
75. Tulloch NL, Muskheli V, Razumova MV, Korte FS, Regnier M, Hauch KD, et al. Growth of engineered human myocardium with mechanical loading and vascular coculture. *Circ Res.* (2011) 109:47–59. doi: 10.1161/CIRCRESAHA.110.237206
76. Bargehr J, Ong LP, Colzani M, Davaapil H, Hofsteen P, Bhandari S, et al. Epicardial cells derived from human embryonic stem cells augment cardiomyocyte-driven heart regeneration. *Nat Biotechnol.* (2019) 37:895–906. doi: 10.1038/s41587-019-0197-9
77. Ronaldson-Bouchard K, Ma SP, Yeager K, Chen T, Song L, Sirabella D, et al. Advanced maturation of human cardiac tissue grown from pluripotent stem cells. *Nature.* (2018) 556:239–43. doi: 10.1038/s41586-018-0016-3
78. Richards DJ, Coyle RC, Tan Y, Jia J, Wong K, Toomer K, et al. Inspiration from heart development: biomimetic development of functional human cardiac organoids. *Biomaterials.* (2017) 142:112–23. doi: 10.1016/j.biomaterials.2017.07.021
79. Varzideh F, Pahlavan S, Ansari H, Halvaei M, Kostin S, Feiz MS, et al. Human cardiomyocytes undergo enhanced maturation in embryonic stem cell-derived organoid transplants. *Biomaterials.* (2018) 192:537–50. doi: 10.1016/j.biomaterials.2018.11.033
80. Nakamura K, Neidig LE, Yang X, Weber GJ, El-Nachef D, Tsuchida H, et al. Pharmacologic therapy for engraftment arrhythmia induced by transplantation of human cardiomyocytes. *bioRxiv [Preprint].* (2021). doi: 10.1101/2021.02.15.431108
81. Pecha S, Yorgan K, Rohl M, Geertz B, Hansen A, Weinberger F, et al. Human iPS cell-derived engineered heart tissue does not affect ventricular arrhythmias in a guinea pig cryo-injury model. *Sci Rep.* (2019) 9:9831. doi: 10.1038/s41598-019-46409-z
82. Miki K, Uenaka H, Saito A, Miyagawa S, Sakaguchi T, Higuchi T, et al. Bioengineered myocardium derived from induced pluripotent stem cells improves cardiac function and attenuates cardiac remodeling following chronic myocardial infarction in rats. *Stem Cells Transl Med.* (2012) 1:430–7. doi: 10.5966/sctm.2011-0038

83. Fernandes S, Naumova AV, Zhu WZ, Laflamme MA, Gold J, Murry CE. Human embryonic stem cell-derived cardiomyocytes engraft but do not alter cardiac remodeling after chronic infarction in rats. *J Mol Cell Cardiol.* (2010) 49:941–9. doi: 10.1016/j.yjmcc.2010.09.008
84. Shiba Y, Filice D, Fernandes S, Minami E, Dupras SK, Biber BV, et al. Electrical integration of human embryonic stem cell-derived cardiomyocytes in a guinea pig chronic infarct model. *J Cardiovasc Pharmacol Ther.* (2014) 19:368–81. doi: 10.1177/1074248413520344
85. Baghbaderani BA, Tian X, Neo BH, Burkall A, Dimezzo T, Sierra G, et al. cGMP-manufactured human induced pluripotent stem cells are available for pre-clinical and clinical applications. *Stem Cell Reports.* (2015) 5:647–59. doi: 10.1016/j.stemcr.2015.08.015
86. Chen VC, Ye J, Shukla P, Hua G, Chen D, Lin Z, et al. Development of a scalable suspension culture for cardiac differentiation from human pluripotent stem cells. *Stem Cell Res.* (2015) 15:365–75. doi: 10.1016/j.scr.2015.08.002
87. Tiburcy M, Hudson JE, Balfanz P, Schlick S, Meyer T, Chang Liao M-L, et al. Defined engineered human myocardium with advanced maturation for applications in heart failure modeling and repair. *Circulation.* (2017) 135:1832–47. doi: 10.1161/CIRCULATIONAHA.116.024145
88. Cai W, Zhang J, Lange WJd, Gregorich ZR, Karp H, Farrell ET, et al. An unbiased proteomics method to assess the maturation of human pluripotent stem cell-derived cardiomyocytes. *Circ Res.* (2019) 125:936–53. doi: 10.1161/CIRCRESAHA.119.315305
89. Mallapaty S. Revealed: two men in China were first to receive pioneering stem-cell treatment for heart disease. *Nature.* (2020) 581:249–50. doi: 10.1038/d41586-020-01285-w
90. Cyranoski D. 'Reprogrammed' stem cells approved to mend human hearts for the first time. *Nature.* (2018) 557:619–20. doi: 10.1038/d41586-018-05278-8

Conflict of Interest: The authors declare that the research was conducted in the absence of any commercial or financial relationships that could be construed as a potential conflict of interest.

frontiers
in Cardiovascular Medicine

ORIGINAL RESEARCH
published: 10 January 2022
doi: 10.3389/fcvm.2021.724183

Deep Neural Network-Aided Histopathological Analysis of Myocardial Injury

Yiping Jiao[1,2†], Jie Yuan[1,2†], Oluwatofunmi Modupeoluwa Sodimu[2], Yong Qiang[1] and Yichen Ding[2,3]*

[1] Key Laboratory of Measurement and Control of CSE, Ministry of Education, School of Automation, Southeast University, Nanjing, China, [2] Department of Bioengineering, Erik Jonsson School of Engineering and Computer Science, The University of Texas at Dallas, Richardson, TX, United States, [3] Hamon Center for Regenerative Science and Medicine, The University of Texas Southwestern Medical Center, Dallas, TX, United States

Deep neural networks have become the mainstream approach for analyzing and interpreting histology images. In this study, we established and validated an interpretable DNN model to assess endomyocardial biopsy (EMB) data of patients with myocardial injury. Deep learning models were used to extract features and classify EMB histopathological images of heart failure cases diagnosed with either ischemic cardiomyopathy or idiopathic dilated cardiomyopathy and non-failing cases (organ donors without a history of heart failure). We utilized the gradient-weighted class activation mapping (Grad-CAM) technique to emphasize injured regions, providing an entry point to assess the dominant morphology in the process of a comprehensive evaluation. To visualize clustered regions of interest (ROI), we utilized uniform manifold approximation and projection (UMAP) embedding for dimension reduction. We further implemented a multi-model ensemble mechanism to improve the quantitative metric (area under the receiver operating characteristic curve, AUC) to 0.985 and 0.992 on ROI-level and case-level, respectively, outperforming the achievement of 0.971 ± 0.017 and 0.981 ± 0.020 based on the sub-models. Collectively, this new methodology provides a robust and interpretive framework to explore local histopathological patterns, facilitating the automatic and high-throughput quantification of cardiac EMB analysis.

Keywords: deep neural network (DNN), heart failure, endomyocardial biopsy, histopathology (HPE), computer-aided diagnosis (CAD)

OPEN ACCESS

Edited by:
Yun Fang,
University of Chicago, United States

Reviewed by:
Helen E. Collins,
University of Louisville, United States
Juhyun Lee,
University of Texas at Arlington, United States

****Correspondence:***
Yichen Ding
yichen.ding@utdallas.edu

† These authors have contributed equally to this work

Specialty section:
This article was submitted to Atherosclerosis and Vascular Medicine, a section of the journal Frontiers in Cardiovascular Medicine

Received: *12 June 2021*
Accepted: *17 December 2021*
Published: *10 January 2022*

Citation:
Jiao Y, Yuan J, Sodimu OM, Qiang Y and Ding Y (2022) Deep Neural Network-Aided Histopathological Analysis of Myocardial Injury. Front. Cardiovasc. Med. 8:724183. doi: 10.3389/fcvm.2021.724183

INTRODUCTION

Heart failure is a major public health issue with a prevalence of over 23 million worldwide (1). Along with endomyocardial biopsy (EMB), non-invasive imaging methods such as an echocardiogram and magnetic resonance imaging (MRI) are the most common tools for diagnosing myocarditis, heart transplant rejection, and chemotherapy-induced injury (2, 3). EMB is a useful but invasive modality for making a definite diagnosis in diseases that are often difficult to diagnose by imaging modality alone. However, current grading methods in assessing histological patterns of myocardial injury are labor-intensive, error-prone, and suffer from a high inter-rater variability (4). Thus, a robust and reproducible method for the quantitative analysis of EMB is urgently needed.

Machine learning methods have been an integral part of biomedical research (5, 6) and clinical work (7, 8), having the great potential to overcome the intra- and inter-observer variability (9, 10) and to improve diagnostic accuracy and efficiency (11). These computational models are based on algorithms that can extract features from clinical data (12). Compared to traditional machine learning methods that rely on expert knowledge to transform raw image data into features (e.g., texture, statistics, and wavelet transform coefficients) (13, 14), deep neural networks (DNN) can achieve better accuracy without defining features explicitly. In the field of cardiovascular diseases, deep learning has been widely implemented for image classification and segmentation in multiple modalities, including echocardiography, coronary artery calcium scoring, coronary computed tomography angiography, single-photon emission computed tomography, positron emission tomography, magnetic resonance imaging, and optical coherence tomography (8, 15–17).

Histopathological image analysis remains the gold standard for diagnosing many diseases. DNN has been proven to be a powerful approach in the analysis of histopathological images of tumor specimens; DNN can predict tumor metastasis (11) and has been shown to be useful for tumor grading (18) and tumor microenvironment analysis (19). While some researchers reported the implementation of DNN into EMB images, the interpretability of DNN output remains challenging.

This study established and validated an interpretable DNN model to assess EMB data of patients with myocardial injury. To extract and classify representative features of myocardial injury on local histological patterns, we adapted a well-established VGG-19 model (20). We then applied the other two methods, gradient-weighted class activation mapping (Grad-CAM) (21) and uniform manifold approximation and projection (UMAP) embedding method (22), to elucidate the model outputs and visualize the intermediate features made by the VGG-19 model. Moreover, we introduced a novel multi-model ensemble strategy to minimize the intra- and inter-observer variability of random dataset partition. Collectively, our method enables automatic quantification of EMB images related to cardiomyopathy, creating a series of visualizable archives for efficient and accurate pathological inspection and providing new insight into cardiac image analysis enhanced by machine learning.

MATERIALS AND METHODS

Data Collection

We used a publicly available dataset provided in a previous study for DNN model development and evaluation (23). Hematoxylin and eosin (H&E) stained EMB tissue samples were collected from left ventricles of 209 patients registered at the University of Pennsylvania, including 94 end-stage heart failure cases diagnosed with either ischemic cardiomyopathy ($n = 51$) or idiopathic dilated cardiomyopathy ($n = 43$), and 115 non-failure cases (23). The non-failure cases were organ donors without a history of heart failure; the hearts were not used for transplantation. Each case included 11 random ROIs within the myocardium, corresponding to 11 specific areas of $50 \times 50\ \mu\text{m}^2$, i.e., 250×250 pixels.

In machine learning, a dataset is usually divided as a training set, validation set, and held-out test set, used for model training, model tuning, and evaluation, respectively. In this study, the aforementioned dataset was divided on case-level into the development set (104 cases, corresponding to 1144 ROIs) for training and validation or multi-model ensemble, and the held-out test set (105 cases, corresponding to 1155 ROIs), removing the crosstalk between development and test sets.

TABLE 1 | Number of cases used in the model development and validation.

Subset partition		Non-failure	Failure
Individual model (Development set)	Training	38	32
	Validation	19	15
Multi-model ensemble (Development set)	Fold-1	12	10
	Fold-2	12	10
	Fold-3	11	9
	Fold-4	11	9
	Fold-5	11	9
Held-out test set		58	47

Each case includes 11 regions of interest (ROIs).

A single model was trained on the well-established development set (23), including 70 cases (770 ROIs) for training and 34 cases (374 ROIs) for validation (**Table 1**). We further employed a multi-model ensemble mechanism using the five-fold-based cross-validation (see **Cross-validation for multi-model ensemble**), where 10 models were trained and integrated to improve accuracy.

Deep Neural Network for Myocardium Assessment

We used VGG-19 network (20) to analyze EMB images. VGG-19 network has been widely used in computational pathology (24, 25). The first part of the model was composed of 16 convolutional layers and five max-pooling layers as the feature extractor. The rest of the model was composed of a global average pooling (GAP) layer and a classification layer with two nodes (**Figure 1A**). In comparison to the original VGG-19 network, our model is light-weighted and compatible with other parts of our framework (see **Regional and feature interpretability**). In our classification task, an input image was processed by all the layers and turned into a probability distribution (p_F or p_N) among all the classes in the output layer (**Figure 1A**). From an overall view, the model receives input image of shape 224 (width) × 224 (height) × 3 (channels), and outputs a Bernoulli distribution, where the p_F activation gives the possibility that the input image is acquired from a heart failure patient. The entire model can be automatically optimized by minimizing the discrepancy between the network activation and desired output for end-to-end training.

Regional and Feature Interpretability

We employed the Grad-CAM method (21) to highlight the potentially injured regions projected for interpretation and implemented the UMAP embedding to visualize inter-sample similarity generated by our VGG-19 model.

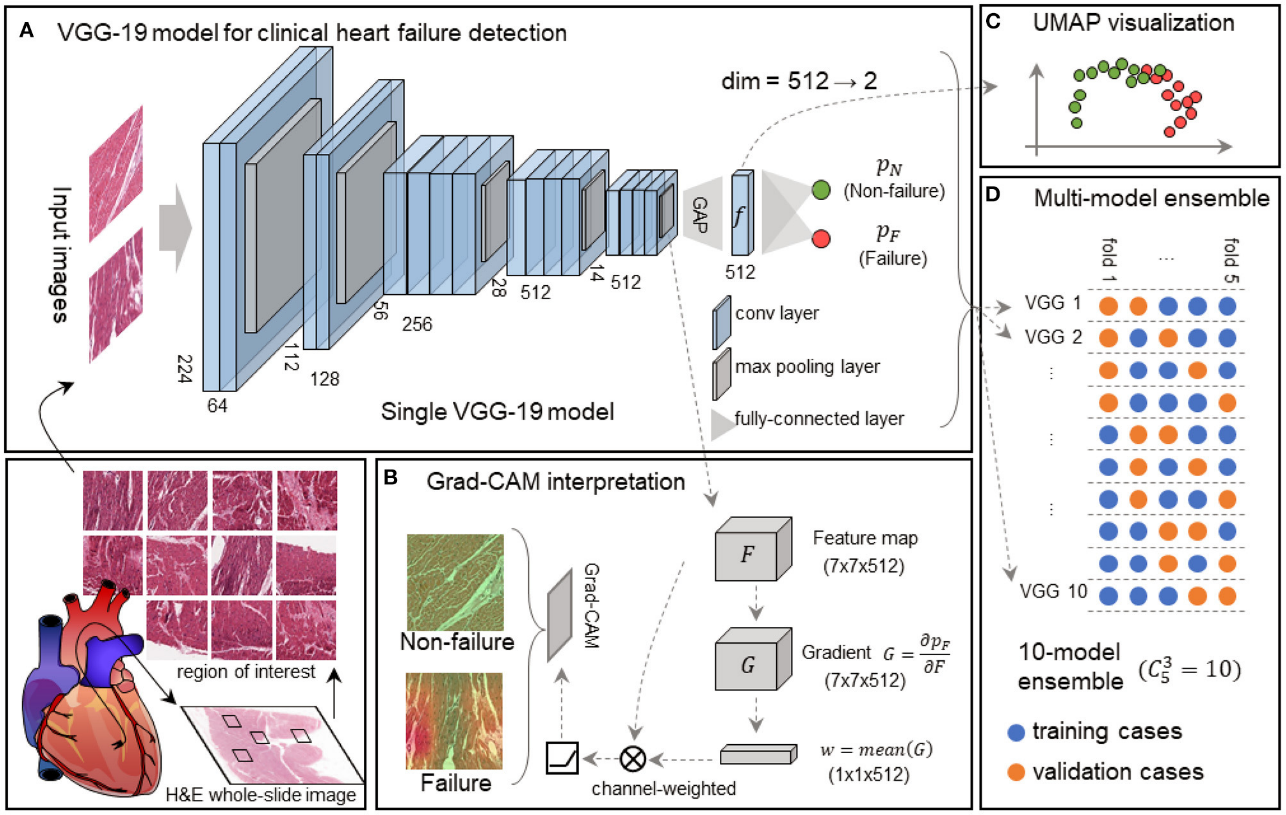

FIGURE 1 | Framework of the interpretable VGG-19 model with Grad-CAM and UMAP embedding for heart failure detection. **(A)** A schematic diagram highlights the basic pipeline from the myocardial section to digital prediction. The feature extractor of this single VGG-19 network includes 16 convolutional layers and 5 max-pooling layers, and the classifier is composed of a global average pooling (GAP) layer and a classification layer. This model is trained to discriminate failure and non-failure regions of interest (ROIs) without explicit pathological patterns. dim, dimension. **(B)** Grad-CAM generates attention maps for failure and non-failure cases, following the convolution and rectified linear unit (ReLU). **(C)** UMAP in the deep feature space converts 512-dimension features to 2-dimension visualization, elucidating the model outputs and intermediate features made by the VGG-19 model. **(D)** The 10-model ensembling is generated by a 5-fold cross-validation manner, and each fold is used for sub-model validation four times.

The 7 × 7 × 512 tensor was obtained from the feature extractor conveys abstract semantic information to the Grad-CAM to generate an attention map (**Figure 1B**) and UMAP to reduce the dimension (**Figure 1C**). We defined the output tensor from the last pooling layer in the VGG-19 model as F, and the predicted failure probability as p_F. Grad-CAM calculated the gradient as $G = \frac{\partial p_F}{\partial F}$, followed by a global-average pooling as a convolutional kernel w. Given an input size of $224 \times 224 \times 3$, the output size of F, G, and w were $7 \times 7 \times 512$, $7 \times 7 \times 512$, and $1 \times 1 \times 512$, respectively. The final attention map (A) is determined as follows:

$$A = ReLU(F \otimes w),$$

where ⊗ represents convolutional operation, and ReLU is defined as:

$$ReLU(x) = x \text{ } if \text{ } x > 0 \text{ } else \text{ } 0.$$

The attention map highlights the regions in an input image that are mostly responsible for prediction. Thus, it provides a way to interpret the decision made by the deep neural network.

In addition to the region-based interpretation, we utilized the UMAP embedding technique to reveal the discrepancy between failing samples and non-failing samples in the feature space. We gathered deep features immediately before the final classification layer. Each input image corresponds to a deep feature vector with a length of 512. Next, we calculated the pair-wise Euclidean distances among all the ROIs, and the distance matrix was processed by UMAP (22), resulting in a 2-D embedding for each ROI. The embedding could be visualized as a scatter plot (**Figure 1C**), reflecting the spatial relationships among samples.

Cross-Validation for Multi-Model Ensemble

Cross-validation is widely used to evaluate the performance of machine learning models reliably in small datasets. The dataset is generally partitioned to K portions, where each portion is known as a "fold." Based on the partition, we usually use arbitrary $m = K - 1$ portions to train a model and evaluate

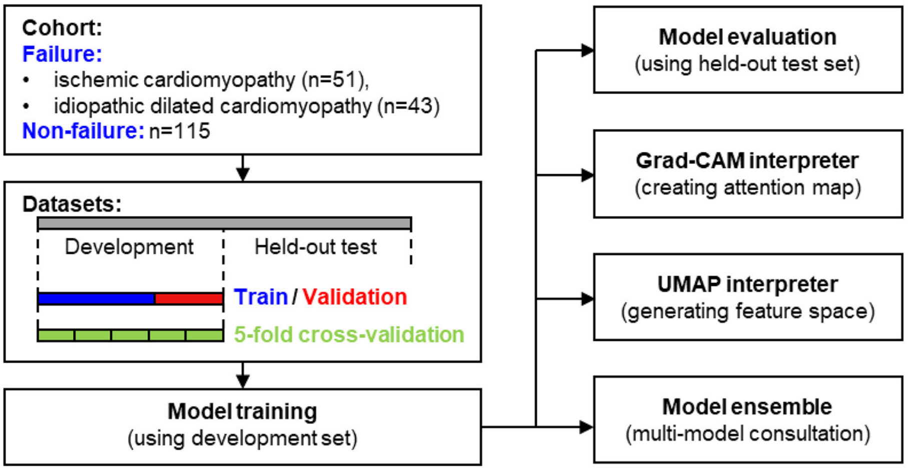

FIGURE 2 | The flowchart of the study.

its performance on the rest of one portion. For this reason, we further introduced this multi-model ensemble mechanism based on cross-validation to mimic multiple human experts for consultation in pathology and minimize the randomity caused by dataset partition. We partitioned the development set into $K = 5$ subsets on case-level (**Table 1**) and used $m = 3$ out of $K = 5$ subsets to train a sub-model and the rest for validation at each time. All the $C_K^m = 10$ models were independently trained with the identical protocol above. This allowed us to generate $C_{K-1}^{K-m-1} = 4$ independent predictions to validate the training process prior to the model deployment on the held-out test set (**Figure 1D**). The final decision from the multi-model ensemble relied on the averaging results to eliminate the discrepancy among individual models. The whole strategy of the multi-model ensemble mechanism is similar to the pathology consultation in which experience and knowledge vary from different experts, providing a comprehensive insight into ambiguous cases.

EXPERIMENTS AND RESULTS

The study flowchart is shown in **Figure 2**. Given the study cohort, image samples, and partitioned datasets, both individual model and multi-model ensemble were trained and evaluated for clinical heart failure detection. Furthermore, we integrated model interpretation techniques, including Grad-CAM-based regional visualization and UMAP-based feature space visualization, to generate positive predictions for specific local histological patterns such as fibrous infiltration and the enlarged myocardial cell nuclei.

Training and Validation of an Individual Model

We established an individual VGG-19 model on 770 training ROIs from 38 non-failure and 32 failure cases. The model was validated using 19 non-failure and 15 failure cases in 100 epochs (**Table 1**). The model was initialized with parameters pre-trained on ImageNet (20). The trainable parameters were then optimized by an Adam optimizer (26) (with a constant learning rate of 10^{-4}) to minimize cross-entropy loss:

$$L = \frac{1}{|C|} \sum\nolimits_{c \in C} - y_c \log(\hat{y}_c),$$

where C is the label set of the dataset, $y_c \in \{0, 1\}$ is the one-hot encoded label of a sample, and $\hat{y}_c$ is the corresponding prediction obtained from the output layer of the network. In response to appearance variation among numerous ROIs, we adopted data augmentation techniques, including random 224-pixel cropping, horizontal and vertical flipping, and stain augmentation (27) in the training process. Both training and validation losses were calculated and recorded at the end of each training period. The optimal network parameters with the lowest validation loss were retrieved for the assessment on the held-out test set (**Figure 3A**).

The confusion matrix on the ROI level showed 588 and 481 correct classifications in 638 non-failure and 517 failure cases, respectively (**Figure 3B**). We further used the proportion of positive predictions of heart failure among 11 ROIs in each patient as the aggregated risk score on the case level, achieving 53 and 46 correct classifications out of 58 non-failure and 47 failure cases, respectively. The AUC values were 0.971 and 0.978 on the ROI- and case-level, respectively.

Grad-CAM-Based Local Visualization

We implemented the Grad-CAM to map the positive confidence to corresponding locations in the raw EMB images, demonstrating that the predictive capability of the VGG-19 model is correlated with dominant morphology such as enlarged nuclei (**Figures 4A,B**), inflammatory infiltration (**Figure 4C**), and perinuclear vacuolation (**Figure 4D**). All the morphologies above were labeled as high attention (arrows in the top panel and corresponding regions in the bottom) in contrast to the medium or low attention in surroundings. The results implied that this deep model could recognize specific

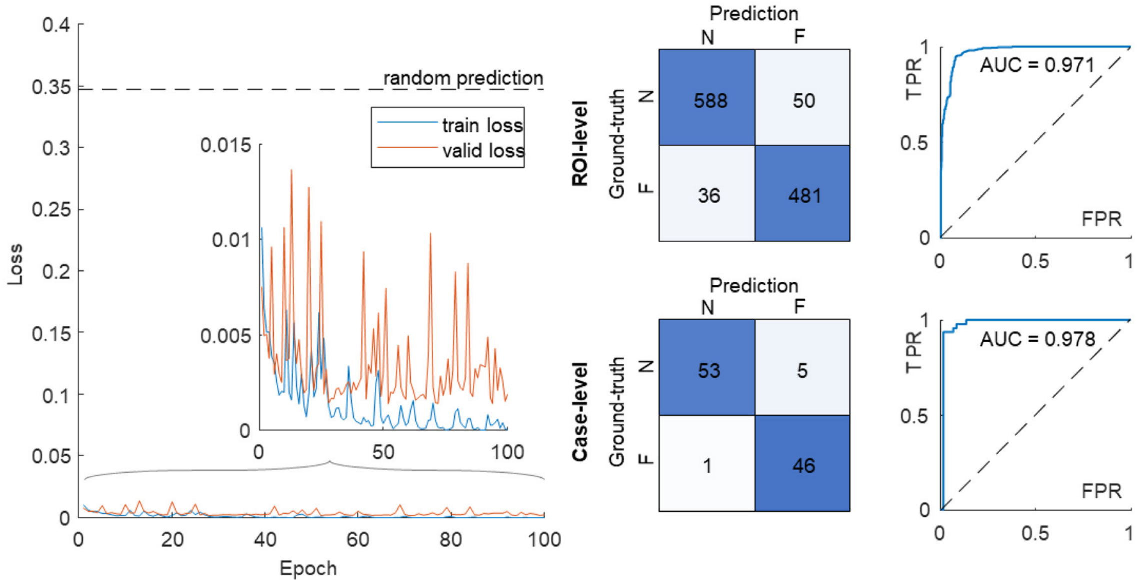

A Training and validation loss

B Confusion matrices and ROC curves

FIGURE 3 | The training process and performance of a single VGG-19 model. **(A)** Training (in blue) and validation (in orange) losses. **(B)** The confusion matrices and ROC curves are shown on the ROI-level (top) and case-level (bottom), respectively. N, non-failure; F, failure; ROC, receiver operating characteristic; AUC, area under ROC curve; FPR, false positive rate; TPR, true positive rate.

morphological patterns in the local area on the ROI. The Grad-CAM provided a straightforward visualization method to interpret the complicated features from the DNN model, guiding us to concentrate on delicate inspection in high attention regions. We further highlighted that Grad-CAM automatically generated attention maps in accordance with pathologies, indicating that this model learned a certain level of pathological knowledge bypassing explicitly defined pathological patterns. Collectively, the attention map visualization improved the creditability and interpretability of the deep models.

UMAP Embedding-Based Global Feature Space Visualization

The UMAP embedding method reduced the dimensionality of the intermediate tensor at the end of the feature extractor in the VGG-19 model, following a GAP layer. We converted all images in the development set and the held-out test set to 512 × 1 column vectors and used the UMAP method to generate 2-D embeddings of all the images. The failure and non-failure samples were mixed together and could not be divided if processed by dimension reduction in the feature space of the original VGG-19 model (**Figure 5A**). In comparison, our retrained model generated a clear boundary between two groups showing regular distribution in the deep feature space (**Figure 5B**). This suggests that the feature extractor is effectively re-modulated in the heart failure detection task.

We further projected all ROIs to the corresponding coordinates in the UMAP space, providing an intuitive distribution of non-failure (in green) and failure (in pink) images (**Figure 5C**). Compared to the failure group, the non-failure images were correlated with densely arranged myocardium cells. Our results indicated that the VGG-19 model was still sensitive to specific applications, and retraining was mandatory to improve the generalization capability.

Multi-Model Ensemble

In addition to the individual model, we employed the multi-model ensemble to mimic multiple human experts for consultation, and each sub-model served as an expert with different background. This method allowed us to verify the predictions made by different models trained on different datasets (**Table 1**). We divided 104 cases in the development set into five portions to generate 10 independent sub-models, and each portion was used for validation (in orange) four times in the development (**Figure 1D**). Thus, each case included 11 × 4 grids in **Figure 6A**. We further implemented these 10 sub-models into the held-out test set (**Figure 6B**), generating 11 × 10 grids for each case to assess the injured regions on 11 ROIs (**Figure 6C**). We mapped out the integrative reports of all 209 cases in **Figure 6**, accentuating the individual prediction of each ROI in each case from all available models. In both development and test sets, most non-failure cases had low failure risk predictions (in green) and vice versa (in red). Besides the predicted likelihood of being a failure, our model could simultaneously generate multiple attention maps, providing more intuitive evidence for further predictive decisions on ambiguous cases (**Figure 6D**).

We averaged corresponding likelihood scores to quantify the prediction on the ROI- and case-level. In comparison with the results of the individual model (**Figure 3B**), the multi-model ensemble performed 604 and 483 correct classifications on the

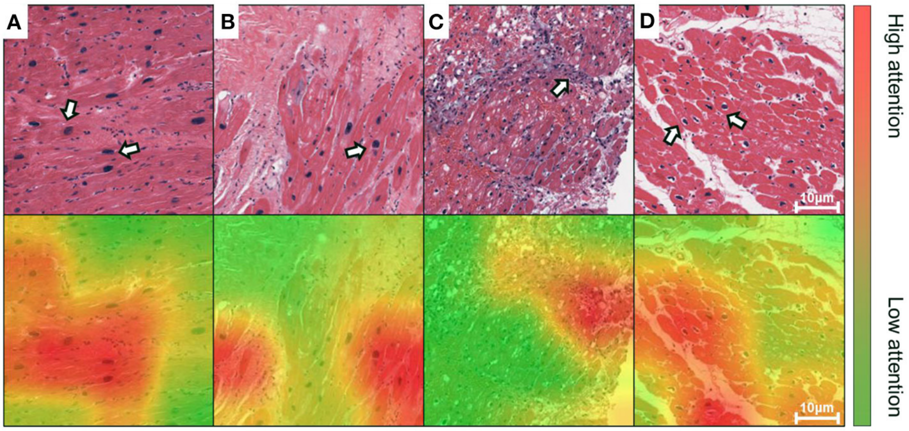

FIGURE 4 | Grad-CAM generates attention maps to visualize the dominant morphology on endomyocardial biopsy (EMB) images. The attention maps are visualized as overlaid heatmaps on top of the H&E stained histopathological images. All suspected injured regions, including **(A,B)** enlarged nuclei, **(C)** inflammatory infiltration, and **(D)** perinuclear vacuolation, are indicated by arrows in the top panel or labeled as high attention in red in the bottom, whereas the other regions with low attention are in green. Scale bars: 10 µm.

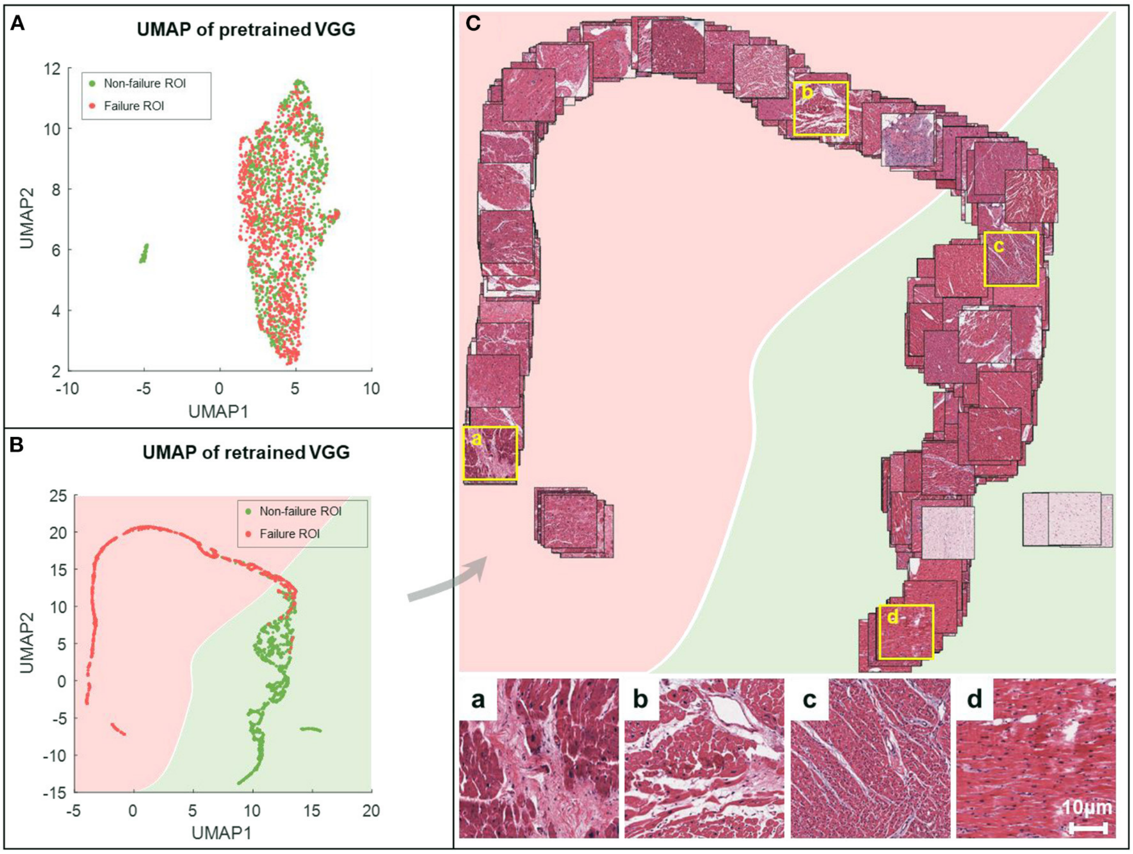

FIGURE 5 | UMAP embeddings of the deep features obtained from VGG-19 networks. All the images are processed by the feature extractor, resulting in features of length 512. These features are then reduced to 2-dimension (2-D) via UMAP (red for failure label, green for non-failure label) for the characterization of spatial relationships on the ROI-level. The 2-D UMAP embeddings are given for pretrained VGG **(A)** and retrained VGG models **(B)**. **(C)** Corresponding EMB images are projected onto the UMAP coordinates for the sake of visualization. For better visual effect, 20% of samples are randomly selected. Representative examples are shown in the bottom, where the first two (a,b) are failure samples, and the others (c,d) are non-failure samples.

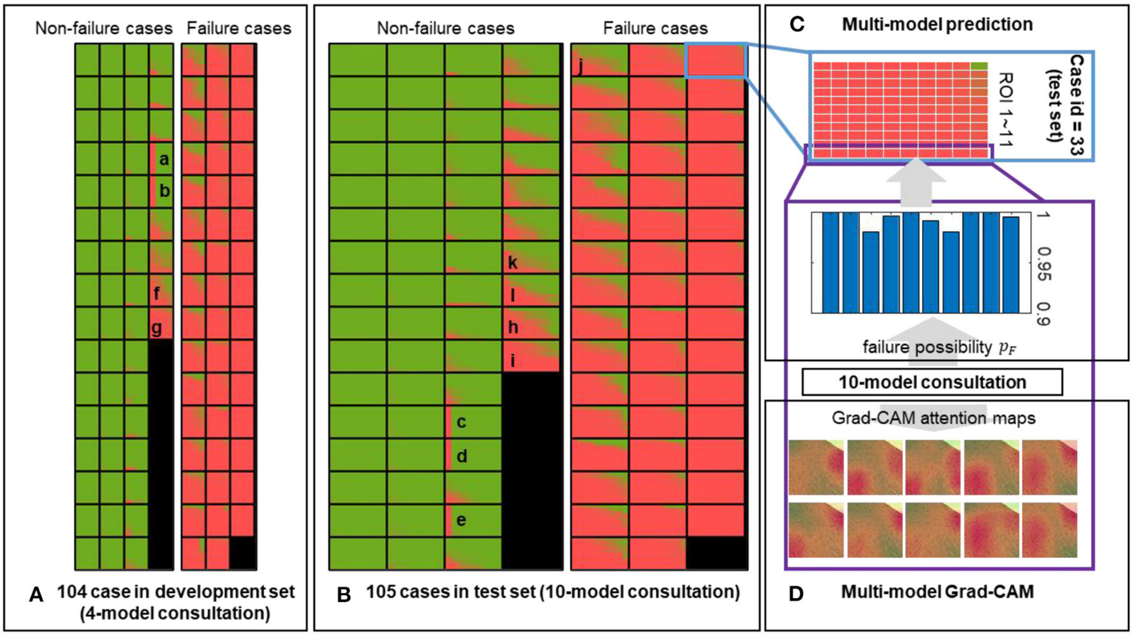

FIGURE 6 | Predictions of the multi-model ensemble. The failure probability predicted for each ROI of each case in the **(A)** development and **(B)** held-out test sets is mapped out. The low and high likelihood of being failure are represented in green and red, respectively. **(C)** An example case from the held-out test set is used to demonstrate the multi-model ensemble. Each block composed of 11 × 10 grids represents a single case, corresponding to the outputs from 10 sub-models applied on 11 ROIs. Each sub-model independently generates a prediction on each ROI, and all 11 × 10 outputs are ensembled to reflect the discrepancy among all sub-models. **(D)** Representative attention maps are generated by 10 sub-models independently on the same ROI, providing the failure probabilities and dominant morphology in the process of a comprehensive evaluation. Image size: 50 × 50 μm^2.

ROI-level, and detected 56 true non-failure and 46 true failure cases on the case-level (**Figure 7**). The AUC values of the ensemble model were 0.985 and 0.992 on the ROI- and case-level, respectively, exceeding the average of the 10 sub-models [AUC = 0.971 ± 0.017 and 0.981 ± 0.020 (mean ± standard deviation), respectively], and the AUC values achieved by random forest (AUC = 0.933 and 0.952), and two pathologists (AUC = 0.75, 0.73, on case-level) (23). The quantitative results demonstrated that our multi-model ensemble reduced the misclassification rate, especially on the non-failure cases, and improved the AUC values on both ROI- and case-levels, suggesting its ability to serve as a great complimentary tool to assist clinical diagnosis.

DISCUSSIONS

While the clinical diagnosis of heart failure relies on ejection fraction and serum biomarker, EMB is always a useful method for making a definite diagnosis in diseases that are difficult to diagnose by imaging modality alone. Computational pathology techniques based on the deep learning method can reduce the workload on pathologists, particularly for regions that have shortages in access to pathological diagnosis services. Nevertheless, the interpretability issue affects people's trust in deep learning systems. This study established and validated an interpretable DNN model to assess EMB histopathology in response to myocardial injury.

We demonstrated that the well-trained VGG-19 network could distinguish heart failure cases from the non-failure ones using local ROIs selected on whole-slide images. Different from traditional methods that rely on explicit pathological patterns such as cell types (28) or morphological features (29), our model was trained with failure or non-failure label solely. However, the attention maps generated by Grad-CAM were well-localized with representative morphologies such as enlarged nuclei and irregular shapes of cells, indicating that the extracted features from our model pertain to a certain level of pathological knowledge. Combined with Grad-CAM and UMAP embedding methods, we further provided an intuitive visualization of the local and global feature patterns of all EMB images learned by the VGG-19 model. Unlike other applications in cancer (24, 30–32), the implementation of this new model in myocardial injury reveals ill-defined histopathological patterns in local regions, providing a guideline and attention maps for well-trained pathologists. Therefore, integrating VGG-19 with Grad-CAM and UMAP embedding methods provides an interpretive DNN model for more accurate histopathological analyses.

Our method can be used to obtain the predictive results of each ROI from all ensembled sub-models, leading to an intuitive illustration of the discrepancy among individual sub-models (**Figure 8**, corresponding to representative results in **Figure 6**). In this study, we emphasized two types of disagreements among sub-models: (1) a significantly different prediction generated by a sub-model (**Figures 8A–E**, corresponding to A–E in **Figure 6**), and (2) in distinguishing false positive or false negative results (**Figures 8F–J**, corresponding to F–J in **Figure 6**). The former disagreement is due to the varied staining appearance of specific cases (**Figures 8A–E**), resulting in an incomprehensive training dataset. Specifically, the data distribution should be inspected prior to model development in response to negative effects introduced by the domain shift (33). The cross-validation protocol employed in this study provides a way to observe such effects in the training dataset. The latter type of disagreement (**Figures 8F–J**) pertains to transitional predictions, an ambiguous case-related false-positive or false-negative result. In some cases, with the label of "non-failure" (e.g., **Figures 8K,L**, corresponding to K and L in **Figure 6**), a few ROIs receive high-risk scores. While the case-level predictions match the ground truth, such circumstance indicates that the case may exhibit severe local injury. To address this issue, we will gather more representative samples, investigate the whole-slide image instead of some specific ROIs, and incorporate other supplementary approaches such as immunohistochemistry staining and polymerase chain reaction (PCR)-based analysis for a comprehensive assessment.

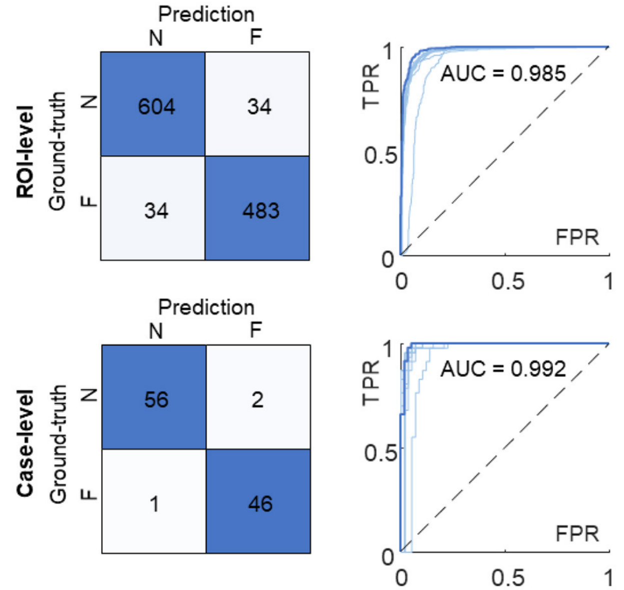

FIGURE 7 | Confusion matrices and ROC curves of the multi-model ensemble. The ROI-level and case-level results are reported at the top and bottom, respectively. The ROC curve and AUC value of the 10-model ensemble (in dark blue) are compared with the ones of individual sub-models (in light blue). N, non-failure; F, failure; ROC, receiver operating characteristic; AUC, area under ROC curve; FPR, false positive rate; TPR, true positive rate.

DNN has been proved as a generalizable tool in assisting cardiovascular disease diagnosis, for example, evaluating cardiac allograft rejection by analyzing histopathological or multiplex immunofluorescence images (4, 34). DNN has also led to breakthroughs in other imaging modalities for cardiovascular diagnosis or research, such as echocardiography, coronary artery calcium scoring, coronary computed tomography angiography, light-sheet microscopy, light-field imaging, etc. (17, 35, 36). Numerous applications such as quantification of receptor status (37), estimation of Ki-67 index (38), or implementation into Ziehl-Neelsen staining (39) and Masson's Trichrome (40) are potentially feasible in cardiovascular studies as well. Besides generic image classification and segmentation, DNN has demonstrated its viability to synthesize pseudo H&E images from Raman spectroscopy and other multi-modality non-linear imaging techniques, augmenting non-invasive and *in vivo* diagnosis (41). Collectively, the proposed framework provides a general pipeline for most of modalities and applications, improving the reliability and credibility of deep learning methods in cardiovascular diagnosis and research.

As a data-driven model, an unbiased and comprehensive training dataset is always preferred in an ideal condition. Our current model can be improved from the following aspects. First, the model was trained supervisory with a case-level label (belonging to failure or non-failure group). While

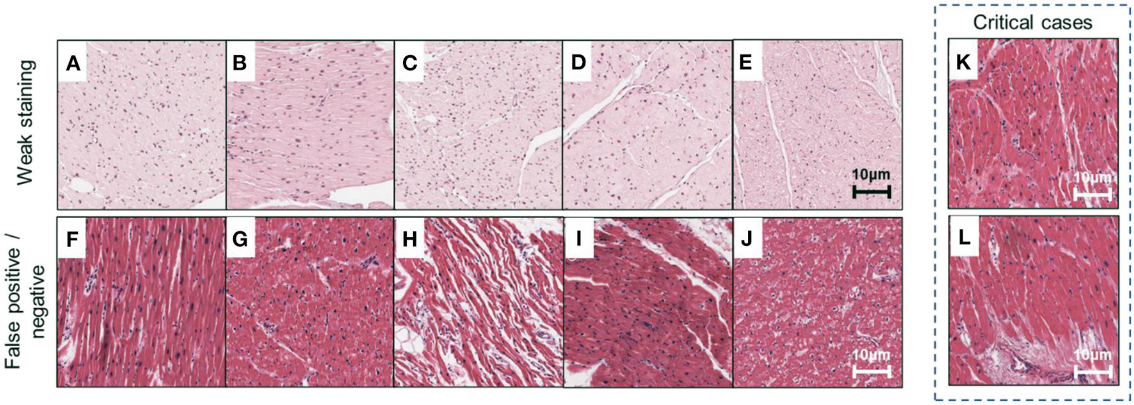

FIGURE 8 | Examples of misclassified cases. Representative ROIs are used as examples to demonstrate two types of misclassification marked in **Figure 6**. **(A–E)** Weak staining; **(F–I)** false-positive cases; **(J)** false-negative cases; **(K,L)** critical cases are correctly classified but confirmed to exhibit severe local injury and receive high-risk scores. Scale bars: 10 μm.

the high attention regions are correlated with pathological patterns, these patterns are not explicitly defined and cannot be quantified by DNNs. We will further introduce additional labels to characterize specific pathological patterns, for example, infiltrated inflammation and myocardial necrosis (12). Second, our data were provided by a single institute. We plan to include more diverse data sources to address the issues of varying data quality, processing protocol, and the equipment used for sample preparation (42). A more robust model covering the sample diversity may further advance future clinical investigations.

CONCLUSION

In this study, we integrated the VGG-19 network with Grad-CAM, UMAP, and multi-model ensemble methods for assessing EMB images from heart failure cases, providing an interpretive classification with high efficiency and accuracy. Three strategies, including the attention maps produced by Grad-CAM, the deep feature visualization via UMAP embedding, and multi-model ensemble, facilitated the interpretability of this VGG-19 model and clarified the dominant morphologies of injured regions on EMB images. Both individual model and multi-model ensemble indicated that DNN-aided diagnosis had great potential to recognize cardiomyopathy. Overall, our method established the basis for quantitative computation and intuitive interpretation of EMB images that can advance the applications of deep learning models in cardiac research.

DATA AVAILABILITY STATEMENT

Publicly available datasets were analyzed in this study. This data can be found at: The image data supporting this study can be found via https://idr.openmicroscopy.org/webclient/?show=project-402.

AUTHOR CONTRIBUTIONS

YJ, JY, and YD contributed to the development of the intellectual design of the project. YJ and JY performed the experiments and prepared the manuscript. All authors contributed to the data analysis, manuscript revision, and final approval.

FUNDING

This work was supported by NIH R00 HL148493 (YD), NSFC 62103098 (JY), and the University of Texas at Dallas.

ACKNOWLEDGMENTS

The authors would like to thank Dr. Anant Madabhushi for sharing the dataset that supports this study. We also thank YW for his help with interpretation of the Grad-CAM attention maps.

REFERENCES

1. Bui AL, Horwich TB, Fonarow GC. Epidemiology and risk profile of heart failure. *Nat Rev Cardiol.* (2011) 8:30–41. doi: 10.1038/nrcardio.2010.165
2. Veinot JP. Endomyocardial biopsy—when, and how? *Cardiovasc Pathol.* (2011) 20:291–6. doi: 10.1016/j.carpath.2010.08.005
3. Pollack A, Kontorovich AR, Fuster V, Dec GW. Viral myocarditis—diagnosis, treatment options, current controversies. *Nat Rev Cardiol.* (2015) 12:670–80. doi: 10.1038/nrcardio.2015.108
4. Peyster EG, Arabyarmohammadi S, Janowczyk A, Azarianpour-Esfahani S, Sekulic M, Cassol C, et al. An automated computational image analysis pipeline for histological grading of cardiac allograft rejection. *Eur Heart J.* (2021) 42:2356–69. doi: 10.1093/eurheartj/ehab241
5. Orringer DA, Pandian B, Niknafs YS, Hollon TC, Boyle J, Lewis S, et al. Rapid intraoperative histology of unprocessed surgical specimens via fibre-laser-based stimulated raman scattering microscopy. *Nat Biomed Eng.* (2017) 1:0027. doi: 10.1038/s41551-016-0027
6. Savastano LE, Zhou Q, Smith A, Vega K, Murga-Zamalloa C, Gordon D, et al. Multimodal laser-based angioscopy for structural, chemical and biological imaging of atherosclerosis. *Nat Biomed Eng.* (2017) 1:0023. doi: 10.1038/s41551-016-0023
7. Esteva A, Kuprel B, Novoa RA, Ko J, Swetter SM, Blau HM, et al. Dermatologist-level classification of skin cancer with deep neural networks. *Nature.* (2017) 542:115–8. doi: 10.1038/nature21056
8. Hannun AY, Rajpurkar P, Haghpanahi M, Tison GH, Bourn C, Turakhia MP, et al. Cardiologist-level arrhythmia detection and classification in ambulatory electrocardiograms using a deep neural network. *Nat Med.* (2019) 25:65–9. doi: 10.1038/s41591-018-0268-3
9. Loh BCS, Then PHH. Deep learning for cardiac computer-aided diagnosis: benefits, issues & solutions. *mHealth.* (2017) 3:45. doi: 10.21037/mhealth.2017.09.01
10. Jahmunah V, Oh SL, Wei JKE, Ciaccio EJ, Chua K, San TR, et al. Computer-aided diagnosis of congestive heart failure using ECG signals – a review. *Physica Medica.* (2019) 62:95–104. doi: 10.1016/j.ejmp.2019.05.004
11. Bejnordi BE, Veta M, Van Diest PJ, Van Ginneken B, Karssemeijer N, Litjens G, et al. Diagnostic assessment of deep learning algorithms for detection of lymph node metastases in women with breast cancer. *JAMA.* (2017) 318:2199–210. doi: 10.1001/jama.2017.14585
12. Peyster EG, Madabhushi A, Margulies KB. Advanced morphologic analysis for diagnosing allograft rejection: the case of cardiac transplant rejection. *Transplantation.* (2018) 102:1230–9. doi: 10.1097/TP.0000000000002189
13. Faust O, Acharya UR, Sudarshan VK, Tan RS, Yeong CH, Molinari F, et al. Computer aided diagnosis of coronary artery disease, myocardial infarction and carotid atherosclerosis using ultrasound images: a review. *Physica Medica.* (2017) 33:1–15. doi: 10.1016/j.ejmp.2016.12.005
14. Ding Y, Gudapati V, Lin R, Fei Y, Packard RRS, Song S, et al. Saak transform-based machine learning for light-sheet imaging of cardiac trabeculation. *IEEE Trans Biomed Eng.* (2021) 68:225–35. doi: 10.1109/TBME.2020.2991754
15. Kang SH, Joe B, Yoon Y, Cho GY, Shin I, Suh JW. Cardiac auscultation using smartphones: pilot study. *JMIR Mhealth Uhealth.* (2018) 6:e49. doi: 10.2196/mhealth.8946
16. Hill NR, Ayoubkhani D, McEwan P, Sugrue DM, Farooqui U, Lister S, et al. Predicting atrial fibrillation in primary care using machine learning. *PLoS ONE.* (2019) 14:e0224582. doi: 10.1371/journal.pone.0224582
17. Al'Aref SJ, Anchouche K, Singh G, Slomka PJ, Kolli KK, Kumar A, et al. Clinical applications of machine learning in cardiovascular disease and its relevance to cardiac imaging. *Eur Heart J.* (2019) 40:1975–86. doi: 10.1093/eurheartj/ehy404
18. Tolkach Y, Dohmgörgen T, Toma M, Kristiansen G. High-accuracy prostate cancer pathology using deep learning. *Nat Mach Intell.* (2020) 2:411–8. doi: 10.1038/s42256-020-0200-7
19. Jiao Y, Li J, Qian C, Fei S. Deep learning-based tumor microenvironment analysis in colon adenocarcinoma histopathological

whole-slide images. *Comput Methods Programs Biomed.* (2021) 204:106047. doi: 10.1016/j.cmpb.2021.106047

20. Simonyan K, Zisserman A. Very deep convolutional networks for large-scale image recognition. *arXiv [Preprint]*. arXiv:1409.1556 (2014).
21. Selvaraju RR, Cogswell M, Das A, Vedantam R, Parikh D, Batra, et al. *Grad-CAM: Visual Explanations from Deep Networks via Gradient-Based Localization*. IEEE International Conference on Computer Vision (ICCV). Venice; IEEE (2017). p. 618–26.
22. McInnes L, Healy J, Melville J. Umap: Uniform manifold approximation and projection for dimension reduction. *arXiv [Preprint]*. arXiv:1802.03426 (2018).
23. Nirschl JJ, Janowczyk A, Peyster EG, Frank R, Margulies KB, Feldman MD, et al. A deep-learning classifier identifies patients with clinical heart failure using whole-slide images of h&e tissue. *PLoS ONE.* (2018) 13:e0192726. doi: 10.1371/journal.pone.0192726
24. Faust K, Bala S, van Ommeren R, Portante A, Al Qawahmed R, Djuric U, et al. Intelligent feature engineering and ontological mapping of brain tumour histomorphologies by deep learning. *Nat Mach Intell.* (2019) 1:316–21. doi: 10.1038/s42256-019-0068-6
25. Kather JN, Pearson AT, Halama N, Jäger D, Krause J, Loosen SH, et al. Deep learning can predict microsatellite instability directly from histology in gastrointestinal cancer. *Nat Med.* (2019) 25:1054–6. doi: 10.1038/s41591-019-0462-y
26. Kingma DP, Ba J. Adam: A method for stochastic optimization. *arXiv [Preprint]*. arXiv:1412.6980 (2014).
27. Tellez D, Litjens G, Bándi P, Bulten W, Bokhorst JM, Ciompi F, et al. Quantifying the effects of data augmentation and stain color normalization in convolutional neural networks for computational pathology. *Med Image Anal.* (2019) 58:101544. doi: 10.1016/j.media.2019.101544
28. Diao JA, Wang JK, Chui WF, Mountain V, Gullapally SC, Srinivasan R, et al. Human-interpretable image features derived from densely mapped cancer pathology slides predict diverse molecular phenotypes. *Nat Comm.* (2021) 12:1613. doi: 10.1038/s41467-021-21896-9
29. Phillip JM, Han KS, Chen WC, Wirtz D, Wu PH. A robust unsupervised machine-learning method to quantify the morphological heterogeneity of cells and nuclei. *NatProtoc.* (2021) 16:754–74. doi: 10.1038/s41596-020-00432-x
30. Faust K, Xie Q, Han D, Goyle K, Volynskaya Z, Djuric U, et al. Visualizing histopathologic deep learning classification and anomaly detection using nonlinear feature space dimensionality reduction. *BMC Bioinform.* (2018) 19:173. doi: 10.1186/s12859-018-2184-4
31. Silva-Rodríguez J, Colomer A, Sales MA, Molina R, Naranjo V. Going deeper through the gleason scoring scale: an automatic end-to-end system for histology prostate grading and cribriform pattern detection. *Comput Methods Programs Biomed.* (2020) 195:105637. doi: 10.1016/j.cmpb.2020.105637
32. Jiang S, Li H, Jin Z. A visually interpretable deep learning framework for histopathological image-based skin cancer diagnosis. *IEEE J Biomed Health Inform.* (2021) 25:1483–94. doi: 10.2307/j.ctv1gt945c.26
33. Stacke K, Eilertsen G, Unger J, Lundström C. A closer look at domain shift for deep learning in histopathology. *arXiv [Preprint]*. arXiv:1909.11575 (2019).
34. Peyster EG, Wang C, Ishola F, Remeniuk B, Hoyt C, Feldman MD, et al. In situ immune profiling of heart transplant biopsies improves diagnostic accuracy and rejection risk stratification. *JACC Basic Transl Sci.* (2020) 5:328–40. doi: 10.1016/j.jacbts.2020.01.015
35. Wang Z, Zhu L, Zhang H, Li G, Yi C, Li Y, et al. Real-time volumetric reconstruction of biological dynamics with light-field microscopy and deep learning. *Nat Methods.* (2021) 18:551–6. doi: 10.1038/s41592-021-01058-x
36. Wang Z, Ding Y, Satta S, Roustaei M, Fei P, Hsiai, et al. A hybrid of light-field and light-sheet imaging to study myocardial function and intracardiac blood flow during zebrafish development. *PLoS Comput Biol.* (2021) 17:e1009175. doi: 10.1371/journal.pcbi.1009175
37. Saha M, Arun I, Ahmed R, Chatterjee S, Chakraborty C. Hscorenet: a deep network for estrogen and progesterone scoring using breast IHC images. *Pattern Recognit.* (2020) 102:107200. doi: 10.1016/j.patcog.2020.107200
38. Negahbani F, Sabzi R, Pakniyat Jahromi B, Firouzabadi D, Movahedi F, Kohandel Shirazi M, et al. Pathonet introduced as a deep neural network backend for evaluation of Ki-67 and tumor-infiltrating lymphocytes in breast cancer. *Sci Rep.* (2021) 11:8489. doi: 10.1038/s41598-021-86912-w
39. Yang M, Nurzynska K, Walts AE, Gertych A. A CNN-based active learning framework to identify mycobacteria in digitized ziehl-neelsen stained human tissues. *Comput Med Imaging Graph.* (2020) 84:101752. doi: 10.1016/j.compmedimag.2020.101752
40. Stritt M, Stalder AK, Vezzali E. Orbit image analysis: an open-source whole slide image analysis tool. *PLoS Comput Biol.* (2020) 16:e1007313. doi: 10.1371/journal.pcbi.1007313
41. Bocklitz TW, Salah FS, Vogler N, Heuke S, Chernavskaia O, Schmidt C, et al. Pseudo-HE images derived from CARS/TPEF/SHG multimodal imaging in combination with raman-spectroscopy as a pathological screening tool. *BMC Cancer.* (2016) 16:534. doi: 10.1186/s12885-016-2520-x
42. Stacke K, Eilertsen G, Unger J, Lundstrom C. Measuring domain shift for deep learning in histopathology. *IEEE J Biomed Health Inform.* (2021) 25:325–36. doi: 10.1109/JBHI.2020.3032060

Conflict of Interest: The authors declare that the research was conducted in the absence of any commercial or financial relationships that could be construed as a potential conflict of interest.

frontiers
in Cardiovascular Medicine

ORIGINAL RESEARCH
published: 10 March 2022
doi: 10.3389/fcvm.2022.766565

A Prediction Equation to Estimate Vascular Endothelial Function in Different Body Mass Index Populations

Xiao Li[1†], Hanying Liu[2†], Yan Zhang[1], Yanting Gu[1], Lianjie Sun[3], Haoyong Yu[2*] and Wenkun Bai[1,4*]

[1] Department of Ultrasound in Medicine, Shanghai Jiao Tong University Affiliated 6th People's Hospital, Shanghai Institute of Ultrasound in Medicine, Shanghai, China, [2] Department of Endocrinology and Metabolism, Shanghai Jiao Tong University Affiliated Sixth People's Hospital, Institute of Shanghai Diabetes, Shanghai, China, [3] Department of Cardiovascular Surgery, The Affiliated Hospital of Qingdao University, Qingdao, China, [4] Department of Ultrasound in Medicine, South Hospital of Shanghai Jiao Tong University Affiliated 6th People's Hospital, Shanghai, China

Edited by:
Yun Fang,
University of Chicago, United States

Reviewed by:
Jessica Faulkner,
Augusta University, United States
Telmo Pereira,
Fisiologia Clínica, Portugal

***Correspondence:**
Haoyong Yu
Yuhaoyong111@163.com
Wenkun Bai
doctor505@hotmail.com

[†] These authors share first authorship

Specialty section:
This article was submitted to
Atherosclerosis and Vascular
Medicine,
a section of the journal
Frontiers in Cardiovascular Medicine

Received: 29 August 2021
Accepted: 14 February 2022
Published: 10 March 2022

Citation:
Li X, Liu H, Zhang Y, Gu Y, Sun L, Yu H
and Bai W (2022) A Prediction
Equation to Estimate Vascular
Endothelial Function in Different Body
Mass Index Populations.
Front. Cardiovasc. Med. 9:766565.
doi: 10.3389/fcvm.2022.766565

Objective: Vascular endothelial dysfunction is considered an early predictor of endothelial injury and the initiating factor of atherosclerosis (AS). Brachial artery flow-mediated dilation (FMD) can detect endothelial injury early and provide important prognostic information beyond traditional cardiovascular (CV) risk factors. This study aimed to find the influencing factors of FMD and develop a simple prediction model in populations with different body mass indices (BMIs).

Methods: In total, 420 volunteers with different BMIs were recruited in our study. Subjects were randomly assigned to the derivation and validation cohorts (the ratio of the two was 1:2) with simple random sampling. The former was used for influencing factors searching and model construction of FMD and the latter was used for verification and performance evaluation.

Results: The population was divided into two groups, i.e., 140 people in the derivation group and 280 people in the verification group. Analyzing in the training data, we found that females had higher FMD than males ($p < 0.05$), and FMD decreased with age ($p < 0.05$). In people with diabetes, hypertension or obesity, FMD was lower than that in normal individuals ($p < 0.05$). Through correlation analysis and linear regression, we found the main influencing factors of FMD: BMI, age, waist-to-hip radio (WHR), aspartate aminotransferase (AST) and low-density lipoprotein (LDL). And we developed a simple FMD prediction model: $\text{FMD} = -0.096\text{BMI}-0.069\text{age}-4.551\text{WHR}-0.015\text{AST}-0.242\text{LDL}+17.938$, where $R^2 = 0.599$, and adjusted $R^2 = 0.583$. There was no statistically significant difference between the actual FMD and the predicted FMD in the verification group ($p > 0.05$). The intra-class correlation coefficient (ICC) was 0.77. In a Bland-Altman plot, the actual FMD and the predicted FMD also showed good agreement. This prediction model had good hints in CV risk stratification (area under curve [AUC]: 0.780, 95 % confidence intervals [95% CI]: 0.708–0.852, $p < 0.001$), with a sensitivity and specificity of 73.8 and 72.1%, respectively.

Conclusions: Males, older, obesity, hypertension, diabetes, smoking, etc. were risk factors for FMD, which was closely related to CV disease (CVD). We developed a simple equation to predict FMD, which showed good agreement between the training and validation groups. And it would greatly simplify clinical work and may help physicians follow up the condition and monitor therapeutic effect. But further validation and modification bears great significance.

Keywords: flow-mediated dilation, prediction equation, vascular endothelial function, atherosclerosis, body mass index

INTRODUCTION

AS is the most common pathological mechanism of coronary artery disease, peripheral artery disease and cerebrovascular disease (1). The chronic accumulation of subendothelial atherosclerotic plaque or the shedding of unstable plaque will cause luminal stenosis to restrict blood flow and cause severe tissue hypoxia, eventually causing myocardial infarction and stroke, which is the most common cause of death in the world (2). Vascular endothelial dysfunction is generally considered an early predictor of endothelial injury and the initiating factor of AS (3). Thus, early recognition of endothelial injury can help take intervention measures as soon as possible to effectively delay or even reverse the process of AS.

The evaluation methods of endothelial function are mainly divided into invasion and non-invasion. In the past, invasive inspections such as coronary angiography and forearm plethysmography (4) were often used. However, these invasive techniques were burdensome for the subjects with low repeatability and high risk characteristics. Especially for healthy people or asymptomatic patients, it was usually inappropriate to perform these examinations. Therefore, some non-invasive technologies have emerged with higher repeatability and accurate and reliable results. Carotid intima media thickness (CIMT) measurement is an effective method for the early assessment of AS (5). With its simple operation and low price, the ultrasound measurement of CIMT is widely used in the clinical screening of vascular diseases. However, there is interobserver variability in measurement, and its accuracy must be improved. Peripheral arterial tonometry (PAT) is an effective method to evaluate the microvascular function (6). The vasomotor function is evaluated by vasodilation after compression, and the results obtained by its automatic detection program are more reliable. Correspondingly, FMD is currently the most commonly used method to evaluate the endothelial function (7). Its result is accurate, reliable and highly repeatable, and it is considered the most important method to non-invasively evaluate the endothelial function.

However, there are many problems in the application of FMD in daily clinical practice. With its high requirements for operation skills, it requires well-trained operators. The discomfort caused by prolonged pressurization makes it unacceptable. The inspect equipment is also expensive, especially in primary hospitals, which results in much more difficult assessments.

Thus, we developed a prediction model based on FMD results with anthropometric measurements and laboratory analysis to facilitate the evaluation of endothelial damage in populations with different BMIs. It was helpful to popularize at primary hospitals and convenient for early detection and early intervention, which we hope to improve the prognosis of atherosclerosis.

METHODS

Participant Selection and Design

This study consequently enrolled subjects from Jan 2021 to April 2021 in the Sixth People's Hospital Affiliated to Shanghai Jiao Tong University, China. Patients with the following conditions were excluded from our study: current malignancy with a life expectancy <6 months; undergoing radiotherapy, chemotherapy, or molecular targeted therapy; severe mental illness or language barriers that prevented normal communication with researchers. In total, 420 subjects aged 18–60 years were recruited, including 108 males and 312 females, all of whom were Chinese. FMD and anthropometric measurements and laboratory analysis were performed on all participants. Hypertension was defined as > 140/90 mm Hg according to the 2018 European Society of Cardiology (ESC)/European Society of Hypertension (ESH) guidelines (8). Criteria for the diagnosis of diabetes was fasting blood glucose (FBG) $\geq$ 7.0 mmol/L or 2-h plasma glucose value $\geq$ 11.1 mmol/L during a 75-g oral glucose tolerance test or the glycated hemoglobin (HbA1c) $\geq$ 6.5% or patient with classic symptoms of hyperglycemia or hyperglycemic crisis, a random plasma glucose $\geq$ 11.1 mmol/L (9). Given that total cholesterol (TC) and/or high-density lipoprotein (HDL) are included as risk assessment factors in many guidelines on the assessment of cardiovascular risk (10–12), we tentatively classified TC $\geq$ 5.2 mmol/l or HDL < 1.0 mmol/l as the dyslipidemia group for ease of analysis. Then, the population was randomly assigned to the derivation and validation cohorts (the ratio of the two was 1:2) with simple random sampling to search for the influencing factors of FMD and construct and verify the equation. The protocol was approved by the Shanghai Jiao Tong University Ethics Committee and conformed to the Declaration of Helsinki. All subjects provided written informed consent to participate in the study.

FMD and CIMT Measurement

FMD was measured according to the guideline (13) with an Omron UNEX EF 38G (UNEX Corporation, Nagoya, Japan) tester, and the probe frequency was 10 MHz. Prior to the FMD examination, subjects should fast (>6 h), avoid exercise

(>24 h), and refrain from caffeine, vitamin C and alcohol (>12 h). Smokers must refrain from smoking for >6 h. When subjects take drugs, they should wait 4 times the half-life of the drug. Then, they should be studied in a quiet, temperature-controlled room and relaxed for at least 10 min to relieve mental stress and physical activity. The blood pressure was measured twice on the right arm in the sitting position, and the average value was obtained. Then, in the supine position with the right arm extended, the cuff was placed on the forearm, and the brachial artery was scanned 3–5 cm above the antecubital fossa. We used an H-shaped probe capturing two short-axis and one long-axis for automatic probe position correction to identify clear vascular boundaries. And a probe-holding device was used to further ensure optimal image. First, the baseline inner diameter of brachial artery was measured; then, the cuff was inflated to a pressure of 50 mmHg higher than the subject's systolic blood pressure and held for 5 min. Afterwards, the cuff was deflated, and the diameter of the artery was measured again over the next 3 min to capture the peak brachial artery diameter. The continuous measurement process was monitoring by automatic edge-detections systems. Finally, the FMD result was automatically calculated by the machine: FMD = [(maximum diameter – diameter at rest)/diameter at rest] × 100 (%). FMD was measured twice for each participant at an interval of 20 min, and the average value was obtained.

CIMT was performed using a MINDRAY DC-8 or a MINDRAY DC-80S ultrasound machine with a 10-MHz linear probe. Patients were examined in the supine position with a slight rotation of the neck to the contralateral side. CIMT was defined as the distance between the lumen-intima boundary and the media-adventitia boundary. And it was measured at ∼1 cm posterior to the common carotid artery bifurcation at a site with uniform intima without plaque lesions. The proximal and distal walls were measured and averaged. Finally, the average value of the left and right common carotid arteries was taken as the average CIMT.

The entire inspection project for FMD and CIMT was completed by two experienced physician with at least 3 years of operating experience and the physicians did not know any information about them.

Clinical and Laboratory Analysis

Operators used a digital scale to measure the height and weight of participants, who had to take off shoes and wear light clothes. Then, we calculated the BMI = body weight (kg)/height squared (m^2). The waist circumference was measured using tape around the abdomen through the midpoint of the lower edge of the costal arch and the anterior superior spine by a trained examiner. Then, the subjects stood upright with legs close together, and the tape was placed horizontally on their front pubic symphysis and the most convex part of the back gluteus maximus to measure the hip circumference. And the WHR was calculated using the formula: WHR = waist circumference (cm)/hip circumference (cm). The systolic blood pressure (SBP) and diastolic blood pressure (DBP) were measured twice in a quiet state for 1 day, and mean values were used for analysis. Mean arterial pressure (MAP) was expressed as MAP = (SBP+2 × DBP)/3.

We searched for cardiovascular risk factors proposed by some guidelines, and on this basis, added variables that may be associated with FMD for model construction: triglyceride (TG), TCHDL, LDL, alanine aminotransferase (ALT), AST, γ-glutamyl transpeptidase (γ-GT), alkaline phosphatase (ALP), free triiodothyronine (FT_3), free tetraiodothyronine (FT_4), thyroid stimulating hormone (TSH), prealbumin (PAB), total bile acid (TPA), total bilirubin (TBiL), direct bilirubin (DBiL), serum creatinine (Scr), serum uric acid (SUA), blood urea nitrogen (BUN), retinol-binding protein (RBP), cystatin C (CysC), FBG, HbA1c, insulin, and C-peptide (CP). Venous blood samples were drawn from all subjects in the early morning after 8 h of fasting. All biochemical determinations were performed in the same laboratory using standard laboratory methods. Insulin was measured by radioimmunoassay (ADVIA Insulin Ready Pack 100, Bayer Diagnostics, Milan, Italy) with intra- and inter-assay coefficients of variation < 5%.

Statistical Analysis

Statistical analyses were performed with the SPSS software, version 26 and MedCalc software, 20.0.3. The normality of distribution was checked with Kolmogorov–Smirnov test. Normally distributed data are expressed as the mean ± standard deviation, whereas data not normally distributed are expressed as the median and interquartile range. Categorical variables were expressed as percentages. Independent two-sample *t*-test and non-parametric test (Mann–Whitney) were used for comparison of quantitative data. Pearson's chi-square ($\chi 2$) was used to compare categorical data. We first analyzed the difference of FMD among subgroups of different genders, different ages and with or without hypertension, diabetes or dyslipidemia. And then we further searched for the influencing factors of FMD through correlation analysis ($p < 0.01$, $r > 0.3$) and linear regression ($p < 0.01$), and constructed a FMD prediction model based on multivariate linear regression (stepwise). Finally, validation and performance evaluation were performed in the validation sample by ICC and Bland–Altman plot. In addition, we analyzed the value of our predictive equation in identifying risk factors for CVD through receiver operating characteristic (ROC) curves. A $p < 0.05$ indicated statistical significance.

RESULTS

Baseline Characteristics and Within-Group Analysis

In total, 420 subjects fulfilled the inclusion criteria and were divided into a derivation group and a verification group by random sampling. The ratio of the two was 1:2, i.e., 140 people in the derivation group and 280 people in the validation group. The demographic and clinical characteristics of the two groups are shown in **Table 1**. There was no statistically significant difference between them ($p > 0.05$).

In the derivation group, we performed sub-group analysis (**Table 2**, **Figure 1**). The initial assessment in gender subgroups revealed that women presented higher FMD than men ($p < 0.05$) (**Figure 1A**), whereas CIMT was not statistically different ($p > 0.05$). In different age groups, we found that younger people

TABLE 1 | Characteristics in the derivation and validation cohorts.

Characteristics	Derivation data set	Validation data set	*P*-value
N (M/F)	140 (38/102)	280 (70/210)	0.64
Age (years)	32.1 ± 8.1	31.3 ± 7.4	0.34
BMI (kg/m^2)	35.5 ± 8.3	35.3 ± 8.7	0.81
HR (beats/min)	86.9 ± 12.7	86.5 ± 12.6	0.75
SBP (mmHg)	130.6 ± 19.7	128.7 ± 17.3	0.32
DBP (mmHg)	85.8 ± 12.9	84.8 ± 12.3	0.42
MAP (mmHg)	100.7 ± 14.2	99.1 ± 14.3	0.26
WHR	1.0 (1.0, 1.0)	1.0 (0.9, 1.0)	0.78
CIMT (mm)	0.6 (0.5, 0.7)	0.6 (0.5, 0.7)	0.23
TG (mmol/l)	1.5 (1.1, 2.4)	1.5 (1.1, 2.3)	0.68
TC (mmol/l)	5.2 (4.5, 6.1)	5.2 (4.4, 5.9)	0.71
HDL cholesterol (mmol/l)	1.2 (1.1, 1.4)	1.3(1.1, 1.4)	0.59
LDL cholesterol (mmol/l)	3.2 ± 0.9	3.2 ± 0.8	0.71
ALT (U/L)	43.0 (27.5, 77.5)	42.5 (25.0, 74.2)	0.93
AST (U/L)	25.0 (18.0, 44.0)	25.5 (18.0, 41.5)	0.91
γ-GT (U/L)	41.0 (27.0, 59.5)	36.0 (23.0, 56.3)	0.37
ALP (U/L)	76.0 (62.5, 92.5)	76.0 (64.0, 93.3)	0.62
FT$_3$ (pmol/L)	5.1 (4.7, 5.4)	5.0 (4.6, 5.5)	0.55
FT$_4$ (pmol/L)	16.3 (15.1, 17.4)	15.9 (14.8, 17.5)	0.76
TSH (mIU/L)	2.2 (1.5, 3.1)	2.5 (1.6, 3.6)	0.05
PAB (mg/L)	273.0 (241.0, 379.0)	272.5 (231.8, 304.0)	0.19
TBA (μmol/L)	2.9 (2.0, 5.4)	3.3 (2.1, 5.3)	0.30
TBiL (μmol/L)	8.7 (6.4, 11.5)	8.5 (6.3, 11.2)	0.28
DBiL (μmol/L)	2.2 (1.6, 3.0)	2.1 (1.7, 2.8)	0.61
Scr (mg/dL)	60.0 (52.1, 71.9)	60.6 (54.0, 68.9)	0.95
SUA (mg/dL)	402.0 (330.5, 453.5)	417.5 (346.8, 464.8)	0.27
BUN (mmol/L)	4.6 (3.9, 5.4)	4.6 (3.9, 5.4)	0.89
RBP (mg/L)	38.0 (32.0, 45.0)	36 (31.0, 42.0)	0.15
CysC (mg/L)	0.7 (0.6, 0.8)	0.7(0.6, 0.8)	0.84
FBG (mmol/l)	5.7 (5.0, 7.2)	5.6(5.1, 6.9)	0.63
HbA1c (%)	5.8 (5.4, 6.8)	5.8 (5.4, 6.7)	0.71
Insulin (μIU/ml)	25.9 (17.6, 38.4)	28.8 (19.9, 44.3)	0.31
CP (ng/ml)	3.9 (3.2, 4.8)	4.1 (3.4, 5.1)	0.56
Current smokers (%)	32 (22.9%)	48 (17.1%)	0.18
Hypertension (%)	30 (21.4%)	38 (13.6%)	0.06
Participants on anti-hypertensives (%)	18 (12.9%)	29 (10.4%)	0.44
Diabetes (%)	40 (28.6)	75 (26.8%)	0.70
Participants on anti-diabetics (%)	17 (12.1%)	39 (13.9%)	0.61
Dyslipidemia (%)	78 (55.7%)	152 (54.3%)	0.78
Participants on lipid-lowering drugs (%)	2 (1.4%)	1 (0.4%)	0.22
FMD (%)	6.4 (5.6, 7.6)	6.2 (5.4, 7.0)	0.51

Data are shown as the mean ± SD or the median (interquartile range).
M/F, male/female; BMI, body mass index; HR, heart rate; SBP, systolic blood pressure; DBP, diastolic blood pressure; MAP, mean arterial pressure; WHR, waist-to-hip ratio; CIMT, carotid intima media thickness; TG, triglyceride; TC, total cholesterol; HDL, high-density lipoprotein; LDL, low-density lipoprotein; ALT, alanine aminotransferase; AST, aspartate aminotransferase; γ-GT, γ-glutamyl transpeptidase; ALP, alkaline phosphatase; FT$_3$, free triiodothyronine; FT$_4$, free tetraiodothyronine; TSH, thyroid stimulating hormone; PAB, prealbumin; TBA, total bile acid; TBiL, total bilirubin; DBiL, direct Bilirubin; Scr, serum creatinine; SUA, serum uric acid; BUN, blood urea nitrogen; RBP, retinol-binding protein; CysC, cystatin C; FBG, fasting blood glucose; HbA1c, glycated hemoglobin; CP, C-peptide; FMD, flow-mediated dilation.

TABLE 2 | Values of FMD and CIMT in subgroups of gender, age, BMI, hypertension, diabetes, dyslipidemia and smokers.

	FMD (%)	*P*-value	CIMT (mm)	*P*-value
Gender				
Male	6.1 (4.9, 7.0)	0.01	0.6 (0.5, 0.6)	0.21
Female	6.7 (5.7, 7.6)		0.6 (0.5, 0.7)	
Age				
≤30	7.0 (5.8, 8.0)	0.00	0.5 (0.5, 0.6)	0.00
>30, ≤39	6.4 (5.5, 7.2)		0.6 (0.5, 0.7)	
>40	5.6 (5.1, 6.5)		0.7 (0.6, 0.8)	
BMI				
<24	10.3 (8.5, 11.9)	0.00	0.5 (0.4, 0.6)[a]	0.00
≥24, <28	7.9 (6.7, 8.3)		0.4 (0.4, 0.5)[a]	
≥28	6.1 (5.4, 7.0)		0.6 (0.5, 0.7)[b]	
Hypertension				
Yes	5.7 (5.0, 6.6)	0.00	0.7 (0.5, 0.8)	0.00
Taking drugs	5.6 (4.8, 6.7)	*0.26*	0.8 (0.6, 0.8)	0.02
Not taking drugs	6.0 (5.2, 6.8)		0.6 (0.5, 0.7)	
No	6.8 (5.7, 7.6)		0.6 (0.5, 0.6)	
Diabetes				
Yes	5.7 (5.3, 6.5)	0.00	0.6 (0.6, 0.7)	0.00
Taking drugs	5.6 (5.0, 6.7)	0.96	0.6 (0.5, 0.7)	0.83
Not taking drugs	5.7 (5.3, 6.3)		0.6 (0.6, 0.8)	
No	6.9 (5.8, 7.9)		0.6 (0.5, 0.6)	
Dyslipidemia				
Yes	6.3 (5.6, 7.3)	0.40	0.6 (0.5, 0.7)	0.21
Taking drugs	6.5 (6.5, 7.1)	0.40	0.8 (0.8, –)	0.04
Not taking drugs	6.3 (5.6, 7.3)		0.6 (0.5, 0.7)	
No	6.7 (5.3, 8.0)		0.6 (0.5, 0.7)	
Smokers				0.22
Yes	6.0 (5.2, 6.9)	0.01	0.6 (0.5, 0.7)	
No	6.8 (5.6, 7.9)		0.6 (0.5, 0.7)	

Data are shown as the median (interquartile range); [a]Compared to [b] BMI ≥ 28, $p < 0.05$.
FMD, flow-mediated dilation; CIMT, carotid intima media thickness; BMI, body mass index.

had higher FMD (**Figure 1B**) and lower CIMT (**Figure 2A**) than older people ($p < 0.05$). Analysis of BMI subgroups revealed that obese people presented lower FMD (**Figure 1C**) and higher CIMT (**Figure 2B**) than non-obese individuals ($p < 0.05$). People with hypertension and diabetes showed lower FMD (**Figures 1D,E**) and higher CIMT (**Figures 2C,D**) than those without such diseases ($p < 0.05$), while taking drugs or not had no significant effect on FMD or CIMT in population with such diseases ($p > 0.05$). Smokers had lower FMD than non-smokers ($p < 0.05$) (**Figure 1F**). However, analysis of the population with or without dyslipidemia revealed that there was no significant difference in FMD or CIMT ($p > 0.05$).

Correlation and Univariate Analysis

Before constructing the prediction equation, we first looked for variables that were clearly related to FMD. We performed bivariate correlation analysis and univariate regression analysis on the above variables and FMD, and screened out 16 potential

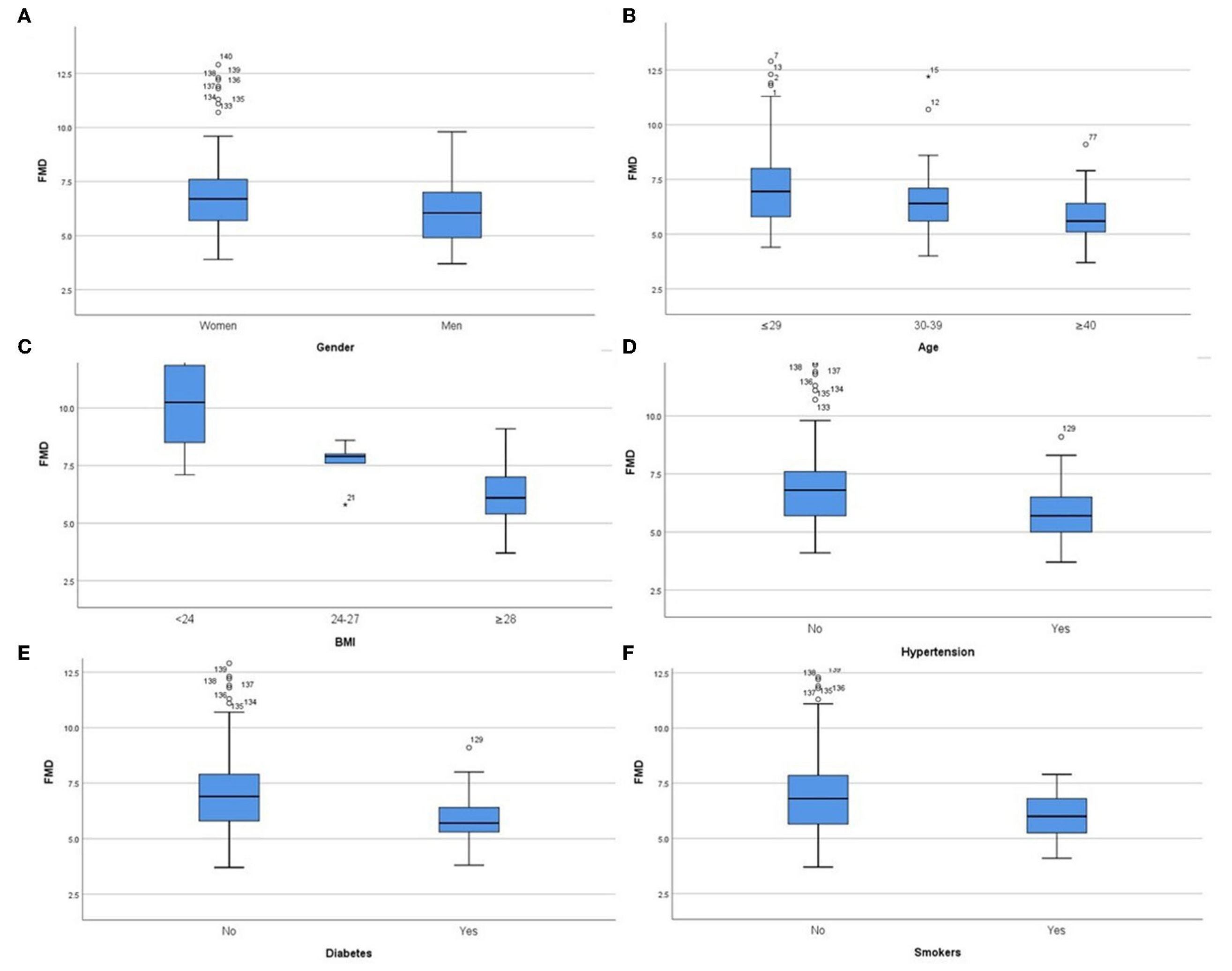

FIGURE 1 | Comparison of FMD values in subgroups of both genders **(A)**, different ages **(B)**, different BMIs **(C)**, hypertension **(D)**, diabetes **(E)** and smoking **(F)**. *P* < 0.05 in all subgroups.

risk factors ($p < 0.01$) after excluding multicollinearity issues, as shown in **Table 3**. Multivariate logistic regression was later performed to screen for significant variables associated with FMD.

Equation Development

After multiple variables combination and modification, we finally selected the following variables for modeling (stepwise, $p < 0.01$), and the expression was:

$$\begin{aligned} \text{FMD} = & -0.096\text{BMI} - 0.069\text{age} - 4.551\text{WHR} \\ & -0.015\text{AST} - 0.242\text{LDL} + 17.938 \end{aligned}$$

R2 = 0.598, and adjusted R2 = 0.582. The regression coefficient and 95% CI of each independent variable are shown in **Table 4**. The independence test of model residuals, i.e., Durbin-Watson test, was 2.184, which indicates good independence between variables. The collinearity analysis show that the VIF values between the independent variables were <2, which indicates that there was no synteny problem among the four independent variables that we introduced. In addition, we draw a residual scatter plot with the standardized predicted value on the X-axis and the standardized residual on the Y-axis (**Figure 3**). The scatter points were randomly distributed, and the slope was almost zero. We believe that there was no possibility of autocorrelation. The scatter plot of the standardized predicted value and dependent FMD shows a linear trend (**Figure 4**).

Verification of Equations

To verify the effectiveness of our model, we compared the actual FMD values to predicted FMD values in the verification group. ICC of them was 0.767 (95% CI: 0.704–0.816; $p < 0.001$). The two-related-sample test (Wilcoxon) shows that there was no statistically significant difference between the actual FMD and the predicted FMD ($P > 0.05$). Next, we drew a Bland–Altman plot (**Figure 5**), which shows that the average value of

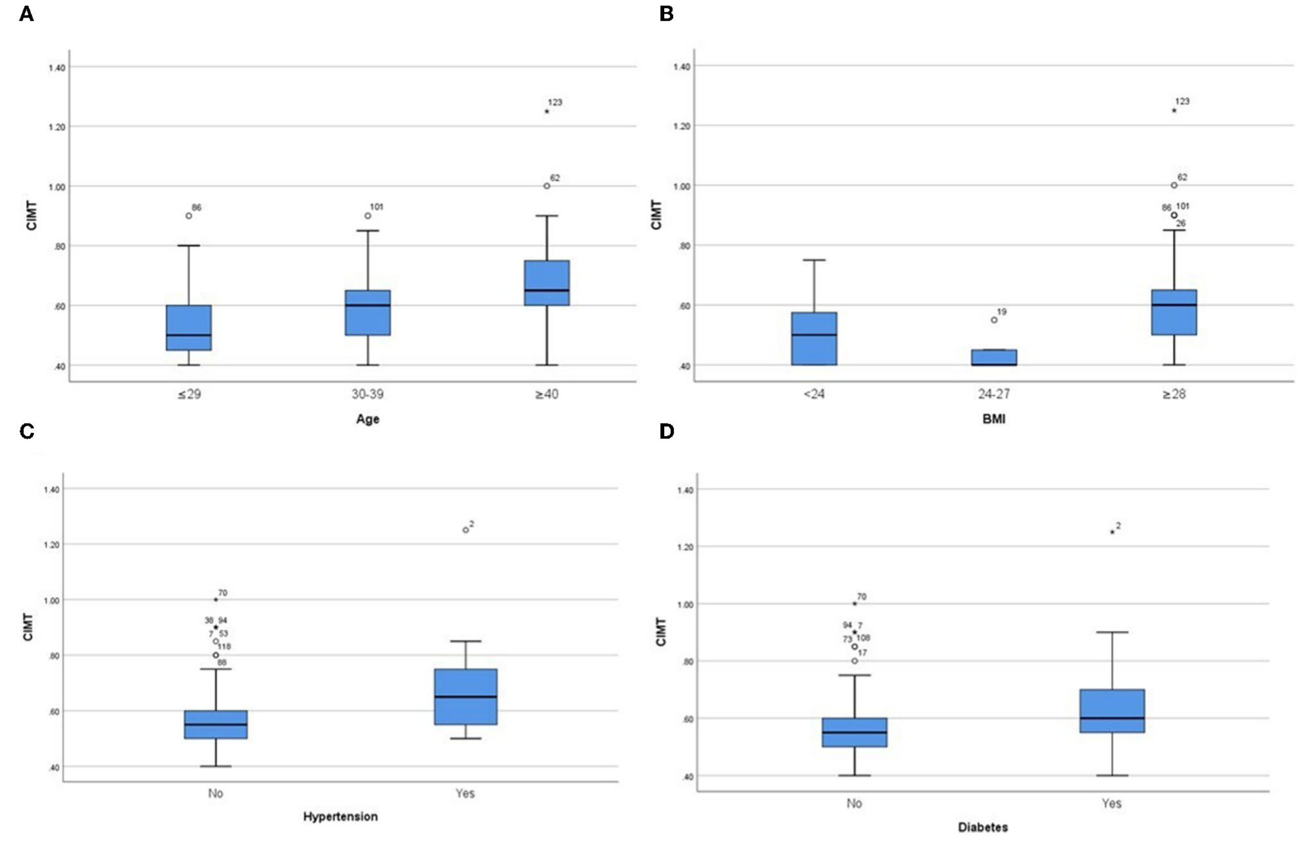

FIGURE 2 | Comparison of CIMT values in subgroups of different ages **(A)**, different BMIs **(B)**, hypertension **(C)** and diabetes **(D)**. $P < 0.05$ in all subgroups.

the differences (middle horizontal solid line) was close to zero (middle horizontal dotted line). Most of the differences between actual FMD and predicted FMD were within the 95% limits of agreement, and only 3% (13/420) of the points lied outside it. We believed that the actual FMD and predicted FMD had high consistency.

To further evaluate the ability of our prediction model to assess CV risk, we divided the validation cohort into groups according to the Framingham Heart Study CV risk stratification updated in 2008 (10-year CV event risk: 0–6%, 6–20% and > 20%) (10). Our study population had no risk >20%, so it was divided into two groups. The AUC of FMD to identify different CV risk stratification was 0.780 (95% CI: 0.708–0.852, $p < 0.001$), with a sensitivity and specificity of 73.8 and 72.1%, respectively (**Figure 6**).

DISCUSSION

The main purpose of this article was to find the influencing factors of vascular endothelial function and establish a simple predictive model of FMD. Endothelial damage is often used as an early marker of various diseases, such as obesity, hypertension, diabetes, and AS. Many studies have shown that FMD can provide important prognostic information beyond traditional CV risk factors (14), and low FMD strongly predicts CV events (15). Therefore, early evaluation of endothelial function is of great significance in diagnosing or monitoring disease progression.

We divided the target population into a derivation group and a verification group through simple random sampling. The ratio of the two was 1:2, which ensured the reliability of the prediction model and reduced the phenomenon of overfitting. The balance test was first performed between them to ensure a random distribution of the indicators. **Table 1** shows that their *p* values were both >0.05, which indicates that there was no significant difference in parameters between them.

We first analyzed the relationship between gender and FMD and found that men had lower FMD than women. Study revealed atherosclerotic CVD prevalence in men was greater than in women until menopause, and some studies showed earlier decrements in endothelial function in men compared to women (16, 17). But sex differences in endothelial function was controversial and others showed similar age-related declines between the sexes (18). After menopause, women may have a higher prevalence of CVD compared to age-matched men (19). This may be due to the lack of protective effects of estrogen. There were few postmenopausal women in our participants (total

TABLE 3 | The correlation and univariate analysis of FMD and 16 variables.

Characteristics	r	*P*-value	R2	*P*-value
BMI	−0.602	0.00	0.362	0.00
WHR	−0.592	0.00	0.350	0.00
γ-GT	−0.462	0.00	0.213	0.00
CP	−0.406	0.00	0.165	0.00
MAP	−0.405	0.00	0.164	0.00
CIMT	−0.374	0.00	0.140	0.00
AST	−0.350	0.00	0.123	0.00
SUA	−0.347	0.00	0.121	0.00
ALT	−0.346	0.00	0.120	0.00
Age	−0.325	0.00	0.106	0.00
HR	−0.318	0.00	0.101	0.00
Insulin	−0.317	0.00	0.101	0.00
LDL	−0.302	0.00	0.092	0.00
FBG	−0.243	0.00	0.059	0.00
smoking	–	–	0.046	0.00
Gender	–	–	0.045	0.01

BMI, body mass index; WHR, waist-to-hip ratio; γ-GT, γ-glutamyl transpeptidase; CP, C-peptide; MAP, mean arterial pressure; CIMT, carotid intima media thickness; AST, aspartate aminotransferase; SUA, serum uric acid; ALT, alanine aminotransferase; HR, heart rate; LDL, low-density lipoprotein; FBG, fasting blood glucose.

TABLE 4 | The regression coefficient and 95% CI of the equation.

Variables	Coefficients	95% CI	*P*-value
BMI	−0.096	(−0.124, −0.068)	0.000
Age	−0.069	(−0.095, −0.043)	0.000
WHR	−4.551	(−7.249, −1.853)	0.000
AST	−0.015	(−0.027, −0.003)	0.001
LDL	−0.242	(−0.463, −0.020)	0.003
Constant	17.938	(15.765, 20.111)	0.000

95% CI, 95% confidence intervals; BMI, body mass index; WHR, waist-to-hip ratio; AST, aspartate aminotransferase; LDL, low-density lipoprotein.

population: 6/420), the results showed that there was no statistical difference in FMD between men and women ($p > 0.05$), but the representativeness was insufficient, and the sample size will be expanded in the future, hoping to conduct in-depth research. The prevalence of CVD increases with age in both men and women. CVD in aging is partly a consequence of the vascular endothelial cell senescence and associated vascular dysfunction (20). Vascular oxidative stress and low-grade inflammation increase with age and is the key mechanism of endothelial diastolic dysfunction (21). Simultaneously, the reduction of estradiol associated with aging (postmenopausal females) (22) and epigenetic modifications (23) may also cause endothelial dilation disorders. This represents a major link between aging and cardiovascular risk.

Many studies have demonstrated impaired endothelial function in obesity, so we compered the FMD values in different BMIs. We found that the group with higher BMI had lower FMD and higher CIMT. This suggested the dual damage of vascular endothelial function and structure related to obesity. Prior study of the impact of obesity revealed FMD decreased in the moderately obese compared with the non-obese (24). This was consistent with our results. An increased CIMT had also been reported in obese patients and weight loss was associated with a reduction in CIMT, consistent with a lowering in risk of cardiovascular events (25, 26). And also, we found that people with diabetes, hypertension and smoking showed lower FMD, all of which suggested an association between FMD and cardiovascular risk factors (12, 27, 28).

Then, we performed bivariate correlation analysis and univariate regression analysis to screen out potential risk factors ($p < 0.01$) to the multivariate logistic regression. After multiple variables combination and modification, we developed a prediction model of FMD, which consisted of BMI, age, WHR, AST and LDL. BMI is a commonly used index to measure the degree of obesity, and BMI≥24 is considered overweight in the Asian population. As we said before, overweight and obesity are factors closely related to vascular endothelial damage (29). Obesity-induced long-term hypoxia, chronic inflammation, oxidative stress and mitochondrial dysfunction are all involved in the development of endothelial dysfunction (30–34). Epigenetics (35) and circulating particles (36, 37) have also been popular mechanisms in recent years. However, obesity-related endothelial damage involves the joint participation of multiple mechanisms, which awaits more in-depth research.

WHR is an important indicator to determine central obesity, and the latter is closely related to an increased risk of CV diseases, even among people with normal BMI (38). Pear-shaped females with normal weight but more fat in the hips and thighs have a lower risk of heart disease and stroke. Fat accumulated in the buttocks and thighs is subcutaneous fat, which has a protective effect. However, the fat of central obesity accumulates in the abdomen, which is visceral fat, and easily releases fatty acids into the blood to cause pathological conditions such as high cholesterol and insulin resistance. This pathological process easily induces early endothelial damage (39, 40).

AST is generally considered a marker of myocardium and liver damage. Perticone et al. reported that AST was closely related to the endothelial function, as evaluated by strain-gauge plethysmography, in both univariate linear analysis and a stepwise multivariate regression model (41). This is consistent with our study. Initial endothelial injury is characterized by endothelial glycocalyx injury, which mediates the release of Syndecan-1 from the endothelium and causes an increase in circulating concentration (42). Researchers found that the concentration of Syndecan-1 was significantly related to AST, and there was an obvious positive correlation between them (43). However, the specific mechanism between AST and vascular endothelial function cannot be fully explained at present, and chronic systemic effects and interorgan communication may promote development.

An increase in pro-atherogenic LDL and its oxidative modifications (ox-LDL) is well known to be a crucial factor in endothelial damage, a key early step and a predictor of the development of AS (44). When the body is continuously

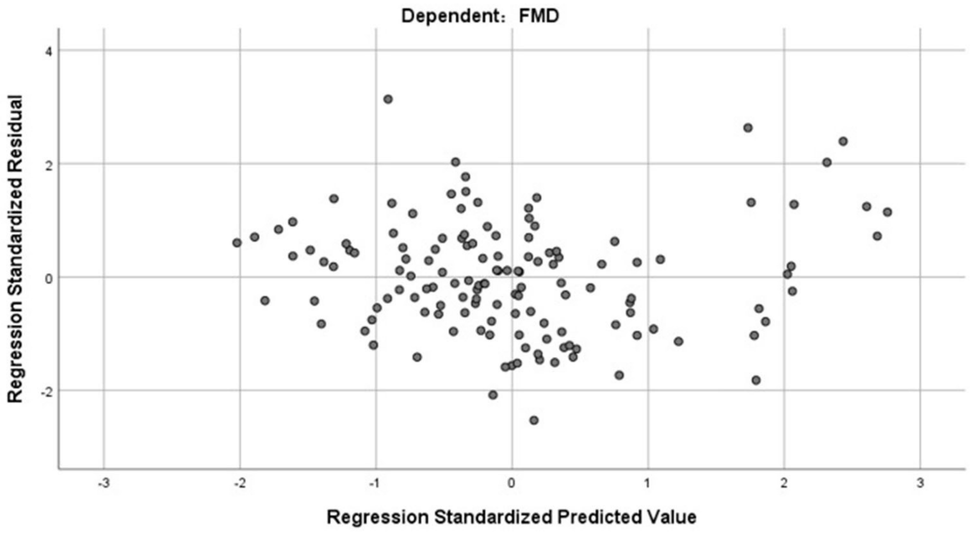

FIGURE 3 | The residual scatter plot of standardized predicted value and standardized residual.

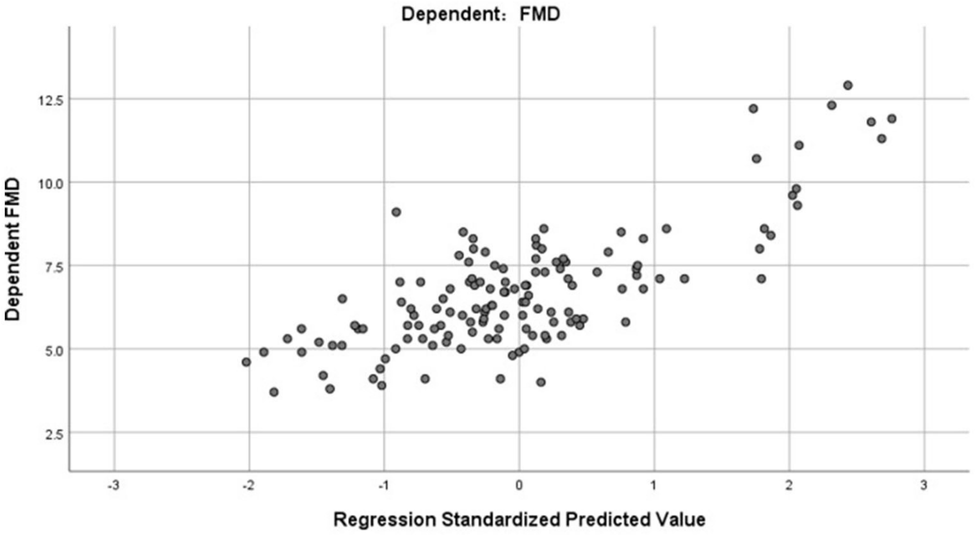

FIGURE 4 | The scatter plot of standardized predicted value and dependent FMD.

exposed to high levels of LDL, inflammatory pathways in vascular endothelial cells are activated to increase local and systemic inflammation, endothelial cell dysfunction and apoptosis, and smooth muscle cell proliferation, resulting in foam cell formation and genesis of AS plaque (45, 46). Therefore, dyslipidemia-induced hyperlipidemic stress is widely recognized as a powerful pathophysiological driver of AS.

However, analysis of these four risk factors also implies that we can improve the function of endotheliocytes through early intervention such as weight loss, a healthy diet and exercise. In some obese people with low FMD, physical exercise or bariatric surgery can increase FMD while losing weight, which suggests the recovery of endothelial injury (14, 47, 48). Aging of endotheliocyte is also not static. Researchers have found that aerobic exercise can significantly prevent endothelial cell aging and change the state of inflammation in the body, especially in elderly individuals (49, 50). The aging rate of endothelial cells after exercise is much lower than that of sedentary peers (51). Mitochondrial-targeted antioxidant supplementation may also play a role in improving age-related vascular dysfunction (52).

Impaired FMD has been associated with conditions predisposing to AS and CVD and represents an early step in the development of subclinical target organ injury and late clinical events (53). Therefore, we intended to evaluate our

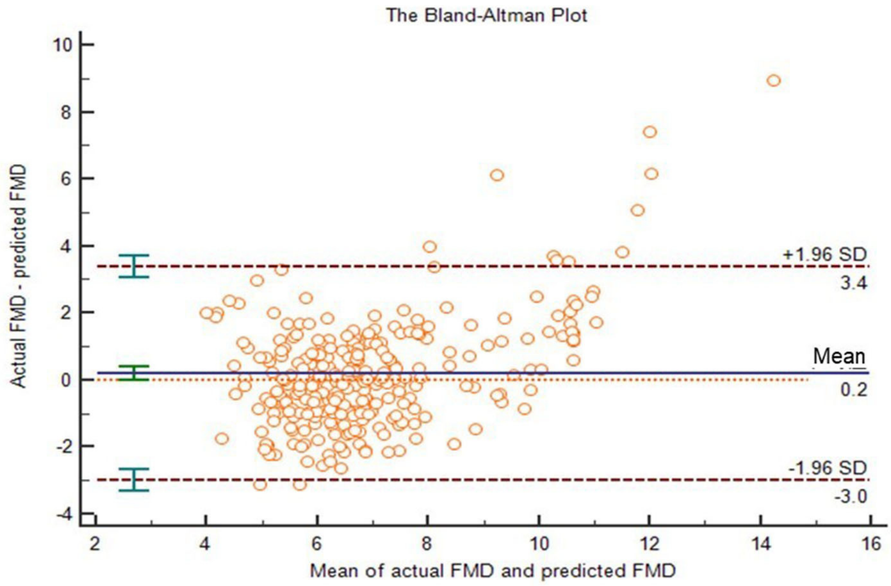

FIGURE 5 | The Bland-Altman plot of actual FMD and predicted FMD. The upper and lower horizontal dotted lines in the picture represented the 95% limits of agreement. The horizontal solid line in the middle represented the average value of the difference. The middle horizontal dotted line indicated the position where the average value of the difference was zero.

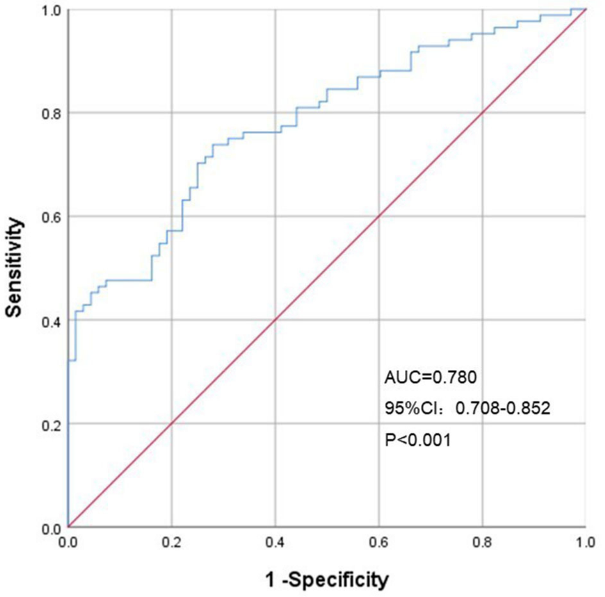

FIGURE 6 | Receiver operating characteristic curves of predicted FMD for Framingham Heart Study CV risk stratification. AUC, area under the curve; CI, confidence interval.

prediction model in identifying CVD risk stratification. The result showed that FMD model can well identify group with higher CVD risk (AUC = 0.780, p<0.001). Several studies have demonstrated the prognostic value of FMD for CVD events (54, 55). However, some scholars believe that the reproducibility of FMD is low and currently not recommend for the assessment of CV risk. That partly because poor standardization between laboratories and lack of guideline adherence. At present, evidence on these issues pertaining to FMD is incomplete. If FMD can be standardized, it may be an important supplement to CV risk stratification.

The 1:2 grouping method improved the adaptability of our equation. It was easy to operate and very suitable for primary hospitals. On one hand, chronic diseases such as hypertension, diabetes, and obesity occupy the majority of community diseases. Doctors in the community are the “gatekeepers” of the health care system, so monitoring and long-term follow-up of such diseases are very important. On the other hand, basic hospitals are not equipped with sufficient hardware facilities, especially expensive and high-tech machines such as FMD equipment. Thus, a simple and reliable evaluation model as an auxiliary method is of great significance.

Our study had several limitations. First, the sample for model construction and verification was relatively small and data was limited to Chinese individuals. In the future, a prediction model will require a larger sample for verification and we hope to extrapolate the model to other ethnic groups. Second, this was a single-center study. Although the ratio of our training group to the validation group was 1:2 to maximize the generalizability of our model, establishing a standardized and accurate model requires the joint participation of multi-center research. Third, the accuracy of our prediction equation was quite modest. It may be suitable for epidemiological purpose or for primary hospitals. Furthermore, there were differences in the ratio of sex and BMI, and the percentage of males and the non-obese was relatively small in our studied population. In response to these problems, our follow-up research must expand the sample size and maintain the internal balance of each variable.

CONCLUSION

Short-term changes or longer-term improvements of vascular endothelial function in interventional trials suggest protective or damaging effects. Therefore, using FMD as a surrogate endpoint to observe changes in endothelial function is timely and simple. We explored the influencing factors of FMD and developed a simple prediction equation. This model will greatly simplify clinical work, but further validation in external populations remains necessary.

DATA AVAILABILITY STATEMENT

The data analyzed in this study is subject to the following licenses/restrictions: Requests to access these datasets should be directed to 1627486196@qq.com.

ETHICS STATEMENT

The studies involving human participants were reviewed and approved by Chinese Clinical Trial Registry ChiCTR2100041860. The patients/participants provided their written informed consent to participate in this study.

AUTHOR CONTRIBUTIONS

XL drafted the manuscript. HL performed the statistical analysis. YZ drafted the figure and legend. YG and LS wrote sections of the manuscript. WB and HY designed the outline of the topic and helped on revising the manuscript. All authors contributed to the article and approved the submitted version.

FUNDING

This project was funded by National Key R&D Program (2021YFC2009100), Shanghai Science and Technology Commission (21Y11910900), Shanghai Sixth People's Hospital Surface Cultivation Project (ynms202110), and Shanghai Pujiang Program (2019PJD036).

ACKNOWLEDGMENTS

The authors would like to thank study participants for their contribution. Authors and participants consent for data to be shared.

SUPPLEMENTARY MATERIAL

The Supplementary Material for this article can be found online at: https://www.frontiersin.org/articles/10.3389/fcvm.2022.766565/full#supplementary-material

Supplementary Figure 1 | The scatter plot of the predicted FMD value and the actual FMD value.

Supplementary Figure 2 | The scatter plot of age and FMD.

Supplementary Figure 3 | FMD in 3 different age groups and different genders.

Supplementary Figure 4 | FMD in 4 different age groups and different genders.

Supplementary Figure 5 | A figure (example captured in one patient of the study sample) of a FMD acquisition.

REFERENCES

1. Gallino A, Aboyans V, Diehm F C, Cosentino, Stricker H, Falk E, et al. Non-coronary atherosclerosis. *Eur Heart J*. (2014) 35:1112–19. doi: 10.1093/eurheartj/ehu071
2. Kruk ME, Gage AD, Joseph NT, Danaei G, García-Saisó S, Salomon JA. Mortality due to low-quality health systems in the universal health coverage era: a systematic analysis of amenable deaths in 137 countries [published correction appears in Lancet. 2018 Sep 20]. *Lancet*. (2018) 392:2203–12. doi: 10.1016/S0140-6736(18)31668-4
3. Balta S. Endothelial Dysfunction and Inflammatory Markers of Vascular Disease. *Curr Vasc Pharmacol*. (2021) 19:243–9. doi: 10.2174/1570161118666200421142542
4. Higashi Y. Assessment of endothelial function. History, methodological aspects, and clinical perspectives. *Int Heart J*. (2015) 56:125–34. doi: 10.1536/ihj.14-385
5. Polak JF, O'Leary DH. Carotid Intima-Media Thickness as Surrogate for and Predictor of CVD. *Glob Heart*. (2016) 11:295–312. doi: 10.1016/j.gheart.2016.08.006
6. Kishimoto S, Matsumoto T, Maruhashi T, Iwamoto Y, Kajikawa M, Oda N, et al. Reactive hyperemia-peripheral arterial tonometry is useful for assessment of not only endothelial function but also stenosis of the digital artery. *Int J Cardiol*. (2018) 260:178–183. doi: 10.1016/j.ijcard.2017.10.069
7. Rodriguez-Miguelez P, Seigler N, Harris RA. Ultrasound assessment of endothelial function: a technical guideline of the flow-mediated dilation test. *J Vis Exp*. (2016) 110:54011. doi: 10.3791/54011
8. Williams B, Mancia G, Spiering W, Agabiti Rosei E, Azizi M, Burnier M, et al. 2018 ESC/ESH Guidelines for the management of arterial hypertension [published correction appears in Eur Heart J. 2019 Feb 1;40(5):475]. *Eur Heart J*. (2018) 39:3021–104. doi: 10.1093/eurheartj/ehy339
9. American Diabetes Association. 2. Classification and Diagnosis of Diabetes: Standards of Medical Care in Diabetes-2019. *Diabetes Care*. (2019) 42:S13–S28. doi: 10.2337/dc19-S002
10. D'Agostino RB Sr, Vasan RS, Pencina MJ, Wolf PA, Cobain M, Massaro JM, et al. General cardiovascular risk profile for use in primary care: the Framingham Heart Study. *Circulation*. (2008) 117:743–53. doi: 10.1161/CIRCULATIONAHA.107.699579
11. Piepoli MF, Hoes AW, Agewall S, Albus C, Brotons C, Catapano AL, et al. 2016 European Guidelines on cardiovascular disease prevention in clinical practice: The Sixth Joint Task Force of the European Society of Cardiology and Other Societies on Cardiovascular Disease Prevention in Clinical Practice (constituted by representatives of 10 societies and by invited experts) Developed with the special contribution of the European Association for Cardiovascular Prevention & Rehabilitation (EACPR). *Eur Heart J*. (2016) 37:2315–81. doi: 10.1093/eurheartj/ehw106
12. Andrus B, Lacaille D. 2013 ACC/AHA guideline on the assessment of cardiovascular risk. *J Am Coll Cardiol*. (2014) 63:2886. doi: 10.1016/j.jacc.2014.02.606

13. Hhijssen DHJ, Bruno RM, van Mil ACCM, Holder SM, Faita F, Greyling A, et al. Expert consensus and evidence-based recommendations for the assessment of flow-mediated dilation in humans. *Eur Heart J.* (2019) 40:2534–47. doi: 10.1093/eurheartj/ehz350
14. Areas GPT, Mazzuco A, Caruso FR, Jaenisch RB, Cabiddu R. Phillips SA, et al. Flow-mediated dilation and heart failure: a review with implications to physical rehabilitation. *Heart Fail Rev.* (2019) 24:69–80. doi: 10.1007/s10741-018-9719-7
15. Maruhashi T, Soga J, Fujimura N, Idei N, Mikami S, Iwamoto Y, et al. Endothelial dysfunction, increased arterial stiffness, and cardiovascular risk prediction in patients with coronary artery disease: FMD-J (Flow-Mediated Dilation Japan) Study A. *J Am Heart Assoc.* (2018) 7:e008588. doi: 10.1161/JAHA.118.008588
16. Brar V, Gill S, Cardillo C, Tesauro M, Panza JA, Campia U. Sex-specific effects of cardiovascular risk factors on endothelium-dependent dilation and endothelin activity in middle-aged women and men. *PLoS ONE.* (2015) 10:e0121810. doi: 10.1371/journal.pone.0121810
17. Writing Group Members, Mozaffarian D, Benjamin EJ, Go AS, Arnett DK, Blaha MJ, et al. Heart Disease and Stroke Statistics-2016 Update: A Report From the American Heart Association [published correction appears in Circulation. 2016 Apr 12;133(15):e599]. *Circulation.* (2016) 133:e38-e360. doi: 10.1161/CIR.0000000000000350
18. Stanhewicz AE, Wenner MM. Stachenfeld NS. Sex differences in endothelial function important to vascular health and overall cardiovascular disease risk across the lifespan. *Am J Physiol Heart Circ Physiol.* (2018) 315:H1569–88. doi: 10.1152/ajpheart.00396.2018
19. Shenouda N, Priest SE, Rizzuto VI, MacDonald MJ. Brachial artery endothelial function is stable across a menstrual and oral contraceptive pill cycle but lower in premenopausal women than in age-matched men. *Am J Physiol Heart Circ Physiol.* (2018) 315:H366–74. doi: 10.1152/ajpheart.00102.2018
20. Jia G, Aroor AR, Jia C, Sowers JR. Endothelial cell senescence in aging-related vascular dysfunction. *Biochim Biophys Acta Mol Basis Dis.* (2019) 1865:1802–9. doi: 10.1016/j.bbadis.2018.08.008
21. Seals DR, Jablonski KL. Donato AJ. Aging and vascular endothelial function in humans. *Clin Sci (Lond).* (2011) 120:357–75. doi: 10.1042/CS20100476
22. Moreau KL. Intersection between gonadal function and vascular aging in women. *J Appl Physiol (1985).* (2018) 125:1881–7. doi: 10.1152/japplphysiol.00117.2018
23. Jin J, Liu Y, Huang L, Tan H. Advances in epigenetic regulation of vascular aging. *Rev Cardiovasc Med.* (2019) 20:19–25. doi: 10.31083/j.rcm.2019.01.3189
24. Suboc TM, Dharmashankar K, Wang J, Ying R, Couillard A, Tanner MJ, et al. Moderate obesity and endothelial dysfunction in humans: influence of gender and systemic inflammation. *Physiol Rep.* (2013) 1:e00058. doi: 10.1002/phy2.58
25. Sönmez HE, Canpolat N, Agbaş A, et al. The Relationship between the Waist Circumference and Increased Carotid Intima Thickness in Obese Children. *Child Obes.* (2019) 15:468–75. doi: 10.1089/chi.2019.0022
26. Skilton MR, Yeo SQ, Ne JY, Celermajer DS, Caterson ID, Lee CM. Weight loss and carotid intima-media thickness-a meta-analysis. *Obesity (Silver Spring).* (2017) 25:357–62. doi: 10.1002/oby.21732
27. Yang X, Li J, Hu D, Chen J, Li Y, Huang J, et al. Predicting the 10-Year Risks of Atherosclerotic Cardiovascular Disease in Chinese Population: The China-PAR Project (Prediction for ASCVD Risk in China). *Circulation.* (2016) 134:1430–40. doi: 10.1161/CIRCULATIONAHA.116.022367
28. Hippisley-Cox J, Coupland C, Brindle P. Development and validation of QRISK3 risk prediction algorithms to estimate future risk of cardiovascular disease: prospective cohort study. *BMJ.* (2017) 357:j2099. doi: 10.1136/bmj.j2099
29. Atawia RT, Bunch KL, Toque HA, Caldwell RB, Caldwell RW. Mechanisms of obesity-induced metabolic and vascular dysfunctions. *Front Biosci (Landmark Ed).* (2019) 24:890–934. doi: 10.2741/4758
30. Reilly SM. Saltiel AR. Adapting to obesity with adipose tissue inflammation. *Nat Rev Endocrinol.* (2017) 13:633–43. doi: 10.1038/nrendo.2017.90
31. Virdis A, Duranti E, Rossi C. Dell'Agnello U, Santini E, Anselmino M, et al. Tumour necrosis factor-alpha participates on the endothelin-1/nitric oxide imbalance in small arteries from obese patients: role of perivascular adipose tissue. *Eur Heart J.* (2015) 36:784–94. doi: 10.1093/eurheartj/ehu072
32. Lee J, Lee S. Zhang H, Hill MA, Zhang C, Park Y. Interaction of IL-6 and TNF-α contributes to endothelial dysfunction in type 2 diabetic mouse hearts. *PLoS ONE.* (2017) 12:e0187189. doi: 10.1371/journal.pone.0187189
33. Bianconi V, Sahebkar A, Atkin SL, Pirro M. The regulation and importance of monocyte chemoattractant protein-1. *Curr Opin Hematol.* (2018) 25:44–51. doi: 10.1097/MOH.0000000000000389
34. Yuan T, Yang T, Chen H, Fu D, Hu Y, Wang J, et al. New insights into oxidative stress and inflammation during diabetes mellitus-accelerated atherosclerosis. *Redox Biol.* (2019) 20:247–60. doi: 10.1016/j.redox.2018.09.025
35. Valencia-Morales Mdel P, Zaina S. Heyn H, Carmona FJ, Varol N, Sayols S, et al. The DNA methylation drift of the atherosclerotic aorta increases with lesion progression. *BMC Med Genomics.* (2015) 8:7. doi: 10.1186/s12920-015-0085-1
36. Leite AR, Borges-Canha M, Cardoso R, Neves JS, Castro-Ferreira R, Leite-Moreira A. Novel Biomarkers for Evaluation of Endothelial Dysfunction. *Angiology.* (2020) 71:397–410. doi: 10.1177/0003319720903586
37. Dimassi S, Chahed K, Boumiza S, Canault M, Tabka Z, Laurant P. et al. Role of eNOS- and NOX-containing microparticles in endothelial dysfunction in patients with obesity. *Obesity (Silver Spring).* (2016) 24:1305–12. doi: 10.1002/oby.21508
38. Chen GC, Arthur R, Iyengar NM, Kamensky V, Xue X, Wassertheil-Smoller S, et al. Association between regional body fat and cardiovascular disease risk among postmenopausal women with normal body mass index. *Eur Heart J.* (2019) 40:2849–55. doi: 10.1093/eurheartj/ehz391
39. Stefan N, Schick F. Häring HU. Causes, Characteristics, and Consequences of Metabolically Unhealthy Normal Weight in Humans. *Cell Metab.* (2017) 26:292–300. doi: 10.1016/j.cmet.2017.07.008
40. Shi J, Yang Z, Niu Y, Zhang W, Lin N, Li X, et al. Large thigh circumference is associated with lower blood pressure in overweight and obese individuals: a community-based study. *Endocr Connect.* (2020) 9:271–8. doi: 10.1530/EC-19-0539
41. Perticone M, Maio R, Caroleo B, Sciacqua A, Suraci E, Gigliotti S. et al. Serum γ-Glutamyltransferase Concentration Predicts Endothelial Dysfunction in Naïve Hypertensive Patients. *Biomedicines.* (2020) 8:207. doi: 10.3390/biomedicines8070207
42. Rehm M, Bruegger D, Christ F, Conzen P, Thiel M, Jacob M, et al. Shedding of the endothelial glycocalyx in patients undergoing major vascular surgery with global and regional ischemia. *Circulation.* (2007) 116:1896–906. doi: 10.1161/CIRCULATIONAHA.106.684852
43. Oda K, Okada H, Suzuki A, Tomita H, Kobayashi R, Sumi K, et al. Factors Enhancing Serum Syndecan-1 Concentrations: A Large-Scale Comprehensive Medical Examination. *J Clin Med.* (2019) 8:1320. doi: 10.3390/jcm8091320
44. Le Master E, Levitan I. Endothelial stiffening in dyslipidemia. *Aging (Albany NY).* (2019) 11:299–300. doi: 10.18632/aging.101778
45. Helkin A, Stein JJ, Lin S, Siddiqui S, Maier KG, Gahtan V. Dyslipidemia Part 1–Review of Lipid Metabolism and Vascular Cell Physiology. *Vasc Endovascular Surg.* (2016) 50:107–18. doi: 10.1177/1538574416628654
46. Hurtubise J, McLellan K, Durr K, Onasanya O, Nwabuko D. Ndisang JF. The Different Facets of Dyslipidemia and Hypertension in Atherosclerosis. *Curr Atheroscler Rep.* (2016) 18:82. doi: 10.1007/s11883-016-0632-z
47. Elitok A, Emet S, Bayramov F. Karaayvaz E, Türker F, Barbaros U, et al. Effect of bariatric surgery on flow-mediated dilation and carotid intima-media thickness in patients with morbid obesity: 1-year follow-up study. *Anatol J Cardiol.* (2020) 23:218–22. doi: 10.14744/AnatolJCardiol.2019.85249
48. Sanches E, Topal B, Proczko M, Stepaniak PS, Severin R, Philips SA, et al. Endothelial function in obesity and effects of bariatric and metabolic surgery. *Expert Rev Cardiovasc Ther.* (2020) 18:343–53. doi: 10.1080/14779072.2020.1767594
49. Wang Y, Xu D. Effects of aerobic exercise on lipids and lipoproteins. *Lipids Health Dis.* (2017) 16:132. doi: 10.1186/s12944-017-0515-5
50. He N, Ye H. Exercise and hyperlipidemia. *Adv Exp Med Biol.* (2020) 1228:79–90. doi: 10.1007/978-981-15-1792-1_5
51. Rossman MJ, Kaplon RE, Hill SD, McNamara MN, Santos-Parker JR, Pierce GL, et al. Endothelial cell senescence with aging in healthy humans: prevention by habitual exercise and relation to vascular endothelial function. *Am J Physiol Heart Circ Physiol.* (2017) 313:H890–H895. doi: 10.1152/ajpheart.00416.2017

52. Rossman MJ, Santos-Parker JR, Steward CAC, Bispham NZ, Cuevas LM. Rosenberg HL, et al. Chronic Supplementation With a Mitochondrial Antioxidant (MitoQ) Improves Vascular Function in Healthy Older Adults. *Hypertension*. (2018) 71:1056–63. doi: 10.1161/HYPERTENSIONAHA.117.10787
53. Lakshmanan S, Shekar C, Kinninger A, Birudaraju D, Dahal S, Onuegbu A, et al. Association of flow mediated vasodilation and burden of subclinical atherosclerosis by coronary CTA. *Atherosclerosis*. (2020) 302:15–9. doi: 10.1016/j.atherosclerosis.2020.04.009
54. Matsuzawa Y, Kwon TG, Lennon RJ, Lerman LO, Lerman A. Prognostic value of flow-mediated vasodilation in brachial artery and fingertip artery for cardiovascular events: a systematic review and meta-analysis. *J Am Heart Assoc*. (2015) 4:e002270. doi: 10.1161/JAHA.115.002270
55. Xu Y, Arora RC, Hiebert BM, Lerner B, Szwajcer A, McDonald K, et al. Non-invasive endothelial function testing and the risk of adverse outcomes: a systematic review and meta-analysis. *Eur Heart J Cardiovasc Imaging*. (2014) 15:736–46. doi: 10.1093/ehjci/jet256

Conflict of Interest: The authors declare that the research was conducted in the absence of any commercial or financial relationships that could be construed as a potential conflictof interest.

frontiers
in Cardiovascular Medicine

PERSPECTIVE
published: 28 March 2022
doi: 10.3389/fcvm.2022.767450

Vascular Inflammation in Mouse Models of Systemic Lupus Erythematosus

Holly Ryan[1], Laurence Morel[2] and Erika Moore[1,3]**

[1] J. Crayton Pruitt Family Department of Biomedical Engineering, University of Florida, Gainesville, FL, United States,
[2] Department of Pathology, Immunology and Laboratory Medicine, University of Florida, Gainesville, FL, United States,
[3] Department of Materials Science and Engineering, University of Florida, Gainesville, FL, United States

Vascular inflammation mediated by overly activated immune cells is a significant cause of morbidity and mortality in systemic lupus erythematosus (SLE). Several mouse models to study the pathogenesis of SLE are currently in use, many of which have different mechanisms of pathogenesis. The diversity of these models allows interrogation of different aspects of the disease pathogenesis. To better determine the mechanisms by which vascular inflammation occurs in SLE, and to assist future researchers in choosing the most appropriate mouse models to study cardiovascular complications in SLE, we suggest that direct comparisons of vascular inflammation should be conducted among different murine SLE models. We also propose the use of *in vitro* vascular assays to further investigate vascular inflammation processes prevalent among different murine SLE models.

Keywords: vascular inflammation, systemic lupus erythematosus, *in vitro* disease modeling, autoimmune disease, mouse models, cardiovascular diseases

OPEN ACCESS

Edited by:
Yun Fang,
University of Chicago, United States

Reviewed by:
Erin Taylor,
University of Mississippi Medical Center, United States
Chieko Mineo,
University of Texas Southwestern Medical Center, United States

****Correspondence:***
Erika Moore
moore.erika@ufl.edu
Laurence Morel
morel@pathology.ufl.edu

Specialty section:
This article was submitted to Atherosclerosis and Vascular Medicine,
a section of the journal Frontiers in Cardiovascular Medicine

Received: *30 August 2021*
Accepted: *18 February 2022*
Published: *28 March 2022*

Citation:
Ryan H, Morel L and Moore E (2022) Vascular Inflammation in Mouse Models of Systemic Lupus Erythematosus. Front. Cardiovasc. Med. 9:767450. doi: 10.3389/fcvm.2022.767450

INTRODUCTION

Systemic lupus erythematosus (SLE) is an autoimmune disease characterized by production of antibodies that react to self-antigens such as DNA and complement components (1). Vasculitis and progression to cardiovascular diseases (CVD) are prevalent and significant contributors to mortality in SLE (2). Although the pathogenesis of CVD in SLE is not fully understood, it is known that abnormalities in immune cells are heavily implicated. Many immune cells, such as T cells and monocytes, are overactive in SLE, causing chronic inflammation and widespread tissue damage, including damage to the heart and vasculature (3). Significant advances toward understanding SLE pathogenesis have been made in the past 60 years due to the use of mouse models that recapitulate certain features of the human disease. However, few studies have addressed cardiovascular complications. Here, we propose that an in-depth systematic characterization of CVD phenotypes in mouse models of SLE in relationship with immune alterations will improve the understanding of the pathogenesis of CVD in SLE. Additionally, we argue that application of *in vitro* biomaterial models will also contribute to increased understanding of CVD pathogenesis in SLE.

CVD IN HUMAN SLE

One of the most serious complications of SLE is CVD, which is a leading cause of death five years past diagnosis (2, 4). With an incidence ranging from 31 to 70% (5–7), CVD presents in SLE patients with diverse manifestations including pericarditis, myocarditis, valvular disease, atherosclerosis, thrombosis, and arrhythmias. This clinical heterogeneity likely reflects a complex etiology as well as the contribution of multiple risk factors. Widespread use of imaging tools has revealed a high frequency of microvascular impairment and myocarditis in SLE patients (6, 8–11), the majority of which do not lead to clinical presentation (12–14). Perfusion abnormalities have also been detected by single-photon emission computerized tomography imaging in 88% of SLE patients, two thirds of which had negative coronary angiograms (15). These results are in agreement with the reduction of myocardial coronary flow reserve on MRI studies found in 44% of SLE patients with angina and a normal angiogram (15). These findings suggest that coronary microvascular dysfunction, which has emerged as a mechanism of myocardial ischemia, heart failure, and arrhythmias distinct from obstructive atherosclerosis, is a common feature in SLE patients, but that the dysfunction is difficult to assess, and probably underdiagnosed.

In addition to coronary effects, vascular inflammation in SLE has further implications throughout the rest of the body. About 11–36% of SLE patients experience vasculitis, which may affect small, medium, or large vessels, causing damage in the integumentary, neurological, digestive, respiratory, and urinary systems (16). Vasculitis is thought to be mediated by immune complex deposition along vessel walls, as well as by direct destruction of vessel components by anti-endothelial cell autoantibodies (3, 16). The binding of immobilized antibodies and immune complexes by innate immune cells such as monocytes sets off an inflammatory response.

Endothelial function deteriorates with increased activity of type-1 interferons (IFNs), an important family of inflammatory cytokines that are upregulated in SLE (3). Endothelial dysfunction is thought to contribute to the dramatically increased risk of hypertension in SLE patients (17). SLE patients are also at risk of developing atherosclerosis and suffering ischemic events such as ischemic stroke or myocardial infarction (3). Atherosclerosis in SLE may be associated with vasculitis since damage to endothelial cells (ECs) is known to lead to CVD (3). New or worsening atherosclerosis occurs in 10% of SLE patients per year, although the precise mechanism by which it occurs is not fully understood (18).

Further study into the mechanisms driving SLE vasculitis is needed to identify targets for treating this serious co-morbidity. Since SLE is widely studied using mouse models, in this review we describe the cardiovascular manifestations of disease in several of the most common SLE mouse models. Unfortunately, most SLE mouse models do not develop cardiovascular complications comparable to those experienced by SLE patients. For this reason, we also propose future work that leverages biomaterial model systems to assist in identifying processes relevant to human SLE-associated CVD.

CVD IN SLE MOUSE MODELS

Several spontaneous and induced mouse models of SLE have been developed since the 1960s, with overlapping but distinct mechanisms of disease, allowing for the study of isolated disease processes. We refer the reader to recent review articles detailing the pathogeneses of several of these models (19–21), as well as to a review article focusing on the development of myocardial infarction or hypertension in several of these models (22). **Table 1** gives a summary of commonly studied CVD manifestations observed in SLE mouse models.

Although there have been few studies comparing microvascular inflammation qualitatively and quantitatively among different SLE mouse models, there are several metrics summarized in **Table 2** by which SLE-associated CVD can be assessed. Overt atherosclerosis can be observed as plaques that are visible by histology in some mouse models such as apolipoprotein E (ApoE) knockouts. Production of reactive oxygen species and associated enzymes in disease vasculature can also be measured using histology in NZB/NZW F1 mice and in some imiquimod-treated models (27, 34, 37). Some strains including MRL/Fas^{lpr}, BXSB, and (NZW/BXSB) F1, may also develop myocardial infarctions (55). NZB/NZW F1 mice and some induced models develop hypertension, which may be used as another measure of CVD progression (23, 25, 27, 32–36, 44).

Since many SLE mouse models do not display overt atherosclerosis and hypertension in the same manner as humans, histological, and blood pressure studies are often insufficient for assessing CVD progression. In these cases, vascular disease can be measured by functional studies in which isolated arteries are forced to contract, and then are exposed to various vasodilators to observe the extent of vasorelaxation (23–25, 27–30, 34, 35, 37–40). This type of study can be done on any mouse model. Another metric of CVD progression is the proliferation of endothelial progenitor cells (EPCs) and their ability to differentiate into mature ECs. EPCs from bone marrow, spleen, and the peripheral circulation of SLE mice often display decreased proliferation and differentiation compared to wild-type mice, suggesting a role for impaired endothelial turnover in SLE-related CVD (24, 30, 38–40, 50, 53). The various methods commonly employed to measure CVD in SLE mouse models are summarized in **Table 2**.

The following sections describe how these metrics have been used to investigate CVD in mouse models of SLE.

Tissue Lesions Detected by Histology

Atherosclerosis

A very common method to assess the extent of CVD in an animal model is to observe vessel micrographs for the presence of atherosclerotic lesions; however, there are few SLE mouse strains that develop atherosclerosis naturally. For this reason, pro-atherogenic mouse models such as ApoE knockouts are often used to investigate how certain cytokines associated with SLE, such as type I IFNs, may contribute to the development of vascular lesions (26). Increasing type I IFN levels by infecting ApoE$^{-/-}$ mice with IFNα-expressing adenovirus has been shown to increase vascular lesions, while the opposite was seen by

TABLE 1 | Cardiovascular manifestations associated with different SLE mouse models.

Mouse models		Cardiovascular manifestations	References
Induced models	Pristane-induced lupus	Pulmonary vasculitis, hypertension	(19, 20, 23–26)
	Imiquimod-induced lupus	Hypertension, increased left ventricular weight	(27, 28)
NZB/NZW F1		Cardiac inflammation, hypertension	(19, 22, 29–38)
NZM strains		Thrombosis in response to endothelial injury, impaired endothelial cell differentiation	(19, 20, 39, 40)
B6.NZM2410.*Sle1.Sle2.Sle3* triple congenic		Enhanced atherosclerosis susceptibility in LDLr or ApoE KO mice	(41–44)
Fas mutation (*gld*.apoE$^{-/-}$, B6.MRL-Fas^{lpr}, and MRL/Fas^{lpr})		Increased risk of atherosclerosis and myocardial infarction in LDLr or ApoE KO mice	(19, 22, 38, 45–54)
Yaa-carrying strains	BXSB	Increased risk of myocardial infarction	(19, 22)
	(NZW/BXSB) F1	Coronary artery disease from anti-phospholipid syndrome and microthrombi, increased risk of myocardial infarction	(22, 55, 56)
	B6.Nba2.*Yaa*	Increased atherosclerosis susceptibility	(57)

TABLE 2 | Experimental measures of CVD in SLE mouse models.

Metric	Results when CVD is present	Mouse model	References
Tissue lesions (histology)	Visible atherosclerotic lesions	Mice susceptible to atherosclerosis such as ApoE or LDLr knockouts or hybrids	(26, 39, 41, 43, 44, 46, 48, 50, 52, 57)
	Myocardial infarction	(NZW/BXSB) F1, MRL/Fas^{lpr}, BXSB	(40, 50)
Hypertension	Increased systolic blood pressure and/or mean arterial pressure	Induced models (pristane or imiquimod); NZB/NZW F1	(23, 25, 27, 31–36, 44)
Endothelial dysfunction	Impaired endothelium-dependent vasorelaxation	Can be used in any model but frequently used in mice that do not develop atherosclerosis, such as NZB/NZW F1; also frequently used in induced models	(23–25, 27–30, 34–40, 48, 53, 54)
	Reduced EPC proliferation/differentiation	Can be used in most models, including pristane or imiquimod-treated mice, NZB/NZW F1, NZM2328, *gld*.apoE$^{-/-}$, and MRL/Fas^{lpr}	(24, 28, 30, 38–40, 50, 53)

knocking out of the IFNα receptor (IFNAR) (39). Knockout of ApoE or low density liproprotein receptor (LDLr) has also been applied to various SLE -specific mouse models to demonstrate the role of SLE pathways in worsening plaque formation in mice that are already prone to atherosclerosis (41, 43, 44, 50, 57). For example, ApoE$^{-/-}$ mice manifest histologically observable vascular lesions upon treatment with pristane, an inflammation-inducing hydrocarbon that promotes type I IFN production (26). The use of type I IFN-increasing agents in mice that are susceptible to atherosclerosis provides evidence that the increase in type I IFNs seen in SLE patients is a major driver behind CVD in these patients.

Another mouse model that has been used in combination with atherosclerosis-prone models is the B6.NZM2410.*Sle1.Sle2.Sle3*, or triple congenic, mouse. This mouse has three NZM2410-derived-SLE susceptibility loci on a C57BL/6 genetic background. Furthermore, this phenotype maps, at least in part, to the overexpression of the lupus susceptibility gene Pbx1-d, which impairs regulatory T cells (43). Triple congenic mice do not develop atherosclerosis spontaneously, but they have been used as bone marrow donors in chimera studies, with atherosclerosis-prone strains as recipients. Chimeras of LDLr$^{-/-}$ (44) or LDLr$^{-/-}$Rag$^{-/-}$ mice (41) with bone marrow from triple congenic mice have shown increased atherosclerosis compared to chimeras with bone marrow from control C57BL/6 mice (42). Mutations in Fas or the Fas ligand (FasL), which disrupt apoptosis, have also been introduced into atherogenic mouse models to simulate the CVD effects of SLE. For example, the FasL mutation in *gld.apoE*$^{-/-}$ mice causes glomerular lesions such as those seen in SLE as well as the vascular lesions typical for ApoE$^{-/-}$ mice (50).

Myocardial Infarction

Although thrombosis and myocardial infarction occur frequently in human SLE patients, there are relatively few SLE mouse strains that develop these complications. Some of the most commonly used mouse strains to study thrombosis and myocardial infarction in SLE are mice with mutations in Fas or FasL, or with overexpression of Toll-like receptor 7 (TLR7).

Fas is a membrane-bound receptor that triggers apoptosis. The Fas/FasL pathway is especially important for inducing apoptosis in activated lymphocytes after infection has been cleared (58). Mutations in Fas or FasL are present in *lpr* and *gld* mice, respectively, and lead to the development of a lupus-like autoimmune pathology. Mice with these mutations often have more obvious CVD than other SLE strains. As they age, MRL/Fas^{lpr} mice develop necrotizing polyarteritis with rare thrombotic occlusion (51, 52). MRL/Fas^{lpr} males tend to develop age-dependent myocardial infarction (22). A recent study examining multiple organs has also shown vascular and perivascular leukocyte infiltrations increased as the mice aged and developed autoimmune pathology (48). These observations suggest that the vascular inflammation and increased risk of myocardial infarction in SLE may be due to active lymphocytes that have failed to receive a normal cell death signal.

The BXSB mouse has a translocation of TLR7 from the X chromosome to the Y chromosome, termed *Yaa*, causing males to develop SLE-like symptoms due to overactivation of the type I IFN pathway, a downstream effect of TLR7 signaling (19). BXSB mice may have increased risk of myocardial infarction, but the risk is lower than for other strains such as (NZW/BXSB) F1 males or MRL/Fas^{lpr} mice (22, 55). (NZW/BXSB) F1 male mice, which are the offspring of the cross between NZW females and BXSB males, have a similar course of disease to that of BXSB males, but with more clearly prevalent coronary vascular disease and myocardial infarction (22). Myocardial infarction in these mice may be due to small coronary artery disease as well as vascular lesions caused by anti-phospholipid autoantibodies (55).

Hypertension

The exact pathogenesis of hypertension in human SLE is not well-understood, but is thought to be related to some combination of endothelial dysfunction, kidney damage, abnormalities in the renin-angiotensin-aldosterone system, dysautonomia, and increased endothelin-1 (17). The degree of hypertension in mice may be measured by tail cuff for systolic blood pressure (33, 34) or by catheterization for mean arterial pressure (35, 36). The main mouse models generally used to study SLE hypertension are pristane-induced models and the NZB/NZW F1 strain. C57BL/6 and BALB/c mice develop increased arterial pressure when treated with pristane, suggesting that that an increase in type I IFN contributes to hypertension (23, 25).

NZB/NZW F1 mice develop spontaneous hypertension that may be avoided by therapeutic intervention to curtail SLE development (32, 33), although one study showed that treating the SLE-like glomerular damage and inflammation seen in this mouse did not decrease blood pressure (33). For this reason, it has been suggested that hypertension and kidney disease in this model are not directly related (33). Hypertension in NZB/NZW F1 mice may be attributable to a variety of influences including increased sensitivity to angiotensin II (31). Inhibition of angiotensin II by the angiotensin-converting enzyme (ACE) inhibitor captopril has been shown to downregulate expression of the type I IFN regulator *Ifr7* (59), so it is possible that the increased angiotensin II sensitivity in NZB/NZW F1 mice causes hypertension mainly *via* increase in type I IFNs.

Endothelial Dysfunction

Vasorelaxation

Another common method of measuring vascular dysfunction is through vasorelaxation studies. These studies are useful because they can be done even if a particular strain of mouse is not prone to developing atherosclerosis or hypertension. In these studies, excised vessels are contracted using a vasoconstrictive agent such as phenylephrine (PE) or U-46619, and then exposed to different vasodilators. Acetylcholine (Ach) causes vasorelaxation in an endothelium-dependent manner by stimulating nitric oxide production, while sodium nitroprusside induces vasorelaxation in an endothelium-independent manner. Vessel response to Ach can be compared to the response to sodium nitroprusside to determine whether impaired vasorelaxation is due to endothelial dysfunction.

Vasorelaxation in response to Ach is impaired in many models of SLE that have type I IFN as a major driver of disease, including ApoE$^{-/-}$ mice exposed to IFNα-expressing adenovirus (39), pristane or imiquimod-treated mice (23–25, 27, 28), NZB/NZW F1 mice (35, 37, 38), and NZM2328 mice (39). Generally, these mice do not display impaired vasorelaxation in response to sodium nitroprusside, which induces vasorelaxation by acting directly on the vascular smooth muscle. These findings demonstrate that models with high levels of type I IFN experience impaired vasorelaxation due to endothelial dysfunction, which is also a common complication in human SLE.

Findings about vasorelaxation in mice with Fas or FasL mutations are variable. Compared to MRL/MpJ, a common control for MRL/Fas^{lpr} mice, MRL/Fas^{lpr} mice have decreased vasorelaxation in response to Ach (53, 54); however, B6.MRL-Fas^{lpr} mice have increased vasorelaxation in response to Ach and to sodium nitroprusside compared to C57BL/6 controls, even in the setting of high proteinuria, which indicates advanced disease (38). B6.MRL-Fas^{lpr} mice experience less severe disease than MRL/Fas^{lpr} mice (47), so the difference in vasorelaxation ability suggests that the *lpr* mutation alone is not sufficient to cause endothelial dysfunction. In addition, B6.MRL-Fas^{lpr} mice do not overproduce type I IFN-regulated genes (38), which seem to be responsible for endothelial dysfunction in most of the other models. For this reason, although B6.MRL-Fas^{lpr} mice are useful for modeling SLE in other respects, they may not be appropriate to use in studies of SLE-related endothelial dysfunction.

EPC Proliferation/Differentiation

Another means of measuring endothelial dysfunction is to investigate the proliferation and differentiation potential of EPCs. In healthy vasculature, EPCs replace old ECs to maintain the integrity and functionality of the endothelium (60). If EPCs are reduced, or if they are unable to differentiate into mature ECs, the turnover of the endothelium is impaired, resulting in vascular disease. Studies on the proliferation and differentiation potential of EPCs have been done on a wide variety of SLE mouse models. EPC differentiation was reduced in pristane- or imiquimod-treated mice (24, 28), in NZB/NZW F1 mice (38), and in ApoE$^{-/-}$ mice exposed to IFNα-expressing adenovirus (39). In aged NZM2328 mice, IFNAR deletion increased the numbers of both bone marrow and circulating EPCs; and in both young and aged female mice, EPCs had increased differentiation ability in the absence of IFNAR (39). These observations corroborate similar findings from vasorelaxation studies, demonstrating that the type I IFN pathway is involved in SLE-related endothelial dysfunction. On the other hand, B6.MRL-Fas^{lpr} mice do not display reduced numbers of EPCs in the bone marrow, or

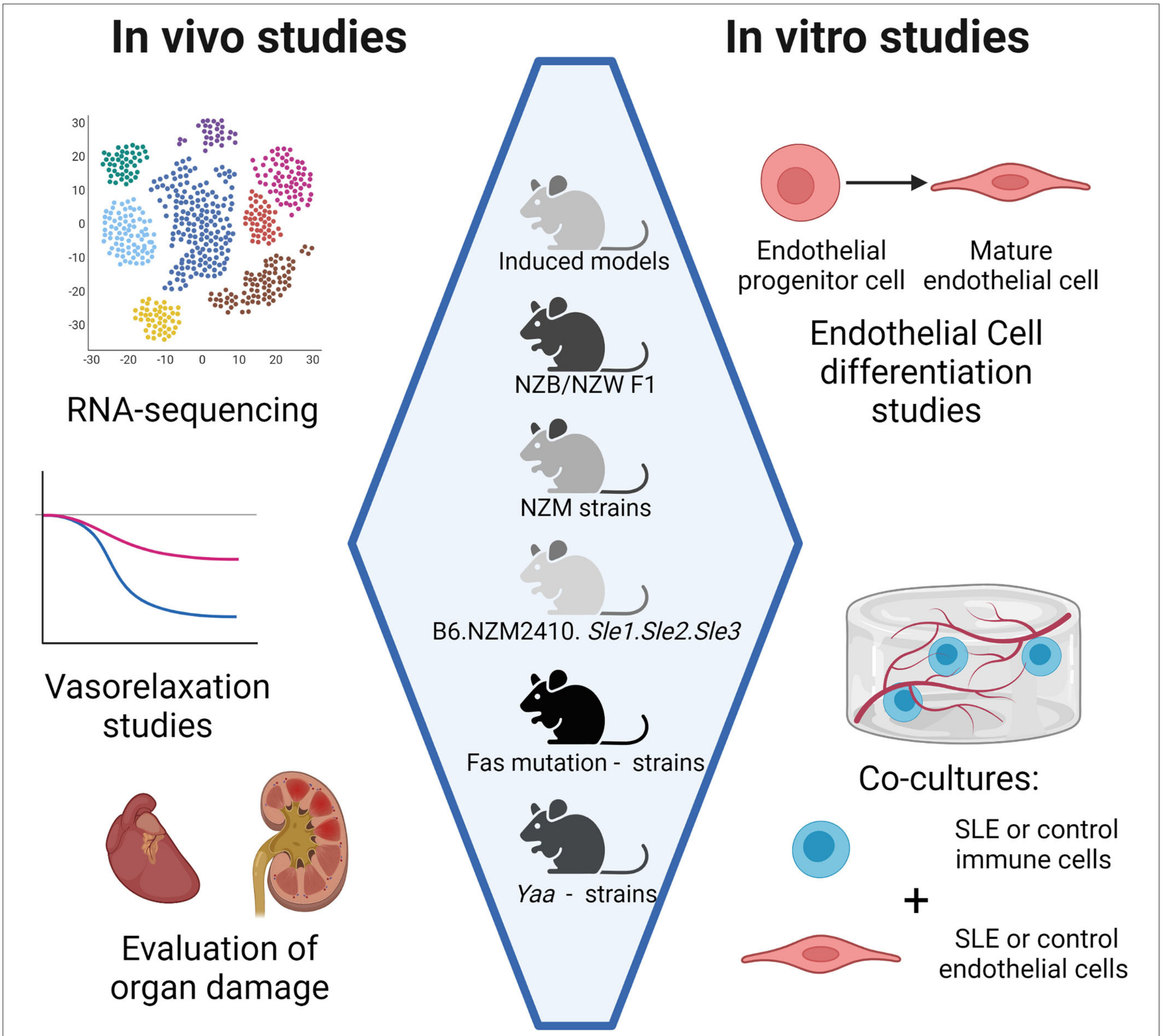

FIGURE 1 | Comparison of CVD development in different SLE mouse models. Head-to-head comparisons among mouse models may be done *in vivo*, *ex vivo*, and *in vitro*. *In vivo* studies include RNA sequencing for expression of inflammatory genes and histology on organs such as the heart for characterization of inflammatory infiltrates. *Ex vivo* studies include vasorelaxation studies on arteries. *In vitro* studies include co-cultures of immune cells and endothelial cells, both of which can be harvested from SLE mouse models. Co-cultures may be indirect, such as in transwell systems, or direct, such as co-encapsulation studies where all cell types are embedded in a hydrogel. Created with BioRender.com.

decreased EPC differentiation (38). Disease is not primarily mediated by type I IFNs in B6.MRL-Fas^{lpr} mice, so this result is unsurprising.

FUTURE DIRECTIONS

Several studies have investigated cardiovascular outcomes in individual SLE mouse models compared to control mice, but thus far very few studies have directly compared cardiovascular outcomes among different SLE mouse models.

Transcriptional signatures between NZB/NZW F1, NZW/BXSB, and NZM2410 mice have been compared to one another and to those of human SLE patients to identify common pathways (61, 62). These studies identified the STAT3- and IL-36A pathways shared between all models. Differences between strains were also seen for some genes, such as increased mitochondrial dysfunction signatures in NZB/W F1 and NZM2410, but not in NZW/BXSB, suggesting that NZB/W F1 and NZM2410 strains have more oxidative stress and so may better simulate human conditions for any future studies on mitochondria in SLE (61). Importantly, such advances have correlated with significant outcomes seen in profiling lupus nephritis in human patients *via* single cell sequencing (scRNAseq) (63, 64). The identification of gene expression pathways that are shared not only among different mouse models but also between mice and humans is an important step toward development of more effective therapeutics.

While the studies mentioned above used histology to study the extent of nephritis, which is a well-known pathology caused by SLE, histological studies of atherosclerosis and other cardiovascular complications of SLE are more challenging. Mice do not develop atherosclerosis with the same pathogenesis as humans; for example, lesions develop in different vessels and have different histological features (65). Some of these changes may be due to the size and hemodynamic properties of mouse vasculature (65). In addition, as discussed in the previous sections, most murine SLE models do not present with overt cardiovascular symptoms. As modeled for lupus nephritis, we suggest that conducting head-to-head comparisons of cardiovascular complications, such as Ach-mediated vasorelaxation, among different SLE mouse models would contribute greatly toward a better understanding of CVD progression in human SLE patients. Since different SLE mouse models have different, well-characterized mechanisms of disease, any differences in endothelial dysfunction among these models could shed more light on the pathways leading to CVD in SLE. This could, in turn, help in identification of potential new treatment options for use in the clinic. Direct comparisons of CVD development among different SLE models would also provide detailed information to assist researchers in the selection of the best mouse models to use in future studies of different aspects of SLE progression.

To better model the contribution of SLE to vascular inflammation in humans, we also propose that *in vitro* studies incorporating immune cells and ECs from different murine SLE models would be useful. Such studies would allow inflammatory pathways common between human and murine SLE cells to be investigated without potential effects from hemodynamic differences. Many types of *in vitro* platforms such as microfluidics devices and transwell assays allow for the study of interactions between diseased inflammatory cells, such as T cells or monocytes, with ECs (66). For example, in one study conducted to observe changes in angiogenesis in the setting of glioblastoma, ECs displayed increased sprouting when co-cultured with tumor-associated macrophages than with unstimulated macrophages (67). We suggest that similar studies using immune cells from SLE mice may also be informative. Since both the immune cells and the ECs of SLE mice tend to be abnormal, researchers may mix and match which cell types come from SLE mice and which come from controls. This flexibility would assist in differentiating whether endothelial dysfunction is due to an intrinsic pathology in ECs themselves, or to their interaction with abnormal immune cells. *In vitro* cultures can also be performed to study the effect of lupus serum on ECs from control mice; for example, on EC production of reactive oxygen species (46).

Currently, some of the most commonly used *in vitro* assays for CVD studies in SLE mouse models are EPC differentiation cultures, since endothelial dysfunction arises when EPCs are not able to mature and replace old ECs (26, 30, 38, 39). In addition to EPC differentiation, EPC function can also be assessed *via* various assays for adhesion and aging (26). Mature EC activity can be assessed through migration assays in which they are allowed to grow through Matrigel and form vascular tubules (26). These types of studies are useful for identifying abnormalities intrinsic to the ECs themselves.

A schematic summarizing studies that may be used to perform comparisons of vascular inflammation among different SLE mouse models is shown in **Figure 1**. As mentioned previously, direct comparisons between kidney gene expression in NZB/NZW F1, NZW/BXSB, and NZM2410 models have been done already (61). We propose that it may be beneficial to include additional models in future studies, such as Fas mutation-carrying strains like *gld*.apoE$^{-/-}$, B6.MRL-Fas^{lpr}, or MRL/Fas^{lpr}, since the disease phenotype in these strains is not mediated by an increase in type I IFN as it is in the other strains. A comparison of vasorelaxation curves as Ach is added to a contracted section of artery could also be made among different models, as could a comparison of histological sections showing the extent of SLE progression and atherosclerosis. For *in vitro* studies, EPC differentiation assays and EC functional assays would help elucidate differences in endothelial dysfunction among different models at the cellular level. Co-culturing ECs with immune cells from different SLE models, or ECs from different SLE models with immune cells from control mice, could also indicate whether endothelial dysfunction is driven primarily by abnormalities in ECs or by abnormalities in immune cells in different models.

We propose that multiple-mouse-model studies of vascular inflammation would contribute greater understanding of the pathogenesis of CVD in human SLE. To aid researchers in the study of cardiovascular dysfunction in SLE, tendencies toward CVD in multiple different murine models of SLE should be compared head-to-head through a variety of *in vitro* and *in vivo* experiments. Comparison of models with different driving mechanisms of disease will help elucidate underlying pathways behind CVD in SLE.

DATA AVAILABILITY STATEMENT

The original contributions presented in the study are included in the article/supplementary material, further inquiries can be directed to the corresponding author/s.

AUTHOR CONTRIBUTIONS

All authors listed have made a substantial, direct, and intellectual contribution to the work and approved it for publication.

FUNDING

The authors gratefully acknowledged funding from the National Institutes of Health NCATS 1KL2TROO1429 (EM), the Rhines Rising Star Larry Hench Professorship (EM), and the FIU/UF Collaborative Grant F020122 (HR/EM).

REFERENCES

1. Dema B, Charles N. Autoantibodies in SLE: specificities, isotypes and receptors. *Antibodies.* (2016) 5:1–32. doi: 10.3390/antib5010002
2. Lee Y, Choi S, Ji J, Song G. Overall and cause-specific mortality in systemic lupus erythematosus: an updated meta-analysis. *Lupus.* (2016) 25:727–34. doi: 10.1177/0961203315627202
3. Liu Y, Kaplan MJ. Cardiovascular disease in systemic lupus erythematosus: an update. *Curr Opin Rheumatol.* (2018) 30:441–8. doi: 10.1097/BOR.0000000000000528
4. Urowitz M, Bookman A, Koehler B, Gordon D, Smythe H, Ogryzlo M. The bimodal mortality pattern of systemic lupus erythematosus. *Am J Med.* (1976) 60:293–9. doi: 10.1016/0002-9343(76)90431-9
5. Abdel-Aty H, Siegle N, Natusch A, Gromnica-Ihle E, Wassmuth R, Dietz R, et al. Myocardial tissue characterization in systemic lupus erythematosus: value of a comprehensive cardiovascular magnetic resonance approach. *Lupus.* (2008) 17:561–7. doi: 10.1177/0961203308089401
6. Seneviratne MG, Grieve SM, Figtree GA, Garsia R, Celermajer DS, Adelstein S, et al. Prevalence, distribution and clinical correlates of myocardial fibrosis in systemic lupus erythematosus: a cardiac magnetic resonance study. *Lupus.* (2016) 25:573–81. doi: 10.1177/0961203315622275
7. O'Neill S, Woldman S, Bailliard F, Norman W, McEwan J, Isenberg D, et al. Cardiac magnetic resonance imaging in patients with systemic lupus erythematosus. *Ann Rheum Dis.* (2009) 68:1478–81. doi: 10.1136/ard.2008.098053
8. Mavrogeni S, Koutsogeorgopoulou L, Markousis-Mavrogenis G, Bounas A, Tektonidou M, Lliossis S, et al. Cardiovascular magnetic resonance detects silent heart disease missed by echocardiography in systemic lupus erythematosus. *Lupus.* (2018) 27:564–71. doi: 10.1177/0961203317731533
9. Strain S, Keegan J, Raphael CE, Simpson R, Sugathapala MH, Prasad SK, et al. Inter breath-hold reproducibility of temporal patterns of coronary artery blood flow. *J Cardiovasc Magn Reson.* (2015) 17:1–2. doi: 10.1186/1532-429X-17-S1-M1
10. Zhang Y, Corona-Villalobos C, Kiani A, Eng J, Kamel I, Zimmerman S, et al. Myocardial T2 mapping by cardiovascular magnetic resonance reveals subclinical myocardial inflammation in patients with systemic lupus erythematosus. *Int J Cardiovasc Imaging.* (2015) 31:389–97. doi: 10.1007/s10554-014-0560-3
11. Puntmann V, D'Cruz D, Smith Z, Pastor A, Choong P, Voigt T, et al. Native myocardial T1 mapping by cardiovascular magnetic resonance imaging in subclinical cardiomyopathy in patients with systemic lupus erythematosus. *Circ Cardiovasc Imaging.* (2013) 6:295–301. doi: 10.1161/CIRCIMAGING.112.000151
12. Doria A, Iaccarino L, Sarzi-Puttini P, Atzeni F, Turriel M, Petri M. Cardiac involvement in systemic lupus erythematosus. *Lupus.* (2005) 14:683–6. doi: 10.1191/0961203305lu2200oa
13. Chen J, Tang Y, Zhu M, Xu A. Heart involvement in systemic lupus erythematosus: a systemic review and meta-analysis. *Clin Rheumatol.* (2016) 35:2437–48. doi: 10.1007/s10067-016-3373-z
14. Miner J, Kim A. Cardiac manifestations of systemic lupus erythematosus. *Rheum Dis Clin North Am.* (2014) 40:51–60. doi: 10.1016/j.rdc.2013.10.003
15. Lin JJ, Hsu HB, Sun SS, Wang JJ, Ho ST, Kao CH. Single photon emission computed tomography of technetium-99m tefrofosmin myocardial perfusion imaging in patients with systemic lupus erythematosus-A preliminary report. *Jpn Heart J.* (2003) 44:83–9. doi: 10.1536/jhj.44.83
16. Barile-Fabris L, Hernández-Cabrera MF, Barragan-Garfias JA. Vasculitis in systemic lupus erythematosus. *Curr Rheumatol Rep.* (2014) 16:1–6. doi: 10.1007/s11926-014-0440-9
17. Munguia-Realpozo P, Mendoza-Pinto C, Sierra Benito C, Escarcega RO, Garcia-Carrasco M, Mendez Martinez S, et al. Systemic lupus erythematosus and hypertension. *Autoimmun Rev.* (2019) 18:102371. doi: 10.1016/j.autrev.2019.102371
18. Kahlenberg JM, Kaplan MJ. The interplay of inflammation and cardiovascular disease in systemic lupus erythematosus. *Arthritis Res Ther.* (2011) 13:1–10. doi: 10.1186/ar3264
19. Li W, Titov AA, Morel L. An update on lupus animal models. *Curr Opin Rheumatol.* (2017) 29:434–41. doi: 10.1097/BOR.0000000000000412
20. Richard ML, Gilkeson G. Mouse models of lupus: what they tell us and what they don't. *Lupus Sci Med.* (2018) 5:e000199. doi: 10.1136/lupus-2016-000199
21. Moore E, Reynolds JA, Davidson A, Gallucci S, Morel L, Rao DA, et al. Promise and complexity of lupus mouse models. *Nat Immunol.* (2021) 22:683–6. doi: 10.1038/s41590-021-00914-4
22. Sanghera C, Wong LM, Panahi M, Sintou A, Hasham M, Sattler S. Cardiac phenotype in mouse models of systemic autoimmunity. *Dis Model Mech.* (2019) 12:1–16. doi: 10.1242/dmm.036947
23. McClung DM, Kalusche WJ, Jones KE, Ryan MJ, Taylor EB. Hypertension and endothelial dysfunction in the pristane model of systemic lupus erythematosus. *Physiol Rep.* (2021) 9:e14734. doi: 10.14814/phy2.14734
24. Kahlenberg JM, Yalavarthi S, Zhao W, Hodgin JB, Reed TJ, Tsuji NM, et al. An essential role for caspase-1 in the induction of murine lupus and its associated vascular damage. *Arthritis Rheumatol. (Hoboken, NJ).* (2014) 66:152–62. doi: 10.1002/art.38225
25. Yan Y, Zhang Z, Chen Y, Hou B, Liu K, Qin H, et al. Coptisine Alleviates Pristane-induced lupus-like disease and associated kidney and cardiovascular complications in mice. *Front Pharmacol.* (2020) 11:929. doi: 10.3389/fphar.2020.00929
26. Ding X, Xiang W, Yi R, Huang X, Lin Q, He X. Neutralizing interferon-α blocks inflammation-mediated vascular injury via PI3K and AMPK in systemic lupus erythematosus. *Immunology.* (2021) 164:372–85. doi: 10.1111/imm.13379
27. de la Visitación N, Robles-Vera I, Moleón-Moya J, Sánchez M, Jiménez R, Gómez-Guzmán M, et al. Probiotics prevent hypertension in a murine model of systemic lupus erythematosus induced by toll-like receptor 7 activation. *Nutrients.* (2021) 13:2669. doi: 10.3390/nu13082669
28. Liu Y, Seto NL, Carmona-Rivera C, Kaplan MJ. Accelerated model of lupus autoimmunity and vasculopathy driven by toll-like receptor 7/9 imbalance. *Lupus Sci Med.* (2018) 5:e000259. doi: 10.1136/lupus-2018-000259
29. Gilbert EL, Ryan MJ. High dietary fat promotes visceral obesity and impaired endothelial function in female mice with systemic lupus erythematosus. *Gend Med.* (2011) 8:150–5. doi: 10.1016/j.genm.2011.03.006
30. Zhao W, Thacker SG, Hodgin JB, Zhang H, Wang JH, Park JL, et al. The peroxisome proliferator-activated receptor-gamma agonist Pioglitazone improves cardiometabolic risk and renal inflammation in murine lupus. *J Immunol.* (2009) 183:2729–40. doi: 10.4049/jimmunol.0804341
31. Venegas-Pont M, Mathis KW, Iliescu R, Ray WH, Glover PH, Ryan MJ. Blood pressure and renal hemodynamic responses to acute angiotensin II infusion are enhanced in a female mouse model of systemic lupus erythematosus. *Am J Physiol Regul Integr Comp Physiol.* (2011) 301:R1286–R92. doi: 10.1152/ajpregu.00079.2011
32. Taylor EB, Ryan MJ. Immunosuppression with mycophenolate mofetil attenuates hypertension in an experimental model of autoimmune disease. *J Am Heart Assoc.* (2017) 6:e005394. doi: 10.1161/JAHA.116.005394
33. Nakagawa P, Masjoan-Juncos JX, Basha H, Janic B, Worou ME, Liao TD, et al. Effects of N-acetyl-seryl-asparyl-lysyl-proline on blood pressure, renal damage, and mortality in systemic lupus erythematosus. *Physiol Rep.* (2017) 5:e13084. doi: 10.14814/phy2.13084
34. Toral M, Robles-Vera I, Romero M, de la Visitación N, Sánchez M, O'Valle F, et al. *Lactobacillus fermentum* CECT5716: a novel alternative for the prevention of vascular disorders in a mouse model of systemic lupus erythematosus. *FASEB J.* (2019) 33:10005–18. doi: 10.1096/fj.201900545RR
35. Ryan MJ, McLemore GR. Hypertension and impaired vascular function in a female mouse model of systemic lupus erythematosus. *Am J Physiol.* (2007) 292:736–42. doi: 10.1152/ajpregu.00168.2006
36. Wolf VL, Phillips TL, Taylor EB, Sasser JM, Ryan MJ. Integrative cardiovascular physiology and pathophysiology: human recombinant relaxin-2 does not attenuate hypertension or renal injury but exacerbates vascular dysfunction in a female mouse model of SLE. *Am J Physiol.* (2019) 317:H234. doi: 10.1152/ajpheart.00174.2019
37. Virdis A, Tani C, Duranti E, Vagnani S, Carli L, Kühl AA, et al. Early treatment with hydroxychloroquine prevents the development of endothelial dysfunction in a murine model of systemic lupus erythematosus. *Arthritis Res Ther.* (2015) 17:277. doi: 10.1186/s13075-015-0790-3
38. Thacker S, Duquaine D, Park J, Kaplan MJ. Lupus-prone New Zealand Black/New Zealand White F1 mice display endothelial dysfunction and

abnormal phenotype and function of endothelial progenitor cells. *Lupus.* (2010) 19:288–99. doi: 10.1177/0961203309353773

39. Thacker SG, Zhao W, Smith CK, Luo W, Wang H, Vivekanandan-Giri A, et al. Type I interferons modulate vascular function, repair, thrombosis and plaque progression in murine models of lupus and atherosclerosis. *Arthritis Rheum.* (2012) 64:2975–85. doi: 10.1002/art.34504
40. Knight JS, Zhao W, Luo W, Subramanian V, O'Dell AA, Yalavarthi S, et al. Peptidylarginine deiminase inhibition is immunomodulatory and vasculoprotective in murine lupus. *J Clin Invest.* (2013) 123:2981–93. doi: 10.1172/JCI67390
41. Wilhelm A, Rhoads J, Wade N, Major A. Dysregulated CD4+ T cells from SLE-susceptible mice are sufficient to accelerate atherosclerosis in LDLr$^{-/-}$ mice. *Ann Rheum Dis.* (2015) 74:778–85. doi: 10.1136/annrheumdis-2013-203759
42. Morel L, Perry D, Sang A, Yin Y, Zheng YY. Murine models of systemic lupus erythematosus. *J Biomed Biotechnol.* (2011) 2011:1–19. doi: 10.1155/2011/271694
43. Li W, Elshikha A, Cornaby C, Teng X, Abboud G, Brown J, et al. T cells expressing the lupus susceptibility allele Pbx1d enhance autoimmunity and atherosclerosis in dyslipidemic mice. *JCI Insight.* (2020) 5:e138274. doi: 10.1172/jci.insight.138274
44. Braun NA, Wade NS, Wakeland EK, Major AS. Accelerated atherosclerosis is independent of feeding high fat diet in systemic lupus erythematosus-susceptible LDLr$^{-/-}$ mice. *Lupus.* (2008) 17:1070–8. doi: 10.1177/0961203308093551
45. Norman MU, James WG, Hickey MJ. Differential roles of ICAM-1 and VCAM-1 in leukocyte-endothelial cell interactions in skin and brain of MRL/faslpr mice. *J Leukoc Biol.* (2008) 84:68–76. doi: 10.1189/jlb.1107796
46. Jacob A, Hack B, Chiang E, Garcia JGN, Quigg RJ, Alexander JJ. C5a alters blood-brain barrier integrity in experimental lupus. *FASEB J.* (2010) 24:1682–8. doi: 10.1096/fj.09-138834
47. Kelley VE, Roths JB. Interaction of mutant lpr gene with background strain influences renal disease. *Clin Immunol Immunopathol.* (1985) 37:220–9. doi: 10.1016/0090-1229(85)90153-9
48. Marczynski P, Meineck M, Xia N, Li H, Kraus D, Roth W, et al. Vascular inflammation and dysfunction in lupus-prone mice-IL-6 as mediator of disease initiation. *Int J Mol Sci.* (2021) 22:2291. doi: 10.3390/ijms22052291
49. Zhang MC, Misu N, Furukawa H, Watanabe Y, Terada M, Komori H, et al. An epistatic effect of the female specific loci on the development of autoimmune vasculitis and antinuclear autoantibody in murine lupus. *Ann Rheum Dis.* (2006) 65:495–500. doi: 10.1136/ard.2005.040832
50. Yao G, Qi J, Zhang Z, Huang S, Geng L, Li W, et al. Endothelial cell injury is involved in atherosclerosis and lupus symptoms in gld.apoE$^{-/-}$ mice. *Int J Rheum Dis.* (2019) 22:488–96. doi: 10.1111/1756-185X.13458
51. Cruse JM, Lewis RE, Dilioglou S. Fate of immune complexes, glomerulonephritis, and cell-mediated vasculitis in lupus-prone MRL/Mp lpr/lpr mice. *Exp Mol Pathol.* (2000) 69:211–22. doi: 10.1006/exmp.2000.2330
52. Berden JH, Hang L, Mcconahey PJ, Dixon FJ. Analysis of vascular lesions in murine sLE. I association with serologic abnormalities. *J. Immunol.* (1983) 130:1699–705. Available online at: http://www.jimmunol.org/content/130/4/1699 (accessed December 24, 2021).
53. Furumoto Y, Smith CK, Blanco L, Zhao W, Brooks SR, Thacker SG, et al. Tofacitinib ameliorates murine lupus and its associated vascular dysfunction. *Arthritis Rheumatol. (Hoboken, NJ).* (2017) 69:148–60. doi: 10.1002/art.39818
54. Knight JS, Subramanian V, O'Dell AA, Yalavarthi S, Zhao W, Smith CK, et al. Peptidylarginine deiminase inhibition disrupts NET formation and protects against kidney, skin and vascular disease in lupus-prone MRL/lpr mice. *Ann Rheum Dis.* (2015) 74:2199–206. doi: 10.1136/annrheumdis-2014-205365
55. Yoshida H, Fujiwara H, Fujiwara T, Ikehara S, Hamashima Y. Quantitative analysis of myocardial infarction in. (NZW x BXSB)F1 hybrid mice with systemic lupus erythematosus and small coronary artery disease. *Am J Pathol.* (1987) 129:477–85.
56. Kolyada A, Porter A, Beglova N. Inhibition of thrombotic properties of persistent autoimmune anti-β2GPI antibodies in the mouse model of antiphospholipid syndrome. *Blood.* (2014) 123:1090–7. doi: 10.1182/blood-2013-08-520882
57. Santiago-Raber ML, Montecucco F, Vuilleumier N, Miteva K, Baptista D, Carbone F, et al. Atherosclerotic plaque vulnerability is increased in mouse model of lupus. *Sci Rep.* (2020) 10:18324. doi: 10.1038/s41598-020-74579-8
58. Nolsøe RL, Kelly JA, Pociot F, Moser KL, Kristiansen OP, Mandrup-Poulsen T, et al. Functional promoter haplotypes of the human FAS gene are associated with the phenotype of SLE characterized by thrombocytopenia. *Genes Immun.* (2005) 6:699–706. doi: 10.1038/sj.gene.6364259
59. Seliga A, Lee MH, Fernandes NC, Zuluaga-Ramirez V, Didukh M, Persidsky Y, et al. Kallikrein-Kinin System suppresses type I interferon responses: a novel pathway of interferon regulation. *Front Immunol.* (2018) 9:156. doi: 10.3389/fimmu.2018.00156
60. Sian P, Lee S, Keong K, Sian PP, Poh KK. Endothelial progenitor cells in cardiovascular diseases. *World J Stem Cells.* (2014) 6:355–66. doi: 10.4252/wjsc.v6.i3.355
61. Bethunaickan R, Berthier CC, Zhang W, Kretzler M, Davidson A. Comparative transcriptional profiling of 3 murine models of SLE nephritis reveals both unique and shared regulatory networks. *PLoS One.* (2013) 8:e77489. doi: 10.1371/journal.pone.0077489
62. Berthier CC, Bethunaickan R, Gonzalez-Rivera T, Nair V, Ramanujam M, Zhang W, et al. Cross-species transcriptional network analysis defines shared inflammatory responses in murine and human lupus nephritis. *J Immunol.* (2012) 189:988–1001. doi: 10.4049/jimmunol.1103031
63. Rao DA, Arazi A, Wofsy D, Diamond B. Design and application of single-cell RNA sequencing to study kidney immune cells in lupus nephritis. *Nat Rev Nephrol.* (2019) 16:238–50. doi: 10.1038/s41581-019-0232-6
64. Der E, Ranabothu S, Suryawanshi H, Akat KM, Clancy R, Morozov P, et al. Single cell RNA sequencing to dissect the molecular heterogeneity in lupus nephritis. *JCI Insight.* (2017) 2:e93009. doi: 10.1172/jci.insight.93009
65. Getz GS, Reardon CA. Animal models of atherosclerosis. *Arterioscler Thromb Vasc Biol.* (2012) 32:1104–15. doi: 10.1161/ATVBAHA.111.237693
66. Silberman J, Jha A, Ryan H, Abbate T, Moore E. Modeled vascular microenvironments: immune-endothelial cell interactions *in vitro*. *Drug Deliv Transl Res.* (2021) 11:2482–95. doi: 10.1007/s13346-021-00970-1
67. Cui X, Morales RTT, Qian W, Wang H, Gagner JP, Dolgalev I, et al. Hacking macrophage-associated immunosuppression for regulating glioblastoma angiogenesis. *Biomaterials.* (2018) 161:164–78. doi: 10.1016/j.biomaterials.2018.01.053

Conflict of Interest: The authors declare that the research was conducted in the absence of any commercial or financial relationships that could be construed as a potential conflict of interest.

Frontiers in Cardiovascular Medicine

ORIGINAL RESEARCH
published: 17 June 2022
doi: 10.3389/fcvm.2022.854287

A Cardiovascular Disease Prediction Model Based on Routine Physical Examination Indicators Using Machine Learning Methods: A Cohort Study

Xin Qian [1†], *Yu Li* [1†], *Xianghui Zhang* [1], *Heng Guo* [1], *Jia He* [1], *Xinping Wang* [1], *Yizhong Yan* [1], *Jiaolong Ma* [1], *Rulin Ma* [1*] *and Shuxia Guo* [1,2*]

[1] *Department of Public Health, Shihezi University School of Medicine, Shihezi, China,* [2] *Department of NHC Key Laboratory of Prevention and Treatment of Central Asia High Incidence Diseases, The First Affiliated Hospital of Shihezi University Medical College, Shihezi, China*

Edited by:
Yun Fang,
The University of Chicago,
United States

Reviewed by:
Yichen Ding,
The University of Texas at Dallas,
United States
Junguk Hur,
University of North Dakota,
United States

***Correspondence:**
Rulin Ma
marulin@shzu.edu.cn
Shuxia Guo
gsxshzu@sina.com

[†] *These authors have contributed equally to this work and share first authorship*

Specialty section:
This article was submitted to Atherosclerosis and Vascular Medicine, a section of the journal Frontiers in Cardiovascular Medicine

Received: 23 January 2022
Accepted: 23 May 2022
Published: 17 June 2022

Citation:
Qian X, Li Y, Zhang X, Guo H, He J, Wang X, Yan Y, Ma J, Ma R and Guo S (2022) A Cardiovascular Disease Prediction Model Based on Routine Physical Examination Indicators Using Machine Learning Methods: A Cohort Study. Front. Cardiovasc. Med. 9:854287. doi: 10.3389/fcvm.2022.854287

Background: Cardiovascular diseases (CVD) are currently the leading cause of premature death worldwide. Model-based early detection of high-risk populations for CVD is the key to CVD prevention. Thus, this research aimed to use machine learning (ML) algorithms to establish a CVD prediction model based on routine physical examination indicators suitable for the Xinjiang rural population.

Method: The research cohort data collection was divided into two stages. The first stage involved a baseline survey from 2010 to 2012, with follow-up ending in December 2017. The second-phase baseline survey was conducted from September to December 2016, and follow-up ended in August 2021. A total of 12,692 participants (10,407 Uyghur and 2,285 Kazak) were included in the study. Screening predictors and establishing variable subsets were based on least absolute shrinkage and selection operator (Lasso) regression, logistic regression forward partial likelihood estimation (FLR), random forest (RF) feature importance, and RF variable importance. The selected subset of variables was compared with L1 regularized logistic regression (L1-LR), RF, support vector machine (SVM), and AdaBoost algorithm to establish a CVD prediction model suitable for this population. The incidence of CVD in this population was then analyzed.

Result: After 4.94 years of follow-up, a total of 1,176 people were diagnosed with CVD (cumulative incidence: 9.27%). In the comparison of discrimination and calibration, the prediction performance of the subset of variables selected based on FLR was better than that of other models. Combining the results of discrimination, calibration, and clinical validity, the prediction model based on L1-LR had the best prediction performance. Age, systolic blood pressure, low-density lipoprotein-L/high-density lipoproteins-C, triglyceride blood glucose index, body mass index, and body adiposity index were all important predictors of the onset of CVD in the Xinjiang rural population.

Conclusion: In the Xinjiang rural population, the prediction model based on L1-LR had the best prediction performance.

Keywords: cardiovascular disease, machine learning, predictive models, routine physical examination indicators, cohort study

INTRODUCTION

Cardiovascular disease (CVD), a chronic and complex disease caused by heart and vascular diseases, is currently the main cause of premature death and chronic disability globally (1, 2). Its treatment usually involves medical and surgical methods. Nevertheless, these treatments cannot cure CVD. Moreover, these treatments have a great impact on the quality of life of individuals with CVD. Therefore, the current management of CVD mainly focuses on preventive measures. Recent studies suggest that ∼80% of premature CVD mortality could be prevented through early intervention (3). In addition, CVD has a slow onset and long incubation period; thus, it is generally at a more serious stage at the time of diagnosis. Therefore, early identification of high-risk groups for CVD is particularly important for its prevention and control (4).

In recent years, an increasing number of CVD prevention and control guidelines recommended the use of CVD risk prediction models to identify high-risk groups who could receive early intervention to reduce CVD risk (5). Most current risk prediction models for CVD were established using traditional statistical methods (6–10). A model is established if it meets the requirements of independence and linearity. Therefore, it cannot reflect the complex relationship between variables, which affects the accuracy of the prediction model and the applicability of external verification (11, 12). The machine learning (ML) algorithm is a traditional statistical method that can effectively solve the problems of non-linearity, variable redundancy, and interaction between variables. Moreover, it can be used to explore the potential risk factors for CVD to improve its predictive performance; hence, it is widely used in the field of CVD prevention and control (13). Despite its advantages, there are still controversies regarding its ability to predict CVD. Related studies reported that the predictive performance of ML algorithms was better than those of traditional statistical methods (14). Contrastingly, studies showed that the predictive performance of logistic regression (LR) was not weaker than that of machine learning algorithms (15, 16).

Xinjiang is located in northwest China and is home to multiple ethnic groups. Uyghur and Kazakh are the main ethnic groups in Xinjiang. Studies found that these populations have high prevalence of CVD risk factors, such as metabolic syndrome, hypertension, and obesity, thereby corresponding with high incidence of CVD (17–20). Most prediction models for CVD are based on European and American populations (6, 9, 21). Although in recent years, Chinese researchers have established predictive models based on Cox regression and ML algorithms, most are based on a feature screening method for predictive modeling (22, 23). Moreover, there are few reports on ethnic minority groups in Xinjiang, and previous studies showed that the Framingham risk score (FRS) and Pooled Cohort Equations (PCEs) were not suitable for identifying groups that had a high risk of CVD among the Uyghur and Kazak populations (24).

Thus, this study aimed to use machine learning algorithms to establish a CVD prediction model that was suitable for the Xinjiang Uyghur and Kazak populations based on routine physical examination indicators. This study also aimed to identify the main factors that affect the occurrence of CVD, to identify groups that had a high risk of CVD in early-stage disease, to provide a theoretical basis for the effective prevention of CVD, and to have important, practical significance for the comprehensive prevention and control of CVD in the Uyghur and Kazak populations.

METHODS

Study Population

Baseline data collection was divided into two phases. In the first stage, a baseline survey was conducted from 2010 to 2012. Through stratified cluster random sampling, the Uyghur population in Jiangbazi Township, Jiashi County, Kashi Prefecture, and southern Xinjiang, and the Kazakhs in Nalati Township, Xinyuan County, Ili Prefecture, and northern Xinjiang were selected. In the second stage, a baseline survey was conducted from September to December 2016, and the Uyghur population of the 51st Regiment of the Third Division of the Xinjiang Corps was selected as the research cohort through stratified cluster random sampling. A total of 19,549 people who were aged ≥18 years and lived in the local area for >6 months were included in the study. The exclusion criteria included CVD

Abbreviations: CVD, cardiovascular disease; ML, machine learning; L1-LR, L1 regularized logistic regression; RF, random forest; SVM, support vector machine; SBP, systolic blood pressure; TyG, triglyceride blood glucose index; BMI, body mass index; BAI, body obesity index; TG, triglycerides; HDL-C, high-density lipoprotein cholesterol; DBP, diastolic blood pressure; WHR, waist-to-hip ratio; LCI, lipoprotein combine index; AI, atherogenic index; LpH, low-high-density lipoprotein ratio; THT, bilirubin comprehensive index; FLR, forward partial likelihood estimation; LR, logistic regression; RF, Random forest; AUC, the area under the receiver operating curve; cNRI, the Net Reclassification Index; IDI, Integrated Discrimination Improvement Index; BS, Brier Score.

TABLE 1 | Comparison of the prediction performance of the optimal model of each algorithm.

Model	AUC	Youden Index	Optimal threshold	Sensitivity (%)	Specificity (%)	PPV (%)	NPV (%)	Proportion of high-risk population (%)	Brier score	Homser-Lemeshow χ^2	*P*-Value
Lasso-AdaBoost	0.798 (0.782, 0.813)	0.472	0.11	73.09	74.10	23.5	96.2	30.4	0.078 (0.070, 0.086)	13.81	0.09
FLR-L1-LR	0.817 (0.801, 0.832)	0.524	0.11	73.49	78.86	27.4	96.5	26.7	0.076 (0.069, 0.084)	11.51	0.17
FLR-RF	0.804 (0.788, 0.820)	0.506	0.08	79.52	71.09	23.0	97.0	33.1	0.077 (0.070, 0.086)	11.59	0.17
FLR-SVM	0.814 (0.798, 0.829)	0.511	0.11	73.90	77.16	26.0	96.5	38.4	0.076 (0.069, 0.084)	16.10	0.04

AUC, area under the receiver operating characteristic curve; PPV, positive predictive value; NPV, negative predictive value; Lasso-AdaBoost, AdaBoost with Lasso regression; FLR-L1-LR, L1 regularized Logistic regression with forward Partial Likelihood Estimation; FLR-RF, random forest with forward Partial Likelihood Estimation; FLR-SVM, support vector machine with forward Partial Likelihood Estimation.

at baseline, those lost to follow-up, and those with incomplete blood information. Follow-up continued until December 2017 for the first stage (median: 6.07 years) and until August 2021 for the second stage (median: 4.94 years). According to the inclusion and exclusion criteria, 5,335 and 7,357 people were included in the first and second stages, respectively, for a total of 12,692 individuals (**Supplementary Figures 1.1, 1.2**). Then do data analysis (**Supplementary Figure 1.3**). All participants provided written informed consent. This study was approved by the Ethics Committee of the First Affiliated Hospital of Shihezi University School of Medicine (NO. SHZ2010LL01).

Data Collection

Data were collected *via* questionnaire, physical examination, and laboratory examination. Questionnaires were completed face-to-face. Anthropometric measurements such as height, weight, waist circumference (WC), hip circumference (HC), and blood pressure were obtained by trained professionals. Blood pressure was measured three times for each participant using a mercury sphygmomanometer after 5-min seated rest, and the average value was calculated. Hypertension was defined as systolic blood pressure (SBP) of $\geq$140 mmHg or diastolic blood pressure (DBP) of $\geq$90 mmHg. Prehypertension was defined as $140 > \text{SBP} \geq 120$ mmHg or $90 > \text{DBP} \geq 80$ mmHg (25). Synthetic indices were calculated based on anthropometric measurements: BMI [weight (kg)/height^2 (m)]; BAI (HC/height$^{1.5}$-18); pulse pressure (SBP–DBP); and waist-to-hip ratio [WHR; WC (cm)/HC (cm)]. A family history of diabetes was defined as a history of diabetes in at least one parent or sibling; the same criteria were used for a family history of stroke and coronary heart disease (CHD). Current smokers were defined as participants who had been smoking for >6 months (26). Drinking was defined as consuming alcoholic beverages (beer, red wine, and white wine) $\geq$2 times a month (27). A 5 ml fasting blood sample was collected from each subject and levels of the fasting blood glucose (FBG), triglycerides (TGs), high-density lipoprotein cholesterol (HDL-C), total cholesterol (TC), low-density lipoprotein cholesterol (LDL-C), and other indicators were obtained using an automatic biochemical analyser (Olympus AU 2700; Olympus Diagnostics, Hamburg, Germany) at the First Affiliated Hospital of Shihezi University School of Medicine. In this study, individuals with diabetes (28) were defined as having FBG level of $\geq$7.0 mmol/L and 2-h postprandial blood glucose level of $\geq$11.1 mmol/L, a previous diabetes diagnosis, and use of blood sugar control drugs. We also calculated other synthetic indices, including TyG, (TG [mg/dl]*FBG [mg/dl]), (LAP) (men: [WC-65]*TC [mmol/L]; women: [WC-58]*TG [mmol/L]); lipoprotein combine index (LCI) (TC*TG [mmol/L]*LDL-C/HDL-C); atherogenic index (AI) (TC [mmol/L]-HDL-C)/HDL-C); atherogenic index of plasma (AIP) (Log[TG/HDL]); LpH (LDL-C/HDL-C ratio); and bilirubin comprehensive index (THT) (TC [mmol/L]/[HDL-C+TBIL (μmol/mL)]).

Data Pre-processing

There were some missing values in the database, and direct deletion of missing values resulted in the loss of sample information. Since there were a few variables with missing values in this study, continuous variables were filled using the mean, while categorical variables were filled using the mode. By standardizing continuous variables, categorical variables were processed by one-hot encoding to reduce the influence of different variable units and quantity levels on the analysis. For the description of missing variables in this study, see **Supplementary Table 1**.

Diagnostic Criteria

The diagnostic criteria for CVD (29) pertained to the detection of ischaemic heart disease, cerebrovascular disease, and related diseases [International Classification of Diseases (ICD)-9: code 390–495]; hospitalization; or death due to CVD (ICD-10) during the follow-up period. Data regarding patient questionnaire answers, medical records, and the diagnosis of CVD during the follow-up period were obtained and recorded. If the same type of CVD event occurred more than once in a patient, the first occurrence of CVD was the final event. The time of onset was recorded. Self-reported patients needed to provide proof of their clinical diagnosis.

Introduction to Predictive Models

Logistic regression belongs to probabilistic nonlinear regression and is one of the most widely used classification models. Logistic regression usually uses regularization to optimize the model. The adjustable parameters include inverse regularization parameters and methods (30). By adding a regularization coefficient to Logistic regression, the parameters of the variable are sparse, so that the weight of most of the feature vectors is 0, thereby reducing the dimension of the variable. SVM is currently one of the most common ML algorithms that can effectively solve the classification problem of small samples and nonlinear and high-dimensional data. It classifies samples by finding a set of hyperplanes in a high-dimensional space, and the samples closest to the hyperplane are called support vectors. When the training data are inseparable, this problem can be solved using the kernel trick (31).That is, the original features of the samples are mapped to a higher dimensional space that makes the samples linearly separable through the mapping function. The RF algorithm is an ensemble learning algorithm based on the decision tree algorithm. The basic idea is to integrate weak classifiers into a more robust model (32). AdaBoost (33) is an ensemble learning algorithm based on boosting. The algorithm first builds a weak learner based on the training data and then according to AdaBoost, increases the weight of the samples that were misclassified by weak learning in the previous round. Then, it reduces the weight of the correctly classified samples, loops this process until the weak learner reaches the specified value, and then linearly combines all weak learners to obtain the final strong classifier by weighted majority voting. In this study, both random forest and Adaboost are ensemble learning algorithms based on decision trees. The decision tree algorithm selects variables by evaluating the characteristics and depth of dividing nodes, reducing the dimension of variables. The integrated model has better generalization error and can effectively reduce the overfitting combination phenomenon.

Model Establishment and Verification

The datasets were randomly divided into training datasets (927CVD/10153) and test datasets (249CVD/2539). The KS test was performed on the training and test datasets, and the *P*-values were both >0.05. The ratio of the training and test datasets was 8:2. We considered four variable selection methods: forward partial likelihood estimation (FLR) with logistic regression (LR), lasso regularization with logistic regression (Lasso-LR), permutation-based selection with random forest (RF), and characteristic importance with RF. Variables were established using a subset of algorithms, such as L1-LR, RF, SVM, and AdaBoost. A prediction model of each algorithm was then established. The optimal prediction model of the same algorithm was then selected by discrimination and calibration, and the most suitable prediction model for the population was obtained by comparing the discrimination, calibration, and clinical effectiveness of the optimal prediction models of different algorithms.

The discrimination of the model was determined by comparing the area under the receiver operating curve (AUC), Net Reclassification Index (cNRI), and Integrated Discrimination Improvement Index (IDI) (34) between models, and the calibration degree was compared by calculating the Brier Score (BS) and Homser–Lemeshow χ^2 (35, 36). This study evaluated the clinical validity of the model using decision curve analysis (DCA) (37). The horizontal axis of the decision curve represents the threshold probability and vertical axis represents the net benefit obtained after subtracting the harm from the benefit under the threshold probability. Using DCA to determine the net benefit that can be obtained using the model to screen high-risk groups compared with assuming that all participants are high-risk groups of CVD and implanting undifferentiated interventions, followed by calculating the net benefit without increasing the number of positive results, can reduce unnecessary interventions.

To avoid over-fitting the problem of the model in the process of model selection and hyper-parameter tuning, we used a 10-fold cross-validation to optimize the parameters of the training set and subsequently selected the optimal model. This method divided the training data in 10 equal, non-repeated parts, nine of which were used for model training, and the remaining one was used for model verification. This process was repeated 10 times, and combination of Bayesian optimisation and grid search was used to select the optimal hyperparameters. The AUC was used as the model selection criterion to determine the hyperparameter value that optimized the model predictive performance. Afterwards, we used the optimal hyperparameter value. We built the model on all training data sets. Finally, the independent test data set was used to make a final evaluation of model performance.

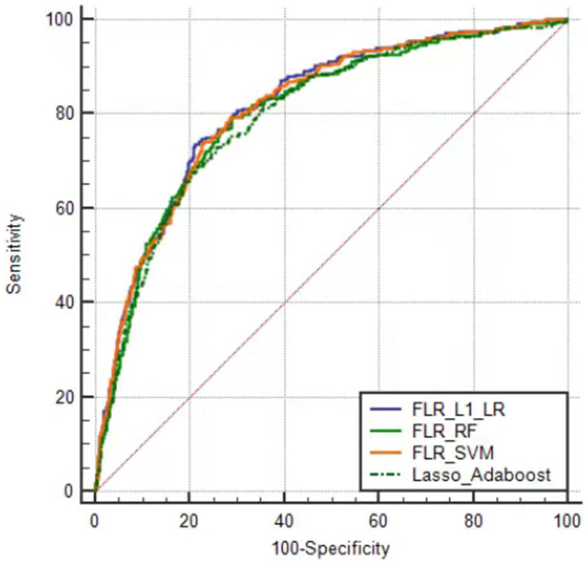

FIGURE 1 | Receiver operator characteristic curves of the optimal prediction model in Xinjiang rural population. FLR-L1-LR, L1 regularized Logistic regression with forwarding Partial Likelihood Estimation; FLR-RF, Random forest with forwarding Partial Likelihood Estimation; FLR-SVM, Support vector machine with forwarding Partial Likelihood Estimation.

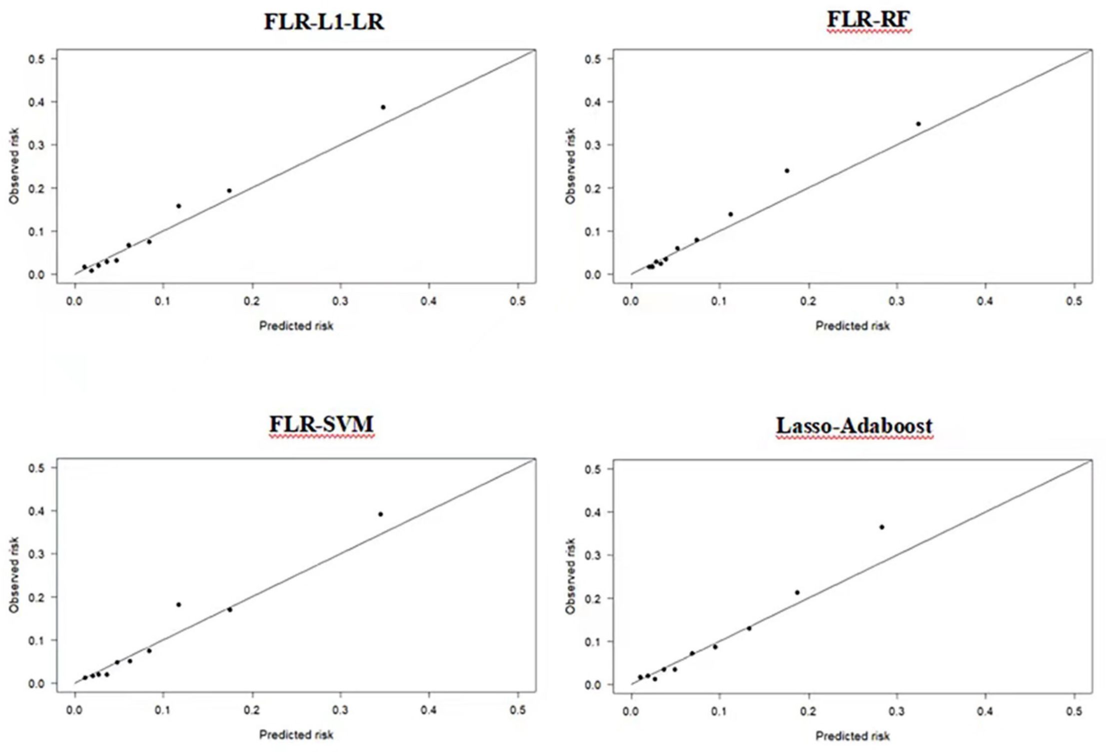

FIGURE 2 | Calibration plots of four ML models in predicting CVD outcomes in Xinjiang rural population. CVD, cardiovascular disease; ML, machine learning; FLR-L1-LR, L1 regularized Logistic regression with forwarding Partial Likelihood Estimation; FLR-RF, Random forest with forwarding Partial Likelihood Estimation; FLR-SVM, Support vector machine with forwarding Partial Likelihood Estimation.

TABLE 2 | Comparison of discrimination performance of optimal prediction models.

Predictive model	AUC difference	*P*-Value	cNRI	*P*-Value	IDI	*P*-Value
Lasso-AdaBoost vs. FLR-L1-LR	0.019	0.002	0.208 (0.078, 0.337)	<0.001	0.032 (0.019, 0.045)	<0.010
Lasso-AdaBoost vs. FLR-RF	0.007	0.334	0.097 (−0.033, 0.228)	0.143	0.016 (0.007, 0.025)	<0.010
Lasso-AdaBoost vs. FLR-SVM	0.016	0.047	0.167 (0.037, 0.296)	0.012	0.029 (0.016, 0.042)	<0.010
FLR-RF vs. FLR-L1-LR	0.012	0.045	0.108 (−0.022, 0.238)	0.105	0.016 (0.003, 0.028)	0.010
FLR-RF vs. FLR-SVM	0.003	0.016	0.072 (−0.058, 0.203)	0.278	0.013 (0.001, 0.026)	0.040
FLR-SVM vs. FLR-L1-LR	0.010	0.118	0.278 (0.149, 0.408)	<0.001	0.003 (0.001, 0.004)	<0.010

AUC, area under the receiver operating characteristic curve; cNRI, continuous Net Reclassification Index; IDI, Integrated Discrimination Improvement Index; Lasso-AdaBoost, AdaBoost with Lasso regression; FLR-L1-LR, L1 regularized Logistic regression with forward Partial Likelihood Estimation; FLR-RF, random forest with forward Partial Likelihood Estimation; FLR-SVM, support vector machine with forward Partial Likelihood Estimation.

Data Analysis

Since machine learning algorithms, such as SVM output, predicted CVD occurrence by default, they did not directly predict CVD probability. We used the Platt scaling method (38) to calibrate the predicted probabilities output using the four models for more accurate prediction of CVD risk and identification of high-risk groups. The data used in this study were unbalanced to enable the use of the threshold probability movement method. The default 0.5 of the model was not used as the standard for dividing the incidence of CVD. However, the optimal threshold probability of each model was determined according to the Youden Index, which was the basis for dividing the high-risk population of CVD. All statistical analyses were performed using the Python 3.7 or R version 4.0. A two-sided test with a *P*-value of <0.05 was considered statistically significant.

RESULTS

Study Population Characteristics

A total of 12,692 people (6,264 men, 6,398 women; average age 41.24 years) were included in this study. A total of 1,176 CVD events were observed during a median follow-up of

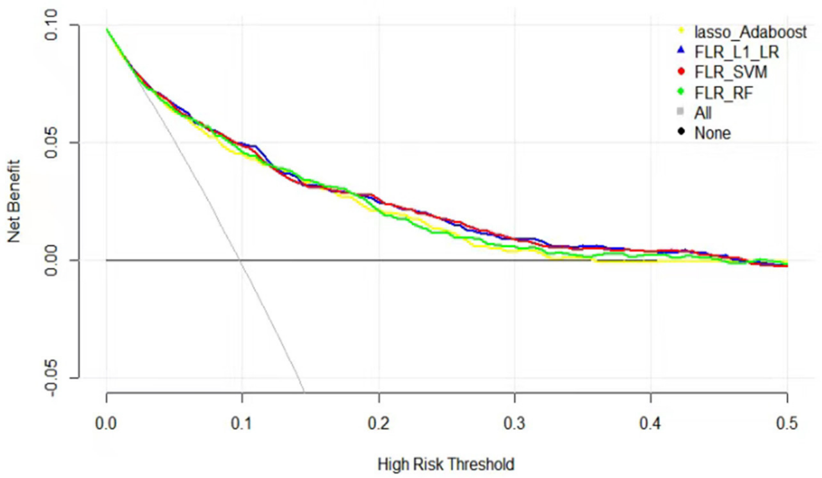

FIGURE 3 | Decision curves for predicting CVD outcomes in Xinjiang rural population using four ML models. CVD, cardiovascular disease; ML, machine learning; FLR-L1-LR, L1 regularized Logistic regression with forwarding Partial Likelihood Estimation; FLR-RF, Random forest with forwarding Partial Likelihood Estimation; FLR-SVM, Support vector machine with forwarding Partial Likelihood Estimation.

4.94 years. The cumulative incidence was 9.26%. Compared with people without CVD events, those with CVD showed a higher trend in study indicators, such as age, BMI, TC, alkaline phosphatase (ALP), WC, and HC. Moreover, subjects with high blood pressure and type 2 diabetes were also at a higher risk of CVD development. The comparison of different characteristics between participants with CVD and those without training and test datasets listed is shown in **Supplementary Tables 2.1,2.2**.

Independent Variable Selection and Optimal Model Construction

The research database included demographic characteristics, physical examination findings, and serology results. There were 62 variables in total. After removing the missing ratio of ≥50% and 11 variables unrelated to the research, a total of 51 variables were included. The following methods were used to filter and establish a subset of variables: FLR-LR (22 variables) and Lasso-LR (34 variables). The top 35 variables were selected according to the built-in random forest importance. The top 30 variables were subsequently selected as the screening subset according to permutation feature importance of RF. The variable subsets formed by the selected variables using the four methods are shown in **Supplementary Tables 3–6**.

To further explore the predictive performance of different variable subsets on different algorithms, we used the above variable subsets and the full variable set to build predictive models using different algorithms to find the algorithm based on the optimal model. Through Bayesian optimization and grid search, the hyperparameter values with the best prediction performance of each model were selected (**Supplementary Tables 7.1–7.4**). The AUC values of different algorithms in the training and test datasets are shown in **Supplementary Table 8**. There was no risk of overfitting and, to comprehensively consider the results of discrimination and calibration, this study concluded that the optimal models based on the four algorithms were Lasso-AdaBoost, FLR-L1-LR, FLR-RF, and FLR-SVM (**Supplementary Tables 9.1–9.4**).

Comparison of Optimal Model Prediction Performance

The predictive performance indicators of the optimal models for each algorithm are listed in **Table 1**. All models have a moderate or higher (AUC value between 0.798 and 0.817) distinguishing ability. The AUC of FLR-L1-LR, FLR-SVM, FLR-RF, and Lasso-AdaBoost was 0.817 (95% CI, 0.801–0.832), 0.814 (95% CI, 0.798–0.829), 0.804 (95% CI, 0.788–0.820), and 0.798 (95% CI, 0.782–0.81), respectively. The receiver operating characteristic (ROC) curve of the prediction model is shown in **Figure 1**.

Compared with other optimal models, the FLR-L1-LR model performed better in terms of Youden index, specificity, and PPV when the optimal threshold was 0.11. BS and Homser–Lemeshow χ^2 also demonstrated that the FLR-L1-LR model was better than others. In the FLR-L1-LR model, 26.7% of the participants were identified as high risk for CVD development (**Table 1**). The results of the calibration curve showed that FLR-L1-LR, FLR-SVM, Lasso-AdaBoost, and FLR-RF predicted the number of patients with CVD to be 234.12, 234.05, 230.55, and 223.93, respectively. The corresponding predicted CVD events/objective CVD events (P/O) values were 94.02, 94.00, 92.59, and 89.93, respectively (**Figure 2**).

To further select a prediction model suitable for this population, we compared the differences between the AUC value, IDI, and cNRI of the optimal models. We found that the AUC values of FLR-L1-LR and FLR-SVM were similar ($P > 0.05$), and both were higher than the AUC values of Lasso-AdaBoost and FLR-RF ($P < 0.05$). The reclassification capabilities of each model were compared with that of the FLR-L1-L model. The cNRI values of FLR-SVM and Lasso-AdaBoost values

TABLE 3 | Comparison of clinical effectiveness of models.

Model	Pt (%)	Net income		Model net income	Advantages of the model[#]
		Treat all	Prediction model		
FLR-L1-LR	5	0.051	0.066	0.015	29
	10	−0.002	0.049	0.051	46
	11[a]	−0.013	0.048	0.061	49
FLR-SVM	5	0.051	0.065	0.014	27
	10	−0.002	0.048	0.050	45
	11[a]	−0.013	0.045	0.058	47
Lasso-AdaBoost	5	0.051	0.063	0.012	23
	10	−0.002	0.045	0.047	43
	11[a]	−0.013	0.043	0.056	46
FLR-RF	5	0.051	0.064	0.013	25
	10	−0.002	0.046	0.048	43
	8[a]	0.02	0.053	0.033	38

[#] *The value was calculated as: (net benefit of the model– net benefit of treat all)/[pt/(1 – pt)] × 100.*

[a] *Select the optimal threshold probability of each model according to AUC.*

Pt, Threshold probability; Lasso-AdaBoost, AdaBoost with Lasso regression; FLR-L1-LR, L1 regularized Logistic regression with forward Partial Likelihood Estimation; FLR-RF, random forest with forward Partial Likelihood Estimation; FLR-SVM, support vector machine with forward Partial Likelihood Estimation.

were 0.278 and 0.208, respectively. Compared with the FLR-L1-LR model, the Lasso-AdaBoost and the FLR-SVM models had a correct classification rate of 21 and 28%, respectively. Similarly, FLR-SVM was compared with Lasso-AdaBoost in terms of the proportion of correct classification. The FLR-SVM had a 17% increased proportion of correct classification compared with that of the Lasso-AdaBoost. The difference between the reclassification capabilities of the remaining models was not statistically significant. The results of the comprehensive discrimination ability of each model, from best to worst, were FLR-L1-LR > FLR-SVM > FLR-RF > Lasso-AdaBoost. This is described in **Table 2**.

The clinical effectiveness of FLR-L1-LR, FLR-SVM, FLR-RF, and Lasso-AdaBoost based on the results of the decision curve are shown in **Figure 3**. It is evident that the clinical application value of the FLR-L1-LR model is higher than that of FLR-SVM, Lasso-AdaBoost, and FLR-RF (**Figure 3**, **Table 3**). Under the optimal threshold, we assumed that all participants were in a high-risk group for CVD. We then administered undifferentiated interventions for primary and secondary prevention. The net benefit of using the FLR-L1-LR model was 0.061. This showed that without increasing the positive results, 49 out of every 1,000 people could avoid unnecessary interventions.

Variable Importance Ranking of the Optimal Model Output

Previous studies indicated that compared with FRS and PCE, the ML algorithm could better determine the nonlinear and complex relationships between variables and outcomes. Furthermore, the ML algorithm identified potential risk factors more effectively (39–41). We further analyzed the relative relationship among the importance rankings of the algorithm variables using the coefficients of variables that could not be obtained based on the Gaussian kernel function. Therefore, this study only highlights the importance of the optimal model variables established by the AdaBoost, RF, and L1-LR algorithms to compare the ability of each variable to predict the incidence of CVD (**Figure 4**). This study found that the risk factors for CVD included factors that reflected the degree and type of body obesity, such as age, sex, ethnicity, DBP, HDL-C level, TC level, BAI, and BMI. Risk factors also included those that reflected glucose and lipid metabolism, such as TyG, LpH level, AI, and occupation type. The indicators were also risk factors for CVD and could predict CVD risk.

DISCUSSION

The results of this study show that the cumulative incidence of CVD in the Xinjiang Uyghur and Kazak populations was 9.26%. The incidence was similar to that in African Americans (42). However, it was higher than those of Han Chinese ancestry (43–45), which may relate to the population's unique genetic background and diet. Here, we used ML algorithms to establish a predictive model and discover the main factors for the occurrence of CVD in this population.

To achieve the best predictive performance of the established model, we selected variables through four variable screening methods. We subsequently established different variable subsets, unlike those in the previous study that only used the feature importance of the RF algorithm to select variables (46). Our results indicate that the subset of variables established using FLR showed the best performance on the L1-LR, RF, and SVM algorithms, similar to the results reported by De Silva et al. (47). Unlike other variable screening methods, FLR focused more on the linear relationship between variables. The model built based on the combination of FLR-screened variable subsets and other ML algorithms had better predictive performance. This may be due to the consideration of the linear relationship of variables based on logistic regression and the in-depth analysis of the nonlinear relationship using different machine learning algorithms.

When the optimal prediction models of the LR, SVM, RF, and AdaBoost algorithms were compared, the prediction performance of the LR-based model was better than that of the other ML algorithm models. These findings are similar to those of a 2019 systematic review (15). There are many possible reasons for this phenomenon. First, the number of variables included in this research was limited, and some ML algorithms were better at dealing with high-dimensional data problems. Moreover, the logistic regression model was established based on the L1 regularization method. This method was better at dealing with small samples and low-dimensional data and was not easily affected by outliers. The established model was more robust.

Second, the performance of the SVM-based prediction model was lower than that of LR but higher than those of RF and

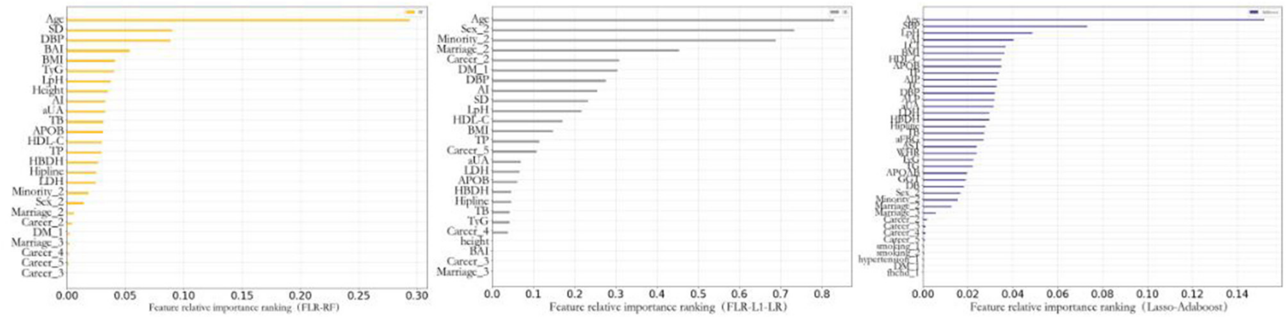

FIGURE 4 | Feature importance of included variables obtained from the random forest with forwarding Partial Likelihood Estimation (FLR-RF), L1 regularized Logistic regression with FLR (FLR-L1-LR), Lasso-AdaBoost model. SD, pulse pressure difference; DBP, diastolic blood pressure; BAI, body obesity index; BMI, body mass index; TyG, triglyceride blood glucose index; LpH, low-high-density lipoprotein ratio; AI, arteriosclerosis index; aUA, uric acid; TB, total bilirubin; APOB, apolipoprotein B; HDL-C, high-density lipoprotein cholesterol; TP, total protein; HBDH, α-hydroxybutyrate dehydrogenase; LDH, lactate dehydrogenase; SBP, systolic blood pressure; LCI, blood lipid index; AIP, Plasma arteriosclerosis index; TC, total cholesterol; ALP, alkaline phosphatase; aFBG, fasting blood glucose; AST, aspartate aminotransferase; WHR, waist-to-height ratio; APOAB, apolipoprotein AB; GGT, γ-glutaminase; DB, Direct Bilirubin; DM, diabetes mellitus; Fhchd, Family history of coronary heart disease.

AdaBoost. These findings are similar to the those reported by Wallert et al. (48). This might be because, although the SVM model based on the Gaussian kernel function could handle the nonlinear relationship among variables well, when dealing with research with fewer variables, its prediction performance was affected by insufficient variables. Prediction performance was lower in the SVM model compared with that of LR. Due to the poor interpretability of SVM and the difficulty of parameter optimisation, the model has fewer clinical application. Nevertheless, its high predictive potential was not ruled out.

Finally, concerning the RF and AdaBoost algorithms, the prediction performance of RF in this study was better than that of AdaBoost, although both integrated learning algorithms. Nevertheless, both were lower than those of LR and SVM, which are consistent with the results of Hae et al. (49). This may be because, compared with a single algorithm, integrated learning algorithms such as RF and AdaBoost require a larger sample size to achieve the optimal model performance (50). Therefore, it did not show optimal performance with the medium sample size of this study.

A comprehensive analysis of the variable importance rankings of the three algorithms revealed that age and systolic blood pressure were the most important predictors. This was similar to the findings of previous studies (9, 51). Furthermore, this study found that compared with a single blood lipid index, composite indicators such as LpH and TyG calculated from multiple blood lipid indicators showed better predictive performance. Similarly, in a study by Huang et al. (52), compared with HDL-C and LDL-C alone, LpH had a stronger correlation with the severity of coronary heart disease. The results of the Tehran Lipid and Glucose Metabolism Study showed that for every standard deviation increase of 1 in TyG, the individual CVD risk increased by 20% (53). In addition, similar studies showed that TyG was an important variable of CVD risk prediction. This was similar to the results of this study (54). BMI and BAI were indicators that reflected the degree and type of body obesity. Moreover, related research showed that it had value in predicting CVD incidence (55, 56). The results of this study also showed that BMI and BAI had strong capabilities of CVD prediction. This may be due to the high-salt and high-fat diets of the Uyghur and Kazakh populations, resulting in high body weight and large hip circumference.

Although we believe that the included population represents the general Uyghur and Kazak populations, this study has certain limitations. First, the variable information included was relatively small. ML algorithms are good at dealing with data relationships between high-dimensional data. The reduced sample information in this study may be the main reason for the limited prediction performance of ML algorithms. Second, this study lacked an independent external verification population, and the prediction accuracy and robustness of extrapolating the established model to other ethnic populations needs to be explored further. Moreover, only the baseline measurement data were used for modeling. Time effect and censored data were not considered during model construction. Finally, although this study uses Plating scaling to deal with this imbalanced dataset, the positive predictive value of different models in this population is low, which may lead to unnecessary intervention in the population.

CONCLUSION

In this study, the performance of the CVD prediction model based on the L1-LR algorithm was higher than those of other ML algorithms. In addition to the traditional single risk factors for cardiovascular disease, complex lipid metabolism indicators, such as LpH and TyG, and obesity indicators, such as BMI and BAI, were found to be important factors for predicting the incidence of CVD in this population.

DATA AVAILABILITY STATEMENT

The raw data supporting the conclusions of this article will be made available by the authors, without undue reservation.

ETHICS STATEMENT

The studies involving human participants were reviewed and approved by Ethics Committee of the First Affiliated Hospital of Shihezi University School of Medicine (No. SHZ2010LL01). The patients/participants provided their written informed consent to participate in this study.

AUTHOR CONTRIBUTIONS

XQ and YL designed the study, analyzed the data, and wrote the manuscript. XHZ, HG, and JH collected and sorted the data. XPW, YZY, and JLM sorted and checked the data. SXG and RLM designed the study, guided the article writing, and modified the manuscript. All authors contributed to the article and approved the submitted version.

FUNDING

This research was funded by the Non-profit Central Research Institute Fund of Chinese Academy of Medical Sciences (2020-PT330-003), the Shihezi University Innovation Outstanding Young Talents Program (Natural Science) (No. CXPY202004), and Shihezi University independently funded and supported school-level scientific research projects (No. ZZZC202018A).

ACKNOWLEDGMENTS

We sincerely thank these rural multi-ethnic residents for their willingness to participate in the study. We are grateful to Nalati Township Hospital, Jiangbazi Township Hospital, and 51st Regiment Hospital for providing study facilities and other assistance.

SUPPLEMENTARY MATERIAL

The Supplementary Material for this article can be found online at: https://www.frontiersin.org/articles/10.3389/fcvm.2022.854287/full#supplementary-material

REFERENCES

1. Roth GA, Johnson C, Abajobir A, Abd-Allah F, Abera SF, Abyu G, et al. Global, regional, and National Burden of Cardiovascular Diseases for 10 Causes, 1990 to 2015. *J Am Coll Cardiol*. (2017) 70:1–25. doi: 10.1016/j.jacc.2017.04.052
2. GBD 2013 Mortality and Causes of Death Collaborators. Global, regional, and national age-sex specific all-cause and cause-specific mortality for 240 causes of death, 1990-2013: a systematic analysis for the Global Burden of Disease Study 2013. *Lancet*. (2014) 385:117–71. doi: 10.1016/S0140-6736(14)61682-2
3. Piepoli MF, Hoes AW, Agewall S, Albus C, Brotons C, Catapano AL, et al. 2016 European Guidelines on cardiovascular disease prevention in clinical practice: The Sixth Joint Task Force of the European Society of Cardiology and Other Societies on Cardiovascular Disease Prevention in Clinical Practice (constituted by representatives of 10 societies and by invited experts)Developed with the special contribution of the European Association for Cardiovascular Prevention and Rehabilitation (EACPR). *Eur Heart J*. (2016) 37:2315–2381. doi: 10.1093/eurheartj/ehw106
4. Liu S, Li Y, Zeng X, Wang H, Yin P, Wang L, et al. Burden of cardiovascular diseases in China, 1990-2016: findings from the 2016 Global Burden of Disease Study. *JAMA Cardiol*. (2019) 4:342–52. doi: 10.1001/jamacardio.2019.0295
5. Joint Task Force for Guideline on the Assessment and Management of Cardiovascular Risk in China. Guideline on the assessment and management of cardiovascular risk in China. *Chin Circ J*. (2019) 34:4—28. (in Chinese). doi: 10.3760/cma.j.issn.0253-9624.2019.01.004
6. Goff DC Jr., Lloyd-Jones DM, Bennett G, Coady S, D'Agostino RB, Gibbons R, et al. 2013 ACC/AHA guideline on the assessment of cardiovascular risk: a report of the American College of Cardiology/American Heart Association Task Force on Practice Guidelines. *Circulation*. (2014) 129:S49–73. doi: 10.1161/01.cir.0000437741.48606.98
7. Kannel WB. D. McGee, and T Gordon A general cardiovascular risk profile: the Framingham Study. *Am J Cardiol*. (1976) 38:46–51. doi: 10.1016/0002-9149(76)90061-8
8. Wilson PW, D'Agostino RB, Levy D, Belanger AM, Silbershatz H, Kannel WB. Prediction of coronary heart disease using risk factor categories. *Circulation*. (1998) 97:1837–47. doi: 10.1161/01.CIR.97.18.1837
9. D'Agostino Sr RB. General cardiovascular risk profile for use in primary care: the Framingham Heart Study. *Circulation*. (2008) 117:743–53. doi: 10.1161/CIRCULATIONAHA.107.699579
10. Hippisley-Cox J, Coupland C, Brindle P. Development and validation of QRISK3 risk prediction algorithms to estimate future risk of cardiovascular disease: prospective cohort study. *BMJ*. (2017) 357:j2099. doi: 10.1136/bmj.j2099
11. Muntner P, Colantonio LD, Cushman M, Goff DC Jr. Validation of the atherosclerotic cardiovascular disease Pooled Cohort risk equations. *JAMA*. (2014) 311:1406–15. doi: 10.1001/jama.2014.2630
12. Tang X, Zhang D, He L, Wu N, Si Y, Cao Y, et al. Performance of atherosclerotic cardiovascular risk prediction models in a rural Northern Chinese population: results from the Fangshan Cohort Study. *Am Heart J*. (2019) 211:34–44. doi: 10.1016/j.ahj.2019.01.009
13. Goldstein BA, Navar AM, Carter RE. Moving beyond regression techniques in cardiovascular risk prediction: applying machine learning to address analytic challenges. *Eur Heart J*. (2017) 38:1805–14. doi: 10.1093/eurheartj/ehw302
14. Jamthikar A, Gupta D, Khanna NN, Araki T, Saba L, Nicolaides A. A special report on changing trends in preventive stroke/cardiovascular risk assessment *via* B-mode ultrasonography. *Curr Atheroscler Rep*. (2019) 21:25. doi: 10.1007/s11883-019-0788-4
15. Christodoulou E, Ma J, Collins GS, Steyerberg EW, Verbakel JY, Van Calster B. A systematic review shows no performance benefit of machine learning over logistic regression for clinical prediction models. *J Clin Epidemiol*. (2019) 110:12–22. doi: 10.1016/j.jclinepi.2019.02.004
16. Nusinovici S, Tham YC, Chak Yan MY, Wei Ting DS, Li J, Sabanayagam C, et al. Logistic regression was as good as machine learning for predicting major chronic diseases. *J Clin Epidemiol*. (2020) 122:56–69. doi: 10.1016/j.jclinepi.2020.03.002
17. Xianghui Z, Yizhong Y, Jia H, Jiaolong M, Hongrui P, Rulin M, et al. Mei, and G. Shuxia Evaluation of screening indices for metabolic syndrome in adult Kazakh in Xinjiang. *Chin J Hypertens*. (2017) 25:55–60.
18. Shuxia G, Jingyu Z, Yihua Z, Shangzhi X, Heng G, Qiang N, et al. Epidemiological characteristics and analysis on hypertension of Kazakstans and Hans in Xinjiang. *J Shihezi Univ*. (2008) 26:538–40. (in Chinese).

19. Jia H, Heng G, Yusong D, Jiaming L, Mei Z, Rulin M, et al. Epidemiological study on overweight and obesity among rural adult residents in Hazakh. Uygur and Han populations in Xinjiang. *Chin J Epidemiol*. (2013) 34:1164–8. (in Chinese).
20. Tao J, Ma YT, Xiang Y, Xie X, Yang YN, Li XM, et al. Prevalanceof major cardiovascular risk factors and adverse risk profiles among three ethnic groups in the Xinjiang Uygur Autonomous Region. *China*. (2013) 12:185. doi: 10.1186/1476-511X-12-185
21. Hippisley-Cox J, Coupland C, Robson J, Brindle P. Derivation, validation, and evaluation of a new QRISK model to estimate lifetime risk of cardiovascular disease: cohort study using QResearch database. *BMJ*. (2010) 341:c6624. doi: 10.1136/bmj.c6624
22. Yang L, Wu H, Jin X, Zheng P, Hu S, Xu X, et al. Study of cardiovascular disease prediction model based on random forest in eastern China. *Sci Rep*. (2020) 10:5245. doi: 10.1038/s41598-020-62133-5
23. Huang YY, Tian WB, Jiang CQ, Zhang WS, Zhu F, Jin YL, et al. A simple model for predicting 10-year cardiovascular risk in middle-aged to older Chinese: Guangzhou Biobank Cohort Study. *J Cardiovasc Transl Res*. (2022) 15:416–26. doi: 10.1007/s12265-021-10163-3
24. Jiang Y, Ma R, Guo H, Zhang X, Wang X, Wang K, et al. External validation of three atherosclerotic cardiovascular disease risk equations in rural areas of Xinjiang, China. *BMC Public Health*. (2020) 20:1471. doi: 10.1186/s12889-020-09579-4
25. Writing Group of 2018. 2018 Chinese guidelines for the management of hypertension. *Chin J Cardiovasc Med*. (2019) 24:24–56. (in Chinese).
26. Cigarette smoking among adults–United States, 1992, and changes in the definition of current cigarette smoking. *MMWR Morb Mortal Wkly Rep*. (1994) 43:342–6.
27. Sun K, Ren M, Liu D, Wang C, Yang C, Yan L. Alcohol consumption and risk of metabolic syndrome: a meta-analysis of prospective studies. *Clin Nutr*. (2014) 33:596–602. doi: 10.1016/j.clnu.2013.10.003
28. Xinjun W, Wen Y. 2012 Diabetes diagnosis and treatment guidelines-American Diabetes Association. *Int J Endocrinol Metab*. (2012) 32:211–4. doi: 10.3760/cma.j.issn.1673-4157.2012.03.020
29. The World Health Organization MONICA Project (monitoring trends and determinants in cardiovascular disease): a major international collaboration. WHO MONICA Project Principal Investigators. *J Clin Epidemiol*. (1988) 41:105–14. doi: 10.1016/0895-4356(88)90084-4
30. Li L, Liu ZP. Biomarker discovery for predicting spontaneous preterm birth from gene expression data by regularized logistic regression. *Comput Struct Biotechnol J*. (2020) 18:3434–46. doi: 10.1016/j.csbj.2020.10.028
31. Cortes C, Vapnik V. Support-vector networks. *Mach Learn*. (1995) 20:273–97. doi: 10.1007/BF00994018
32. Breiman, L. Random forests. *Mach Learn*. (2001) 45:5–32. doi: 10.1023/A:1010933404324
33. Hastie T, Rosset S, Zhu J, Zou H. Multi-class adaboost. *Statist Interf*. (2009) 2:349–60. doi: 10.4310/SII.2009.v2.n3.a8
34. Pencina MJ, D'Agostino Sr RB. Evaluating the added predictive ability of a new marker: from area under the ROC curve to reclassification and beyond. *Stat Med*. (2008) 27:157–72. doi: 10.1002/sim.2929
35. Rufibach K. Use of Brier score to assess binary predictions. *J Clin Epidemiol*. (2010) 63:938–9. doi: 10.1016/j.jclinepi.2009.11.009
36. Lemeshow S, Hosmer Jr DW. A review of goodness of fit statistics for use in the development of logistic regression models. *Am J Epidemiol*. (1982) 115:92–106. doi: 10.1093/oxfordjournals.aje.a113284
37. Tsalatsanis A, Hozo I, Vickers A, Djulbegovic B. A regret theory approach to decision curve analysis: a novel method for eliciting decision makers' preferences and decision-making. *BMC Med Inform Decis Mak*. (2010) 10:51. doi: 10.1186/1472-6947-10-51
38. Platt JC. Probabilistic outputs for support vector machines and comparisons to regularized likelihood methods. In: *Advances in Large Margin Classifiers*. MIT Press (2000). p. 61–74. doi: 10.1016/j.enpol.2006.07.010
39. Mortazavi BJ, Downing NS, Bucholz EM, Dharmarajan K, Manhapra A, Li S-X, et al. Analysis of machine learning techniques for heart failure readmissions. *Circ Cardiovasc Qual Outcomes*. (2016) 9:629–640. doi: 10.1161/CIRCOUTCOMES.116.003039
40. Ambale-Venkatesh B, Yang X, Wu CO, Liu K, Hundley WG, McClelland R, et al. Cardiovascular event prediction by machine learning: the multi-ethnic study of atherosclerosis. *Circ Res*. (2017) 121:1092–101. doi: 10.1161/CIRCRESAHA.117.311312
41. Jiang F, Jiang Y, Zhi H, Dong Y, Li H, Ma S, et al. Artificial intelligence in healthcare: past, present and future. *Stroke Vasc Neurol*. (2017) 2:230–43. doi: 10.1136/svn-2017-000101
42. DeFilippis AP, Young R, Carrubba CJ, McEvoy JW, Budoff MJ, Blumenthal RS, et al. An analysis of calibration and discrimination among multiple cardiovascular risk scores in a modern multiethnic cohort. *Ann Intern*. (2015) 162:266–75. doi: 10.7326/M14-1281
43. Wang L, Lee Y, Wu Y, Zhang X, Jin C, Huang Z, et al. A prospective study of waist circumference trajectories and incident cardiovascular disease in China: the Kailuan Cohort Study. *Am J Clin Nutr*. (2021) 113:338–47. doi: 10.1093/ajcn/nqaa331
44. Zhong VW, Van Horn L, Cornelis MC, Wilkins JT, Ning H, Carnethon MR, et al. Associations of dietary cholesterol or egg consumption with incident cardiovascular disease and mortality. *JAMA*. (2019) 321:1081–95. doi: 10.1001/jama.2019.1572
45. Liu W, Hu B, Dehghan M, Mente A, Wang C, Yan R, et al. Fruit, vegetable, and legume intake and the risk of all-cause, cardiovascular, and cancer mortality: a prospective study. *Clin Nutr*. (2021) 40:4316–23. doi: 10.1016/j.clnu.2021.01.016
46. Jiang Y, Zhang X, Ma R, Wang X, Liu J, Keerman M, et al. Cardiovascular disease prediction by machine learning algorithms based on cytokines in Kazakhs of China. *Clin Epidemiol*. (2021) 13:417–28. doi: 10.2147/CLEP.S313343
47. De Silva K, Jonsson D, Demmer RT. A combined strategy of feature selection and machine learning to identify predictors of prediabetes. *J Am Med Inform Assoc*. (2020) 27:396–406. doi: 10.1093/jamia/ocz204
48. Wallert J, Tomasoni M, Madison G, Held C. Predicting two-year survival versus non-survival after first myocardial infarction using machine learning and Swedish national register data. *BMC Med Inform Decis Mak*. (2017) 17:99. doi: 10.1186/s12911-017-0500-y
49. Hae H, Kang SJ, Kim WJ, Choi SY, Lee JG, Bae Y, et al. Machine learning assessment of myocardial ischemia using angiography: development and retrospective validation. *PLoS Med*. (2018) 15:e1002693. doi: 10.1371/journal.pmed.1002693
50. van der Ploeg T, Austin PC, Steyerberg EW. Modern modelling techniques are data hungry: a simulation study for predicting dichotomous endpoints. *BMC Med Res Methodol*. (2014) 14:137. doi: 10.1186/1471-2288-14-137
51. Tokgozoglu L, Torp-Pedersen C. Redefining cardiovascular risk prediction: is the crystal ball clearer now? *Eur Heart J*. (2021) 42:2468–71. doi: 10.1093/eurheartj/ehab310
52. Huang Z-S, Zhong J-L, Luo Y-T, Peng L, Li S-H, Liu J-L. Correlation between LDL-C/HDL-C ratio and the severity of coronary artery lesion in patients with coronary heart disease. *J Sun Yat-sen Univ*. (2018) 39:303–8.
53. Barzegar N, Tohidi M, Hasheminia M, Azizi F, Hadaegh F. The impact of triglyceride-glucose index on incident cardiovascular events during 16 years of follow-up: Tehran Lipid and Glucose Study. *Cardiovasc Diabetol*. (2020) 19:155. doi: 10.1186/s12933-020-01121-5
54. Sanchez-Inigo L, Navarro-Gonzalez D, Fernandez-Montero A, Pastrana-Delgado J, Martinez JA. The TyG index may predict the development of cardiovascular events. *Eur J Clin Invest*. (2016) 46:189–97. doi: 10.1111/eci.12583
55. Lam BC, Koh GC, Chen C, Wong MT, Fallows SJ. Comparison of Body Mass Index (BMI), Body Adiposity Index (BAI), Waist Circumference (WC), Waist-To-Hip Ratio (WHR) and Waist-To-Height Ratio (WHtR) as predictors of cardiovascular disease risk factors in an adult population in Singapore. *PLoS ONE*. (2015) 10:e0122985. doi: 10.1371/journal.pone.0122985
56. Moliner-Urdiales D, Artero EG, Lee DC, Espana-Romero V, Sui X, Blair SN. Body adiposity index and all-cause and cardiovascular

disease mortality in men. *Obesity*. (2013) 21:1870–6. doi: 10.1002/oby.20399

Conflict of Interest: The authors declare that the research was conducted in the absence of any commercial or financial relationships that could be construed as a potential conflict of interest.

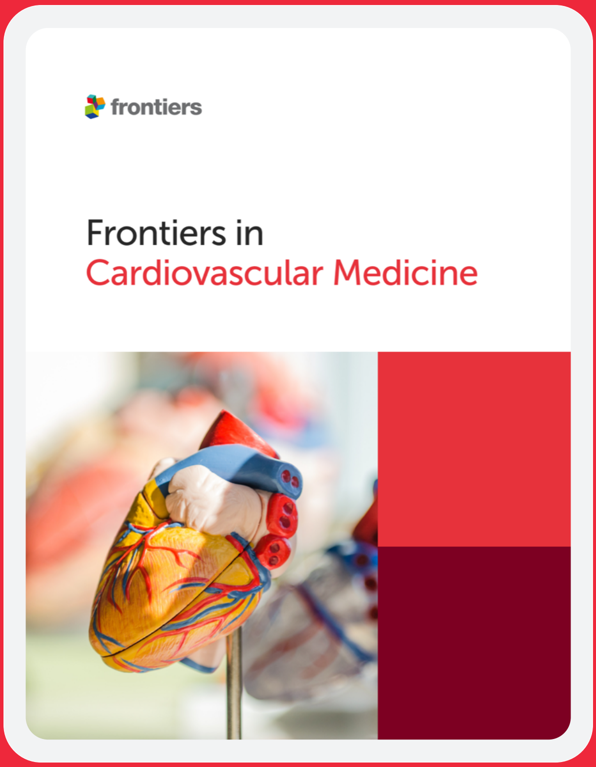

frontiers

Frontiers in
Cardiovascular Medicine

Frontiers

Avenue du Tribunal-Fédéral 34
1005 Lausanne, Swizerland
frontiersin.org

Contact us

+41 (0)21 510 17 00
frontiersin.org/about/contact